Progress in Theoretical Chemistry and Physics A 24
Series Editors: J. Maruani · S. Wilson

Anders Lund
Masaru Shiotani *Editors*

EPR of Free Radicals in Solids I

Trends in Methods and Applications

2nd Edition

Springer

EPR of Free Radicals in Solids I

Progress in Theoretical Chemistry and Physics

VOLUME 24

For further volumes:
http://www.springer.com/series/6464

EPR of Free Radicals in Solids I

Trends in Methods and Applications

Second Edition

Edited by

ANDERS LUND
University of Linköping, Sweden

MASARU SHIOTANI
University of Hiroshima, Japan

Springer

Editors
Anders Lund
Department of Physics, Chemistry and Biology
Linköping University
Linköping
Sweden

Masaru Shiotani
Graduate School of Engineering
Hiroshima University
Higashi-Hiroshima
Japan

ISSN 1567-7354
ISBN 978-94-007-4892-7 ISBN 978-94-007-4893-4 (eBook)
DOI 10.1007/978-94-007-4893-4
Springer Dordrecht Heidelberg New York London

Library of Congress Control Number: 2012951322

PTCP Aim and Scope

Progress in Theoretical Chemistry and Physics

A series reporting advances in theoretical molecular and material sciences, including theoretical, mathematical and computational chemistry, physical chemistry and chemical physics and biophysics.

Aim and Scope

Science progresses by a symbiotic interaction between theory and experiment: theory is used to interpret experimental results and may suggest new experiments; experiment helps to test theoretical predictions and may lead to improved theories. Theoretical Chemistry (including Physical Chemistry and Chemical Physics) provides the conceptual and technical background and apparatus for the rationalisation of phenomena in the chemical sciences. It is, therefore, a wide ranging subject, reflecting the diversity of molecular and related species and processes arising in chemical systems. The book series *Progress in Theoretical Chemistry and Physics* aims to report advances in methods and applications in this extended domain. It will comprise monographs as well as collections of papers on particular themes, which may arise from proceedings of symposia or invited papers on specific topics as well as from initiatives from authors or translations.

The basic theories of physics – classical mechanics and electromagnetism, relativity theory, quantum mechanics, statistical mechanics, quantum electrodynamics – support the theoretical apparatus which is used in molecular sciences. Quantum mechanics plays a particular role in theoretical chemistry, providing the basis for the valence theories, which allow to interpret the structure of molecules, and for the spectroscopic models employed in the determination of structural information from spectral patterns. Indeed, Quantum Chemistry often appears synonymous with Theoretical Chemistry: it will, therefore, constitute a major part of this book series. However, the scope of the series will also include other areas of theoretical

chemistry, such as mathematical chemistry (which involves the use of algebra and topology in the analysis of molecular structures and reactions); molecular mechanics, molecular dynamics and chemical thermodynamics, which play an important role in rationalizing the geometric and electronic structures of molecular assemblies and polymers, clusters and crystals; surface, interface, solvent and solidstale effects; excited-state dynamics, reactive collisions, and chemical reactions.

Recent decades have seen the emergence of a novel approach to scientific research, based on the exploitation of fast electronic digital computers. Computation provides amethod of investigationwhich transcends the traditional division between theory and experiment. Computer-assisted simulation and design may afford a solution to complex problems which would otherwise be intractable to theoretical analysis, and may also provide a viable alternative to difficult or costly laboratory experiments. Though stemming from Theoretical Chemistry, Computational Chemistry is a field of research in its own right, which can help to test theoretical predictions and may also suggest improved theories.

The field of theoretical molecular sciences ranges from fundamental physical questions relevant to the molecular concept, through the statics and dynamics of isolated molecules, aggregates and materials, molecular properties and interactions, and to the role of molecules in the biological sciences. Therefore, it involves the physical basis for geometric and electronic structure, states of aggregation, physical and chemical transformations, thermodynamic and kinetic properties, as well as unusual properties such as extreme flexibility or strong relativistic or quantum-field effects, extreme conditions such as intense radiation fields or interaction with the continuum, and the specificity of biochemical reactions.

Theoretical Chemistry has an applied branch – a part of molecular engineering, which involves the investigation of structure-property relationships aiming at the design, synthesis and application of molecules and materials endowed with specific functions, now in demand in such areas as molecular electronics, drug design and genetic engineering. Relevant properties include conductivity (normal, semi- and supra-), magnetism (ferro- and ferri-), optoelectronic effects (involving nonlinear response), photochromism and photoreactivity, radiation and thermal resistance, molecular recognition and information processing, biological and pharmaceutical activities, as well as properties favouring self-assembling mechanisms and combination properties needed in multifunctional systems.

Progress in Theoretical Chemistry and Physics is made at different rates in these various research fields. The aim of this book series is to provide timely and in-depth coverage of selected topics and broad-ranging yet detailed analysis of contemporary theories and their applications. The series will be of primary interest to those whose research is directly concerned with the development and application of theoretical approaches in the chemical sciences. It will provide up-to-date reports on theoretical methods for the chemist, thermodynamician or spectroscopist, the atomic, molecular or cluster physicist, and the biochemist or molecular biologist who wish to employ techniques developed in theoretical, mathematical and computational chemistry in their research programmes. It is also intended to provide the graduate student with a readily accessible documentation on various branches of theoretical chemistry, physical chemistry and chemical physics.

Preface

During the last 10 years, significant progress has been made in the study of free radical processes in solids by applying modern EPR (ESR) methods. The progress has been possible by instrumental advancements in continuous wave (CW) and pulse EPR, by development of sensitive detection methods, by the application of sophisticated matrix isolation techniques and by the advancement in quantitative EPR, to mention a few recent experimental trends. On the theoretical side, methods based on first principles have been developed and applied for the calculation of hyperfine couplings, zero-field splittings and g-factors as well as in spectral simulations. Software for these purposes, developed during the last decade, is also available. Not all of those developments can be treated in detail in a single volume. We have therefore asked several main contributors to the development of the field to present chapters in selected areas, where recent reviews seem to be missing. In this respect, the book is an update of a previous edition of this work, with a similar organization of the content.

The first volume is concerned with trends in experimental and theoretical methods. In the first chapter, CW EPR and ENDOR methods for studies of radical structure in single crystals and powders are reviewed. Most of the following seven chapters give accounts of novel developments that so far are only available in the journal literature. The chapter by Brustolon and Barbon describes the different pulsed techniques as applied to radicals and spin probes in solid matrices. Methods to extract dynamical parameters from CW and pulsed EPR are summarised in the chapter by Benetis and Dmitriev, which also contains an account of relaxation phenomena. New simulation schemes, including the influence of dynamics, are also presented. Single crystal measurement is the most straightforward but not always applicable method for complex systems, where often only powder spectra can be obtained. For these systems, analyses by simulation techniques based on exact diagonalisation are beginning to replace the previously used perturbation methods, as described in the chapter by Hanson and coworkers. An extended version of the software presented in the previous edition is outlined, including now also procedures for the analysis of pulse EPR and several other new features. The software is available commercially. Studies of quantum effects in isotopically labelled methyl

radicals trapped in inert matrices at low temperature are a major part of the chapter by Shiotani and Komaguchi. A detailed theoretical analysis was possible due to the extremely high resolution of the EPR spectra at low temperature. The chapter by Boyd and coworkers illustrates the usefulness of advanced quantum chemistry methods for the theoretical interpretation of hyperfine coupling tensors. Ab initio and density functional methods are applicable even for the biological systems. The calculated parameters have been frequently employed for the assignment of experimental spectra in recent work. The methods for the calculation of *g*-tensors have been developed even more during the last 10 years as described in the chapter by Kaupp. The accurate *g*-tensor data obtained by high-field EPR measurements can for instance now be analyzed taking into account environmental interactions with the radical. A new chapter on the calculation of the zero-field splitting tensors was introduced in this edition. The subject is of relevance for high-spin clusters and molecules treated in two chapters in the second volume. The theory is also applicable in EPR studies of systems containing pairs of radicals.

The second volume presents applications involving studies of radiation and photo-induced inorganic and organic radicals in inert matrices. High-spin molecules and complexes are also considered as well as radical processes in photosynthesis. Recent advancements in environmental applications including EPR dosimetry are summarised. There are trends both towards simplification by using matrix isolation in frozen noble gas matrices with accompanying increase of resolution as illustrated in the chapter by Kunttu and Eloranta and in the work by Shiotani and Komaguchi in the first volume, and towards studies of complex systems treated in the chapters by Takui et al., by Baumgarten, Kawamori and by Feldman. In the former case an overview of the matrix isolation technique for the studies of atoms and small radicals embedded in solid rare gases is presented, while Feldman presents recent development in the EPR studies of reactive intermediates from irradiation of moderately large organic molecules using matrix isolation. Two chapters address the issue of high-spin systems, the one by Baumgarten in organic systems, the other by Takui et al. also in metal-based molecular clusters. Both subjects have relevance for the development of molecular magnets. The potential application of EPR for quantum computing is also considered in a newly written chapter, with emphasis on pulse ENDOR methods. The chapter by Kawamori describes studies of plant photosystem II by pulsed EPR, dual mode CW EPR and pulsed electron–electron double resonance, the latter to obtain distances between radical pairs trapped after illumination. Accurate measurement of the concentration of radicals is an important issue in EPR dosimetry and other kinds of quantitative EPR, which is addressed in the chapter by Yordanov et al. This subject relates to other applications of EPR in the environmental sciences, discussed in a chapter by Rhodes. In this context, myon spin resonance provides new means to considerably lower the detection limit in heterogeneous systems. In the final chapter, recent developments of optical detection to lower the detection limit and to obtain time-resolution in the characterisation of defect centres in semiconductor materials are presented by Chen.

The titles of the chapters have been retained from the old edition, with one exception. The content of each chapter in the new edition differs in general from that

in the old by the addition of new results and deletion of older material, however. The size has nevertheless increased, in part also due to the inclusion of two new chapters. Some technical problems with the printing of figures, figure legends and the index of the previous work have been corrected. The chapters of the first edition were frequently referred to as additional reading in a work we recently prepared for a broader audience [Anders Lund, Masaru Shiotani, Shigetaka Shimada: 'Principles and Applications of ESR Spectroscopy', Springer (2011)]. We hope that the new edition will be of value for this purpose as well as for future research involving free radicals.

Anders Lund
Masaru Shiotani

Contents

Contributors

Fuqiang Ban Department of Chemistry, Dalhousie University, Halifax, NS, Canada

Antonio Barbon Department of Chemical Sciences, University of Padova, Padova, Italy

Nikolas-Ploutarch Benetis Department of Pollution Control, Technological Education Institution, TEI, West Macedonia, Kozani, Greece

Simon Benson Centre for Advanced Imaging, The University of Queensland, Brisbane, QLD, Australia

Russell J. Boyd Department of Chemistry, Dalhousie University, Halifax, NS, Canada

Marina Brustolon Department of Chemical Sciences, University of Padova, Padova, Italy

Yurij Dmitriev A. F. Ioffe Physico-Technical Institute, St Petersburg, Russia

James W. Gauld Department of Chemistry and Biochemistry, University of Windsor, Windsor, ON, Canada

Graeme R. Hanson Centre for Advanced Imaging, The University of Queensland, Brisbane, QLD, Australia

Martin Kaupp Institut für Chemie, Theoretische Chemie, Technische Universität Berlin, Berlin, Germany

Masahiro Kitagawa Department of System Innovation, Graduate School of Engineering Science, Osaka University, Toyonaka, Osaka, Japan

Kenji Komaguchi Department of Applied Chemistry, Graduate School of Engineering, Hiroshima University, Higashi-Hiroshima, Japan

Wei Liu Department of Materials Science and Chemical Engineering, School of Chemical Engineering, Dalian University of Technology, Dalian, China

Anders Lund Department of Physics, Chemistry and Biology, The Emeritus Academy, Husett, Linköping University, Linköping, Sweden

Christopher J. Noble Centre for Advanced Imaging, The University of Queensland, Brisbane, QLD, Australia

Kazunobu Sato Department of Chemistry and Molecular Materials Science, Graduate School of Science, Osaka City University, Osaka, Japan

Daisuke Shiomi Department of Chemistry and Molecular Materials Science, Graduate School of Science, Osaka City University, Osaka, Japan

Masaru Shiotani Department of Applied Chemistry, Graduate School of Engineering, Hiroshima University, Higashi-Hiroshima, Japan

Kenji Sugisaki Department of Chemistry and Molecular Materials Science, Graduate School of Science, Osaka City University, Osaka, Japan

Takeji Takui Department of Chemistry and Molecular Materials Science, Graduate School of Science, Osaka City University, Osaka, Japan

Kazuo Toyota Department of Chemistry and Molecular Materials Science, Graduate School of Science, Osaka City University, Osaka, Japan

Stacey D. Wetmore Department of Chemistry and Biochemistry, University of Lethbridge, Alberta, Canada

Chapter 1
Continuous Wave EPR of Radicals in Solids

Anders Lund and Wei Liu

Abstract Continuous wave (CW) EPR and ENDOR methods for studies of the structure, dynamics and reactions of radicals in crystalline and powdered samples are reviewed. Improvements of the standard Schonland procedure to obtain the hyperfine (*hfc*)- and nuclear quadrupole (*nqc*)-coupling tensors from single crystal measurements are described, including the resolution by ENDOR measurements of the so-called Schonland ambiguity. An account of the influence of the *g*-anisotropy on the intensity is included in a brief review of EPR studies of powders. The microwave saturation properties are discussed in the context of quantitative EPR using software for the analysis of CW power saturation curves and for simulations of saturated EPR spectra taking into account the different microwave power dependence of the allowed and forbidden ($\Delta m_{\mathrm{I}} = 1$) hyperfine lines. The analysis of powder ENDOR spectra by simulations is described in considerable detail, with special emphasis on the combined influence of *hfc* and *nqc* of comparable magnitudes. Studies of the dynamics of free radicals, particularly on surfaces are summarized, including recent results concerning the adsorption/desorption and diffusion of nitrogen oxides. Software for the simulation of EPR and ENDOR powder spectra, for the analysis of internal and slow motion, and for the analysis of single crystal data, are described including addresses for downloading, when available.

A. Lund (✉)
Department of Physics, Chemistry and Biology, The Emeritus Academy, Husett,
Linköping University, S-581 83 Linköping, Sweden
e-mail: alund@ifm.liu.se

W. Liu
Department of Materials Science and Chemical Engineering, School of Chemical Engineering,
Dalian University of Technology, Dalian 116024, China
e-mail: liuwei08@dlut.edu.cn

A. Lund and M. Shiotani (eds.), *EPR of Free Radicals in Solids I*, Progress in Theoretical Chemistry and Physics 24, DOI 10.1007/978-94-007-4893-4_1,

1.1 Introduction

Continuous wave electron paramagnetic resonance, CW-EPR, has been in use since 1945 to study paramagnetic species. Other abbreviations are ESR and EMR, the latter standing for electron magnetic resonance. Studies by EPR of free radicals in solids have been made for about 50 years. Several treatises have appeared both on the general technique [1–10] and on applications [11–18]. In previous general treatises most emphasis was on electronic structure, and how this structure was deduced from measurements of *g*-, hyperfine (*hfc*) and for nuclei with $I \geq 1$ also nuclear quadrupole coupling (*nqc*) tensors. Numerous EPR studies of radicals formed in radiation chemistry processes were reported especially in early works [11–13]. The treatise [13] dealing with studies of primary radiation effects and damage mechanisms in molecules of biological interest is also valuable as a source of information of ENDOR spectroscopy of primary paramagnetic components formed after irradiation in liquid helium. Other specialised treatises of free radicals in solids involve studies of inorganic systems [11], disordered systems [14], radical ionic systems [15] and radicals on surfaces [16]. The book by Rånby and Rabek [17] about EPR spectroscopy in polymer research contains more than 2,500 references. The development of advanced methods in this field has been treated in a recent work [18]. Recent literature reviews are also contained in the series of books issued annually by the Royal Society of Chemistry [19]. The tabulated data in the Landolt Börnstein data base [20] provide useful structural information.

The progress in CW-EPR methodology during the last decade has mainly been in high field EPR. The primary advantage in studies of free radicals is the possibility to resolve the *g*-value anisotropy of a radical or to separate spectra of radicals with different *g*-factors [21]. The technique has been discussed in recent review articles [22–25], in book chapters [26], and monographs [27]. Solid state EPR studies of free radicals at high field are therefore only briefly reviewed here.

The measurement of parameters used to determine the electronic structure has been considered in great detail in the past. In this chapter the used methods are discussed and procedures for the analysis of the experimental data are given. The analysis of single crystal data by variants of the Schonland procedure [28] is accordingly first reviewed, hopefully in sufficient detail to enable the non-specialist to understand the principles of extracting *g*-, *hfc*- and *nqc*-coupling tensors from single crystal EPR and ENDOR data. This procedure cannot be straight-forwardly applied when either the nuclear quadrupole interaction is of comparable magnitude to the hyperfine energy, or when the hyperfine interaction is exceptionally large. The first case is of concern in studies of radicals with appreciable *nqc* due e.g. to ^{23}Na, ^{27}Al, ^{35}Cl, ^{37}Cl, and occasionally ^{14}N, and other nuclei with nuclear spin $I \geq 1$. The second case is less likely to cause problems with modern high field spectroscopy, but is still of relevance in EPR studies at X-band and in the analysis of high-precision ENDOR data. Methods to treat those cases have been developed several years ago [29], but have apparently not been generally applied in subsequent EPR studies of free radicals.

The analysis of EPR and ENDOR spectra of radicals rigidly trapped in glassy, polycrystalline or amorphous "powder" samples is frequently assisted by computer simulations, often employing exact theory in recent studies. Tools for the simulation of EPR and ENDOR spectra that have been implemented in several recent programs are described in Sect. 1.3.4 and in more detail in Chap. 5. Calculations of the *hfc*- and *g*-tensors as described in Chaps. 6 and 7 are often employed in combination with simulations in order to interpret EPR and ENDOR powder spectra.

The measurement and analysis of dynamic parameters like relaxation times, rates of internal motion within radicals and external motion of radicals, are treated in varying detail in the textbook literature [1–18]. The measurement of relaxation times by continuous wave EPR is only briefly mentioned in modern treatments, because of the development of pulsed EPR. In quantitative EPR control of power saturation is of interest to ensure that spin concentration is correctly measured, however. The degree of saturation is governed by the relaxation times, and since quantitative measurements are made with CW-EPR, relaxation data obtained with the same technique are relevant. The methods of analysis of saturation curves developed several years ago have therefore been reviewed and an up-dated technique involving computer-based fitting to all the data, rather than the use of a few special data points used earlier is described.

The analysis of dynamics in liquids involving chemical exchange *i.e.* processes involving jumps of a nucleus from one environment to another, different environment has been treated in previous texts [1–4]. In favourable cases the dynamics of chemical exchange in solids involves only nuclei with approximate isotropic hyperfine couplings, *e.g.* from hindered rotation of methyl groups in β-position to the radical centre and from ring puckering observed in many cyclic radical systems. In this chapter studies of the dynamics of free radicals on surfaces are emphasized, while recent investigations of radicals and radical cations in low temperature solid matrices are reviewed in Chap. 4. The simulation methods developed for exchange in liquids can then be applied [30]. The method fails, however, when nuclei with anisotropic *hfc* undergo exchange. Methods of analysis for this case are described in Chap. 3.

The analysis of dynamics in condensed phase, studied by introducing spin probes or labels in the material is a vast subject that has been treated in detail elsewhere, particularly in the polymer [18] and biological fields [31] and is accordingly largely omitted here. In this chapter only the results with NO_x probe molecules adsorbed on surfaces are briefly summarised, including recent results concerning adsorption/desorption processes in zeolites.

1.2 Radical Structure

Radicals trapped in solid materials usually possess anisotropic *g*- and hyperfine coupling tensors. The effect of the nuclear Zeeman term must be taken into account even in EPR for nuclei with large magnetic moments like ^{1}H and ^{19}F. For nuclear

spin I $\geq$ 1 nuclear quadrupole couplings might have to be considered in ENDOR, for strong interactions also in EPR, resulting in the spin-Hamiltonian (1.1).

$$\mathrm{H} = \mu_B \mathbf{BgS} + \mathbf{IAS} - g_N \mu_\mathbf{N} \mathbf{BI} + \mathbf{IQI} \tag{1.1}$$

The analysis of hyperfine couplings by EPR and ENDOR is simplified when the high field approximation $hfc \ll h\nu$ (ν = microwave frequency) applies. The combined effects due to *hfc*, *nqc* and nuclear Zeeman interactions can be accounted for by 1st order perturbation theory based on the operator (1.2).

$$H' = \mathbf{IAu}S_u + \mathbf{IQI} - g_N \mu_N \mathbf{BI} \tag{1.2}$$

Here S_u is the electron spin component along the effective Zeeman field direction $\mathbf{u} = \mathbf{gB}/gB$. The second term applies for nuclei with I $\geq$ 1. The analysis of *hfc* and *nqc* in single crystal spectra is very often made to first order, commonly by the Schonland method discussed below.

1.2.1 Analysis of Single Crystal Spectra

The most informative method to determine the tensor data is by single crystal measurements. The Schonland method [28] originally developed for the determination of the principal *g*-values in electron spin resonance is applicable also for the determination of *hfc* tensors from ESR and ENDOR data and in principle even for *nqc* tensors of nuclei with I $\geq$ 1. Non-linear least squares procedures are more directly applicable to this case, however.

The directions of the **g**, **A** and **Q** principal axes do as a rule not coincide with each other or with the crystallographic axes. In experimental single crystal studies the orientation of each axis is commonly specified by the three direction cosines with respect to the crystallographic axes. The nine direction cosines for the three axes cannot be varied independently, however. The three Euler angles [32] specifying the orientation of the three principal axes are therefore often preferred for theoretical purposes. Several different conventions have been adopted for the definition of these angles, however.

1.2.2 The Schonland Method

The *g*-Tensor. The *g*-factor with the magnetic field B along the unit vector $\boldsymbol{l}$ is given by:

$$g^2 = \boldsymbol{l}\mathbf{g}^2\boldsymbol{l} \tag{1.3}$$

In the Schonland procedure the g-factors are measured by EPR as functions of the angle of rotation of the crystal with respect to the magnetic field in three different planes. It is usual, but not necessary, to make the measurements in mutually orthogonal planes xy, yz and zx. For the rotation in the xy-plane with $\boldsymbol{l} = (\cos\theta, \sin\theta, 0)$ one obtains (1.4), where $\mathbf{T}^{g} = \mathbf{g}^2$ has been introduced to conform with the notation in [28].

$$g^2 = \frac{T^g_{xx} + T^g_{yy}}{2} + \frac{T^g_{xx} - T^g_{yy}}{2}\cos(2\theta) + T^g_{xy}\sin(2\theta) \tag{1.4}$$

The expressions for the orientation dependence of g^2 in the yz and zx planes are obtained by cyclic permutations of the subscripts in (1.4). In Schonland's original treatment a fitting of the equations to the data was performed individually for each plane. The principal values and directions were obtained by diagonalization of the $\mathbf{g^2}$ tensor. The principal directions for $\mathbf{g^2}$ and $\mathbf{g}$ coincide, while the principal g-values were calculated as the square roots of the principal values of $\mathbf{g^2}$. In theory the g-tensor may be asymmetric. The $\mathbf{g}^2$ tensor in (1.3) is then replaced by the symmetric tensor $\mathbf{g}^{T}\mathbf{g}$, where $\mathbf{g}^{T}$ is the transposed tensor. The energy of the EPR transition is not affected by a possible asymmetry of the g-tensor. In the following it is assumed, unless otherwise stated, that the g-tensor as well as the *hfc*- and *nqc*-tensors can be represented by symmetric 3×3 matrices.

The *hfc*-Tensor. In the case of a dominant electron Zeeman energy the energy due to the hyperfine and nuclear Zeeman terms, $E_{\pm}(m_{\mathrm{I}})$ is to first order given by (1.5) for $m_S = \pm ½$, respectively.

$$E_{\pm}(m_I) = G_{\pm} m_I \tag{1.5}$$

The quantity $G_{\pm}$ [33] contains contributions from the hyperfine coupling tensor $\mathbf{A}$ and from the nuclear Zeeman term $\nu_{\mathrm{N}} = g_{\mathrm{N}}\mu_{\mathrm{N}}\mathrm{B}/\mathrm{h}$, both given in frequency units in (1.6). $\mathbf{E}$ is the unit tensor.

$$G^2_{\pm} = \boldsymbol{l}\left(\pm\frac{\mathbf{gA}}{2} - \nu_N\mathbf{E}\right)\left(\pm\frac{\mathbf{Ag}}{\mathbf{2}} - \nu_N\mathbf{E}\right)\boldsymbol{l} \tag{1.6}$$

Different modifications of the Schonland procedure have been adopted depending on the relative magnitudes of the hyperfine and nuclear Zeeman terms, the degree of g-anisotropy and also if EPR or ENDOR is employed.

EPR. When the nuclear Zeeman energy is negligible compared to the hyperfine term, $\nu_{\mathrm{N}} \ll \mathrm{K}$, the energy for the allowed $\Delta m_{\mathrm{S}} = 1$, $\Delta m_{\mathrm{I}} = 0$ transition is obtained from (1.7) and (1.8) [34].

$$\Delta E = g\mu_B B + K \cdot m_I \tag{1.7}$$

$$K^2 g^2 = \boldsymbol{l}\mathbf{g}\mathbf{A}^2\mathbf{g}\boldsymbol{l} \tag{1.8}$$

The measurement of the hyperfine coupling, K, as a function of the angle of rotation of the crystal, makes it possible to obtain the tensor $\mathbf{T}^h = \mathbf{gA^2g}$ by the Schonland procedure. The $\mathbf{A}^2$ tensor, obtained by multiplying this tensor from the left and right with $\mathbf{g}^{-1}$ is then diagonalized yielding $|A_p| = \sqrt{(\mathrm{A}^2)_p}$ for the principal values A_p. The signs are not obtained. The principal directions of $\mathbf{A}$ and $\mathbf{A}^2$ coincide. This procedure (neglect of ν_N) was often adopted to obtain *hfc* tensors from EPR measurements on transition metal ions in early work [35]. The method is usually not applicable for the analysis of single crystal EPR spectra of organic free radicals featuring anisotropic proton hyperfine structure due to the unusually large ^{1}H nuclear g-factor.

The opposite case with $\nu_\mathrm{N} \gg K$ is rare at X-band and lower frequencies, but is of interest for measurements at the higher frequency bands which have recently become commercially available. The expression (1.9) applies when g is isotropic [36].

$$K = \boldsymbol{l}\mathbf{A}\boldsymbol{l} \tag{1.9}$$

The relative signs of the principal values of the A-tensor can in principle be obtained by EPR measurements under this condition.

When none of the two extreme cases is applicable the procedure to obtain the *hfc* tensor by EPR is rather difficult. A common complication occurs for example in X-band measurements of the hyperfine structure due to an α–H hydrogen atom in organic radicals of the type $>\dot{\mathrm{C}}_\alpha$-H, According to a classical model [33] the magnetic fields $\mathbf{B}_+$ and $\mathbf{B}_-$ acting on the proton are obtained by vector addition of $\mathbf{B}_\mathrm{N}$ due to the externally applied magnetic field and that due to the magnetic moment of the electron with opposite directions, $\pm\mathbf{B}_\mathrm{A}$, depending on the value of m_S, Fig. 1.1. The phenomenon is commonly referred to as the "direct field effect".

The four-line EPR line pattern occurring in this case is conventionally, but somewhat misleadingly attributed to the occurrence of allowed $\Delta m_\mathrm{I} = 0$ and forbidden $\Delta m_\mathrm{I} = 1$ transitions. The intensities of the lines depend on the angle α between the effective fields and accordingly on the strength of the applied magnetic field, see *e.g.* [36] for a quantum mechanical treatment.

$$I_i = \cos^2\frac{\alpha}{2}, \quad I_o = \sin^2\frac{\alpha}{2} \tag{1.10}$$

The Eq. (1.11) derived by Poole and Farach [37] can be applied when both the inner and outer doublets are observed. The *hfc* tensor can then directly be obtained in single crystal measurements by the Schonland method from the relation:

$$l\mathbf{A^2}l = T_0^2 + T_i^2 - (2B_N)^2 \tag{1.11}$$

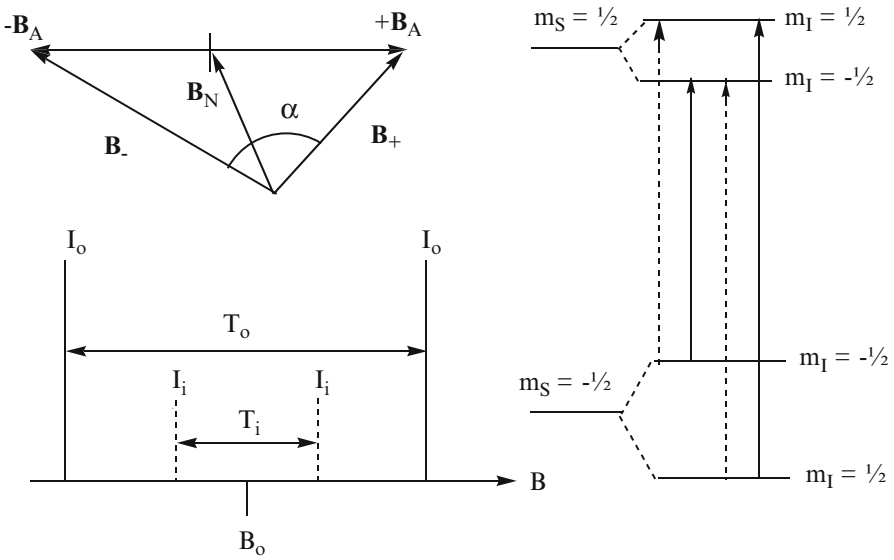

Fig. 1.1 Effective fields $\mathbf{B}_+$ ($m_S = +½$) and $\mathbf{B}_-$ ($m_S = -½$) acting on a nucleus (I = ½) with an anisotropic *hfc* and a nuclear Zeeman term of comparable magnitudes. $\mathbf{B}_A$ is due to the hyperfine coupling, $\mathbf{B}_N$ to the applied magnetic field. The magnitude of $\mathbf{B}_N$ corresponds to the nuclear Zeeman energy. The inner (i) and outer (o) hyperfine lines are indicated (Adapted from Ref. [69] with kind permission of © Springer 2011)

This method has been applied in some cases [38]. In principle, the so called Schonland ambiguity in determining the principal values might then be resolved, by adapting the procedure developed in ENDOR, see Sects. 1.2.2.1 and 1.2.2.2. Poor resolution of the allowed and forbidden lines often makes the interpretation difficult, however. The early work by McConnell and co-workers to obtain the first EPR single crystal data of the malonic acid radical $(HOOC)_2\dot{C}_\alpha$–H including an interpretation of the forbidden transitions must therefore be considered as an extra-ordinary achievement [39]. The ^{1}H *hfc* tensor of this radical has turned out to be typical for a whole class of π-electron radicals and the data have served as a reference in numerous later studies of similar species, both experimentally and theoretically.

Q-band measurements may in some cases be employed to reduce the intensity of the forbidden transitions [40], while a method to determine the *hfc* tensor by an analysis of X-band single crystal data using a non-linear fit [41] employing the general equation (1.6) might not be appropriate when the allowed and forbidden lines overlap. The ENDOR technique has therefore more often been employed in modern applications for reasons of higher resolution and simpler analysis of the data.

ENDOR. In this case it is not necessary to make any assumption regarding the relative magnitudes of the nuclear Zeeman and hyperfine energies. For an I = ½ nucleus two lines with frequencies $\nu_{\pm}$ appear corresponding to the two values of $m_S = \pm ½$. In case of an isotropic g-factor Eq. (1.6) simplifies to (1.12) and (1.13).

$$\nu_{\pm}^2 = \boldsymbol{l}\mathbf{T}_{\pm}^2\boldsymbol{l} \tag{1.12}$$

$$\mathbf{T}_{\pm} = \pm ½\mathbf{A} - \nu_N E \tag{1.13}$$

If ν_N is constant during the measurements, *i.e*. the static magnetic field strength is constant, the tensor $T_{\pm}^2$ can be obtained by a Schonland type fit. After diagonalization, the absolute values of the principal values are obtained as in (1.14).

$$|t_{\pm}|_p = \left|\pm ½A_p - \nu_N\right| \tag{1.14}$$

The uncertainty in evaluating the principal values A_p from (1.14) is reduced if the two ENDOR transitions corresponding to $m_S = \pm ½$ can both be observed. In this case one has:

$$(t_-)_p^2 - (t_+)_p^2 = 2\nu_N \cdot A_p \tag{1.15}$$

The low frequency line has been difficult to observe in earlier applications, in part attributed to a low intensity due to the hyperfine enhancement effect discussed in Sect. 1.3.2. The signs of the couplings were, however, known from theoretical considerations in several systems of interest, for instance of α–H ($A_p < 0$) and β–H ($A_p > 0$) couplings in carbon-centered π-electron radicals. Observation of both ENDOR transitions might become of practical relevance in the future for the resolution of the so called Schonland ambiguity in the determination of the *hfc* tensor. The subject is discussed in Sect. 1.2.2.2.

ENDOR from Nuclei with I ≥ 1. More complicated equations result in the presence of *nqc* for nuclei with I ≥ 1. When the contributions from the hyperfine and nuclear Zeeman interactions dominate over that caused by the *nqc* the ENDOR transitions (±½, $m_I \rightarrow m_I - 1$) occur at frequencies given by (1.16) and (1.17) [42, 43].

$$\nu_{\pm} = G_{\pm} + 3P_{\pm}\,(m_I - ½) \tag{1.16}$$

$$G_{\pm}^2 P_{\pm} = \boldsymbol{l}\mathbf{T}_{\pm}\mathbf{Q}\mathbf{T}_{\pm}\boldsymbol{l} \tag{1.17}$$

It is assumed that g is isotropic so that $\mathbf{T}_{\pm}$ is given by (1.13).

A simple method [43] involving separate measurements of G_+ and P_+ (or G_- and P_-) is illustrated for the case of $I = 1$ corresponding to the energy diagram in Fig. 1.2. The magnitudes of G_+ and P_+ are obtained from ν_1 and ν_2 as a function of orientation in three crystal planes. The quantities can therefore be determined separately.

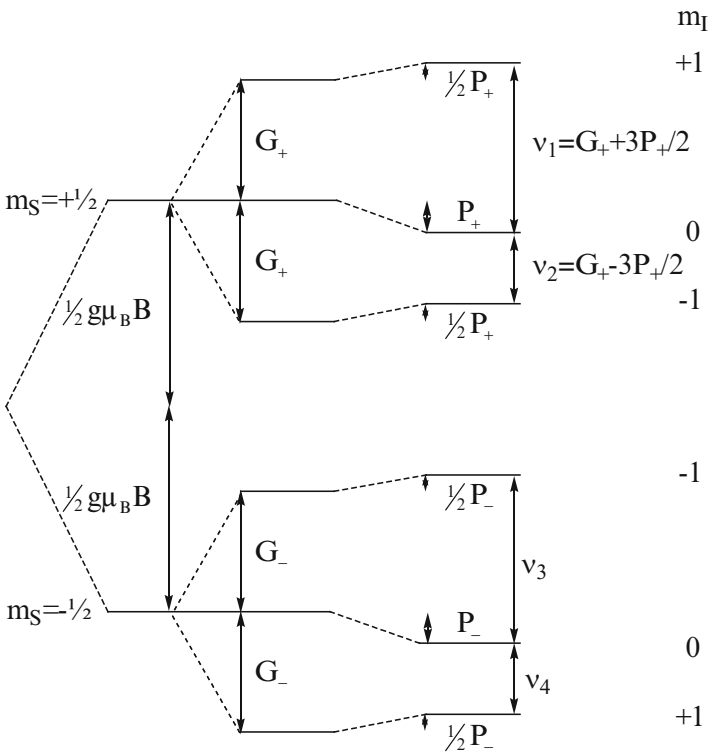

Fig. 1.2 Energy level diagram for a radical with nuclear spin $I = 1$

The ENDOR tensor $\mathbf{T}_{\pm}$ is first obtained from the Schonland fit of $G_{\pm}$ to the experimental data. Next the tensor $\mathbf{T}^{q}_{\pm} = \mathbf{T}_{\pm}\mathbf{Q}\mathbf{T}_{\pm}$ is calculated from a similar Schonland fit to the experimental $G^2_{\pm}P_{\pm}$data. The tensor $\mathbf{Q}$ is finally calculated and diagonalized to obtain the principal values and directions of the *nqc*-tensor. The principal values estimated by this method can differ significantly from those obtained in early work assuming parallel principal axes for $\mathbf{A}$ and $\mathbf{Q}$. A procedure to obtain the tensors by a non-linear least squares fitting to the directly measured frequencies described in Sects. 1.2.3 and 1.2.4 has been applied more recently [44].

ENDOR of Radicals with *g*-Factor Anisotropy. The issue is of less importance for organic radicals due to the small g-anisotropy, but may have to be considered for some inorganic species. In the favourable situation when the $m_S = \pm ½$ pairs of transitions are observable one may employ a fitting to the relation (1.18).

$$\nu_+^2 + \nu_-^2 - 2\nu_N^2 = {}^1\!/_2\mathbf{u}\mathbf{A}^2\mathbf{u} \tag{1.18}$$

According to this equation the hyperfine tensor can be obtained from a modified Schonland fitting procedure employing the unit vector $\mathbf{u} = \mathbf{g}\boldsymbol{l}/g$ to specify the

direction of the effective magnetic field. The Schonland method cannot be applied to obtain the *hfc* tensor from the ENDOR frequencies when only one of the two ENDOR lines is observed, however. The evaluation of the *nqc*-tensor **Q** for nuclei with I $\geq$ 1 from the expression (1.19) [42, 43] is also more difficult due to the *g*-anisotropy.

$$G_{\pm}^{2} P_{\pm} = \boldsymbol{l} \left(\pm \frac{\mathbf{gA}}{2g} - \nu_N \mathbf{E} \right) \mathbf{Q} \left(\pm \frac{\mathbf{Ag}}{2g} - \nu_N \mathbf{E} \right) \boldsymbol{l} \tag{1.19}$$

We refer to Sect. 1.2.3 for a brief discussion of methods to obtain the *hfc*- and *nqc*-tensors under those conditions.

Correction of ENDOR Frequencies. The Schonland method is directly applicable to obtain *hfc* tensors with ENDOR, provided that the magnetic field and accordingly the nuclear frequency ν_N can be kept constant. This condition cannot always be realized, however, due to instrumental effects and/or the influence of an anisotropic *g*-factor. The problem can be solved either by taking account of the change in ν_N or by adjustment of the measured ENDOR data to a common value of the nuclear frequency. The latter method is common for slight variations in magnetic field strengths, but the applied procedure is not always described. We briefly consider this approach for a radical with anisotropic *g*- and *hfc*-tensors in Appendix A.1.

1.2.2.1 The Schonland Ambiguity

An uncertainty in the signs of the off-diagonal tensor elements, due to a wrong sense of the rotation of the crystal commonly occurs in practical applications of the Schonland method. An ambiguity of this type is difficult to avoid when several crystals are used for the measurements in the three different crystal planes normally employed. Geometric [28] and numeric analyses [45] show, however, that only two cases with different principal values need to be considered, one with correct sense or with wrong sense in two crystal planes, the other with wrong sense in a single or all three planes. Assume for instance that the components T_{xz} and T_{yz} of a symmetric tensor, *e.g.* $\mathbf{T} = \mathbf{g}\mathbf{g}^{\mathrm{T}}$ were obtained with wrong sign due to wrong sense of rotation in the xz and yz planes The principal values are then obtained from an eigenvalue equation, written in component form in (1.20).

$$\begin{aligned} T_{xx} \cdot R_x' + T_{xy} \cdot R_y' - T_{xz} \cdot R_z' &= t' \cdot R_x' \\ T_{xy} \cdot R_x' + T_{yy} \cdot R_y' - T_{yz} \cdot R_z' &= t' \cdot R_y' \\ -T_{xz} \cdot R_x' - T_{yz} \cdot R_y' + T_{zz} \cdot R_z' &= t' \cdot R_z' \end{aligned} \tag{1.20}$$

The relations apply for each of the three principal values (t') and the corresponding three sets of direction cosines (R_x', R_y', R_z'). The corresponding correct values are denoted t and (R_x, R_y, R_z), respectively. The correct equations are regained by

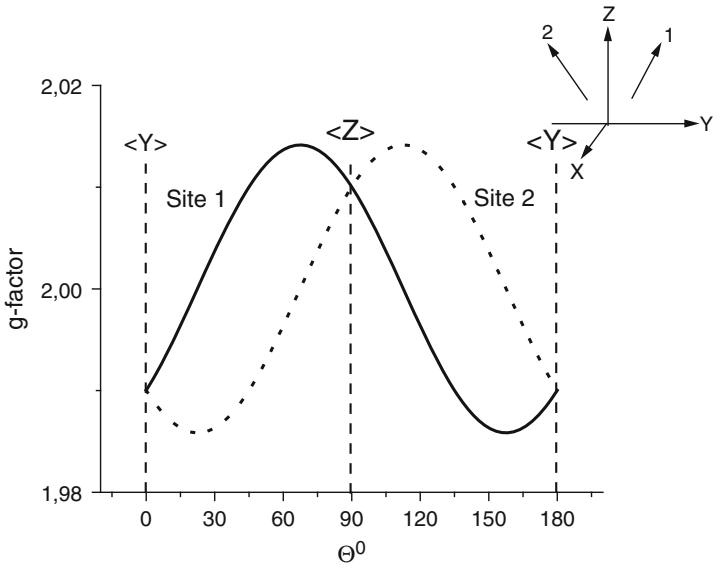

Fig. 1.3 *g*-Factor variation in a plane showing site-splitting due to a single species trapped in two equivalent but differently oriented positions, "sites" in the crystal (Adapted from Ref. [69] with kind permission of © Springer 2011)

the substitution $R_x' = R_x$, $R_y' = R_y$, $R_z' = -R_z$. The principal values are therefore equal, $t' = t$. Analogous results apply when T_{xy} and T_{xz} or T_{yz} and T_{xy} are obtained with the wrong sign. One can show in a similar way that a wrong sign of a single element or all three elements all give the same principal values. Those values differ in general from the correct ones. Uncertainty in the sense of rotation of the crystal in the magnetic field accordingly gives rise to just two sets of principal values. Within each set the magnitudes of the direction cosines agree, while the sign of either R_x, R_y or R_z can be ambiguous due to wrong sense of rotation. A similar change of sign also occurs between the different sites in crystals of higher symmetry than triclinic. The different signs of the direction cosines obtained by the Schonland method are then often found to agree with those expected from crystal symmetry. The principal *g*-values of the two symmetry-related sites 1 and 2 in Fig. 1.3 with coordinates (x, y, z) and (x, −y, z) would for example have opposite signs of the R_y direction cosine. An assignment of the spectra to specific sites can then not be obtained experimentally. The sites are therefore frequently assigned by comparison of the direction cosines with those obtained from the crystal structure.

The ambiguity between the two sets of principal values can be resolved by measurements in a fourth "skew" plane [28], in favourable cases also by recording the powder spectrum. As a rule only one of the two tensors reproduces the experimentally determined variation of the EPR or ENDOR line positions in the skew plane or the line-shape of the powder sample.

1.2.2.2 The Schonland Ambiguity in ENDOR

A simpler procedure to resolve the Schonland ambiguity is applicable by ENDOR measurements when the two ENDOR transitions corresponding to $m_S = \pm ½$ can be observed. Only one of the two tensors was found to be compatible with the observed angular dependence of the two frequencies [45]. The observation is of relevance in practical applications and is therefore further discussed below.

When the *g*-factor is isotropic the ENDOR frequencies due to ^{1}H or other I = ½ nuclei are to first order given by (1.12) and (1.13), which can be expanded as in (1.21).

$$\nu_{\pm}^2 = \frac{1}{4}\boldsymbol{l}\mathbf{A}^2\boldsymbol{l} \mp \nu_N \boldsymbol{l}\mathbf{A}\boldsymbol{l} + \nu_N^2 \tag{1.21}$$

The static magnetic field **B** is along the unit vector $\boldsymbol{l} = \mathbf{B}/B$. The nuclear frequency ν_N is constant if the measurements are performed at a fixed magnetic field strength *B*. The equivalent relations (1.22) and (1.23) suggest a probable reason for the resolution of the ambiguity when both transitions are observable.

$$\nu_+^2 + \nu_-^2 - 2\nu_N^2 = \frac{1}{2}\boldsymbol{l}\mathbf{A}^2\boldsymbol{l} \tag{1.22}$$

$$\nu_+^2 - \nu_-^2 = -2\nu_N \boldsymbol{l}\mathbf{A}\boldsymbol{l} \tag{1.23}$$

Thus, relation (1.22) implies that the magnitudes of the principal values and the corresponding principal directions of the tensor $\mathbf{A^2}$ can be deduced by application of the Schonland method when both ν_+ and ν_- are measured. The close analogy with (1.11) in the EPR analysis according to Poole and Farach is notable. The *hfc* tensor **A** can also be obtained by a similar analysis based on the relation (1.23). We assume that measurements were correctly made in the xz- and yz-planes, and examine the influence of a wrong sense of rotation for the angle θ in the xy-plane using the Eqs. (1.24) and (1.25).

$$2\left(\nu_+^2 + \nu_-^2 - 2\nu_N^2\right) = \left(\mathbf{A}^2\right)_{xx}\cos^2\theta + \left(\mathbf{A}^2\right)_{yy}\sin^2\theta + \left(\mathbf{A}^2\right)_{xy}\sin(2\theta) \tag{1.24}$$

$$\frac{\nu_-^2 - \nu_+^2}{2\nu_N} = A_{xx}\cos^2\theta + A_{yy}\sin^2\theta + A_{xy}\sin(2\theta) \tag{1.25}$$

The quantities A_{xy} and $(\mathbf{A}^2)_{xy}$ would both be experimentally obtained with reversed sign. For consistency the value obtained by matrix multiplication as in (1.26) should, however, be applied.

$$\left(\mathbf{A}^2\right)_{xy} = -A_{xx}\cdot A_{xy} - A_{xy}\cdot A_{yy} + A_{xz}\cdot A_{zy} \tag{1.26}$$

This quantity differs from the value $-(\mathbf{A}^2)_{xy}$ obtained experimentally in the sign of the 3rd term. The tensors obtained by an analysis of the data using both (1.22) and (1.23) are therefore not consistent in case of wrong sense for the angle in a single plane. The result corroborates the conclusion reached by a numerical analysis [45].

1.2.3 Non-linear Least Squares Methods

Non-linear least squares procedures have been employed in several instances for the analysis of single crystal EPR and ENDOR data, *e.g.* to refine the tensor elements obtained by the Schonland method, to obtain simultaneous fittings of two or more tensors, or to obtain a tensor employing exact theory rather than by first order analysis.

First Order Analysis of *hfc*-Tensor ($\mathbf{I} = ½$). A procedure to derive the *hfc* tensors from the ENDOR data similar to that described by Nelson et al. [46] is often applied in recent applications. In this method, the data obtained in the three crystal planes are analysed in a single step using a six-parameter linear regression routine to obtain the tensor elements from the polar angles (θ, φ) of the rotation axes, the angle of rotation α, and the corresponding measured ENDOR frequency. Refinements including a total of nine angles (θ, φ) and the starting angle α_0 for each plane were made using a nonlinear refinement procedure converging to minimum root mean square value for the complete data set, for details see the original papers [46].

First Order Analysis of *hfc*- and *nqc*-Tensors when $|\mathbf{P}_\pm| \ll |\mathbf{G}_\pm|$ ($\mathbf{I} \geq \mathbf{1}$). A direct fit of the theoretical ENDOR frequencies (1.16) to the experimental data by a non-linear least squares procedure can be made using (1.6) and (1.19) [44]. The procedure was developed to determine the ^{14}N *hfc* and *nqc* tensors in a nitrogen-containing radical, but applies for arbitrary nuclear spin values. The method might be more satisfactory from an accuracy point of view than the original Schonland procedure.

First Order Analysis of *hfc*-and *nqc*-Tensors when $|\mathbf{P}_\pm| \approx |\mathbf{G}_\pm|$ ($\mathbf{I} \geq \mathbf{1}$). When the nuclear and hyperfine interactions are much weaker than the electronic Zeeman energy a perturbation treatment based on the perturbation operator (1.2) is in principle applicable. An easily overlooked fact is that the energies have to be calculated by diagonalization of this operator [47, 48] due to the degeneracy with respect to nuclear spin. We refer to previous work for the analysis of single crystal ENDOR data under those conditions [49, 50]. The limited number of applications makes it difficult to evaluate the potential of the method, however.

Higher Order and Exact Analysis. Higher order perturbation theory can be applied to the case when the first order analysis is inadequate, *e.g.* when the *hfc* is large. The second order corrections given in [42, 51] are in a suitable form to be applied in single crystal analysis of EPR and ENDOR data. Energy cross terms might have to be taken into account in the case of several interacting nuclei [52].

Table 1.1 Software for single crystal analysis

Program	Order	Available from	Code
MAGRES	1	[46]	Fortran77
TENSOR	1	[55]	–
ENDPAQ	1	[44]	Fortran77
EasySpin	Exact	http://www.easyspin.org/	Matlab 6.5.1
EPR-NMR	Exact	http://www.chem.queensu.ca/eprnmr/	Fortran77
Schon_fit	1	This work	Matlab 6.5.1

Fitting procedures involving exact diagonalisation of the spin-Hamiltonian at each crystal orientation have been applied e.g. in a study of a rare earth metal ion complex [53]. The derivatives of the energies with respect to the parameters P_i employed in the fitting were obtained from (1.27) in accordance with the Hellmann-Feynman theorem [54].

$$\frac{\partial E_k}{\partial P_i} = \left\langle k \left| \frac{\partial H}{\partial P_i} \right| k \right\rangle \tag{1.27}$$

Here |k> is the eigenvector corresponding to the eigenvalue E_k. An adaptation of the method for free radical systems should be useful particularly in ENDOR where the line positions are accurately measured. We are not aware of recent applications of this method, however.

1.2.4 Software for Single Crystal Analysis

Computer programs for this purpose are often developed in laboratories specialized in single crystal measurements, but the programs are not always published. The computer programs that the authors are aware of are listed in Table 1.1.

The MAGRES [46] and TENSOR [55] programs are particularly designed for the analysis of g and hyperfine data. While the nuclear quadrupole tensor of nuclei with $I \geq 1$ might be obtained with those programs by using the stepwise procedure described in Sect. 1.2.2, the ENDPAQ program [44] is directly applicable.

The Schon_fit program is a simplified replacement for software in obsolete code referred to in our previous work [49], based on the original Schonland method. Axial symmetry constraints commonly employed in the analysis of defects in crystals of high symmetry [56] can be taken into account relatively easily. The NMR-EPR and Easyspin programs should be better suited when the conditions $|hfc| \ll h\nu$ (ν = microwave frequency) or $|nqc| \ll |hfc|$ do not apply. The first case implies that the high-field approximation is invalid, the second situation can occur for radicals containing nuclei with $I \geq 1$ having large quadrupole moments and occasionally also with ^{14}N, see *e.g.* [57, 58]. We refer to the references in Table 1.1 and Appendix A.1 for additional information about the programs.

1.3 Analysis of Powder Spectra

Single crystals are not always available for measurements *e.g.* of radicals in biochemical materials, while in other cases the paramagnetic species are intentionally trapped in a disordered matrix or in a frozen solution. This section is accordingly concerned with the problem of extracting anisotropic g- and/or hyperfine couplings from an analysis of CW EPR and ENDOR spectra in rigid amorphous matrices, frozen solutions, multiphase systems and in polycrystalline samples. The term 'powder spectrum' is frequently used in the following.

1.3.1 EPR Powder Spectra

g-Tensors. Visual analysis can be employed to obtain the g-tensor for well-resolved powder spectra, but due to the slight anisotropy typical for most organic radicals, high-field EPR measurements are then usually required. High field studies have increased in importance both in basic studies and for applications in the chemical, biological and environmental fields during the last decade, following initial work [21]. Principal g-values in the range 2.0024–2.0072 of phenoxyl radicals were then resolved with an uncertainty of $\pm 5 \times 10^{-5}$. Such small anisotropy is practically impossible to determine at low frequency, but was clearly resolved at the 2 mm band because of the 15 times better g-factor resolution as compared to that of the X-band. The resolution of g-anisotropy has been a major reason for the use of high frequency and correspondingly high field EPR in recent applications, for instance in studies of radicals and metal sites in proteins [26, 27]. The new experimental methods to determine accurate g-tensors with high field EPR have also caused a revival of theoretical research to predict these quantities in free radical systems (Chap. 7) following early seminal work [59].

The resonances of two species with different g-factors, g and $(g + \Delta g)$ are separated by

$$\Delta B = \frac{h}{\mu_B} \frac{\Delta g}{g \cdot (g + \Delta g)} \cdot \nu. \tag{1.28}$$

The field separation (ΔB) and thus the g-factor resolution increases with the microwave frequency ν. The anisotropy of the g-factor is also better resolved; the degree of resolution depends on the difference between the g-components, on the linewidth, and on the frequency band of the spectrometer. At a line-width of 1 mT measurements at W-band would for example be required to resolve an anisotropy of $\Delta g \approx 10^{-3}$ according to Table 1.2, where conventional symbols for the frequency bands were employed.

Regular electromagnets can be used up to Q-band frequencies and corresponding magnetic fields, while at W-band and higher superconducting magnets

Table 1.2 Bands, wavelengths (λ), frequencies (ν), fields (B) at $g = 2$, and resolution (ΔB) for $\Delta g = 10^{-3}$ in multi-frequency EPR

Band	L	S	X	K	Q	W	mm	Sub-mm
λ (cm)	30	10	3.0	1.25	0.88	0.32	0.10–0.30	<0.10
ν (GHz)	1	3	9	24	34	95	110–300	>300
B (T)	0.0357	0.107	0.321	0.857	1.215	3.394	3.93–10.72	>10.72
ΔB (mT)[a]	0.018	0.054	0.16	0.43	0.61	1.70	1.96–5.36	>5.36

[a] $\Delta B(mT) = 71.4477 \frac{\Delta g}{g \cdot (g + \Delta g)} \cdot \nu(gHz)$

are employed. Commercial equipment is at present available up to a microwave frequency of 263 GHz, while spectrometers operating at even higher frequencies have been constructed in specialised laboratories.

Radicals present in frozen solutions, in enzymes, in photosynthetic systems, in catalytic systems, in soil etc. have recently been characterized by their g-factor anisotropy using high field EPR [21, 60–66], see Chap. 7 for additional examples.

Although the increased spectral resolution of anisotropic g-factors might be the most important feature of high field EPR in free radical research some other characteristics have also been considered [22]:

1. The analysis of hyperfine couplings in EPR spectra is simplified when the high field approximation applies. Hyperfine couplings can be read directly as line separations at high field.
2. Hyperfine couplings obtained by the angular selection method with the field set at anisotropic g_x, g_y and g_z features can give single-crystal-like ENDOR spectra from randomly oriented samples. The enhanced resolution of g-anisotropy at high magnetic field increases orientation selectivity of ENDOR spectra in amorphous systems.

At present, multi-frequency and high field studies are mostly carried out in CW-mode. Pulsed EPR may become more generally accessible, however, by the rapid progress in this field. These developments are, nonetheless, beyond the scope of this chapter, and we refer to Chap. 2 and previous reviews [22, 25].

Hyperfine Coupling Tensors. Splittings due to hyperfine interactions are (to first order) independent of the microwave frequency. Measurements at different frequencies can therefore clarify if an observed spectrum is split by Zeeman interactions (different g-factors) or not. As schematically shown in Fig. 1.4, the ^{14}N hyperfine splittings at $g_x = 2.0094$, $g_y = 2.0066$, $g_z = 2.0026$ of the Tempone radical [67] can be resolved at microwave frequencies of 94 and 263 GHz, while features due to hyperfine structure and g-anisotropy are not well separated at 9.5 GHz.

Line-broadening due to anisotropic hyperfine couplings with nuclei like ^{1}H and ^{14}N occurs frequently in powder EPR spectra of free radicals. The anisotropy is large (*ca.* 50% of the isotropic coupling) for the α–H coupling of radicals of the type $\rangle \dot{C}_{\alpha}$–H frequently observed in organic, polymeric and biological samples. The three principal values are all different [39], resulting in a smeared spectrum. The smearing

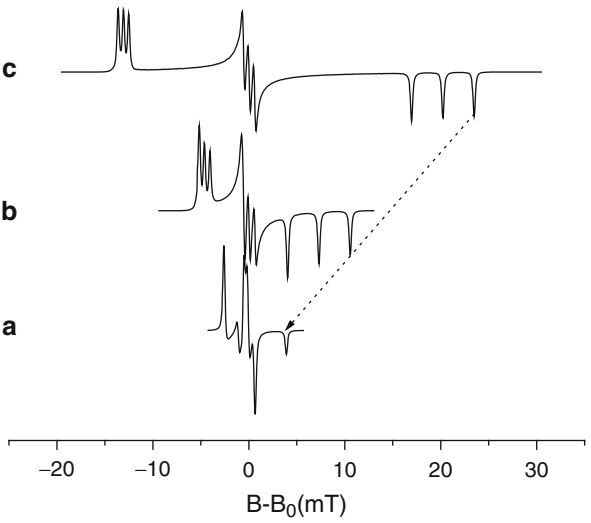

Fig. 1.4 Schematic powder EPR spectra centred at field B_0 corresponding to $g = 2.0066$. Features due to g-and ^{14}N *hfc*-anisotropy are resolved at (**b**) 94 GHz and, (**c**) 263 GHz but overlap at (**a**) 9.5 GHz. The spectra were calculated with $g_x = 2.0094$, $g_y = 2.0066$, $g_z = 2.0026$, $A_x = 15.49$ MHz, $A_y = 16.27$ MHz, $A_z = 91.06$ MHz for the Tempone radical [67]

can become more pronounced and/or additional lines can appear due to the earlier described direct field effect (Sect. 1.2.2). The effect is most pronounced when the anisotropic coupling and the nuclear Zeeman energy are of comparable magnitudes, very often occurring at X-band for radicals with anisotropic hyperfine couplings due to ^1H and occasionally to ^{19}F, the two nuclei with the largest nuclear *g*-factors among the stable isotopes. The smearing and the appearance of additional lines are well understood [33], and could be accounted for as early as 1965 with the first general computer program for simulations of free radicals in amorphous systems [36]. We refer to the original literature [33, 39] for details. Simulations of powder spectra featuring such effects have been frequently employed in recent studies. Software for this purpose is given in Table 1.3.

Complications due to the direct field do not appear for isotropic couplings, and are usually not of major concern for so-called β–H in radicals of the types $\rangle\dot{C}_\alpha–C_\beta H_2–$, $\rangle\dot{C}_\alpha–CH_3$ and other couplings with small anisotropy, and even for anisotropic couplings due to ^{14}N and other nuclei with small nuclear *g*-factors. The *hfc* anisotropy in nitrogen-centred free radicals is often approximately axially symmetric, giving line-shapes that in several cases can be analysed by inspection, *e.g.* for NO_2 stabilized in Vycor glass in early work [68] and for spin labels in frozen matrices [23, 24]. In the first case the X-band EPR spectrum at 4.8 K was well resolved and could be simulated using anisotropic *g*-factors and hyperfine couplings ($g_x = 2.0051, g_y = 1.9913, g_z = 2.0017, A_x = 50.0$ G, $A_y = 46.0$ G, $A_z = 65.5$ G), in the latter case high field measurements at low temperature were required to resolve the *g*-anisotropy. Forbidden hyperfine transitions were not observed, although such transitions might be visible under certain circumstances at high field measurements of nitrogen-centred radicals [69].

Table 1.3 Programs for simulation of powder EPR and ENDOR spectra

Program	Order	Available from	Code
EasySpin (general)[a]	Exact	http://www.easyspin.org/	MatLab 6.5.1
EPR-NMR (general)[b]	Exact	http://www.chem.queensu.ca/eprnmr/	Fortran77, exe
RIGMAT (EPR, S = ½)[c]	2	http://www.EPR-spectsim-softw.fr/programs	APL
HMLT[c]	Exact	—"—	—"—
XEMR (general)[d]	Exact	http://sourceforge.net/projects/xemr/files/	Source, binary
XSOPHE (general)[e]	Exact	http://www.bruker-biospin.com/xsohpe.html	Exe (commercial)
— (EPR)[f]	Exact	H, Weihe	Exe
Simfonia	1–2	http://www.bruker-biospin.de/EPR/software/emx.html	Exe (commercial)
MSPEN/MSGR[g]	Exact	[99]	Fortran77
GENDOR[h]		http://chemgroups.northwestern.edu/hoffman/endor_files/simulationprograms.htm	Visual Basic
ENDOR F2[i]	1–2	A. Lund, alund@ifm.liu.se	Fortran77, exe

[a]Matlab toolbox for simulating EPR and ENDOR spectra. MatlLab version 6.5.1 or higher must be installed on the computer and is not provided with EasySpin. Details are given in [108]
[b]EPR-NMR simulation of single crystal and powder spectra. The program runs on any computer capable of running 32-bit Fortran77. The program has been developed by Prof. J.W. Weil
[c]EPR simulation programs for the simulation of radicals or metal ions in rigid glassy or polycrystalline matrices prepared by Dr C. Chachaty. APL must be installed on the computer
[d]Spectrum manipulation and EPR and ENDOR simulation package written for Linux systems. The program is written and maintained by Dr. J. Eloranta
[e]The simulation software suite is described in Chap. 5
[f]General spin Hamiltonians can be treated. The program has been developed by Dr H. Weihe, Department of Chemistry, University of Copenhagen
[g]Simultaneous EPR and ENDOR powder spectra synthesis by direct Hamiltonian diagonalization. The program developed by Dr. A. Kreiter and Prof. J. Hüttermann, is described in [99]
[h]Simulation of powder ENDOR spectra featuring angular selection due to *g*-factor anisotropy
[i]Simulation of powder ENDOR spectra treating hyperfine-, quadrupole- and nuclear Zeeman interactions as a joint perturbation. The reader is referred to the original paper for details [58]

Powder EPR spectra of species with hyperfine structure due to several nuclei are often difficult to analyse by visual inspection, and complementary data and/or simulations are often required, at least when the principal axes of the corresponding coupling tensors do not coincide. It is therefore remarkable that the ^{19}F *hfc* tensor of the trifluoromethyl radical, $\dot{C}F_3$, could be accurately determined by an analysis of the X-band spectrum in rigid noble gas matrix at an early stage [70]. The complex shape of the EPR spectrum was attributed to the different orientations of the principal directions of the three ^{19}F hyperfine couplings tensors, with equal, strongly anisotropic principal values and was supported by simulations at a much later stage, completely confirming the original analysis [69]. Spectra of this type are most conveniently simulated by one of the exact methods exemplified in Table 1.3. We refer to the literature for an account of the complications occurring in an analysis based on perturbation theory [70].

Hyperfine coupling data obtained from theory, particularly DFT (Density Functional Theory) calculations, have proved to be useful to predict both isotropic and anisotropic hyperfine couplings. The theoretical data are in certain applications quite accurate as exemplified by the agreement between simulated and experimental spectra for a series of fluorocarbon anion radicals [69, 71].

Nuclear Quadrupole Couplings. Nuclear quadrupole couplings that are smaller than the hyperfine coupling do not influence the shape of the EPR spectra to a first approximation. Exceptions occur for species containing nuclei with large nuclear quadrupole moments, Rigorous procedures for the analysis of single crystal [29] and powder [72] EPR spectra were given in early work on inorganic radicals with ^{35}Cl and ^{37}Cl nuclear quadrupole couplings of comparable magnitudes to the corresponding hyperfine couplings. The software used may no longer be available, however. We refer to [73] for a related analysis of a metal-ion complex by a combined experimental and computational study and to procedures applicable to radicals for the analysis of ENDOR powder spectra presented in Sect. 1.3.2. Software to simulate spectra of this type by exact methods and by treating the nuclear quadrupole-, the nuclear Zeeman- and the hyperfine terms as a joint small perturbation, are further discussed in Sect. 1.3.4.

1.3.1.1 EPR Intensity in Disordered Systems

The factor $|\mathrm{G}|^2$ in (1.29) takes into account the influence of the g-factor anisotropy on the intensity of an EPR transition in a single crystal with the static and microwave magnetic fields along the unit vectors $\boldsymbol{l} = \mathbf{B}/B$ and $\mathbf{r} = \mathbf{B}_1/B_1$, respectively, [42].

$$|G|^2 = 0.25\mu_B^2 B_1^2 \left(\mathbf{r}^T\mathbf{g}^T\mathbf{g}\mathbf{r} - \left(\boldsymbol{l}^T\mathbf{g}^T\mathbf{g}\mathbf{r}\right)^2/g^2\right) \tag{1.29}$$

The corresponding transposed quantities are indicated by superscript T in (1.29). The g-tensors obtained experimentally are usually symmetric, *i.e.* $\mathbf{g^T} = \mathbf{g}$. Theoretical calculations often yield unequal values for the off-diagonal elements, $g_{\mathrm{xy}} \neq g_{\mathrm{yx}}$ may for instance occur. This possibility is taken into account in (1.29). The intensity depends only on the symmetric tensor $\mathbf{g}^T\mathbf{g}$, however.

For a disordered system the intensity is obtained by performing the averages indicated by bars in (1.30) and (1.31).

$$\overline{\mathbf{r}^T\mathbf{g}^T\mathbf{g}\mathbf{r}} = \sum_{i=1}^{3}\sum_{j,k=1}^{3} g_{ij}g_{ik}\overline{r_j r_k} = \frac{1}{2}\left(Trace(\mathbf{g}^T\mathbf{g}) - g^2\right) \tag{1.30}$$

$$\overline{\left(l^T\mathbf{g}^T\mathbf{g}\mathbf{r}\right)^2}/g^2 = \sum_{m,n=1}^{3} u_m u_n \sum_{j,k=1}^{3} g_{mj}g_{nk}\overline{r_j r_k} = \frac{1}{2}\left(\mathbf{u}^T\mathbf{g}^T\mathbf{g}\mathbf{u} - g^2\right) \tag{1.31}$$

here $\mathbf{u} = \mathbf{g}\boldsymbol{l}/g$ has been introduced.

Equations (1.30) and (1.31) follow from the expression (1.32), obtained under the normal experimental condition with B perpendicular to B_1 [74].

$$\overline{r_j r_k} = (\delta_{jk} - l_j l_k) \tag{1.32}$$

Taking into account the 1/g factor for field-swept EPR [75] the $|G|^2$ factor of a disordered solid is accordingly given by (1.33):

$$|G|^2 = \frac{\mu_B^2 B_1^2}{8g} \left(Trace(\mathbf{g}^T\mathbf{g}) - \mathbf{u}^T\mathbf{g}^T\mathbf{g}\mathbf{u}\right) \tag{1.33}$$

The factor is nearly constant for most organic free radicals, but can be of significance for some inorganic radicals. An expression valid for a symmetric tensor [74] is obtained by inserting $\mathbf{g}^2$ in place of $\mathbf{g}^T\mathbf{g}$ in (1.33).

1.3.2 Powder ENDOR Spectra

ENDOR measurements on radicals in powder samples usually aim at deducing structural properties from an analysis of hyperfine- and nuclear quadrupole interactions that are too small to be resolved by EPR. Interactions with nuclei of the matrix can provide information about the trapping site and thus about the solvation structure of the radicals. The subject has been treated in textbooks [3, 4, 10, 14, 18, 69], numerous articles, *e.g.* [58, 76–99] and recent reviews [100–102] about radicals on surfaces, in frozen matrices, and in biological systems.

Hyperfine enhancement and angular selection effects are well known examples of factors affecting the ENDOR intensities. Hyperfine enhancement effects [91–93] can cause differences in intensities of the $m_S = \pm ½$ lines even in liquids, while angular selection [94, 96] due to anisotropic g-factors occurs only in powders. In the ENDOR spectra of systems with pronounced g-anisotropy the ENDOR spectrum obtained at a specific magnetic field setting contains contributions from a limited range of orientations, *e.g.* along a line or in a plane for an axially symmetric system with the field set at $g_{||}$ and $g_{\perp}$. Methods to analyse ENDOR spectra in those cases have been described [95–102] and are usually incorporated in software developed for the simulation of powder ENDOR spectra. The poor agreement between experimental and simulated intensities that is nevertheless commonly observed may at least in part be due to relaxation effects that are not taken into account in any software for solid state ENDOR we are aware of. (Simulations that take such effects into account seem to have been employed only to analyse ENDOR spectra in the liquid state [103].)

Hyperfine Coupling Anisotropy. The hyperfine coupling parameters of well resolved powder spectra can be extracted by a visual analysis analogous to that applied in EPR. The principle is indicated in Fig. 1.5 for an axially symmetric ^{1}H *hfc* tensor, with $|A_{||}| < |A_{\perp}| < 2\cdot\nu_H$. Absorption-like peaks separated by $A_{||}$ in the

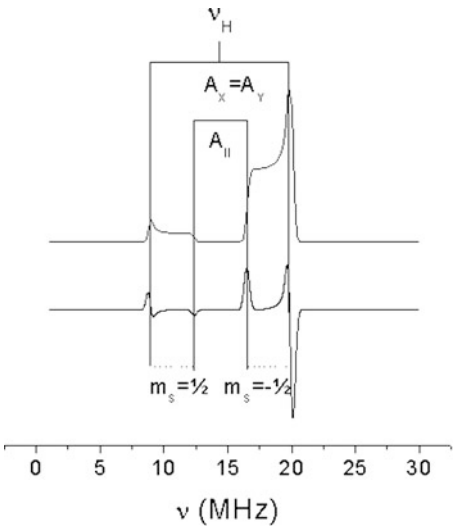

Fig. 1.5 Schematic X-band powder ENDOR spectrum due to an axially symmetric ^{1}H hyperfine structure with $|A_{||}| < |A_{\perp}| < 2{\cdot}\nu_H$. Absorption-like peaks separated by $A_{||}$ in the 1st derivative spectrum occur due to the step-wise increase of the amplitude in the absorption spectrum (Adapted from Ref. [69] with kind permission of © Springer 2011)

1st derivative spectrum occur due to the step-wise increase of the amplitude in the absorption spectrum. The difference in amplitude commonly observed between the $m_S = \pm ½$ branches is caused by the hyperfine enhancement effect on the ENDOR intensities [91–93].

Angular Selection. The recording of ENDOR spectra with the magnetic field locked at different positions of the EPR spectrum, *e.g.* at $g_{\perp}$ and $g_{||}$ in case of axial symmetry, is a common procedure to extract weak anisotropic hyperfine couplings from powder samples. Coupling constants corresponding to those obtained from a single crystal with the magnetic field oriented along the principal axes of the *g*-tensor can be obtained from an analysis of the ENDOR spectra. The structure of transition metal ions and metalloproteins have been probed [96, 100], and software taking angular selection effect into account for the simulation of powder ENDOR spectra has been developed, see Sect. 1.3.4.

In many free radical systems the g-anisotropy is quite small and it is then impossible at X-band to obtain single crystal like ENDOR spectra, which instead are made up of a large number of orientations. Computer simulations are then essential for the analysis. When the nuclear and hyperfine interactions are much weaker than the electronic Zeeman energy a perturbation treatment is applicable. A program developed by Erickson [58] has been used in the simulations for this chapter. Several nuclei with any value of nuclear spin I can be handled. A spin Hamiltonian of the type (1.2) was assumed for each nucleus. This Hamiltonian arises when the electronic Zeeman term is the dominating one, while the hyperfine, quadrupole and nuclear Zeeman interactions are treated, simultaneously, as a joint perturbation. Thus, no assumption needs to be made regarding their relative magnitude or the relative orientation of the principal axes of the tensors. The ENDOR frequencies for the $m_S = \pm ½$ electron states are obtained by diagonalisation of the perturbation matrix corresponding to (1.2) for each nucleus.

The powder line shape at the frequency ν and static magnetic field B is assumed to have the form (1.34) proposed in [99] using slightly different notation.

$$Y'(B,\nu) = \int_{\theta=0}^{\pi} \sin\,\theta d\theta \int_{\phi=0}^{2\pi} \varphi d\varphi \sum_{ij} s(B-B_{ij}) V_{ij}^2 \left\{ \sum_k t(\nu-\nu_{ik}) W_{ik}^2 + \sum_l t(\nu-\nu_{jl}) W_{jl}^2 \right\} \tag{1.34}$$

Indices i and k denote nuclear states within the $m_S = -½$ manifold, while j and l refer to levels with $m_S = +½$. The EPR line shape function s (in absorption) is a weighting function to select the transitions that contribute to the ENDOR signal, and thus gives rise to the angular selection at the magnetic field B. Only those nuclear transitions that have an energy level in common with the EPR transition $|-½\,\mathrm{i}> \leftrightarrow |½\,\mathrm{j}>$will contribute to the signal. The ENDOR line shape function, *t,* is in first derivative to obtain the first derivative spectrum $Y'(B, \nu)$ by integration over the polar angles (θ, φ). The ENDOR intensities for the transitions between the states $|-½\,\mathrm{i}> \leftrightarrow |-½\,\mathrm{k}>$ and $|½\,\mathrm{j}> \leftrightarrow |½\,\mathrm{l}>$ in (1.35) were calculated to first order by an analytic formula applying for a powder sample.

$$W_{ik}^2(\theta,\phi) = \frac{1}{2}\left(\frac{B_2}{B}\right)^2 (\boldsymbol{\alpha}^* \mathbf{T}^2 \boldsymbol{\alpha} - \boldsymbol{\alpha}^* \mathbf{T}\boldsymbol{l} \cdot \boldsymbol{\alpha}\mathbf{T}\boldsymbol{l}) \tag{1.35}$$

T is the ENDOR tensor (1.13), $\boldsymbol{l}$ is the unit vector specifying the direction of the static magnetic field B (not the radiofrequency field B_2), and $\boldsymbol{\alpha}$ is a complex vector with the components $<\mathrm{i}|\mathrm{I_x}|\mathrm{k}>$, $<\mathrm{i}|\mathrm{I_y}|\mathrm{k}>$ and $<\mathrm{i}|\mathrm{I_z}|\mathrm{k}>$. The formula for the ENDOR intensities by this method predicts enhancement effects analogous to those given in classical treatments [91–93], and in addition takes into account the influence of nuclear quadrupole interactions for nuclei with $I \geq 1$. The influence can be significant as shown in Fig. 1.6 for the ^{14}N spectral region of the powder ENDOR spectrum of the radical $H_2\dot{C}NHCOC_6H_5$ in X-irradiated hippuric acid. An analysis (c) that ignores the *nqc* cannot account for the experimental powder spectrum (a), while the simulation in (b) provides a satisfactory fit. The reader is referred to the original paper [58] for additional details and applications.

A limitation of the analysis of powder ENDOR is that the directions of the principal axes for the hyperfine couplings cannot in general be obtained unless the *g*-anisotropy is sufficient for angular selection to occur. Measurements at high field may be necessary to achieve angular selection due to the small *g*-anisotropy of most radicals. Theoretical modeling is another useful complement for the interpretation of powder ENDOR spectra, see [65, 66] for an example of applying those techniques.

1.3.3 Simulation of ENDOR Spectra

Due to the lower resolution of powder ENDOR spectra compared to spectra from liquids and single crystals, computer assisted analysis by simulation is often

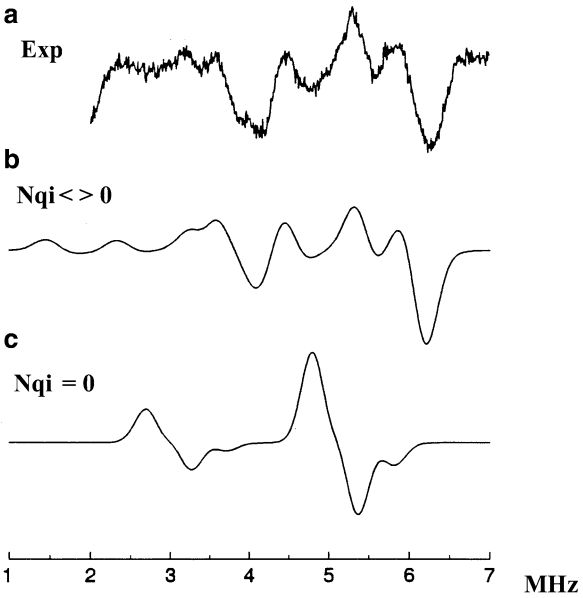

Fig. 1.6 Experimental (**a**) and simulated (**b**), (**c**) powder ENDOR spectra at 110 K of $H_2\dot{C}NHCOC_6H_5$ radical in X-irradiated hippuric acid. Only the region of ^{14}N-signals is shown. The simulations were made including (**b**) and excluding (**c**) the *nqc* using $\mathbf{A}(^{14}N) = (-7.38, -8.77, -9.44)$ MHz, $\mathbf{Q}(^{14}N) = (-0.843, +0.582, +0.261)$ MHz [104] (Adapted from Ref. [58] with kind permission of © Elsevier 1996)

required. Brief descriptions of general programs as well as dedicated software for ENDOR simulation are given in Table 1.3. In general, the positions of the ENDOR lines can be accurately simulated. The experimental intensities are more difficult to reproduce even taking into account the different intensities of the ENDOR lines due to the hyperfine enhancement effect. ENDOR powder spectroscopy in conjunction with simulations has, nevertheless, become a usable alternative in recent applications. A few examples are given below.

Confirmation of Single Crystal Analysis. This application may seem redundant, but is motivated *e.g.* by the so-called Schonland ambiguity in determining the *hfc* tensors from single crystal measurements. It is only very recently that methods to eliminate the ambiguity [45] have been proposed, and the procedures are not always applicable. An investigation to clarify the radical structure of *l*-alanine [105] is taken as an example in Fig. 1.7.

In Fig. 1.7b and c are shown powder ENDOR spectra obtained with the applied magnetic field B at the centre (b) and at the outermost high field (c) line of the EPR spectrum in Fig. 1.7a of irradiated alanine together with their simulations. The ENDOR signals were attributed mainly to $R1 = CH_3\dot{C}HCOOH$ in (b) and $R2 = H_3N^+\dot{C}(CH_3)COO^-$ in (c) [105].

A possible reason for the disagreement between the relative intensities of the experimental and simulated curves is that the influence of relaxation is not taken into account in the simulations. The line positions are, however, in good agreement. The stick spectra represent the assigned *hfc* tensor principal values as deduced from the previous single crystal study. The simulations were performed with the program ENDOR-F2 described briefly in Sect. 1.3.2, in more detail in [58].

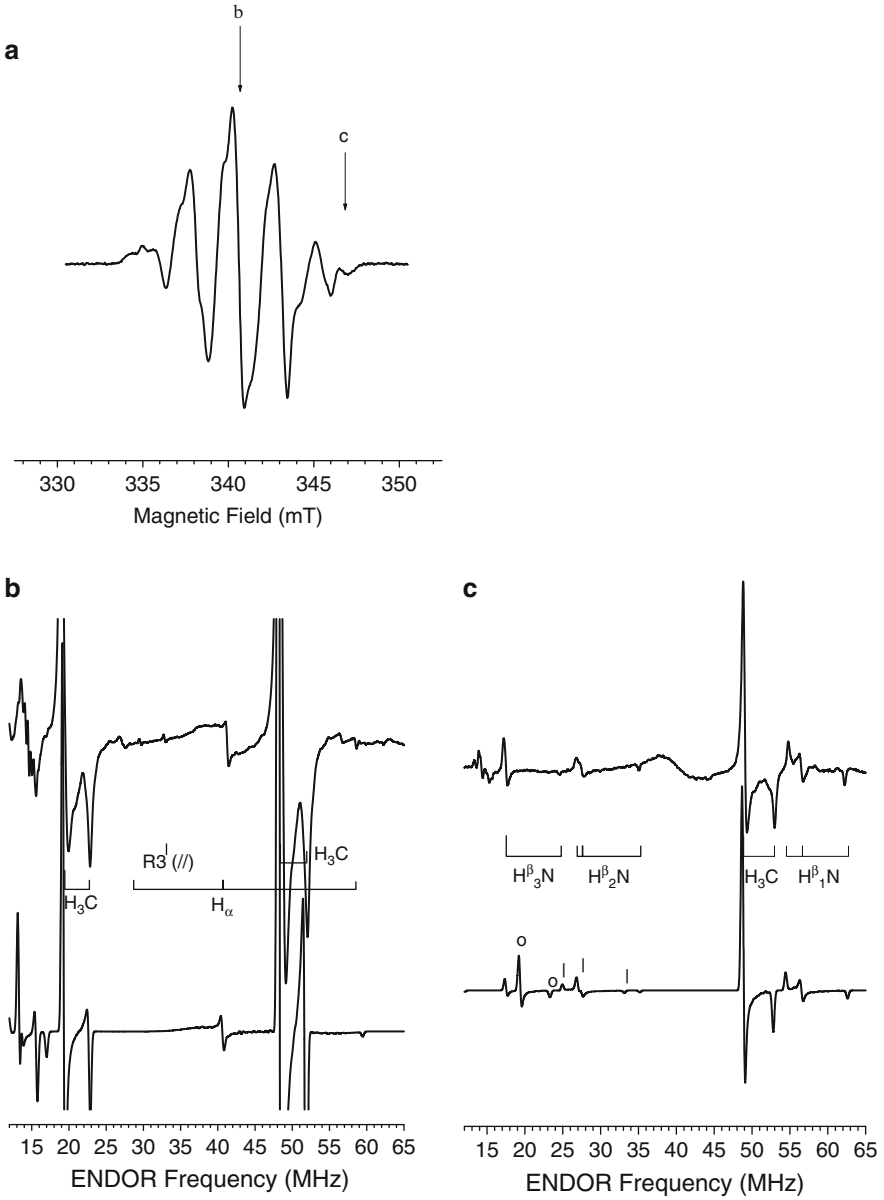

Fig. 1.7 (**a**) First-derivative X-band EPR spectrum from a polycrystalline sample of alanine x-irradiated at 295 K and measured at 221 K. The arrows indicate field positions of ENDOR spectra in (**b**) and (**c**). (**b**) Experimental (*top*) and simulated powder ENDOR spectrum due to radical R1 at 221 K. The experimental spectrum was obtained by saturating the central EPR line at arrow "b" in (**a**). (**c**) Experimental (*top*) and simulated powder ENDOR spectrum due to radical R2 at 221 K. The experimental spectrum was obtained by saturating the EPR line at arrow "c" in (a). (Adapted from Ref. [105] with kind permission of © The American Chemical Society 2002)

Solvation Structure. The resolution of hyperfine structure by ENDOR is a well-established method to obtain the structure of the trapping sites of paramagnetic species in work on single crystals. Information about the local geometry of ions or molecules surrounding the species can also be obtained from powder spectra. The ^{7}Li *hfc* tensors deduced from simulations of the powder spectra of an irradiated powder sample of lithium formate employed as an EPR-dosimeter agreed for instance well with those obtained from a single crystal study [106]. The observed stability of CO_2^- radicals formed by X-irradiation was attributed to the solvation by surrounding Li^+-ions. A limitation of the analysis was that the directions of the principal axes for the hyperfine couplings could not be obtained since the *g*-anisotropy was insufficient for angular selection to occur. The shape of the experimental powder ENDOR spectrum in [106] was for example reproduced by simulating the individual contributions from each ^{7}Li and was insensitive to the relative orientation of the tensor axes. The analysis of the experimental spectra was therefore combined with theoretical modelling.

Surface Complex Structures. The analysis of orientation-selective ENDOR experiments benefits from the improved resolution of the different *g*-components at high field, *e.g.* at W-band. This procedure was well illustrated by work to clarify the structures of the adsorption complexes of nitric oxide (NO) interacting with metal ions in zeolites. These structures are of interest from an applied view to elucidate the catalytic decomposition of NO into N_2 and O_2 over transition metal ion-exchanged zeolites. Complexes with alkali-metal ions such as Na^+—NO were recently re-examined with high field EPR, pulsed ENDOR and ESEEM methods. The readers are referred to the original works [65, 66] and a recent monograph [69] for more details.

1.3.4 EPR and ENDOR Simulation Software

Computer methods for the analysis of less resolved spectra were developed and applied at an early stage for $S = ½$ complexes [107]. Simulations were also necessary to analyse EPR spectra of systems containing several nuclei. Definite procedures for the simulation of EPR spectra of radicals of this type in amorphous solid samples were published already in 1965 [36]. Advanced simulation methods are required for $S = ½$ species containing nuclei with $I \geq 1$ featuring hyperfine and *nqc* nuclear quadrupole couplings of comparable magnitudes as realised in early work [72]. Recently developed free-ware and commercial software for simulations of systems with arbitrary electron and nuclear spin values are presented in Table 1.3, with notes based on the descriptions by the developers. Some previously commonly used programs [36, 48] were excluded as they have not been maintained. The programs of the general type are usually applicable both for EPR and ENDOR simulations. Exact calculations can be performed with several of the recently developed programs. Those programs can also handle systems with S>½. With some of the programs an automatic fitting can be made to obtain the *g*- and *hfc* tensors of an experimental powder EPR spectrum. The references in Table 1.3 may

be consulted for details. Hyperfine enhancement and angular selection effects are taken into account in the programs dedicated to the simulation of powder ENDOR spectra. Several commercial and free-ware program packages can be downloaded electronically, where updates are also reported.

1.4 Saturation Properties of Radicals

CW-microwave saturation studies were performed at an early stage to obtain the spin–lattice and spin-spin relaxation times of paramagnetic centres in inorganic solids [109–112]. Similar investigations of radicals trapped in frozen glasses and organic solids were also made at an early stage [113, 114]. The interest in this old method has been revived in several new applications of quantitative EPR. The microwave saturation properties are for instance of interest for the performance of potential dosimeter materials and may be used to characterize the radicals found in products that have been treated by irradiation. Such studies often involve measurements at high microwave power to increase the sensitivity. An automatic fitting procedure of saturation curves is described in Sect. 1.4.1. Methods to predict the EPR line shape at saturation are outlined in Sect. 1.4.2, taking into account the different saturation properties of allowed ($\Delta m_{\mathrm{I}} = 0$) and forbidden ($\Delta m_{\mathrm{I}} = 1$) hyperfine lines.

1.4.1 Relaxation Times

Two limiting cases termed homogeneous and inhomogeneous broadening give rise to different shapes of the saturation curves [109, 110]. In the first case the resulting EPR absorption is a Lorentz function, $L(\mathrm{B})$ in (1.36). The quantity t equals one in the limit of no saturation. It increases with the microwave power, causing an increase by the factor t of the line-width. The Lorentz shape usually occurs in liquids, while an inhomogeneous line often observed in solid samples is assumed to be an envelope of narrow homogeneous lines, with the envelope approximated by a Gauss function, $G(\mathrm{B})$ in (1.36). The corresponding widths are denoted ΔB_L and ΔB_G, respectively.

$$L(B) \propto \frac{1}{t^2 + \left(\frac{B-B_0}{\Delta B_L}\right)^2}, \quad G(B) \propto e^{-\left(\frac{B-B_0}{\Delta B_G}\right)^2} \tag{1.36}$$

The first derivative amplitudes of homogeneous (A_{hom}) and inhomogeneous (A_{Inhom}) lines as function of microwave power P with P_0 as a relaxation dependent parameter are obtained from (1.37):

$$A_{Hom.} \propto \frac{\sqrt{P}}{(1 + \frac{P}{P_0})^{3/2}}, \quad A_{In\,\mathrm{hom.}} \propto \frac{\sqrt{P}}{\sqrt{1 + \frac{P}{P_0}}} \tag{1.37}$$

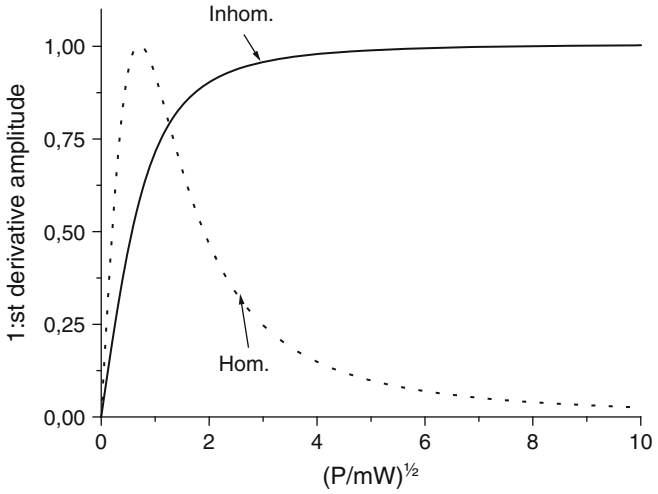

Fig. 1.8 Schematic shapes of saturation curves for homogeneous and inhomogeneous EPR-lines (Adapted from Ref. [69] with kind permission of © Springer 2011)

The amplitude can reach a maximum at a particular microwave power and approach zero at saturation for a homogeneous line or come to a constant level in the inhomogeneous case, Fig. 1.8.

One detail that is occasionally overlooked is that the power dependence of a homogeneously broadened line is different for the absorption and the first derivative. The maximum amplitude of the derivative occurs at $P = P_0/2$, while the absorption signal reaches a maximum at $P = P_0$. General equations for the power dependence of higher derivatives have been obtained [115]. The power dependence of an inhomogeneously broadened line does not depend on if the spectrum is in absorption or derivative mode, however.

It is often observed that a fitting of the data cannot be made to any of the two limiting cases. Two methods are proposed to handle this case. In the first the amplitude is assumed to be:

$$A \propto \frac{\sqrt{P}}{\left(1 + \frac{P}{P_o}\right)^{\alpha}} \tag{1.38}$$

where a reasonable range for the empirical parameter α is $½ \leq \alpha \leq 3/2$, when the first derivative is recorded. The estimated value of $\alpha = 0.83 \pm 0.01$ obtained by employing a least squares fit of Eq. (1.38) to the saturation curve data for a γ-irradiated glycyl-glycine powder sample [49] indicated that an intermediate situation between homogeneous and inhomogeneous saturation occurs. This might imply that the assumption of a Lorentzian line-width much smaller than the Gaussian width is not valid.

The limitation with this analysis is that it mainly serves to characterise saturation curves with a few phenomenological parameters. When values of T_1 and T_2 are required the analysis must be modified. Several variants of similar methods have been developed for this case. Castner calculated the amplitude of the absorption signal as a function of the microwave field strength [110]. The line-shape was a convolution of a Gaussian with a Lorentzian function. Maruani extended Castner's method to multiple-level systems (S > ½) and applied the analysis to polycrystalline systems using graphical methods [112]. These methods were designed for the case when absorption curves could be obtained but were also applied to the analysis of derivative spectra, in cases where the difference between the saturation behaviour of the absorption and the derivative was small [114]. Zhidkov et al. have taken into account the effect of field modulation to obtain saturation curves for the derivative signal of Lorentzian spin packets with a Gaussian or Lorentzian distribution [111]. Formulae for the first derivative amplitude were developed. The following numerical procedure makes use of all measured data, rather than the few used in earlier treatments to obtain the relaxation times T_1 and T_2, alternatively T_2 and the microwave power P_0 at saturation [116].

1.4.1.1 Fitting to Microwave Saturation Curves

The method to obtain relaxation times from CW microwave saturation measurements for an inhomogenously broadened line in [116] was based on the assumption that the EPR line shape is a convolution of a Gauss and a Lorentz function [109–112], i.e. the Voigt function g(r) in (1.39). The function was evaluated by a standard procedure [117], while its derivative $g^{'}$(r) employed in the fitting to the experimental peak-peak amplitude (A_{pp} in Fig. 1.9) was obtained numerically.

$$g(r) \propto \int_{-\infty}^{\infty} \frac{e^{-a^2 r^2}}{t^2 + (r - r')^2} dr' \tag{1.39}$$

The parameters t^2 and a affecting the shape of the saturation curve are given by (1.40), where the gyromagnetic ratio γ, the amplitude of the microwave magnetic field B_1, the transition probability β and the spin–lattice and spin-spin relaxation times T_1 and T_2 have been introduced.

$$t^2 = 1 + \gamma^2 B_1^2 \beta T_1 T_2 = 1 + s^2, a = \frac{\Delta B_L}{\Delta B_G} \tag{1.40}$$

The amplitude is related to the input microwave power as in (1.41).

$$B_1 = k\sqrt{Q_L P} = K\sqrt{P} \tag{1.41}$$

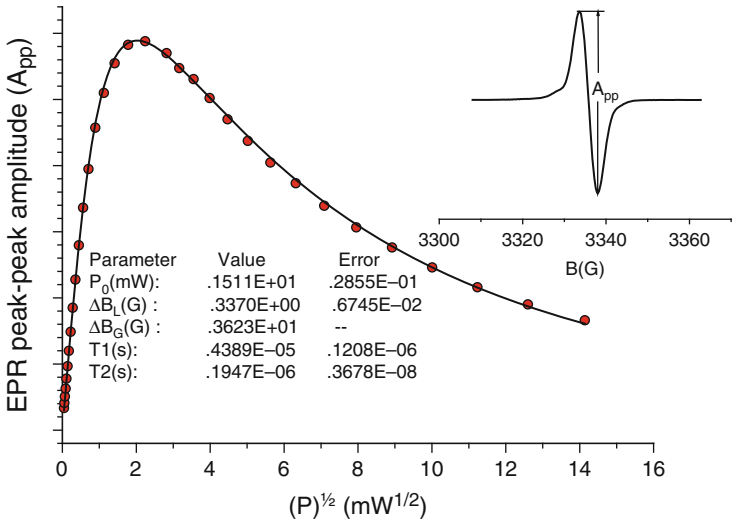

Fig. 1.9 Experimental (•) and theoretical (—) *saturation curves* (Data provided by Prof. E. Sagstuen) obtained as the peak-peak amplitudes A_{pp} (*inset*) against $\sqrt{P}$ (P = microwave power) for $\dot{S}O_3^-$ radicals trapped in an X-irradiated powder of $(NH_4)_2S_2O_6$

The value of the constant K is often difficult to estimate depending on an uncertainty in the quality factor Q_L with the sample inserted, therefore the quantity P_0 was introduced:

$$P_0 = \frac{1}{K^2\gamma^2\beta T_1 T_2} \tag{1.42}$$

The values of P_0 and ΔB_L obtained by a non-linear least squares fit to the experimental saturation curve were employed in (1.43) to calculate the relaxation times for a system with $\beta = 1$.

$$T_1 = \frac{\Delta B_L}{K^2\gamma P_0}, \quad T_2 = \frac{1}{\gamma \Delta B_L} \tag{1.43}$$

The saturation curves must be recorded under slow passage conditions, that is, conditions such that the time between successive field modulation cycles is sufficiently long for each spin packet to relax between cycles. The spin system is then continually in thermal equilibrium and the true line shape is observed. A convenient formulation of the slow passage condition [118] is given by the expression (1.44), where ν_m is the modulation frequency and B_m is the modulation amplitude.

$$2\pi\nu_m B_m << \Delta B_L / T_1 \tag{1.44}$$

CW-EPR spectra are usually recorded with $\nu_m = 100$ kHz, but to obtain reliable values of relaxation times it is preferable to use the lowest modulation frequency available on the instrument.

The method has been employed to analyze the microwave saturation properties of materials of interest in EPR-dosimetry. In this context the parameters P_0, ΔB_L, and ΔB_G obtained from the fit schematically shown in Fig. 1.9 are usually the most relevant. A comparison of the corresponding relaxation times obtained by this method with those obtained by pulsed EPR is not straight-forward, however. The relaxation times previously obtained by CW saturation of the radiation-induced radicals in glycyl-glycine [119], were for instance probably affected by spectral diffusion processes [120]. Biexponential decay was frequently observed in the pulsed measurements [120–122], while slow passage conditions might not always have been achieved in the CW experiments. A comparison of data for some systems of interest as EPR dosimeters [49] nevertheless indicated that the shortest relaxation times obtained in pulsed experiments could be roughly estimated using the CW-method.

1.4.2 Microwave Power Effects on EPR Spectral Shape

To achieve high sensitivity in CW-EPR it is advantageous to apply high microwave power. Under microwave saturation conditions the intensity of $\Delta m_I = 1$ lines, particularly from distant protons, can increase considerably. The spectral shape is affected, which introduces uncertainties in the read-out of the intensity. It is therefore an advantage if the effects of power saturation can be taken into account by simulation. The theory for microwave saturation has proved useful also to simulate spectra of radicals under saturation conditions. Two approaches have been attempted [123, 124].

In the first method [123] the influence of microwave saturation was taken into account by the saturation factor $(1 + \beta_l P/P_0)^{-\alpha}$ for each transition (l) with transition probability β_l in a spectrum of L lines in Eq. (1.45):

$$S(B, P) = \sum_{l=1}^{L} \frac{\beta_l}{(1 + \beta_l P/P_0)^{\alpha}} G\left(\frac{B - B_l}{\Delta B_G}\right) \tag{1.45}$$

A Gaussian line-shape G of line-width ΔB_G that is unaffected by saturation was employed, i.e. inhomogeneous broadening was assumed.

The experimental and simulated X-band spectra of the radical $\dot{C}H(COOH)_2$ in an X-irradiated malonic acid single crystal are seen to be in agreement over a wide microwave power range, Fig. 1.10a. The saturation factor accounts for the difference in saturation between allowed and spin flip lines, the latter being caused by weak anisotropic hyperfine coupling with protons at neighbour malonic acid molecules.

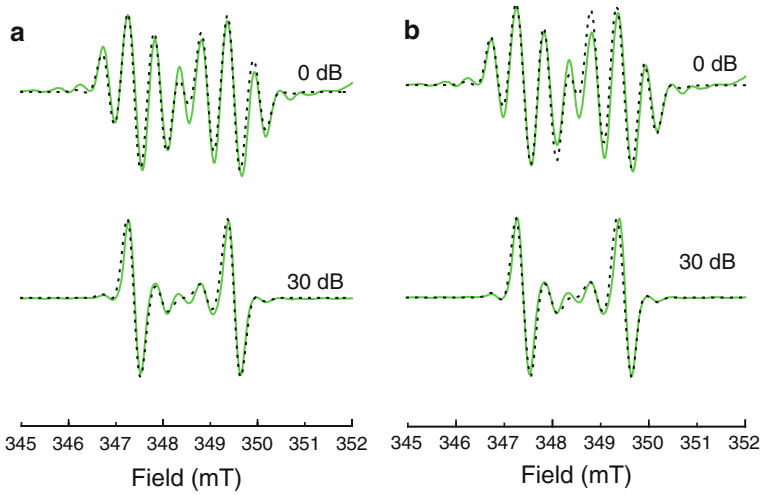

Fig. 1.10 X–band EPR spectra of X-irradiated malonic acid single crystal recorded at room temperature with magnetic field at $\theta = 49.9°$, $\phi = -39.8°$ in the axes system in [124], (**a**) with simulations (*dashed curves*) using (1.45) with $\alpha = 0.68$, $P_0 = 0.1$ mW, $\Delta B_G = 3.0$ G, (**b**) using (1.39) with $\Delta B_G = 2.0$ G, $\Delta B_L = 0.018$ G, $P_0 = 0.04$ mW

In the second method a theory utilising the saturated Voigt line shape function (1.39) was employed as a physically more satisfactory method for the simulation of EPR spectra at saturation [124]. The simulations with this method were also in good agreement with the experimental data, Fig. 1.10b.

1.4.3 Software for Microwave Saturation Analysis

Software for the analysis of microwave saturation data are rarely reported in recent literature although related issues have been considered from a theoretical point of view [125]. The programs described in [116, 123, 124] were therefore employed in the present work. We refer to [116] for details about software (MarLun_fit) for the analysis of saturation curves. The simulation programs KvaSat [123] and MarSat [124] were adapted from locally used software [48, 126].

1.5 Motional Effects

The internal motion, mobility and kinetics of radicals in solid matrices can be experimentally examined at different temperatures by conventional CW-EPR, while the theoretical analysis can be quite demanding. Some examples are presented below.

1.5.1 Internal Motion

Intramolecular motions occur frequently even in free radicals trapped in solids. The analysis is in general made by comparison with theoretical spectra obtained when different configurations of the radical interchange. Density matrix theory within the Liouville formalism has usually been employed. The EPR spectra can in favourable cases be analyzed by software designed for the simulation of chemical exchange in liquids [30]. The procedure is applicable when the hyperfine coupling constants of the nuclei involved in the dynamics are isotropic. This applies, approximately, for radicals with protons in β-position with respect to the radical centre, and for cyclic radicals undergoing ring puckering. In the opposite case with anisotropic hyperfine structure non-perturbative simulations of the temperature-dependent EPR line-shapes were employed in early studies of mobile end-groups in simple radicals [127]. Powder spectra can also be analysed by this method, treated in detail in Chap. 3. A complementary use of simulations of the temperature dependent EPR spectra by the density matrix formalism and potential energy surface calculations has recently been proposed as a means to obtain a detailed picture of the motions of larger radicals [128].

Recent studies of the dynamics of radicals and radical ions trapped in matrices are reviewed in Chap. 4. Earlier studies of the dynamics of cyclic radicals are therefore only briefly summarized below, while more recent studies of the matrix dependent activation barriers for different types of internal motion of cation radicals trapped in zeolites are treated in more detail. The analysis developed in [30] for exchange-broadened isotropic EPR spectra could be applied even when the substituents were attached to a radical centre containing nuclei with anisotropic *hfc*, since those nuclei were usually not involved in the dynamics.

Cyclic Radicals. Ring puckering may occur for the twisted or envelope conformations of five-membered ring radicals. The spectral changes with temperature of cation radicals of tetrahydrofuran (THF) produced in γ-irradiated solid solutions of trichlorofluoromethane were accordingly accounted for in terms of ring puckering with an activation energy of 6.9 kJ/mol in an initial work [129], in agreement with a later study of perdeuterated THF cation radicals [82]. Recent studies of related systems have mainly concentrated on the formation mechanism, structure and decomposition reactions of cation radicals, based on quantum chemical calculations and low-temperature EPR results. However, ring puckering was also reported to occur in the tetrahydropyran radical cation trapped in the frozen CF_3CCl_3 matrix [130].

Chemical exchange assigned to puckering motion and/or conversion between two conformations of a twisted structure could account for the reversible changes of the EPR spectra of the five-membered radical species with activation energies in the range 5–15 kJ/mol. The conversion between the dynamic structures of radical cations of cyclohexane and related molecules with low activation energy discussed in Chap. 4 might occur by site-jumping on potential surfaces with shallow energy barriers, while for the five-membered rings reorganisation of the molecular structure is required, particularly for the proposed puckering motion.

The internal motion of some heterocyclic cation- and neutral radical species containing nitrogen was interpreted in terms of the conversion between two energetically equivalent structures. The temperature dependent changes of the EPR line-shape were in several cases governed by the averaging of the ^{14}N hyperfine anisotropy, attributed to the reorientation of the principal axes between two twisted structures. It was confirmed that the so-called modified Heinzer method is not applicable in those cases. We refer to the original papers [131–141] for details.

Modified Heinzer Method. In contrast to the Heinzer model for isotropic spectra, a decomposition of the Liouville matrix in blocks of size '*n* x *n*' where *n* is the number of sites has not proved possible when the *hfc* is anisotropic. In view of the associated higher demands on computer power an approach has been attempted, in which the small block-size could be retained [132, 140, 141]. In this model the anisotropic *hfc* was treated as an effective coupling as in a rigid structure [36] for each site. The modified version of the Heinzer program also allows to use different linewidths for lines with different values of the nuclear quantum number.

As mentioned, the treatment is insufficient for cases with different orientations of the principal axes between different sites, but is applicable to systems in which the anisotropic couplings are not affected by the dynamics. Several cases of dynamics in zeolites mentioned below have been studied recently by this so-called modified Heinzer method.

Dynamics of Radicals in Zeolites. The structure and reactivity of radicals on surfaces have been considered in previous works, see *e.g.* [16, 101] for reviews. Until recently, detailed studies of the dynamics of radicals trapped in the cages and channels of zeolites have not been made, however. Liu et al. found that the confined space affected the stability and motion of radicals trapped at those cavities and channels [142–145]. The radicals were generated by γ-irradiation of the zeolites, containing amine molecules used as templates during synthesis of the zeolite.

$[(CH_3)_3N]^{+\bullet}$ and $[(CH_3)_3NCH_2]^{+\bullet}$ radical cations in γ-irradiated Al-offretite, SAPO-37 and SAPO-42 show different stability and dynamics. The strongly temperature dependent EPR spectra observed in the temperature range 140–270 K for the $[(CH_3)_3NCH_2]^{+\bullet}$ species in Al-offretite and SAPO-42 were attributed to methyl-group rotation about the C-N bond, Fig. 1.11. The methylene group, with anisotropic *hfc* due to the two H-atoms, did not take part in the exchange process. Quite good fits were obtained in simulations, as shown in Fig. 1.12. The dynamics involved a three-site jump model for each methyl group, combined with free rotation of the methylene group about the N–CH_2 bond. The exchange rates were in the order SAPO-37 < Al-offretite <SAPO-42 in the temperature range of 110–300 K. In SAPO-37 the size of the sodalite cage (∼6 Å) was too small to permit exchange rates that are observable by CW-EPR (*ca.* 10^7 s^{-1}), whereas in Al-offretite with wider cages (∼6 × 7.4 Å) and main channels (∼6.5 Å) and in SAPO-42 with large (∼11 Å) channels internal motion is feasible because of less interaction with the matrix. The activation energy in Al-offretite was $E_a = 9$ kJ/mol, and in SAPO-42 $E_a = 11$ kJ/mol. Strongly temperature dependent EPR spectral line-

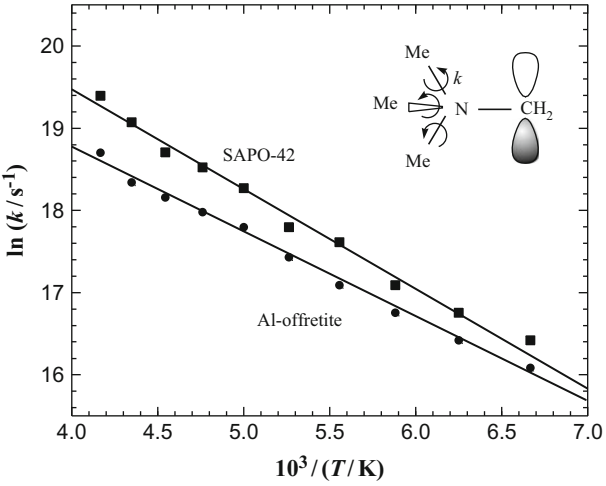

Fig. 1.11 Arrhenius plots of the exchange rates, ln k (s^{-1}) *vs.* T^{-1} (K^{-1}) for $[(CH_3)_3NCH_2]^{+\bullet}$ in SAPO-42 (■) and Al-offretite (●) (Adapted from Ref. [143] with kind permission of © The Royal Society of Chemistry 2000)

shapes were also apparent in the range 77–300 K for the triethylamine (Et_3N) and tripropylamine (Pr_3N) radical cations generated in γ-irradiated $AlPO_4$-5 from the corresponding templates. The anisotropic ^{14}N hyperfine couplings $A_{||} = 4.4$ mT, $A_{\perp} = 0$ mT in $Et_3N^{+\cdot}$ and $A_{||} = 4.0$ mT, $A_{\perp} = 0$ mT in $Pr_3N^{+\cdot}$were constant, *i.e.* not averaged by the motion in the temperature range 77–300 K. A two-site model with exchanging methylene protons at the C_β position accounted for the temperature dependence of the EPR spectra in both cases, when analysed with the modified Heinzer program. The activation energies $E_a = 9.1$ kJ/mol for $Et_3N^{+\cdot}$ and $E_a = 11.4$ kJ/mol for $Pr_3N^{+\cdot}$correlated well with the potential energy curves for the hindered rotation of the methylene groups although the calculated value at the UHF/3-21G* level for $Pr_3N^{+\cdot}$was slightly lower than the experimental one [142, 144]. A possible explanation is that the $Et_3N^{+\cdot}$ diameter is smaller than the ring channel size while $Pr_3N^{+\cdot}$has the same diameter as the channel, and therefore may interact with the channel wall.

In conclusion the CW EPR method allows studies of internal motion not only in the liquid phase as studied before but also of radicals trapped in the solids. When the radicals are trapped in zeolite matrices the size of the channels or cages affects the dynamics. Similar effects may also occur in other matrices, although the results are less clear. The Heinzer method [30] is still applicable, even when some of the hyperfine couplings are anisotropic, provided that the corresponding nuclei do not take part in the exchange process.

Internal Motion Studied by ENDOR. Brustolon and coworkers have developed ENDOR methods [146–150] for studies of rotation rates of methyl groups and the libration of bonds at β-position of the radical. The temperature dependence of β–H

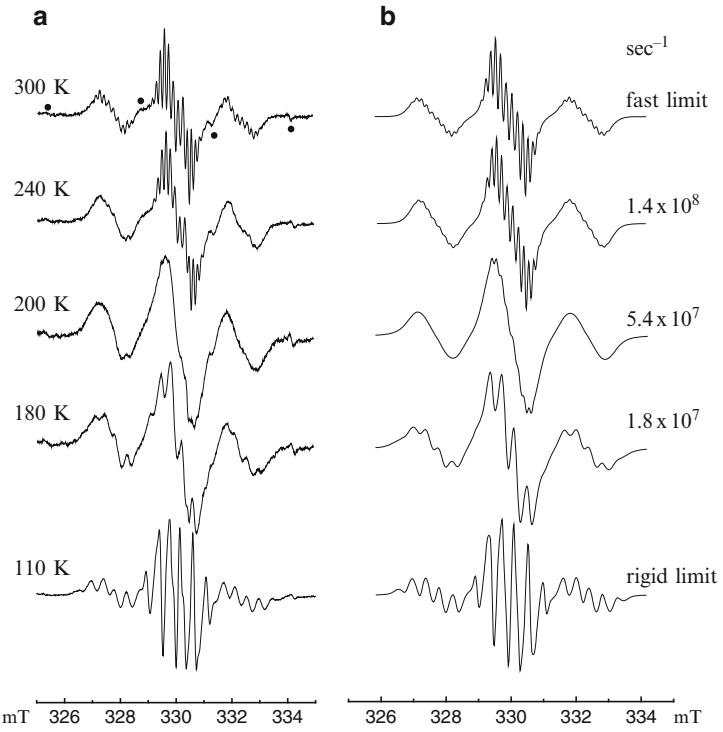

Fig. 1.12 (**a**) Temperature dependent EPR spectra of $[(CH_3)_3NCH_2]^{+\bullet}$ generated and stabilized in γ-irradiated Al-offretite. The lines marked (•) are attributed to $[(CH_3)_3N]^{+\bullet}$. (**b**) EPR spectra simulated using the three-site exchange model for the methyl hydrogen rotation of $[(CH_3)_3NCH_2]^{+\bullet}$. The best-fit m_I and temperature dependent linewidths employed were: $\Delta B_{pp} = 0.12$ mT ($m_I = \pm 1$) and 0.08 mT ($m_I = 0$) for the 300 K spectrum; $\Delta B_{pp} = 0.20$ mT ($m_I = \pm 1$) and 0.10 mT ($m_I = 0$) for the spectra above 200 K; $\Delta B_{pp} = 0.20$ mT ($m_I = \pm 1$) and 0.20 mT ($m_I = 0$) below 200 K. The other EPR parameters used are the same as those of $[(CH_3)_3NCH_2]^{+\bullet}$ in the SAPO-42 system [144]. (1 mT = 10 G) (Adapted from Ref. [143] with kind permission of © The Royal Society of Chemistry 2000)

hfc in heterocyclic radicals obtained by X-irradiation of glutarimide has for example been analysed by the latter method, see [49, 151, 152] and Chap. 3 for additional details.

1.5.2 Diffusion of Radicals

Spin labels *i.e.* stable free radicals containing a nitroxide (−NO) group covalently linked to the object under study are frequently employed to examine the dynamics of polymers and biopolymers. The molecular motion at particular sites of the polymer has been investigated by this method, employing CW-EPR measurements at

different temperatures. Spin probes as defined in [153] are paramagnetic molecules that add non-covalently and may diffuse in the medium. The spin-probe method can also detect molecular motions of solid polymers from an analysis of the EPR spectra of the probe moving with the polymer chain segment. Computer simulations are frequently employed to extract information of the mobility in the low-motional region. We refer to the literature for information about this topic and of modern applications in the study of polymers [18] and biopolymers [31, 154] using spin labels and spin probes.

Nitrogen oxides have been employed in studies by Shiotani and coworkers [68, 155–159] of diffusion dynamics in heterogeneous systems. EPR spectra of NO_2 adsorbed on zeolites were obtained from 4 K up to the temperature at which excessive broadening sets in. The spectra were analyzed based on the slow-motion EPR theory developed by Schneider and Freed [31]. The type and degree of motion depended on the properties of the zeolite. Rotational diffusion of NO_2 predominated in X- and Y-zeolites. In other cases like in Na-ZSM5, Na-mordenite and K-and L-type zeolites the simulations did not agree well with the experimental spectra, however, and the possibility of translational diffusion along the zeolite channels was considered. Heisenberg spin exchange can then occur between the NO_2 molecules. In Na-ZSM-5 zeolites with different SiO_2/Al_2O_3 ratios for instance, the corresponding EPR spectra of NO_2 at 10 K differed considerably. At lower Al_2O_3 content the concentration of Na^+ ions is higher, and it was assumed that the mobility of NO_2 was hindered by the presence of the exchangeable cations. The spectral broadening increased with temperature, depended on the structure and the size of the channels, being more pronounced in multiple-channel zeolites than in single-channel ones, and also increased with increasing channel size. These observations were consistent with the assumption that the exchange rate increased with increasing diffusion speed. The simulated slow-motional EPR spectra differed significantly from the experimental ones in several other cases, however. A possible explanation is that diffusion occurs with a distribution of rates. A procedure to analyse this case has been described [156]. A series of theoretical slow-motional spectra with different exchange rates was calculated. Next, a principal component analysis of the spectra was made to obtain a collection of eigenspectra and corresponding eigenvalues [160]. The spectra with the 4–5 largest eigenvalues were then used as a basis to approximate the experimental spectra. Finally, the weight of each rate in the experimental spectrum was calculated. The fit to the experimental spectra obtained at different temperatures was much improved, indicating that the assumption of a distribution of rates at each temperature was reasonable. The width of the distribution could also be estimated. In the NO_2/mordenite system for example the distribution was relatively narrow at temperatures below 110 K and broadens above 160 K. Similar EPR methods have been applied to the distribution of radical species in irradiated DNA [161]. One advantage with this technique over other methods is that the number of eigenspectra is an order of magnitude fewer than the number of slow-motional spectra. The number of studies in the EPR field with this and related techniques is, however, small, and it may be too early to conclude if the method is of general applicability in analysing motional effects by EPR.

Adsorption-Desorption. The studies by Pöppl and coworkers contain several EPR applications of general interest for the characterisation of adsorption and desorption processes in zeolites [65, 66]. Nitric oxide exhibits orbital degeneracy in the gaseous state. Upon adsorption the degeneracy is lifted and it is possible to observe a conventional EPR spectrum, with anisotropic g-factors that depend on the strength of the adsorption. Experimentally, the difference between the g-factors is small, resulting in low resolution at X-band. Measurements were therefore made at W-band to obtain the g-tensor for NO in Na-A and Na-ZSM-5 zeolites. Only one component of the ^{14}N *hfc* tensor could be resolved by EPR, while the smaller couplings perpendicular to the N–O axis were determined with ENDOR. It was also possible to observe interaction with Na^+ ions by ENDOR, and from this a geometric model of the NO–Na^+ complex was constructed. An EPR method to study the desorption behaviour of NO on ZSM-5 and Na-A was developed in which desorbed NO was detected in the gas phase above a certain temperature. The desorption activation energies determined from the temperature dependent line-width of the adsorbed NO followed the relation E_A (Na-ZSM-5)<E_A (Na-A)≪E_A (H-ZSM-5) reflecting the difference between the adsorption strength at an aluminum center and the weak interaction with the sodium cation. In all cases the magnitude of the activation energies and the low desorption temperatures showed that the NO molecules were physically adsorbed. The detailed information [65, 66] that has been collected for the adsorption-desorption of NO on zeolites using EPR is remarkable.

A peculiar property of the Na-A zeolite/NO system is the formation of NO-NO radical pairs separated by about 4.5 Å [162, 163]. The two NO molecules are probably aligned along their N-O bond axes. A confirmation of this model is complicated by the difficulty of simulating the EPR spectra when the axes are not aligned. This difficulty seems to have been overcome in modern software (see Chap. 5) which should open the possibility to deduce the structure of radical pairs in this and similar systems by simulations.

1.5.3 Free Radical Kinetics in Solids

The kinetics of free radical reactions has been investigated in several EPR applications. The mechanisms of relevance for the design of polymer processing, for the deterioration and mechanical fracture of the polymers, and for the polymerization in the solid state have for instance been elucidated by kinetic studies [164]. The intermediate radical species in solid polymers have a long lifetime. The variation of the intensity and the spectrum shape with time can therefore be readily obtained by CW-EPR. Measurements of the lifetime of radicals in materials exposed to ionizing radiation reviewed in Chap. 8 of Vol. II, is of relevance for the control of food, for geological dating, and for fundamental studies of dispersive kinetics [165] etc.

Table 1.4 Software for analysis of motional effects in CW-EPR spectra

Program	Order	Available from	Code
EXREXN	1	QCPE[a]	Fortran
XEMR	Exact	http://sourceforge.net/projects/xemr/	
EPRL[b], PC[c], PC.NEW[d], NLSL. MOMD[e]	1	ftp.ccmr.cornell.edu/pub/freed	Fortran
EasySpin	Exact	http://www.easyspin.org/	Matlab 6.5.1

[a]The QCPE services seem to be suspended, and the original program might therefore not be available. Heinzer's intramolecular exchange model is, however, implemented in the XEMR software package. A slightly modified stand-alone version of ESREXN used for the preparation of this chapter can be obtained by contacting liuwei08@dlut.edu.cn

[b]The basic simulation programs for CW spectrum calculation including the program EPRBL used to determine the truncated basis sets

[c]The original PC version of the CW spectrum simulation programs

[d]A version of the NLSL programs suitable for running on a PC with WINDOWS 98/2000/NT/XP

[e]The least squares version of the program described by Budil et al. [168]

The decay of radicals in solid matrices was analyzed by the kinetic equations applicable to gases and liquids in early studies, see e.g. [166]. A more realistic scheme involving a diffusion-controlled bimolecular reaction proposed for the decay reaction of the polymer radicals [164] is of the form (1.46):

$$\frac{C_0}{C} = 1 + A\sqrt{t} + Bt \tag{1.46}$$

C_0 and C are the concentrations at time zero and t, respectively. Values of A and B were determined by computer modeling, from which the diffusion constant was estimated employing relations for A and B obtained by theory [164].

1.5.4 Software for the EPR Analysis of Motional Effects

Different software packages have been employed for the analysis of internal motion and for the motion of the entire radical. Procedures for the latter analysis in the slow motional region are well documented, while computer programs for the former are not always available or are in obsolete code. Commonly available software that the authors are aware of are listed in Table 1.4.

The program ESREXN [167] simulates multiline exchange- broadened EPR spectra from the coupling constants, the line widths, and the populations of the different chemical configurations. The rate constants and certain other constants are further required as part of the input data. ESREXN also makes use of the line shape equation derived by Norris. The original program might not be available. Heinzer's intramolecular exchange model is, however, implemented in the XEMR software. A slightly modified stand-alone version of ESREXN was used for the preparation of this chapter.

XEMR is a spectrum manipulation and simulation package written for Linux systems that includes Norris exchange model, and Heinzer's intramolecular exchange model in the simulation. These line-shape models can be integrated over the angular variables to obtain powder spectra.

A number of programs for the CW spectrum simulation of reorienting nitroxide radicals used as spin labels including original versions of well-known programs described in [31, 168] and their most recent updates are freely available. Relevant software packages are included in Table 1.4.

Simulation of slow-motional effects is performed in the EasySpin package with the program *chili* to obtain CW-EPR spectra of systems with one unpaired electron and one or more nuclei in the slow-motional regime. CW- EPR spectra of a slow tumbling nitroxide radical can for instance be simulated. For full details of the algorithm see [31, 169]. The EasySpin program runs with Matlab 6.5.1 or higher. It is developed and maintained by Dr. S. Stoll.

A.1 Appendix

A.1.1 Single Crystal Analysis by the Original Schonland Method

The Schon_fit program in Table 1.1 is based on the original Schonland method as a simplified replacement for software in obsolete code referred to in our previous work [49]. The variation of the g-factor in a crystal plane was analyzed by a least squares fit to the experimental data using an equation of the type (1.4), by which three tensor elements with estimated uncertainties were obtained. Measurements in three mutually orthogonal crystal planes were employed to obtain the complete tensor. The principal values were computed with uncertainties estimated by the relation (1.55) originally given in different notation in [28]. The uncertainties (1.56) of the principal directions considered in [28, 46] were not computed, however. We refer to the literature [28, 46, 170] for procedures to obtain the statistical uncertainties from the propagating errors.

The variation of the hyperfine couplings in EPR measurements can be analyzed in the same manner as for the g-factor. The influence of the nuclear Zeeman term and of possible g-anisotropy was not taken into account in the software, however. Analysis of single crystal ENDOR data to obtain *hfc*-tensors can be made assuming that the measurements were obtained at or adjusted to a fixed magnetic field. Procedures for the adjustment, see e.g. [171], were not implemented. With these simplifications the program could be compactly written (ca 50 lines of Matlab code).

Axial symmetry constraints, commonly employed in the analysis of defects in crystals of high symmetry [56], can be taken into account by applying (1.49) below. The number of parameters can then be reduced, and measurements in three crystal planes are not always required as schematically illustrated in Fig. 1.13 for the ^{33}S *hfc* of the $\dot{S}O_3^-$ radical in an X-irradiated $K_2S_2O_6$ crystal.

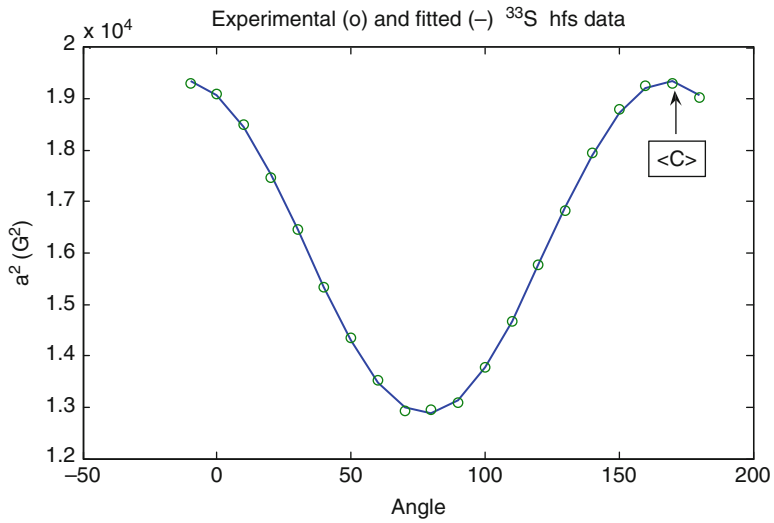

Fig. 1.13 Experimental (o) and fitted variations of a^2 (a $=^{33}$S hyperfine coupling) for a $\dot{S}O_3^-$ radical in the ac plane of $K_2S_2O_6$, X-irradiated at room temperature. The values $A_{||} = 138.9$ G, $A_\perp = 113.0$ G were obtained from an analysis of Q-band EPR measurements (Data provided by Prof. E. Sagstuen) by assuming axial symmetry about the hexagonal crystal axis <c>

A.1.1.1 Axial Symmetry

An axially symmetric *g*- or *hfc*-tensor is commonly specified by the principal values $T_\parallel$, $T_\perp$ and the direction of the symmetry axis. The tensor elements in an arbitrary system (x, y, z) are then given by (1.47):

$$T_{ij} = \delta_{ij} T_\perp + \left(T_\parallel - T_\perp\right) e_i e_j \tag{1.47}$$

with i, j = x, y, z.

The coupling parameters ($T_\parallel$, $T_\perp$) and the polar angles (θ, ϕ) for the unit vector $\mathrm{e} = (\sin\theta\cos\varphi, \sin\theta\sin\varphi, \cos\theta)$ along the symmetry axis completely determine the tensor. An alternative specification, obtained by eliminating the direction cosines of the symmetry axis in (1.47) is based on (1.48).

$$\left(T_{ii} - T_\perp\right)\left(T_{jj} - T_\perp\right) = T_{ij}^2 \tag{1.48}$$

The first alternative might be suitable for a least squares fitting to the data by a non-linear procedure, while the second can be used with the Schonland method. Assume for instance that the tensor components T_{xx}, T_{yy} and T_{xy} had been obtained from a least squares fit to the data in the xy-plane, in which case equation (1.49) applies:

$$T_\perp = \frac{T_{xx} + T_{yy}}{2} \pm \sqrt{\left(\frac{T_{xx} - T_{yy}}{2}\right)^2 + T_{xy}^2} \tag{1.49}$$

The + and – signs correspond to $T_{\parallel} < T_{\perp}$ and $T_{\parallel} \geq T_{\perp}$, respectively. An additional measurement along the z axis to obtain T_{zz} is required to calculate $T_{\parallel} = \text{trace}(\mathbf{T}) - 2T_{\perp}$. The sign ambiguity in (1.49) would be resolved by measurements in two crystal planes, both expected to show the same maximum or minimum g-value or hyperfine splitting associated with $T_{\perp}$. Expressions applicable to the yz and zx planes are obtained by cyclic permutations of the indices in Eq. (1.49).

A.1.1.2 Propagation of Errors

The probable errors in the determination of the principal values and the directions of the principal axes are usually estimated from the uncertainties of the tensor elements [28, 46, 170]. The propagation of errors derived by a first order perturbation method is reproduced below in matrix notation.

The principal values t_q and principal vectors $\mathbf{c}_q$ are obtained from the eigenvalue equation:

$$\mathbf{T}\mathbf{c}_q = t_q \mathbf{c}_q \tag{1.50}$$

Errors in the elements of the tensor $\mathbf{T}$ give rise to corresponding uncertainties in t_q and $\mathbf{c}_q$.

$$(\mathbf{T} + \Delta\mathbf{T})\left(\mathbf{c}_q + \Delta\mathbf{c}_q\right) = \left(t_q + \Delta t_q\right)\left(\mathbf{c}_q + \Delta\mathbf{c}_q\right) \tag{1.51}$$

The errors $\Delta\mathbf{c}_q$ are expressed as a linear combination (1.52) of the principal vectors.

$$\Delta\mathbf{c}_q = \sum_{s \neq q} d_s \mathbf{c}_s \tag{1.52}$$

Equation (1.53) is obtained by combining (1.50), (1.51) and (1.52), neglecting 2nd order terms:

$$\sum_{r \neq q} d_r t_r \mathbf{c}_r + \Delta\mathbf{T}\mathbf{c}_q = \Delta t_q \mathbf{c}_q + t_q \sum_{r \neq q} d_r \mathbf{c}_r \tag{1.53}$$

Equation (1.54) is derived after multiplication with $\mathbf{c}_s$, taking into account that the principal vectors are orthonormal.

$$d_s t_s + \mathbf{c}_s \Delta\mathbf{T}\mathbf{c}_q = \Delta t_q \delta_{sq} + t_q d_s \tag{1.54}$$

The errors are accordingly estimated by the expressions (1.55) and (1.56):

$$\Delta t_q = \mathbf{c}_q \Delta\mathbf{T}\mathbf{c}_q \tag{1.55}$$

$$\Delta\mathbf{c}_q = \sum_{s \neq q} \frac{\mathbf{c}_s \Delta\mathbf{T}\mathbf{c}_q}{t_q - t_s} \mathbf{c}_s \tag{1.56}$$

References

1. Carrington A, McLachlan AD (1967) Introduction to magnetic resonance with applications to chemistry and chemical physics. Harper & Row, New York
2. Wertz JE, Bolton JR (1972) Electron spin resonance: elementary theory and practical applications. McGraw-Hill Book Company, New York
3. Weil JA, Bolton JR (2007) Electron paramagnetic resonance: elementary theory and practical applications, 2nd edn. Wiley, New York
4. Atherton NM (a) (1973) Electron spin resonance: principles and applications. Ellis Horwood, Chichester; (b) (1993) Principles of electron spin resonance. Ellis Horwood, New York
5. Poole CP, Farach HA (1987) Theory of magnetic resonance, 2nd edn. Wiley, New York
6. Ayscough PB (1967) Electron spin resonance in chemistry. Methuen & Co Ltd, London
7. Bljumenfeld LA, Wojewodski WW, Semjonov AG (1966) Anwendung der paramagnetischen Elektronenresonanz in der Chemie, AkademischeVerlagsgesellschaft. Guest &Portig K-G, Leipzig
8. Gordy W (1980) Theory and applications of ESR. Wiley, New York
9. Rieger PH (2007) Electron spin resonance – analysis and interpretation. RSC Publishing, Cambridge
10. Brustolon MR, Giamello E (eds) (2009) Electron paramagnetic resonance: a practitioner's toolkit. Wiley, Hoboken
11. Atkins PW, Symons MCR (1967) The structure of inorganic radicals. An application of ESR to the study of molecular structure. Elsevier Publishing Company, Amsterdam
12. Pshezhetskii SYa, Kotov AG, Milinchuk VK, Roginski VA, Tupilov VI (1974) EPR of free radicals in radiation chemistry. Wiley, New York
13. Box HC (1977) Radiation effects, ESR and ENDOR analysis. Academic, New York
14. Yordanov ND (ed) (1992) Electron magnetic resonance in disordered systems. World Scientific, Singapore
15. Lund A, Shiotani M (eds) (1991) Radical ionic systems. Kluwer Academic Publishers, Dordrecht
16. Lund A, Rhodes C (eds) (1995) Radicals on surfaces. Kluwer Academic Publishers, Dordrecht
17. Rånby B, Rabek JF (1977) ESR spectroscopy in polymer research. Springer, Berlin
18. Schlick S (ed) (2006) Advanced ESR methods in polymer research. Wiley, Hoboken
19. Royal Society of Chemistry (1973–2010) Electron paramagnetic resonance. Thomas Graham House, Cambridge
20. Springer Materials. The Landolt-Börnstein Database, http://www.springermaterials.com/navigation
21. Bresgunov AYu, Dubinsky AA, Poluektov OG, Lebedev YaS, Prokofev AI (1992) The structure of phenoxyl radicals as studied by 2 mm band ESR. Mol Phys 75:1123–1131
22. Riedi PC, Smith GM (2002) Progress in high-field EPR. In: Royal Society of Chemistry (ed) Electron paramagnetic resonance, vol 18. Thomas Graham House, Cambridge, pp 254–303
23. Huber M (2009) Introduction to magnetic resonance methods in photosynthesis. Photosynth Res 102:305–310
24. Savitsky A, Möbius K (2009) High-field EPR. Photosynth Res 102:311–333
25. Goldfarb D (guest editor) (2009) Modern EPR spectroscopy. PCCP 11:6537–6860
26. Grinberg O, Berliner LJ (eds) (2004) Very high frequency (VHF) ESR/EPR, vol 22, Biological magnetic resonance. Kluwer Academic Publishers, Dordrecht
27. Möbius K, Savitsky A (2009) High-field EPR spectroscopy on proteins and their model systems. Royal Society of Chemistry, Cambridge
28. Schonland DS (1959) On the determination of the principal g-values in electron spin resonance. Proc Phys Soc 73:788–792

29. (a) Byberg JR, Jensen SJK, Muus LT (1966) ESR spectra from paramagnetic centers in irradiated $KClO_4$. I. The ClO_2 center. J Chem Phys 46:131–137; (b) Byberg JR (1995) Single crystal study of ClOO. Matrix effects in the EPR and IR spectra of ClOO trapped in $KClO_4$. J Phys Chem 99:13392–13396
30. Heinzer J (1971) Fast computation of exchange-broadened isotropic ESR spectra. Mol Phys 22:167–177
31. Schneider DJ, Freed JH (1989) Calculating slow-motional magnetic resonance spectra: a user's guide. In: Berliner LJ, Reuben J (eds) Spin labelling. Theory and applications, Biological Magnetic Resonance 8, vol III. Plenum, New York, pp 1–76
32. Synge JL, Griffith BA (1959) Principles of mechanics, 3rd edn. McGraw-Hill Book Company, New York, pp 259–261
33. Weil JA, Anderson YH (1961) Direct field effects in electron paramagnetic resonance (EPR) hyperfine spectra. J Chem Phys 35:1410–1417
34. Lund A, Vänngård T (1965) Note on the determination of the principal fine and hyperfine coupling constants in ESR. J Chem Phys 42:2979
35. Pake GE (1962) Paramagnetic resonance. Benjamin, New York
36. Lefebvre R, Maruani J (1965) Use of computer programs in the interpretation of electron paramagnetic resonance spectra of dilute radicals in amorphous solid samples. 1. High field treatment. X-band spectra of π-electron unconjugated hydrocarbon radicals. J Chem Phys 42:1480–1496
37. Poole CP Jr, Farach HA (1971) Influence of the nuclear Zeeman term on anisotropic hyperfine patterns in electron spin resonance. J Magn Reson 4:312–321
38. Bergene R (1977) Free radicals in pyrimidines: single crystals of dihydro-6-methyl uracil irradiated and observed at 77 K. Int J Radiat Biol 31:17–34
39. McConnell HM, Heller C, Cole T, Fessenden RW (1960) Radiation damage in organic crystals. I. $CH(COOH)_2$ in malonic acid. J Am Chem Soc 82:766–775
40. Lindgren M, Gustafsson T, Westerling J, Lund A (1986) ESR characterization of the hydroxyalkyl radical in single crystals of 1,6- hexanediol and 1,8-octanediol and crystal structure of 1,6-hexanediol. Chem Phys 106:441–446
41. Claesson O, Lund A, Jørgensen JP, Sagstuen E (1980) Electron spin resonance of irradiated crystals of 2-thiouracil; hyperfine coupling tensor for nuclei with $I = ½$. J Magn Reson 41:229–239
42. Iwasaki M (1974) Second-order perturbation treatment of the general spin Hamiltonian in an arbitrary coordinate system. J Magn Reson 16:417–423
43. Thuomas KÅ, Lund A (1975) Evaluation of hyperfine and quadrupole tensors from ENDOR measurements on single crystals. J Magn Reson 18:12–21
44. Sørnes AR, Sagstuen E, Lund A (1995) ^{14}N Quadrupole and hyperconjugative hyperfine coupling in 2-aminoethyl hydrogen sulfate X-irradiated at 295 K. Single crystal ENDOR analysis, UHF-INDO MO calculations. J Phys Chem 99:16867–16876
45. Vrielinck H, DeCooman H, Tarpan MA, Sagstuen E, Waroquier M, Callens F (2008) Schonland ambiguity in the electron nuclear double resonance analysis of hyperfine interactions: principles and practice. J Magn Reson 195:196–205
46. (a) Nelson WH (1980) Estimation of errors in eigenvectors and eigenvalues from magnetic resonance results by use of linear data-fitting techniques. J Magn Reson 38:71–78; (b) Nelson WH, Nave CR (1981) ESR and ENDOR studies of radicals produced in hydroxyproline single crystals by x-irradiation at low temperature. J Chem Phys 74:2710–2716
47. Thuomas KÅ, Lund A (1976) Analysis of EPR with large quadrupole interaction. J Magn Reson 22:315–325
48. Lund A, Erickson R (1998) EPR and ENDOR simulations for disordered systems: the balance between efficiency and accuracy. Acta Chem Scand 52:261–274
49. Lund A, Shiotani M (eds) (2003) EPR of free radicals in solids. Kluwer Academic Publishers, Dordrecht
50. Westerling J, Lund A (1988) ^{23}Na hyperfine and quadrupolar interactions with CO_2^- in sodium hydrogen oxalate. An ENDOR study. Chem Phys Lett 147:111–115

51. Rockenbauer A, Simon P (1973) Second-order perturbation treatment of spin Hamiltonian for low symmetry. J Magn Reson 11:217–218
52. Weil JA (1975) Comments on second-order spin-hamiltonian energies. J Magn Reson 18:113–116
53. Fox B, Holuj F, Baylis WE (1973) A new fitting procedure. The ESR spectrum of Gd^{3+} in $Ca(OH)_2$. J Magn Reson 10:347–354
54. Hellmann H (1937) Einführung in die Quantenchemie. Franz Deuticke, Leipzig, p 285
55. Ponti NA, Oliva C (1992) Tensor: a program to extract hyperfine tensors from single crystal EPR and ENDOR data. Comput Chem 16:233–238
56. (a) Son NT, Henry A, Isoya J, Katagiri M, Umeda T, Gali A, Janzén E (2006) Electron paramagnetic resonance and theoretical studies of shallow phosphorous centers in 3C-4H-, and 6H-SiC. Phys Rev B 73:075201–075216; (b) Son NT, Isoya J, Umeda T, Ivanov IG, Henry A, Ohshima T, Janzén E (2010) EPR and ENDOR studies of shallow donors in SiC. Appl Magn Reson 39:49–85
57. Lee HI, Doan PE, Hoffman BM (1999) General analysis of ^{14}N ($I = 1$) electron spin echo envelope modulation. J Magn Reson 140:91–107
58. Erickson R (a) (1996) Simulation of ENDOR spectra of radicals with anisotropic hyperfine and nuclear quadrupolar interactions in disordered solids. Chem Phys 202:263–275; (b) (1995) Electron magnetic resonance of free radicals. Theoretical and experimental EPR, ENDOR and ESEEM studies of radicals in single crystal and disordered solids. Dissertation, Linköping University
59. Stone AJ (a) (1963) g factors of aromatic free radicals. Mol Phys 6:509–515; (b) (1964) g tensors of aromatic hydrocarbons. Mol Phys 7:311–316
60. YaS L, Rakhimov RR, Prokof'ev AI, Brezgunov AYu (1992) Fast molecular dynamics: novel effects studied by 3 cm and 2 mm band EPR. Pure Appl Chem 64:873–881
61. Rakhimov RR, Benetis NP, Lund A, Hwang JS, Prokof'ev AI, Lebedev YS (1996) Intramolecular and reorientation dynamics of bis(triphenylphosphine)- 3,6-di-tert-butyl-4,5-dimethoxy-o-semiquinone complex of copper(I) in viscous media. Chem Phys Lett 255:156–162
62. Lakshmi KV, Reifler MJ, Brudvig GW, Poluektov OG, Wagner AM, Thurnauer MC (2000) High-field EPR study of carotenoid and chlorophyll cation radicals in photosystem II. J Phys Chem B 104:10445–10448
63. Okafuji A, Schnegg A, Schleicher E, Möbius K, Weber S (2008) G-tensors of the flavin adenine dinucleotide radicals in glucose oxidase: a comparative multifrequency electron paramagnetic resonance and electron ─ nuclear double resonance study. J Phys Chem B 112:3568–3574
64. Christoforidis KC, Un S, Deligiannakis Y (2007) High-Field 285 GHz Electron paramagnetic resonance study of indigenous radicals of humic acids. J Phys Chem A 111:11860–11866
65. Pöppl A, Rudolf T, Monikanolen P, Goldfarb D (2000) W- and X-band pulsed electron nuclear double-resonance study of a sodium ─ nitric oxide adsorption complex in NaA zeolites. J Am Chem Soc 122:10194–10200
66. (a) Rudolf T, Pöppl A, Hofbauer W, Michel D (2001) X, Q and W band electron paramagnetic resonance study of the sorption of NO in Na-A and Na-ZSM-5 zeolites. PCCP 3:2167–2173; (b) Rudolf T, Böhlmann W, Pöppl A (2002) Adsorption and desorption behavior of NO on H-ZSM-5, Na-ZSM-5, and Na-A as studied by EPR. J Magn Res 155:45–56
67. Brustolon M, Maniero AL, Corvaja C (1984) EPR and ENDOR investigation of tempone nitroxide radical in a single crystal of tetramethyl-1,3-cyclobutanedione. Mol Phys 51:1269–1281
68. Shiotani M, Freed JH (1981) ESR studies of NO_2 adsorbed on surfaces. Analysis of motional dynamics. J Phys Chem 85:3873–3883
69. Lund A, Shiotani M, Shimada S (2011) Principles and applications of ESR spectroscopy. Springer, Dordrecht/London

70. (a) Maruani J, McDowell CA, Nakajima H, Raghunathan P (1968) The electron spin resonance spectra of randomly oriented trifluoromethyl radicals in rare-gas matrixes at low temperatures. Mol Phys 14:349–366; (b) Maruani J, Coope JAR, McDowell CA (1970) Detailed analysis of the singularities and origin of the 'extra' lines in the ESR spectrum of the CF_3 radical in a polycrystalline matrix. Mol Phys 18:165–176
71. (a) Shiotani M, Person P, Lunell S, Lund A, Williams F (2006) Structures of tetrafluorocyclopropene, hexafluorocyclobutene, octafluorocyclopentene and related perfluoroalkene radical anions revealed by electron spin resonance spectroscopic and computational studies. J Phys Chem A 110:6307–6323; (b) Shiotani M, Lund A, Lunell S, Williams F (2007) Structures of the hexafluorocyclopropane, octafluorocyclobutane, and decafluorocyclopentane radical anions probed by experimental and computational studies of anisotropic electron spin resonance (ESR) spectra. J Phys Chem A 111:321–338
72. Herring FG, McDowell CA (1972) Electron spin resonance spectrum of the chlorodisulfanyl (S_2Cl) radical in inert matrices at 4.2 K. J Chem Phys 57:4564–4570
73. Kokatam S, Ray K, Pap J, BillE GWE, LeSuer RJ, Rieger PH, Weyhermüller T, Neese F, Wieghardt K (2007) Molecular and electronic structure of square-planar gold complexes containing two 1,2-di(4-tert-butylphenyl)ethylene-1,2-dithiolato ligands: [Au(2L)2] 1+/0/1-/2-. A combined experimental and computational study. Inorg Chem 46:1100–1111
74. Lund A, Andersson P, Eriksson J, Hallin J, Johansson T, Jonsson R, Loefgren H, Paulin C, Tell A (2008) Automatic fitting procedures for EPR spectra of disordered systems: matrix diagonalization and perturbation methods applied to fluorocarbon radicals. Spectrochim Acta 69A:1294–1300
75. Aasa R, Vänngård T (1975) EPR signal intensity and powder shapes: a reexamination. J Magn Reson 19:308–315
76. Clarkson RB, Belford RL, Rothenberger KS, Crookham HC (1987) ENDOR of perylene radicals adsorbed on alumina and silica-alumina powders. I. The ring protons. J Catal 106:500–511
77. Wu Y, Piekara-Sady L, Kispert LD (1991) Photochemically generated carotenoid radicals on nafion film and silica gel: an EPR and ENDOR study. Chem Phys Lett 180:573–577
78. Erickson R, Lindgren M, Lund A, Sjöqvist L (1993) Ionic radicals on silica surfaces – an EPR, ENDOR and ESE study of benzene radical cations adsorbed on HY and silica gel. Colloids Surf A 72:207–216
79. Erickson R, Lund A, Lindgren M (1995) Analysis of powder EPR and ENDOR spectra of the biphenyl radical cation on H-ZSM-5 zeolite, silica gel and in $CFCl_3$ matrix. Chem Phys 193:89–99
80. Gerson F, Qin XZ (1988) The radical cation of naphthalene: first correct analysis of its ESR spectrum. Chem Phys Lett 153:546–550
81. Gerson F (1994) Applications of ENDOR spectroscopy to radical cations in freon matrixes. Acc Chem Res 27:63–69
82. Lindgren M, Erickson R, Benetis NP, Antzutkin ON (1993) The [^{2}H8]THF radical cation in 1,1,1-trichloro-2,2,2-trifluoroethane and trichlorofluoromethane. An EPR and ENDOR study. J Chem Soc Perkin Trans II:2009–2014
83. O'Malley PJ, Babcock GT (1986) Powder ENDOR spectra of p-benzoquinone anion radical: principal hyperfine tensor components for ring protons and for hydrogen-bonded protons. J Am Chem Soc 108:3995–4001
84. Van Doorslaer S, Callens F, Maes F, Boesman E (1995) Single-crystal and powder electron-nuclear double resonance of $RbCl:O_2^-$: a comparison between the spin Hamiltonian parameters obtained from both experiments. Phys Rev B 51:12480–12490
85. Kadam RM et al (a) (1998) ENDOR and EPR studies of benzene radical cations in halocarbon matrices: the static Jahn–Teller distortion of the monomer and geometry of the dimer cation. Chem Phys Lett 290:371–378; (b) (1999) Studies of radical cations of methyl-substituted benzene in halocarbon matrices. J Phys Chem A 103:1480–1486; (c) (1999) An EPR, ENDOR and ESEEM study of the benzene radical cation in $CFCl_3$ matrix: isotopic substitution effects on structure and dynamics. PCCP 1:4967–4973

86. Itagaki Y, Kadam RM, Lund A, Benetis NP (2000) Structure of dimeric radical cations of benzene and toluene in halocarbon matrices: an EPR, ENDOR and MO study. PCCP 2:2683–2689
87. Dalton LR, Kwiram AL (1972) ENDOR [electron-nuclear double resonance] studies in molecular crystals. II. Computer analysis of the polycrystalline ENDOR spectra of low-symmetry materials. J Chem Phys 57:1132–1145
88. LoBrutto R, Wei YH, Mascarenhas R, Scholes CP, King TE (1983) Electron nuclear double resonance and electron paramagnetic resonance study on the structure of the NO-ligated heme alpha 3 in cytochrome c oxidase. J Biol Chem 258:7437–7448
89. Bender CJ, Sahlin M, Babcock GT, Barry BA, Chandrasekar TK, Salowe SP, Stubbe J, Lindström B, Pettersson L, Ehrenberg A, Sjöberg BM (1989) An ENDOR study of the tyrosyl free radical in ribonucleotidereductase from escherichia coli. J Am Chem Soc 111:8076–8083
90. Tommos C, Tang X-S, Warncke K, Hoganson CW, Styring S, McCracken J, Diner BA, Babcock GT (1995) Spin-density distribution, conformation, and hydrogen bonding of the redox-active tyrosine YZ in photosystem II from multiple-electron magnetic-resonance spectroscopies: implications for photosynthetic oxygen evolution. J Am Chem Soc 117:10325–10335
91. Whiffen DH (1966) ENDOR transition moments. Mol Phys 10:595–596
92. Toriyama K, Nunome K, Iwasaki M (1976) ENDOR studies of methyl radicals in irradiated single crystals of lithium acetate dihydrate. J Chem Phys 64:2020–2026
93. Schweiger A, Günthard HsH (1982) Transition probabilities in electron-nuclear double- and multiple-resonance spectroscopy with non-coherent and coherent radio-frequency fields. Chem Phys 70:1–22
94. Rist GH, Hyde JS (1970) Ligand ENDOR of metal complexes in powders. J Chem Phys 52:4633–4643
95. (a) Hoffman BM, Martinsen J, Venters RA (1984) General theory of polycrystalline ENDOR patterns. g and hyperfine tensors of arbitrary symmetry and relative orientation. J Magn Reson 59:110–123; (b) Hoffman BM, Gurbiel RJ (1989) Polycrystalline ENDOR patterns from centers with axial EPR spectra. General formulas and simple analytic expressions for deriving geometric information from dipolar couplings. J Magn Reson 82:309–317
96. Hurst GG, Henderson TA, Kreilick RW (1985) Angle-selected ENDOR spectroscopy. 1. Theoretical interpretation of ENDOR shifts from randomly orientated transition-metal complexes. J Am Chem Soc 107:7294–7299
97. Attanasio D (1989) Structural information from powder endor spectroscopy. Possibilities and limitations. J Chem Soc Faraday Trans 185:3927–3937
98. Gochev GP, Yordanov ND (1993) Polycrystalline "Endor Crystallography", A new methodological approach. J Magn Reson A 102:180–182
99. Kreiter A, Hüttermann J (1991) Simultaneous EPR and ENDOR powder-spectra synthesis by direct Hamiltonian diagonalization. J Magn Reson 93:12–26
100. Kappl R, Bracic G, Hüttermann J (2009) Probing structural and electronic parameters in randomly oriented metalloproteins by orientation-selective ENDOR spectroscopy. Biol Mag Reson 28(Part 1):63–103
101. Goldfarb D (2006) High field ENDOR as a characterization tool for functional sites in microporous materials. Phys Chem Chem Phys 8:2325–2343
102. Murphy DM, Farley RD (2006) Principles and applications of ENDOR spectroscopy for structure determination in solution and disordered matrices. Chem Soc Rev 35:249–268
103. Kurreck H, Kirste B, Lubitz W (1988) Electron nuclear double resonance spectroscopy of radicals in solution – application to organic and biological chemistry. VCH Verlagsgesellschaft, Weinheim
104. Chacko VP, McDowell CA, Singh BC (1980) ^{14}N and ^{1}H ENDOR studies of x-irradiated single crystals of hippuric acid. J Chem Phys 72:4111–4116
105. Heydari MZ, Malinen E, Hole EO, Sagstuen E (2002) Alanine radicals. 2. The composite polycrystalline alanine EPR spectrum studied by ENDOR. Thermal annealing, and spectrum simulations. J Phys Chem A 106:8971–8977

106. Komaguchi K, Matsubara Y, Shiotani M, Gustafsson H, Lund E, Lund A (2007) An ESR and ENDOR study of irradiated ^{6}Li-formate. Spectrochim Acta Part A 66:754–760
107. Vänngård T, Aasa R (1963) ESR (electron spin resonance) line shapes of polycrystalline samples of S' = 1/2 transition element ions. Proceedings of the first international conference on paramagnetic resonance, vol II, Academic, New York, pp 509–519
108. Stoll S, Schweiger A (2006) EasySpin. A comprehensive software package for spectral simulation and analysis in EPR. J Magn Reson 178:42–55
109. Portis AM (1953) Electronic structure of F centers: saturation of electron spin resonance. Phys Rev 91:1071–1079
110. Castner TG Jr (1959) Saturation of the paramagnetic resonance of a V center. Phys Rev 115:1506–1515
111. Zhidkov OP, YaS L, Mikhailov AI, Provotorov BN (1967) Deduction of relaxation parameters from saturation in non-uniformly broadened lines. Theor Exp Chem 3:135–139
112. Maruani J (1972) Continuous saturation of "dispersion" singularities and application to molecular triplet states. J Magn Reson 7:207–218
113. Zimbrick J, Kevan L (1967) Paramagnetic relaxation of trapped electrons in irradiated alkaline ices. J Chem Phys 47:2364–2371
114. Gillbro T, Lund A (1974) Relative concentrations and relaxation properties of isomeric alkyl radicals in γ-irradiated n-alkane single crystals. Chem Phys 5:283–290
115. Schneider F, Plato M (1971) Elektronenspin-Resonanz. Verlag Karl Thiemig, München
116. Lund A, Sagstuen E, Sanderud A, Maruani J (2009) Relaxation-time determination from continuous-microwave saturation of EPR spectra. Radiat Res 172:753–760
117. Gautschi NW (a) (1969) Algorithm 363. Complex error function. Commun ACM 12:635; (b) (1970) Efficient computation of the complex error function. SIAM J Num Anal 7:187–198
118. Schlick S, Kevan L (1976) The application of differential saturation to distinguish radial and angular modulation mechanisms of electron spin-lattice relaxation. J Magn Reson 22:171–181
119. Copeland ES (1973) A simple method for estimating H1 in ESR experiments–the microwave power saturation of γ-irradiation induced glycylglycine radicals. Rev Sci Instrum 44:437–442
120. Harbridge JR, Eaton SS, Eaton GR (2003) Electron spin-lattice relaxation processes of radicals in irradiated crystalline organic compounds. J Phys Chem A 107:598–610
121. Brustolon M, Segre U (1994) Electron spin-lattice relaxation-time and spectral diffusion in gamma-irradiated l-alanine. Appl Magn Reson 7:405–413
122. Olsson S, Sagstuen E, Bonora M, Lund A (2002) EPR dosimetric properties of 2-methyl-alanine: EPR, ENDOR and FT-EPR investigations. Radiat Res 157:113–121
123. Sagstuen E, Hole EO, Haugedal SR, Lund A, Eid OI, Erickson R (1997) EPR and ENDOR analysis of X-irradiated L-alanine and $NaHC_2O_4H_2O$. Simulation of microwave power dependence of satellite lines. Nukleonika 42:353–372
124. Sagstuen E, Lund A, Itagaki Y, Maruani J (2000) Weakly coupled proton interactions in the malonic acid radical: single crystal ENDOR analysis and EPR simulation at microwave saturation. J Phys Chem A 104:6362–6371
125. Zamoramo-Ulloa R, Flores-Llamas H, Yee-Madeira H (1992) Calculation of the relaxation times for an inhomogeneously broadened ESR line. J Phys D Appl Phys 25:1528–1532
126. Lund A, Thuomas KÅ, Maruani J (1978) Calculation of powder ESR spectra with hyperfine and quadrupole interactions. Application to mono- and dichloroalkyl radicals. J Magn Reson 30:505–514
127. Benetis NP et al (a) (1990) Intramolecular dynamics in small radicals with anisotropic magnetic interactions. 1. ESR lineshapes of carboxymethyl(1-) trapped in irradiated zinc acetate single crystal. Appl Magn Reson 1:267–281; (b) (1994) Rotation of deuterated methylene groups in the diffusional regime. Isotope effect of anisotropic α-deuterons on ESR lineshapes of $\bullet CD_2$-COO- radical in irradiated ZnAc dihydrate single crystal. Chem Phys Lett 218:551–556

128. (a) Brynda M, Berclaz T, Geoffroy M (2000) Intramolecular motion in dibenzobarrelenephosphinyl radical: a single crystal EPR study at variable temperature. Chem Phys Lett 323:474–481; (b) Brynda M, Dutan C, Berclaz T, Geoffroy M, Bernardinelli G (2003) Intramolecular motion in the triptycenegermanyl radical: single crystal EPR study at variable temperature and DFT calculations, J Phys Chem Solids 64:939–946; (c) Brynda M, Dutan C, Berclaz T, Geoffroy M (2002) Dynamic phenomena in barrelenephosphinyl radicals: a complementary approach by density matrix analysis of EPR spectra and DFT calculations. Curr Top Biophys 26:35–42
129. Kubodera H, Shida T, Shimokoshi K (1981) ESR evidence for the cation radicals of tetrahydrofurans and dimethyl ether produced in a γ-irradiated frozen matrix of trichlorofluoromethane. J Phys Chem 85:2583–2588
130. Naumov S, Janovsky I, Knolle W, Mehnert R (2003) Radical cations of tetrahydropyran and 1,4-dioxane revisited: quantum chemical calculations and low-temperature EPR results. Phys Chem Chem Phys 5:3133–3139
131. Sjöqvist L, Lund A, Maruani J (1988) An ESR investigation of the dynamical behavior of the cyclopentane cation in CF_3CCl_3. Chem Phys 125:293–298
132. Sjöqvist L (1991) The electron structure and dynamics of organic radical cations studied by ESR spectroscopy. Dissertation, Linköping University
133. Sjöqvist L, Lindgren M, Lund A (1989) Internal motion of the cyclopentyl radical in $CF_2ClCFCl_2$: an ESR investigation. Chem Phys Lett 156:323–327
134. Lloyd RV, Wood DE (1977) Electron paramagnetic resonance study of inversion barriers and conformations in substituted cyclopentyl radicals. J Am Chem Soc 99:8269–8273
135. Toriyama K (1991) ESR studies on cation radicals of saturated hydrocarbons. Structure, orbital degeneracy, dynamics and reactions. Top Mol Organ Eng 6:99–124
136. Sjöqvist L, Lindgren M, Shiotani M, Lund A (1990) Mirror inversion of the low-symmetry ground-state structures of the methylcyclohexane and 1,1-dimethylcyclohexane radical cations. An electron paramagnetic resonance study. J Chem Soc Faraday Trans 86:3377–3382
137. Melekhov VI, Anisimov OA, Sjöqvist L, Lund A (1990) The electronic structure of cis- and trans-decalin radical cations in halocarbon matrices: an ESR and MNDO study. Chem Phys Lett 174:95–102
138. Shiotani M, Sjoeqvist L, Lund A, Lunell S, Eriksson L, Huang MB (1990) An ESR and theoretical ab initio study of the structure and dynamics of the pyrrolidine radical cation and the neutral 1-pyrrolidinyl radical. J Phys Chem 94:8081–8090
139. Antzutkin ON, Benetis NP, Lindgren M, Lund A (1993) Molecular motion of the morpholin-1-yl radical in $CF_2ClCFCl_2$ as studied by ESR. Use of residual anisotropy of powder spectra to extract dynamics. Chem Phys 169:195–205
140. Sjöqvist L, Benetis NP, Lund A, Maruani J (1991) Intramolecular dynamics of the C_4H_8NH radical cation. An application of the anisotropic exchange theory for powder ESR lineshapes. Chem Phys 156:457–464
141. Benetis NP, Sjöqvist L, Lund A, Maruani J (1991) Theoretical comparison and experimental test of the secular and nonperturbative approaches on the ESR lineshapes of randomly oriented, anisotropic systems undergoing internal motion. J Magn Reson 95:523–535
142. Liu W (2001) Structure and molecular dynamics of radicals trapped in organic–inorganic composites. Dissertation, Hiroshima University
143. Liu W, Wang P, Komaguchi K, Shiotani M, Michalik J, Lund A (2000) Structure and dynamics of $[(CH_3)_3N–CH_2]^{+\bullet}$ radical generated in γ-irradiated Al-offretite. PCCP 2:2515–2519
144. Liu W, Yamanaka S, Shiotani M, Michalik J, Lund A (2001) Structure and dynamics of triethylamine and tripropylamine radical cations generated in $AlPO_4$-5 by ionizing radiation: an EPR and MO study. PCCP 3:1611–1616
145. Liu W, Shiotani M, Michalik J, Lund A (2001) Structure and dynamics of triethylamine and tripropylamine radical cations generated in $AlPO_4$-5 by ionizing radiation: an EPR and MO study. PCCP 3:3532–3535
146. Brustolon M, Cassol T, Micheletti L, Segre U (1986) Methyl dynamics studied by ENDOR spectroscopy - a new method. Mol Phys 57:1005–1014

147. Brustolon M, Cassol T, Micheletti L, Sagre U (1987) ENDOR studies of methyl dynamics in molecular-crystals. Mol Phys 61:249–255
148. Brustolon M, Maniero AL, Sagre U (1988) An ENDOR study of the slow intramolecular motion in the CH_2COO^- radical. Mol Phys 65:447–453
149. Brustolon M, Sagre U (1994) Structure and dynamics of radicals in solids by EPR and ENDOR spectroscopies. J Chim Phys Chim Biol 91:1820–1829
150. Bonon F, Brustolon M, Maniero AL, Segre U (1992) Hindered motions in a ketone-urea inclusion compound. An ESR and ENDOR study. Appl Magn Reson 3:779–795
151. Salih NA, Eid OI, Benetis NP, Lindgren M, Lund A, Sagstuen E (1996) Reversible conformation change of free radicals in X-irradiated glutarimide single crystals studied by ENDOR. Chem Phys 212:409–419
152. Eid OI (1999) Glutarimide, sodium hydrogen oxalate single crystals: an ESR/ENDOR study. Dissertation, University of Khartoum
153. Likhtenshtein GI (1993) Biophysical labelling methods in molecular biology. Cambridge University Press, New York
154. Hubbell WL, Gross A, Langen R, Lietzow MA (1998) Recent advances in site-directed spin labeling of proteins. Curr Opin Struct Biol 8:649–656
155. Li H (1998) Bonding and diffusion of molecules in zeolites by ESR and ENDOR. Dissertation, Linköping University
156. Li H, Yahiro H, Shiotani M, Lund A (1998) SER Spectrum: A novel information imaging to characterize molecular dynamics of NO_2 on Na − mordenite. J Phys Chem B 102:5641–5647
157. Yahiro H, Nagata M, Shiotani M, Lindgren M, Li H, Lund A (1997) Motional dynamics of NO_2 adsorbed on cation-exchanged mordenites. Nukleonika 42:557–563
158. Biglino D, Li H, Erickson R, Lund A, Yahiro H, Shiotani M (1999) EPR and ENDOR studies of NO_x and Cu^{2+} in zeolites: bonding and diffusion. PCCP 1:2887–2896
159. Yahiro H, Shiotani M, Freed JH, Lindgren M, Lund A (1995) ESR studies of nitrogen oxides adsorbed on zeolite catalysts: analysis of motional dynamics. Study Surf Sci Catal 94:673–680
160. Wadsworth H (ed) (1990) Handbook of statistical methods for engineers and scientists. McGraw-Hill, New York
161. Barnes J, Bernhard W (1995) The distribution of electron trapping in DNA - one-electron-reduced oligodeoxynucleotides of adenine and thymine. Radiat Res 143:85–92
162. Kasai PH, Bishop RJ (1976) ESR studies of zeolite chemistry and catalysis. In: Rabo JA (ed) ACS monograph, vol 171. American Chemical Society, Washington, DC, pp 350–391
163. Yahiro H, Lund A, Aasa R, Benetis NP, Shiotani M (2000) Association forms of NO in sodium ion-exchanged A-type zeolite: Temperature-dependent Q-Band EPR spectra. J Phys Chem A 104:7950–7956
164. Shimada S, Hori Y, Kashiwabara H (1977) Free radicals trapped in polyethylene matrix. 2. Decay in single crystals and diffusion. Polymer 18:25–31
165. Plonka A (2001) Dispersive kinetics. Springer, Dordrecht
166. (a) Kinell PO, Lund A, Vanngard T (1964) Electron spin resonance study of γ-irradiated solid dextran. Arkiv Kemi 23:193–203; (b) Lund A, Nilsson G, Samskog PO (1986) Structure and reactions of reduction products in crystalline and polymeric materials by combining pulse radiolysis and ESR. Radiat Phys Chem 27:111–121
167. Heinzer J (1972) EXREXN: simulation of exchange-broadened isotropic ESR spectra. QCPE 11:209
168. Budil DE, Lee S, Saxena S, Freed JH (1996) Nonlinear least-squares analysis of slow-motional EPR spectra in one and two dimensions using a modified Levenberg-Marquardt algorithm. J Magn Reson A 120:155–189
169. Earle KA, Budil DE (2006) Calculating slow-motion ESR spectra of spin-labeled polymers. In: Schlick S (ed) Advanced ESR methods in polymer research. Wiley, Hoboken
170. Fouse GW, Bernhard WA (1978) Analysis of error in eigenvalues and eigenvectors determined from EPR data. J Magn Reson 32:191–198
171. Mahgoub AS, Lund A, Lindgren M (1994) ENDOR study of ^{133}Cs hyperfine couplings with SO_3^- radicals in x-irradiated piezoelectric $Cs_2S_2O_6$ single crystals. J Mater Chem 4:223–227

Chapter 2
Pulse EPR of Paramagnetic Centers in Solid Phases

Marina Brustolon and Antonio Barbon

Abstract We present an overview of the most used Electron Spin Echo techniques and their applications to the study of structure and dynamics of paramagnetic centers in solid phases. A short theoretical section presents the tools necessary to understand the experiments. Three sections describe the experiments that are used to get information on the spin and spatial dynamics of the system, on the distribution of paramagnetic centers in the solid matrix, and on their local environment. Many examples of applications to different paramagnetic centers in various research fields are given.

2.1 Introduction

Pulse EPR spectroscopy has been developed later than pulsed NMR. The pioneering work started in the 1960s, and a further development bringing pulse EPR to become a quite common spectroscopic tool, with pulsed spectrometers also available commercially, had to wait the 1980s. The basic principles of pulse EPR and NMR are the same, as is the physics of the nuclear and electron spins. In fact both types of spectroscopies use the same theoretical approach and models [1]. However, much more stringent conditions for EPR, as faster relaxation times (three orders of magnitude) and larger spectral ranges (three-four orders of magnitude), have required further technological developments. Today, also with the best available technology it is in general impossible to achieve a non selective excitation of all the EPR spectrum, and an important part of the initial time signal cannot be recorded due to the presence of the tail of the excitation pulse (dead time). These limitations

M. Brustolon (✉) • A. Barbon
Department of Chemical Sciences, University of Padova, Via Marzolo 1, 35131 Padova, Italy
e-mail: marinarosa.brustolon@unipd.it; antonio.barbon@unipd.it

A. Lund and M. Shiotani (eds.), *EPR of Free Radicals in Solids I*, Progress in Theoretical Chemistry and Physics 24, DOI 10.1007/978-94-007-4893-4_2,

make impossible at the moment for pulse EPR to have a fate similar to that of pulsed NMR, that of completely substituting CW-EPR.

Pulse EPR methods have been, however, a fundamental step towards to the so-called "modern EPR spectroscopy", a term used to refer to the techniques developed in the last 20 years for the study of electron spins in more and more complex systems. Thanks to impressive methodological and instrumental developments, the EPR spectroscopists today have a wealth of methods at their disposal. A comparison of the modern methods with the traditional CW X-band EPR spectroscopy at 9.5 GHz shows flexibilities in the resonance frequencies, today available in the range 1–600 GHz, in the acquisition methods (continuous wave, time resolved or pulse), and in the multiple irradiations with different frequencies. By exploiting a convenient combination of these options the researcher is today able to obtain structural and dynamic information on complex systems, in the field of physics, chemistry, materials science and biology.

As far as pulse EPR methods in solid systems are concerned, most techniques are based on the Electron Spin Echo (ESE) phenomenon, and they can be grouped into three major types, each devoted to a specific kind of information:

a. Methods oriented to get information on the dynamics of the system, based on spin relaxation properties: ESE for the determination of T_1, T_2 and T_M; electron spin echo detected EPR (EchoEPR).
b. Methods oriented to get information on the spatial distribution of paramagnetic probes (local concentration, probe-probe distance). These methods are based on spin relaxation originated by dipolar coupling between electrons: ESE for the determination of Instantaneous Diffusion, $2 + 1$ ESE, Pulsed Electron Double Resonance (PELDOR), called also Double Electron Electron Resonance (DEER), and Double Quantum Coherence (DQC) ESR for probe-probe distance. These methods are sometimes referred to as Dipolar Electron Spectroscopy.
c. Methods oriented to get information on the local environment of paramagnetic centers *via* the interaction with nuclear spins. These methods include one and two dimensional Electron Spin Echo methods, i.e. Electron Spin Echo Envelope Modulation (ESEEM) and HYperfine Sub-level CORrElation (HYSCORE), pulse electron–nuclear double resonance (pulse ENDOR). These methods are sometimes referred to as Hyperfine Spectroscopy.

A rather general method of simulating electron-spin echo experiments has been derived and implemented in EasySpin [2], a widely used software for CW-EPR and ENDOR simulations. It enables the numerical simulation of spectra from many pulse EPR and ENDOR experiments where electron-spin echoes are detected [3].

In this contribution we will describe the simplest pulse experiments and give the basic principles for understanding them. We tried to give a good descriptive physical insight into the pulse experiments, but only general outlines of the formal treatments will be given, providing the references to the papers and books where the theory is fully developed. We recommend the extensive compendium by Arthur Schweiger and Gunnar Jeschke [4], still unsurpassed for a thorough grounding in pulse EPR. Other books treating specific aspects of pulse EPR are reported in Refs. [5–14].

We choose to exclude in general a description of the instrumentation and detailed descriptions of the more technical aspects of the experiments, as for example phase cycling or treatments of data. On the other hand we will describe a number of applications to different fields of the methods outlined above.

2.2 Elements of Theory

The aim of this section is to give the basic concepts and definitions in pulse EPR techniques. General theoretical treatments are reported in Refs. [4–6, 8, 15–19].

Pulse experiments are normally performed in three steps: preparation of the system, evolution (mixing) and detection. The preparation is given by a sequence of pulses applied to the sample to create non-equilibrium magnetization. During the evolution time different processes make the system to evolve, then modifying its non-equilibrium state. In some experiments a mixing period can be present at this stage. A net non-zero transverse magnetization is eventually detected. In pulse techniques applied to solid samples an echo is formed along the detection axis in the *xy* plane, perpendicular to the static field B_0. The variation of the echo intensity depending on the preparation and evolution steps can be related to the properties of the system.

A classical approach can be used to treat the dynamics of a single $S = 1/2$ spin, or an ensemble of non-interacting $S = 1/2$ spins. This approach (which is often referred to as *vector model*) is equivalent to the quantum mechanical one for this case (since an $S = 1/2$ spin in a magnetic field has two energy levels only), and it can be fruitfully used to have an insight of the events during a pulse experiment for more complex systems.

2.2.1 Classical Treatment of Free Induction Decay and Electron Spin Echo

The classical equation of the evolution of the magnetization vector **M** given by the sum of identical electron spins $\boldsymbol{\mu}$ in a magnetic field **B** is:

$$\frac{d\mathbf{M}}{dt} = -\gamma_a \mathbf{M} \times \mathbf{B} \tag{2.1}$$

where γ_a is the absolute value of the electron magnetogyric ratio $\gamma_a = |\gamma| = g_e \mu_B / \hbar$.

In a magnetic resonance experiment the field has a static component, B_0, assumed to be along the **k** director of the z axis, and a field B_1(t) oscillating in the plane perpendicular to z at a microwave (mw) frequency ω.

The equation of motion of the single components of the magnetization can be conveniently described in a right-hand rotating frame at frequency ω with the x axis parallel to B_1, so that B_1 is time independent in this axes system.

In the rotating frame Eq. (2.1) is written as

$$\begin{aligned}\frac{dM_x}{dt} &= -(\gamma_a B_0 - \omega)M_y = -\Delta\omega M_y \\ \frac{dM_y}{dt} &= (\gamma_a B_0 - \omega)M_x - \gamma_a B_1 M_z = \Delta\omega M_x - \omega_1 M_z \\ \frac{dM_z}{dt} &= \gamma_a B_1 M_y = \omega_1 M_y \end{aligned} \tag{2.2}$$

where $\Delta\omega = \gamma_a B_0 - \omega = \omega_0 - \omega$ and $\omega_1 = \gamma_a B_1$ is called nutation or Rabi frequency. For $\Delta\omega = 0$ (resonance condition) the motion of the magnetization is therefore a precession around the B_1 direction at frequency ω_1. After a time t_p the magnetization is tilted by an angle $\theta_p = \gamma B_1 t_p = \omega_1 t_p$.

The motion in presence of B_1 is more complex if the pulse is applied with an offset resonance $\Delta\omega \neq 0$. In this case the nutation is around an effective field tilted from B_1 by an angle $\zeta = \arctan(\omega_1/\Delta\omega)$ with a nutation frequency $\omega_{eff} = (\Delta\omega^2 + \omega_1^2)^{1/2}$.

So far the model does not take into account the spin relaxation. Bloch introduced in a phenomenological way two relaxation terms, relative to two separated relaxation processes: a transverse and a longitudinal relaxation processes, with times T_2 and T_1 [16].

$$\begin{aligned}\frac{dM_x}{dt} &= -\Delta\omega M_y - \frac{M_x}{T_2} \\ \frac{dM_y}{dt} &= \Delta\omega M_x - \omega_1 M_z - \frac{M_y}{T_2} \\ \frac{dM_z}{dt} &= \omega_1 M_y - \frac{M_z - M_0}{T_1} \end{aligned} \tag{2.3}$$

These equations give the basis to describe a simple real experiment: the Free Induction Decay (FID) of an ensemble of spins with the same frequency $\Delta\omega$ (isochromats).

A longitudinal relaxation of the magnetization requires an exchange of energy between the spin system and some degree of freedom of the surrounding (*e.g.*, molecular rotations or vibrations). During the transverse relaxation process on the other hand the total amount of magnetization energy accumulated in the spin system is invariant. Therefore the relaxation of the transverse components of the magnetization is generally faster than the longitudinal one. In solids the difference is usually large and $T_2 \ll T_1$.

Let us apply a mw pulse of frequency ω to a system with equilibrium magnetization $\mathbf{M} = M_0\mathbf{k}$ for a time $t_{\pi/2} = \pi/2\omega_1 \ll T_1, T_2$. This is called a $\pi/2$ pulse. The effect of the pulse is to bring the magnetization $\mathbf{M}$ from the z to the -y direction.

After the pulse, the evolution of the system in the rotating frame is given by the solution of the Eq. (2.3) with initial conditions $\mathbf{M}(t=0) = -M_0\mathbf{j}$. The solution is

$$\begin{aligned} M_x &= M_0 \sin(\Delta\omega t)\exp(-t/T_2) \\ M_y &= -M_0 \cos(\Delta\omega t)\exp(-t/T_2) \\ M_z &= M_0[1-\exp(-t/T_1)] \end{aligned} \tag{2.4}$$

In resonance condition ($\Delta\omega = 0$) during the free evolution time following the end of the pulse the magnetization lies along -*y* and decays for the transverse and longitudinal relaxations. The Fourier Transform (FT) of the FID gives a lorentzian line with half width at half height of $1/T_2$ and centred at zero frequency. The same lineshape would be obtained by the CW-EPR spectrum centred at the resonance field. If the resonance condition is not met, the magnetization decays and rotates in the *xy* plane at a frequency $\Delta\omega = \omega_0 - \omega$. The FT of the FID is then a lorentzian line of the same width but centred at $\Delta\omega$ which corresponds to a shift $\Delta B = \hbar\Delta\omega/g\beta$ in the CW-EPR spectrum.

In principle FT-EPR and CW-EPR spectra give the same information. However, for solid samples FT-EPR cannot be used for experimental limitations. In a solid sample the magnetic anisotropic interactions are not (or only partially) averaged by the molecular reorientation, and therefore it is almost impossible to have an isochromatic spin system (apart from conditions of very strong spin exchange in concentrated spin systems). Groups of spins with the same resonance frequency are called *spin packets*. Due to the large number of hyperfine and superhyperfine interactions of each electron spin, many EPR lines are overlapping, and this gives rise to an inhomogeneous line broadening in the CW-EPR spectrum. The FT of a rectangular pulse of width τ_p at frequency ω_0 contains frequency components in the excitation bandwidth $\omega_0 \pm \delta\omega$, with $\delta\omega \approx 1/\tau_p$ [4]. When the excitation bandwidth is larger than the overall frequency extension of the EPR spectrum, the pulse excites all the electron spins (non selective pulse), whereas if only a part of the spectrum is excited the pulse is selective. For the larger frequency extension of the EPR spectra in solids, due to dipolar hyperfine and g anisotropies, the EPR pulse is usually strongly selective in these cases. Therefore one should take into account the shape of the pulse, and analyze separately different regions of the spectrum to obtain a meaningful result. Each signal moreover would be composed of the sum of the FIDs of all the resonating spin packets, interfering with each other.

A more convenient pulse EPR method for solids requires more than just a pulse. A convenient sequence of pulses can produce an electron spin echo, which is generally at the basis of all applications of pulse EPR to probes in solid state. In a spin echo experiment a number of spin packets with resonance frequencies within the excitation bandwidth will be rotated into the *xy* plane, where they will then start to precess, each with its frequency ω_{0i} (see Fig. 2.1). Due to their different resonance frequencies the spin packets are dephasing very rapidly, with a characteristic time $T_2^* << T_2$. This dephasing is reversible; the spin packets can be re-phased at time 2τ by applying a π pulse after a time τ. At time 2τ the components of spin packets will refocus all along the *y* direction to form an echo (Hahn echo).

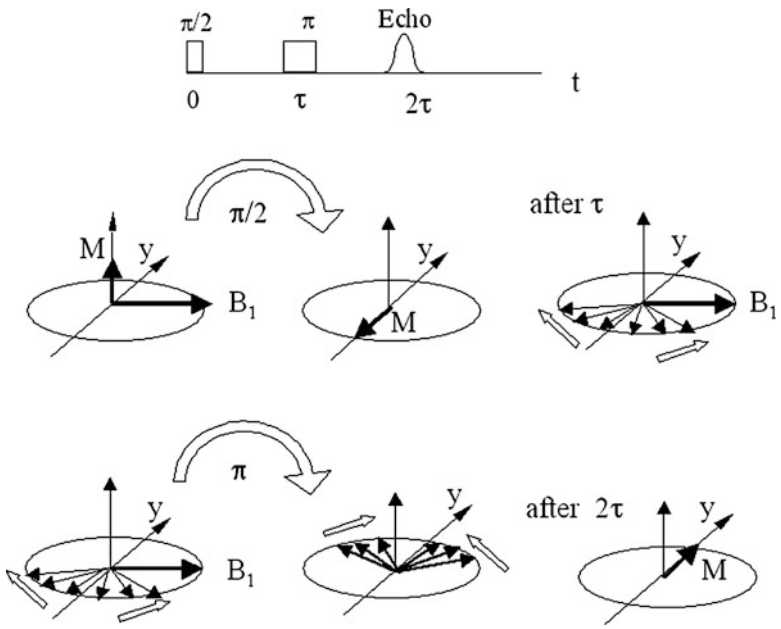

Fig. 2.1 Vector model of the Hahn echo formation

Beside the dephasing processes that lead to the reversible decay of the total *xy* magnetization, the *xy* component of each spin packet decays irreversibly during τ with characteristic time T_{2i}, due to stochastic interactions and other effects (see Sect. 2.2.4). As a consequence on increasing τ the total echo intensity decays with a characteristic time T_M (phase memory time). The $\pi/2-\tau-\pi-\tau$ -echo sequence is called Hahn Echo or 2p-ESE (see Figs. 2.1 and 2.2) [20, 21].

By using selective pulses and by recording the echo intensity on sweeping the magnetic field, one obtains the so-called echo-detected EPR, with a spectral profile dependent on τ, and different from CW-EPR. The use of this spectroscopy will be discussed in Sect. 2.3.2.2.

The classical magnetization vector picture given above is not any more adequate for $S>1/2$, or when interactions between spins are taken into account. A quantum-mechanical treatment is therefore necessary. We will give here only the results of this treatment, referring to the specialized literature for the derivation.

2.2.2 *Quantum Mechanical Treatment of Pulse Experiments*

The Bloch equations are a convenient model for spin systems as far as the spins are not interacting between them. In presence of such an interaction a quantum

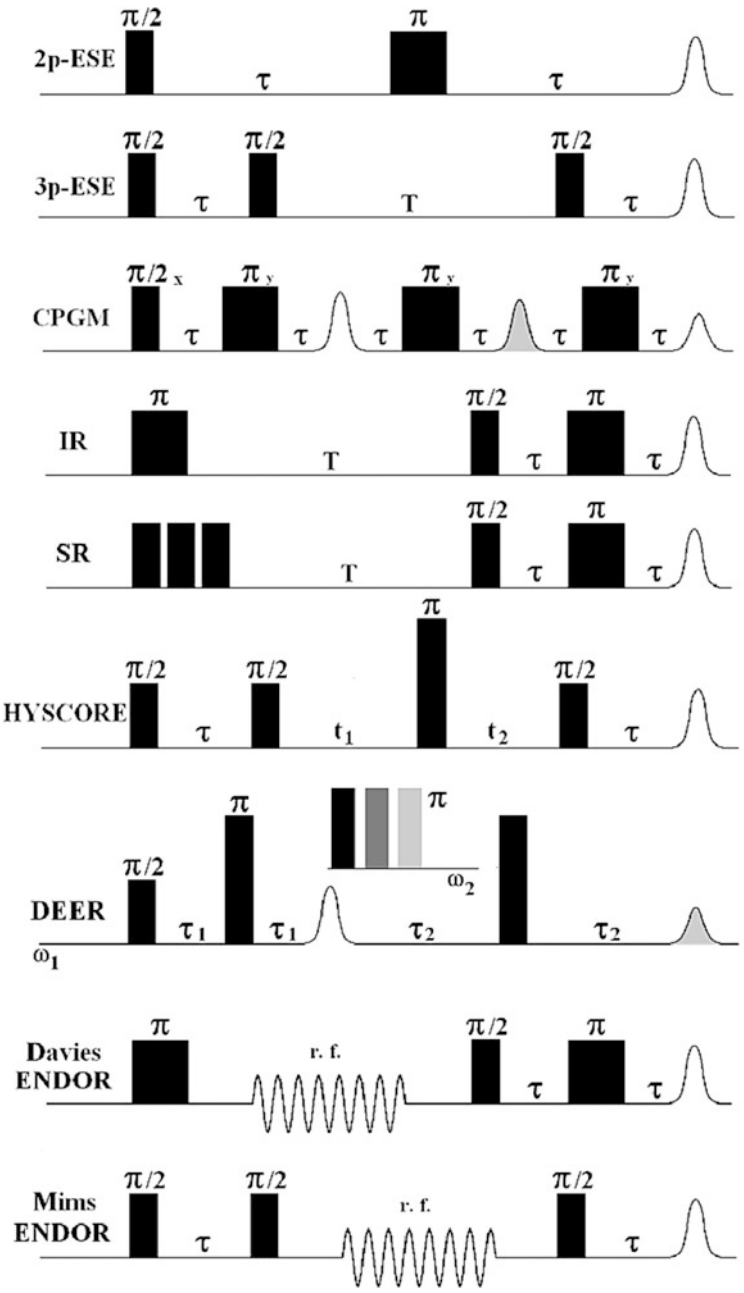

Fig. 2.2 Pulse sequences used in the described experiments. Echoes with opposite signs are indicated with different shadowing

mechanical description of the experiments is necessary. To this aim the concept of *density matrix* must be introduced. A density matrix relative to the spin system $\sigma(t)$ is generally used for treating of spin dynamics [18].

For a single spin $S = 1/2$ the wavefunction can be expressed in the basis of the eigenfunctions of the spin Hamiltonian, $|\alpha >$ and $|\beta >$:

$$|\psi >= c_\alpha \, |\alpha\rangle + c_\beta \, |\beta\rangle \tag{2.5}$$

where c_α and c_β are complex coefficients; we can also write

$$|\psi >= e^{-i\varphi_\alpha} \, |c_\alpha| \, |\alpha\rangle + e^{-i\varphi_\beta} \, \left|c_\beta\right| \, |\beta\rangle \tag{2.6}$$

The state of an ensemble of spins all with the same wavefunction is called a *pure state*. All the spins have the same phase in the pure state, and the state is said to be *coherent*.

For this system we can define a density matrix σ

$$\sigma = \begin{vmatrix} |c_\alpha|^2 & c_\alpha c_\beta^* \\ c_\alpha^* c_\beta & \left|c_\beta\right|^2 \end{vmatrix} \tag{2.7}$$

The expectation value of any operator A in terms of the density matrix is given by:

$$\langle A\rangle = tr\,\{\sigma \cdot A\} \tag{2.8}$$

Then the expectation values of the components $<S_x>$, $<S_y>$, $<S_z>$, of the spin operator S are given by

$$\begin{aligned} < S_x > &= \frac{1}{2}(c_\alpha^* c_\beta + c_\alpha c_\beta^*) = |c_\alpha||c_\beta| \cos \Delta\varphi \\ < S_y > &= \frac{1}{2}(c_\alpha^* c_\beta - c_\alpha c_\beta^*) = |c_\alpha||c_\beta| \sin \Delta\varphi \\ < S_z > &= \frac{1}{2}(|c_\alpha|^2 - |c_\beta|^2) \end{aligned} \tag{2.9}$$

The state of an ensemble of spins with different wave functions $|\psi_k >$ is called a *mixed state*. The elements of the density matrix for a mixed state are given by averages of the elements in matrix Eq. (2.7) [22]:

$$\sigma = \begin{vmatrix} \overline{|c_\alpha|^2} & \overline{c_\alpha c_\beta^*} \\ \overline{c_\alpha^* c_\beta} & \overline{\left|c_\beta\right|^2} \end{vmatrix} \tag{2.10}$$

For a system at thermal equilibrium the diagonal elements of the density matrix are the equilibrium *populations*, whereas the off diagonal terms, called *coherences,* are equal to zero:

$$\overline{c_i^* c_j} = \overline{c_i c_j \exp(i\,\Delta\varphi_{ij})} = 0 \tag{2.11}$$

as the phase differences are random.

The components of the macroscopic magnetization are proportional to the ensemble averages of Eq. (2.9). Therefore the diagonal elements of the density matrix are related to the longitudinal magnetization, whereas the off diagonal elements are related to transverse one. In a system at thermal equilibrium in an external magnetic field the transverse magnetization is zero and only the longitudinal magnetization is present.

During the preparation period the spin system is prepared by a sequence of pulses and both coherences and polarized non-equilibrium states can be created. In the evolution period the system evolves under the influence of the spin Hamiltonian, and different types of magnetization transfers may take place. In the detection period coherences are detected as transverse magnetization.

The time evolution of the density matrix during the different periods is described by the Liouville-von Neumann equation, derived from the time-dependent Schrödinger equation [4, 18],

$$\frac{\mathrm{d}\sigma(t)}{\mathrm{d}t} = -\frac{i}{\hbar}\left[H(t), \sigma(t)\right] \tag{2.12}$$

where $H(t)$ is the spin Hamiltonian. Its formal solution is:

$$\sigma(t) = \exp\left[-\frac{i}{\hbar}\int_0^t H(t')\mathrm{d}t'\right]\sigma(0)\exp\left[\frac{i}{\hbar}\int_0^t H(t')\mathrm{d}t'\right] \tag{2.13}$$

By selecting a suitable rotating frame system, the Hamiltonian can often be made time-independent within each evolution period. Then the evolution of the density matrix can be obtained in successive steps in which a static Hamiltonian acts on the system. In each step, from t to $t + t_1$, the evolution of the density operator is obtained as

$$\sigma(t + t_1) = \exp\left[-\frac{i}{\hbar}\mathrm{H}t_1\right]\sigma(t)\exp\left[\frac{i}{\hbar}\mathrm{H}t_1\right] \tag{2.14}$$

The echo intensity at the end of an experiment is obtained as

$$\langle M(t_1 + t_2 + t_3 + \cdots)\rangle = tr\{\sigma(t_1 + t_2 + t_3 + \cdots)\cdot M\} \tag{2.15}$$

Accordingly, with this procedure the magnetization arising from any pulse EPR experiment could be obtained.

2.2.3 2p- and 3p-ESE Experiments

In the following we will use the concept of density matrix to describe the 2p-ESE and 3p-ESE experiments on the basis of the modifications of its elements during the different steps of the experiment. Complete calculations can be found for example in refs. [1, 8]. For a spin system $S = 1/2$, $I = 1/2$, coupled by a weak hyperfine interaction either isotropic or anisotropic, the spin Hamiltonian H is

$$\begin{aligned} H &= \nu_e S_z - \nu_N I_z + S\mathbf{T}I \\ &\approx \nu_e S_z - \nu_N I_z + T_{xz} I_x S_z + T_{yz} I_y S_z + T_{zz} I_z S_z \end{aligned} \tag{2.16}$$

where ν_e and ν_N are the electron and nuclear resonance frequency and $\mathbf{T}$ is the hyperfine tensor; for weak couplings the terms in S_x and S_y can be neglected [16].

It is convenient to use a basis of four coupled spin functions $\alpha\alpha$, $\alpha\beta$, $\beta\alpha$, $\beta\beta$, product of the electronic and nuclear eigenfunctions of the Zeeman terms in Eq. (2.16). In Fig. 2.3 (bottom) one can see the definitions of the elements of spin density matrix $\boldsymbol{\sigma}$ for this spin system. Spin populations (P) along the trace and coherences off diagonal are indicated. The coherences corresponding to allowed ($\Delta m_s = \pm 1, \Delta m_I = 0$) and forbidden ($\Delta m_s = \pm 1, \Delta m_I = \pm 1$) EPR transitions are indicated respectively with *EPR* and *f*, those corresponding to ENDOR transitions ($\Delta m_s = 0, \Delta m_I = \pm 1$) with *ENDOR*.

Let us first describe the 2p-ESE experiment for a $S = 1/2$, $I = 1/2$ system with an isotropic hyperfine interaction. In Fig. 2.3, upper stripe, the effect on σ of the $\pi/2$ and π pulses is shown. The populations are transferred to EPR coherences by a $\pi/2$ pulse, and after a time τ the π pulse changes the phases of the coherences, as indicated by the arrows. The complete treatment shows that the rephasing of the coherences is taking place after another interval τ, then the rephased electron coherence is detected.

When an anisotropic hyperfine coupling is present, allowed and forbidden EPR transitions can both be excited. In fact the quantization axis for the nucleus is determined by the resultant of the applied field and of the anisotropic hyperfine field, the two fields having different directions; then the eigenfunctions of the Hamiltonian Eq. (2.16) are a mixing of α and β nuclear states. The effect of a $\pi/2$ pulse for such a system is shown in Fig. 2.3, lower stripe. The pulse excites coherences on allowed (dark grey) and forbidden (light grey) electron transitions. The effect of the π pulse is shown on just one of the allowed coherences created previously. It has the effect of inverting the phase of the coherence, but also of redistributing (branching) the coherence considered on all the electron spin transitions (with probabilities depending on the angle between applied and hyperfine fields). This effect can be considered as the consequence of the probability that also the nuclear spin flips during the mw pulse. This branching prevents a complete rephasing of the spin packets, as the four magnetic vectors, in phase immediately after the pulse, precess

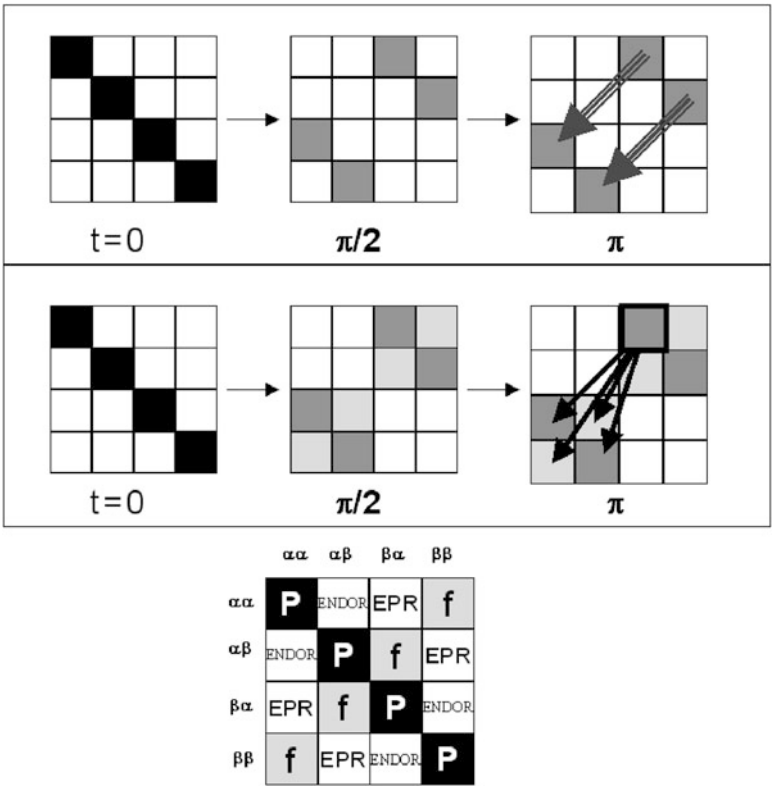

Fig. 2.3 Evolution of the density matrix during a 2p-ESE experiment for a $S = 1/2$, $I = 1/2$ spin system, coupled either with isotropic (*upper stripe*) or anisotropic (*lower stripe*) interaction. *Bottom*: definition of the density matrix elements; P is the population of the single spin state; ENDOR, EPR are coherences corresponding to allowed transitions; f correspond to prohibited transitions

then with different frequencies. This effect is the basis for observation of ESEEM, as we will discuss in Sect. 2.5.1.

The effect on the density matrix of the pulse sequence in 3p-ESE or stimulated echo is shown schematically in Fig. 2.4. An anisotropic coupling for the $S = 1/2$, $I = 1/2$ system is considered. The first $\pi/2$ pulse creates the same electron coherence pattern as for the 2p-ESE (*b*). Then the magnetization evolves freely during τ. In the vector model the spin packets rotate in the *xy* plane and they will distribute in the plane with different phases depending on their Larmor frequencies. Let us take into account those spin packets which after τ are again aligned along the axis perpendicular to B_1 (therefore along *y* or –*y*). They will be rotated

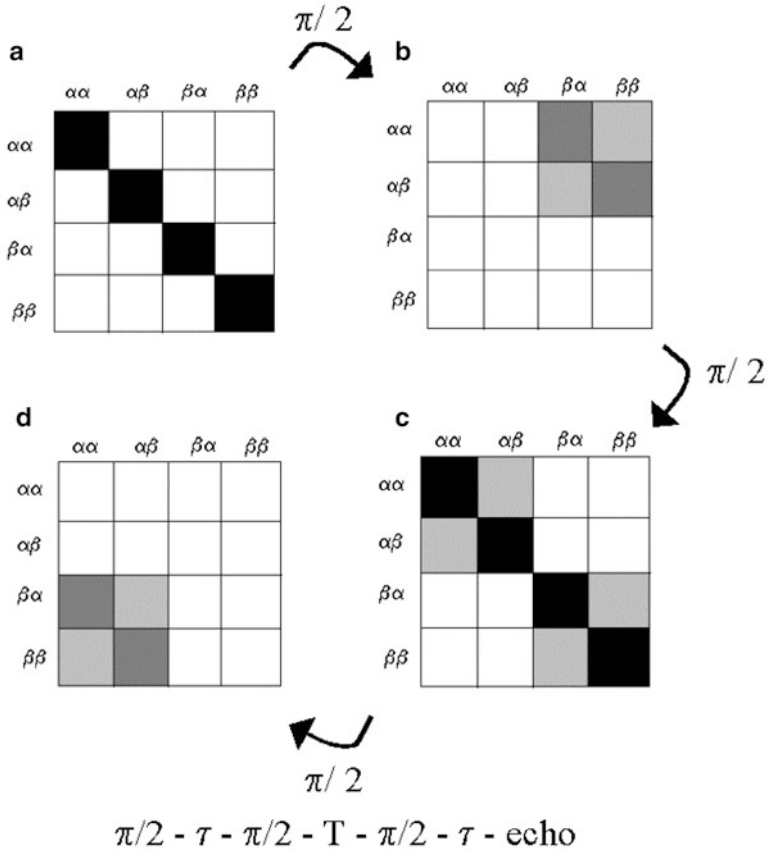

Fig. 2.4 Evolution of the density matrix during a 3p-ESE experiment for a coupled $S = 1/2$, $I = 1/2$ spin system

respectively along $-z$ or $+z$ by the second pulse, therefore giving a contribution to the magnetization along the z axis. As one can see in Fig. 2.4, diagonal elements in σ are in fact created by the second $\pi/2$ pulse. On the other hand the spin packets which after τ are aligned along x will be unaffected by the $\pi/2$ pulse. Therefore the z polarization after the second pulse has a modulation at frequency $\pi/2\tau$.

It should be noted that the electron spin polarization is decaying with rates depending on the spin-lattice relaxation and in general on *spectral diffusion*, as explained later. These relaxations are slower than the rate of dephasing in the xy plane typical of the 2p-ESE, and therefore the decaying of the stimulated echo with time T is slower than the Hahn echo decay on increasing τ. Besides the electron spin polarization, the second $\pi/2$ pulse creates also nuclear coherences, as can be seen in c in the figure. Finally, the third $\pi/2$ pulse transfers the polarization back to xy plane, where it starts to precess. We should expect to detect an FID, that is in

fact formed, but due to the modulation of the polarization it refocuses after a time τ. Therefore the *stimulated echo* is in reality a FID [4].

2.2.4 Spin Relaxation and Echo Decay

By varying the time delays between pulses we can follow the decay of the electron magnetization due to stochastic processes, and the effect of hyperfine dipolar coupling with nearby nuclei (Electron Spin Echo Envelope Modulation, ESEEM). Both effects can be described in the quantum mechanical frame by the time evolution of the density matrix elements.

The general evolution of the density operator under a time-independent Hamiltonian H in the presence of relaxation processes is given by the quantum mechanical master equation [4, 16–18].

$$\frac{d\sigma(t)}{dt} = -\frac{i}{\hbar}\left[\mathrm{H}, \sigma(t)\right] - \Gamma\left\{\sigma(t) - \sigma_0\right\} \tag{2.17}$$

where σ_0 is the equilibrium density operator and Γ the relaxation superoperator that accounts for the dissipative interactions between the spin system and the lattice.

The matrix elements of the relaxation superoperator Γ_{klkl} describe the decay of the element σ_{kl} of the density matrix, while elements Γ_{klmn} describe relaxation between elements σ_{kl} and σ_{mn}. The correspondence to Bloch equations for the $S = 1/2$ system is recovered by setting $\Gamma_{kkll} = \pm 1/2T_1$ and $\Gamma_{mnmn} = 1/T_2$ (with $\mathrm{m} \neq \mathrm{n}$).

The two terms in Eq. (2.17) refer respectively to the evolution of the spin system under the Hamiltonian, and to its evolution due to stochastic processes provided by the other degrees of freedom of the sample. The first term gives rise to the ESEEM effect when the Hamiltonian contains operators of hyperfine dipolar coupling of the electrons with the nuclear spins. The second term produces the decay of the magnetization towards thermal equilibrium. The usual treatment of the echo decays in solids is that of calculating the ESEEM modulation $V_m(t)$ by the quantum mechanical procedure, and considering the whole time evolution of the echo intensity $V(t)$ as given by the product of $V_m(t)$ with a phenomenological decay function $V_d(t)$ [23] due to all the relaxation mechanisms :

$$V(t) = V_m(t)V_d(t) \tag{2.18}$$

The spin relaxation processes affecting the longitudinal and transverse relaxation rates are discussed respectively in Sects. 2.3.1 and 2.3.2. The expressions for $V_d(t)$ obtained for the 2p-ESE are given in the Appendix. Some expressions for $V_m(t)$ are discussed in Sect. 2.5.1.

An example of the application of Eq. (2.18) is shown in Fig. 2.5. In the figure one can see two ESE spectra at different temperatures for a nitroxide radical doping a single crystal. Both $V_d(t)$ and $V_m(t)$ change with the temperature. $V_d(t)$ can be fitted

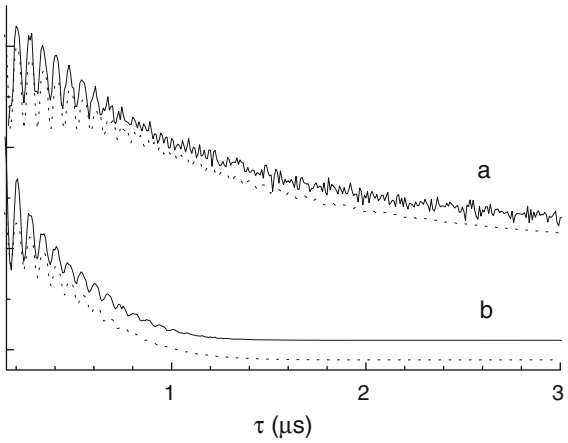

Fig. 2.5 Echo decays of 4-oxo-2,2,6,6-tetramethyl-1-piperidinyloxy (Tempone) doping substitutionally a single crystal of the diketone 2,2,4,4-tetramethyl-cyclobutan-1,3-dione (*upper solid lines*) for *a*: T = 300 K; *b*: T = 50 K and the relative simulations (*lower dotted lines*) (Adapted from Ref. [24]). The decay at T = 300 K is obtained from a crystal deuterated in the methylene positions. The simulation of the modulation is obtained by assuming dipolar couplings respectively (*a*) with the four methyl groups of the radical; (*b*) with the eight methyl groups of the first shell of host molecules (Adapted from Ref. [24])

with one linear exponential for T = 300 K, as the relaxation process is dominated by the motions of the radical in the matrix. On the other hand, the decay is fitted with a gaussian for T = 50 K, since at this temperature the dominant relaxation mechanism is the fast flip-flop of neighbor proton spins. The modulation is simulated as due to the four freely rotating methyl groups of the radical at 300 K, and to the eight methyl groups of the host neighbor molecules at 50 K.

2.2.5 Product Operator Method

A convenient method for treating the spin dynamics in pulse magnetic resonance experiments is that of decomposing the density operator in a set of product operators [1, 4, 18].

This method combines elements of both vector model and density matrix approach. It makes the physical picture easier and is advantageous when one is interested to put in evidence only some properties of the evolution of the system relative to some operators. The method is based on the expansion of the density operator on a suitable base of operators B_s,

$$\sigma(t) = \sum_{s=1}^{n^2} b_s(t) B_s \tag{2.19}$$

where the time dependence is given by the coefficients $b_s(t)$. B_s elements belong to the Liouville space obtained by direct product of the basis set of the single spins [4] that, for spin systems, are normally Cartesian spin operators.

The theory is commonly used to calculate the spin physics of pulse sequence in NMR [25]. For pulse EPR experiments, the theory can be found in Ref. [4], Sect. 4.2.3.

2.3 Methods Oriented to Get Information on the Dynamics of the System: Determination of T_1, T_2 and T_M; Electron Spin Echo Detected EPR (ED-EPR)

2.3.1 Spin-Lattice Relaxation

The measurement of electron spin-lattice relaxation rates with CW-EPR techniques can be done with the *progressive saturation* technique which is illustrated in this book in Chap. 1.

The methods used by pulse EPR for measuring electron spin-lattice relaxation times T_1 are mostly *inversion recovery* and *saturation recovery* (with a long unique saturating pulse, or with a train of short pulses).

A drawback of these techniques is the intrinsic selectivity of the preparation pulses, as usually the width of the spectrum is larger than the bandwidth of the pulses [26]. Thus only a part of the spin packets is affected by the pulse. As a consequence, the dynamics of the electron spins after the preparation procedure is determined by more than one process, and the recovery is given in general by a multiexponential expression [27]:

$$V(t) = \sum_j V_{0j}[1 - n \ \exp(-t/T_{1j})] \tag{2.20}$$

($n = 1$ for the saturation recovery, $n = 2$ for inversion recovery)

Very often two main processes are active, *i.e.* the exchange of energy between the spins and the *lattice*, and the exchange of energy between the spins affected by the pulses and those not affected. The first process is the true spin-lattice relaxation, the second one is the so called *spectral diffusion* [28]. The saturation recovery experiments should be designed in particular to exclude as much as possible the interference of spectral diffusion.

The resulting traces are described usually by a sum of two exponentials, and a least-squares fitting yields the rates of spectral diffusion, generally faster, and of the spin-lattice relaxation.

When a distribution of relaxation times due to intrinsic disorder in the sample is present, the recovery curves are given by stretched exponentials

$$V(t) = V_0[1 - n\exp(-(t/T_1)^{\beta})] \tag{2.21}$$

where β depends on the distribution of relaxation times.

2.3.1.1 Spin-Lattice Relaxation Processes

Phonons and spin-lattice relaxation: The exchange of energy between the spin system and the lattice takes place by exchange of phonons. This latter can occur in different ways [27, 29].

The *direct process* is the emission of a phonon with frequency equal to the electron Larmor frequency into a lattice mode of the same frequency. By emission of the phonon the spin state changes. This process therefore involves only low frequency phonons, and it is important only at very low temperatures. It should be noted that the importance of this mechanism is related to the working frequency of the spectrometer [30]. For X-band EPR the direct process exhibits a temperature dependence $1/T_1 = aT$ above 1–2 K.

The *Raman process* involves a simultaneous interaction with two lattice modes whose difference frequency is the Larmor frequency ω_0. This process can be considered as an inelastic scattering between the paramagnetic species and a phonon of frequency ω_A higher than the Larmor frequency ω_0, which is absorbed taking the paramagnetic system to a virtual state, and then emitted at a minor frequency ω_B, where $\omega_A - \omega_B = \omega_0$. The temperature dependence at low temperature is given by $1/T_1 \propto T^9$ for half-integer S systems (Kramer systems), and $1/T_1 \propto T^7$ for integer S (non-Kramer systems). In the high temperature limit, $1/T_1 \propto T^2$ [31].

The *Orbach-Aminov process* involves the absorption of a phonon with transition from the ground state to a real excited state, and then transition back to the ground state in a different spin state. To be effective, it requires the presence of low lying excited states. The temperature dependence is given by $T_1 \propto 1/[\exp(-\Delta/k_B T)-1]$.

The relaxation induced by the *spin-orbit coupling* is due to the interaction between an electron spin and its orbital motion around an atomic nucleus. Different types of mechanisms can be found, like the Elliot-Yafet or the D'yakonov-Perel mechanisms, or others giving different contributions to relaxations, like the Dresselhaus or the Rashba contributions [32]. These mechanisms are particularly effective in systems where electrons are mobile. In such systems very short relaxation times can be found because the probability for an electron of meeting scattering centers is rather high. For these systems $T_1 = T_2$.

Motions and spin-lattice relaxation: Intramolecular and intermolecular motions with frequencies near the electron Larmor frequency can affect the spin-lattice

relaxation. At X-band some *intramolecular motions* (as e.g. conformational interconversion or methyl groups rotations) can have a frequency similar to the electron Larmor frequency. In particular for methyl groups rotations the time modulation of the beta protons hyperfine coupling constant (h.c.c.) has been shown to be a powerful mechanism for non secular relaxations [33, 34].

The effect of *tunneling* modes for protons in glassy solutions of radicals has also been considered a possible spin-lattice relaxation mechanism [35].

Magnetic interactions between different paramagnetic species can affect relaxation properties.

The spin-lattice relaxation of a species A can be affected by the presence of a faster relaxing species B. The influence on the T_1 values of species A by species B depends on the spectra of the two species, on their spin exchange and dipole-dipole interaction. In the cases in which it is possible to distinguish the effect on the relaxation of species A due to the presence of species B, information on the distance of the two species can be achieved [4, 36].

2.3.1.2 Methods for Measuring T_1

All the pulse methods used for measuring the spin-lattice relaxation rates consist of two steps. The first step is the preparation of the spin system to a non equilibrium population distribution, the second is the observation of the equilibrium recovery. Experiments taking advantage also of magnetic field sweeps or jumps have been described, and a review can be found in Ref. [4].

Saturation recovery with CW-EPR detection. This method has been used for many years [27]. A long pulse of microwaves partially saturate the EPR signal, that is then followed in its evolution towards equilibrium recovery by the monitoring of the CW-EPR signal.

Saturation recovery with pulsed detection of recovery. The EPR signal is saturated with a long cw pulse, or with a train of shorter pulses (see Fig. 2.2). Then the recovery of the magnetization can be followed either by a detection pulse giving rise to a FID, or by a two pulses sequence giving rise to an echo. This second method is normally used for solid state samples, due to the fast decay time T_2^* of the FID for paramagnetic species in solids.

Inversion recovery. The spin state populations are inverted by a convenient mw pulse, and then the recovery of the signal is followed by observing the echo (see Fig. 2.2). Due to the limited spectral range affected by the inverting pulse, this method is not usually convenient for systems giving rise to a spectrum wider than the latter spectral range, *i.e*. wider than ca. 10 G. In fact a single pulse can in the latter case "burn a hole" in the EPR spectrum, and therefore the recovery would be due to a competition between spin-lattice relaxation and spectral diffusion. To ascertain the importance of spectral diffusion in the recovery it is convenient to compare the form of the inversion recovery and saturation recovery curves, where in the second

case the use of trains of saturating pulses allows to extend the saturated range and therefore to reduce the extent of spectral diffusion. Usually the cross checking of the results of the two techniques is useful to have a better insight into the physical meaning of the measured relaxation times. For a direct measure of spectral diffusion rate, see Sect. 2.4.2.1.

Two modifications of a conventional inversion-recovery experiment which exclude the effect of spectral diffusion on the measured spin-lattice relaxation times of rapidly tumbling nitroxide spin labels have been proposed [26].

Stimulated or 3p-ESE. In 3p-ESE (see Fig. 2.2) during time T a non equilibrium magnetization is stored along z, see Fig. 2.4, and therefore it decays in principle with time T_1. Therefore it should be possible to measure T_1 by following the intensity of the stimulated echo by varying the time delay T. The drawback is that the effects of spectral and spin diffusion are more important in this case than in the other described experiments [4]. Therefore a comparison between the rate of stimulated echo decay with the rates of magnetization recoveries gives a criterion for assessing the importance of diffusion of non equilibrium magnetization in the system.

Decay of photoexcited species. Photoexcitation with a laser pulse can create paramagnetic species with non equilibrium populations, and their kinetics to the equilibrium can be followed by probing the magnetization with a two pulses echo on varying the time after the laser pulse [37]. A contribution of both chemical and spin lattice kinetics can be present.

PELDOR (DEER) for measuring Spectral Diffusion. As the major drawback of pulsed methods for measuring T_1 is the intermixing of spin-lattice relaxation and spectral diffusion, Pulsed Electron Double Resonance (PELDOR) is used to measure the contribution of spectral diffusion processes (see for example Ref. [38]). PELDOR will be described in detail in Sect. 2.4.2.1.

2.3.1.3 Applications and Examples

Radicals in glassy phases. A series of nitroxide radicals in different glassy phases have been studied in the temperature range between 20 and 150 K by Du, Eaton and Eaton [39]. The T_1 values have been found to depend on the temperature and on the resonance field. The relaxation is explained by a two phonons Raman process, but the relevant vibrations have been considered as belonging to the molecule itself and not to the lattice modes. At higher temperatures effects due to the increasing mobility of the radicals in the matrices are relevant. The dependence of T_1 on the orientation of the probe in the magnetic field is attributed to the symmetries of the vibrational modes and to the orientation dependence of the spin-orbit coupling. A similar analysis has been reported for a series of semiquinones in a wider temperature range [40].

The T_1 values have been determined for the frozen solutions of radical anions of fullerene C_{60}^- [41] and of a series of mono and bisadducts [42] fulleropyrrolidines. The values obtained were much shorter than the usual ones for organic radicals. The T_1 values increase, approaching the usual values, on increasing the stiffness of the

fullerene sphere going from C_{60}^- to the anions of monoadducts and to bisadducts. The short T_1 has been attributed to the near degeneracy of the π-electrons energy levels of fullerenes, allowing fast radiationless transitions between the different electronic states.

Radicals in molecular crystals. The T_1 values obtained with various pulsed methods (inversion recovery, echo-detected saturation recovery, and PELDOR) on a series of radicals produced by γ- irradiation of polycrystalline samples have been compared. For each sample the relaxation times measured by the various methods are found to be different, apart for 2,4,6-tri-*tert*-butyl-phenoxy radical, which has a single-line EPR spectrum, and as a consequence spectral diffusion is unimportant [43].

Crystalline L-alanine is used for EPR dosimetry of ionizing radiation dose. The spin-lattice relaxation properties of the radical produced by irradiation have been characterized with several EPR techniques. Due to rapid spectral diffusion in the irradiated alanine samples at room temperature, the estimated relaxation times are strongly dependent upon the measurement technique [44, 45]. In general two characteristic times are measured, the shorter one always attributed to spectral diffusion. In Ref. [44] it was shown that with a saturation recovery experiment a biexponential recovery is obtained. The time attributed to spin-lattice relaxation obtained by using more selective saturating (80 ns) and less selective detection pulses (16 ns) was very similar to the value measured by an independent cw electron and nuclear double resonance experiment, Longitudinally Modulated ENDOR technique [46]. Ghim et al. [47] measured the saturation and inversion recovery of irradiated alanine at different EPR frequencies at room temperature. They found that in any case the recovery curves were given by the sum of two exponentials, and the contribution of the faster relaxing component, *i.e*. the spectral diffusion contribution, decreases with increasing microwave frequency. In addition to the changing weights of the two components, the two characteristic times increased with increasing microwave frequency. A more recent similar study shows how the recovery times for alanine radical in dosimeters depend upon the type of dosimeter [48].

The effect of methyl groups rotation on spin-lattice relaxation has been observed in irradiated alanine at different temperatures [34]. Previous ENDOR amplitude studies had shown that the cross electron-nuclear flip-flop relaxation was strongly affected by the modulation of the hyperfine coupling of beta protons due to the methyl group rotation in the radical [33]. The fast component of the inversion recovery curves at different temperatures is completely dominated by the same relaxation mechanism. Clear-cut results are obtained by comparing the different values of the latter fast component for recoveries obtained on different methyl protons hyperfine lines, respectively affected and non affected by the exchange. The slow component of the recovery is shown on the other hand to be dominated by the relaxation process due to the rotation of neighbor $-CH_3$ and $-NH_3$ groups in the undamaged molecules [34].

Triplet states. Spin lattice relaxation has been studied in naphtalene doped with quinoxaline at very low temperature ($T<2$ K) at variable magnetic field. It was

shown that the direct process is taking place, dominated by the coupling with the $\Delta m_S = 2$ transition of the triplet states [30].

Transition metals complexes. In Cu(II) complexes in glassy frozen solution the EPR spectrum is dominated by the g anisotropy, and a striking dependence of T_1 on the resonance field has been obtained, attributed to local intramolecular vibrations modulating anisotropically the spin – orbit coupling [4, 49].

$[Fe_3S_4]^+$ clusters ($S = 1/2$) in four proteins have been studied by pulsed X- and Q-band EPR. The T_1 values have been determined by saturation recovery technique in the range 2–4.2 K. The T_1 values vary sharply across the EPR envelope, due to a distribution in cluster properties. The temperature dependence of $1/T_1$ is analyzed in terms of the Orbach mechanism involving a doublet excited state at 20 cm^{-1} above the ground state [50].

The T_1 values at different temperatures have been measured by inversion recovery for the S_2 state multiline signal of the Mn cluster in Photosystem II oxygen evolving complex in different states [51]. The temperature dependence of T_1 shows that the signal relaxes via an Orbach relaxation pathway, indicative of a low lying excited state at an energy varying in the range 33.8–39.7 cm^{-1} above the ground state.

High−spin Fe(III) octaethylporphyrin in single crystal of the Ni analogue shows T_1 values obtained by inversion recovery that are originated by an Orbach process below 6 K, through the intermediate Kramers states. A D value of 7 cm^{-1} was obtained from the temperature dependence. A spin−lattice relaxation time $T_1 = 4.15$ μs was obtained for the magnetic field perpendicular to the porphyrin plane, 20 times longer than with the field in the plane. This allows to obtain information on the states mixing due to spin orbit interaction [52].

Other systems. The spin lattice relaxation has been measured by saturation recovery with a train of saturating pulses in metallic silver nanoparticles embedded in amorphous SiO_2 and crystalline TiO_2 matrices in the range 4–300 K. T_1 of the order of 10^{-2} to 10^{-1} s have been obtained, the temperature dependence being different in the two matrices, with a Raman-type temperature dependence in the TiO_2 matrix [53].

Hydrogenated amorphous silicon (a-Si:H) spin-lattice relaxation in undoped [31] and n- and p- doped [54] a-Si:H has been measured. The recovery traces are given by stretched exponentials. Dangling bond signals recover with times of the order of 10^{-2} to 10^{-4} s, whereas conduction electrons signals recover with times of the order of 10^{-5} to 10^{-7} s.

The kinetics of spin lattice relaxation of C_{60}^+ radicals in C_{60} powder at room temperature shows a stretched exponential behavior, Eq. (2.21), which is attributed to a distribution of relaxation times. A strong effect of the presence of oxygen on the spin lattice relaxation suggests that the distribution of T_1 values might be due to different interactions of the cation with the adsorbed oxygen [55]. Long T_1 relaxation times are found for $N@C_{60}$, which make this material a suitable candidate for quantum information processing devices [56].

T_1 measurements on inorganic and organic materials have shown that spintronics, a new emerging sector of technology, could benefit by the use of semiconductive

organic materials because of the much longer relaxation times compared to inorganic materials [32]. In Ref. [57] a protocol is described for measuring distances of radicals from metal centers in a protein by saturation recovery.

2.3.2 Transverse Relaxation

The measurement of the electron spin transverse relaxation in the solid phase is performed by using echo experiments. The relaxation is characterized by the rate $1/T_M$ of the irreversible dephasing of the xy magnetization, where T_M is the so called *phase memory time*. This parameter is related but not coincident with the T_2 transverse relaxation time of single spin packets, as explained later.

Two methods are currently used to measure the spin dephasing in the xy plane: the 2p-ESE decay (or Hahn echo decay) and the Carr-Purcell-Meiboom-Gill (CPMG) experiment (see Fig. 2.2). In 2p-ESE decay a series of echoes each obtained at an increasing delay time between the two pulses are observed, whereas in the CPMG experiment the same echo is refocused periodically for several times. The refocusing of the initial spin packets minimizes the effect of the different magnetic energy transfer processes [58]. As a consequence the decay times obtained from CPMG experiments are normally longer than those obtained from 2p-ESE decay [59].

2p-ESE decay is much more popular than CPMG being an easier experiment, suitable also for systems with short phase memory times. Moreover a considerable amount of theoretical work allows to correlate the shape of the decay curves to the relaxation mechanisms [28, 60, 61].

Large differences in phase memory times can be found at different positions of the EPR spectrum, for the residual mobility of the paramagnetic species, or their interactions with the environment, or for different contributions of Instantaneous Diffusion (see next section). In field-swept echo detected EPR (EchoEPR, echo-detected electron paramagnetic resonance, ED EPR), the intensity of the Hahn echo is recorded as a function of the magnetic field B_0 at a fixed time delay τ between the two pulses. Comparing line shapes taken at different time delays allows one to detect the field-dependent contribution to relaxation. As different field positions in the spectra of disordered solids are related to different orientations of the paramagnetic probes, one gets the orientation dependent contributions to the spin relaxation. For samples where the phase memory time T_M varies substantially for the different spin packets, the relative intensities of the EPR lines in CW-EPR and EchoEPR spectra can be very different.

2.3.2.1 Processes of Spin Dephasing

The loss of phase memory is due to: (i). processes affecting the individual spin packets, similar to those giving rise to the homogeneous EPR linewidth in solution, originating from the residual intramolecular and intermolecular motions in the

matrix modulating in time the hyperfine and g tensor parameters; (ii). collective relaxation processes, due to magnetic interactions between different spin packets, and to the interaction with the nuclear spins bath.

The relative importance of the relaxation mechanisms at a given temperature depends on the selectivity of the pulses, on the concentration of the radicals, on their residual mobility in the solid matrix, on the presence of intramolecular motions such as methyl group rotation and on the concentration and type of nuclear spins in the diamagnetic matrix.

In a system with electron spins not interacting between them, neither with the nuclear spins bath, the collective relaxation processes could be neglected. In this case the echo decay would give $1/T_2$, the homogeneous linewidths of the spin packets (in the hypothesis of the same homogeneous linewidth for all of them). The residual motions of the paramagnetic centers in the solid matrix, as librational, intramolecular, etc. give rise to a relaxation behaviour that can be modelled by using the same theory developed for relaxation in liquids. In particular, for "fast" motions the relaxation effects can be analyzed in the framework of the well known Redfield-Freed theory [62, 63] by taking into account the orienting effects of the anisotropic environment [64].

The different processes bringing about the spin dephasing due to spin-spin interactions have been treated in a series of theoretical and experimental works [28, 60, 61, 65, 66]. In the following we give a very short account of them.

Let us consider the relaxation mechanisms due to the electron-electron interactions. The pulses are in general selective, and they excite only a part of the spin packets in the sample (usually called spins A, whereas spins B are not excited). Time dependent dipolar interactions A-A and A-B both contribute to the dephasing of spins A. Very often the time dependence of A-A interaction is dominated by the flipping of the spins produced by the pulses themselves (*instantaneous diffusion*). In this case a clear dependence of $1/T_M$ on the microwave power is found. On the other hand both interactions A-A and A-B are modulated in time by the intrinsic processes of the spin system, *i.e*. spatial and spin dynamics.

The dephasing of spins A can be produced by a relaxation of the first kind, *i.e*. a time fluctuation of the dipolar magnetic interaction parameters due to spatial dynamics. A relaxation of the second kind is due to random modulation of the electron-electron dipolar interaction via spin flips of the coupled spins. These spin flips can be due mainly to spin-lattice relaxation (the so called T_1 samples) or to spin flip-flops (T_2 samples) [22, 28, 66]. The intrinsic relaxation processes and instantaneous diffusion contribute to the rate of spin dephasing in an additive way if the former are not much faster than the latter one [28].

Also nuclear-electron dipolar interactions contribute to the spin dephasing. The most important contribution comes from the bath of the matrix protons, which fluctuate because of the nuclear flip-flop transitions. When this relaxation mechanism is important, the concentration and type of matrix protons is determining the rate of the echo decay [67].

All these relaxation mechanisms give rise to an echo decay (measured by 2p-ESE or CPMG) that can be represented by a stretched exponential. The effective

decay function and the temperature dependence of T_M depend on the dominating relaxation mechanism, and can give information on the dynamics and concentration of the spins.

Theoretical treatments take into account the evolution of the density matrix under the time dependent dipolar interactions between the observed spin packets (spins A) and all the spins present in the system (spins A, spins B and nuclear spins). A detailed treatment can be found in Ref. [60].

In the Appendix the 2p-ESE decay functions for relaxation processes described above are reported.

As for longitudinal relaxation, transverse relaxation can be induced by a residual motion (intra- or inter-molecular) that affects the resonance field value of the species. This effect is well known for paramagnetic species in solution [16].

2.3.2.2 Methods

2-p ESE decay. The 2p-ESE experiment has been described in Sect. 2.2.3. The choice of the pulses length and power depends on the system and on the desired information. Short pulses have a wider bandwidth than long pulses, therefore the number of excited spin packets is higher for short pulses, and an echo of higher intensity is expected. On the other hand, as discussed above, different pulse lengths determine different relative concentration of A- and B-spins, therefore affecting also the dephasing rate. Moreover shorter pulses give rise to a more complex ESEEM modulation, since they can excite a larger range of allowed and forbidden EPR transitions.

The echo decay functions are always stretched exponentials of type:

$$V_d(2\tau) = V_0 \exp\left[(-2\tau/T_M)^x\right] \tag{2.22}$$

The explicit forms are given in the Appendix. From the value of the x exponent one can get information on the mechanism that determines the transverse relaxation.

For the determination of Instantaneous Diffusion, see Sect. 2.4.1.

CPMG. This pulse sequence has been introduced for NMR by Carr and Purcell, and modified by Meiboom and Gill [1]. For a scheme of the pulse sequence see Fig. 2.2. A $\pi/2$-τ-π sequence is used to refocus the magnetization at $t = 2\tau$, where an echo is formed. If a π pulse is applied after a time 3τ, another echo will be formed at time 4τ. In this manner successive π-pulses at $(2n+1)\tau$ $(n = 0,1,2,..)$ form progressively decaying echoes at $(2n+2)\tau$. The advantage is that with a single experiment several points are obtained, reducing the acquisition time. On the other hand the time resolution is limited by the spectrometer dead time t_d, since the condition $\tau \geqslant t_d$ must hold.

It has been shown that the relative contribution from the spectral and spin diffusion to the dephasing is reduced in this experiment with respect to the 2p-ESE decay due to shorter τ values for each recorded echo. In fact the relative contribution to the dephasing of the diffusion terms compared to the T_2 term depends on τ, and it can be decreased on decreasing τ [1, 58, 68].

The intensities of unwanted echoes overlapping regular echoes can be strongly reduced by using a hard $\pi/2$ pulse, followed by more selective long pulses [68]. To overcome the problem of the cumulative effects due to the deviation of the pulse rotation from π a 90° phase shift between subsequent π pulses is used [1].

A detailed full analysis of CPMG experiments has been carried out by Schwartz et al. for the case of EPR of nitroxides in viscous solution both in fast and slow motional regime [58]. This method is applicable to situations in which slow reorientations of the molecules are possible, like, for example, in soft glasses close to the melting point. The method is based upon the evaluation of the eigenvectors and the eigenvalues of the stochastic Liouville operator. The primary echo is calculated to be a sum of exponential decays with characteristic times related to the differences of eigenvalues.

A systematic comparison of the results obtained from 2p-ESE decay and CPMG on various irradiated polycrystalline organic and inorganic solids can be found in Ref. [69].

EchoEPR. EchoEPR spectra are obtained by recording the two pulse (or more rarely the three pulses) echo intensity, for a given τ, as function of the magnetic field B_0. In general the latter for a given B_0 and τ can be calculated by [70]:

$$E(2\tau, B_0) = E_{CW}(B_0)V_m(2\tau, B_0)V_d(2\tau, B_0) \tag{2.23}$$

where E_{cw} is the intensity of the CW-EPR spectrum, V_m and V_d the nuclear modulation and decay functions. The dependence of the echo intensity on the nuclear modulation can help in disentangling EchoEPR spectra due to species with different modulations [71]. However in general the effect of the modulation is strongly reduced by using long selective pulses. To get a better spectral resolution $\Delta\omega$ the echo is integrated with a window $\Delta t_{obs} > 2\pi/\Delta\omega$. [4, 59].

For an oriented paramagnetic center the terms in Eq. (2.23) depend on the orientation of the magnetic field with respect to the molecular axes. For a disordered distribution the angular dependence has to be integrated over all the possible orientations of the magnetic field. For $S = 1/2$ coupled with a nuclear moment I, by neglecting the effect of the nuclear modulation, the EchoEPR spectrum can be computed by the expression [72]:

$$E(2\tau, B_0) = \sum_{M=-I}^{I} \frac{1}{4\pi} \iint \sin\theta d\theta d\varphi f\left[(B_0 - B_M(\theta, \varphi))/\delta\right] R_M(2\tau, \theta, \varphi) \tag{2.24}$$

where $f\left[(B_0 - B_M(\theta, \varphi))/\delta\right]$ is the residual lineshape function, and $R_M(2\tau, \theta, \varphi)$ the relaxation decay function for the particular spin packet.

EchoEPR spectral profiles are generally different with respect to the cw ones. This can be due to any anisotropic decay of the magnetization, and/or to the effect of instantaneous diffusion that depends on the concentration of the spin packets resonating at each field value.

2.3.2.3 Applications

Phase memory times by 2p-ESE. By means of the analysis of the electron spin echo decay of nitroxide radicals, a wealth of information has been obtained on the spin relaxation mechanisms of the spin probes. A correct analysis therefore allows exploiting the echo decay results and provide an insight into dynamical and structural properties of condensed phases of different types (see for example Refs. [73, 74]).

At very low temperatures in diluted nitroxide glassy solutions in proton-containing solvents the fluctuations of nuclear spins dominate the echo dephasing [24, 28, 61, 75, 76]. The protons of the matrix are known to produce dephasing of the electron spins thanks to the random modulation of the local magnetic field due to their nuclear flip-flop transitions. The echo decay depends therefore on the proton concentration, but also on the type of protons. Particularly effective in producing dephasing are methyl groups, suggesting an important contribution from tunneling processes. Eaton et al. determined a dependence of the rate of dephasing on the barrier hindering the methyl groups rotations [67, 76]. At higher concentration of radicals and in deuterated solvents the instantaneous diffusion dominates [76].

On increasing the temperature the echo decay becomes more and more dominated by relaxation processes related to different motions of the probes: contributions from the softening of the glassy phase and from the intramolecular motions of the probe itself can be present.

In Ref. [24] a detailed study of the echo decay at different temperatures for the tempone radical hosted in a single crystal allows to study the effect on the dephasing of the intrinsic motions of the probe. Methyl groups rotation, conformational interconversion and a libration in the matrix contribute to the echo decay for $T>80$ K, giving rise to a minimum in phase memory time $T_M<150$ ns in the range 130–210 K.

Echo decay and motions. The temperature dependence of phase memory time can be used to study the motion of the paramagnetic species in a given matrix.

Echo decays of hydrazinium ions in lithium hydrazinium sulphate (LHS) show two local minima for T_M, at 115 K and at 175 K [77]. The minimum at 115 K is attributed to hydrazinium ion librations, whereas the one at 175 K is produced by the hindered rotation of the $-NH_3^+$ group. The minima are explained as due to the transitions from slow to fast limit motions as compared with the splitting between the hyperfine proton lines.

An application of the CPMG method to a study of rotational motions in *t*-butyl groups of the phenoxy radical formed in γ-irradiated single crystal of 4-methyl-2,6-di-*t*-butyl phenol in the temperature range 130–290 K has allowed to detect three different kinds of motions. The resulting values of the dynamical parameters are in good agreement with those obtained for the undamaged precursor molecule by previous NMR studies [78].

Applications of EchoEPR spectroscopy. EchoEPR spectra are particularly suitable to study the anisotropy of spin relaxation in disordered solid systems. This

method has been applied to study nitroxides in organic glasses [79, 80] and spin probes in membranes at cryogenic temperatures [81]. A review [82] reports echo detected EPR studies on spin-labelled lipids in membranes, by using both 2p echo-detected spectra for determining rapid rotational motions, and 3p echo-detected spectra for slower motions.

The anisotropic librational motion of semiquinones in photosynthetic reaction centers of Rhodobacter sphaeroides R26 and in frozen isopropanol solution have been studied by Rohrer et al. [83] at W-band. The high magnetic field allows a sensitive detection of the orientation-dependent echo-decay functions, thanks to spectral resolution of the anisotropic Zeeman interaction.

The symmetries of different coordinating sites of Fe(III) incorporated into aluminosilicate and aluminophosphate sodalite affect the relaxation times of the paramagnetic ions, the ones with a more symmetric environment relaxing more slowly. X- and W-band EchoEPR spectroscopies allow to distinguish between them [84].

Extensive use of the capabilities of the EchoEPR technique has been done in a study on Cu(II)-doped inorganic glasses. X- and S-band EchoEPR yield information on the local symmetry of the Cu(II) coordination polyhedra, the chemical nature of the atoms in the second and higher coordination spheres, the distribution of the parameters of the static spin Hamiltonian and the low-temperature motions of the dopant-containing structural units [85].

When more paramagnetic species with different relaxation properties contribute to a CW-EPR spectrum, EchoEPR can help in disentangling their spectral contributions. As an example, we report an EchoEPR study on irradiated tooth enamel [86]. Ionizing radiations produce CO_2^- radicals in different sites that are characterized by different mobilities and relaxation properties, with overlapping CW-EPR spectra. We have acquired EchoEPR spectra of tooth enamel samples respectively UV and γ-irradiated. Spectra with a long delay ($\tau = 5\ \mu s$) detect only the orthorhombic slowly relaxing species, and are identical for the two samples. On the other hand spectra with a short delay ($\tau = 200$ ns) due to mobile radicals with a partially motionally averaged axial g tensor can be detected only in the UV irradiated sample.

EchoEPR has also been used to study the motion of molecules in their triplet state. The comparison between the spectra profiles of CW-EPR and EchoEPR spectra of a 4-4′ disubstituted dithiophene in triplet state allowed to detect different anisotropic types of motions in glassy toluene and in a channel inclusion compound [87]. This behaviour has been attributed to spin relaxation due to modulation of the Zero Field Splitting tensor induced by fast librational motions of the dithiophene triplet.

2.4 Methods Oriented to Get Information on the Spatial Distribution of Paramagnetic Probes

The determination of the spatial distribution of paramagnetic probes can be done by using different effects: the instantaneous diffusion, from which the local or microscopic concentration of radicals can be obtained, the electron-electron

interaction strength that can be obtained by measuring the modulation of the echo in the out-of-phase component, or by using a two-frequencies experiment, where the modulation is created by an artificial spin flip of the coupled spins.

2.4.1 Instantaneous Diffusion and Spin Concentration

The contribution to the 2p echo dephasing by the microwave pulses themselves is called instantaneous diffusion. When instantaneous diffusion contributes to the spin dephasing the relaxation rate is dependent on the microwave power, and this effect is used as a clue to instantaneous diffusion [88–91]. If this is the case, for non selective pulses the echo intensity depends on the tilting angles θ_i of the i-th pulse; if $2\theta_1 = \theta_2$ the echo intensity is given by the expression:

$$V_d(2\tau) \propto \sin^3\theta_1 \exp(-2\tau / T_M) \tag{2.25}$$

the phase loss rate has the form:

$$1/T_M = A + B \cdot \sin^2(\theta_1) \tag{2.26}$$

where A is the contribution due to any other process, and B is due to instantaneous diffusion and given by:

$$B = (4\pi^2\gamma^2\hbar C \Big/ 9\sqrt{3}) = b \cdot C \tag{2.27}$$

where $b = 8.2\ 10^{-13}$ cm^{3}s^{-1}, and C is the concentration of the spins affected by the pulses in spins/cm^3 [65]. The selectivity of the pulses can be taken into account [88].

Determination of the Instantaneous Diffusion. When instantaneous diffusion is a relevant relaxation mechanism, a study of the microwave power dependence of the echo decay can give the microscopic average concentration of radicals in the sample. This determination has been done in a number of cases [88–90] and is very important in the field of dosimetry of ionizing radiation, as the biological damage of a radiation is determined mostly by the way in which the energy is released [92].

The effect of instantaneous diffusion can be detected in EchoEPR spectra, as shown in Fig. 2.6. In the figure one can see two EchoEPR spectra of partially deuterated irradiated ammonium tartrate, obtained with different mw power levels [70]. The spectrum with low power (upper trace) is similar to the cw one, showing the main spectrum due to the radicals with ^{12}C and weak sidebands due to radicals with ^{13}C. On the other hand in the EchoEPR spectrum with higher power level the instantaneous diffusion affects strongly the phase memory times of the spin packets corresponding to the more concentrated radical (with ^{12}C), whereas the instantaneous diffusion contribution to the total relaxation is much smaller for the

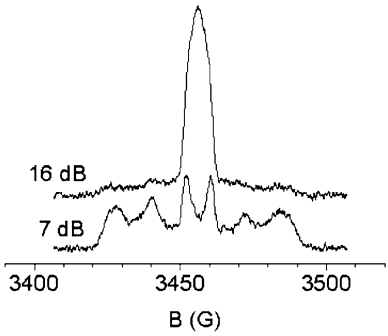

Fig. 2.6 EchoEPR of partially deuterated irradiated ammonium tartrate at room temperature. The main CW-EPR spectrum is given by a single line for this orientation of the single crystal in the magnetic field. Satellite lines are due to molecules with ^{13}C in natural abundance. The two EchoEPR spectra are obtained at different microwave attenuations by means of a 2p-ESE sequence with a $\pi/2$ pulse of 24 ns, a π pulse of 48 ns and a τ of 1,216 ns (More details are given in Ref. [70]. Reprinted from Ref. [70] with kind permission of © Springer, 2001)

satellite bands, due to the much lower concentration of the relative species, thus giving a stronger signal for these lines.

2.4.2 Determination of Distance Between Spin Probes

The fine interaction parameter D between two localized electron spins at a distance $r \sim 2$ nm is $D \sim 3.4$ G [93], therefore contributing only to the linewidth in a CW-EPR spectrum. On the other hand, for distances of this order of magnitude or larger it is possible to obtain information on the electron-electron distance by pulse EPR. A very concise summary of the experiments follows. Reviews of the methods can be found in refs. [4, 94–96].

2.4.2.1 Methods: PELDOR (DEER)

The insertion of an extra pulse between the $\pi/2$ and π pulses of a 2p-ESE sequence produces an increase of dephasing rate depending on the dipolar interactions between the spins giving rise to the echo. This pulse sequence has been called $2 + 1$, to distinguish the role of the pulses. By varying the position of the extra pulse one gets a modulation of the echo intensity giving information between the distances between spin probes [97, 98]. In a more convenient version of this experiment the extra pulse (pumping pulse) is at a different mw frequency with respect to the two pulses producing the echo. This latter technique is called either PELDOR [75] (Pulsed Electron Electron Double Resonance) or DEER (Double Electron-Electron Resonance).

A 2p-ESE sequence with a fixed interpulse delay τ generates a spin echo by selectively exciting a collection of *A*-type spins (on-resonance, at microwave frequency ν_1, probe pulse). The selective pumping π-pulse at microwave frequency ν_2 gives rise to flips of spins *B* changing the dipolar interactions with spins *A*. The effect of the introduction of this extra pulse is double: on varying the position of the pump pulse with respect to the first pulse of the exciting sequence, a PELDOR signal decay occurs [100] with a time depending on $1/\omega_{ee}$, where ω_{ee} is the dipolar spin coupling [99]; moreover, in the case of distributions of spin-spin distances within a limited range (as for example in biradicals with rigid structures or in crystals) the echo envelope is modulated. The modulation depends on the fine interaction between the two electrons [99]. The π-pulse on-resonance with the *B*-type spins (pump pulse), inserted at time $\tau_1 < \tau$ after the first $\pi/2$-pulse of the 2p-ESE sequence, generates a phase gain $\omega_{ee}\tau_1$ to the precession frequency of *A*-type spins, due to dipolar interaction ω_{ee}, that can not be reversed by the π-pulse of the echo sequence. On varying the time τ_1 of the pump pulse a modulation of the echo amplitude is created:

$$\omega_{ee} = \frac{g_A g_{B'} \mu_B^2 \mu_0}{4\pi\hbar} \frac{1}{r^3} (3\cos\beta_{AB'} - 1) \tag{2.28}$$

where g_A and $g_{B'}$ are the *g*-factors of the two partners, and $\beta_{AB'}$ is the relative orientation of the radicals with respect to the external field [101].

For pairs of spins at a fixed distance but with a complete orientational disorder with respect to the field direction, as in a powder samples, the Fourier Transform of the modulation gives the well known Pake distribution of frequencies [102]. If a peaked distribution of distances is present, for each distance a typical Pake distribution of frequencies is obtained; in this case a deconvolution procedure is required to extract the information on the distances from the Fourier Transform of the modulation. For broad distributions the modulation is undetectable and only an exponentially decaying PELDOR signal is observed [100].

It should be noted that in addition to the electron-electron dipolar interaction in some cases also the exchange coupling constant J and its distribution can influence PELDOR data, and must be taken into account [103].

The most used PELDOR pulse sequence is a four pulses version, which has been introduced to allow the detection of the modulation with zero dead-time. This is achieved by introducing a further π-pulse in the ESE sequence to refocus again the first formed echo like in the CPGM sequence [102], see Fig. 2.2.

Various analysis programs for PELDOR data have been developed; among these the DEERAnalysis software [104] has been implemented for the four pulses experiment and it provides an automatic routine to obtain directly distribution distances by fitting the time profile patterns.

Distance measurements are carried out usually at X-band, but they can also be performed at higher frequencies [14, 105]. Significantly improved sensitivity is observed by using Q-band [106]. At W band and higher frequencies the PELDOR traces for pair of paramagnetic centers with g-anisotropy offer additional

information such as the relative orientations of the g-tensors of the two coupled paramagnetic centers [105–107].

A further technique allowing to measure distances between spin probes is DQC-ESR (double quantum coherence ESR) [108] and the modulation of the out-of-phase echo (see further).

Out-of-phase ESEEM. This technique has been applied to the measurement of electron-electron distance in spin-correlated radical pairs. The modulation of the out-of-phase echo is dominated by spin-spin couplings between the two radicals [93, 124]. Exchange and dipolar interactions can be both measured.

Important information on light-induced structural changes as the distance between acceptor and donor cofactors in the reaction centers has been obtained from the study of the radical pairs formed following photoexcitation in photosynthetic systems (see Refs. [37], [125] and references therein).

2.4.2.2 Some Applications of PELDOR

Spin probes and biological systems. Over the last 10 years PELDOR has emerged as a powerful new biophysical method that measures distances (1.5–8 nm) between paramagnetic probes via the dipolar electron electron coupling (a review can be found in Ref. [109]). The availability of the site-directed spin labelling in proteins or other molecules such as nucleic acids [110] has extended strongly the possibility of the use of this technique [111]. It has been applied to a large variety of nucleic acids as well as proteins and protein complexes. Small nitroxide spin labels, paramagnetic metal ions, amino acid radicals or intrinsic clusters and cofactor radicals have been used as paramagnetic centres [112–116]. A common approach is to perform a doubly covalent spin-labeling of a macromolecule with nitroxide spin labels, and a single spin-labeling in systems already containing a paramagnetic center as a metal ion, or in systems that forms aggregates or oligomers (spin-clusters). Recently complexes of Gd(III) have been used as probes for W-band PELDOR [117]. A specific study on the use of Cu(II) as probes for PELDOR is reported in Ref. [118].

The method has been nicely calibrated for RNA residues, and a rather high correlation is found between the measured inter-nitroxide distances with those predicted from the parent RNA structure [113].

Other successful applications to complex structures are for example those to dimers or self-assembled systems of human serum albumin (HSA) [119] or to s pin-labeled fatty acids [120].

At W band and higher frequencies, the DEER traces for pair of paramagnetic centers with a g-anisotropy depend also on the relative orientation of the *g*-tensors of the two spin labels with respect to the inter-spin vector. At 180 GHz, this further information has allowed for example to define the relative orientations of two radicals embedded in the active dimeric ribonucleotide reductase enzyme in solution [105].

Synthetic systems. Synthetic systems have also been studied by PELDOR, obtaining information on the local ordered structure which cannot be reached by any other method [101]. By a CW-EPR and PELDOR study on systems of spin-carrying counterions and oppositely charged, rodlike Ru(II) coordination polymers, it has been shown that the spatial distribution of divalent counterions reflects the spatial distribution of charges on the polyion [121].

The Gd(III)-nitroxide spin pair has also shown to be a nice partnership for the use of PELDOR technique, and a good substitute for the nitroxide – nitroxide pair of spin labels and potentially provides a link to other experimental approaches dealing with structural information [122].

Radiation damages. DEER has been used to measure the distribution of radicals produced by ionizing radiations on ammonium tartrate irradiated at high temperature [123] and on DNA crystals irradiated at low temperature [100].

In the former study the PELDOR spectra yielded the distributions of distances between pairs of radicals produced by the same radiation event, two to five crystal cells apart. The inter-radical distributions are strongly dependent on the radiation quality, and can be correlated to the specific matter-radiation interactions for the various beams [123].

In Ref. [100] the radical density and spatial extent have been obtained from the analysis of PELDOR contribution to echo decay, providing the first direct experimental determination of track characteristics in irradiated DNA.

2.5 Methods Oriented to Get Information on the Local Environment of Paramagnetic Centers *via* the Interaction with Nuclear Spins

The determination of hyperfine interactions is important both for assessing the structure of the paramagnetic species and for obtaining information on the 3D local geometry around the electron spin probe. CW-EPR spectra of paramagnetic species in solid state exhibit generally broad lines, due to the magnetic anisotropies and to the large number of hyperfine dipolar couplings. The poor resolution hinders the determination of the hyperfine couplings, except those large with respect to the inhomogeneous linewidths.

2.5.1 The Determination of Hyperfine Interactions

A wealth of pulse EPR methods have been developed to obtain information on the hyperfine interactions, sometimes referred to collectively as Hyperfine Spectroscopy. They allow to detect nuclei surrounding the paramagnetic probe in a range of distances up to 0.5 nm. The most popular ones, which have been extensively

used in all fields, from biology to material science, are 2p and 3p ESEEM, 4p hyperfine-sublevel correlation (HYSCORE) [126] and Mims and Davies ENDOR.

All ESEEM pulse sequences have in common that they consist only of microwave pulses with one microwave frequency and that they generate an electron spin echo, whose intensity is detected as a function of one or two inter-pulse distances. The detected modulation of this echo intensity reflects the nuclear interactions. In pulse ENDOR, the sample is irradiated with a combination of microwaves and radio waves, both pulsed.

In principle ENDOR and ESEEM give the same information, i.e. frequencies related to the nuclear resonance transitions, but ESEEM methods are more suitable than ENDOR to resolve small hyperfine interactions. For a weakly coupled nucleus with $I = 1/2$ the ENDOR frequencies $\nu_{\alpha,\beta}$ are given for a particular orientation *(l,m,n)* of the magnetic field in an arbitrary reference system by

$$\nu^2{}_{\alpha,\beta} = \frac{1}{4}\left\{\left[\left(T_{xx} \mp 2\nu_N\right) l + T_{xy}m + T_{xz}n\right]^2 + \left[T_{xy}l + \left(T_{yy} \mp 2\nu_N\right) m + T_{zy}n\right]^2 + \left[T_{xz}l + T_{yz}m + \left(T_{zz} \mp 2\nu_N\right) n\right]^2\right\} \tag{2.29}$$

where ν_N is the nucleus Larmor frequency, T_{ij} are the components of the hyperfine coupling tensor in the reference system. If $|\nu_\alpha - \nu_\beta|$ is of the order of magnitude of the ENDOR linewidths the nuclear spin contributes to the so-called matrix ENDOR band. In this case only the ESEEM technique can give information on the number and hyperfine tensors of weakly coupled nuclei.

On the other hand, the condition for observing ESEEM is the simultaneous excitation of allowed and forbidden EPR transitions. As a consequence, due to the limited bandwidth of microwave pulses, only small couplings can be studied with ESEEM. This condition is not stringent in the case of ENDOR techniques that therefore allow the determination also of large couplings. The two types of techniques are in conclusion complementary. This is true also by considering the relative intensities in different frequency ranges, since ESEEM is particularly suited to determine low frequencies, as the modulation depths are more pronounced at low frequency, whereas the sensitivity of pulse ENDOR is higher for high radio-frequency transitions.

All these methods can be applied at different microwave frequencies, increasing further the flexibility of EPR spectroscopy. The EPR spectroscopist has therefore today a really large variety of methods at his disposal. Working at mw frequency higher than X-band improves in general the resolution, by separating the nuclear resonance frequencies and by enhancing the orientational selection due to Zeeman anisotropy [127–129]. ENDOR benefits more from a higher magnetic field than ESEEM, as for this latter the echo modulation depth diminishes at higher frequencies. HYSCORE experiments are better performed in the microwave range 2–35 GHz, as high frequency HYSCORE would need high-power microwave pulses, which are at present only attainable in prototype spectrometers [130, 131].

2.5.1.1 Methods: ESEEM Spectroscopy

The most popular experiments are 2p- and 3p- ESEEM, but other pulse sequences have been also proposed [4, 8, 23, 132, 133].

2p-ESEEM. The ESEEM effect due to the hyperfine interaction with a nuclear spin can be detected when the mw pulse creates coherences corresponding to the relative allowed and forbidden EPR transitions, see Fig. 2.3. After the $\pi/2$ pulse the four coherences (the "allowed" σ_{13} and σ_{24}, and the "forbidden" σ_{14} and σ_{23}) precess in the xy plane each with its frequency. After precessing for a time τ at frequency ω_{ij} each coherence *ij* has acquired a phase $\Delta\varphi_{ij} = \omega_{ij}\tau$.

The π pulse has the effect of reversing the phase of all the coherences, but also it can induce a nuclear spin flip, as discussed in the theory section. As a consequence, only a fraction of each initial coherence σ_{ij} is refocused after time τ, i.e. the fraction which has conserved the same frequency after the π pulse. The other fractions are now precessing at a different frequency $\omega_{ij} + \Delta\omega$, and therefore they will refocuse at different times with respect to τ, unless their frequency jump $\Delta\omega$ is such that $\Delta\omega\tau = 2n\pi$. The echo intensity recorded for different τ is therefore showing a "modulation", with frequencies that are the differences between those of the allowed and forbidden EPR transitions, i.e. the ENDOR frequencies and their combination [23, 134, 135].

A straightforward analysis for this system can be done with a density matrix approach to obtain the function $V_m(t)$ in Eq. (2.18) for a 2p-ESEEM experiment.

The result for the $S = 1/2$, $I = 1/2$ system is [6]

$$\begin{aligned} V_m(2\tau) &= 1 - 2k\left[\sin^2(\pi\nu_\alpha\tau)\sin^2(\pi\nu_\beta\tau)\right] = \\ &= 1 - \frac{k}{2}\left[1 - \cos(2\pi\nu_\alpha\tau) - \cos(2\pi\nu_\beta\tau)\right. \\ &\quad \left. + \frac{1}{2}\cos(2\pi\nu_+\tau) + \frac{1}{2}\cos(2\pi\nu_-\tau)\right] \end{aligned} \tag{2.30}$$

where ν_α and ν_β are respectively the two ENDOR frequencies, $\nu_+ = \nu_\alpha + \nu_\beta$ and $\nu_- = \nu_\alpha - \nu_\beta$ and k the modulation depth

$$k = \left(\frac{\nu_N B}{\nu_\alpha \nu_\beta}\right)^2 \tag{2.31}$$

The B parameter, given in a generic reference system *xyz* in which the external magnetic field is in the plane *xy* with direction cosines *(l,m,0)*, is [136]:

$$B = \sqrt{\left(T_{xz}l + T_{yz}m\right)^2 + \left[\left(T_{xx} - T_{yy}\right)lm - T_{xy}\left(l^2 - m^2\right)\right]^2} \tag{2.32}$$

In the expression above we can note that combination frequencies appear in the spectrum with opposite sign and with half intensity with respect to the ENDOR frequencies. When the applied field is along the principal directions of the hyperfine tensor $B = 0$, then the modulation depth is also equal to zero.

Analytical expressions have been obtained also for a nucleus with $I = 1$ as

$$V_m(2\tau) = 1 - \frac{16k}{3}\sin^2(\pi\nu_\alpha\tau)\sin^2(\pi\nu_\beta\tau) + \frac{16k^2}{3}\sin^4(\pi\nu_\alpha\tau)\sin^4(\pi\nu_\beta\tau) \quad (2.33)$$

For weak interactions the term in k^2 can be neglected and an expression similar to the $S = 1/2$, $I = 1/2$ case is obtained.

For $I > 1/2$ systems, non-negligible nuclear quadrupolar interactions have to be taken into account. For the solution of these problems we send the reader to selected publications [8, 15, 23], where details for analytical as well as numerical solutions are given.

It can be seen that if n interacting nuclei are present, the modulation function is given by the product of the modulation functions of each single nucleus as [23]

$$V_m^{tot} = \prod_{i=1}^{n} V_m^i \quad (2.34)$$

The effect of the power and length of the pulses on the modulation has been analyzed in Ref. [137, 138]. Pulses of 10 ns can excite allowed and forbidden transitions in a range of several gauss (typical values are around 10 G ca).

Modulation of the echo intensity can also be induced by electron-electron interactions. This effect is observed in photoproduced radical pairs [93, 124]. In these systems the normal in-phase echo is zero, whereas a modulated out-of-phase echo is observed; the modulation frequency depends on the electron-electron distance, as discussed shortly in Sect. 2.4.2.

3p-ESEEM. In 3p-ESEEM the modulation of the echo envelope is observed by increasing the T delay between the second and third $\pi/2$ pulses, see Fig. 2.2. This technique offers the advantage that the echo modulation usually occurs on longer time scales, thus obtaining a better frequency resolution respect to 2p-ESEEM. For the latter experiment the echo decay is determined by transverse relaxation processes. On the other hand in 3p-ESEEM during T the decay is due to slower processes like electron spin-lattice relaxation, spectral diffusion and transverse nuclear relaxation, as a consequence of the polarization and coherences present in this evolution period (see Fig. 2.4).

The analysis done for the 2p-ESEEM can be extended to 3p-ESEEM. The modulation of the stimulated echo depends on the nuclear coherences present during time T. (see Fig. 2.4). During T the matrix elements corresponding to nuclear coherences precess at the ENDOR frequencies ν_α and ν_β. Therefore these frequencies only are seen in the modulation of the stimulated echo.

Exact solutions can be obtained for the $S = 1/2$, $I = 1/2$ case, for which the expression is [6]:

$$\begin{aligned} V_m(2\tau + T) &= 1 - k\left[\sin^2(\pi\nu_\alpha\tau)\sin^2\left(\pi\nu_\beta(\tau + T)\right)\right. \\ &\quad \left. + \sin^2\left(\pi\nu_\beta\tau\right)\sin^2(\pi\nu_\alpha(\tau + T))\right] \\ &= 1 - \frac{k}{2} + \frac{k}{4}\left\{\cos(2\pi\nu_\alpha\tau) + \cos\left(2\pi\nu_\beta\tau\right)\right. \\ &\quad + \left[1 - \cos\left(2\pi\nu_\beta\tau\right)\right]\cos(2\pi\nu_\alpha(\tau + T)) \\ &\quad \left. + \left[1 - \cos(2\pi\nu_\alpha\tau)\right]\cos\left(2\pi\nu_\beta(\tau + T)\right)\right\} \end{aligned} \tag{2.35}$$

It is worth to note that the combination frequencies ν_+ and ν_- are absent when T is varied, therefore the spectrum is simpler with respect to 2p-ESEEM.

Another important point is that modulations due to the two frequencies ν_α and ν_β are weighted by factors that depend on τ, that are equal to zero when the condition $\nu\tau = n$ is fulfilled. The latter condition gives rise to the so called *blind spots*: for particular values of τ, some frequencies are not appearing in the spectrum. One can use this condition to eliminate, for example, modulation due to one type of nuclei to put in evidence the modulations due to other nuclei. On the other hand, to be sure to detect all the modulation frequencies, several decays corresponding to different τ values must be recorded. A systematic variation of both T and τ is also possible, giving rise to a 2D-experiment. However, the same information given by such experiment is given with better resolution by HYSCORE, described below.

Similarly, for the 3p-ESEEM of a $S = 1/2$, $I = 1$ system with negligible quadrupolar interaction, one obtains

$$\begin{aligned} V_m(2\tau + T) =& 1 - \frac{4k}{3}\left\{\sin^2(\pi\nu_\alpha\tau)\cdot\left[1 - \cos(2\pi\nu_\beta(\tau + T))\right] + \right. \\ &+ \left.\sin^2\left(\pi\nu_\beta\tau\right)\cdot[1 - \cos(2\pi\nu_\alpha(\tau + T))]\right\} + \\ &+ \frac{4k^2}{3}\left\{\sin^4(\pi\nu_\alpha\tau)\cdot\left[1 - \cos(2\pi\nu_\beta(\tau + T))\right] + \right. \\ &+ \left.\sin^4\left(\pi\nu_\beta\tau\right)\cdot[1 - \cos(2\pi\nu_\alpha(\tau + T))]\right\} \end{aligned} \tag{2.36}$$

As for the 2p-ESEEM, other cases require particular treatments to obtain analytical or numerical solutions [8, 15, 23].

HYSCORE. HYSCORE [139] is a two-dimensional experiment derived from the 3p-ESE where a π pulse has been introduced in between the second and third $\pi/2$ pulses (see Fig. 2.2). The effect of the introduction of a π pulse is a transfer of population from one m_s manifold to the other, and a mixing of nuclear coherences in one manifold with those of the other manifold. In the following evolution time these new created coherences evolve with new frequencies corresponding to correlations

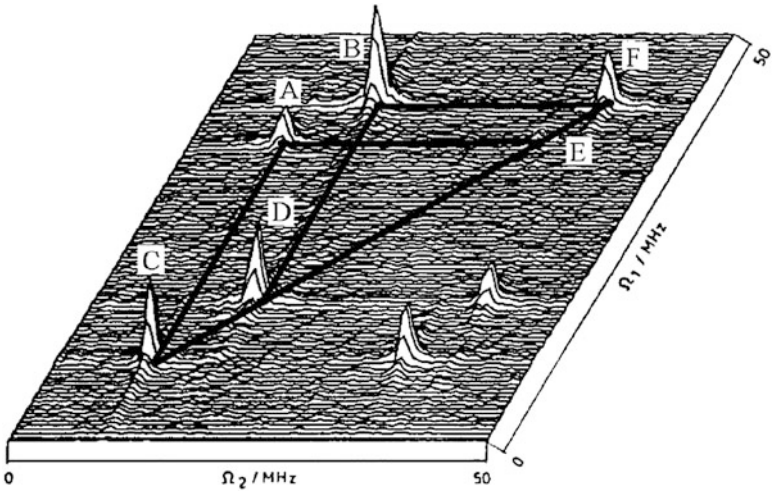

Fig. 2.7 HYSCORE absolute value spectrum of an irradiated succinic acid single crystal at room temperature. Pulse separation $\tau_1 = 200$ ns, pulse width 10 ns for $\pi/2$ and 14 ns for π. Recorded data matrix (130, 130) with steps of 8 ns; zero filled to (256, 256) and apodized in t_1 and t_2 prior to FT (Adapted from Figure 8 in Ref. [140]). In the text the labelling of the peaks is explained. Cross-peaks are expected between nuclear transitions that belong to the same manifold. Cross peaks between *C* and *E* (peak *A*) and between *D* and *F* (peak *B*), and the relative symmetric peaks with respect to the diagonal (not labeled in the figure) present, then indicating that *C* and *E* belong to one spin site and that *D* and *F* belong to a different site (Adapted from Figure 8 in Ref. [140] by kind permission of Dr Hoefer, Bruker-Biospin, Germany)

between sublevels of the two m_s manifolds. These correlations show up as cross peaks in the 2D-FT of the modulation of the echo.

The echo intensity is recorded by varying t_1 and t_2. After a double FT with respect to these times, a 2D spectrum with axes ω_1 and ω_2 is obtained. The correlation of two ENDOR frequencies $\omega_\alpha, \omega_\beta$, relative to the same nucleus, is indicated by a cross peak corresponding to the two frequencies. Since only pairs of frequencies belonging to the same paramagnetic center are correlated, this technique allows disentangling the spectra due to different species. As an example, in Fig. 2.7 one can see the HYSCORE absolute value spectrum of an irradiated succinic acid single crystal at room temperature.

The two pairs of peaks on the diagonal (C, D, E and F) are the regular ESEEM peaks originating from two α-proton couplings. They are attributed to two different sites in the crystal. Moreover, if two types of nuclei are detected, with frequencies $\omega_{\alpha1}, \omega_{\beta1}, \omega_{\alpha2}, \omega_{\beta2}$, cross peaks appear also at $\omega_{\alpha1}, \omega_{\beta2}$ and $\omega_{\beta1}, \omega_{\alpha2}$.

If the two h.c.c.'s of nuclei 1 and 2 have the same sign, $\omega_{\alpha1}, \omega_{\beta2}$ and $\omega_{\alpha2}, \omega_{\beta1}$ are pairs of high/low (or low/high) frequencies, whereas if the two h.c.c.'s of nuclei 1 and 2 have opposite sign $\omega_{\alpha1}, \omega_{\beta2}$ and $\omega_{\alpha2}, \omega_{\beta1}$ are pairs of high/high (or low/low) frequencies. Therefore the relative signs of the h.c.c.'s are obtained.

With respect to 1D technique, the resolution is therefore improved. Moreover, it overcomes the problem of instrumental deadtime that introduces lineshape

distortion and loss of broad lines in the 1D spectra. Thus this technique is particularly useful in the study of disordered samples and broad signals.

Details on the theory of HYSCORE with ideal and non-ideal pulses can be found in refs. [141, 142]. Extension of the analysis to systems with $S>1/2$, typical of metals, can be found in Ref. [143].

Signal analysis. The time trace of ESEEM is normally very little informative without proper analysis. One way to proceed is to perform a spectral analysis in order to extract the frequency components out of the ESEEM signal, that are related to hyperfine interactions. Normally this is achieved by subtracting the unmodulated part of the signal, very often well approximated by an exponential decay, and then by performing the Fourier Transform of the modulated signal. Standard procedures are available to reach this goal [144].

ESEEM signals suffer from strong limitations due either to the instrumental dead time or to the limited extent of the signal. To improve the signal-to-noise ratio and to avoid introduction of artifacts on the spectrum, some advanced mathematical methods are currently available. A discussion about the comparison among the methods can be found in Refs. [4, 145]. An efficient approach for powder samples, within the point-dipole approximation, is to use the spherical approximation model [146] to fit directly the time profile from structural information. This has the advantage that time profiles are calculated by assuming a given geometry (distances of paramagnetic nuclei from the paramagnetic center, number of equivalent nuclei).

2.5.1.2 Methods: Pulse ENDOR Spectroscopy

ENDOR spectroscopy takes advantage of the use of a second radiating field in the radiofrequency (rf) band to induce nuclear transitions. CW-ENDOR is a very well known and powerful spectroscopy, however the interplay of the relaxation rates often limits its applicability. Pulse ENDOR spectroscopy in general overcomes the problem of unfavourable relaxation properties; however, it requires the detection of the ESE signal, therefore the transverse relaxation time must be longer than ≈ 100 ns. Therefore in general pulse ENDOR requires low temperatures.

By application of microwave and radiofrequency pulses, selective transfer of either polarization or coherence can be obtained. Several methods are available for this spectroscopy. We limit ourselves to introduce the most popular pulse sequences based on polarization transfer: the Davies [147] and the Mims [148] sequences.

During the preparation step a spin polarization inversion is obtained by application of a proper microwave sequence. This part of the experiment is followed by application of a selective rf pulse that induces a nuclear spin transitions. The inverted polarization of the spin packets with nuclear transitions on-resonance with the rf field is transferred to microwave off-resonance spin packets in the Davies experiment. In the Mims experiment, the inverted spin packets simply exchange polarization between nuclear sublevels. The transfer is complete if the pulse is a nuclear π-pulse.

The magnetization unaffected by the rf pulse is monitored in the detection step by means of an electron spin echo. ENDOR transitions are then determined in these techniques as a reduction of the echo intensity by sweeping the frequency of the rf pulse.

Radiofrequency is applied to the sample in the EPR cavity by means of a properly positioned broadband radiofrequency coil [149, 150]. Typically, nuclear transitions are obtained with c.a. 10 μs pulses. Low temperatures are normally used to have longer relaxation times for the inverted magnetization.

It should be noted that pulse ENDOR at W-band (95 GHz) has many advantages with respect to X-band, in particular because of the much larger separation in frequency of the lines due to different types of nuclei. Therefore pulse ENDOR at W-band is one of the more powerful spectroscopies in particular for paramagnetic centers in disordered and biological systems [151, 152]. A further advantage of this technique in the latter systems is the better orientation selection which is possible for the increased separation of the EPR peaks corresponding to the g-tensor principal directions due to the higher field [83]. At Q-band the capability of pulse ENDOR is illustrated with experimental examples in a short review [153].

Davies ENDOR. Davies ENDOR pulse sequence is presented in Fig. 2.2. The magnetization is rotated by a selective microwave π-pulse (generation of polarization). Then, during the mixing period, a selective rf pulse is sent to the sample (polarization transfer) and, finally, the magnetization is monitored by a 2p-ESE ($\pi/2$-τ-π-τ) sequence (detection of the polarization). If the rf pulse is resonant with a nuclear transition also the electron polarization is affected and, as a consequence, also the intensity of the echo. The theoretical maximum effect is the complete quenching of the echo intensity [4].

As several microwave pulses are involved, attention has to be paid to the bandwidth of the different pulses in order to have good selectivity and sensitivity [4]. The bandwidth of the first pulse determines the bandwidth of the inverted packets when broad lines are present. As the pulse must be selective, then the bandwidth of the first pulse is a lower limit for the hyperfine interactions that can be seen with pulse ENDOR. Moreover, the bandwidth of the echo sequence has to be matched to the bandwidth of the rotated spin packets in order not to generate echo signals from unaffected magnetization, and to have the maximum intensity effect. Spectral diffusion processes can induce a modification of the initial bandwidth.

Mims ENDOR. Mims ENDOR (see Fig. 2.2) is based on a stimulated echo sequence obtained with unselective microwave pulses, to which a rf pulse is added between the second and the third $\pi/2$ pulses. As discussed in Sect. 2.2, the z polarization after the second pulse has a modulation at frequency $\pi/2\tau$. It can be shown that the effect of a resonant rf pulse is to reduce this periodic polarization and therefore the amplitude of the stimulated echo.

For an $S = 1/2$, $I = 1/2$ system, it can be shown [4] that by averaging over all resonance offsets of an infinitely broad EPR line, the echo intensity after nuclear inversion depends on τ as $V = [1 + \cos(a_{iso}\tau)]/4$. In Mims ENDOR therefore blind spots occur as in stimulated echo ESEEM.

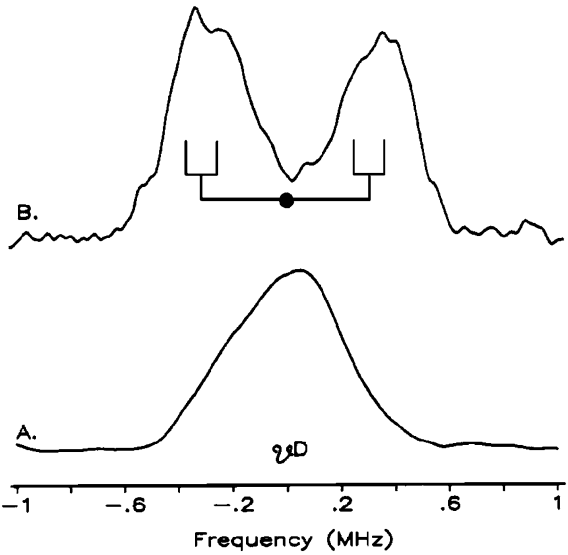

Fig. 2.8 Comparison between the CW-ENDOR (*a-bottom*) and the Mims ENDOR (*b-top*) spectra of the $[2Fe–2S]^+$ cluster of Anabaena ferredoxin in frozen D_2O solvent (From Ref. [154]). The two spectra are plotted as function of $\delta\upsilon = \upsilon\text{-}\upsilon_D$. Experimental conditions: (**a**) $B_0 = 12670$ G, $\upsilon_e = 34.54$ GHz, scan rate 0.25 MHz/s, 200 scans. (**b**) $B_0 = 3357$ G, $\upsilon_e = 9.15$ GHz, mw pulse 16 ns, rf width 40 μs, $\tau = 420$ ns, 64 scans (Reprinted from Ref. [154] with kind permission of © The American Chemical Society 1992)

This technique is convenient for measuring hyperfine couplings smaller than c.a. 5 MHz, whereas for larger couplings Davies ENDOR is a better choice [4].

In Fig. 2.8 the CW-ENDOR and the Mims ENDOR spectra of the $[2Fe–2S]^+$ cluster of *Anabaena* ferredoxin in D_2O solvent are shown (from Ref. [154]). The CW-ENDOR spectrum (Fig. 2.8a) is dominated by the broad *distant ENDOR* signal from deuterons. On the other hand, a resolved ^2H ENDOR spectrum is obtained with the Mims sequence (Fig. 2.8b) at the high-field edge of the EPR spectrum from which a splitting of about 0.60 MHz can be obtained. In fact in Mims ENDOR the *distant ENDOR* signal is not visible because the rf pulse length is shorter than the time for the spin diffusion processes, a necessary condition to obtain the signal [154].

2.5.1.3 Applications

In applications of EPR spectroscopy today it is customary to exploit more techniques among those listed above to determine the different spin Hamiltonian parameters. Thanks to this approach modern EPR is a really powerful tool to get insights in complex systems in biology as well as in material sciences. The number of applications makes impossible to give an exhaustive account of all them. Here, we merely give a few examples to give the reader an idea about the wide applicability of the hyperfine techniques. Most of the work found in recent literature is devoted to the resolution of biological structures. The combined use of pulse EPR techniques, in case integrated with the information coming from other techniques, can clarify the electronic structure of the active centers in enzymes, the redox state and the

spin state on the metals in proteins, the paths in electron-transfer chains, and give structural and functional information on structures containing paramagnetic sites [155], either naturally present or introduced as a spin probe. In this regard the site-directed spin labelling is becoming a standard tool in many biological labs.

Paramagnetic metals. The pulsed techniques described here make possible the determination of the superhyperfine interactions of the weakly coupled nuclei surrounding a paramagnetic metal ion.

Metal complexes. For many aspects this is a field very close to metalloproteins [156] discussed below. Some of the most important applications to metallo-centers are reviewed in Refs. [8, 157, 158]. A Q-band pulse ENDOR spectrometer for the study of transition metal ion complexes in solids is described in [127].

Zeolites and inorganic catalysts. Hyperfine spectroscopy has been used to distinguish and characterize paramagnetic centers of vanadia supported on silica, titania, and magnesia [159]; to interpret the EPR spectra of VO^{2+}-exchanged zeolites [160]; to characterize monocyclopentadienyl Ti(III) catalysts [161]. Inclusion of NO in Na-A zeolites and the interaction of NO with $^{23}Na^{+}$ has been studied with ESEEM spectroscopy [162]. ESEEM technique has been used in the determination of the coordination geometry of zeolite-encapsulated copper(II)-histidine (CuHis) complexes [151]. The advantages of high field ENDOR for the characterization of microporous materials can be found in Ref. [163].

A review by S. Van Doorslaer et al. showed the wealth of detail and information on the structure and mechanism on asymmetric catalysts that can be obtained by pulse techniques [164].

Metalloproteins and biological systems. A review by Prisner, Rohrer and MacMillan is devoted to biological application of pulse EPR [165]. Cammack et al. reviewed the studies of hyperfine interactions in [2Fe–2S] proteins by EPR and ENDOR [166]. The information obtained by EPR methods on the oxygen-evolving complex of photosystem II has been reviewed by Britt et al. [167], and for photosystem I a review can be found in Ref. [168]. High-field ENDOR studies on proteins containing native paramagnetic sites are reported in [169]. Another review reports the applications of pulsed (and cw) ENDOR to photosynthetic systems up to 2009 [170]. Overviews focusing on information about metalloproteins obtained by Hyperfine Spectroscopy techniques are found in [171–173]. A book chapter on EPR methods to study specific metal-ion binding sites in RNA can be found in Ref. [174].

A ^{57}Fe Q-band ENDOR and HYSCORE study in the [FeFe]-hydrogenase is reported in Ref. [175]. The same techniques have been used to clarify coordination property of the Nitrate reductase A (NarGHI). Figure 2.8 shows the HYSCORE spectrum of ubisemiquinone (USQ). The spectrum exhibits cross peaks at nitrogen frequencies (indicated by arrows in A), only in presence of NarGHI; the same peaks are absent when a mutant with the His66 substituted by a Tyr (H66Y) is used, proving the coordination of USB to NarGHI [176].

Pulse techniques have been applied to the study of blue copper proteins [177, 178], to copper binding sites in prion proteins [179], to proteins and enzymes with

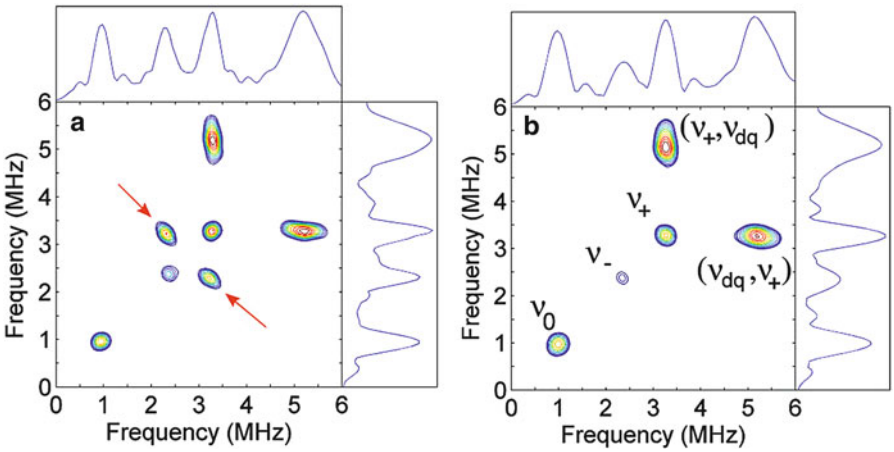

Fig. 2.9 HYSCORE spectrum of USQ in the enriched inner-membrane (*E. coli*) vescicles (**a**) stabilized in NarGHI from an menaquinone-deficient *E. coli* strain and (**b**) stabilized in the single-point mutant H66Y-NarGHI from an LCB3063 strain (Adapted from Ref. [176] with kind permission of © The American Chemical Society 2010)

Mn(II) or VO^{2+} paramagnetic probes substituting Mg(II), as H^+-ATPase [180] (Fig. 2.9).

Anisotropic hyperfine components of chemically prepared carotenoid radical cations have been determined by 1D and 2D ESEEM and pulse ENDOR study [181]. A method to identify possible carotenoid radicals in biological systems by Mims ENDOR has been suggested [182].

In Ref. [183] it is shown as pulse ENDOR helps in the study of photochemical processes in photosynthesis, giving information on hyperfine interactions in short-lived intermediate states such as radical pairs and triplet states. A study by ^{55}Mn pulse ENDOR at 34 GHz of the S-0 and S-2 states of the oxygen-evolving complex in photosystem II can be found in Ref. [170]. Multifrequency Pulsed EPR Studies of biologically relevant Mn(II) complexes are reported in Ref. [184].

High-field (95 GHz) pulse EPR and electron-nuclear double resonance (ENDOR) techniques have been used to determine coordinates of ligand protons in the Mn(II) binding site of concanavalin [185].

The coordination structure and oxidation state of the VO^{2+} ion in vivo in bone samples has been determined with ESEEM spectroscopy [186].

Inorganic systems and glasses. Paramagnetic species in $6Li_2O\ 3P_2O_5\ 6SiO_2$ and $6Na_2O\ 3P_2O_5\ 6SiO_2$ glasses produced under γ -ray irradiation, assigned to the $Q^{n=2}$-type center (POHC-defect), have been studied by ESEEM [187].

Cu(II)-doped inorganic glasses [85] and borate glasses [188] have been studied. Fe(III) incorporated into $AlPO_4$-20 has been studied by X- and W-band pulse EPR spectroscopies [84]. Structure of Cu(II)-histidine complexes in frozen aqueous

solutions has been determined from high-field pulsed electron nuclear double resonance [189].

In Ref. [190] a W-band ^{17}O pulse ENDOR electron nuclear double resonance study of gadolinium complexes with water is reported. A study on blue ultramarine pigments can be found in Ref. [191].

Fullerene systems. Pulse EPR and ENDOR techniques have been used to study several endohedral fullerenes. Pulse ENDOR experiments on ^{14}N atoms encapsulated in C_{60} ($S = 3/2$) allowed to detect a symmetry lowering induced by a phase transition in polycrystalline C_{60} at $T_c = 258$ K [192]. Hyperfine interaction of the ^{13}C nuclei in the librating C_{60} molecules was detected using pulse ENDOR in both phases.

Pulse EPR investigations of anisotropic interactions in $M@C_{82}$ ($M = Sc,Y,La$) in frozen solutions allowed to obtain the principal values of the hyperfine tensor $\boldsymbol{A}$ of the ^{89}Y nuclear spin ($I = 1/2$) with the electron spin on the C_{82} cage in $Y@C_{82}$. The relative orientation of $\boldsymbol{g}$ and $\boldsymbol{A}$ tensors were determined by applying three- and four-pulse electron spin echo envelope modulation techniques (ESEEM) [193].

Semiconductors. Pulse ENDOR applied to non oriented and oriented Feast-type polyacetylene [194] allowed the determination of the spin density distribution of neutral solitons (radical electrons) present in the system. By fitting the ENDOR lineshape, a distribution over ca 60 carbon units has been found, with alternant even/odd distribution for the nearest-neighbor units.

A High-Frequency pulsed EPR and ENDOR study on Semiconductor Quantum Dots is reported in Ref. [195].

Appendix

The 2p echo decays are all given by a stretched exponential function

$$V_d(2\tau) = V_0 \exp(-2\tau/T_M)^x \tag{2.37}$$

1. In the case of relaxation due to time modulation of anisotropic terms of the spin Hamiltonian, solution of Eq. (2.17) in fast motion régime (Redfield limit) [16], $x = 1$,

$$1/T_M = \Delta^2 \frac{\tau_c}{1+\omega^2\tau_c^2} \tag{2.38}$$

   where Δ is the magnetic anisotropy (in frequency units) averaged by the motion and τ_c is the correlation time of the motion.

2. In the case of instantaneous diffusion, $x = 1$ and with $2\theta_1 = \theta_2$ (see Sect. 2.4.1)

$$1/T_M = A + B \cdot \sin^2(\theta_2/2) \tag{2.39}$$

Table 2.1 Analytical expressions for echo decay in the presence of spectral diffusion for given models and approximations

Relaxation mechanism	x	$(1/T_M)^x$	Model	Reference
Nuclear spin flip-flop	7/4	m		[75]
B-electronic spin flip-flop	1/2	$2\Delta\omega_B\sqrt{\tau_c/\pi}$	Gauss-Markov ($\tau/\tau_c >>1$)	[60]
B-electronic spin flip-flop	3/2	$2\Delta\omega_B\sqrt{1/6\pi\tau_c}$	Gauss-Markov ($\tau/\tau_c<<1$)	[60]
B-electronic spin flip-flop	1/2	$2\Delta\omega_B\sqrt{\tau_c/2\pi}$	Sudden-jump ($\tau/\tau_c>>1$)	[60]
B-electronic spin flip-flop	2	$\Delta\omega_B/2\tau_c$	Sudden-jump ($\tau/\tau_c<<1$)	[60]

$\Delta\omega_B = 4\pi^2\gamma_A\gamma_B\hbar C_B/9\sqrt{3}$, $\tau_c$is the correlation time of the electronic flip-flop process and $m = 32\pi(3a\gamma_e\gamma_N\hbar)^{3/4}n$W 0.01840 where W is the nuclear flip-flop frequency

where A is the contribution due to any other process, and B is due to instantaneous diffusion and it is proportional to the concentration see Eq. (2.27), and θ_2 is the tilting angle of the π pulse (assuming non selective pulses).

In the case of spin-spin interactions (spectral diffusion) the values of the exponent and of $1/T_M$ depend on the particular process and model, see Table 2.1.

The general expression found for the echo intensity is obtained from solution of Eq. (2.13) as [60]:

$$V_Y(2\tau + T) = n(\omega_k)\hbar^2\gamma\omega_k/(4kT)\,Re\left[\exp\left[i\int_0^{2\tau} s(t')\delta\omega_k(t')dt'\right]\right] \quad (2.40)$$

where ω_k is the resonance frequency of the k-th spin packet, $\delta\omega_k$ its frequency shift due to coupled-spin flips, and s(t') is a step function (equal to +1,0 or –1 during the different free evolutions).

Evaluation of the integral can be performed on the basis of the type of spin-flip mechanism with different models. The expression is given for the three pulses (stimulated) echo, for the 2p-echo the time T = 0.

References

1. Slichter CP (1990) Principles of magnetic resonance. Springer, Berlin
2. Stoll S, Schweiger A (2006) EasySpin, a comprehensive software package for spectral simulation and analysis in EPR. J Magn Reson 178:42–55
3. Stoll S, Schweiger A (2007) EasySpin: a comprehensive software package for spectral simulation and analysis. In: Hemminga MA, Berliner L (eds) EPR in biological magnetic resonance, vol 27. Springer, Berlin, pp 299–321
4. Schweiger A, Jeschke G (2001) Principle of pulse electron paramagnetic resonance. Oxford University Press, New York
5. Kevan L, Schwartz RN (eds) (1979) Time domain electron spin rersonance. Wiley, New York
6. Kevan L, Bowman MK (eds) (1990) Modern pulsed and continuous-wave electron spin resonance. Wiley, New York
7. Keijzers CP, Reijerse EJ, Schmidt J (eds) (1989) Pulse EPR: a new field of applications. North Holland, Amsterdam

8. Dikanov SA, Tsvetkov YD (1992) Electron spin echo envelope modulation (ESEEM) spectroscopy. CRC Press, Boca Raton
9. Chasteen ND, Snetsinger PA (2000) ESEEM and ENDOR spectroscopy. In: Que L (ed) Physical methods in bioinorganic chemistry, spectroscopy and magnetism. University Science Books, Sausalito, pp 187–231
10. Hoff AJ (ed) (1989) Advanced EPR applications in biology and biochemistry. Elsevier, Amsterdam
11. Kosman DJ (1984) Electron spin resonance. In: Rousseau DL (ed) Structural and resonance techniques in biological research. Academic, New York, pp 89–244
12. Mims WB, Peisach J (1981) Electron spin echo spectroscopy and the study of metalloproteins. In: Berliner LJ, Rubens J (eds) Biological magnetic resonance, vol 3. Plenum Press, New York, pp 213–263
13. Schmidt J, Singel DJ (1987) Fashioning electron-spin echoes into spectroscopic tools – a study of aza-aromatic molecules in metastable triplet-states. Annu Rev Phys Chem 38: 141–161
14. Thomann H, Dalton LR, Dalton LA (1984) Biological application of time domain ESR. In: Berliner LJ, Reuben J (eds) Biological magnetic resonance, vol 6. Plenum, New York, pp 143–186
15. Mehring M, Weberuβ VA (2001) Object oriented EPR classes of objects, calculations and computations. Academic, New York
16. Atherton NM (1993) Principles of ESR. Ellis Horwood and Prentice Hall, London
17. Weil JA, Bolton JR, Wertz JE (1994) Electron paramagnetic resonance elementary theory and practical application. Wiley, New York
18. Ernst RR, Bodenhausen G, Wokaun A (1987) Principles of nuclear magnetic resonance in one and two dimensions. Oxford University Press, Oxford
19. Freed JH (1976) Theory of slow tumbling ESR spectra for nitroxides. In: Berliner LJ (ed) Spin labeling. Theory and applications. Academic, New York, pp 53–132
20. Hahn EL (1950) Spin echoes. Phys Rev 80:580–594
21. Carr HY, Purcell EM (1954) Effects of diffusion on free precession in nuclear magnetic resonance experiments. Phys Rev 94:630–638
22. Abragam A (1961) Principles of nuclear magnetism. Clarendon, Oxford
23. Kevan L (1990) Developments in electron spin-echo modulation analysis. In: Kevan L, Bowman MK (eds) Modern pulsed and continuous-wave electron spin resonance. Wiley, New York, pp 231–283
24. Brustolon M, Barbon A, Maniero AL, Romanelli M, Brunel LC (1999) Dynamics and spin relaxation of tempone in a host crystal. An ENDOR, high field EPR and electron spin echo study. Phys Chem Chem Phys 1:4015–4023
25. Kingsley PB (1995) Product operators, coherence pathway, and phase cycling part I: product operators, spin-spin coupling, and coherence pathway. Con Magn Res 7:29–45; Kingsley PB (1995) Product operators, coherence pathway, and phase cycling part II. Coherence pathways in multipulse sequences: spin echoes, stimulated echoes, and multiple-quantum coherences. Con Magn Res 7:115–136
26. Koptyug IV, Bossmann SH, Turro NJ (1996) Inversion-recovery of nitroxide spin labels in solution and microheterogeneous environments. J Am Chem Soc 118:1435–1445
27. Bowman MK, Kevan L (1979) Electron spin-lattice relaxation in nonionic solids. In: Kevan L, Schwartz RN (eds) Time domain electron spin rersonance 67–106. Wiley, New York
28. Salikhov KM, Tsvetkov YD (1979) Electron spin-echo studies of spin-spin interactions in solids. In: Kevan L, Schwartz RN (eds) Time domain electron spin rersonance 231–277. Wiley, New York
29. Gordy W (1980) Theory and applications of electron spin resonance. In: Weissberger A (ed) Techniques of Chemistry, XVth edn. Wiley, New York
30. Renk KF, Sixl H, Wolfrum H (1977) Spin lattice relaxation in triplet states of naphthalene crystals at very high magnetic fields. Chem Phys Lett 52:98–101
31. Durny R, Yamasaki S, Isoya J, Matsuda A, Tanaka K (1993) New results of spin-lattice relaxation in a-Si-H by pulsed Esr. J Non-Cryst Solids 166:223–226

32. Naber WJM, Faez S, van der Wiel WG (2007) Organic spintronics. J Phys D Appl Phys 40:R205–R228
33. Brustolon M, Cassol T, Micheletti L, Segre U (1987) Endor studies of methyl dynamics in molecular-crystals. Mol Phys 61:249–255
34. Rakvin B, Maltar-Strmecki N, Cevc P, Arcon D (2001) A pulse EPR study of longitudinal relaxation of the stable radical in gamma-irradiated L-alanine. J Magn Reson 152:149–155
35. Bowman MK, Kevan L (1977) An electron spin-lattice relaxation mechanism involving tunneling modes for trapped radicals in glassy matrixes. Theoretical development and application to trapped electrons in.gamma.-irradiated ethanol glasses. J Phys Chem 81:456–461
36. Eaton SS, Seiter M, Budker V, Du JL, Eaton GR (1998) Interspin distances determined by time domain EPR of spin-labeled high-spin methemoglobin. Inorg Chim Acta 273:354–366
37. Stehlik D, Moebius K (1997) New EPR methods for investigating photoprocesses with paramagnetic intermediates. Annu Rev Phys Chem 48:745–784
38. Eaton GR, Harbridge JR, Eaton SS (2002) Electron spin-lattice relaxation in radicals containing two methyl groups, generated by gamma-irradiation of polycrystalline solids. J Magn Reson 159:195–206
39. Du JL, Eaton GR, Eaton SS (1995) Temperature, orientation, and solvent dependence of electron spin-lattice relaxation rates for nitroxyl radicals in glassy solvents and doped solids. J Magn Reson Ser A 115:213–221
40. Eaton SS, Kathirvelu V, Sato H, Eaton GR (2009) Electron spin relaxation rates for semiquinones between 25 and 295 K in glass-forming solvents. J Magn Reson 198:111–120
41. Shell-Sorokin AJ, Mehran F, Eaton GR, Eaton SS, Viehbeck A, O'Toole TR, Brown AA (1992) Electron spin relaxation times of C_{60}^- in solution. Chem Phys Lett 195:225–232
42. Brustolon M, Zoleo A, Agostini G, Maggini M (1998) Radical anions of mono- and bis-fulleropyrrolidines: an EPR study. J Phys Chem A 102:6331–6339
43. Eaton GR, Harbridge JR, Eaton SS (2003) Electron spin-lattice relaxation processes of radicals in irradiated crystalline organic compounds. J Phys Chem A 107:598–610
44. Brustolon M, Segre U (1994) Electron spin-lattice relaxation-time and spectral diffusion in gamma-irradiated L-Alanine. Appl Magn Reson 7:405–413
45. Nagakawa K, Eaton SS, Eaton GR (1993) Electron spin relaxation times of irradiated alanine. Appl Radiat Isot 44:73–76
46. Angelone R, Forte C, Pinzino C (1993) Relaxation-time measurements by longitudinally modulated endor spectroscopy on irradiated L-Alanine single-crystal. J Magn Reson Ser A 101:16–22
47. Ghim BT, Du JL, Pfenninger S, Rinard GA, Quine RW, Eaton SS, Eaton GR (1996) Multifrequency electron paramagnetic resonance of irradiated L-alanine. Appl Radiat Isot 47:1235–1239
48. Eaton GR, Eaton SS (2005) Electron spin relaxation times for the alanine radical in two dosimeters. Appl Radiat Isot 62:129–132
49. Du JL, Eaton GR, Eaton SS (1995) Temperature and orientation dependence of electron-spin relaxation rates for Bis(Diethyldithiocarbamato)Copper(Ii). J Magn Reson Ser A 117:67–72
50. Hoffman BM, Telser J, Lee HI (2000) Investigation of exchange couplings in [Fe3S4](+) clusters by electron spin-lattice relaxation. J Biol Inorg Chem 5:369–380
51. Lorigan GA, Britt RD (2000) Electron spin-lattice relaxation studies of different forms of the S2 state multiline EPR signal of the Photosystem II oxygen-evolving complex. Photosynth Res 66:189–198
52. Takui T, Nishio T, Yokoyama S, Sato K, Shiomi D, Ichimura AS, Lin WC, Dolphin D, McDowell CA (2001) Ground-state high-spin iron (III) octaethylporphyrin as studied by single-crystal cw/pulsed ESR spectroscopy. Synthetic Met 121:1820–1821
53. Kordas G, Mitrikas G, Trapalis CC (1999) Electron spin-lattice relaxation of silver nanoparticles embedded in SiO2 and TiO2 matrices. J Chem Phys 111:8098–8104
54. Malten C, Mueller J, Finger F (1997) Pulsed ESR studies on doped microcrystalline silicon. Phys Status Solidi B 201:R15–R16

55. Fedoruk GG (2000) Paramagnetic relaxation kinetics of the cation radical C_{60}^+ in C_{60} powder. Phys Solid State 42:1182–1185
56. Porfyrakis K, Zhang JY, Morton JJL, Sambrook MR, Ardavan A, Briggs GAD (2006) The effects of a pyrrolidine functional group on the magnetic properties of N@C_{60}. Chem Phys Lett 432:523–527
57. Hirsh DJ, Brudvig GW (2007) Measuring distances in proteins by saturation-recovery EPR. Nat Protoc 2:1770–1781
58. Schwartz LJ, Stillman AE, Freed JH (1982) Analysis of electron spin echoes by spectral representation of the stochastic Liouville equation. J Chem Phys 77:5410–5425
59. Holczer K, Schmalbein D, Baker P (1988) Electron spin-echo spectroscopy: a domain of the ESP 380 FT spectrometer. Bruker Rep 113
60. Romanelli M, Kevan L (1997) Evaluation and interpretation of electron spin-echo decay. 1. Rigid samples. Concept Magn Res 9:403–430; ibid. (1998) Evaluation and interpretation of electron spin echo decay. Part II: molecular motions. Concept Magn Res 10:1–18
61. Brown IM (1979) Electron spin-echo studies of relaxation processes. In: Kevan L, Schwartz RN (eds) Molecular solids in time domain electron spin resonance. Wiley, New York, pp 195–230
62. Redfield AG (1966) The theory of relaxation processes. Adv Magn Reson 1:1–32
63. Freed JH, Fraenkel GK (1963) Theory of linewidths in electron spin resonance spectra. J Chem Phys 39:326–348
64. Nordio PL (1976) General magnetic resonance theory. In: Berliner LJ (ed) Spin labeling. Theory and applications. Academic, New York, pp 5–53
65. Raitsimiring AM, Salikhov KM, Umanskii BA, Tsvetkov YD (1974) Instantaneous diffusion in the spin echo of paramagnetic centers stabilized in a solid host. Sov Phys Solid State 16:492–497; ibid, Fiz Tverd Tela 16:756
66. Doetschmen DC, Thomas GD (1995) Electron spin dephasing model for molecular reorientation: exact solutions. Chem Phys Lett 232:242–246
67. Zecevic A, Eaton GR, Eaton SS, Lindgren M (1998) Dephasing of electron spin echoes for nitroxyl radicals in glassy solvents by non-methyl and methyl protons. Mol Phys 95: 1255–1263
68. Kurshev VV, Raitsimring AM (1990) Carr-Purcell train in the conditions of partial excitation of magnetic-resonance spectrum. J Magn Reson 88:126–129
69. Eaton GR, Harbridge JR, Eaton SS (2003) Comparison of electron spin relaxation times measured by Carr-Purcell-Meiboom-Gill and two-pulse spin-echo sequences. J Magn Reson 164:44–53
70. Brustolon M, Romanelli M, Bonora M, Barbon A, Lund A (2001) Selective detection of EchoEPR signals due to naturally substituted ^{13}C radicals in a single crystal of ammonium tartrate. Appl Magn Reson 20:171–188
71. Goldfarb D, Kevan L (1998) Effect of nuclear modulation on field-swept electron spin-echo spectra. J Magn Reson 76:276–286
72. Dzuba SA (2000) Libration motion of guest spin probe molecules in organic glasses: CW EPR and electron spin echo study. Spectrochim Acta A 56:227–234
73. Hiromitsu I, Kevan L (1987) Effect of cholesterol on the solubilization site and the photoionization efficiency of chlorophyll-a in dipalmitoylphosphatidylcholine vesicle solutions as studied by electron-spin-resonance and optical-absorption spectroscopies. J Am Chem Soc 109:4501–4507; Hiff T, Kevan L (1989) Electron-spin echo modulation studies of doxylstearic acid spin probes in frozen vesicles – interaction of the spin probe with D_2O and effects of cholesterol additino. J Phys Chem 93:1572–1575; Martini G, Ristori S, Romanelli M, Kevan L (1990) Adsorption of nitroxide D_2O solutions on X-zeolite and Y-zeolite studied by electron-spin-resonance and electron-spin echo spectroscopies. J Phys Chem 94: 7607–7611
74. Saxena S, Freed JH (1997) Two-dimensional electron spin resonance and slow motions. J Phys Chem A 101:7998–8008
75. Milov AD, Salikhov KM, Tsvetkov YD (1973) Phase relaxation of hydrogen atoms stabilized in an amorphous matrix. Sov Phys Solid State 15:802–806

76. Lindgren M, Eaton GR, Eaton SS, Jonsson BH, Hammarstrom P, Svensson M, Carlsson U (1997) Electron spin echo decay as a probe of aminoxyl environment in spin-labeled mutants of human carbonic anhydrase II. J Chem Soc Perk T 2:2549–2554
77. Goslar J, Hilczer W, Morawsky P (2000) Low temperature dynamics of hydrazinium ions in lithium hydrazinium sulphate (LHS) studied by electron spin echo (ESE) technique. Solid State Ion 127:67–72
78. Brustolon M, Maniero AL, Bonora M, Segre U (1996) Electron spin relaxation times and internal motions of radicals in the solid state investigated by ENDOR and pulsed EPR. Appl Magn Reson 11:99–113
79. Dzuba SA (1996) Librational motion of guest spin probe molecules in glassy media. Phys Lett A 213:77–84
80. Kirilina EP, Grigoriev IA, Dzuba SA (2004) Orientational motion of nitroxides in molecular glasses: dependence on the chemical structure, on the molecular size of the probe, and on the type of the matrix. J Chem Phys 121:12465–12471; Dzuba SA, Kirilina EP, Salnikov ES (2006) On the possible manifestation of harmonic-anharmonic dynamical transition in glassy media in electron paramagnetic resonance of nitroxide spin probes. J Chem Phys 125:054502; Dzuba SA, Salnikov ES, Kulik LV (2006) CW EPR, echo-detected EPR, and field-step ELDOR study of molecular motions of nitroxides in o-terphenyl glass: dynamical transition, dynamical heterogeneity and beta-relaxation Appl Magn Reson 30:637–650
81. Isaev NP, Dzuba SA (2008) Fast stochastic librations and slow rotations of spin labeled stearic acids in a model phospholipid bilayer at cryogenic temperatures. J Phys Chem B 112:13285–13291
82. Bartucci R, Erilov DA, Guzzi R, Sportelli L, Dzuba SA, Marsh D (2006) Time-resolved electron spin resonance studies of spin-labelled lipids in membranes. Chem Phys Lipids 141:142–157
83. Rohrer M, Gast P, Mobius K, Prisner TF (1996) Anisotropic motion of semiquinones in photosynthetic reaction centers of Rhodobacter sphaeroides R26 and in frozen isopropanol solution as measured by pulsed high-field EPR at 95 GHz. Chem Phys Lett 259:523–530
84. Arieli D, Vaughan DEW, Strohmaier KG, Thomann H, Bernardo M, Goldfarb D (1999) Studies of Fe(III) incorporated into AlPO(4)-20 by X- and W-band EPR spectroscopies. Magn Reson Chem 37:S43–S54
85. Stosser R, Sebastian S, Scholz G, Willer M, Jeschke G, Schweiger A, Nofz M (1999) Pulse EPR spectroscopy of Cu^{2+}-doped inorganic glasses. Appl Magn Reson 16:507–528
86. Marrale M, Longo A, Brai M, Barbon A, Brustolon M, Fattibene P (2011) Pulsed EPR analysis of tooth enamel samples exposed to UV and gamma-radiations. Radiat Res 46:789–792
87. Barbon A, Bortolus M, Brustolon M, Comotti A, Maniero AL, Segre U, Sozzani P (2003) Dynamics of the triplet state of a dithiophene in different solid matrixes studied by transient and pulse EPR techniques. J Phys Chem B 107:3325–3331
88. Brustolon M, Zoleo A, Lund A (1999) Spin concentration in a possible ESR dosimeter: An electron spin echo study on X-irradiated ammonium tartrate. J Magn Reson 137:389–396
89. Brown IW (1973) Concentration dependent relaxation times in organic radical solids. J Chem Phys 58:4242–4251
90. Eaton SS, Eaton GR (1993) Irradiated fused-quartz standard sample for time-domain EPR. J Magn Reson A 102:354–356
91. Boscaino R, Gelardi FM (1992) Instantaneous diffusion in spin-echo dynamics: a frequency-domain experimental investigation. Phys Rev B 46:14550–14558
92. Marrale M, Brai M, Barbon A, Brustolon M (2009) Analysis of the spatial distribution of free radicals in ammonium tartrate by pulse EPR techniques. Radiat Res 171:349–359
93. Hoff AJ, Gast P, Dzuba SA, Timmel CR, Fursman CE, Hore PJ (1998) The nuts and bolts of distance determination and zero- and double-quantum coherence in photoinduced radical pairs. Spectrochim Acta A 54:2283–2293
94. Lakshmi KV, Brudvig GW (2001) Pulsed electron paramagnetic resonance methods for macromolecular structure determination. Curr Opin Struct Biol 11:523–531

95. Tsvetkov YD, Grishin YA (2009) Techniques for EPR spectroscopy of pulsed electron double resonance (PELDOR): a review. Instrum Exp Tech 52:615–636
96. Jeschke G, Pannier M, Spiess HW (2000) Double electron–electron resonance, distance measurements. In: Berliner LJ, Eaton SS, Eaton GR (eds) Biological systems by EPR 493–512. Kluwer Academic/Plenum Publishers, New York
97. Kurshev VV, Raitsimring AM, Tsvetkov YD (1989) Selection of dipolar interaction by the 2 + 1 pulse train ESE. J Magn Reson 81:441–454
98. Astashkin AV, Hara H, Kawamori A (1998) The pulsed electron-electron double resonance and "2 + 1" electron spin echo study of the oriented oxygen-evolving and Mn-depleted preparations of photosystem II. J Chem Phys 108:3805–3812
99. Milov AD, Maryasov AG, Tsvetkov YD, Raap J (1999) Pulsed ELDOR in spin-labeled polypeptides. Chem Phys Lett 303:135–143
100. Bowman MK, Becker D, Sevilla MD, Zimbrick JD (2005) Track structure in DNA irradiated with heavy ions. Radiat Res 163:447–454
101. Jeschke G (2002) Determination of the nanostructure of polymer materials by electron paramagnetic resonance spectroscopy. Macromol Rapid Commun 23:227–246
102. Martin RE, Pannier M, Diederich F, Gramlich V, Hubrich M, Spiess HW (1998) Determination of end-to-end distances in a series of TEMPO diradicals of up to 2.8 nm length with a new four-pulse double electron electron resonance experiment. Angew Chem Int Ed 37:2833–2837; Pannier M, Veit S, Godt A, Jeschke G, Spiess HW (2000) Dead-time free measurement of dipole-dipole interactions between electron spins. J Magn Reson 142:331–340; Schiemann O, Piton N, Plackmeyer J, Bode BE, Prisner TF, Engels JW (2007) Spin labeling of oligonucleotides with the nitroxide TPA and use of PELDOR, a pulse EPR method, to measure intramolecular distances. Nat Protoc 2:904-923
103. Margraf D, Cekan P, Prisner TF, Sigurdsson ST, Schiemann O (2009) Ferro- and antiferromagnetic exchange coupling constants in PELDOR spectra. Phys Chem Chem Phys 11:6708–6714
104. Jeschke G, Chechik V, Ionita P, Godt A, Zimmermann H, Banham J, Timmel CR, Hilger D, Jung H (2006) DeerAnalysis2006 – a comprehensive software package for analyzing pulsed ELDOR data. Appl Magn Reson 30:473–498
105. Denysenkov VP, Prisner TF, Stubbe J, Bennati M (2006) High-field pulsed electron-electron double resonance spectroscopy to determine the orientation of the tyrosyl radicals in ribonucleotide reductase. Proc Natl Acad Sci USA 103:13386–13390
106. Ghimire H, McCarrick RM, Budil DE, Lorigan GA (2009) Significantly improved sensitivity of Q-Band PELDOR/DEER experiments relative to X-band is observed in measuring the intercoil distance of a leucine zipper motif peptide. Biochemistry 48:5782–5784
107. Sicoli G, Argirevic T, Stubbe J, Tkach I, Bennati M (2010) Effects in 94 GHz orientation-selected PELDOR on a rigid pair of radicals with non-collinear axes. Appl Magn Reson 37:539–548; Denysenkov VP, Biglino D, Lubitz W, Prisner TF, Bennati M (2008) Structure of the tyrosyl biradical in mouse R2 ribonucleotide reductase from high-field PELDOR. Angew Chem Int Edit 47:1224–1227; Savitsky A, Dubinskii AA, Flores M, Lubitz W, Mobius K (2007) Orientation-resolving pulsed electron dipolar high-field EPR spectroscopy on disordered solids: I. Structure of spin-correlated radical pairs in bacterial photosynthetic reaction centers. J Phys Chem B 111:6245–6262
108. Saxena S, Freed JH (1996) Double quantum two-dimensional Fourier transform electron spin resonance: distance measurements. Chem Phys Lett 251:102–110; Freed JH, Borbat PP, Mchaourab HS (2002) Protein structure determination using long-distance constraints from double-quantum coherence ESR: Study of T4 lysozyme. J Am Chem Soc 124:5304–5314
109. Reginsson GW, Schiemann O (2011) Pulsed electron-electron double resonance: beyond nanometre distance measurements on biomacromolecules. Biochem J 434:353–363
110. Sowa GZ, Qin PZ (2008) Site-directed spin labeling studies on nucleic acid structure and dynamics. Prog Nucleic Acid Re 82:147–197
111. Jeschke G, Polyhach Y (2007) Distance measurements on spin-labelled biomacromolecules by pulsed electron paramagnetic resonance. Phys Chem Chem Phys 9:1895–1910

112. Fajer PG (2005) Site directed spin labelling and pulsed dipolar electron paramagnetic resonance (double electron-electron resonance) of force activation in muscle. J Phys-Condens Mat 17:S1459–S1469
113. Cai Q, Kusnetzow AK, Hideg K, Price EA, Haworth IS, Qin PZ (2007) Nanometer distance measurements in RNA using site-directed spin Labeling. Biophys J 93:2110–2117
114. Schiemann O, Prisner TF (2007) Long-range distance determinations in biomacromolecules by EPR spectroscopy. Q Rev Biophys 40:1–53
115. Krstic I, Hansel R, Romainczyk O, Engels JW, Dotsch V, Prisner TF (2011) Long-range distance measurements on nucleic acids in cells by pulsed EPR spectroscopy. Angew Chem Int Edit 50:5070–5074
116. Borovykh IV, Ceola S, Gajula P, Gast P, Steinhoff HJ, Huber M (2006) Distance between a native cofactor and a spin label in the reaction centre of Rhodobacter sphaeroides by a two-frequency pulsed electron paramagnetic resonance method and molecular dynamics simulations. J Magn Reson 180:178–185
117. Yagi H, Banerjee D, Graham B, Huber T, Goldfarb D, Otting G (2011) Gadolinium tagging for high-precision measurements of 6 nm distances in protein assemblies by EPR. J Am Chem Soc 133:10418–10421
118. Yang ZY, Kise D, Saxena S (2010) An approach towards the measurement of nanometer range distances based on Cu(2+) ions and ESR. J Phys Chem B 114:6165–6174
119. Bennati M, Weber A, Antonic J, Perlstein DL, Robblee J, Stubbe JA (2003) Pulsed ELDOR spectroscopy measures the distance between the two tyrosyl radicals in the R2 subunit of the E-coli ribonucleotide reductase. J Am Chem Soc 125:14988–14989
120. Junk MJN, Spiess HW, Hinderberger D (2011) DEER in biological multispin-systems: a case study on the fatty acid binding to human serum albumin. J Magn Reson 210:210–217
121. Hinderberger D, Schmelz O, Rehahn M, Jeschke G (2004) Electrostatic site attachment of divalent counterions to rodlike ruthenium(II) coordination polymers characterized by EPR spectroscopy. Angew Chem Int Edit 43:4616–4621
122. Lueders P, Jeschke G, Yulikov M (2011) Double electron-electron resonance measured between Gd(3+) ions and nitroxide radicals. J Phys Chem Lett 2:604–609
123. Carmieli R, Mi QX, Ricks AB, Giacobbe EM, Mickley SM, Wasielewski MR (2009) Direct measurement of photoinduced charge separation distances in donor-acceptor systems for artificial photosynthesis using OOP-ESEEM. J Am Chem Soc 131:8372–8373
124. Tang J, Thurnauer MC, Norris JR (1994) Electron-spin echo envelope modulation due to exchange and dipolar interactions in a spin-correlated radical pair. Chem Phys Lett 219:283–290
125. Iwaki M, Itoh S, Hara H, Kawamori A (1998) Spin-polarized radical pair in photosystem I reaction center that contains different quinones and fluorenones as the secondary electron acceptor. J Phys Chem B 102:10440–10445
126. Calle C, Sreekanth A, Fedin MV, Forrer J, Garcia-Rubio I, Gromov IA, Hinderberger D, Kasumaj B, Leger P, Mancosu B, Mitrikas G, Santangelo MG, Stoll S, Schweiger A et al (2006) Pulse EPR methods for studying chemical and biological samples containing transition metals. Helv Chim Acta 89:2495–2521
127. Hoentsch J, Rosentzweig Y, Heinhold D, Koehler K, Gutjahr M, Poeppl A, Voelkel G, Boettcher R (2003) A Q-band pulsed ENDOR spectrometer for the study of transition metal ion complexes in solids. Appl Magn Reson 25:249–259
128. Kababya S, Nelson J, Calle C, Neese F, Goldfarb D (2006) Electronic structure of binuclear mixed valence copper azacryptates derived from integrated advanced EPR and DFT calculations. J Am Chem Soc 128:2017–2029
129. Bennati M, Prisner TF (2005) New developments in high field electron paramagnetic resonance with applications in structural biology. Rep Prog Phys 68:411–448
130. Cruickshank PAS, Bolton DR, Robertson DA, Hunter RI, Wylde RJ, Smith GM (2009) A kilowatt pulsed 94 GHz electron paramagnetic resonance spectrometer with high concentration sensitivity, high instantaneous bandwidth, and low dead time. Rev Sci Instrum 80:103102

131. Goldfarb D, Lipkin Y, Potapov A, Gorodetsky Y, Epel B, Raitsimring AM, Radoul M, Kaminker I (2008) HYSCORE and DEER with an upgraded 95 GHz pulse EPR spectrometer. J Magn Reson 194:8–15
132. Kevan L (1979) Modulation of electron spin-echo decay in solids, Ch. 8. In: Kevan L, Schwartz RN (eds) Time domain electron spin rersonance. Wiley, New York, pp 279–342
133. Mims WB, Peisach J (1989) ESEEM and LEFE of metalloproteins and model compounds in advanced EPR applications. In: Hoff AJ (ed) Biology and biochemistry. Elsevier, Amsterdam, pp 1–58
134. Atherton NM (1993) Bruker lecture – the nuclear zeeman interaction in electron resonance. Chem Soc Rev 22:293–298
135. Schweiger A (1991) Pulsed electron spin resonance spectroscopy: basic principles, techniques, and examples of applications. Angew Chem Int Ed Engl 30:265–292
136. Brustolon M, Maniero AL, Jovine S, Segre U (1996) ENDOR and ESEEM study of the radical obtained by gamma irradiation of a single crystal of ammonium tartrate. Res Chem Intermediat 22:359–368
137. Braunschweiler L, Schweiger A, Fauth JM, Ernst RR (1985) Selective excitation in electron spin-echo modulation experiments. J Magn Reson 64:160–166
138. Barkhuijsen H, de Beer R, Pronk BJ, Vanormondt D (1985) Partial excitation in electron spin-echo envelope modulation spectroscopy. J Magn Reson 61:284–293
139. Hoefer P, Grupp A, Nebenfuehr H, Mehring M (1986) Hyperfine sublevel correlation (HYSCORE) spectroscopy - a 2d electron-spin-resonance investigation of the squaric acid radical. Chem Phys Lett 132:279–282
140. Hoefer P (1988) Bruker Rep 118
141. Szosenfogel R, Goldfarb D (1998) Simulation of HYSCORE spectra obtained with ideal and non-ideal pulses. Mol Phys 95:1295–1308
142. Gemperle C, Aebli G, Schweiger A, Ernst RR (1990) Phase cycling in pulse EPR. J Magn Reson 88:241–256
143. Benetis NP, Dave PC, Goldfarb D (2002) Characteristics of ESEEM and HYSCORE spectra of $S > 1/2$ centers in orientationally disordered systems. J Magn Reson 158:126–142
144. Press WH, Flannery BP, Teukolsky SA, Vetterling WT (1986) Numerical recipes, the art of scientific computing. Cambridge University Press, Cambridge
145. van Ormond D (1989) Instrumentation. In: Keijzers CP, Reijerse EJ, Schmidt J (eds) Pulse EPR: a new field of applications. North Holland, Amsterdam, pp 43–78
146. Kevan L (1989) Advances in electron spin echo modulation analysis and applications to cations and zeolites and to photoionization in micelles and vesicles. In: Keijzers CP, Reijerse EJ, Schmidt J (eds) Pulse EPR: a new field of applications. North Holland, Amsterdam, pp 127–134
147. Davies ER (1974) A new Pulse ENDOR technique. Phys Lett A 47:1–2
148. Mims WB (1965) Pulsed ENDOR experiments. Proc R Soc Lond A 283:452–457
149. Forrer J, Pfenninger S, Eisenegger J, Schweiger A (1990) A pulsed ENDOR probehead with the bridged loop-gap resonator – construction and performance. Rev Sci Instrum 61:3360–3367
150. Bietsch W, vin Schuetz JU (1993) Bruker Rep 139
151. Grommen R, Manikandan P, Gao Y, Shane T, Shane JJ, Schoonheydt RA, Weckhuysen BM, Goldfarb D (2000) Geometry and framework interactions of zeolite-encapsulated copper(II)-histidine complexes. J Am Chem Soc 122:11488–11496
152. Epel B, Slutter CS, Neese F, Kroneck PMH, Zumft WG, Pecht I, Farver O, Lu Y, Goldfarb D (2002) Electron-mediating Cu-A centers in proteins: a comparative high field H-1 ENDOR study. J Am Chem Soc 124:8152–8162
153. Gromov IA, Harmer J (2007) Radio frequencies in EPR: conventional and advanced use. Appl Magn Reson 31:627–647
154. Fan C, Kennedy MC, Beinert H, Hoffman BM (1992) ^{2}H mims pulsed ENDOR of hydrogen bonds and exogenous ligands to the metal clusters of iron-sulfur proteins. J Am Chem Soc 114:374–375

155. Lubitz W, Reijerse E, van Gastel M (2007) [NiFe] and [FeFe] hydrogenases studied by advanced magnetic resonance techniques. Chem Rev 107:4331–4365
156. Hadjiliadis N, Deligiannakis Y, Louloudi M (2000) Electron spin echo envelope modulation (ESEEM) spectroscopy as a tool to investigate the coordination environment of metal centers. Coordin Chem Rev 204:1–112
157. Pilbrow JR (1990) Transition ion electron paramagnetic resonance. Oxford University Press, New York
158. Calle C, Eichel RA, Finazzo C, Forrer J, Granwehr J, Gromov I, Groth W, Harmer J, Kalin M, Lammler W, Liesum L, Madi Z, Stoll S, Van Doorslaer S, Schweiger A (2001) Electron paramagnetic resonance spectroscopy. Chimia 55:763–766
159. Luca V, MacLachlan DJ, Bramley R (1999) Electron paramagnetic resonance and electron spin echo study of supported and unsupported vanadium oxides. Phys Chem Chem Phys 1:2597–2606
160. Carl PJ, Isley SL, Larsen SC (2001) Combining theory and experiment to interpret the EPR spectra of VO^{2+}-exchanged zeolites. J Phys Chem A 105:4563–4573
161. Van Doorslaer S, Shane JJ, Stoll S, Schweiger A, Kranenburg M, Meier RJ (2001) Continuous wave and pulse EPR as a tool for the characterization of monocyclopentadienyl Ti(III) catalysts. J Organomet Chem 634:185–192
162. Biglino D, Bonora M, Volodin A, Lund A (2001) Pulsed EPR study of the $(NO)_2$-Na^+ triplet state adsorption complex. Chem Phys Lett 349:511–516
163. Goldfarb D (2006) High field ENDOR as a characterization tool for functional sites in microporous materials. Phys Chem Chem Phys 8:2325–2343
164. Van Doorslaer S, Caretti I, Fallis IA, Murphy DM (2009) The power of electron paramagnetic resonance to study asymmetric homogeneous catalysts based on transition-metal complexes. Coordin Chem Rev 253:2116–2130
165. Prisner T, Rohrer M, MacMillan F (2001) Pulsed EPR spectroscopy: biological applications. Annu Rev Phys Chem 52:279–313
166. Shergill JK, Cammack R, Weiner JH (1993) Electron spin-echo envelope modulation studies of the [3Fe–4S] cluster of Escherichia coli fumarate reductase. J Chem Soc Faraday Trans 89:3685–3689
167. Peloquin JM, Britt RD (2001) EPR/ENDOR characterization of the physical and electronic structure of the OEC Mn cluster. Biochim Biophys Acta 1503:96–111
168. Deligiannakis Y, Rutherford AW (2001) Electron spin echo envelope modulation spectroscopy in photosystem I. Biochim Biophys Acta 1507:226–246
169. Goldfarb D, Arieli D (2004) Spin distribution and the location of protons in paramagnetic proteins. Annu Rev Biophys Biomol Struct 33:441–468
170. Kulik L, Lubitz W (2009) Electron-nuclear double resonance. Photosynth Res 102:391–401
171. Van Doorslaer S, Vinck E (2007) The strength of EPR and ENDOR techniques in revealing structure-function relationships in metalloproteins. Phys Chem Chem Phys 9:4620–4638
172. Hoffman BM (2003) ENDOR of metalloenzymes. Acc Chem Res 36:522–529
173. Lyubenova S, Maly T, Zwicker K, Brandt U, Ludwig B, Prisner T (2010) Multifrequency pulsed Electron earamagnetic resonance on metalloproteins. Acc Chem Res 43:181–189
174. Hunsicker-Wang L, Vogt M, DeRose VJ (2009) EPR methods to study specific metal-ion binding sites in RNA. In: Herschalag D (ed) Biophysical, chemical, and functional probes of RNA structure, interactions and folding: part A, vol 468, Methods in enzymology. Academic, San Diego, pp 335–367
175. Silakov A, Reijerse EJ, Albracht SPJ, Hatchikian EC, Lubitz W (2007) The electronic structure of the H-cluster in the [FeFe]-hydrogenase from Desulfovibrio desulfuricans: a Q-band Fe-57-ENDOR and HYSCORE study. J Am Chem Soc 129:11447–11458
176. Grimaldi S, Arias-Cartin R, Lyubenova S, Ceccaldi P, Prisner T, Magalon A, Guigliarelli B (2010) HYSCORE evidence that endogenous mena- and ubisemiquinone bind at the same Q aite (Q(D)) of Escherichia coli nitrate reductase A. J Am Chem Soc 132:5942–5943

177. van Gastel M, Coremans JW, Mol J, Jeuken LJ, Canters GW, Groenen EJ (1999) The binding of imidazole in an azurin-like blue-copper site. J Biol Inorg Chem 4:257–265
178. Slutter CE, Gromov I, Epel B, Pecht I, Richards JH, Goldfarb D (2001) Pulsed EPR/ENDOR characterization of perturbations of the Cu(A) center ground state by axial methionine ligand mutations. J Am Chem Soc 123:5325–5336
179. Burns CS, Aronoff-Spencer E, Dunham CM, Lario P, Avdievich NI, Antholine WE, Olmstead MM, Vrielink A, Gerfen GJ, Peisach J, Scott WG, Millhauser GL (2002) Molecular features of the copper binding sites in the octarepeat domain of the prion protein. Biochemistry 41:3991–4001
180. Schneider B, Sigalat C, Amano T, Zimmermann JL (2000) Evidence for changes in the nucleotide conformation in the active site of H^+-ATPase as determined by pulsed EPR spectroscopy. Biochemistry 39:15500–15512
181. Konovalova TA, Dikanov SA, Bowman MK, Kispert LD (2001) Detection of anisotropic hyperfine components of chemically prepared carotenoid radical cations: 1D and 2D ESEEM and pulsed ENDOR study. J Phys Chem B 105:8361–8368
182. Focsan AL, Bowman MK, Molnar P, Deli J, Kispert LD (2011) Carotenoid radical formation: dependence on conjugation length. J Phys Chem B 115:9495–9506
183. Lubitz W (2003) Photochemical processes in photosynthesis studied by advanced electron paramagnetic resonance techniques. Pure Appl Chem 75:1021–1030
184. Stich TA, Lahiri S, Yeagle G, Dicus M, Brynda M, Gunn A, Aznar C, DeRose VJ, Britt RD (2007) Multifrequency pulsed EPR studies of biologically relevant manganese(II) complexes. Appl Magn Reson 31:321–341
185. Carmieli R, Manikandan P, Kalb AJ, Goldfarb D (2001) Proton positions in the Mn^{2+} binding site of concanavalin A as determined by single-crystal high-field ENDOR spectroscopy. J Am Chem Soc 123:8378–8386
186. Dikanov SA, Liboiron BD, Thompson KH, Vera E, Yuen VG, McNeill JH, Orvig C (1999) In vivo electron spin-echo envelope modulation (ESEEM) spectroscopy: first observation of vanadyl coordination to phosphate in bone. J Am Chem Soc 121:11004–11005
187. Kordas G (2001) Investigation of the medium range structure of phosphosilicate glasses by cw-EPR, 1D-ESEEM and HYSCORE spectroscopies. J Non-Cryst Solids 281:133–138
188. Kordas G, Goldfarb D (2008) Characterization of borate glasses by W-band pulse electron-nuclear double resonance spectroscopy. J Chem Phys 129:154502
189. Manikandan P, Epel B, Goldfarb D (2001) Structure of copper(II) -histidine based complexes in frozen aqueous solutions as determined from high-field pulsed electron nuclear double resonance. Inorg Chem 40:781–787
190. Raitsimring AM, Astashkin AV, Baute D, Goldfarb D, Caravan P (2004) W-band ^{17}O pulsed Electron Nuclear Double Resonance study of gadolinium complexes with water. J Phys Chem A 108:7318–7323
191. Arieli D, Vaughan DEW, Goldfarb D (2004) New synthesis and insight into the structure of blue ultramarine pigments. J Am Chem Soc 126:5776–5788
192. Weiden N, Kass H, Dinse KP (1999) Pulse electron paramagnetic resonance (EPR) and electron-nuclear double resonance (ENDOR) investigation of $N@C_{60}$ in polycrystalline C_{60}. J Phys Chem B 103:9826–9830
193. Knorr S, Grupp A, Mehring M, Kirbach U, Bartl A, Dunsch L (1998) Pulsed ESR investigations of anisotropic interactions in $M@C_{82}$ (M = Sc, Y, La). Appl Phys A-Mater 66:257–264
194. Kaess H, Hoefer P, Grupp A, Kahol PK, Weizenhofer R, Wegner G, Mehring M (1987) Electron-spin delocalization in feast-type (Durham Route) polyacetylene - Pulsed ENDOR investigations. Europhys Lett 49:47–951
195. Baranov PG, Orlinskii SB, Donega CD, Schmidt J (2010) High-frequency EPR and ENDOR spectroscopy on semiconductor quantum dots. Appl Magn Reson 39:151–183

Chapter 3
Dynamical Effects in CW and Pulsed EPR

Nikolas-Ploutarch Benetis and Yurij Dmitriev

Abstract Typical molecular processes with EPR accessible dynamical parameters are listed and evaluation of their timescales according to the different EPR methods used for this purpose is reported. The detection and description of the dynamics of cyclic and some other small radicals and related nitroxide labels isolated in solids and the connection to the structural parameters are given. Both fast-motion averaging and the method of lineshape modification due to chemical exchange are outlined. Some usually overlooked anomalies concerning the activation parameters of the thermally activated rotary motion and their relation to the microscopic variables of the spin-motion system are discussed. The definition of the thermodynamic limits differentiating diffusional motion from quantum motion and the particular ways of the couplings of these motions to the spin system are exemplified. Several experiments manifesting their difference, such as comparison of EPR spectra for classical and for tunnelling rotors, as well as severely distorted EPR spectra including totally quenched (stopped) methyl-type rotors are reviewed and explained. Spin-lattice relaxation and broadening are discussed for fast and slow motions in solids and the characterization of the different dynamics according to the effects of motion on the ESE (Electron Spin Echo) decay are considered in the framework of pulsed EPR. Finally, some standard biological applications in determining the timescales and the motional pattern of disordered matter at the molecular level are described with emphasis to the relatively recent pulsed EPR techniques and some relevant developments. Also the classical EPR methods for dynamics investigations will be reviewed focusing in the application of fundamental theoretical tools.

N.-P. Benetis (✉)
Department of Pollution Control, Technological Education Institution, TEI, West Macedonia, Kozani 501 00, Greece
e-mail: niben@teikoz.gr; niben@otenet.gr

Y. Dmitriev
A. F. Ioffe Physico-Technical Institute, 26 Politekhnicheskaya Street, 194021 St Petersburg, Russia
e-mail: dmitrievyurij@gmail.com

A. Lund and M. Shiotani (eds.), *EPR of Free Radicals in Solids I*, Progress in Theoretical Chemistry and Physics 24, DOI 10.1007/978-94-007-4893-4_3,

3.1 Introduction

The update of this chapter from 2003 was augmented by including many newer (and older) experimental data of methyl radical EPR isolated in different "inert" gas matrices at low temperatures with relevant interpretations. Some understandable, some less obvious, these results indicate that this simple radical at cryogenic temperatures is a complicated enough quantum system. Also among the new reviewed literature included in this chapter update it is exciting to understand why the inner doublet of the EPR quartet of methyl radicals isolated in silica gel obtains so unexpected higher intensity than 3:1 to the outer lines at 77 K in Shiga and Lund [1] and Pariiskii et al. [2].

Considering the experimental work of Dmitriev on the CH_3 radical isolated in Ar cryocrystal for example it is interesting to notice the unpredictability of the EPR lineshape at 1.5 K, at liquid He temperature, as well as at temperatures like 20 K and higher. Shiotani's spectra [3] of methyl radical at cryogenic temperatures are extremely sharp and isotropic while the same system in Dmitriev's spectra [4] display a lot of anisotropy, additional line splitting or/and superposition and significantly greater broadening. Similar results of other researchers, Eloranta et al. [5] are reviewed. It is obvious however, that systems with sharp and isotropic EPR spectra of methyl radical indicate extremely good thermal isolation from the matrix rendering the free 3D quantum rotation visible by the Pauli exclusion of certain transitions, due to the nuclear spin coupling to rotation.

Dynamics' objective is to determine which motion will take place under the influence of given forces [6]. *Motional dynamics* phenomena and *spin dynamics* phenomena to be discussed in this chapter concern the paramagnetic species – neutral or ionic radicals, metal ions complexes and nitroxides – as they interact with their closest environment in solid matrices, leading to modification of the EPR measurables.

One cannot avoid considering some properties of *fluid motional dynamics* as detected by EPR, either because of their similarities or due to their contrasting characteristics compared to dynamics in solids. For instance even though the environment of the paramagnetic probes in composite phases such as silica gel, *zeolites* and *liquid crystals*, particularly *membranes*, is highly anisotropic, the very slow and restricted overall motion of some large units can coexist with much faster *local motions* and internal rotary motions.

In most cases, approximate simulation of the macroscopic magnetic properties can be obtained from first principles. The spins are usually treated *quantum mechanically* while the rest of the degrees of freedom, the *motional part* of the environment with which the spins interact, are treated as *classical systems* with a continuum of energy levels, or at least as *random processes*. Interestingly, some of the motional degrees of freedom have to be treated quantum mechanically [7] and vice versa, some fast relaxing electron spins must be included in the "lattice" [8], as will be seen in Sect. 3.6.

Often, very crude dynamical models, such as the Arrhenius law of exponential temperature dependence of the rate of thermally activated processes, work nicely at the macroscopic level [6, 9]. As it was seen however, the activation model of Arrhenius was not always consistent with the microscopic model for hindered rotational motion [10, 11]. In some cases neither *free diffusion* nor the *jump model* were particularly successful to describe a classical rotor in presence of a periodic *restoring force* [10] and more general models, such as a Smoluchowski drift diffusion model, was necessary in order to account for the motional subsystem. The rotation of methyl-type rotors at liquid –He temperature had to be described quantum mechanically [3, 7] Mixed quantum and a classical description of the motion was employed within the *transition regime* between *inertial* and *diffusional limit* at intermediate temperatures [11]. For many classical rotors it appears that the motion does not really stop even for temperatures lower than the melting point.

Methyl-type radicals, for which the planar methyl radical $^{\bullet}CH_3$ with $\boldsymbol{D_3}$ symmetry is a prototype, or similar small fragments with nitrogen instead of carbon and/or protons exchanged by deuteron, can be isolated in inert gas matrices at cryogenic temperatures. Their EPR spectra at liquid He temperatures display quantum effects such as *extremely sharp* and easily saturated EPR signals and in general behave rather differently than strongly hindered rotors. The spectral properties of these rotors indicate that there is not good thermal contact to the lattice, a fact also verified by the apparent free rotation of these radicals at very low temperatures. Because of the lack of thermal energy, those rotors stop at temperatures close to and under 5 K in spite that they are not hindered [3].

Almost all biological ESEEM (Electron Spin Echo Envelope Modulation) applications of paramagnetic metal ions are possible only under cryogenic conditions [12] and the same situation is found also in some *triplets* [13, 14]. This is predominantly due to the *homogeneous broadening* of the EPR lines that arises when the anisotropic interactions of the electron spin are modulated by *thermal motion* at higher temperatures. The ESE (Electron Spin Echo) methods eliminate the *inhomogeneous* broadening, but the homogeneous broadening is also usually large and it is still always there to "report" about the dynamics. Some direct FID (Free Induction Decay) methods are possible in EPR, however. In particular motional narrowed spectra of e.g. nitroxides can routinely be obtained by *one-shot registration* [15] after a single pulse, and subsequent FFT (Fast Fourier Transformation) of the time resolved signal. Also, special soft pulse sequences involving Extended Time Excitation (ETE) [16], allow for the whole ESEEM signal to be registered by using a single two-pulse echo experiment [17].

Relaxation rates in relatively spin-dense systems of radicals and echo decay starts to become substantial along with the realization of effects such as *spin-diffusion*, *spectral-diffusion*, and *instantaneous diffusion*. The relaxation phenomena that are important in solids have to be considered in this case and if the concentration of the paramagnetic centers is still rather low, even the pure *nuclear spin diffusion* can also affect the electron spins by modulations of the local electron-nuclear *S-I* dipole-dipole interaction [18–20]. These phenomena will be outlined in Sect. 3.9.3 along with the pulsing of inhomogeneous lines, and will be used for the interpretation of the Echo Detected EPR spectra of nitroxides.

Several important concepts such as *spin-diffusion* are also known from the nuclear magnetism (NMR) and the book of Abragam [21], which is an important source of additional reading, also for other general concepts such as the *spin temperature*, concerning primarily solids. One of the important early successes of spin diffusion was the explanation of the strong enhancement of the relaxation rates and the broadening of solid diamagnetic samples by introduction of very small amount of *paramagnetic impurities* [21, 22].

3.2 Types of Dynamical Processes Accessible by EPR

In the following we list several kinds of dynamics that have been typically investigated by EPR (sometimes in combination with NMR) and collect the *timescales* of the corresponding dynamical processes in Table 3.1. The classification used is certainly not unique, but the collected cases constitute an almost complete overview of the most common motions studied by magnetic resonance in solids and fluids.

The term *libration* refers to small-amplitude overall *restricted-reorientation* motion [23]. A model of libration in ref. [24] concerns molecules undergoing oscillations about some axis fixed in the molecular frame. This motion is very important in modulating the magnetic interactions for partially immobilized anisotropic systems, such as nitroxide radicals, used in studies of polycrystalline phase or glassy materials. Libration can induce very similar reorientation effects as internal motion in cyclic nitroxides [18]. For the lower temperatures, $T < 200$ K, libration was the cause of the overall restricted reorientation of tempone around the N-O axis. At higher temperatures, $T > 230$ K, the motion of a characteristic direction of the (hyperfine) hf tensor of the nitrogen atom was induced by *intramolecular* conformation change of the tempone molecule between two possible *twisted-crossover* conformations of the 6-membered ring, see Fig. 3.1. A more sophisticated motional model involving libration [25] was investigated to describe aggregates with long-range order with simultaneous local motions.

A different type of *restricted motion* is the overall molecular rotation occurring around a certain axis defined with respect to the molecular frame found for instance at temperatures lower than 144 K in the morpholine radical [34] with a ring skeleton similar to that of tempone. The relevant *correlation time* was ca 10^{-7} s, in the temperature range where this motion was accessible by CW EPR.

The interconversion of this molecule between two stable chair conformations was not possible at that temperature range due to the high barrier, a fact verified also by the absence of the exchange of the protons of the ring [34]. On the other hand, the morpholine skeleton was flat enough to rotate inside the matrix cavities around an axis with a restricted direction.

Except for the above pure cases, some exchange processes can act simultaneously, e.g. in small saturated cyclic hydrocarbon radical ions under matrix isolation, where several kinds of ring conformers are possible [26, 27].

Table 3.1 Dynamic range of the most usual motions at the molecular level

Intramolecular processes

- *Conformation changes*, i.e. motions involving internal molecular degrees of freedom
  (i) *Hindered rotation* and *torsional oscillations* of small fragments such as methyl with respect to the rest of the molecule [29–32]
  (ii) *Methyl rotation*: fast [33] $10^{-10} < \tau_C < 10^{-7}$, slow $10^{-5} < \tau_C < 10^{-2}$
  (iii) *Twist-crossover interconversion* [18] in 6-membered-rings, as in cyclic nitroxides $\tau_C \sim 10^{-7}$
  (iv) *Puckering motion* and generally large amplitude pseudorotation type of motion in saturated 4-, 5-, and 6-membered rings: $\tau_C < 10^{-8}$, see also Chap. 1 in this book
- *Exchange of protons* or any other small group between different sites
- *Exchange of electrons* $\tau_C \sim 10^{-10}$ to 10^{-12}
- *Isomerization* of some kind e.g. *valence isomerization*
- *Pseudorotation* due to the Jahn-Teller effect
- *Spin-Rotation* coupling[a] in methyl radical
- Overall *tumbling-rotation* [15]. Slow motion: $\tau_R \geq 10^{-6}$, fast motion: $\tau_R \leq 10^{-11}$
- Overall *restricted rotation* of molecules [34] and molecular fragments [3]
- Overall small-amplitude *librational motion* [35], slow motion at ca 77 K, $\tau_C > 3.\ 10^{-9}$
- *Libration* of ring protons [36]
- Large-amplitude localized *vibrations* of paramagnetic particles [37]

Intermolecular processes

- *Diffusion of defects* and *radicals* in crystals [9]
- *Exchange of small fragments* between a molecule and the surrounding bulk [22]
- *Electron transfer*, ref. [38] page 207, $\tau_C \sim 2.\ 10^{-8}$
- *Proton transfer*, ref. [38] page 204, $\tau_C \sim 6.\ 10^{-9}$
- *Translational motion* (Heisenberg spin-exchange [39]). Liquids $10^{-11} < \tau_C < 10^{-9}$
- *Ion-pair interconversions* (association- dissociation) $\tau_C \sim 10^{-9}$
- *Electron-spin exchange*, ref. [38] page 204, $\tau_C \sim 7.\ 10^{-11}$
- Tempone in perdeuteriated toluene [15] at 21° C, $\tau_C \sim 2.\ 10^{-7}$
- *Doppler effect* and *collisions in gases*, Abragam [21] pages 427, 322

The correlation times τ_C (s) are sensitive to temperature. If single values are reported they refer to specific experimental situation of the given reference

[a]Spin-rotation coupling is traditionally the relaxation mechanism of fast rotating minor molecules signifying the coupling of the electron spin with the angular momentum. In treating quantum rotors it means the mixing of the rotation with the nuclear–spin degrees of freedom of the molecule

Another interesting case is the correlation between the *overall reorientation* (tumbling) and some *intramolecular* reorganizations [28] that can occur in parallel in the coordination sphere of metal complexes with bulky ligands in viscous solutions.

It is worth noting that large-amplitude localized vibrations may considerably influence measured EPR parameters. This is especially true for light atoms H, D and also Mu (Muonium). At low enough sample temperatures only the ground vibration levels are populated with different vibration amplitudes for the above isotopes. Because of the distinct delocalization of the isotopes in the matrix cage the averaged EPR parameters turn out to be different.

This temperature independent isotope effect was observed in H and D atoms trapped in solid gases at 10 K [40] and at liquid helium temperatures [41]. The

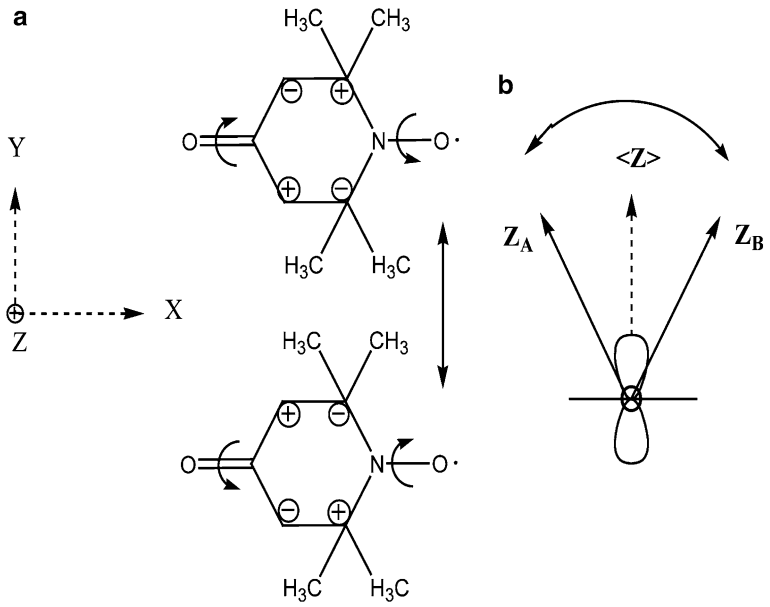

Fig. 3.1 (**a**) The tempone molecule performs restricted reorientation in the host matrix around the molecular *x*-axis. (**b**) Exchange between twist crossover conformers of the molecule [18]

finding was explained using the model of a particle harmonic oscillation in the cage of spherical symmetry [42]. The isotope effect and dynamics contribution to the hf constant**s** was also observed and explained by vibrational averaging for H, D and Mu in alkali halides in *substitutional* and *interstitial* positions of the impurity atoms [43]. With smaller energy interval between vibrational levels of the atomic impurities and higher sample temperatures, the excited vibrational levels become populated and the Fermi contact hyperfine interaction of hydrogen isotopes changes with variation of the sample temperature [44]. The isotope effect on the *superhyperfine interaction* (shf) for the interstitial and substitutional H- and D-atoms in alkali halides using ENDOR (Electron Nuclear DOuble Resonance) technique was studied by Spaeth [43] while Dmitriev studied the same effect for H and D trapped in solids Xe using CW-EPR [45]. Both sets of experiments showed that the shf interaction is smaller for deuterium centres compared to hydrogen ones.

3.3 Conformational Reorganization and Libration

Many detailed conformation studies of *saturated hydrocarbon rings* by EPR, involving temperature dependent lineshape simulations for the determination of the experimental *activation parameters*, exist in literature [26, 27]. More systematic

coverage of the subject with examples of several studied systems, are given in Chap. 1 of this edition. Selected examples of conformation studies will be discussed further in Sect. 3.5.1 together with the EPR-lineshapes in exchanging systems, where also some questions about the equivalence between the *microscopic barriers* and the experimental *activation energies* are raised [10, 11].

Averaging of the tensorial magnetic parameters with respect to overall motion is usually performed directly over the orientation dependent parameters of the spin-Hamiltonian. The set of the magnetic parameters used in simulations that include dynamics is assumed to be obtained in as low temperature as possible, and it is implicitly assumed that the rotational invariants (trace and determinant) of these parameters do not change significantly with temperature.

The contribution of each ring proton of the rigid unsaturated rings with conjugated π-bond systems to the hf interaction can be estimated by using the semi-empirical relations of Heller-McConnell type seen in Eq. (3.1) [46].

$$a = a_0 + a_2 \cos^2 \vartheta \tag{3.1}$$

On the other hand, in the versatile saturated 5- and 6-heterocyclic rings containing nitrogen, such as pyrrolidine and piperidine skeletons (involved in cyclic nitroxides), thermally induced deformations occurring by interconversion between the stable conformations of the ring carbons, modulate the hf couplings at relatively high temperatures. Each intermediate stable configuration determines automatically the location of the axial and equatorial protons, as well as the configuration of the C-NO-C fragment of the ring in cyclic nitroxides, and by this way their hf parameters.

The effect of averaging of the magnetic parameters for conditions of rapid motion in cyclic nitroxides is given in [47] for several internal motions and can be used in high resolution EPR studies.

3.3.1 Saturated Rings and Cyclic Nitroxides

Here are some examples of processes which are responsible for the most important intramolecular *large-amplitude* motions [47, 48] affecting the average of the magnetic parameters of small cyclic radical ions and nitroxides.

(a) *Ring puckering* can be seen as part of the conformational changes giving finally the *chair* and *boat* transformations of the 6-rings and the "*envelope*" structure of the 5-membered rings.

  (a1) 5-membered rings conformations: (i) *Envelope* (ii) *Twist*
  (a2) 6-membered rings conformations: (i) *Chair* and (ii) *Boat* (iii) *Twist-crossover*, see Fig. 3.1.

(b) *Pyramidal* (out of plane) *inversion/distortion* of the C-NO-C fragment vs. planar sp^2 hybridization.

(c) *Pseudorotation.* The above three types of distortions can "rotate" around the ring, exchanging position with the neighbouring corners of the polygon. This rotation does not involve any actual displacement of mass in the plane of the ring, therefore the adjective pseudo (= false in Greek)
(d) *Internal rotation* of the methyl groups.

Some experimentally obtained, widely varied, activation energies for different nitroxide molecules are reproduced further as they were reported in ref. [47], where they were compared also to *ab-initio* computations.

Chair-chair interconversion activation energy: 7–8 kJ/mol (ca 902 K).

Methyl rotation activation energy: 20–30 kJ/mol (ca 3,000 K!) in 4-methyl and 4-propyl substituted piperidine-1-oxide [47].

The pyramidal inversion barrier of the C_2NO fragment at the nitrogen atom is referred to as a small one, compared to the above two processes. The energy difference between the axial and equatorial configurations of the NO-fragment was 2–3 kJ/mol (ca 300 K).

Comparing also to the regular methyl rotation with a potential barrier of ca 1,000 K, e.g. 9 kJ/mol (1,082 K) in tempone [18] and the inversion of ammonia which needs ca 3,047 K to be activated, it is obvious that: (a) The activation energies for methyl rotation in nitroxides are relatively high while the pyramidal inversion at the nitrogen atom has a relatively small value.

3.3.2 Hyperfine Interaction of Beta Protons

As an example about how the averaging can be performed one can take the usual dihedral-angle dependence of the scalar hyperfine spin coupling for the internal rotation of the beta-protons with respect to the carbon with the unpaired p_z electron, ruled to a good approximation by the relation (3.1). The first term in the above equation, with a value of $a_0 \sim 10$ MHz, is sometimes ignored compared to the major contribution from the second term, which is proportional to $a_2 \sim 140$ MHz.

The dihedral angle ϑ between the two planes defined by the p_z axis and the C−H bond, having in common the C−C bond, varies in time with rotation or by thermally activated hindered rotary motion of the methyl fragment. In the latter case it can be considered as a stochastic process $\vartheta(t)$ and through the cosine square dependence the contact coupling is also modulated randomly by motion. The average of the above relation for a very "flat" potential, i.e. a freely rotating methyl, is $<a> = a_0 + a_2/2$. For high potential barriers the hf coupling depends on the *twist angle* ϑ_0, an important parameter in the configuration of the quenched (stopped) rotor, determining the relative position of the wells of the potential energy function of the methyl fragment compared to the direction of the p_z orbital [10, 11]. The motional effects of the methyl fragment on the EPR lineshape will be discussed in Sect. 3.7.2 for the different conditions of *diffusional* (classical) and *inertial* (quantum) rotation.

It can be generally shown that for several motional models, in particular for libration, the average $<\cos^2\vartheta>$ is not always 1/2 but at least it takes the same functional form shown in the following Eq. (3.2), see refs. [29, 36] and citations there:

$$< \cos^2\vartheta > \; = \; (1/2)\,[1 + \cos(2\vartheta_0)\,F(\alpha)] \tag{3.2}$$

Where one can obtain the following functions $F(\alpha)$ of the libration amplitude α.

(i) Uniform distribution [29] $F(\alpha) = \text{sinc}\,\alpha \equiv (\sin\alpha)/\alpha$
(ii) Two-site jump exchange [26] $F(\alpha) = \cos\alpha$
(iii) Classical harmonic oscillator [49] $F(\alpha) = J_0(2\alpha)$, where J_n are the Bessel functions of the first kind [50]
(iv) Stochastic harmonic oscillator [51] $F(\alpha) = \exp\{- < \alpha^2 >\}$

The averages $<\cos^2\vartheta>$ of the above shown models were tested in the following system: A proton detachment from a carbon in the ring of glutarimide in X-ray irradiated single crystal of this substance generated a carbon-centered radical with a pure p_z orbital [36]. The hyperfine couplings of the two protons in beta position with respect to the radical site changed reversibly between 5.1–3.8 and 1.2–2.2 mT in the temperature range 100–375 K. The correlated motion of the two beta protons of the ring was considered as a possible source of the temperature effects on the EPR lineshapes. A chemical exchange model considering the temperature-dependent amplitude of the motion (libration or reorientation due to conformation changes) was used successfully to analyze the situation.

3.4 Fundamental Dynamical Parameters

The range of the reorientation correlation times that may give visible effects on the EPR lineshape extends between the pico-second regime, $\tau_R \sim 10^{-12}$ s (*fast motion*) to $\tau_R \sim 10^{-5}$ s (*slow motion*), depending also on the strength of the interaction of the spin with the molecular motion. Close to the fastest and the slowest limits within the above range, and often before the limits are reached, a change in the correlation time cannot further alter the CW EPR lineshape. Beyond these limits, other magnetic resonance methods such as pulsed EPR can still be sensitive.

High- frequency/high-field EPR [52] offers a great advantage in studying dynamics of regular organic radicals with typically small **g**-tensor anisotropy. By estimating the lineshape variation of the nitroxides with temperature the dynamical range of the CW-EPR method becomes extended toward faster motions. Already the 95 GHz W-band CW lineshape of tempone doped in a single crystal of a host with similar structure and exchanging between two environments with different g-values, was sensitive to motion, while the X-band of the same sample was already fast-motion averaged [18].

Sometimes both CW and pulsed EPR are combined as e.g. the phase transition in solid ethanol doped with nitroxyl radicals was studied by continuous and pulsed EPR spectroscopy [53]. Similarly, the appearance of the crystalline state from the ethanol glass was for the first time directly monitored in the course of an EPR experiment. Both methods were successfully applied in studying the structural and dynamic characteristics of bis (leucine) oxalyl diamide ethanol gels [54].

The advantage of accessibility of dynamical information to both faster and slower timescales of motion can also be exploited by pulsed-EPR. This is primarily due to two factors, the volatility of the pulsed methods to adjust in each particular case at hand, and the elimination of the *inhomogeneous broadening*. Dzuba et al. [55] used very early a straightforward and innovative experimental pulse-EPR method to study the internal rotation of the methyl group in the radical anion CH_3-$^{\bullet}$CH-CO_2^-, obtained in irradiated single crystal of L-alfa-alanine. This method relied on the selective saturation of the different EPR transitions of the methyl spectrum by a nutation of about 90°, followed by a two-pulse sequence with a short and constant pulse delay. The amplitudes of the generated echoes was registered for variable waiting time after the first saturating pulse and was employed on the top of the T_1 processes to simulate the kinetics of the magnetization signal. By this way correlation times in the range of 10^{-5} to 10^{-2} s were obtained, which are indeed too long to be accessible by regular CW-EPR. The same investigators [55] performed later extensive studies on the effect of restricted reorientation (libration) by using Echo-Detected EPR spectra of several nitroxide probes.

Detailed dephasing kinetics of echo signals contains information about the dynamics of systems within an wide range of timescales. The two parameters that are necessary to determine the "stretched" exponential decay of the echo, discussed later in connection to Eq. (3.13), are also often adequate according to theory to discriminate the actual mechanism of the motional and spin dynamics among several alternatives.

Another task of studying dynamics is to understand the fundamental microscopic principles and identify the parameters that give rise to the macroscopic measurables. One can connect the reorientation correlation time with more fundamental quantities, such as the dimensions of the molecule and the *viscosity coefficient* η, utilizing the dynamical information from EPR. In such an analysis, the connected quantities depend on the motional model used, as for example Stokes' expression for the *transnational diffusion* constant D for the archetype Brownian particle is given by $\mathrm{D} = k\,T/(6\pi\,a\,\eta)$ where a is the radius of the molecule considered approximately as spherical [21]. For a tumbling molecule one usually assumes that the orientation Ω (Euler angles) of a predefined molecular frame at time t (with initial condition Ω_0 at time 0) satisfies the diffusion equation in the angular space Ω covering the surface of the unit sphere. The *reorientation diffusion constant* and the Stokes' constant for *rotation* are closely related to the *translational diffusion constant*, given in the above relation [21]. The quantity D is identical to the self-diffusion constant measured by the Carr-Purcell method [56]. The experimentally important temperature dependence of the correlations times is discussed further in this text, first in the next subsection and later under the Redfield relaxation limit, see Eq. (3.6).

3.4.1 More Accurate Models of Methyl Fragment Rotation

Two rather accurate theoretical models of the dynamics of hindered rotation, one classical [10] and one quantum mechanical [11], were thoroughly tested by simulations of experimental EPR lineshapes of the methyl hyperfine structure in methyl malonic acid radical CH_3-$^{\bullet}C(COOH)_2$.

(Model I) The classical model of diffusion in the presence of a periodic potential (Smoluchowski drift diffusion model.)

(a) Both the *free diffusion* and the *site jump model* were shown to be inadequate to reproduce the EPR lineshapes in the experimentally important region $0.32 < V_3/k\,T < 5.62$ of many rotors, where V_3 is the *barrier height*.
(b) The separate-harmonic-oscillators model for the high-barrier limit was not consistent with reasonable barriers but it gave a reasonably good Arrhenius fit with pre-exponential factor $2.08\,D\,V_3/k\,T$, where D is the diffusion constant. As a byproduct of this study we obtained that,
(c) The widely used relation for the isotropic hf-couplings in Eq. (3.1) must be corrected by a linear cosine term $\sim a_1 \cos\vartheta$ in systems with pyramidal distortion in the alfa-carbon, derived earlier by Suryanarayana and Sevilla [46]. This term was also introduced in our Model II of pure quantum treatment coming next.
(d) The rigid limit of this purely classical case gave unexpectedly a quartet of equal intensities, which is also the result of the quantum theory for the *stopped methyl rotor*, see further in Fig. 3.12b. This is an indication that the stopped rotor quartet is a consequence of the symmetry of the rotor rather than the quantum effects of motion.

(Model II) The quantum rotor in presence of a periodic potential.

(a) The Arrhenius barrier for activated methyl rotation was found to be 754 K and was thus significantly different from the potential barrier used in the Hamiltonian of the quantum rotor $V_3 = 618$ K. This was as unexpected as that,
(b) the deuteriated methyl rotor Arrhenius barrier differed also from both the above values being 387 K
(c) the deuteriated rotor behaved classically even at the lowest temperatures.
(d) The methyl rotor was also behaving classically above 50 K. A more detailed discussion about quantum effects of motion on the EPR spectra is undertaken in Sect. 3.7 of this chapter.

The above brief account for the extensive treatments given in Refs. [10, 11], shows that it can be worth to be careful in describing the dynamics of some quantum systems with exchange symmetry of identical, light particles in terms of the Arrhenius parameters due to the insensitivity of the experimental fits to the well known law. Furthermore, the macroscopically determined activation energies can be different from the microscopic potential barrier.

3.4.2 Forms and Phases of Solids Subjected to Dynamics Studied by EPR

The interactions of the electron spin in disordered solids results in *inhomogeneous* broadening due to anisotropic Zeeman interaction and unresolved hf interaction, as well as eventually the ZFS for higher electronic multiplets. The solid-state-EPR spectra can be broadened in addition by field inhomogeneities. It is assumed that the spectrum of a *polyoriented* sample is made up of a broad envelope of *homogeneously* broadened peaks from spins resonating at different frequencies, each associated with a certain orientation. The different peaks define the *spin packets*. Another definition of a spin packet was given recently in [57], being described as an ensemble of spin systems that experience the same, time averaged, local fields. This definition specifies in a better way the role of dynamics instead of the regular definition that is strictly applicable to the rigid limit of inhomogeneously broadened EPR spectra.

One has to deal with EPR measurements in *disordered* solids, which are categorized as either *glasses* or *polycrystalline* matter. The EPR lineshapes of such samples correspond to what are usually called *powder spectra.* In that case, one of the most appropriate methods to study such systems is ESEEM (Electron Spin Echo Envelope Modulation), and particularly the 2D-HYSCORE (HYperfine Sublevel CORrElation) technique. This method is usually combined with pulsed ENDOR, since complementary information is always desirable.

The *microcrystalline* and the *amorphous* solids can be modelled similarly in simulations of EPR spectra at low temperatures where motional dynamics can be disregarded. If dynamics is important, the magnetic behaviour of the *microcrystalline* state is different than the amorphous *glassy* state and it is possible to discriminate between them by using Field-Sweep Pulse-Detected EPR [58], further called Echo-Detected EPR (ED EPR). The *pulse delay* dependence of the echo-detected lineshape in glassy materials is namely more prominent. The reason for that is the difference in the *spin-diffusion* conditions that equalizes the *spin temperature* across the whole sample of the above two different kinds of disordered solids. While the spin packets within each microcrystallite are isolated in space and the magnetization of each spin packet develops independently thus minimizing spin diffusion, in the amorphous glassy state the spin packets can interact with each other in the regions of overlap and are more sensitive to cross correlation that increases the spin-spin relaxation rate. The explanation given in ref. [58] was: librations of the molecules near their equilibrium positions in amorphous materials not present in crystalline states.

Concerning the effect of different solid structures on the EPR lineshape of impurity radicals, the terms "*ordered*" and "*disordered*" may slightly shift meanings reflecting the actual order of the radical environment. As an example, relatively narrow methyl radical hf lines are recorded in fused silica [60] while very broad signals were observed for CH_3 in quench-condensed solid Kr [59, 61], see Fig. 3.2. It means that in spite that silica glass is *amorphous* lacking *long-range* order,

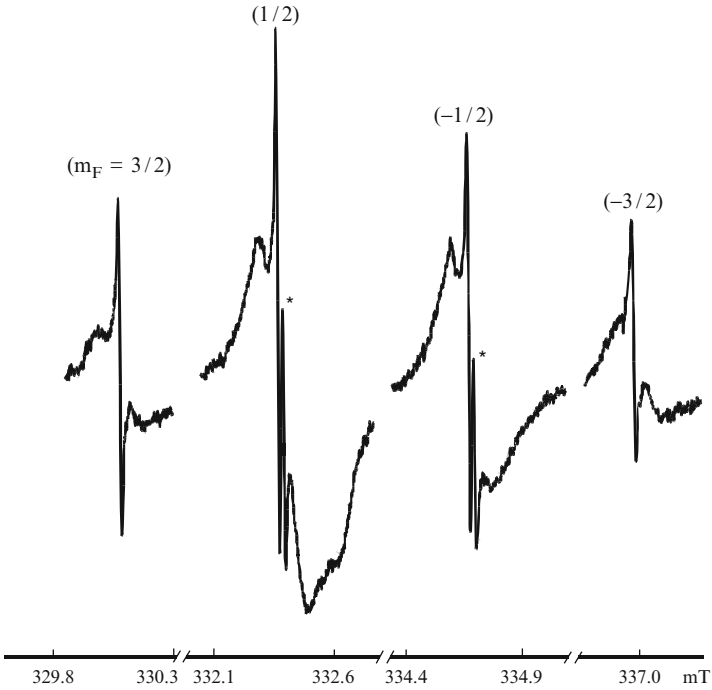

Fig. 3.2 The 4.2 K EPR spectrum of methyl radicals trapped in solid krypton. Resonance frequency: $f_{res} = 9344.22$ MHz. The narrow lines of the "*E*" symmetry doublet are marked by *stars*. The projection m_F corresponds to the F_z component of the total nuclear spin. The narrow *A*- and *E*-lines of 0.022–0.033 mT width are attributable to the CH_3 centers in perfect fcc (face centered cubic) structure in the polycrystalline Kr, while the broad A- and E-transitions of 0.18 mT are a fingerprint of the highly disordered Kr surroundings (Reproduced from Ref. [59] with kind permission of © The American Institute of Physics (2008))

it should exhibit much better "ordering" at the *nanoscale* level compared to the quench-condensed Kr (crystalline in the steady-state). In fact X-ray measurements show very high density of stacking faults for the "*amorphous at the nanoscale level*" quench-condensed Kr [62], which is consistent with the EPR lineshapes indicating long-range disorder.

Except for isotropic liquids with short range order and crystalline matter with long range order, *liquid crystals* may exhibit long range order up to 10^6 Å, i.e. almost within the macroscopic mm range. An important remark is that even though the environment of a paramagnetic solute in liquid crystal solvents is highly anisotropic some restricted-reorientation rates of local nature can be relatively fast [25, 63]. The elongated phospholipid molecules in membranes execute fast overall rotation about their long axes whose directions are restricted by the packing of the membrane lamellae [64].

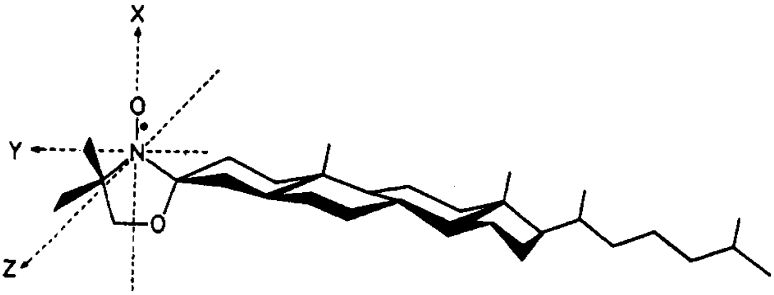

Fig. 3.3 The elongated and relatively flat cholestane nitroxide probe that was inserted in a multibilayer film consisting of the macroscopically oriented lipid dimyristoyl phosphatidyl-choline (L-alfa) during the study of the motional dynamics (Reproduced from Ref. [25] with kind permission of © Elsevier (1995))

A dense fluid which consists of "spherical" molecules is generally characterized by *short-range order* and *long-range disorder*, which can usually be described by a *pair distribution function* [9, 63]. The orientational averaging of the second rank harmonic, $S = <P_2(\cos\vartheta)>$, actually the Legendre polynomial, where the angle ϑ is defined between a molecular and a static laboratory direction, is the simplest parameter discriminating ordered from disordered solids. The average S is called the *order parameter* and vanishes in the absence of an orientation *restoring potential*. Equivalently, for a constant potential energy the orientation probability density is *uniform* and factors out in the calculation of the average S, which obtains the value zero by symmetry. On the contrary the physics of oriented systems requires that the orientation distribution has necessarily some tensorial components of second rank (or higher) rendering the value of the order parameter finite. E.g. for an ensemble of elongated molecules it is required at least a cylindrical symmetry giving $S \neq 0$.

In a particular lamellar system, Fig. 3.3, the libration axis, which was restricted by a potential was allowed to change direction [25]. That treatment demonstrated both theoretically and experimentally the implications of the structural order of the environment on the dynamics by a combined study of CW- and ED-EPR lineshapes. One could easily follow the limiting cases that were obtained using a truncated Hamiltonian and only two simple dynamics parameters, a *correlation time* and the average *amplitude* of libration, see Sect. 3.10 for details.

3.4.3 Estimation of the Amplitude of Libration in Nitroxides

The libration amplitude in anisotropic systems can be determined by using the field separation of the outer peaks A_{zz} of the CW-EPR spectrum in nitroxides affected by slow overall reorientation motion [24]. This method was based on the estimation of

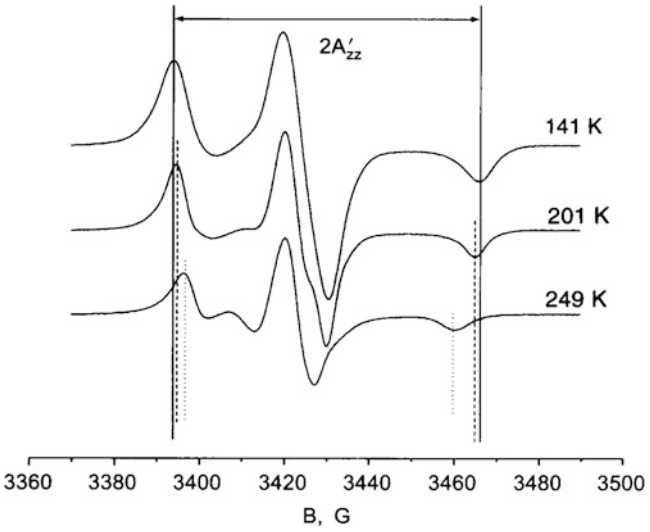

Fig. 3.4 The EPR lineshape of a partially immobilized nitroxide with large residual anisotropy. Libration around the *x*-axis of the molecule decreases the field separation between the outer peaks compared to completely immobilized molecule (Reproduced from Ref. [23] with kind permission of © Springer (1998) [23])

restricted reorientations from CW-EPR lineshapes of nitroxides developed by Freed and collaborators [65], a situation similar to libration, with the difference of the small amplitude in the latter type of motion.

Commonly the *x*-axis of the principal hf molecular frame in a nitroxide probe is assumed to be directed along the N-O bond, while the *z*-molecular axis is along the p_z orbital containing the unpaired electron. Furthermore A_{yy} has a similar value as A_{xx}, while A_{zz} is the largest hyperfine component. Sometimes, however, even in "simple" cases such as the nitroxide 3-carboxy-proxyl, some complications may arise concerning the interpretation of the libration restricted around a certain axis, see ref. [66].

For fast librational motion around the *x*-axis and assuming small amplitude librations, one can derive a simple relation between the time averaged parallel hyperfine component A'_{zz} and the mean square amplitude of the libration angle $<\alpha^2> \approx <\sin^2\alpha>$, shown in the following Eq. (3.3).

$$A'_{zz} = A_{zz} - \left(A_{zz} - A_{yy}\right) < \alpha^2 > \tag{3.3}$$

The A'_{zz} component is directly related to the field separation ΔH of the outer spectral peaks of the CW spectrum of the nitroxide by the simple relation $\Delta H = 2\,A'_{zz}$. The effects of the restricted motion on the nitroxide lineshape are shown in Fig. 3.4. The averaging of the anisotropic components of the hf (hyperfine) tensor was rather mild compared to unrestricted rotation, leaving a large amount

of *residual anisotropy* to the EPR lineshape even for fast motions. The relatively small decrease of A'_{zz} with temperature was still significant to obtain data for the librational amplitude $<\alpha^2>$.

In order to gain some feeling of the librational amplitude range, we mention that the *standard deviation* of the libration angle $<\alpha^2>^{1/2}$ for tempone in doped glassy alfa-D-glucose varied in the interval from 11° to 22°, for temperatures between 295 and 340 K [24]. This method was used to disentangle the *libration amplitude* and the *correlation time* of libration that were obtained as a product in Echo-Detected EPR studies [24, 25].

3.4.3.1 Relation to the Order Parameter

A variation of the method of the field separation of the outer peaks of a powder spectrum for the estimation of the restricted slow reorientation correlation time is discussed here. It was shown by Freed and collaborators [65] that the reorientation correlation time τ_R for slow isotropic reorientation was directly related to a particular quantity S, defined as the ratio of the field separation of the outer peaks of the EPR lineshape in the presence and in the absence of motion, by the following relation.

$$\tau_R = a(1 - S)^b \text{with } S = A'_{zz}/A_{zz} \tag{3.4}$$

The two involved parameters a and b depend on the *motional model*, the *intrinsic linewidth* and the *hyperfine parameters,* and could be obtained by fitting the experimental spectra provided that a certain model of simulation of the EPR lineshape including slow motional dynamics was available.

Similarly, a simple relation between τ_R and S was determined from simulated spectra of morpholine radical for which we had experimental data from powder samples [34]. The measurable S was shown to be intimately related to the *order parameter*. The variation of the measured S values (after elimination of the contribution of the isotropic hyperfine proton couplings) for relatively fast motion was computed using the second expression in Eq. (3.4).

The theoretical values of S for different angles of the z-dipolar axis with respect to the rotation axis are shown in Fig. 3.5. The principal dipolar z-axis of the nitrogen was assumed to perform jumps between three sites, simulating a rotation around an axis perpendicular to the (average) molecular plane (see further in Fig. 3.8). The computed values of S were almost indistinguishable from the values of the second order harmonic $Y_{2,0}(\beta)$, indicating an intimate relation to the order parameter S. Furthermore, from the intercept of the experimentally obtained curve S, shown as a straight line in the lower part of Fig. 3.5, with the theoretical curve we could accurately "read" the angle β in the diagram. This angle is the opening of the cone on which the p_z-orbital is confined during the rotation-like process.

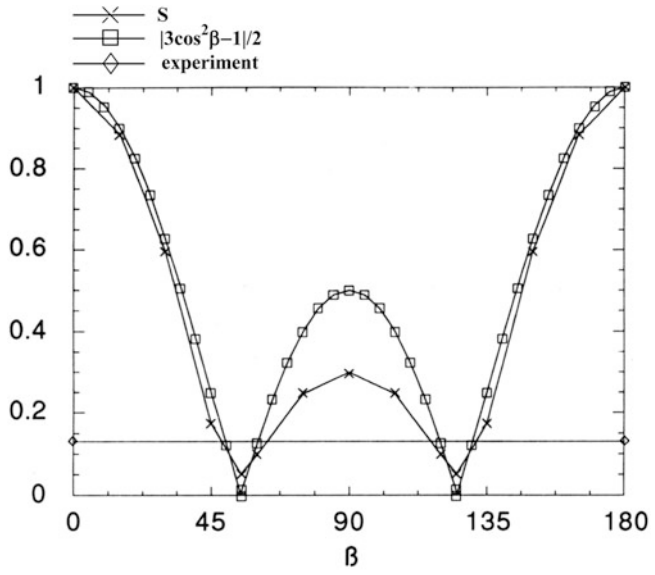

Fig. 3.5 The angular dependence of the quantity $S = A'_{zz}/A_{zz}$ (×) was essentially the same as for the second order harmonic in $Y_{2,0}(\beta)$ (□), while the horizontal line that intersects these curves at ca 0.13 represents the experimental value. S defines the ratio of the field separation of the outer peaks of the CW EPR spectrum of morpholine for relatively fast restricted reorientation by the same quantity for immobilized molecules [34]. The angle β is defined between the rotation axis and the z-direction of the nitrogen hyperfine tensor **A**. (Reproduced from Ref. [34] with kind permission of © Elsevier (1996))

3.5 Chemical Exchange

CW spectra have been used from the early days of EPR to study the dynamics in systems with *chemical reorganization* [67], or as they are simply called *chemically exchanging* systems, see also Chaps. 1 and 4 in this book. A general treatment for the EPR lineshapes of isotropic exchange within the density matrix formalism given by Heinzer develops there [67]. The exchange processes can give rise to line broadening and/or to modification of the entire EPR-lineshape pattern if they alter the magnetic environment, site, of the unpaired electron.

If motion exchanges the hf parameters of two lines, a resolved slow exchange spectrum acquires initially extra broadening in excess to the *intrinsic broadening* of each line, at the original transition frequencies, cf. Fig. 3.6a. The excess broadening is equal to the inverse lifetime of the corresponding site. For faster exchange the *lifetime broadening* of the exchanging transitions, shifts gradually the two lines to an intermediate position, cf. Fig. 3.6b, so that they at last overlap and finally *coalesce* to a single broad signal. The new lines of the spectrum created by this way start to sharpen by motion with further increasing exchange rate, Fig. 3.6c. For

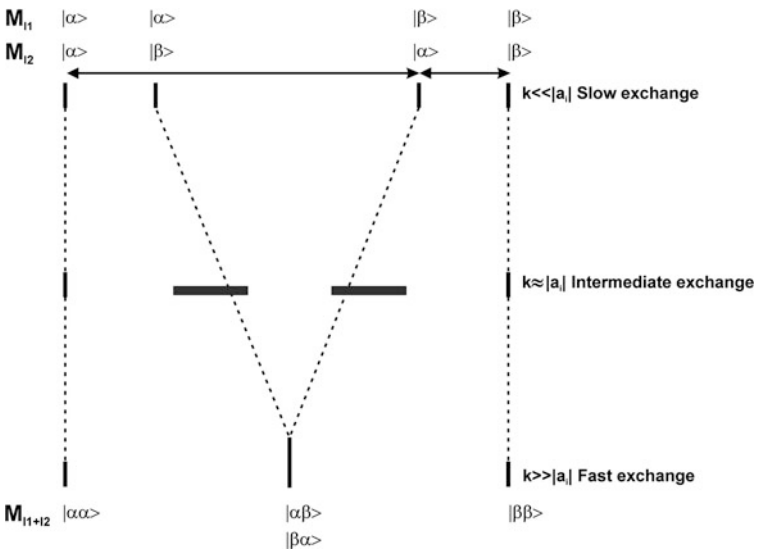

Fig. 3.6 Alteration of the hyperfine lineshape due to chemical exchange in a radical containing two isotropic nuclei with spin $I = 1/2$ for the three characteristic domains of dynamics for the exchange process: (a) higher $k \ll |a_i|$, *slow exchange*, (b) middle $k \cong |a_i|$, *intermediate* (coalescence), (c) lower, $k \gg |a_i|$, *fast limit* of exchange. All possible EPR transitions with the same total nuclear projection $M_I = M_{1I} + M_{2I}$, mix by motion and their resonance position is altered

really fast exchange the motionally narrowed final spectrum has a totally different appearance than the original.

Each of the three domains of exchange-dynamics, slow, intermediate-coalescence, and fast, with the corresponding spectral transformations seen in Fig. 3.6 can be followed quantitatively with relatively simple approximate expressions for the *linewidth* and the *resonance positions* of the exchanging peaks. The relevant parameter for the simple two-site exchange is the *lifetime* of the interconverting sites (particles) or its inverse, proportional to the *rate of reaction*, see e.g. ref. [38], page 214. The most rapid modification of the lineshape with the temperature variation happens close to rates (in MHz) that approach the hyperfine interactions, usually 0.1–3.5 mT for radicals in solids, i.e. 3–100 MHz. The corresponding exchange correlation times are usually longer than 10^{-8} s, demonstrating that exchange is generally a *slower process* compared e.g. to the pico-second (10^{-12} s) timescales of reorientation correlation in ambient fluids.

For further increase of the temperature over the fast exchange limit, no additional change can be observed in the lineshape rendering faster rate constants inaccessible to plain CW EPR. At the other extreme of low temperatures, slower motions cannot either alter the lineshape, and thus also slower motions are inaccessible for CW EPR. However, in some cases even these "extreme" rates can be studied by using high- field EPR [52], the lower ENDOR (Electron Nuclear DOuble Resonance) frequencies of the coupled nuclei in [29, 68, 69], or pulsed EPR methods [55, 70, 71].

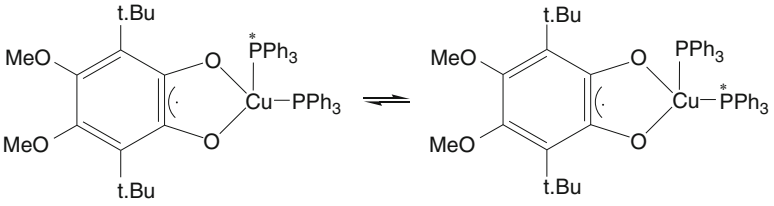

Fig. 3.7 Intramolecular exchange of the ligand triphenyl phosphine between two sites in the o-semiquinone complex of monovalent copper [28]. The unpaired electron is localized on the quinone ligand in this complex (Adapted from Ref. [28] with kind permission of © Elsevier (1996))

3.5.1 The Exchange Lineshape of Anisotropic Systems

We give further an example of intramolecular exchange concerning the phenyl phosphine ligands in a Cu-complex, see Fig. 3.7. The triphenyl phosphine ligands contain two magnetically inequivalent ^{31}P nuclei ($I = 1/2$), one in *equatorial* and one in *axial position*, which were found to have isotropic hf couplings [28]. Their exchange was observed in the CW lineshape as alteration of the nuclear spin projections $|\alpha\beta>$ and $|\beta\alpha>$ of the two phosphorous nuclei. The corresponding peaks were first broadened for slow exchange while for intermediate rates they coalesced to almost disappearance for the higher measurement temperatures. These phenomena were clearly recognizable in spite of the complexity of the system, involving: (a) Additional couplings to the two different magnetic isotopes of copper ^{63,65}Cu ($I = 3/2$) and (b) Anisotropic interactions modulated by the *slow tumbling* of the complex in the viscous medium giving asymmetric broadening.

The significant result of this work, studied by the temperature dependent CW-EPR linewidths, was that there is a connection between *chemical kinetics* and *motional dynamics* for bulky complexes with ligands that stick out to the bulk of the solution. Thus, a whole "cage" of particles extended even outside the complex ion has to be included in the model of certain intramolecular reactions [28] in order to explain their kinetics.

In studying anisotropic systems several additional theoretical difficulties appear, e.g. the interactions are no longer secular and additional kind of sites may be (indirectly) defined through the orientation change of the **g**-tensor and/or the hf **A**-tensor. In that case one has to include in the motional part of the problem except for spin populations, corresponding to diagonal elements of the density matrix, even spin-spin interactions that may involve extra couplings in the usually blocked density matrix. If one chooses to work with the density matrix formalism the creation of an exchange (super)operator in the combined space of the EPR transitions and the sites is straightforward, leading to a simplified form of the SLE (Stochastic Liouville Equation) [72, 73]. The mathematical problem of the kinetics for exchanging particles under chemical reorganization is relatively easy

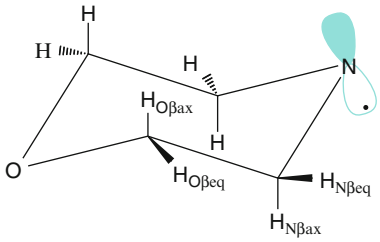

Fig. 3.8 Geometry of the saturated 6-membered ring of morpholine radical, indicating how the chair C_S conformation affects the orientation of the p_z orbital at the nitrogen nucleus (Adapted from Ref. [34] with kind permission of © Elsevier (1993))

to derive from the chemical equations describing the reorganization at hand. It is also straightforward to implement the population equations in the Liouville type numerical simulation of the EPR lineshapes, and also in simulations of the ESEEM signal [71]. The chemical reactions describing the reorganization of the system lead usually to non-linear kinetics, however, and the equation of motion has to be linearized as a first step. After that, the numerical matrix formalism is straightforward to apply [67] to the simulations using density matrix theory even for systems with anisotropy [73], where the meaning of site is generalized as discussed in the beginning of this subsection.

Except for simulations based on the *density matrix* formalism the simpler method of a *modified* form of the *Bloch equations* has also often been employed. The Bloch equations, which describe the magnetization classically, are valid for simpler two-level systems and weak spin-spin coupling [74, 75] but they give equivalent results as the more general density matrix formalism in the regime of their validity. They can be modified in particular for the purpose of simulating chemically exchanging systems to give the so-called *McConnell equations* [76], which have been derived for first order reactions.

Our most accurate treatment of anisotropic systems was a non-perturbative solution of the problem given by Benetis et al. [73, 77, 78]. This treatment revealed that one has to be careful when the high field approximation is applied to lineshape simulations of exchanging spin-systems, in particular in systems with *strong anisotropy* and/or *extensive reorganization* [34]. It was found that the nonperturbative exchange theory for the CW lineshape was necessary to reproduce faithfully the residual anisotropy in the spectra of randomly oriented morpholine molecules in cold Freons, subjected to restricted rotational motion in the matrix, see Figs. 3.5 and 3.8. The high field approximation gave a less accurate simulation of the lineshapes for this system, failing to reproduce the lineshape at intermediate rates and overestimating consistently the field separation of the outer peaks over the whole range of exchange rates [34]. This failure was attributed to the difficulty of incorporating the varying quantization axes for the nuclear spins of the high-field sublevel Hamiltonians obtained for each site in the computation of the exchange process.

One has to point out an important fact about the exchange dynamics for internal rotation of methyl-type fragments. For the high temperature *diffusion limit* the deuteron substitution does not change significantly the thermal activation parameters of the Arrhenius law. This is in contrast to the quantum rotational regime that is controlled by *inertial effects* at very low temperatures close to 5 K and sometimes up to 20–30 K. There, the dynamics of deuteron substituted methyl have very different characteristics compared to regular methyl, as it will be analysed further in Sect. 3.7.1. Thus, each of the following pairs displayed almost identical barriers. (a) The methyl fragment $-CH_3$ and the deuteriated analogue $-CD_3$ in acetic acid anion radicals [79] and (b) The methylene fragment $-CH_2$ and $-CD_2$ in irradiated crystals of Zn-acetate single crystal [77]. The rate of rotation in the first pair was $k_H = 3.3 \times 10^{11}$ Hz $\times \exp(-2.2$ kcal mol$^{-1}/R\ T)$ for proton and $k_D = 4.8 \times 10^{11}$ Hz $\times \exp(-2.5$ kcal mol^{-1}/R T) for deuteron, in the temperature range 77–170 K. In the second pair the rate of rotation was identical for both the proton and the deuteron fragments, $k = 6.73 \times 10^{12}\, Hz \times \exp(-7.17$ kcal mol$^{-1}/R\ T)$, in the temperature range 170–300 K.

3.6 Magnetic Relaxation

3.6.1 Spin-Lattice Relaxation in Very Cold Solids

The most well documented theoretical treatment concerning electronic spin-lattice relaxation times T_1 at liquid He temperatures refers to dilute paramagnetic metal ions hosted in ionic crystals. The important relaxation mechanisms for the corresponding sub-5 K temperatures regime occur through modulation of the ligand field by the crystal-lattice vibrations, a really inefficient mechanism, see Table 3.2.

The temperature dependence of the T_1 relaxation time can be written by adding together three main contributions to a single expression in Eq. (3.5), Abragam and Bleaney [80], page 65.

$$\frac{1}{T_1} = a\ \coth\left(\frac{h\nu}{2kT}\right) + bT^n + \frac{c}{\exp(\Delta/kT) - 1} \tag{3.5}$$

The symbol T is the *lattice absolute temperature*, assuming that the electron spin is in equilibrium with the lattice. The constant a of the first term is the magnitude of the *direct spin-phonon processes*. The second term is due to *Raman processes* and b determines the magnitude of this source of relaxation. The third term and the value of c depend on the contribution of the *Orbach process*. The variable Δ represents the crystal field splitting. The constants a, b, and c can have widely varying values from system to system depending on which is the dominating part.

The exponent n for the Raman two-phonon process can take several unusually large integer values, such as e.g. $n = 5$ for multiplets with small splitting, $n = 7$

Table 3.2 Order of magnitude of the electron-spin relaxation times induced by different motions or relaxation mechanisms under various lattice-temperature conditions

Temperature-conditions	Mechanism **Electron-spin-relaxation**	Longitudinal relaxation time T_1 s	Transversal relaxation time T_2 s
Cryogenic (liquid He) 1–5 K	• Electromagnetic bath: photons [81][a]	$10^8 \; ! < T_1$	–
	• Lattice vibrations[a]: phonons	$10^3 < T_1$	–
	– Direct process	$10 < T_1$	–
	– Raman processes	$10^{-3} < T_1 < 1$	–
	– Orbach process		
Low (*liquid* N_2) 77 K	• Slow tumbling	10^{-12}	–
	• Exchange	–	10^{-8}
Room temperature	• Tumbling	10^{-6}	10^{-6}
	• Gas collisions	10^{-4}	10^{-4}
	Nuclear-spin-relaxation		
Slow motion	• Paramagnetic impurities [81]	$T_1 < 10^{-3}$	$10^{-7} \leq \tau_C \leq T_2$
Other	• Other	sec-min	$T_2 \leq T_1$

T_2 values were occasionally deduced from the homogeneous broadening

[a]All spin-lattice relaxation times in this regime are theoretical and they are heavily overestimated due to the failure of the early attempts to assign an appropriate relaxation mechanism to solids' spin dynamics, but they have a fundamental interest indicating also the inefficient coupling of the spins with the lattice at lowest temperatures

for non Kramers doublets, and $n = 9$ for Kramers doublets, implying a strong temperature dependence. The strong temperature dependence is also a characteristic of the other two terms in Eq. (3.5), but the absolute values of the overall coefficients are small.

One can use some of the tendencies given by the above equation as indicative even for the relaxation conditions in other cases such as covalent crystals and powders according to detailed discussion found in ref. [82]. For these systems the spin-phonon interaction mechanisms result to relatively small values of relaxation rates compared to the rates due to thermal motion, which can modulate the *orientation* of the anisotropic interactions and/or the *distances* between interacting spins quantitatively. Since thermal motion is not possible in the limited range of the sub-5 K region, the crystalline-lattice *zero-level vibrations* are the only possible motions that are left to modulate the magnetic interactions. As they do not display large amplitudes and they are high-frequent and coherent, they are usually inefficient at inducing fast spin relaxation, if not many-particle (synergetic) and/or particular quantum effects occur. Finally for temperatures higher than ca 40 K, with the onset of *thermally activated* processes and the resulting classical random motions that induce spin relaxation rates larger by several orders of magnitude, the spin-phonon interaction mechanisms totally lose importance and can be neglected.

3.6.2 The Redfield Relaxation Limit

This is the classical theory of relaxation primarily concerning fluids, but still useful in the examination of the solid state for reasons that will be explained in Sects. 3.8, 3.9, and 3.10.1.

The characterization of the spin-motion dynamics as *fast*, is determined by the relation $<|H_{SL}|>\cdot\tau_C \ll 1$, where $H_{SL}(t)$ is the time dependent interaction between the spin S and the *lattice* L with zero average $<H_{SL}(t)> = 0$, and where the parameter τ_C of the lattice is the *correlation time*. One of the assumptions of the Redfield-relaxation theory is the so called *strong narrowing* condition [83] which implies that $\tau_C \ll T_{1,2}$, where T_1 and T_2 are the *spin-lattice* and *spin-spin relaxation times*, respectively. Equivalently it means that the fluctuations of the lattice are faster than the fluctuations in the decaying macroscopic magnetization.

Even for liquids, the particular conditions of *low temperature* and/or for *high viscosity*, renders the electron spin of relatively bulky molecules and complex ions into the thermodynamic limit of motion called the *slow-motion regime*. In that limit the Redfield theory of narrowing is not valid because the fluctuations of the spin and the motional degrees of freedom become of the same order of magnitude and can be statistically correlated [8].

In the Redfield regime, both relaxation times are relatively long, in particular the transversal relaxation time T_2, as the term *strong narrowing* refers to its inverse, i.e. the small linewidths corresponding to narrower lines. However, T_2 decreases monotonically with increasing correlation time τ_C, i.e. for slower motion and the lines broaden. This is apparent in Fig. 3.9 where also the different behavior of the *longitudinal relaxation time* is shown in the right half of the diagram where the condition $\omega_{0S}\cdot\tau_C \leq 1$ is no longer valid. The variable ω_{0S} here is the electron Larmor frequency. Notice that the relation $T_1 \geq T_2$ is always true, and particularly that for the solid state the pure inequality $T_1 > T_2$ is always the case.

The left part of the diagram in Fig. 3.9, which is called the *extreme narrowing region*, corresponds to faster motions while the right part corresponds to slower motions, as the correlation times become larger from left to right. An interpretation of the *extreme narrowing* condition $\omega_{0S}\cdot\tau_C \leq 1$ is that the fluctuations of the lattice are faster even in comparison to the electron Larmor frequency, that is, $\omega_{0S} \leq 1/\tau_C$. Equivalently, the lattice changes many times during each Larmor period in average, and consequently the precessing spins feel an average lattice interaction, which by definition vanishes.

For the higher temperatures corresponding to extreme narrowing, the *spin-lattice* relaxation time T_1 becomes equal to, and follows along with, the *transversal relaxation* time T_2 in a monotonically increasing fashion with further increasing temperature. (The primed quantity T_2' to be defined later in Eq. (3.8) designating the *adiabatic part* of the transversal relaxation time T_2 has strictly this property.) In this regime, the relaxation rates are shown to be *proportional* to the correlation time, i.e. $1/T_{1,2} \propto \tau_C$, and most importantly the spin dynamics can be characterized as *field independent*.

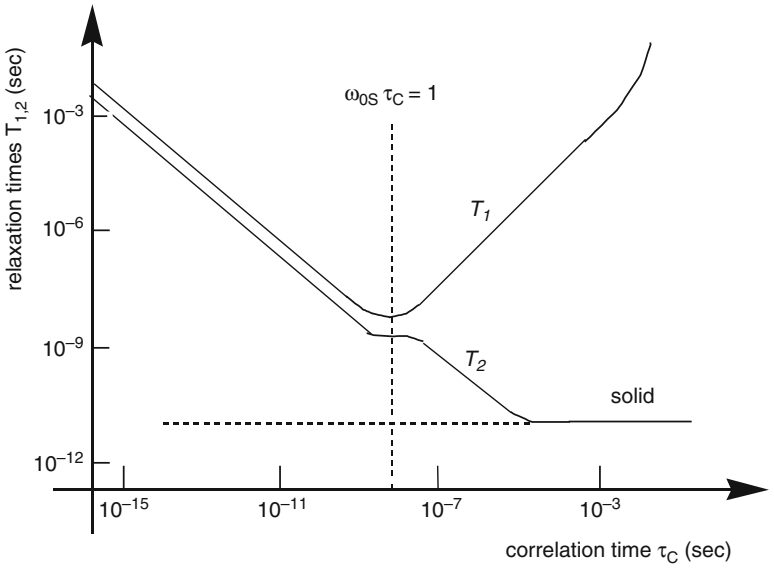

Fig. 3.9 *Correlation time* τ_C ($\propto 1/T$) dependence of the *longitudinal* T_1 and the *transversal* T_2 electron- spin *relaxation times* in fluids of varying viscosity and solids. The *left* part of the diagram until the *vertical broken line* at $\omega_{0S} \cdot \tau_C = 1$, is the high temperature *extreme narrowing* regime. Except for the region far out to the *right*, designated as solid in this figure, the Redfield, also called *strong narrowing* conditions [83], are tacitly assumed [33]

The lattice motions are usually considered as *thermally activated* processes and the correlation times exhibit normally a temperature dependence of Arrhenius type, i.e.

$$\tau_C = \tau_C{}^{\infty} \exp(E_\alpha / kT) \tag{3.6}$$

This temperature dependence is particularly steep for the lower temperatures until the realm of temperatures equivalent to the activation energy, i.e. for $T \cong E_a/k$.

While according to the above discussion *slower modulations* give *faster relaxation* the opposite is also possible in several systems, i.e. faster modulation gives faster spin relaxation. Most prominent and interesting example is the longitudinal relaxation at very cold conditions, seen in the previous Sect. 3.6.1.

Another example, where one has a similar behaviour of increasing spin-lattice relaxation rate $1/T_1$ with increasing temperature T, is coming from the region of the Redfield *strong narrowing* but only within the slower motions, the non-extreme narrowing region of the Redfield [83] regime. It implies that the lattice fluctuations are too slow and the *spectral density* $J^{(n)}$, which has the general Lorentzian shape,

$$J^{(n)}(\omega) \propto \overline{|H_{SL}(t)|^2}\, \frac{\tau_C}{1 + n^2\, \omega^2\, \tau_C^2} \tag{3.7}$$

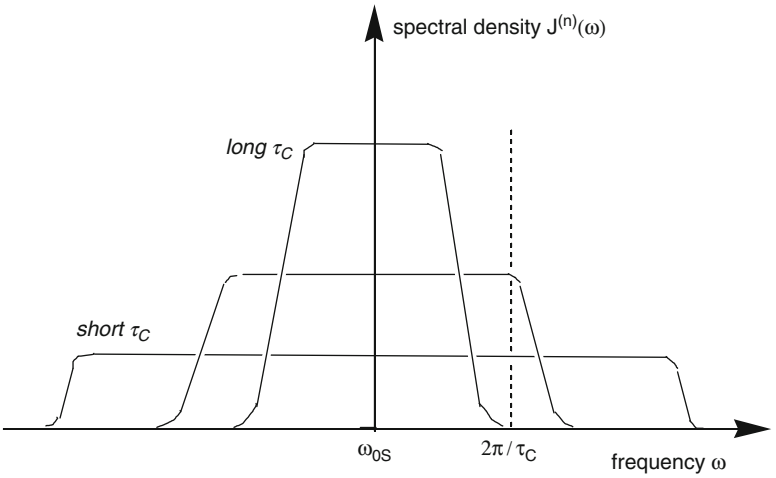

Fig. 3.10 The *spectral density* functions $J^{(n)}(\omega)$ for $n \neq 0$, i.e. the Fourier transforms of *decaying correlation functions* of the lattice variables according to the original Bloembergen-Purcell-Pound BPP [84] – Wangness-Bloch WB [85] – Redfield [83] theory about *magnetic relaxation*. The relaxation for long *correlation time* τ_C (slow motion) is efficient only for transitions inside a narrow region with frequencies $\omega_{0S} \pm 2\pi/\tau_C$, compared to shorter τ_C (faster motion) [86]

indicates that there is no strong component in the relaxation power spectrum for large resonance frequencies ω_{0S}. This happens when the motion obtains large enough modulation rate $1/\tau_C$, i.e. when the matching $\tau_C \cdot \omega_{0S} \approx 1$ occurs (vertical line in Fig. 3.10). For the faster motions on the other hand the resulting white relaxation spectrum becomes inefficient for all frequencies. These conclusions are based on the assumption that the total relaxation power, which corresponds to the area under the spectral density in Fig. 3.10, remains constant for different correlation times.

The integer n in Eq. (3.7) corresponds to the step of the ladder operators $S_{\pm n}$ for the electron spin S in the random part of the spin Hamiltonian. The ladder operators induce transitions $|\Delta M_S| = n$, with $n = 0, 1, 2$, between the Zeeman levels M_S. Notice that for the *adiabatic* or *secular* term with $n = 0$, the spectral density is monotonically increasing with the correlation time τ_C, and is frequency/field independent. Finally notice the quadratic dependence of the spectral density in Eq. (3.7) on the interaction strength $|H_{SL}|^2$; the interaction can be e.g. the hyperfine interaction (hfi).

3.6.3 Broadening

The main contribution to the homogeneous broadening in solids is *adiabatic* [87], merging from the *secular* terms of the Hamiltonian, including *spin flips* of like

spins, and comes from terms of the electron-Zeeman interaction for anisotropic **g**-tensor which contains the secular S_z operator, as well as the dipolar interaction. When motion becomes faster the *lifetime broadening* due to mutual transitions of the spin system and the lattice can become significant and contribute to the total broadening. The *lifetimes* of the spin states become shortened due to more frequent transitions between different spin states, during which the exchange of energy with the lattice takes place. However, the lifetime broadening is significant only when efficient motional narrowing is already active and the total broadening is small.

Thus, the higher the temperature the smaller the total linewidth even with the contribution of the lifetime broadening of the states, due to the smallness of the correlation time and the overall proportionality $1/T_2 \propto \tau_C$. Notice that this does not mean that we can neglect the contribution of the lifetime broadening, i.e. terms with $n \neq 0$ in Eq. (3.7), in calculating the total broadening, because it becomes significant relative to the adiabatic part for fast motion ($1/T_2'$, see also Sect. 3.6.2).

As an outline of the above discussion the following expressions in Eqs. (3.8) and (3.9) can be given for the total broadening that is strictly valid only for *two-level* spin systems.

$$1/T_2 = 1/T_2' + 1/2T_1 \tag{3.8}$$

T_1 is the spin-lattice relaxation time. This very useful relation separates the two possible sources of broadening, i.e. the *adiabatic* and the *lifetime broadening*. Sometimes, also the following relation is given, also in NMR, which includes in addition the *inhomogeneous broadening* $|\gamma \cdot \Delta H|$.

$$1/T_2^* = 1/T_2 + |\gamma \cdot \Delta H| \tag{3.9}$$

The star signifies that the total broadening of an EPR line is not only due to relaxation, the term designated by $1/T_2$, but also by field inhomogeneity, at least for fast motion. The pattern of these expressions with the different contributions remains the same even in more complex situations [21]. The point here is that each *spin packet* only contains the first two contributions (homogeneous) shown in Eq. (3.8).

For systems dense in unpaired electron spins the most efficient term of the dipolar Hamiltonian and the scalar spin-spin (exchange) interaction is the *flip-flop* term proportional to the bilinear operators $S_{1+} \cdot S_{2-}$ and $S_{1-} \cdot S_{2+}$.

3.6.4 Electron-Spin Dynamics Through Nuclear Relaxation

It is a well-known fact that even small amounts of paramagnetic impurities enhance the nuclear relaxation rates in both liquid solutions and diamagnetic crystals. On purpose, one can introduce salts of paramagnetic ions in solution or dope the diamagnetic crystals with paramagnetic ions. Concentrations already in the *ppm*

(part per million) range are most of the times enough for a significant enhancement of the nuclear spin relaxation and increased linewidths of the NMR spectra.

The mechanisms of these strongly "disproportional" effects are, however, different in the liquids and in the solids.

The average distance of radicals in a uniform and isotropic solution with concentration C is given by $R \sim C^{-1/3}$. To give an idea about this distance, for particle concentrations of e.g. ca $10^{18}/\text{cm}^3$, $C = 1$ mM, one obtains an average distance of about 90 Å. This is a substantial distance for the electron spins to exert any direct interaction to each other, although experimental data about Heisenberg exchange effects start at concentrations of this order of magnitude [15].

There are thus necessarily processes that bring the electron spins to a "closer contact", at least in a statistical way, to each other and to all the nuclei of the sample, which act as the "lattice". In liquids this is not particularly difficult to understand since the particles in a fluid can rapidly change positions, and furthermore the Brownian motion of all the involved species can contribute to the energy balance during mutual spin flips of the "unlike" nuclear and electron spins [21]. This guarantees the conservation of energy while motion allows also for many reencounters at a high rate. Thus in liquids it is reasonable with a great relaxation effect from impurities of relatively few paramagnetic centers. In solids, the mechanism must be of a different nature because, excluding diffusion, the particles are static. Thus, the mobility of liquids is replaced partially by the fast (and independent from the mutual interaction) *electron spin relaxation*. Furthermore, nuclear *spin diffusion* replaces the possibility of "closer spatial approach" of the electron to all nuclei by the effects of the *S-I* spin interaction of a paramagnetic center over the entire sample. The mechanism of spin diffusion involves spin flips between neighboring nuclear spins which transfer polarization disturbances throughout the sample [21] and was originally introduced by Bloembergen in 1949.

The nuclear relaxation enhancement offers a way of determining indirectly the relaxation rates, both $1/T_1$ and $1/T_2$, of the electron spin. These rates are normally many orders of magnitude higher than for nuclear relaxation, a fact that makes the direct measurement of the electron spin relaxation difficult. Several theories of computing the nuclear relaxation in paramagnetic systems of varying levels of accuracy have been developed in the past. One of the most complete theories involving *slow motions for the electron spin* was developed starting with the original reference by Benetis et al. [8]. In that treatment the electron spin was considered as a part of the lattice for the nuclei along with the regular motional degrees of freedom. Furthermore, all possible correlations between the electron spin and the motional subsystems were retained in this model.

The nuclear relaxation effects of paramagnetic "impurities" are still today extensively used to extract structural and dynamical information about *paramagnetic metal complexes* in solution [22]. Among the dynamical processes accessible by this method is the *overall reorientation* of the whole complex, *internal motions* such as *vibration-distortion* [88] and internal *rotations* [89], as well as *exchange* of the ligands from the first coordination sphere to the bulk [90].

3.7 Inertial Effects

Turning to *quantum effects* of rotation on the methyl radical EPR, we notice that the coupling of the nuclear spin with quantum rotation, *spin-rotation coupling* (Table 3.1a), in the Hamiltonian is occurring through the hyperfine interaction, either isotropic or anisotropic. The methyl-type rotors XY_3 (where the element X belongs to the carbon or the nitrogen group [91] of the periodic table and Y is proton or deuteron) in inert-gas matrices can be approximated as *pure quantum rotors* that occupy only the first few rotational levels at the lowest experimental temperatures. This becomes possible because the *rotational constants* of the lightest of the above radicals are of the order of 7 K, and sometimes even larger, being thus several orders of magnitude larger than the rotational constants of regular heavy molecules, with low symmetry.

Most importantly, rotors with kinetic energies of this magnitude can be considered as free when this kinetic energy is compared to the typical potential energies in relatively inert host matrices. This is only possible for "ultra light" and "highly symmetric" rotors, where interaction with the matrix is not large enough to quench quantum rotation [92]. The experimental low temperature EPR lineshapes are not affected significantly by interaction with the lattice since thermal motion is not adequate to populate higher quantum states.

The citation of the term "ultra light" is used to designate the very small *moment of inertia* of the methyl-like XY_3 rotors about their symmetry axes because they pass through the heavy central atom X. Methyl has $\boldsymbol{D}_3$ symmetry, see Fig. 3.11. The citation of the term "highly symmetric" rotors is used since only basic exchange symmetry between the peripheral Y = H, D atoms of the radicals was enough to give certain quantum effects [3] in the EPR spectra of the rotors, see discussion about mixed- isotope proton-deuteron methyls in next section.

The EPR quartet of the CH_3 rotors attached on silica gel surfaces display unusually high intensity of the inner doublet compared to the classical Fig. 3.12d high temperature 1:3:3:1 methyl quartet [1, 2]. Besides anisotropy, this peculiarity can in part be explained by referring to the energy diagram of Fig. 3.11, displaying the regular free 3D methyl rotation properties.

For pyramidal deviation of the CH_3 radical due to matrix-carbon interaction, the $\boldsymbol{C}_3$ symmetric instead of a planar $\boldsymbol{D}_3$ rotor could be adopted giving identically a *symmetric-top*. Small deviations from planarity are not able to modify significantly the moment of inertia of methyl. Furthermore, if a significant amount of the potential energy of the matrix-radical interaction must be added to the kinetic energy rendering the total quantum energy much larger than ca. 7 K corresponding to the rotational constant B of the rotors, seen in the vertical axis of the figure. The important issue of the state occupancy here is the adjustment by considering the degeneracy of the angular momentum laboratory projection quantum number $L = 0, \pm 1$ of the $J = 1$ rotational states, see Fig. 3.11.

In that case we obtain totally a sixfold rotational degeneracy in the first excited rotational level $|J = 1, M = \pm 1, L>$, actually all of them E symmetric nuclear spin doublets, where $M = \pm 1$ are the molecular angular momentum projections,

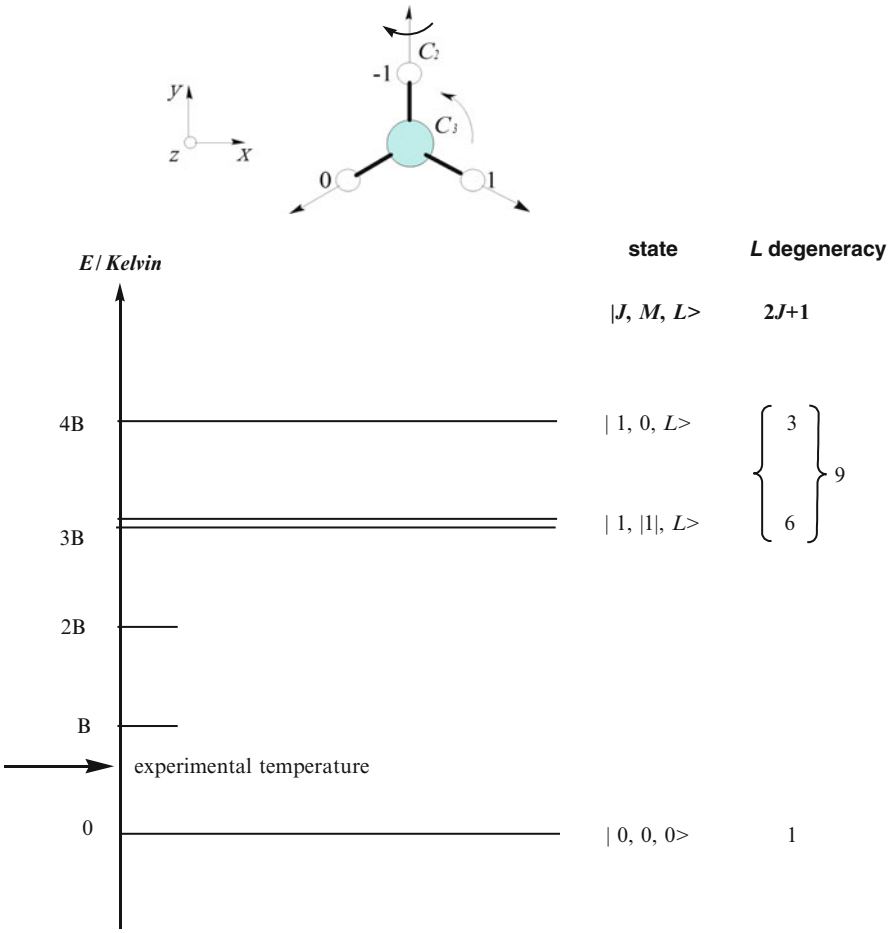

Fig. 3.11 The symmetric-top free-methyl rotor, i.e. a planar, methyl fragment of $\boldsymbol{D}_3$ symmetry [3] considered in three dimensions. The rotational C_3 and C_2 axes are indicated in the figure while the three protons are indexed by -1, 0, and 1. The rotational energy level diagram indicates that the first excited "parallel" rotation level $|J, M, L> = |1, \pm 1, L>$ has totally sixfold rotary degeneracy due to the laboratory projection $L = 0, \pm 1$ of the angular momentum $J = 1$, while $M = \pm 1$ are the two opposite molecular projections. The experimental temperature indicated in the energy diagram is 4.2 K (Aadapted from Ref. [93] with kind permission of © IOP-science (2009))

see the total nuclear spin-up $F_z = 1/2$ states, in the next Eq. (3.10). The spin-down $F_z = -1/2$ states are obtained by exchanging α to β in the equation.

$$\begin{cases} \Psi^{(A)}_{\alpha,\beta,\alpha}(1,+1,L) = |1,+1,L\rangle\ [\varepsilon^*\ |\beta,\alpha,\alpha\rangle + |\alpha,\beta,\alpha\rangle + \varepsilon\ |\alpha,\alpha,\beta\rangle] \\ \Psi^{(A)}_{\alpha,\beta,\alpha}(1,-1,L) = |1,-1,L\rangle\ [\varepsilon\ |\beta,\alpha,\alpha\rangle + |\alpha,\beta,\alpha\rangle + \varepsilon^*\ |\alpha,\alpha,\beta\rangle] \end{cases} \tag{3.10}$$

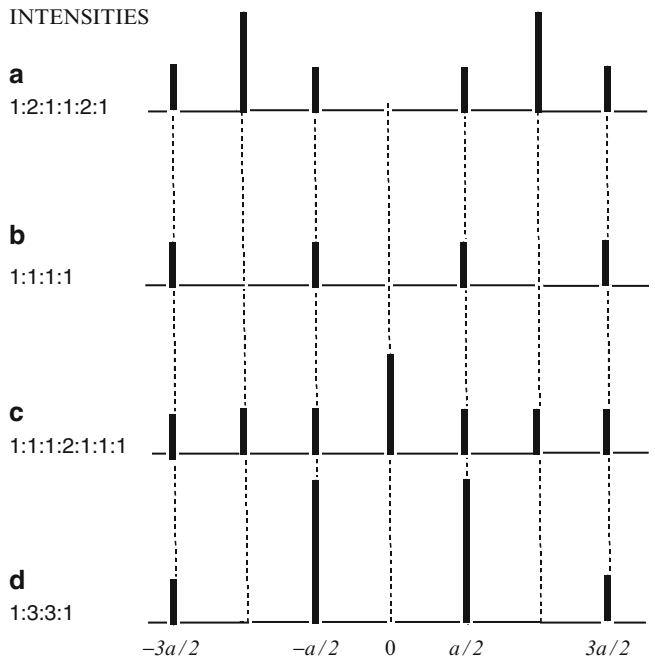

Fig. 3.12 Basic EPR stick-spectra for a *hindered methyl rotor* with *isotropic beta protons* with hf coupling according to Eq. (3.1) along with the appropriate limiting conditions for the motion, see text for details. (**a**) *Stopped classical rotor* $\tau_{exch} \rightarrow \infty$. (**b**) *Stopped quantum-rotor* ($\ell = 0$) for negligible barrier or strongly- hindered diffusional rotor. (**c**) *Tunneling quantum rotor* (superposition of $\ell = 0$ and $\ell = \pm 1$ rotational levels). (**d**) Fast classical- ($\tau_{exch} \rightarrow 0$) and very rapid high energy quantum-rotor (high rotational quantum numbers ℓ). The quantum mechanical z-projection quantum number of the rotational angular momentum is denoted by ℓ. Notice that the stopped quantum rotor in (**b**) requires negligible barrier and that it is also obtained for classical treatment of motion [10]

The imaginary number $\varepsilon = \exp(i\, 2\pi/3)$ signifies the period of the $\boldsymbol{C}_3$ symmetry and $L = 0, \pm 1$ the laboratory projections of the rotational angular momentum. The A nuclear spin states $\Psi^{(A)}_{n,n,n}(1, \pm 1, L)$ for the equal nuclear spin projections, $n = \alpha$ or β, that should give total nuclear spin $F_z = \pm 3/2$ are excluded due the requirements of the $\boldsymbol{C}_3$ group for the particular case of the three protons with nuclear spin $I = 1/2$. On the other hand the E nuclear–spin, totally symmetric $\mathbf{R} \otimes \mathbf{I}$ states in Eq. (3.10), are allowed by symmetry. Thus going up to the energy of the first excited "parallel" rotational levels $|1, \pm 1, L>$ and before reaching the "perpendicular" rotational levels $|1, 0, L>$ we obtain a quartet ratio 1:7:7:1, comparable to the experimental 1:8.5:13:2.5 quartet of ref. [2]. When the rotational level $|1, 0, L>$ is also populated at even higher temperatures, a new totally symmetric quartet is available changing the theoretical intensity ratio to 1:2.5:2.5:1. This is actually not compatible with the lowest temperature 1:1:1:1 quantum quartet but approaches the higher temperature 1:3:3:1 quartet since the system at 77 K approaches the classical quartet. On the other hand the rotational level $|1, 0, L >$ is forbidden for the planar D_3 rotor.

Our tentative interpretation of the unusual EPR methyl quartet found in silica gel based on a straightforward *zeroth order free rotor* approximation is under further investigation in our laboratory [94]. We believe that it constitutes a semi-quantitative explanation to be compared to qualitative explanations of other groups found in Sect. 3.7.3.2. There are indications that the above model explains certain peculiarities and helps understanding some recent experimental data of CH_3 spectra in solids. In particular, it is seen that this model sheds light on similar peculiarities observed in our and Eloranta's group recent experimental results. Thus, the *A/E* peak intensity ratio for CH_3 in CO and CO_2 matrices went below 0.5 with the sample temperature increasing, as reported by Kiljunen et al. [95]. More surprisingly, in solid N_2 for low sample temperatures they observed inner/outer line peak intensity ratio significantly greater than for the high ones. In our preliminary results of radical CH_3-N_2O matrix experiments, the P_A/P_E population ratio falls so steeply with rising sample temperature as if the energy gap between the radical rotation levels is far above 20 K [94]. It is also observed that the same dependence retains in general, for CO, CO_2, N_2 and Ar matrices. The greater the radical-matrix interaction, the further the shifts into the high sample-temperature region of the *A/E* peak-intensity ratio *vs.* temperature dependence.

The assumption of radical non-planarity during strong matrix–radical interaction agrees with Misochko et al. [96] who observed rather large **g-**tensor anisotropy of type I CH_3 and CD_3 radicals formed upon low temperature photolysis in solid argon. They stated that the observation of **g-**tensor anisotropy is good evidence for a nonplanar structure of type I radicals. They refer to the **g-**tensor anisotropy of the SiH_3 radical [97] which is known to be a pyramidal type molecule.

3.7.1 Quantum-Rotation of Small Radicals in Inert Matrices

Matrix isolation methods of radicals in inert gas matrices were developed during a long period of time by Shiotani's group. The group was particularly specialized in experimental CW-EPR methods on radicals under *rare-* (*noble*) *gas-matrix* isolation, a specialization posing particular skills. For more information about *matrix isolation* of free radicals see Chaps. 4 and 9 in this edition. In particular the rare-gas matrix isolation is very important for testing experimentally the *quantum effects* on the lineshapes of "ultra-light" and "highly symmetric" methyl-type rotor radicals. The quantum mechanical *spin-rotation coupling* (Table 3.1a) by the hf-interaction modifies radically the classically expected EPR lineshape of methyl radicals kept in relatively inert matrices close to the liquid He temperature 4.2 K. Considering the interaction of the alfa-proton methyl rotor, with the Ar (Argon) molecules of the host matrix [3] it was shown that, at least for the lowest experimental temperatures $T < 20$ K, a *freely-rotating planar-rotor model* was adequate to account for the experimental findings [98]. In other words, no appreciable hindering potential by the rare-gas matrix was found to apply in these systems.

Still, several significant new *quantum effects* other than *tunnelling* were discovered and explained semiquantitatively [3] by using group theory. It was possible, for example, to observe and identify the EPR signal from the *stopped methyl-rotor* ($J = 0$) for both the usual proton-methyl radical and the deuteron-substituted methyl radical, at the lowest experimental temperatures close to 4.2 K. The observed severe distortion of the lineshapes involving exclusion of several EPR transitions was attributed to the symmetry of the $\boldsymbol{D}_3$ point group of the radical and the Pauli principle of exchanging indistinguishable Bosons or Fermions.

The quantum effects were most dramatic for the deuteriated methyl rotor where the expected classical 1:3:6:7:6:3:1 septet had collapsed to a mere singlet (!) at the lowest experimental temperatures. The severely distorted EPR spectrum of the stopped deuteriated methyl CD_3 in Ar matrix at 4.1 K is seen in figure 5, ref. [3]. The experimentally observed singlet conforms to a single allowed EPR transition of the *antisymmetric* (with respect to exchange of any two deuterons) nuclear-spin wave function, coupled to the lowest rotation state with zero angular momentum ($J = 0$).

$$\Psi_{000}^{A_2}(-1,0,1) = \frac{1}{\sqrt{6}}\,|000\rangle\ \{[\,|-1,0,1\rangle + |\,1,-1,0\rangle + |0,1,-1\rangle\,] - [\,|1,0,-1\rangle + |-1,1,0\rangle + |0,-1,1\rangle\,]\} \tag{3.11}$$

All the expressions derived by Benetis and Sørnes for the lowest mixed rotational and nuclear-spin part of the quantum states of the system which are allowed by exchange symmetry under low temperature conditions are found in ref. [3]. Even mixed CH_2D and CHD_2 rotors, which have solely fundamental $\boldsymbol{C}_2$ symmetry, were characteristically affected by exclusion of EPR transitions [3].

Among the new interpreted quantum effects was the observed extreme sharpness of the experimental EPR spectra at the lowest temperatures, unexpected for anisotropic systems. Further theoretical investigation, including full simulation of the experimental spectra has to be performed, however, in order to obtain information about dynamics for temperatures higher than 20 K where the effects of thermal motion start to appear in the experimental spectra.

Preliminary data show that also other systems, such as the nitrogen-based rotors NH_2 and $NH_3{}^+$, exhibit similar properties as the *isoelectronic species*, H_2O^+ and CH_3, respectively [91]. On the other hand, the classical thermal motion increasingly affects heavier and non-planar methyl-type rotor radicals, such as SiH_3. Studies of similar heavier hydrides of groups IV and V of the periodic table showed a systematically increasing importance of the interaction of the host molecules with the inert-gas matrix and increased classical behaviour [91].

Regarding the information about dynamics contained in the spectra of the pure quantum rotors one should not expect the same kind of parameters as in the case of classical motions. An immediate difference is that the rotation is not any more a part of the lattice, and thus we cannot obtain a parameter such as *correlation time* of rotation. We can instead extract the *rotational frequencies* expected for the rotors

or equivalently the *rotational quantum number* from the effects on the EPR spectra. The *barriers of rotation* of methyl type quantum rotors in the inert Ar gas matrix was definitely much smaller than the *rotational constant B*, which is of the order of 5–8 K, since the radical was performing free rotation up to the first two decades of K. As a comparison we report the rotation constant of the H_2 molecule [99], which is one order of magnitude larger, that is, $B = 7.35$ meV $= 86.30$ K.

The motion of methyl rotors has been found to be important in understanding the experimental ESEEM (Electron Spin Echo Envelope Modulation) and ENDOR properties in solid state for experiments performed at very low temperatures. In ESE (Electron Spin Echo) studies of methyl- substituted nitroxides it was obvious that nuclear and electron spin relaxation was affected very distinctly by the quantum properties of methyl-rotation [18, 100] in addition to the effects of the classical relaxation theory. The experimental facts about the effect of the hindered internal rotation of methyl fragments in nitroxides have not been understood in detail so far.

3.7.2 Hindered Rotation of "Light" Molecular Fragments

The quantum effects of rotary motion discussed above are normally important and can be observed at the lowest experimental temperatures close to 5 K in systems that contain the lightest possible atoms, protons and deuterons. They result in relatively *temperature independent* EPR lineshapes, since they are *inertia dependent* through a quantum mechanical spin-rotation Hamiltonian as opposed to classical diffusional motion involving lattice thermal contact. The quantum effects become of minor importance between 40 and 60 K, giving ultimately place to classical effects of motion [11] at even higher temperatures. The vibrational degrees of freedom of the crystal lattice act here as a *thermal reservoir* to which the rotation is primarily coupled, and indirectly the spins [31].

Usually the rotary motion of methyl fragments of larger molecular units is substantially hindered by *intramolecular*, but also by *intermolecular* forces, depending on the phase of the solid (crystal lattice), represented by potential barriers of the order of 1,000 K. Cases of much smaller barriers, e.g. toluene with barrier 6.8 K(!) with almost free rotation, and much higher potential barriers than 1,000 K, up to 2,000–3,000 K with strongly hindered rotation also exist [101]. The high value 3,000 K is usually referred to the methylene fragment $-\dot{C}H_2$.

The strongly hindered methyls perform torsional oscillations, where the motion is not possible to stop in the classical meaning, i.e. by freezing it at very low temperature. Those quantum systems perform zero-level oscillations if the barriers are too high, or otherwise tunnel (coherently) to adjacent wells [30, 92] for lower barriers. In the case of very low barriers compared to the splitting of the pure rotational states, such as for light, protonated methyl rotors in frozen inert gases, the rotation stops per definition when only the lowest rotational level with zero angular momentum ($\ell = 0$) is populated. The EPR spectra of the *stopped quantum rotors* are characteristic [3], i.e. four equally intense lines shown in Fig. 3.12b, and occur at the lowest liquid He temperatures due the lack of adequate thermal excitation.

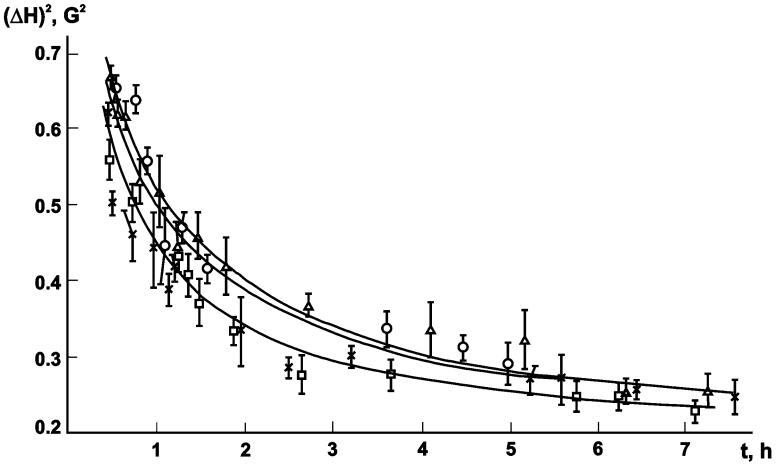

Fig. 3.13 Time variation of the squared width of the EPR lines of nitrogen atoms stabilized in H_2 matrix. The figure shows results recorded in four runs at different sample temperatures: 4.2 K *circles* and *squares*, and 1.2 K crosses and triangles. The theoretical curves were calculated supposing distinct values of the o-p conversion rate (See ref. [106] for details. Reproduced from Ref. [106] with kind permission of © The American Institute of Physics (1990))

Freed [30] seems to be the first to recognize and interpret the quantum effects of spin-rotation coupling (Table 3.1a) on the CW-EPR spectra in the case of a *hindered methyl rotor* at low temperatures, and derived the *tunnelling-rotor septet* seen in Fig. 3.12c, obtained also experimentally [102–104]. In the same figure two more characteristic cases of experimentally obtained spectra are shown, in addition to the above two, using as a model the identical methyl fragment for different thermodynamic conditions. The stick spectra of this figure have been approximately computed using identical magnetic parameters. The underlying physics for the differences is briefly explained in the legend of Fig. 3.12.

Except for studying the motional dynamics of paramagnetic matrix impurities the dynamics of the matrix particles may be the subject of study by EPR spectroscopy of different paramagnetic species as probes. In the next section, we consider a variety of methyl radical EPR lineshapes in solid gases and discuss recent experiments which utilize methyl-like quantum rotors as potential spin probes to trace matrix structure and dynamics.

We present first certain studies concerning modifications in the structure of frozen molecular hydrogen accessible by EPR. This quantum solid is occasionally used as a matrix for low temperature isolation of methyl radical.

The slow temporal narrowing of the EPR lineshape of nitrogen N-atoms trapped in solid normal H_2 (3:1 ortho-H_2 to para-H_2 mixture) seen in Fig. 3.13 was used to study the stimulated ortho-para conversion of the matrix molecules [105, 106] which leads to para- H_2 solid consisting of "spherical" molecules executing no (identifiable) rotational motion.

Another combined EPR and NMR study was utilized to investigate the process of ortho-para conversion in solid molecular hydrogen containing small amounts of atomic hydrogen impurity [107].

3.7.3 Methyl Radical as a Probe of Quantum Properties in Matrix Dynamics

The EPR lineshape of methyl radicals depends on the state of the radical rotation which, in turn, is governed by the kind of the matrix hosting the radical, the sample temperature and the methyl isotopomer used.

With a C–H bond length of 1.088 Å, methyl radical is sufficiently small to allow the particle to embed in the lattice without disturbing seriously the nearest surroundings. One obvious disadvantage of methyl radical as a potential spin probe lies in its strong chemical reactivity. This implies use of inert matrices and, preferably, low sample temperatures. On the other hand, methyl radicals were studied in certain matrices at room temperatures also, see for example [108]. Not only the small size but also the simplicity of its molecular structure is another advantage of using the CH_3 radical, encouraging calculation of the EPR radical spectra on the basis of based first quantum principles.

This brief review will focus on the effect of the solid state dynamics on the lineshape of the methyl radical EPR spectrum.

3.7.3.1 In the Bulk of Single Crystals

According to theoretical studies, see ref. [109] and references cited therein, the CH_3 radical possesses three different principal values of the proton hyperfine tensor and should yield anisotropic EPR spectra at certain experimental conditions. This is in agreement with the experimental data obtained for CH_3 radicals studied by EPR in a single crystal of $CH_3COONa \cdot 3D_2O$ at 20 K [110]. At a sample temperature of 20 K, the CH_3 EPR spectrum consisted of eight anisotropic hyperfine transitions, while at 77 K it appeared as a nearly isotropic 1:3:3:1 quartet [110]. Consistently Rogers and Kispert [111] observed a near 1:3:3:1 quartet for CH_3 in $CH_3COONa \cdot 3H_2O$ single crystal kept at 77 K and measured the slight axially symmetric hyperfine coupling anisotropy with $A_{||} = -2.18$ mT and $A_{\perp} = -2.25$ mT. They explained the result suggesting fast rotation of the radical around its threefold axis resulting in averaging of the A_{xx} and A_{yy} principal values. Toriyama et al. [112] carried out ENDOR (Electron Nuclear DOuble Resonance) studies of methyl radicals in γ- irradiated single crystals of $CH_3COOLi \cdot 2H_2O$. The proton hyperfine coupling $\mathbf{A} = (-21.30, -21.61, -20.57)$ G tensor turned out to deviate somewhat from axial symmetry being also far from the principal values of the CH_3 proton coupling tensor $(-11.21, -33.46, -21.54)$ G in the rigid state [110]. To explain the residual orthorhombic

symmetry of the hf coupling tensor Toriyama et al. suggested that the CH_3 radical undergoes hindered oscillation about one of the crystallographic axes located in the plane of the radical, *c*, in addition to rapid reorientation about the threefold axis pointing in the direction of another crystallographic axis, *b*. The authors suggest that the deviation of the observed spectrum from the cylindrical symmetry relates to no cylindrical symmetry in the crystal field around the *b* axis.

Thus, one might conclude that in single crystals the radicals execute, at temperatures as high as the liquid nitrogen, fast rotation around the C_3 axis accompanied by restricted oscillations about the C_2 axis, while, at temperatures below approximately 20 K, the torsional rotation is strongly hindered and the EPR lineshape corresponds to orthorhombic symmetry. However, the situation is not as simple as that. Kubota et al. stressed that the methyl radical trapped in crystals other than discussed in ref. [110] showed no eight- line pattern even at 4 K. Thus the character of the radical rotation is extremely sensitive to the matrix environment of the radical. Below, this inference will obtain support when considering CH_3 in polycrystals.

3.7.3.2 On a Solid Surface and in Voids of Single Crystals

Pariiskii et al. [2] reported the EPR spectrum of methyl radicals adsorbed on a silica gel surface at 77 K. The spectrum consisted of four lines with the unusual amplitude ratio 1:8.5:13:2.5 and different linewidths, 0.1–0.2 mT, for the spectral components. The authors notify the line asymmetry of the transitions. The non-binomial distribution of amplitudes was attributed to incomplete averaging of the anisotropic hyperfine and spin- orbit interactions resulting to different widths of the spectral components. Combined qualitative analysis of the amplitude and linewidths distribution of the hf components led the authors to conclude that, though the radical rotation around the C_3 symmetry axis (perpendicular to the sample surface) was the key motion affecting the shape of the EPR spectrum, torsional rotations about two other main coordinate axes also contributed somewhat to the neutralization of the anisotropy. With decreasing sample temperature, the amplitude ratio changed in favor of the outer lines [113]. At the liquid helium temperature 4.2 K, new additional lines emerged explained by group theoretical considerations concerning additional splitting of the torsional states of the radical about the C_3 symmetry axis in the presence of a large rotation barrier [113].

In experiments by Gardner and Casey [114], methyl radicals adsorbed on a silica gel surface showed, at 77 K, not only non- binomial distribution of the line amplitudes but also lines with unsymmetrical shape. In treating the experimental results, Gardner and Casey applied the theory by Freed and Frankel [115] which linked the tumbling of a system with sets of equivalent nuclei and anisotropies in the hyperfine interaction and **g-**tensors to a relaxation mechanism dependent on the nuclear spin quantum number m_F. They obtained correlation times for tumbling motion though no model for the nature of "tumbling" was suggested.

The non- binomial distribution of the amplitudes of the hyperfine quartet was also reported by Shiga and Lund [1] for CH_3 radicals adsorbed on silica gel surfaces at 77 K. As opposed to the earlier study [2], the spectrum revealed narrower lines and asymmetry of the separate hyperfine components and was analyzed in terms of axially symmetric **g** and hyperfine coupling tensors: $|A_\perp| = 2.26 \pm 0.02$ mT, $|A_{||}| = 2.19 \pm 0.02$ mT, $\Delta g = g_\perp - g_{||} = (3 \pm 1) \times 10^{-4}$.

A thorough study of the temperature dependence of the proton and deuterium isotropic hyperfine splittings was undertaken by Garbutt et al. [116] for carbon-13- enriched methyl radicals stabilized on the surface of porous Vycor glass. A decrease in the absolute value of the isotropic splitting with increasing sample temperature was found over the range 77–400 K and was compared to the theoretical prediction by Schrader [117]. The calculation in the latter work was carried out using semiempirical nonionic valence bond theory. The hf splitting was obtained by averaging the hf interaction over the ground and excited vibration states of the molecule in the out- of- plane bending mode. Later on, *ab initio* nonempirical calculations were published where basis sets of contracted Gaussian orbitals [118] and molecular dynamics [119] were employed. Except for the hyperfine splitting, Garbutt et al. obtained a wealth of information on the temperature behavior of the four proton lines of the methyl radical, including linewidth, line asymmetry, and line intensity ratio. This information is a fingerprint of the rotational motion of the radical. The linewidths of the proton hf components decreased constantly for the more upfield ones, showing thus some deviation from findings in silica gel samples [2, 114]. On the other hand, a sequence of the relative intensities measured as the area under the first derivative proportional to the amplitude of the absorption line follows qualitatively the first derivative amplitudes of refs. [1, 2, 114]. The asymmetry of the hf first derivative lines also showed temperature dependence, decreasing with temperature increase and becoming unobservable at 350 K. The sequence of the hf line asymmetries matched that of refs. [1, 114]. The overall information on the temperature behavior of proton and carbon hf splittings, proton line widths, spectral asymmetries and intensities allowed the authors of ref. [116] to suggest rotational and translational motions of the radical on the surface of porous Vycor glass. The authors showed that matrix effects on the EPR lineshape of the methyl radical and its parameters were most prominent at low temperatures and pointed out the usefulness of methyl radical EPR in characterizing the surface of Vycor glass.

Very recently, both the matrix and temperature effects on the isotropic hf coupling for the surface adsorbed CH_3 radical were tested theoretically by means of DFT (Density Functional Theory) and direct *ab initio* MD (Molecular Dynamics) methods using cluster models [120]. ESR studies performed on methyl radicals stabilized on the surface of porous Vycor glass at 77 K yielded the anisotropic shape [121], typical for CH_3 on the silica gel surface. As with other cases of the surface CH_3, the $m_F = -1/2$ hf component turned out to be the narrowest one allowing partial resolution of the second order splitting. As a result, a poorly resolved high-field component of the *E*-symmetry doublet was recorded overlapping the $m_F = -1/2$ hf component of the *A*-symmetry quartet.

In zeolites, methyl radicals studied at temperatures over 77 K yielded an EPR spectrum with nearly classical hf line intensity ratio, 1:3:3:1 and with small or no anisotropy. Noble et al. obtained EPR spectra of CH_3 radicals stabilized in Linde Type A synthetic zeolite at 77 K [122]. The spectrum consisted of four lines with relative intensities (going from low to high field) 1.0:3.1:2.8:0.9. Slight anisotropy of the hf coupling tensor could be supposed considering the shape of the $m_F = \pm 3/2$ components. Danilczuk et al. employed EPR to study paramagnetic species stabilized in Na- A zeolite exposed to gaseous methane and γ-irradiated at 77 K [123]. At temperatures above 77 K they found the methyl isotropic quartet with intensity ratios 1:3:3:1 and peak- to- peak first derivative linewidth 0.3 mT at 210 K. The authors concluded that the CH_3 radicals were not adsorbed on the surface of the zeolite framework but rather freely rotated in the α-cages. The EPR signal of CH_3 in the 1973 Maxixe- type beryl single crystal was found to be axially symmetric, with the symmetry axis oriented along the crystal c- axis and $|A_{||}| > |A_{\perp}|$, $g_{||} > g_{\perp}$ [108]. In the same work Andersson assumed that the radical was located in a plane perpendicular to the beryl channel direction, quickly jumping in its plane and the EPR parameters were, therefore, averaged over all directions in this plane. The inequalities found in beryl turned out to be opposite to those reported by Shiga and Lund for CH_3 on a silica gel surface. Andersson explained the difference by different effect of the matrix surroundings in the channel on the parallel and perpendicular EPR parameters.

3.7.3.3 In Powders and Glasses

Using a ^{60}Co source for irradiation of a high- purity synthetic fused silica, Friebele et al. obtained stable methyl radicals, CH_3 [60]. EPR measurements were made at −170°C. When the measurements were performed with small modulation and power amplitudes, a marked asymmetry of the lines and in addition dependence of the linewidth on the nuclear spin quantum number m_F was observed. Although the line amplitudes followed no longer the classical high-temperature ratio, 1:3:3:1, the integrated intensities determined by double integration of each first derivative hf line did follow this ratio. The hf lines showed asymmetry with respect to the base line[1] and their shape was suggesting a powder. The authors mentioned the temperature dependence of the EPR spectrum of the methyl radical in irradiated silica and assumed that tumbling of the radical averaged the angular effects of the **g**-tensor and hf anisotropy, but gave rise to a relaxation that was dependent of m_F. Based on linewidth analysis, a correlation time 9.2×10^{-8} s for the radical tumbling was calculated. A double line structure was detected for the narrowest $m_F = -1/2$ transition. The structure was attributed to second order hf interactions

[1]The authors of the original article tried to avoid mixing of two asymmetries: the asymmetry of amplitude distribution of the set of the CH_3 hf components and the asymmetry of the shape of the individual lines.

removing the degeneracy of the $m_F = -1/2$ states. An identical splitting of the $m_F = +1/2$ component was not observed because the much larger linewidth of this component obscured the second- order splitting. The radicals were supposedly located in interstitial positions of the silica.

Most studies of methyl radicals in powders were carried out with radicals trapped in polycrystalline solid gases frequently referred to as *cryocrystals*. High- resolution EPR spectra of CH_3 in solid Ar generated from photolysis of CH_3I trapped in the matrix was published by Cirelli et al. [124]. At 10 K, the spectrum consisted of four almost symmetrical lines with non- binomial amplitude distribution.

Marked asymmetry of the amplitude distribution of the hf lines is also evident from the 4 K EPR spectrum of CH_3 in Ar presented by McKinley and Michl [125]. The methyl radicals were generated in the argon matrix from CH_3I during codeposition with Cs atoms.

Misochko et al. [96] studied samples prepared by codeposition of two effusive beams, Ar: CH_4 (CD_4) and Ar: F_2 onto a substrate cooled to 12–16 K. The methyl radicals were formed during the codeposition as well as due to subsequent photolysis of the sample followed by chemical reactions in the matrix. Asymmetry in the amplitude distribution was observed and analyzed for the CD_3 hf transitions. Considering the case of rapidly tumbling methyl radical with averaged spectrum anisotropy, the authors estimated a correlation time of 10^{-9} s for the motion of the CD_3 radicals at sample temperature 13 K. Saturation curves plotted for different CH_3 hyperfine components were divided into two groups: outer lines with easier saturability as compared to the inner lines with shorter spin- lattice relaxation time. The authors noted that the inner, $m_F = \pm 1/2$ lines were actually an unresolved superposition of components with $F = 1/2$ and $F = 3/2$, where F is the total nuclear spin of the three protons. The width of all lines decreased slightly with increasing sample temperature up to 24 K.

Dmitriev reported high- resolution spectra for methyl radicals obtained in cryocrystals by condensation from gas discharge onto a low temperature substrate [4]. Methyl radicals, CH_3, stabilized in solid Ar at 4.2 K showed a sequence of amplitude ratios as 1:1.9:3.4:2.1 [59].

The asymmetry of the distribution was explained as incomplete average of the anisotropy of the g- and hyperfine coupling tensors. Experimental results were obtained in matrices of pure Ar, Kr and Ar: Kr (1:1) solid gas mixtures. Comparing the results, the author came to the conclusion that, in solid Ar, the inequalities $|A_{||}| > |A_{\perp}|$ and $g_{||} > g_{\perp}$ hold for the CH_3 radicals [4], assuming axial symmetric **g-** and **A-**tensors. The anisotropies, defined as $\Delta A = |A_{\perp}| - |A_{||}|$, $\Delta g = g_{\perp} - g_{||}$, were estimated to be $\Delta A \approx -0.021$ mT and $\Delta g \approx -5 \times 10^{-5}$ [59]. The observed spectrum was composed of the lowest rotational A- symmetry quartet. All the hyperfine transitions became saturated in the same manner and had the same spin- lattice relaxation time. In a temperature range 1.6–4.2 K the spectrum revealed no marked change in anisotropy.

Popov et al. [5] studied the rotation of methyl radicals, CH_3, in a solid argon matrix in the temperature range 14–35 K and observed axially symmetric EPR spectra. The radicals were produced by dissociating methane by plasma bursts

generated either by a focused 193 nm laser radiation or using a radio frequency discharge device during the gas condensation on the substrate.

With very narrow EPR lines, the authors were able to resolve a splitting of the low- field, $m_F = +3/2$, line which was due to the axial symmetry of the spectrum. The anisotropies were found to be $\Delta A \approx -0.01$ mT and $\Delta g \approx -2.5 \times 10^{-5}$. The spectrum was ascribed to the ground rotational state of the CH_3 radicals with the totally symmetric nuclear spin function $F = 3/2$. The anisotropy was visible only at the lowest sample temperatures. At low resolution, the anisotropy resulted in varying peak heights due to the diverse overlapping at the resonance, 1:1.6:2.5:1.6.

High- resolution EPR spectra of methyl radicals in solid Ar matrix were obtained by X- ray radiolysis of Ar matrix containing 0.2 mol % CH_4 [3]. The samples were studied in the temperature range 4.2–40 K. At the lower temperatures, the spectrum of the CH_3 radicals was a quartet of very narrow, symmetric lines with equal amplitudes. No asymmetry of the sequence of amplitude ratios emerged. The spectrum was attributed to the "*A*" lines of the CH_3 radical. The distance between adjacent hf lines increased with higher resonance field. The same observation was later reported for the gas- phase deposited CH_3 in Ar, Kr and Ne [4, 93, 126]. The splitting variation was explained by the second- order shift of the proton hf coupling.

To the best of our knowledge, the EPR spectrum of CH_3 in Ar was the first CH_3 spectrum where the *E*-symmetry doublet was well resolved and studied [3]. Later on, the *E*-symmetry pattern was also observed in solid Ar [5, 126] and Kr [61] matrices. In all those studies the lineshape of the *E*-symmetry spectrum showed strong dependence on the sample temperature with considerable line broadening as the sample temperature decreased.

Dmitriev and Benetis [126] observed the *E*- symmetry doublet of CH_3 in solid Ar which suggested anisotropy of both the **g**- and **A**-tensors. At higher temperatures the anisotropy appeared as different widths and amplitudes of the components of the doublet. In Fig. 3.14a, the doublet lines are marked by stars.

As the temperature decreased, the components became non- symmetric, and finally, the $m_F = 1/2$ hf components showed splitting. The modification of the spectrum was recorded in a temperature range 30–12 K. The splitting made it possible to obtain the signs of the anisotropies which, as opposed to the *A*- symmetry quartet, turned out to be positive, $\Delta A > 0$ and $\Delta g > 0$. The ratio of *E*- to *A*- symmetry line intensities plotted vs. sample temperature evidenced relative increase in the *E*-line intensity with increasing temperature complying with more populated higher rotation states [3, 5, 61].

A model of free rotation about the C_3- axes and a hindered C_2- type rotation (thermally activated as assumed by Popov et al.) was proposed to explain experimental results for CH_3 in Ar [4, 5] and Kr [127]. In solid Kr matrix the EPR spectrum of the CH_3 radicals revealed no anisotropy in the 17–31 K temperature range [61], or markedly smaller anisotropy compared to Ar matrix in the range 1.6–4.2 K [59, 126, 127]. No anisotropy was observed in *p*- H_2 matrix [126].

The matrix effects on the EPR spectrum anisotropy and the isotropic hf constant of the *A*- symmetry pattern of trapped methyl radicals were studied in some detail [126]. The experimental results were correlated to the matrix- radical interaction. The largest anisotropy was found for solid Ne [93, 128], the "tightest" of the

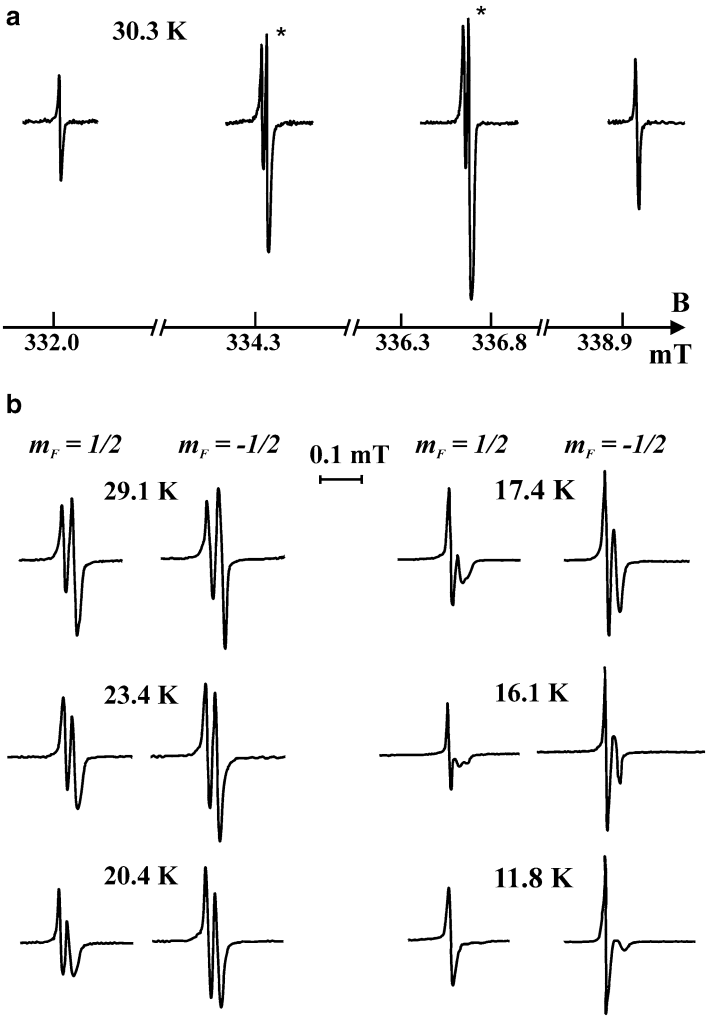

Fig. 3.14 EPR spectra of CH_3 radicals in Ar matrix at different sample temperatures. The resonance microwave frequency is $f_{res} = 9402.99$ MHz. The projection m_F corresponds to the F_z component of the total nuclear spin (Reproduced from Ref. [126] with kind permission of © The American Chemical Society (2010))

four matrices under comparison. The finding suggests that the repulsive Pauli exclusion forces between the host-matrix molecules and the methyl radical govern the anisotropy [126]. An empirical linear correlation of the matrix shifted isotropic hf coupling constants to the matrix- radical interaction including van der Waals attraction and Pauli repulsion was proposed, Fig. 3.15.

The correlation based approximation of the CH_3 radical free state hits almost exactly the mean value of the hf coupling constant measured for the free radical by Davis et al. in jet- cooled slit discharge experiments [129]. Thus, the value of

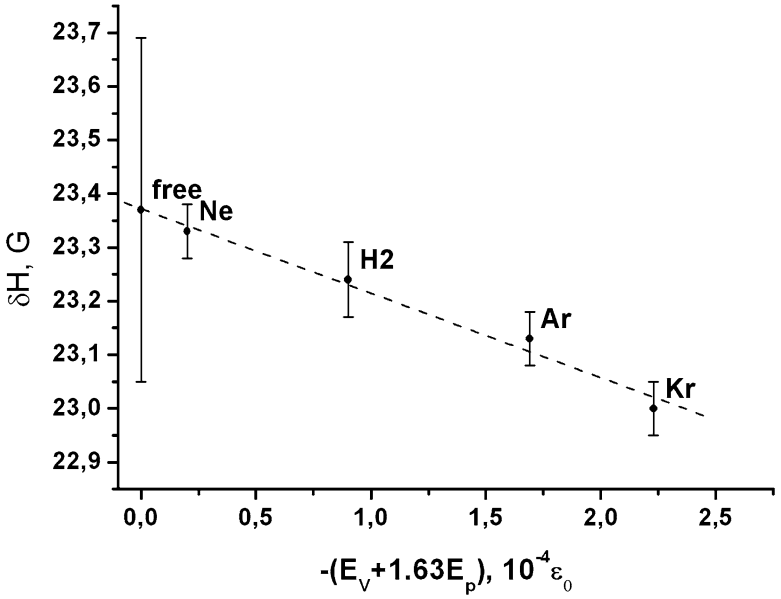

Fig. 3.15 The spacing between the hf components of CH_3 affected by both van der Waals attraction, E_B, and Pauli repulsion, E_p (Reproduced from Ref. [126] with kind permission of © The American Chemical Society (2010))

−2.337 mT [126, 129] for the free CH_3 radical is a target for *ab- initio* calculations of the isotropic hf coupling constants and can be compared to theoretical results available at present [120].

Besides narrow lines, the EPR spectra of methyl radicals trapped in the solid Kr matrix [59, 61] revealed a pattern of very broad lines, 0.18 mT, Fig. 3.2. This finding suggests that apart from the regular fcc lattice, crystal regions with highly disordered local structure of the matrix are also present which host the major part of the impurity CH_3 molecules.

In a study on CH_3 in solid CH_4 Jackel and Gordy [91] found that a contribution of the higher rotation states of the radical to the EPR spectrum occurs noticeably down to the surprisingly low sample temperature of 2.1 K. In the recent publications [59, 93] an *E*- symmetry doublet contributing to the overall EPR spectrum for sample temperatures from 4.2 K down to even 1.5 K was reported for CH_3 trapped in solid Kr from the gas phase Fig. 3.2.

EPR spectra of CH_3 in van der Waals matrices of linear molecules yield a characteristic lineshape which was not observed in other host-substances. Dmitriev and Zhitnikov reported axially symmetric EPR spectrum for methyl radical, CH_3, at liquid helium temperatures obtained in a solid carbon monoxide, CO, matrix by the gas deposition technique [127].

The spectrum in Fig. 3.16 showed large anisotropic splittings of the $m_F = 3/2$ and $m_F = 1/2$ hyperfine components. As opposed to the Ar, Kr, and plausibly Ne matrices, the hf anisotropy ΔA and Δg were positive. Based on the experimental

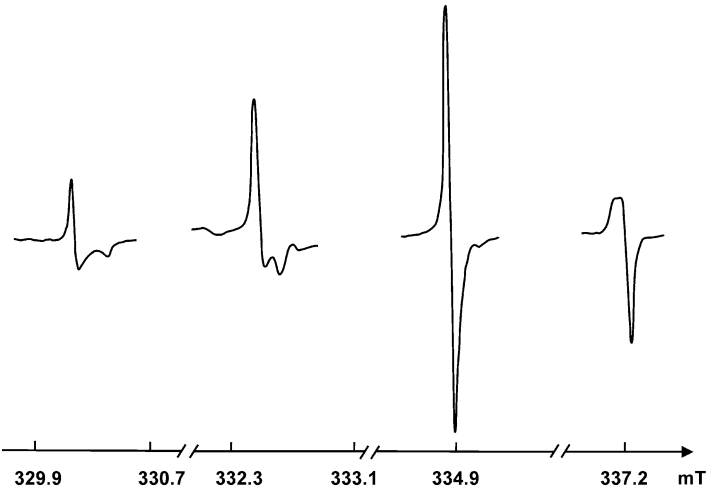

Fig. 3.16 EPR spectrum of CH_3 radicals in solid CO at 4.2 K. The microwave resonance frequency, $f_{res} = 9354.70$ MHz (Reproduced from Ref. [127] with kind permission of © Springer (2001))

results for the van der Waals matrices, Dmitriev suggested [4] that $\Delta A > 0$ is characteristic for the EPR spectrum of the CH_3 in matrices where the radical rotates almost freely around the C_3-symmetry axis while the axis itself experiences no reorientation, pointing in a certain direction. This is e.g. the case of CH_3 in CO matrix, and the rotationally excited CH_3 in Ar. On the other hand $\Delta A \leq 0$ is characteristic of the radicals in matrices where they rotate freely (the isotropic spectrum in the p-H_2 matrix) or when the C_3-symmetry axes are allowed to execute fast reorientation (Ar, Kr, Ne matrices).

Kiljunen et al. [95] obtained methyl radicals in CO, CO_2 and N_2 solids and observed "CO-matrix" EPR spectra for the CH_3 radicals in all these matrices with $\Delta A > 0$ and $\Delta g > 0$. The authors interpreted the experimental results by locking of the C_3 axis of the radicals to a crystalline direction that allows for free rotation about that axis.

In the CO_2 matrix, four additional weak transitions were found [95] which were tentatively assigned to "nonrotating" CH_3 radicals. This feature did not emerge in CO and N_2 matrices. Another possibility for the appearance of additional CH_3 transitions was suggested by Brotikovskii et al. [113] explaining their experimental results for CH_3 on silica gel surfaces at 4.2 K, concerning additional splitting of the torsional states on the basis of group theoretical considerations.

3.7.3.4 Deuterium Isotopomers

CD_3 radicals obtained in solid Ar by X-radiolysis [3] showed strong quantum effect on the EPR line shape. An unusual septet observed at 4.1 K exhibited a relative

intensity ratio 1.0:3.8:7.0:105:8.7:4.3:1.5, indicating that the spectrum consisted of a very strong transition at $m_F = 0$ seen in Eq. (3.11), superimposed on a much weaker classical high- temperature spectrum due to motional averaging.

Furthermore, a double quintet was observed for the CHD_2 radical at 4.2 K. The central triplet of each quintet was much stronger than the outer lines and had an intensity ratio of 1:1:1 being, thus, far from the "binomial" one 1:2:3:2:1, expected for the high- temperature spectrum. The triplet can be assigned to the following three wavefuntions.

$$\psi_{-1}^{B} = [\,|-1,\ 0\rangle - |0,-1\rangle]\,\Big/\sqrt{2};\ \ \psi_{1}^{B} = [\,|0\ 1\,\rangle - |1\ 0\rangle]\,\Big/\sqrt{2};$$
$$\psi_{0}^{B} = [\,|1,-1\rangle - |-1,\ 1\rangle]\,\Big/\sqrt{2} \tag{3.12}$$

They are the only ones allowed by the Pauli principle for the lowest rotational level ($J = 0$) and correspond to the antisymmetric B irreducible representation regarding the $\boldsymbol{C}_2$ symmetry of CHD_2. Only the deuteron-spin projections of the nuclear I factor out of the $\mathbf{R} \otimes \mathbf{I}$ spin-rotational states at the symmetric $|J, M, L> = |0\ 0\ 0>$ ground rotational level are given in the above expressions for simplicity (the quantum-numbers in the ket are explained in legend of Fig. 3.11).

The 4.2 K spectrum of CH_2D was a triplet of triplets. Instead of expected binomial intensity distribution 1:2:1 of the major triplet, all lines were of equal intensity. Due to the exchange of the protons by the C_2 symmetry axis, the major 1:1:1 triplet of CH_2D can be attributed to the totally symmetric A nuclear spin states of the two protons with total spin $F = 1$.

The above experimental results presented in Chap. 4 were explained in ref. [3] by application of the Pauli principle on the zeroth order free 3D rotational states. As it was explained in that work, the fundamental symmetry operation for the observed effects was the exchange of the protons or deuterons of the radical species CH_2D and CHD_2 by the C_2 rotation symmetry, assuming that they are indistinguishable Fermions and Bosons, respectively.

Similar results for CD_3 and CHD_2 radicals were obtained in experiments performed in H_2 [130], D_2 and Ne matrices [131] at temperatures of 1.6–4.2 K, Fig. 3.17. This figure shows the temperature dependence of the ratio of the central line amplitude of the CD_3 hf septet to the amplitude of the nearest hf transition of the septet. The data were obtained in H_2, D_2 and Ne matrices.

Thus, the methyl radical features stimulate one to consider it as a potential spin probe of certain radical- matrix interactions. EPR spectroscopy at liquid He temperature in combination with *ab initio* molecular dynamics calculations of this simple radical may play an important role for testing basic quantum theory of the effects originating from the weak the spin- lattice coupling.

The **A**-tensor of the radical, and, possibly the **g**-tensor, is orthorhombic. Depending on the radical- matrix interaction and the matrix structure the tensors are averaged due to the radical motion to give either orthorhombic [110], axially symmetric, or isotropic EPR spectrum. Due to the small moment of inertia, the

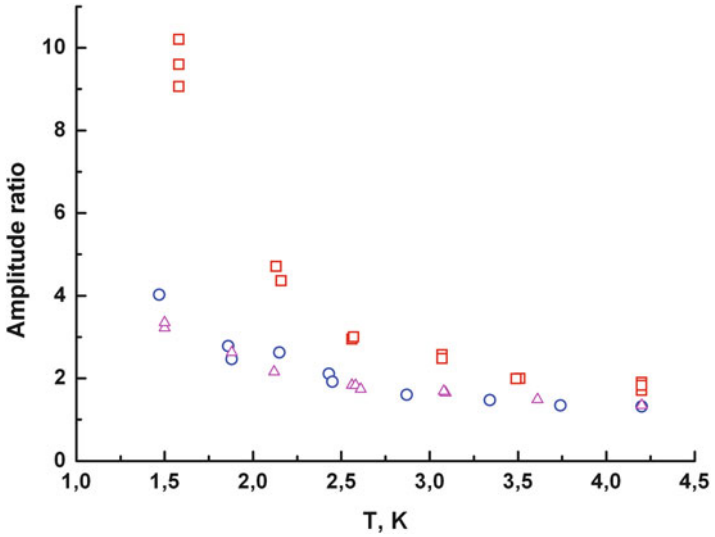

Fig. 3.17 The temperature dependence of the relative intensity of the CD_3 central component ($m_F = 0$) to the neighbor transitions ($m_F = \pm 1$) for the radical trapped in low-temperature solids: H_2, *squares*; D_2, circles; Ne, *triangles* (Reproduced from Ref. [131] with kind permission of © The American Institute of Physics (2005))

radical possesses large energy gaps between the adjacent rotational levels. The excited rotation levels contribute, partly, with the *E*-symmetry EPR doublet in addition to the ground- state *A*-symmetry quartet.

Being quite different, the *E*-symmetry contribution may be extracted from the overall EPR spectrum giving information about a barrier to the rotation which is determined by the matrix surroundings of the radical. Depending on details of the radical- matrix interaction certain transitions may be excluded from, or on the contrary, emerge in the EPR spectrum. The radicals that execute fast rotation about the C_3-axis with prohibited reorientation of the axis are actually allowed to perform libration motions about the C_2-axis. The amplitudes of these motions are governed by the radical- matrix interaction and the matrix structure and influence the EPR lineshape.

3.8 Dynamics by ENDOR Spectroscopy

ENDOR (Electron Nuclear DOuble Resonance) spectra are free from unresolved hf structure from nearby and distant nuclei that usually broadens the EPR lineshape, rendering ENDOR a preferable method for the determination of small hf interactions. It has also been demonstrated that investigation of dynamics is possible by temperature dependence of CW-ENDOR lineshapes in a parallel fashion as

chemical exchange alteration of the EPR lineshapes described in Sect. 3.5, as it can be seen in the detailed book of Kurreck [69]. The intensity distribution of the CW-ENDOR lineshapes however is more complicated than the EPR as it is heavily depending on the sensitive balance of the different electronic and nuclear relaxation pathways. This was also one of the reasons that the pulsed ENDOR recently became a popular alternative to the CW technique, since the interpretation of the pulsed ENDOR spectra are free from complicated kinetics of the signal.

A usually successful combination in the investigation of disordered solids is the pulse ENDOR with ESEEM (Electron Spin Echo Envelope Modulation) and HYSCORE (HYperfine Sublevel CORrElation). In a work specialized in high electronic spin multiplet $S > 1/2$ [132] we presented a novel expression for what is usually called an ideal ENDOR lineshape of disordered systems, which does not include effects of relaxation or enhancement due to electron mixing. For $S = 5/2$ for instance we can ideally have as many as five overlapping pairs of HYSCORE ridges from different allowed EPR transitions and the best way to disentangle this pattern is using the ENDOR lineshapes.

Several theoretical aspects of the spin dynamics in connection with the ENDOR-lineshape intensity distribution were early investigated by Freed [133]. A long-standing subject of investigation by the group of Brustolon [29] is the methyl rotation. In particular ENDOR *enhancement* was used in several temperature dependent CW ENDOR-linewidth studies for the investigation of this motion. Relatively simple radicals, such as those from γ-irradiated L-alanine, CH_3-$^{\bullet}$CH-COOH, and simple methyl substituted aromatics, were used as models during development of this method in both single crystals and in powders, and the values of the activation parameters for the methyl rotation by standard methods could be reproduced rather well. What was in addition very appealing with the temperature ENDOR enhancement studies of this group was the apparent simplicity of the theoretical temperature dependence, expressed by a single spectral density of Lorentzian form [29].

The expression for the enhancement curve for which we see an example of in Fig. 3.18, has the same form as the spectral density appearing in the discussion about the Redfield theory, i.e. Eq. (3.7) with $n = 1$. This is the result of the dominance of a single cross-relaxation pathway determining the EPR *desaturation* and the ENDOR line intensity, as it was deduced by a detailed theoretical consideration by Freed [133].

3.9 Pulsed-EPR Techniques

Random reorientation should average out the nuclear modulations of the ESEEM signal [15], and even restricted motion in crystals would severely broaden the corresponding Fourier-transforms at intermediate rates [71]. Freed and co-operators in an early spin-echo application investigated the effects of the slow reorientation

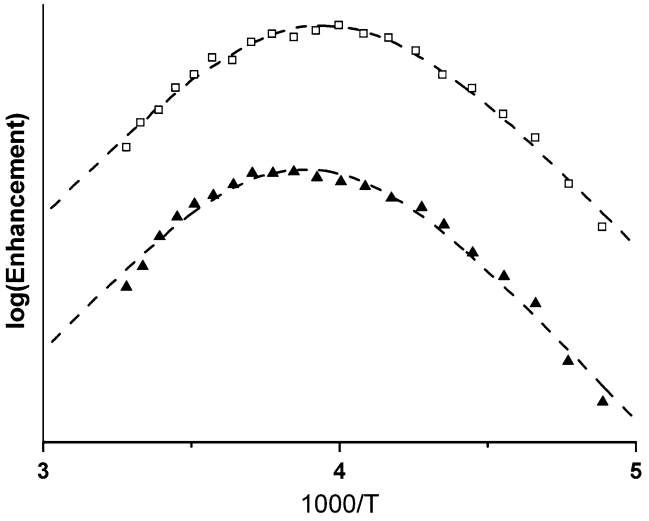

Fig. 3.18 Typical temperature dependence of ENDOR enhancement from methyl rotation. In this case it includes the maximum of the Lorentz spectral density (Reproduced from Ref. [29] with kind permission of © Elsevier (1992))

on both the nuclear modulations and the ESE (Electron Spin Echo) *phase memory decay* in viscous fluids [70, 134]. They calculated the temperature dependence of the *phase memory* (*decay*) *time* T_M of the primary echo signals and compared with *spin-echo* experiments for the tempone probe in glycerol/water solutions where slow motion conditions prevailed. Some experimental T_2 data from CW spectra of tempone were also compared, see figure 2, ref. [15]. The phase memory decay rate $1/T_M$ went apparently through a maximum at about 0°C and decreased for higher temperatures. Furthermore, The three most known models of random reorientation, i.e. *Brownian diffusion*, *free diffusion*, and *jump model* were related to the experimental data considering that the phase memory decay time is given by the simple relations $T_M \propto (\tau_R)^b$, with $b \cong 1/2$, 2/3 and 1 for the above three models, respectively [134]. They explained that in the *slow exchange limit* it is reasonable with an exchange broadening equal to ${\tau_R}^{-1}$, the jump frequency. This is analogous to the *lifetime broadening* of the simple site exchange since each jump changes randomly the orientation-"site" and thus the resonance frequency of the electron spin, leading to *spectral diffusion*.

The above dependence of the *relaxation time* T_M on the rotation *correlation time* τ_R in the slow motion regime conforms to model simulations of the destruction of the nuclear ESE envelope modulations through faster decay of the time resolved signal in single crystals by motion [71]. In the latter case, the random reorientation of the hfi tensor was modelled by a simple two-site exchange of the principal axes of the hf interaction of the probe molecule between two extreme positions through

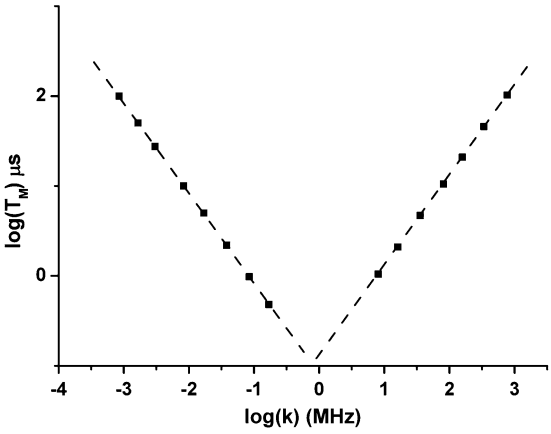

Fig. 3.19 Phase memory decay time T_M dependence on the rate of random jumps k between two possible dipolar frames of a radical in a single crystal according to model simulations of the primary ESEEM (Reproduced from Ref. [71] with kind permission of © Elsevier (1995))

intramolecular or intermolecular reorganization. In spite of the clear difference in the motion of the two systems, i.e. the viscous fluid with unrestricted reorientation vs. the single crystal with a restricted reorientation, respectively, the theoretical dependence of the phase memory decay time T_M on the *exchange/reorientation rate* was astonishingly similar. The "linear" relations $T_M \propto (\tau_{exch})^{\pm 1}$ were found in the single crystal *exchange model*, which is identical to reorientation for the *jump diffusion model* in the slow motion region discussed above.

The relevant diagram in Fig. 3.19 displays furthermore two distinct branches as in the reorientation case of figure 2, ref. [15], one for the slow motion and one for fast motion, corresponding to the two different exponents $+1$ and -1, respectively, in the above relation, $T_M \propto (\tau_{exch})^{\pm 1}$. In the left, slow motion branch of Fig. 3.19 the phase memory is lost faster for faster motions, while in the fast motion branch to the right in the same figure the phase memory is lost slower for faster motions. Accordingly, the two branches pass through a maximum phase memory decay rate $1/T_M$ in the same way as the typical longitudinal relaxation rate $1/T_1$ does, and not the typical transversal relaxation rate $1/T_2$ in the Redfield regime. The latter exhibits instead a monotonically decreasing behaviour with increasing temperature, as it was shown in Fig. 3.9.

The explanation of the single crystal two-"site" exchange case agrees with the standard CW lineshape results, where the random jumps of the resonance frequency between two discrete values destroy the hyperfine structure due to *lifetime broadening*. For very fast exchange the individual slow motion lines overlap and finally a narrowed average spectrum appears.

Similar results were found for the hindered rotation of the methylene fragment – CH_2 in irradiated zinc acetate dihydrate crystals by other investigators [135], in a work where even the nonsecular nuclear-*I*-part effects were discussed. It is worth to notify that such terms, which are necessary for regular spin echo modulation, are usually less important when exchange dynamics corresponding to unrestricted overall motion are affecting the lineshape in powders. On the other hand they give

significant deviations to the distance between the outer peaks of the CW-EPR lines for restricted motion and contribution of forbidden transitions to the spectra in single crystals [77].

Finally, the group of Brustolon studied the restricted conformational changes of the saturated tempone ring by ESE and ESEEM, while the *libration* of the same molecule was more appropriately studied by high-field EPR [18]. In that work the above discussed dip in the relaxation time was verified by the total disappearance of the echo signal in the temperature range 130–210 K, and similar observations were made about the relaxation behaviour of several nitroxide labels by the Institute of Chemical Kinetics and Combustion [136].

A simpler exchange theory for echo modulation in nitroxides induced by the motion of a classically rotating methyl fragment of the probe molecule was developed by the group of Dzuba [137]. The corresponding experimental verification was performed for several methyl substituted nitroxides using a variation of the stimulated echo sequence with variable pulse delay τ between the first and the second pulse instead of the regular T variation.

3.9.1 ESEEM and Tunnelling Frequency

Normally, the tunnelling frequency 3Δ of hindered methyl fragments attached to larger units (radicals) is obtained indirectly, involving complicated experimental setups. Thus, under favourable experimental conditions, the tunneling frequency may be accurately determined from first-order EPR transition sidebands, optimally observed by electron–electron double resonance ELDOR, see [138] and references there.

According to our theoretical prediction, however, one can register directly the tunnelling frequency in the ESEEM Fourier Transformed spectrum of a Hahn-echo sequence and detecting 90° out of phase from the (Microwave) MW field [138]. It was derived there that nuclear modulations can be observed in the Electron Spin Echo (ESE) experiment of methyls even with isotropic hyperfine interaction α under the condition that the latter is smaller than 3Δ. A doublet of equal intensity about the tunnelling frequency split by $a/2$ and two equally intense peaks with inverted intensity, one at the double tunnelling frequency and one close to zero, are expected, signifying a great potential applicability for this method. However, due to the high frequency harmonics involved, this method was limited by the contemporary instrumental development. Choosing appropriate known systems with relatively high potential barrier the prediction of that theory can be applied, at least in certain systems, see ref. [138].

The principle for the above described Echo Modulation for a hindered rotating methyl under quantum conditions of motion is the slightly different mixing of the torsional states with the nuclear-spin states in the two electron spin manifolds by the contact term of the hfi. This is a totally different possibility of echo modulation compared to regular ESEEM nuclear modulations based on purely

magnetic interactions as the cause of nuclear mixing. Due to the similar physics [7], i.e. by partially allowing forbidden EPR transitions due to mixing of the nuclear spin with the rotational degree of freedom by the hfi, the ESEEM spectra should copy the *tunnelling sidebands* (compare *spin flip satellites*) of CW EPR lineshapes for tunnelling methyls observed occasionally also experimentally [102].

3.9.2 Two-Dimensional Experiments

Within the ESEEM (Electron Spin Echo Envelope Modulation) techniques, the *primary Hahn echo* and the *three- pulse stimulated echo* were also used as the basis for the design of two-dimensional methods [139]. A classical example of generalizing a one-pulse sequence to two dimensions is a series of ED-EPR experiments taken for several values of the pulse delay τ of the Hahn echo. One can finally collect the entire τ series in a two-dimensional spectral representation, where in one dimension is plotted the resonance field and in the other the homogeneous broadening [15].

A brief list of the main classical two-dimensional methods contains three of them: (a) EPR- SECSY (Spin Echo Correlated Spectroscopy), (b) EPR- COSY (Correlation Spectroscopy) and (c) 2D-ELDOR [140] (Electron-electron Double Resonance). These methods discussed by Gorcester and Freed [15] were based to the transfer of the FT-NMR (Fourier transform NMR) to EPR called FT-EPR (Fourier Transform EPR) [14].

Concerning the pulsed ELDOR, another series of pulse sequences was proposed during 2003 with the purpose of a direct evaluation of unpaired electron distances in disordered solids [57]. It is interesting to note that among the first theoretical computations and experimental measurements of the electron-electron two-pulse signal modulations were performed as early as 1969 by a Russian team [141].

3.9.3 Spectral Diffusion

The echo decay in a *primary* or a *stimulated echo* experiment is due to different intrinsic relaxation processes which for a certain *temperature* depend on the *concentration* of the radicals and their *residual mobility*, as well as on the *interaction* with the nuclear magnetic isotopes, particularly protons, present in the diamagnetic matrix. In the case of broad inhomogeneous EPR lines a pulse excites only a limited part of the spectrum, usually a bandwidth of about 0.9 mT of the CW transition for moderate MW (MicroWave) power, and thus only excites a limited group of *spin packets*.

In order to organize the discussion of the mechanisms of the echo decay in solids and to distinguish the relaxation mechanisms that are due to the effect of the pulse,

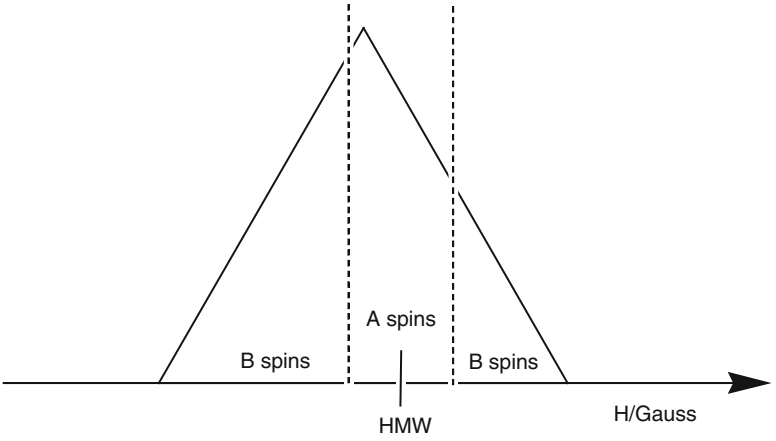

Fig. 3.20 The separation of an inhomogeneously broadened signal into two parts, a region with the **A** spins, actually spin packets which are directly excited by a MW (MicroWave) pulse, and the rest of the EPR band with the so called **B** spins that are not directly affected by the pulse [20]. The **A**-spin and **B**-spin regions depend in simpler cases on the central MW frequency $\sim H_{MW}$ and the intensity of the MW field $\sim H_1$

one usually labels the spin packets affected directly by the pulse as spins **A**, and the ones not affected by the pulse but interacting with the first, as spins **B**. A simple example of this division of the EPR signal is shown in Fig. 3.20.

Starting with the intrinsic interactions, we have so far mostly referred to relaxation mechanisms which depend on the thermal fluctuations of the parameters of the spin Hamiltonian. Using the previous assignment, they affect both the directly involved spins **A** as well as the **B** spins. These interactions are thus similar to the *scalar* mechanism of the *first kind* to be distinguished from the mechanisms similar to the scalar mechanism of the *second kind* [21]. In the latter, the modulation of the interaction necessary to give relaxation to the spins **A** is due to the independent fluctuations of the spin orientation of the **B** spins due to their spin-lattice relaxation [18]. We emphasize that this classification is only in analogy to the effect of the *contact term* of the scalar hyperfine interaction and that we have here in addition to consider the intermolecular interactions between the **A** spins and the unobserved spins **B** spins modulated by mutual spin flips.

The **B** spins generate local fields at the positions of the **A** spins, that directly participate in the formation of the ESE (Electron Spin Echo) signal, through the dipolar interaction. Considering a primary, $\pi/2$-τ-π-τ-echo, sequence if the **B** spins do not change orientation during the interpulse periods τ they induce static resonant frequency shifts which contribute to the inhomogeneous broadening of the signal that is unimportant for the echo decay. If however the orientation of the **B**-spins is randomly modulated in some way, e.g. by an independent relaxation mechanism, the fluctuations of the *local field* at the positions of the **A** spins give migrations of the resonance frequencies which result in *spectral diffusion*. Spectral diffusion gives *irreversible dephasing* to the electron-spin precession.

Furthermore, the random modulation of the **B** spins causing spectral diffusion can be of two kinds: (a) In T_1- type systems the random changes of the spin orientation of the **B** spins by spin- lattice relaxation are mediated to the **A** spins by the *S*-*S* interactions. (b) In T_2-type systems the mutual spin flip-flops between **A** and **B** spins are the reason for this kind of spectral diffusion [19].

The relative importance of the above two mechanisms for the ESE decay varies with *temperature* and radical *concentration*. For systems at relatively high temperature, and thus shorter T_1, as well as dilute matter with respect to paramagnetic centers, the flip-flops are infrequent and random variation of the spin orientation by the spin-lattice interaction dominates in producing spectral diffusion. For lower temperatures and higher concentrations of the paramagnetic centers the flip-flop mechanism is the most important mechanism.

Except for the above adiabatic [87] mechanisms of spin dephasing by spin-resonant frequency shifts there is one more way for the acceleration of the echo decay of the **A** spins which is due to a phenomenon related to spin diffusion called *spin-excitation transfer*. Part of the excitation of the **A** spin by the MW pulse can migrate to **B** spins by mutual flip-flops and cannot participate in the formation of the echo increasing thus the apparent decay of the signal.

In addition to the **B** electron spins in the sample, even the spins of the matrix nuclei are also included in the definition of the **B** spins as they can enhance *spectral diffusion*. A necessary condition is that there is an *S*-*I* coupling to the **A** spins and that the nuclei have a strong and independent relaxation mechanism. They cause dephasing of the electron spins as *spectral diffusion* can be induced by random modulation of the local fields at the position of the electron by the nuclear spin flips. One should remember that the nuclear spin system in solids is rather dense. It consists usually of the abundant proton nuclei, a fact that compensates for their smaller gyromagnetic ratio in comparison to the electrons. They are interacting with each other, and via this dipole-dipole mechanism, the nuclear spin flips are transferred by nuclear spin diffusion to the rare paramagnetic centers.

3.9.4 Instantaneous Diffusion

Generally speaking, the kinetics of dephasing of the echo signals according to the above mechanisms has a "*stretched exponential*" [142] functional form with a great variation of the parameters x and τ_m.

$$I(t) = A \exp[-(t/\tau_m)^x] \tag{3.13}$$

The point here is that these two parameters can specify rather well the dynamics of the system. An example is the *instantaneous diffusion* mechanism which can be shown to display exponential decay with rate $1/\tau_m$, for $x = 1$.

The instantaneous diffusion is a source of ESE decay due to the dipolar *S*-*S* interaction among only the **A** spins. The decay in this case is brought about by the

local-field changes resulting from the *spin flips* induced by the second MW pulse of the primary echo. The instantaneous diffusion depends on the concentration of the **A** spins and the extent of the perturbation caused by the pulse on them, that is the *nutation angle*, and results in a very simple exponential decay. A detailed analysis of the instantaneous diffusion computed under rather general conditions revealed the following relationship for the phase memory decay time [23].

$$\frac{1}{T_M} = \frac{4\pi^2}{9\sqrt{3}} \gamma^2 \hbar \, C < \sin^2(\vartheta/2) >_g \tag{3.14}$$

C is the concentration and γ is the gyromagnetic ratio of the **A** spins, while the average with respect to the lineshape g(H) indicated in the above equation is an important quantity to be computed. It is a measure of the involvement of the variable nutation angles of the different parts of the inhomogeneous EPR lineshape to the decay. The angle $\vartheta \equiv \vartheta(H)$ here is the nutation angle that the second pulse in the primary echo tilts the magnetization resonant at field H. The nutation angle depends on the amplitude of the MW field H_1, giving thus a reliable experimental way to recognize the instantaneous diffusion mechanism by variation of H_1. We reproduce the suggestive form of this averaging given in refs. [23, 142] for pulse duration t_p.

$$< \sin^2(\vartheta/2) >= \\ = \int \frac{dH \, g(H) \frac{H_1^2}{(H-H_0)^2+H_1^2} \sin^2\left(\frac{\gamma t_p}{2}\sqrt{(H-H_0)^2+H_1^2}\right)}{\int dH \, g(H)} \tag{3.15}$$

Application of this type of phase decay in the Echo-Detected EPR (ED-EPR) spectra of spin-labelled peptides [23] is described next.

3.10 Librational Motion Studied by ED-EPR

The *Echo-Detected* ED-EPR method was used for the study of the relaxation due to librational motion in several nitroxides [58] such as tempone, 2, 2, 6, 6- tetramethyl-4- piperidone-1- oxide, and other nitroxides tailored for specific cases, see Fig. 3.3.

The experimental approach consists simply in obtaining the echo-detected ED-EPR spectrum for different *pulse delays* τ, the time interval between the first and the second pulse, in the primary echo [58]. Several structural and dynamical parameters are involved in the amount of the alteration of the ED-EPR spectra by the τ variation as long as the librational motion is not frozen, a condition imposing a minimum required temperature. This phenomenon is due to phase memory relaxation induced

by libration. A temperature of 77 K was thus adequate in most cases to freeze the motion and to forbid a further τ dependence to be observed but not always, since the phenomenon of instantaneous diffusion could be active.

One idea was to use the nitroxides for the structural and dynamical investigation of *glassy* vs. the *crystalline* phases and by this way discriminate between these components in different frozen biological samples [58]. As it was known previously that the glassy state has a *cryoprotective activity* for cells, while the formation of crystalline ice is considered as the basic cause of cell death at low temperatures, the interest of such a study is great for cryogenic life preservation. An early application of ED-EPR of this kind [58] is reviewed in the next section. Some newer theoretical developments of the same group are found in refs. [23–25, 66], including a model of dynamics combining a classical theoretical approach with important experimental results [35]. However, the assigned, single type of overall librational motion was not always consistent with the experimental data [35, 136].

3.10.1 Glasses and Polycrystallites

In general, glassy materials displayed a more substantial alteration of the ED-EPR lineshape with an increase of the *pulse delay* τ than crystalline matter. Stronger sensitivity with respect to τ variation was indeed observed in the *amorphous* glassy phase in comparison to the *crystalline*. The sensitivity of the pulse-delay dependent modification of the spectra varied also in the different regions of the inhomogeneously broadened line. Most sensitive was the high field component of the ^{14}N hf triplet, which for this reason obtained an additional minimum in the glassy series, see figure 1 in Ref. [58]. It was concluded that this type of dependence could be attributed to the differential magnetic phase relaxation (*phase memory time* T_M) of the nitroxide for the different orientations with respect to the external field.

A quantitative explanation of this behaviour was achieved by considering the spin relaxation due to small- amplitude *librations* of the nitroxide molecular probe.

The required expressions for the orientation dependent relaxation (decay) factors $R_m(2\tau, \vartheta, \varphi)$ of the primary echo signal were derived within the limit of the Redfield relaxation theory in ref. [24] for each pair (ϑ, φ) of polar angles and each nuclear projection $m \equiv M_I = 0, \pm 1$, of the hyperfine lines of ^{14}N.

The decay of the primary two-pulse echo consisted in an *adiabatic* contribution arising from the electron-spin dephasing and a *non-adiabatic* contribution arising from the modulation of the electron spin resonance frequency by the jumps of the nitrogen nuclei projections [24].

The most important adiabatic part for the simple case *of small libration angles* α and for libration around the x-axis of the nitroxide is seen in Eq. (3.16). Actually the non-adiabatic (lifetime) part was discarded in the simulations of that work assuming slow motions, that is $\tau_C > 3 \times 10^{-9}$ s, also in agreement with the inefficiency of the non-adiabatic part for slow motions.

$$r_a(\vartheta,\varphi) = \tau_C < \alpha^2 > \sin^2\vartheta\cos^2\vartheta\sin^2\varphi \times [\omega(g_{xx} - g_{zz} + m(A_{xx}^2 - A_{zz}^2)/a_0]^2 \tag{3.16}$$

Except for the trigonometric factors of the field orientation, the Cartesian **g**-tensor components g_{ij}, the spectrometer operating frequency ω, the Cartesian hyperfine tensor components A_{ij}, and the average $\mathbf{a}_0$ of the "vector" $\mathbf{a} = (A_{zx}, A_{zy}, A_{zz})$, are involved in this relation. We note that the above cited adiabatic part of the relaxation rate is proportional to the product $<\alpha^2>\cdot\tau_C$. The proportionality to the correlation time agrees with the adiabatic part of the Redfield theory, for $n = 0$ in Eq. (3.7) as it should. Notice, however, that with increasing temperature the product $<\alpha^2>\cdot\tau_C$ can either increase or decrease since $<\alpha^2>$ is an increasing quantity while τ_C is a decreasing one, cf. Eq. (3.6).

Simulations of the Echo-Detected EPR spectra of the cholestane nitroxide are shown in figure 3 of ref. [25] for macroscopically oriented lamellar samples consisting of the lipid dimyristoyl phosphatidyl-choline (L-alfa) multibilayer film. Two orientations of the lamellae were studied defined by considering samples with the director parallel and perpendicular to the magnetic field. In addition, variable orientation of the libration axis in the molecular frame and different values of the product $\tau \cdot <\alpha^2>\cdot\tau_C$ were considered in the simulations in order to relate to the experimental ED EPR spectra.

3.10.2 Multilayer Aggregates

The study of biologically important lipid *multibilayer aggregates* [25] by Echo-Detected EPR (ED- EPR) was undertaken in the experimental and theoretical work of Dzuba and collaborators. The experimental spectra of the dopand, i.e. the particularly elongated *cholestane* spin label shown in Fig. 3.3, depended drastically on the orientation of the multibilayer with respect to the field as shown in Fig. 3.21. This property shows that the label exhibits long range order in the aggregate as it is oriented with respect to the macroscopic *director* of the multibilayer, i.e. the optical axis of the membrane normal to the lamellar surface.

The variation of the lineshapes with the pulse delay τ could be fitted to the product $<\alpha^2>\cdot\tau_C$, used as a single parameter, where α is the angle of the torsional motion and τ_C the correlation time of the responsible stochastic process of libration. The indicated average of the angle is evaluated with respect to time and the above relation is strictly valid for small libration angles. The ED-EPR method alone could not allow for the separate determination of both the variance $<\alpha^2>$ of the libration angle and the correlation time τ_C, and was therefore combined with a separate determination of the former by CW-EPR, as shown in Fig. 3.4.

One should note that in the research of *phospholipid bilayers* the NMR spectroscopy offers a non-invasive method for structure and dynamics investigation. Lipid bilayers are considered as adequate models for *cell membranes*. Commonly

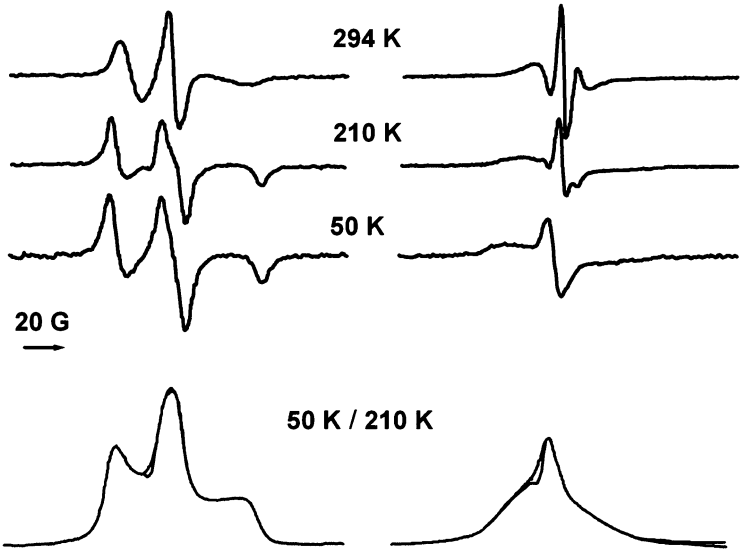

Fig. 3.21 The CW EPR spectra of the elongated and relatively flat cholestane nitroxide spin-label shown in Fig. 3.3, in an oriented *lamellar phase* for several temperatures and for two orthogonal orientations of the multibilayer surface with respect to the external magnetic dc field, one parallel (*left vertical series*) and one perpendicular (*right vertical series*), figure 1 in ref. [25]. The integrated CW absorption spectra in the lower panel, which are nearly unchanged in the interval 50–210 K, were compared to theoretical Echo-Detected EPR traces [25] that exhibited significant temperature dependence (Reproduced from Ref. [25] with kind permission of © Elsevier (1995))

Deuteron and Phosphorus NMR powder spectra give excellent results for non-oriented samples such as e.g. multi-lamellar bilayers in the *gel* and the "*liquid crystalline*" phase at physiological/ambient temperatures [64, 143]. The biologically interesting results from Cross Polarization ^{31}P-NMR wideline simulations are in very good agreement with EPR measurement. Such is the case of phospholipid model membranes modulated by insertion of the peptidomimetic antihypertensive drug Losartan in the lamellar structure [144].

3.10.3 Peptide Chain Mobility

Extensive use of nitroxide spin labels, mostly in studying substances of biological interest and glassy polymers, owes to features such as: (1) sensitivity of the lineshape of the radical EPR spectrum to the state of its rotation (2) great longevity of this stable radical. Being invaluable source of information on the dynamics properties of the above mentioned biological substances, the nitroxides cannot however be used in studying solids with no cavities of large size to host them. The

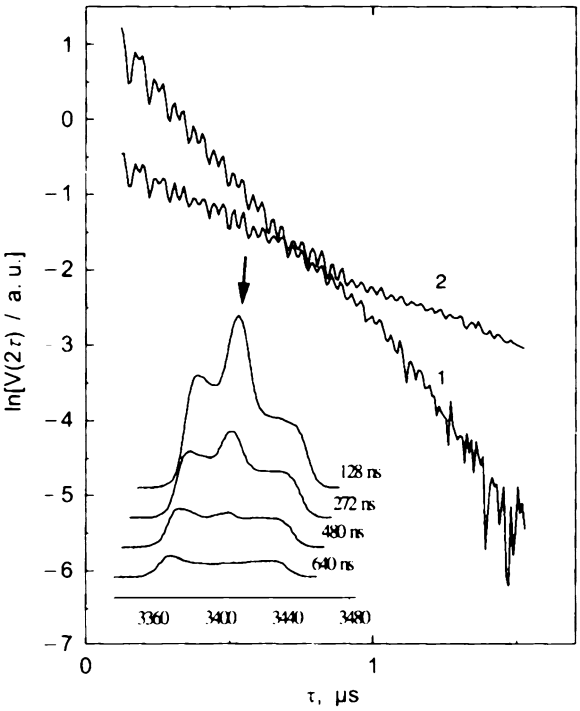

Fig. 3.22 Determination of the (local) radical concentration by using the properties of the instantaneous diffusion, see text (Reproduced from Ref. [23] with kind permission of © Springer (1998))

van der Waals volume for TEMPO, one of the smallest nitroxides, was estimated to be 150 $Å^3$ [145], which corresponds to 6.6 Å van der Waals diameter. This value is close to the distance of 6.57 Å between the unpaired electrons of the TEMPO crystal taken to be on the nitrogen atoms [146]. Such great van der Waals diameters exceed the nearest neighbor distances in a large variety of solids. Hence, a nitroxide radical trapped in a crystal lattice would cause local tension which would break the dynamics of the pure lattice.

In spite of such structural perturbations, the *local mobility* of peptides as well as *unfolding* and *denaturation* of larger proteins can be studied by spin labelling. Mutant proteins or polypeptides with predefined residue(s) at certain position(s) of the aminoacid chain by appropriate nitroxides can be used.

Three labelled variants of the small natural peptide peptaibol, containing only ten aminoacid residues, were prepared by substitution of one amino-isobutyric acid residue by 2,2,6,6-tetramethyl-piperidine-1-oxyl-4-carboxylic acid, at the two terminal and one intermediate positions, and were studied by Dzuba et al. [23]. The dependence of the ED-EPR on the *pulse delay*, the *temperature*, and the *nutation angle* variation were used to study the librational dynamics and eventual deviations of the *local concentration* of the label. By observing the lower left part of Fig. 3.22 we notice that the variation of the pulse delay τ affects most significantly the central hf-component of the nitroxide triplet. In contrast to the *spectral diffusion*, the effect

of *instantaneous diffusion* on the spectra of partially immobilized nitroxides can be seen as the selective decrease of the central peak intensity of the nitroxide with the increase of the pulse delay τ.

The instantaneous diffusion has furthermore an exponential decay rate proportional to the concentration of the irradiated **A** spin packets, which is largest just at the central hf component $M_I = 0$ of the ^{14}N nucleus. Inspection of the intensity distribution of the immobilized nitroxide spectra, e.g. in Fig. 3.21 and Fig. 3.22, shows this fact indicating that relatively more spin packets can be affected by irradiating just the middle region of the inhomogeneous spectrum. The central peak attains also for this reason the largest dynamical range concerning pulse-delay variation dependence of the intensity when the decay is due to instantaneous diffusion. This is demonstrated very well in the lower left part of Fig. 3.22, where the pulse-delay dependent variation of the central peak is by far more impressive compared to the variation of the intensity of the two outer peaks.

An application of the nutation angle variation is also displayed in Fig. 3.22, which with clarity demonstrates that (a) the decay of the ESE signal is *exponential*, as the instantaneous diffusion mechanism predicts, and also that (b) the decay rate varies with the change of the (Microwave) MW field intensity. Thus, computing the average $<\sin^2(\vartheta/2)>_g$ according to Eq. (3.15) for two different values of the MW field intensity H_1, the authors in [23] obtained a larger value of the average for the greater nutation angle and a corresponding greater slope of the time domain signal in the semilogarithmic plot (the vertical axis is logarithmic) shown in the higher middle of Fig. 3.22.

One important issue here was the potential determination of *local* deviations of the concentration of a given radical with respect to the bulk value in the sample. By using the above instantaneous diffusion data and the slopes of the two curves in Fig. 3.22 the authors in [23] were able to compute the concentration C according to Eq. (3.14). This is not necessarily equal to the average concentration of the sample but to the effective concentration of *paramagnetic centers* within a narrow resonance- frequency band (**A** spins). In that particular case the experimental value was however equal to the average concentration.

3.10.4 Protein Mobility Studies

An important application of the nitroxide spin labels' EPR is found in a series of studies concerning the mobility of selected regions of certain macromolecules such as peptides [23] and enzymes [100] in particular. Usually the *dephasing* of the Electron Spin Echo signal is of interest in this method. It is generally accepted that for dilute solutions of organic radicals at low temperature, *electron spin echo dephasing* is dominated by the interaction between the free radical and the nuclear spins (protons) in the surrounding medium.

Herzog and Hahn [147] first recognized the importance of *spin diffusion* mediated by nuclear spin *flip-flops* on the dephasing of the electron spin echo. Secular

flip-flop transitions among the nuclear spins, which are induced by the terms $I_{1+} \cdot I_{2-} + I_{1-} \cdot I_{2+}$ of the nuclear-pair dipolar Hamiltonian modulate the electron-nuclear *S-I* hyperfine coupling providing an efficient mechanism of the second kind for echo dephasing for the electron spin. This relaxation mechanism in many ways resembles the way that the **B** electron spins, that are not directly affected by the pulse, give fluctuations to the z-component of the resonating **A** spins through their spin-lattice T_1-relaxation (Sect. 3.9.3). In the case of relatively dilute electron spins both nuclear and electron **B** spins are treated similarly, also including *semisecular* terms of their electronic Hamiltonian, i.e. isolated flips or flops, where the energy balance is assisted by the mediation of the "lattice". The latter processes are heavily depending on the state of the matter and on *cross relaxation*.

A statistical treatment for the fluctuation of the z-component of the magnetization of the **B** spins for different theoretical models can be cast to a *stretched*-exponential-decay [18, 142] function shown in Eq. (3.13). Extensive theoretical derivations of the *stretched exponential* forms for different models are found in ref. [142]. Except for the usual *exponential* and *Gaussian decays* (for exponential power of time $x = 1$ and 2, respectively) this relation also includes other possible cases such as $x = 1/2$, 3/2, and 7/4, at least theoretically. The echo decay function of ESEEM can in practice equally well, if not better, be fitted by considering exponential polynomials in the time variable t, which naturally include exponential and Gaussian decays. *Third order* decays are supported by the *self-diffusion* mechanism, in connection with the field gradients and the Carr-Purcell sequence [56], but higher integer powers can hardly find theoretical support.

The stretched- exponential-decay function was used qualitatively in order to simulate the envelope of the electron spin echo decaying signal of spin labels in various model solvents as well as of spin labels attached to different positions in Human Carbonic Anhydrase II (HCA II). The different solvents were classified tentatively according to the values of the two parameters of this function [18, 100], i.e. the *phase memory decay time* T_m, and the exponent x, at a temperature of 40 K. Similarly these parameters were evaluated for spin labels attached to different positions in HCA II [100 iii]. By such a study one could obtain information about the mechanism determining T_2 relaxation by the magnetic nuclei surrounding the spin label. An interesting observation in several studied systems with this method was the great sensitivity of the dephasing rates to the groups of slowly-to-rapidly rotating methyl groups confined in the sphere of interaction of the electron spin [18, 100].

Earlier results have shown that the ESR line- shape associated with an introduced spin-label can give very useful information in terms of local structure and mobility at the position of the spin-label, such as the structure of equilibrium folding intermediates. This method was applied in the investigation of the degree of folding of partially *denaturated mutant* protein HCA II containing label molecules in different positions of the primary chain by CW EPR lineshape simulations [148]. The dependence of the measured *phase memory time* (T_M) on the degree of denaturation can be assumed to be due to the mobility variation of the label in different mutants containing the label at different residue positions used for this purpose.

Acknowledgments NPB would like to thank the so many people that gave him the opportunity to work with this text. First of all Professor Anders Lund from Linköping University and Professor Dimitrios Galaris in Ioannina University in Greece. Also Professor Rimma Samoilova and Professor Sergei Dzuba as well as Professor Yuri Tsvetkov from the Institute of Chemical Kinetics and Combustion in Novosibirsk are highly acknowledged. I thank Dr. Eugenia Kirillina for all practical help in "Academ Gorodok" and for teaching me some dynamics of nitroxides and I am also thankful to theorist Alexandr Maryasov who also borrowed him his Russian(!) version of Abragam and finally to Dr. Martina Huber for correcting the first manuscript. Finally Mari Löfkvist is acknowledged for the language corrections. For the new update during 2011 NPB wants to thank the President of the TEI of Western Macedonia, Prof. George Charalambidis. YD acknowledges an unbelievable patience of his wife who found strength to survive days, rich of experimental work, data processing and preparing manuscripts. Furthermore, she supported me incredibly by giving birth to our beloved tiny son.

References

1. Shiga T, Lund A (1973) *g* factor and hyperfine coupling anisotropy in the electron spin resonance spectra of methyl-, ethyl-, and allyl-type radicals adsorbed on silica gel. J Phys Chem 77:453–455
2. Pariiskii GB, Zhidomirov GM, Kazanskii VB (1963) Electron paramagnetic resonance spectrum of the methyl radical adsorbed on a silica gel surface. J Struct Chem 4:336–338
3. Yamada T, Komaguchi K, Shiotani M, Benetis NP, Sørnes AR (1999) High resolution EPR and quantum effects on CH_3, CH_2D, CHD_2 and CD_3 radicals under argon-matrix isolation conditions. J Phys Chem A 103:4823–29
4. Dmitriev YA (2004) High- resolution EPR and the origin of the spectrum anisotropy of CH_3 radicals in Ar, Kr, and CO matrices at liquid helium temperature. Phys B 352:383–389
5. Popov E, Kiljunen T, Kunttu H, Eloranta J (2007) Rotation of methyl radicals in a solid argon matrix. J Chem Phys 126:134504
6. Symon KR (1974) Mechanics, 3rd edn. Addison-Wesley Publ Comp, Boston
7. Sørnes AR, Benetis NP (1998) The EPR spectrum of the general $>C^{\cdot}\text{-}CX_3$ quantum rotor. Chem Phys 226:151–170
8. Benetis N, Kowalewski J, Nordenskiöld L, Wennerström H, Westlund P-O (1983) Nuclear spin relaxation in paramagnetic systems. The slow motion problem for electron spin relaxation. Mol Phys 48:329–346
9. McQuarrie DA (1976) Statistical mechanics. Harper & Row, New York
10. Sørnes AR, Benetis NP (1997) The methyl-rotor electron-spin dynamics in the Smoluchowsky drift diffusional model framework. J Magn Reson 125:52–64
11. Sørnes AR, Benetis NP, Erickson R, Mahgoub AS, Eberson L, Lund A (1997) Effect of isotopic substitution on the electron spin dynamics of the $CH_3C{\cdot}(COOH)_2$ radical in x-irradiated methyl malonic acid powder: intrinsic potentials and activation energies. J Phys Chem A 101:8987–8994
12. Deligiannakis Y, Louloudi M, Hadjiliadis N (2000) Electron spin envelope modulation (ESSEM) spectroscopy as a tool to investigate the coordination environment of metal centers. Coord Chem Rev 204:1–113
13. Schmidt J, Singel DJ (1987) Fashioning electron spin echoes into spectroscopic tools: a study of azaaromatic molecules in metastable triplet states. Ann Rev Phys Chem 38:141–161
14. Bowman MK (1990) Chapter 1. In: Kevan L, Bowman MK (eds) Modern pulsed and continuous-wave electron spin resonance. Wiley, New York
15. (i) Gorcester J, Millhauser GL, Freed JH (1989) Chapter 5. In: Hoff AJ (ed) Advanced EPR: applications in biology and biochemistry. Elsevier, Amsterdam; (ii) Gorcester J, Millhauser GL, Freed JH (1990) Chapter 3. In: Kevan L, Bowman M (eds) Modern pulsed and continuous-wave electron spin resonance. Wiley, New York

16. Schweiger A (1990) Chapter 2. In: Kevan L, Bowman M (eds) Modern pulsed and continuous-wave electron spin resonance. Wiley, New York
17. Dzuba SA, Borovykh IV, Hoff AJ (1998) Simple two-pulse detection scheme in pulsed EPR for studying low-frequency nuclear coherences. J Magn Reson 133:286–290
18. Barbon A, Brustolon M, Maniero AL, Romanelli M, Brunel L-C (1999) Dynamics and spin relaxation of tempone in a host crystal. An ENDOR, high field EPR and electron spin echo study. Phys Chem Chem Phys 1:4015–4023
19. Salikhov KM, Tsvetkov YuD (1979) Chapter 7. In: Kevan L, Schwartz RN (eds) Time domain electron spin resonance. Wiley, New York
20. Brown IM (1979) Chapter 6. In: Kevan L, Schwartz RN (eds) Time domain electron spin resonance. Wiley, New York
21. Abragam A (1961) The principles of nuclear magnetism. Clarendon Press, Oxford. Page references of specific topics of interest here: *Spin-packet* page 397, *spin-diffusion* pages 378–389 and 103-111, and additional information in pages 10–38 and 133–144. *Spin temperature* pages 133–144. *Relaxation due to paramagnetic impurities* pages 378–398. Notice that definition of *spin diffusion* in pages 59 and 61, concerns actually the *self-diffusion* of spin-bearing molecules measured when an external *field gradient* is applied on the top of the static field. An extensive consideration of the broadening in *solid state* is given in Abragam Chapter X, but it concerns nuclear relaxation. Many important aspects and definitions about electron spin relaxation at very low temperatures are found in the book of Abragam A, Bleaney B (1970) Electron paramagnetic resonance of transition ions. Dover Publications, inc., New York, but are specialized to paramagnetic metal ions
22. Kowalewski J, Nordenskiöld L, Benetis N, Westlund PO (1985) Theory of nuclear spin relaxation in paramagnetic systems in solution. Progr NMR Spectrosc 17:141–185
23. Toropov YuV, Dzuba SA, Tsvetkov YuD, Monaco V, Formaggio F, Crisma M, Toniolo C, Raap J (1998) Molecular dynamics and spatial distribution of TOAC spin-labelled peptaibols studied in glassy liquid by echo-detected EPR spectroscopy. Appl Magn Reson 15:237–246
24. Dzuba SA (1996) Librational motion of guest spin probe molecules in glassy media. Phys Lett A 213:77–84
25. Dzuba SA, Watari H, Shimoyama Y, Maryasov AG, Kodera Y, Kawamori A (1995) Molecular motion of the cholestane spin label in multibilayer in the gel phase studied using echo-detected EPR. J Magn Reson 115:80–86
26. Sjöqvist L, Benetis NP, Lund A, Maruani J (1991) Intramolecular dynamics of the $C_4H_8NH^+$ radical cation. An application of the anisotropic exchange theory for powder ESR lineshapes. Chem Phys 156:457–464
27. (i) Lindgren M, Erickson R, Benetis NP, Antzutkin O (1993) The THF-d8 radical cation in CF_3CCl_3 and $CFCl_3$. An EPR and ENDOR study. J Chem Soc Perkin Trans 2:2009–2014; (ii) Lindgren M, Benetis NP, Matsumoto M, Shiotani M (1995) A study of the dynamic equilibrium between symmetrical and distorted 1, 2, 3-trimethyl-cyclohexane radical cations. Appl Magn Reson 9:45–59
28. Rakhimov RR, Benetis NP, Lund A, Hwang JS, Prokof'ev AI, Lebedev YS (1996) Intramolecular and reorientation dynamics of bis (triphenyl phosphine)-3, 6-di-tert- butyl-4, 5-dimethoxy-o-semiquinone complex of copper(I) in viscous media. Chem Phys Lett 255: 156–1622
29. Bonon A, Brustolon M, Maniero AL, Segre U (1992) An ENDOR study of the tempera-ture dependence of methyl tunneling. Chem Phys 161:257–63
30. Freed JH (1965) Quantum effects of methyl-group rotations in magnetic resonance: ESR splittings and linewidths. J Chem Phys 43:1710
31. Clough S, Poldy F (1969) Study of tunneling rotation of methyl groups by electron spin resonance and electron nuclear double resonance. J Chem Phys 51:2076
32. Brustolon M, Cassol T, Micheletti L, Segre U (1986) Methyl dynamics studied by ENDOR spectroscopy: a new method. Mol Phys 57:1005–1014
33. Carrington A, McLachlan AD (1967) Introduction to magnetic resonance. Harper, New York

34. Antzutkin ON, Benetis NP, Lindgren M, Lund A (1993) Molecular motion of the morpholine-1-yl radical in $CF_2ClCFCl_2$ as studied by ESR. Use of residual anisotropy of powder spectra to extract dynamics. Chem Phys 169:195–205
35. Kirillina EP, Dzuba SA, Maryasov AG, Tsvetkov YuD (2001) Librational dynamics of nitroxide molecules in a molecular glass studied by echo-detected EPR. Appl Magn Reson 21:203–221
36. Salih NA, Eid OI, Benetis NP, Lindgren M, Lund A, Sagstuen E (1996) Reversible conformation change of free radicals in x-irradiated glutarimide single crystals studied by ENDOR. Chem Phys 212:409–419
37. Spaeth JM (1969) Influence of zero-point vibration on the superhyperfine interactions of hydrogen and deuterium centres in KCl. Phys Stat Sol 34:171–181
38. Wertz JE, Bolton JR (1972) Electron spin resonance. Elementary theory and practical applications. McGraw-Hill, New York
39. Adrian FJ (1988) Analytic solution of the stochastic-Liouville model of spin exchange. J Chem Phys 88(5):3216–3220
40. Morton JR, Preston KF, Strach SJ, Adrian FJ, Jette AN (1979) Anisotropic hyperfine interactions of rare-gas nuclei near trapped hydrogen atoms. J Chem Phys 70:2889–2893
41. Zhitnikov RA, Dmitriev YA (1990) Isotopic effect in EPR spectra of stabilized atoms. Zhurnal Tekhnicheskoi Fiziki 60:154–159 (Technical Physics in English translation)
42. Dmitriev YA, Zhitnikov RA (1990) Hyperfine interaction in hydrogen and deuterium atoms stabilized in frozen- gas matrices. Optika i Spectroskopiya 69:1231–1237 (Optics and Spectroscopy in English translation)
43. Spaeth JM (1986) Atomic hydrogen and muonium in alkali halides. Hyperfine Interact 32:641–658
44. (i) Roduner E, Percival PW, Han P, Bartels DM (1995) Isotope and temperature effects on the hyperfine interaction of atomic hydrogen in liquid water and ice. J Chem Phys 102:5989–5997; (ii) Matsuda Y (2003) Encapsulation of atomic hydrogen into silsesqui-oxane cages and EPR of encapsulated hydrogen atoms. Appl Magn Reson 23:469–480
45. Dmitriev YA (1993) The influence of hydrogen and deuterium zero-point vibrations on electron spin resonance parameters of the atoms matrix-isolated in solid Xe. J Phys Condens Matter 5:5245–5254
46. (i) Heller C, McConnell HM (1960) Radiation damage in organic crystals. II. Electron spin resonance of $(CO_2H)CH_2CH(CO_2H)$ in β-succinic acid. J Chem Phys 32:1535; (ii) Suryanarayana D, Sevilla MD (1984) INDO study of the anion radicals of acetic acid and acetamide. Nonplanarity and barriers to methyl group rotation. J Phys Chem 84:3045–3049
47. Rockenbauer A, Györ M, Hankovszky HO, Hideg K (1987) Chapter 5. In: Electron spin resonance. R Soc Chem 11A:145–182
48. Lister DG, Macdonald JN, Owen NL (1978) Internal rotation and inversion. An introduction to large amplitude motions in molecules. Academic, London
49. Stone EW, Maki AH (1962) Hindered internal rotation and E.S.R. [electron spin resonance] spectroscopy. J Chem Phys 37:1326
50. Arfken G (1970) Mathematical methods for physicists, 2nd edn. Academic, New York
51. Benetis NP, Sørnes AR, unpublished
52. Lebedev YS (1979) Chapter 8. In: Kevan L, Schwartz RN (eds) Time domain electron spin resonance. Wiley, New York
53. Kveder M, Merunka D, Ilakovac A, Makarević J, Jokić M, Ravkin B (2006) Direct evidence for the glass-crystalline transformation in solid ethanol by means of a nitroxide spin probe. Chem Phys Lett 419:91–95
54. Kveder M, Andreis M, Makarević J, Jokić M, Ravkin B (2006) EPR study of low molecular weight organogels by means of nitroxide spin probe. Chem Phys Lett 420:443–447
55. Dzuba SA, Salikhov KM, Tsvetkov YuD (1981) Slow rotations ($\tau \geq 10^{-5}$ s) of methyl groups in radicals studied by pulse ESR spectroscopy. Chem Phys Lett 79:568
56. Carr HY, Purcell EM (1954) Effects of diffusion on free precession in nuclear magnetic resonance experiments. Phys Rev 94:630–638

57. Schweiger A, Jeschke G (2001) Principles of pulse electron paramagnetic resonance. Oxford University Press, Oxford
58. Dzuba SA, Golovina YeA, Tsvetkov YuD (1993) Echo-induced EPR spectra of spin probes as a method for identification of glassy states in biological objects. J Magn Reson B 101: 134–138
59. Dmitriev YA (2008) Peculiarities of EPR spectra of methyl radicals in quenched- condensed krypton films. Low Temp Phys 34:75–77
60. Friebele EJ, Griscom DL, Rau K (1983) Observation of the methyl radical CH_3 in irradiated high- purity synthetic fused silica. J Non-Cryst Solids 57:167–175
61. Kiljunen T, Popov E, Kunttu H, Eloranta J (2009) Rotation of methyl radicals in a solid krypton matrix. J Chem Phys 130:164504
62. Strzhemechny MA, Galtsov NN, Prokhvatilov AI (2003) Quench deposited Kr–H_2 and Ar–H_2 mixtures: in quest of impurity–hydrogen gels. Low Temp Phys 29:522–526
63. Luckhurst GR (1972) Chapter X. In: Muus LT, Atkins PW (eds) Electron spin relaxation in liquids. Plenum Press, New York
64. Benetis NP, Kyrikou I, Mavromoustakos T, Zervou M (2005) Static 31P CP NMR multilamellar bilayer broadlines in the absence and presence of the bioactive dipeptide beta-Ala-Tyr or Glu. Chem Phys 314:57–72
65. Goldman SA, Bruno GV, Freed JH (1972) Estimating slow-motional rotational correlation times for nitroxides by electron spin resonance. J Phys Chem 76:1858–1860
66. Buitink J, Dzuba SA, Hoekstra FA, Tsvetkov YuD (2000) Pulsed EPR spin-probe study of intracellular glasses in seed and pollen. J Magn Reson 142:364–368
67. (i) Heinzer J (1971) Fast computation of exchange-broadened isotropic E.S.R. spectra. Mol Phys 22:167; (ii) Heinzer J (1972) Quantum chemistry program exchange. In: QCPE program 209, ESREXN, Indiana University, Bloomington
68. Segre U, Brustolon M, Maniero AL, Bonon F (1993) EPR and ENDOR relaxation study of molecular motions of a ketone-urea inclusion compound. J Phys Chem 97:2904
69. Kurreck H, Kirste B, Lubitz W (1988) Electron nuclear double resonance spectroscopy of radicals in solution. VCH, Weinham
70. Schwartz LJ, Stillman AE, Freed JH (1982) Analysis of electron-spin echoes by spectral representation of the Stochastic Liouville Equations. J Chem Phys 77:5410–5425
71. Nordh UE, Benetis NP (1995) Extension of the accessible dynamical range of reorganization in ESEEM simulations of single crystals. Chem Phys Lett 244:321
72. Sjöqvist L, Lund A, Maruani J (1988) An ESR investigation of the dynamical behavior of the cyclopentane cation in CF_3CCl_3. Chem Phys 125:293
73. Benetis NP, Sjöqvist L, Lund A, Maruani J (1991) Theoretical comparison and experimental test of the secular and nonperturbative approaches of the ESR lineshapes of randomly oriented, anisotropic systems undergoing internal motion. J Magn Reson 95:523–535
74. Ladd JA, Wardale HW (1974) Chapter 5. In: Orville-Thomas WJ (ed) Internal rotation in molecules. Wiley, New York
75. Ernst RR, Bodenhausen G, Wokaun A (1991) Principles of nuclear magnetic resonance in one and two dimensions. Clarendon, Oxford, 71
76. McConnell HM (1958) Reaction rates by nuclear magnetic resonance. J Chem Phys 28:430
77. Benetis NP, Lindgren M, Lee H-S, Lund A (1990) Intramolecular dynamics in small radicals with anisotropic magnetic interactions. ESR lineshapes of $\cdot CH_2$-COO^- trapped in irradiated ZnAc single crystal. J Appl Magn Reson 1:267–281
78. Benetis NP, Mahgoub AS, Lund A, Nordh UE (1994) Rotation of deuterated methylene groups in the diffusional regime. Isotope effect of anisotropic alfa-deuterons on ESR lineshapes of $\cdot CD_2$-COO^- radical in irradiated ZnAC dihydrate single crystal. Chem Phys Lett 218:551–556
79. Erickson R, Nord U, Benetis NP, Lund A (1992) ESR lineshapes and methyl rotation in the acetic acid anion radical. Chem Phys 168:91–98
80. Abragam A, Bleaney B (1970) Electron paramagnetic resonance of transition ions. Dover Publications, New York

81. Benetis NP (1984) Nuclear-spin relaxation in paramagnetic metal complexes and the slow-motion problem for the electron spin. Dissertation, University of Stockholm, Stockholm
82. Bowman MK, Kevan L (1979) Chapter 3. In: Kevan L, Schwartz RN (eds) Time domain electron spin resonance. Wiley, New York
83. (i) Redfield AG (1957) On the theory of relaxation processes. IBM J Reson Dev 1:19–31; (ii) Redfield AG (1965) The theory of relaxation processes. Adv Magn Reson 1:1–32
84. Bloembergen N, Purcell EM, Pound RV (1948) Relaxation effects in nuclear magnetic resonance absorption. Phys Rev 73:679–712
85. (i) Wangsness RK, Bloch F (1953) The dynamical theory of nuclear induction. Phys Rev 89:728–739; (ii) Bloch F (1956) Dynamical theory of nuclear induction. II. Phys Rev 102:104–135
86. Slichter CP (1990) Principles of magnetic resonance, 3rd edn. Springer, Berlin
87. Beware that the term *adiabatic* has been used in several other magnetic resonance contexts concerning both solids and liquids. In the present case we mean the use of the *S*-secular Hamiltonian. The quantum mechanical or Ehrenfest sense of adiabaticity according to Abragam, The principles of nuclear magnetism. Clarendon press, Oxford 1961, pages 135–136, is the one where the variation of the magnetic field, or generally any other external parameter of the system, is applied in such a way that *no spin transitions are induced*. Thus, the populations of the levels are maintained during the change, while obviously heat has to flow to or from the ensemble to compensate the parametric change in the energy (Hamiltonian). Such can also be the so called *sudden change* that con-serves the *spin temperature*. The *thermodynamic sense* of an *adiabatic transformation* on the other hand, has the pro-found interpretation of prohibited exchange of energy between the spins and the lattice. Such a *reversible change* of the system close to equilibrium is also *isentropic*, i.e. it is conserving the entropy, Abragam pages 144–149. Examples belonging in this sense of adiabaticity are the cases of *adiabatic demagnetization* and *adiabatic fast passage*, or simply *fast passage*, discussed in detail also for nuclei by E. Fukushima, S.B.W. Roeder in Experimental pulse NMR. A nuts and bolts approach. Addison-Wesley Publishing Company, Inc, London 1981. Adiabatic fast passage means slow enough rate of change of the field through resonance in order to be *reversible* but fast enough so that exchange of energy with the lattice by $T1$ processes not to be possible, see also Slichter's book Principles of magnetic resonance, 3rd edn. Springer, Berlin 1990, Chapter 6
88. Westlund PO, Benetis N, Wennerström H (1987) Paramagnetic proton nuclear magnetic relaxation in the Ni^{2+} hexa-aquo complex. A theoretical study. Mol Phys 61:177–194
89. Benetis N, Kowalewski J (1985) Nuclear spin relaxation in paramagnetic systems ($S = 1$) in the slow motion regime for the electron spin. IV. Motional anisotropy and non-coinciding dipole-dipole and zero-field splitting tensors. J Magn Reson 65:13–33
90. Benetis N, Kowalewski J, Nordenskiöld L, Wennerström H, Westlund PO (1984) Nuclear spin relaxation in paramagnetic systems ($S = 1$) in the slow-motion regime for the electron spin. II. The dipolar T_2 and the role of scalar interaction. J Magn Reson 58:261–281
91. Jackel GS, Gordy W (1968) Electron spin resonance of free radicals formed from group-IV and group-V hydrides in inert matrices at low temperature. Phys Rev 176:443–452
92. Press W (1981) Tracts in molecular physics, vol 92. Springer, Berlin
93. Benetis NP, Dmitriev Y (2009) Internal rotation and matrix interaction effects on the EPR spectra of methyl radicals isolated in "inert" cryogenic matrices. J Phys Condens Matter 21:103201
94. Dmitriev YuA, Benetis NP (2012) Anomalous EPR intensity distribution of the methyl radical quartet adsorbed on the surface of porous materials. Comparison with solid gas matrix isolation. Submitted to PCCP September 2012
95. Kiljunen T, Popov E, Kunttu H, Eloranta J (2010) Rotation of methyl radicals in molecular solids. J Phys Chem A 114:4770–4775
96. Misochko EY, Benderskii VA, Goldschleger AU, Akimov AV, Benderskii AV, Wight CA (1997) Reactions of translationally excited and thermal fluorine atoms with CH_4 and CD_4 molecules in solid argon. J Chem Phys 106:3146–3156

97. Morehouse RL, Christiansen JJ, Gordy W (1966) ESR of free radicals trapped in inert matrices at low temperature: CH_3, SiH_3, GeH_3 and SnH_3. J Chem Phys 45:1751–1758
98. Shiotani M, Yamada T, Komaguchi K, Benetis NP, Lund A, Sørnes AR (1998) The meeting on tunneling reactions and low temperature chemistry. JAERI-Conf 98–014:58–63
99. Dag S, Gülseren O, Ciracia S, Yildirim T (2003) Quantum rotation of hydrogen in single- wall carbon nanontubes. http://www.ncnr.nist.gov/staff/taner/nanotube/dynamics.html. Accessed 13 Oct 2003
100. (i) Lindgren M, Eaton GR, Eaton SS, Jonsson B-H, Hammarström P, Svensson M, Carlsson U (1997) Electron spin echo decay at a probe of aminoxyl environment in spin-labeled mutants of carbonic anhydrase. J Chem Soc Perkin Trans 2:2549; (ii) Zecevic A, Eaton GR, Eaton SS, Lindgren M (1998) Dephasing of electron spin echoes for nitroxyl radicals in glassy solvents by non-methyl and methyl protons. Mol Phys 95:1255; (iii) Huber M, Lindgren M, Hammarström P, Mårtensson L-G, Carlsson U, Eaton GR, Eaton SS (2001) Phase memory relaxation times of spin labels in human carbonic anhydrase II: pulsed EPR to determine spin label location. Biophys Chem 94:245–256
101. Owen NL (1974) Chapter 6. In: Orville-Thomas WJ (ed) Internal rotation in molecules. Wiley, New York
102. Mottley C, Kispert LD, Clough S (1975) Electron-electron double resonance study of coherent and random rotational motion of methyl groups. J Chem Phys 63:4405
103. Heller C (1962) Electron spin resonance and internal rotation of the methyl group in the $CH_3{}^{\cdot}C(COOH)_2$ radical. J Chem Phys 36:175
104. Wells JW, Box HC (1968) Magnetic resonance studies on irradiated crystals of chloroacetyl DL-alanine. J Chem Phys 48:2542–2546
105. Zhitnikov RA, Dmitriev YA, Kaimakov ME (1989) EPR observation of stimulated ortho-para conversion in solid H_2 and D_2. Fizika Nizkikh Temperatur 15:651–653 (Sov J Low Temp Phys in English translation)
106. Dmitriev YA, Zhitnikov RA (1990) Ortho-para conversion in solid H_2 stimulated by atomic nitrogen impurities. Fizika Nizkikh Temperatur 16:94–101 (Sov J Low Temp Phys in English translation)
107. Shevtsov V, Frolov A, Lukashevich I, Ylinen E, Malmi P, Punkkinen M (1994) The ortho-para conversion in solid hydrogen catalyzed by hydrogen atoms. J Low Temp Phys 95:815–833
108. Andersson LO (2008) EPR investigation of methyl radical, the hydrogen atom and carbon oxide radicals in Maxixe- type beryl. Phys Chem Miner 35:505–520
109. (i) McConnell HM, Strathdee J (1959) Theory of anisotropic hyperfine interactions in π-electron radicals. Mol Phys 2:129–138; (ii) Zhidomirov GM, Schastnev PV (1966) Calculation of anisotropic hyperfine interaction in radicals with π-electrons. J Struct Chem 7:57–62; (iii) Lee JY, Rogers MT (1976) Tunneling rotation of the methyl radical in solids. J Chem Phys 65:580–581; (iv) Chipman DM (1983) Theoretical study of the properties of methyl radical. J Chem Phys 78:3112–3132; (v) Feller D, Davidson ER (1984) *Ab initio* configuration interaction calculations of the hyperfine structure in small radicals. J Chem Phys 80:1006–1017
110. Kubota S, Iwaizumi M, Ikegami Y, Shimokoshi K (1979) Anisotropic hyperfine interaction in the electron spin resonance spectrum of the methyl radical trapped in $CH_3COONa{\cdot}3D_2O$ crystal at low temperatures. J Chem Phys 71:4771–4776
111. Rogers MT, Kispert LD (1967) Methyl radical in irradiated single crystal of sodium acetate trihydrate. J Chem Phys 46:221–223
112. Toriyama K, Nunome K, Iwasaki M (1976) ENDOR studies of methyl radicals in irradiated single crystals of $CH_3COOLi{\cdot}2H_2O$. J Chem Phys 64:2020–2026
113. Brotikovskii I, Zhidomirov GM, Kazanskii VB (1972) Quantum effects of anisotropic rotation in the ESR of the methyl radical. Theor Exp Chem 8:653–659
114. Gardner CL, Casey EJ (1968) Tumbling of methyl radicals adsorbed on a silica gel surface studied by electron spin resonance. Can J Chem 46:207–210

115. Freed JH, Fraenkel GK (1963) Theory of linewidths in electron spin resonance spectra. J Chem Phys 39:326–348
116. Garbutt GB, Gesser HD, Fujimoto M (1968) Temperature dependence of the hyperfine interactions, linewidths, and line asymmetries in methyl radicals stabilized on porous glass surfaces. J Chem Phys 48:4605–4614
117. Schrader DM (1967) Theory of temperature dependence of the hyperfine interactions in the methyl radical. J Chem Phys 46:3895–3904
118. Ellinger Y, Pauzat F, Barone V, Douady J, Subra R (1980) *Ab initio* study of the vibrational dependence of hyperfine coupling constants in the methyl, silyl, and formaldehyde anion radicals. J Chem Phys 72:6390–6397
119. Tachikawa H, Igarashi M, Ishibashi T (2002) *Ab initio* molecular dynamics (MD) calculations of hyperfine coupling constants of methyl radicals. Chem Phys Lett 352:113–119
120. (i) Takada T, Tachikawa H (2009) DFT and direct *ab initio* MD study on hyperfine coupling constants of methyl radicals adsorbed on model surface of silica gel. J Mol Catal A: Chem 311:54–60; (ii) Fernandez B, Christiansen O, Bludsky O, Jorgensen P, Mikkelsen K (1994) Theory of hyperfine coupling constants of solvated molecules: applications involving methyl and ClO_2 radicals in different solvents. J Chem Phys 104:629–635; (iii) Ishii N, Shimizu T (1994) Density-functional-theory calculations of isotropic hyperfine coupling constants of radicals. Chem Phys Lett 225:462–466
121. Garbutt GB, Gesser HD (1970) Electron spin resonance studies on porous VYCOR glass: various surface interactions, second order splitting, and a linewidth temperature study. Can J Chem 48:2685–2694
122. Noble GA, Serway RA, O'Donnell A, Freeman ES (1967) Stability of methyl radicals in a zeolite matrix. J Phys Chem 71:4326–4329
123. Danilczuk M, Pogocki D, Lund A, Michalik J (2006) EPR and DFT study on the stabilization of radiation- generated methyl radicals in dehydrated Na- A zeolite. J Phys Chem B 110:24492–24497
124. Cirelli G, Russu A, Wolf R, Rudin M, Schweiger A, Gunthard HH (1982) Detection of ENDOR spectra of paramagnetic species isolated in solid argon. Chem Phys Lett 92: 223–224
125. McKinley AJ, Michl J (1991) EPR- ENDOR spectroscopy of matrix-isolated NH_3^+ and CH_3 radicals. J Phys Chem 95:2674–2679
126. Dmitriev YuA, Benetis NP (2010) EPR line-shape anisotropy and hyperfine shift of methyl radicals in solid Ne, Ar, Kr, and *p*-H_2 gas matrices. J Phys Chem A 114:10732–10741
127. Dmitriev YA, Zhitnikov RA (2001) EPR study of methyl radicals. Anisotropy and tumbling motion in low- temperature matrices. J Low Temp Phys 122:163–170
128. Dmitriev YuA (2005) EPR of matrix isolated methyl radicals. J Low Temp Phys 139:541–549
129. Davis S, Anderson DT, Duxbury G, Nesbitt DJ (1997) Jet- cooled molecular radicals in slit supersonic discharges: sub- doppler infrared studies of methyl radical. J Chem Phys 107:5661–5675
130. Dmitriev YA, Zhitnikov RA (2003) EPR spectra and rotation of CH_3, CH_2D, CHD_2, and CD_3 radicals in solid H_2. Low Temp Phys 29:519–521
131. Dmitriev YA (2005) EPR spectra of deuterated methyl radicals trapped in low temperature matrices. Low Temp Phys 31:423–428
132. Benetis NP, Dave P, Goldfarb D (2002) Characteristics of ESEEM and HYSCORE spectra of $S > 1/2$ centers in orientationally disordered systems. J Magn Reson 158:126–142
133. Freed JH (1979) In: Dorio MM, Freed JH (eds) Multiple electron resonance spectroscopy. Plenum Press, New York
134. Stillman AE, Schwartz LJ, Freed JH (1980) Direct determination of rotational correlation time by electron-spin echoes. J Chem Phys 73:3502–3503
135. Kispert LD, Bowman MK, Norris JR, Brown MS (1982) Electron spin echo studies of the internal motion of radicals in crystals: phase memory vs correlation time. J Chem Phys 76: 26–30

136. Dzuba SA, Maryasov AG, Salikhov KM, Tsvetkov YuD (1984) Superslow rotations of nitroxide radicals studied by pulse EPR spectroscopy. J Magn Reson 58:95–117
137. (i) Kulik LV, Dzuba SA, Grigoryev IA, Tsvetkov YD (2001) Electron dipole-dipole interaction in ESEEM of nitroxide biradicals. Chem Phys Letts 343:315–324; (ii) Kulik LV, Grigor'ev IA, Salnikov ES, Dzuba SA, Tsvetkov YD (2003) Electron spin-echo envelope modulation induced by slow intramolecular motion. J Phys Chem A 107:3692–3695
138. Sørnes AR, Benetis NP (1998) Theory of electron spin-echo envelope modulation in isotropic tunneling methyl rotor systems. Chem Phys Lett 287:590
139. Dikanov SA, Tsvetkov YuD (1992) Electron spin echo envelope modulation (ESEEM) spectroscopy. CRC Press, Boca Raton
140. Gamliel D, Freed JH (1990) Theory of two-dimensional ESR with nuclear modulation. J Magn Reson 89:60–93
141. Yudanov VF, Salikhov KM, Zhidomirov GM, Tsvetkov YuD (1969) Modulation effects in the electron spin echo of biradical systems. Teor Eksp Khim 5:663–668
142. Romanelli M, Kevan L (1997) Evaluation and interpretation of electron spin-echo decay Part I: Rigid samples. Concept Magn Reson 9:403; ibid (1998) Evaluation and interpretation of electron spin echo decay Part II: Mol Motions 10:1
143. Fotakis Ch, Christodouleas D, Zoumpoulakis P, Kritsi E, Benetis NP, Mavromoustakos T, Reis H, Gili A, Papadopoulos MG, Zervou M (2011) Comparative biophysical studies of Sartan class drug molecules Losartan and Candesartan (CV-11974) with membrane bilayers. J Phys Chem B 115:6180–92
144. (i) Theodoropoulou E, Marsh D (1999) Interactions of angiotensin II non-peptide AT1 antagonist losartan with phospholipid membranes studied by combined use of differential scanning calorimetry and electron spin resonance spectroscopy. Biochim Biophys Acta 1461:135–146; (ii) Theodoropoulou E, Marsh D (2000) Effect of angiotensin II non-peptide AT1 antagonist losartan on phosphatidyl ethanolamine membranes. Biochim Biophys Acta 1509:346–360
145. Chernova DA, Vorobiev AKh (2009) Molecular mobility of nitroxide spin probes in glassy polymers. Quasilibration model. J Polym Sci, Part B: Polym Phys 47:107–120
146. Shibaeva RN (1975) Structure of organic paramagnetic nitroxyl radicals. J Struct Chem 16:318–332
147. Herzog B, Hahn EL (1956) Transient nuclear induction and double nuclear resonance in solids. Phys Rev 103:148–166
148. Owenius R (2001) Studies of local interactions between and within proteins using site-directed labeling techniques. Dissertation, Linköping University, Sweden

Chapter 4
Deuterium Labeling Studies and Quantum Effects of Radicals in Solids

Masaru Shiotani and Kenji Komaguchi

Abstract Recent progress in deuterium (D or ^{2}H) labeling studies of radicals in the solid state is reviewed. Emphasis is placed on quantum effects at low temperature. The high-resolution EPR (ESR) spectra of selectively D-labeled methyl radicals were radiolytically generated together with a hydrogen atom methyl radical pair in an Ar matrix at cryogenic temperatures. The methyl radical spectra are discussed in terms of nuclear spin-rotation couplings using a three-dimensional free quantum-rotor model. A hydrogen atom hydrogen molecule ($H\cdots H_2$) pair formation in Ar is discussed in terms of D-isotope effects on quantum mechanical tunneling reaction. The H_2 molecule as a "quantum solid" for high-resolution EPR spectroscopy is presented. D-effects on zero-point vibrational energy (ZPVE) are presented in combination with Jahn-Teller (*J*-*T*) distortion of some chemically important radical cations of methane, tetramethylsilane, cyclohexane and related radical cations whose mother molecules have high symmetrical structures such as T_d and D_{3d}. D-isotope effects on methyl group conformations are exemplified using selectively deuterated dimethylether and monofluoromethane radical cations; the experimental results were also interpreted in terms of ZPVE incorporated with the mass difference of the two hydrogen isotopes. Furthermore, a D-labeling study on bimolecular homolytic substitution (S_H2) reactions by methyl radical in solid methylsilane (CH_3SiH_3) is presented.

M. Shiotani (✉) • K. Komaguchi
Department of Applied Chemistry, Graduate School of Engineering,
Hiroshima University, Higashi-Hiroshima, Japan
e-mail: mshiota@hiroshima-u.ac.jp

A. Lund and M. Shiotani (eds.), *EPR of Free Radicals in Solids I*, Progress in Theoretical Chemistry and Physics 24, DOI 10.1007/978-94-007-4893-4_4,

4.1 Introduction

Static and dynamic structures and physical-chemical properties of reaction intermediates such as ionic and neutral radicals have attracted much attention because they play an important role in chemical reactions [1–13]. In the previous book, "Radical Ionic Systems: Properties in Condensed Phases" [2], we presented a chapter about "Deuterium labeling studies of cation radicals". In that chapter we have noted as follows: Use of selectively deuterium (D or ^{2}H) labeled compounds is essential for an unequivocal assignment of the EPR (ESR) spectra of organic radicals because of the difference in magnetic properties, *i.e.* nuclear spin and magnetic moment, between ^{1}H- and D-atoms. In addition the D-labeling is expected to give rise to important isotope effects on the static and dynamic structures of the radicals due to the mass difference, *i.e.* D-isotope effects. However, only a limited number of molecules have been subjected to D-labeling EPR studies because the synthesis of D-labeled compounds is often difficult and troublesome, time consuming and expensive.

In the last two decades considerable progress has been made in this field, *i.e.* strong and clear D-isotope effects have been observed on structures, conformations, molecular dynamics and reactions of organic radicals. In this chapter we review "D-labeling studies and quantum effects of radicals in low temperature solids". Here, in terms of "quantum effects" we present some topics related to "nuclear spin-rotation couplings" [14–22] associated with "the Pauli principle" [16, 18], "quantum tunnelling" [2, 11, 23], "H_2 molecule as a quantum solid" [24, 25], "Jahn-Teller (*J-T*) or *pseudo J-T* distortion" [1, 2, 5, 26–42] *etc*. In most cases, D-isotope effects on zero-point vibrational energy (ZPVE) play an important role. We emphasize that low temperature matrix-isolation EPR methods are useful to study "quantum effects" of radicals in solids.

The first three sections address quantum effects in high-resolution EPR of D-labeled radicals in either solid argon (Ar) or H_2 matrix at low temperature. In Sect. 4.2 we present high-resolution EPR spectra of selectively D-labeled methyl radicals, CH_3, CD_3, CHD_2 and CH_2D [14]. The experimental EPR spectra are explained in terms of nuclear spin-rotation couplings using a three-dimensional free quantum-rotor model. An application of the Pauli principle in combination with D_3 point group symmetry results in important selection rules for the EPR transitions of D-labeled methyl radicals. In addition, we present high-resolution EPR spectra and the characterization of a hydrogen atom methyl radical pair ($H\cdots CH_3$) generated radiolytically in Ar [43]. Section 4.3 deals with hydrogen atom hydrogen molecule ($H\cdots H_2$) pair formation reactions in solid Ar [23, 44]. The reactions can proceed *via* quantum mechanical tunnelling in which D-isotope effects play a critically important role. Section 4.4 deals with solid H_2 molecules as a "quantum solid" for high-resolution EPR spectroscopy. In addition to some small organic radicals in the *para*-H_2 matrix, partial orientation and motional dynamics of stable NO_2 as a spin probe in the solid H_2 matrix are presented [45]. Furthermore, the formation of H_6^+ radical cations in the irradiated solid para-H_2 matrix and the identification of the cations using the D-labeling method are presented [46, 47].

Further, we present distorted structures of some small organic radical cations due to *J-T* or *pseudo J-T* effects, where D-isotope effects on ZPVE of a C–H bond stretching vibration [26, 33, 35] play a key role. Section 4.5 is concerned with ^{1}H/D isotope effects on ZPVE combined with *J-T* distortion of radical cations such as methane radical cations [34, 35] and tetramethylsilane radical cation (TMS^+) [31, 36, 48, 49] whose mother molecules have degenerate highest occupied molecular orbitals (HOMO) in a high symmetrical structure of T_d or D_{3h}. Section 4.6 presents D-labeling EPR studies of selectively deuterated dimethylether (DME) [26] and monofluoromethane (CFH_3) [50, 51] radical cations in combination with *ab initio* and density functional theory (DFT) calculations, where D-effects on methyl group conformations are demonstrated. The D-isotope effects on temperature-dependent ^{1}H *hf* splittings can be interpreted in terms of ZPVE incorporated with the mass difference of the two hydrogen isotopes. In Sect. 4.7 we further discuss D-effects of ZPVE on static and dynamic *J-T* distortions of chemically important cyclohexane radical cations (cC6$^+$) using selectively deuterated compounds [5, 28, 29]. Asymmetrically distorted structures of alkane radical cations due to *pseudo J-T* effects are also demonstrated by the EPR studies using partially deuterated silacyclohexane (cSiC5) radical cations [27, 41, 42].

In the last section, we present our recent D-labeling study showing direct EPR evidence for the bimolecular homolytic substitution (S_H2) reactions by methyl radicals in the solid methylsilane (CH_3SiH_3) at cryogenic temperatures [52–54]. Furthermore enormously large ^{1}H/D isotope effects on H-atom abstraction from CH_3SiH_3 are presented.

4.2 High-Resolution EPR and Nuclear Spin-Rotation Coupling of Methyl Radicals

This section deals with high-resolution isotropic EPR spectra of D-labeled methyl radicals radiolytically generated and isolated in solid argon (Ar) matrix at a low temperature range of 4.2–40 K [14].

The methyl radical is the most simple and fundamentally important alkyl radical and its EPR spectra under different conditions have attracted much attention: they include methyl radicals isolated in inert gas matrices [55–58], adsorbed on solid surfaces [59, 60], and trapped in organic media [61–63] at low temperatures. Quantum effects of the methyl radical itself have not been reported previously although the tunneling rotation of methyl hydrogens in β-proton systems (·CRR'-CH_3) have been reported [15–22]. On the other hand, among all available inert gases, Ar is potentially capable of providing one of the most appropriate matrices to observe high-resolution EPR spectra because it has no nuclear spin, including all stable isotopes. However, even in an Ar matrix, EPR spectra of the CH_3 radical reported earlier [57, 58] did not distinctly reflect its intrinsic high-resolution potential because of, for example, unresolved super-hyperfine (*hf*) splittings due to ^{127}I ($I = 5/2$) atom concomitantly generated with the CH_3 radical by photolysis of

methyl iodide (CH_3I) in the matrix. In order to prevent such unnecessary broadening of the EPR spectra due to the interactions between the CH_3 radical and other radicals or molecules, we employed the X-ray radiolysis of an Ar matrix containing selectively deuterated methanes at 4.2 K to generate the radical [14]. The high-resolution EPR spectra observed for CH_3, CD_3, CHD_2 and CH_2D are explained in terms of a three-dimensional free quantum-rotor model; *that is*, in contrast to the β-proton systems, the ^{1}H *hf* coupling is isotropic in its intrinsic nature and no hindering barrier for the rotation is present. The problem can be treated theoretically in terms of nuclear spin-rotation couplings associated with the Pauli principle and results in an interesting exclusion of EPR transitions for the selectively deuterated methyl radicals [14].

In addition to the isolated methyl radicals, high-resolution EPR spectra of a hydrogen atom methyl radical pair ($H\cdots CH_3$) were observed for X-ray irradiated Ar mixed with methanes at 4.2 K [43]. The EPR spectra of the radical in a triplet state are characterized by a forbidden transition at $\Delta m_s = \pm 2$ and an electron–electron dipole transition at an allowed $\Delta m_s = \pm 1$ band. The latter makes it possible to evaluate the separation distance of the paired radicals and discuss their orientation in space.

4.2.1 EPR Spectra of Methyl Radicals in Solid Argon: CH_3, CH_2D, CHD_2 and CD_3

Figure 4.1 shows the high-resolution isotropic EPR spectra of the D-labeled methyl radicals, CH_3, CH_2D, CHD_2 and CD_3, isolated in a solid Ar matrix at 4.2 and 20 K [14].

4.2.1.1 CH_3 Radical

A highly resolved quartet EPR spectrum with an equal-intensity was observed below 6 K and attributed to the isolated CH_3 radical with isotropic ^{1}H *hf* splitting of 2.315 mT (after the second-order *hf* correction): A_1-lines in D_3 symmetry. Upon increasing the temperature above 12 K, a new doublet, *E*-lines, with the identical *hf* splitting appeared at $m_F = \pm 1/2$ positions. The line positions were 0.024 mT higher than the inner $m_F = \pm 1/2$ lines of A_1-lines: the difference in the resonance lines originates from the second-order *hf* shift between the total nuclear spins of $F = 1/2$ (*E*-lines) and $F = 3/2$ (A_1-lines). The intensity of the *E*-lines increased with increasing temperature and became two times stronger than that of $m_F = \pm 1/2$ (A_1-line) at 40 K. Based on the temperature dependence of the *E/A* intensity ratio, an effective rotational energy splitting between the *A* and *E* levels in the matrix were discussed. Because of the very high spectral resolution with a linewidth of 0.007 mT, the spectra of CH_2D radicals as well as of $^{13}CH_3$ were clearly observed with their natural abundance of 0.015% (D) and 1.1% (^{13}C) at 20 K.

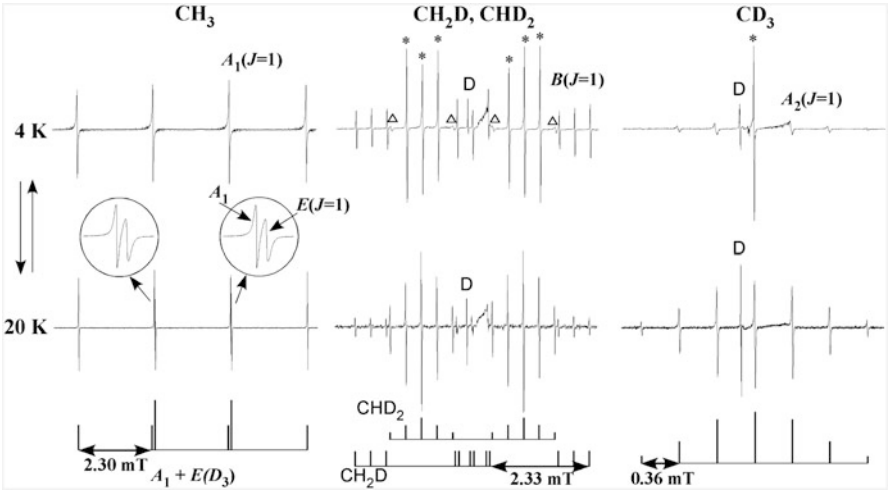

Fig. 4.1 The high-resolution EPR spectra of CH_3 (*left*), CH_2D and CHD_2 (*middle*) and CD_3 (*right*) were observed in an Ar matrix at 4.2 and 20 K. The radicals were generated by X-ray irradiation of the Ar matrix containing *ca.* 0.1 mol% CH_4, CH_2D_2, or CD_4. At the lower temperatures close to 4.2 K, the EPR lineshapes of these radicals are dominated by *hf* patterns with anomalous intensity, attributed to quantum effects [14]

4.2.1.2 CD_3 Radical

Quantum effects of the perdeuterated methyl radical CD_3 on the EPR lineshape were also observed. A strong singlet was superimposed on the central peak of the septet with *hf* splitting of 0.359 mT. The septet shows a relative intensity ratio of 1.0:3.8:7.0:105:8.7:4.3:1.5 at 4.1 K; the ratio is close to a binomial intensity of 1:3:6:7:6:3:1 except for the central line. It was concluded that the CD_3 spectrum was observed with the superposition of a "classical" high-temperature spectrum due to a freely rotating CD_3 with a very strong transition at the central line. Obviously the CD_3 (D: *boson* with $I = 1$) spectra behave very much differently from the CH_3 spectra. The central line intensity rapidly decreased with increasing temperature and the spectral intensity already reached the binomial one at 10 K.

4.2.1.3 CH_2D and CHD_2

Partially deuterated methyl radicals, CH_2D and CHD_2, were generated in the Ar matrix using CH_2D_2 as a solute. The 4.2 K spectrum of the CHD_2 radical consists of a double quintet due to one ^{1}H-atom and two D-atoms with *hf* splittings of 2.315 and 0.359 mT, respectively. The central triplet of the quintet has a narrower linewidth of 0.01 mT and a very strong transition at $m_F = 1, 0, -1$ with a 1:1:1 intensity ratio, whereas the outer two lines (at $m_F = \pm 2$) have about four times broader linewidths. Upon warming to 10 K, the peak intensities were rapidly changed and reached a binomial one of 1:2:3:2:1 which were attributable to a freely rotating CHD_2.

On the other hand, the 4.2 K CH_2D spectrum is a triple triplet due to two equivalent ^{1}H-atoms and one D-atom. The triplet *hf* lines due to the two ^{1}H-atoms are of equal intensity, but not of a binomial one, 1:2:1. Similarly to the case of CH_3, upon warming above 15 K, three new *hf* lines became visible at the higher field side of each of the central triplet by 0.024 mT and the relative intensity of the new line to the old line reached a limiting value of 1:1 at 40 K (Fig. 4.1). The relative spectral intensity ratio of [CHD_2] *vs.* [CH_2D] is *ca.* 8:1 at 4.2 K. The value is quite different from a statistical value of 1:1 expected from CH_2D_2 molecule used as a solute. The result indicates that light hydrogen (^{1}H) can be detached from the methane molecule much easier than the deuterium.

4.2.2 Nuclear Spin-Rotation Couplings

Applying the Pauli principle the observed 1:1:1:1 quartet (A_1-lines) of CH_3 (^{1}H: *fermion* with $I = 1/2$) is attributable to the four totally symmetric A_1 nuclear spin states coupled with the rotational ground state, $J = 0$, in D_3 symmetry [14, Chapter 3]. On the other hand, the *E*-lines are attributable to the nuclear spin states coupled with the $J = 1$ rotational state [14]. In the earlier study of β-proton rotors with C_{3v} symmetry ($^{\bullet}CR_1R_2$-CH_3 type of radical) [16–18] the isotropic *hf* splitting of a quadratic cosine form couples the degenerate rotational states with projections $J_z = \pm 1$ and split them, giving the characteristic triplet called *E*-lines. For the present D_3 rotor the *E*-lines, however, are almost superimposed on the A_1-lines at $m_F = \pm 1/2$.

The CD_3 radical at 4 K shows an abnormally strong singlet at the center of the spectrum. Consistent with this observation, the Pauli principle allows only one spin-rotation state at the lowest rotational level $J = 0$ with the anti-symmetric nuclear spin function of A_2 in D_3 symmetry [14]. For the same reason as for the CH_3 radical, the expected *E*-lines do not shift from their original positions, but are superimposed on the A_2-lines. Here the second order *hf* shifts are not of significance because of the 6.5 smaller *hf* splitting of the deuteron (D) than of the proton (^{1}H). Note that, on the contrary, the CD_3 rotor in C_{3v} symmetry (β-CD_3) is expected to show the intensity ratio of 1:2:2:3:2:2:1 for *A*-lines (A_2 for D_3 symmetry) at $J = 0$.

The reader can refer to Refs. [13, 14, Chapter 3] for the nuclear spin-rotation couplings in CH_2D and CHD_2 radicals and for details on the temperature dependence of the relative intensity of the *E*-lines to the A_1-lines in CH_3 radical.

4.2.3 Radical Pair of H···CH_3 in Solid Argon

A singlet molecule decomposes into a pair of doublet species (radicals) by ionizing radiation (or photolysis), and a pairwise trapping of radicals is inherent in radiation damage processes. When a pair of radicals is trapped with a distance less than *ca.*

2 nm, a singlet or triplet state of radical pairs is formed, the latter being observed by EPR. A number of EPR studies have been reported for the radical pairs generated in irradiated organic crystals, which include a pioneer work on a dimethylglyoxime single crystal by Kurita [64]. However, a limited number of EPR studies have been carried out on the radical pairs of fundamentally important primary organic species such as an "H-atom methyl radical" pair (H···CH_3) trapped in organic compounds. Gordy et al. have first presented an EPR spectrum attributable to the H···CH_3 radical pair separated by one methane molecule in irradiated solid methane at 4.2 K [65]; the separation distance of 0.68 nm has been evaluated from the observed axially symmetric electron–electron dipole coupling tensor. Toriyama et al. have reported the spatial distribution of the H···CH_3 (D···CD_3) pair in irradiated solid CH_4 (CD_4) at 4.2 K [66]. Here we present highly resolved EPR spectra of selectively D-labeled radical pairs trapped in irradiated solid Ar matrices [43].

As mentioned in the above section, the high-resolution EPR spectra of a series of D-labeled methyl radicals were observed for X-irradiated solid Ar incorporated with various D-labeled methane molecules such as CH_4, CH_2D_2 and CD_4 at 4.2 K [43]. When the irradiated samples were recorded with higher microwave powers and amplitude gains, the EPR spectra due to the triplet radical-pairs such as H···CH_3, H···CHD_2, D···CH_2D and D···CD_3 were clearly observed at both bands of the allowed $\Delta m_s = \pm 1$ and the forbidden $\Delta m_s = \pm 2$ transitions in addition to the spectra of isolated H (D) atoms and CH_3 (CH_2D, CHD_2 and CD_3) radicals.

Here we focus on the high-resolution spectra of H···CH_3 radical pairs. Three different sets of doublets with 25.1–26.3 mT splittings, which were further split into a quartet with 1.16 mT, were observed at the $\Delta m_s = \pm 2$ band. The splittings for the double-quartets are very close to one-half of the isotopic ^{1}H *hf* splittings typical of isolated H-atoms ($a_{iso} = 51.8$ mT) and CH_3 radicals ($a_{iso} = 2.3$ mT). This leads us to attribute the observed double-quartets to the triplet state of the H···CH_3 radical pair, which lies below the singlet state by $2J$ (the singlet-triplet separation) with $|J| \gg a_{iso}$(isotropic *hf* splitting of H atom) = 1.4 GHz. At the allowed $\Delta m_s = \pm 1$ transition, the ^{1}H *hf* lines with one-half of a_{iso}(H) and a_{iso}(CH_3) splittings are further split into anisotropic doublets due to $d_{||}$ and d, parallel and perpendicular components of the electron–electron dipole coupling (*i.e.* zero-field splittings). At least three different sets of fine structure parameters, d (= |–d|, d: the perpendicular component of the fine structure coupling tensor) = 4.2, 4.9 and 5.1 mT, were clearly resolved in the spectrum. The formation of the radical pairs was further confirmed by observing the corresponding spectra of D···CD_3 radical pairs for irradiated CD_4 in Ar, and H···CHD_2 and D···CH_2D pairs for irradiated CH_2D_2 in Ar, see Fig. 4.2 [43]. Noteworthy is that only two distinct pairs, H···CH_3 and D···CD_3 were observed for the equimolar mixture of CH_4-CD_4 system (Fig. 4.2a). The result demonstrates that the hydrogen atom and the methyl radical formed in pairs originate from the same methane molecule.

The separation distance R between the H atom and the CH_3 radical in pair can be evaluated from the experimental value of d using the following relation based on the assumption of a point-dipole interaction model: $R = (3g\beta/2d)^{1/3}$, where g is the g-value of the radical and β is the Bohr magneton of the electron [67].

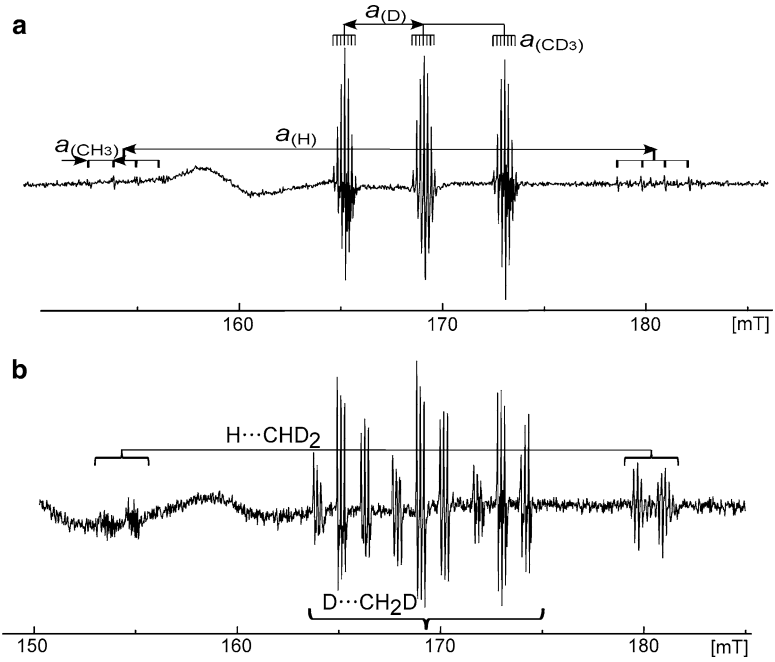

Fig. 4.2 EPR spectra ($\Delta m_s = \pm 2$) of "hydrogen atom methyl radical" pairs trapped in a solid Ar matrix at 4.2 K. (**a**) H···CH_3 and D···CD_3, (**b**) H···CHD_2 and D···CH_2D. The radical pairs were generated by X-ray irradiation to the solid Ar mixed with CH_4–CD_4 (0.25 mol% each) and CH_2D_2 (0.5 mol%), respectively. The broad singlet at *ca.* 160 mT comes from unidentified triplet species (Adapted from Ref. [43] with kind permission of © The American Chemical Society 2007)

Replacing d by the observed values of 4.2, 4.9 and 5.1 mT, the separation distances of $R = 0.87$, 0.83, and 0.82 nm are evaluated, respectively. It is known that there are three different trapping sites in the solid Ar, *i.e.* the interstitial tetrahedral site (I_t), the interstitial octahedral site (I_o), and the substitutional site of the *fcc* lattice [43]. Assuming that the CH_3 radical as a counterpart occupies a substitutional site that the mother molecule is expected to originally occupy, the most probable location of the counter H-atom is the I_t site directed away from the methyl radical by a distance of 0.87 nm or the I_o site by a distance of 0.88 nm. The calculated distances well correspond to the experimental R values, especially $R = 0.87$ nm, see Fig. 4.3. The observed H-atom gives a *hf* splitting of 51.8 mT after the second-order *hf* correction; the splitting being significantly larger than that in the gas phase, 50.8 mT. It is known that the H-atom, which is trapped in a narrower site such as the interstitial tetrahedral one, generally gives a larger ^{1}H *hf* splitting than the gas-phase splitting [23, 68, 69]. This provides an additional support for the suggested trapping site of the coupled H-atom.

In the end we note that the radical pairs of H···NH_2 and D···ND_2 trapped in solid Ar and Kr at 4 K have been observed by EPR [70]. Furthermore, Knight

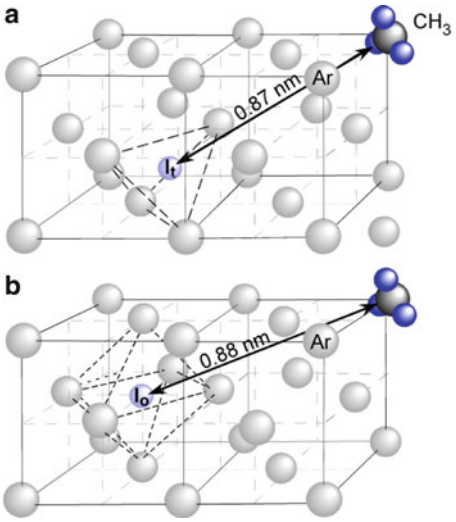

Fig. 4.3 Schematics showing proposed trapping sites for the H···CH_3 radical pair with $d = 4.2$ mT (*i.e.*, $R = 0.87$ nm) in solid Ar. The CH_3 radical occupies a substitutional site in the Ar crystalline lattice (*fcc*). The counter H-atom occupies either (**a**) the interstitial tetrahedral site, I_t, at a distance of 0.87 nm from the CH_3 radical, or (**b**) the interstitial octahedral site, I_o, at a distance of 0.88 nm, or both

and his collaborators have reported EPR studies on the triplet state radical pairs of D-substituted hydrogen atoms, H···H, H···D and D···D generated and trapped in rare gas matrices at 4.2 K and discussed the results in terms of a theoretical model treating these spin-pairs as weakly interacting atoms [71, 72]. The triplet radical pairs of isotope substituted nitrogen atoms, $^{14}N\cdots{}^{14}N$, $^{14}N\cdots{}^{15}N$ and $^{15}N\cdots{}^{15}N$ have also been reported by Knight et al. [73].

4.3 Hydrogen Atom Hydrogen Molecule Complex Formation in Solid Argon

As mentioned in the foregoing section, Ar can potentially provide a suitable matrix for high-resolution EPR because all the stable isotopes of Ar have a nuclear spin quantum number of $I = 0$ and are chemically inert. In addition, the closest inter-atomic distance of solid Ar with the face center cubic (*fcc*) structure is 0.376 nm, which is almost the same as that of a solid hydrogen molecule with the hexagonal close-packed (*hcp*) structure, 0.379 nm [68, 69]. Thus, the H_2 molecules incorporated are expected to disperse homogeneously in the solid Ar and occupy its substitutional site. Hydrogen atoms were generated in a solid Ar matrix at cryogenic temperatures by means of X-ray radiolysis and subjected to an EPR study on fundamental reaction processes between the hydrogen atom and the hydrogen molecule. Super-*hf* couplings due to an H_2 molecule were observed for the H-atoms generated in the solid Ar matrix and discussed in terms of a hydrogen atom hydrogen molecule pair formed *via* tunneling reactions. D-labeling and quantum effects on the pair formation in the Ar matrix are presented.

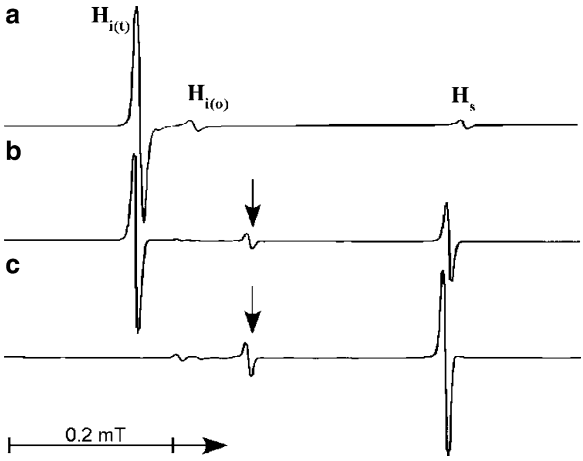

Fig. 4.4 Temperature dependence of the low-field components of the EPR spectra observed for H-atoms in a solid Ar matrix containing *ca.* 1.0 mol% H_2; (**a**) observed at 4.2 K just after X-ray radiolysis at the same temperature, (**b**) observed at 13 K after annealing the sample from 4.2 K, and (**c**) observed at 20 K (Adapted from Ref. [23] with kind permission of © Elsevier 1997)

4.3.1 Hyperfine Splittings and Locations of H-Atoms

Figure 4.4 shows low-field components of the EPR spectra of H-atoms generated by the X-ray radiolysis and trapped in a solid Ar matrix at 4.2 K. Three different doublet spectra with ^{1}H *hf* couplings, 51.54 mT, 51.42 mT, and 50.73 mT are visible in the spectra [23]. The ^{1}H *hf* couplings larger than the theoretical value, 50.8 mT, in the gas phase suggest that the H-atoms are trapped in the narrower sites in the solid Ar matrix as a result of the Pauli exclusion effect in preference to the van der Waals attraction interaction. Referring to this suggestion the observed H-atoms are attributable to those trapped in three different sites, *i.e.* interstitial tetrahedral site ($H_{i(t)}$), interstitial octahedral site ($H_{i(o)}$), and substitutional site (H_s), respectively. Immediately after the radiolysis (Fig. 4.4a) the doublet with 51.54 mT splitting gives rise to the most intense spectrum, suggesting that more than 90% of H-atoms generated predominately occupy the narrowest $H_{i(t)}$ site.

On annealing the sample to 13 K, the H-atoms in $H_{i(t)}$ can migrate to H_s sites with concomitant decrease in the total number of radicals due to the recombination reaction, $H + H \rightarrow H_2$. The migration is completed below 20 K. On the other hand, a new doublet with a ^{1}H *hf* coupling of 51.18 mT, indicated by the arrow in Fig. 4.4, appeared at 13 K. Figure 4.5 shows the low-field components of the EPR spectra at 20 K corresponding to the newly appeared H- and D-atoms in an Ar matrix containing small amount of H_2, D_2 and HD. In turn, the peak with the strongest intensity (Fig. 4.4c) is attributable to H-atoms in the substitutional site. In a solid Ar matrix containing HD, the doublet further splits into isotropic nine lines with super-*hf* splittings of 0.068 mT and 0.062 mT for the outer three and inner three lines, respectively; the relative peak intensity is 1:1:2:1:2:1:2:1:1, see Fig. 4.5c. This observation is in a sharp contrast with the doublets without any super-*hf* splittings observed for the Ar matrix containing H_2 (see Fig. 4.5a). On the other hand, the five isotropic super-*hf* lines with 0.062 mT splitting with a relative intensity of 1:1:2:1:1

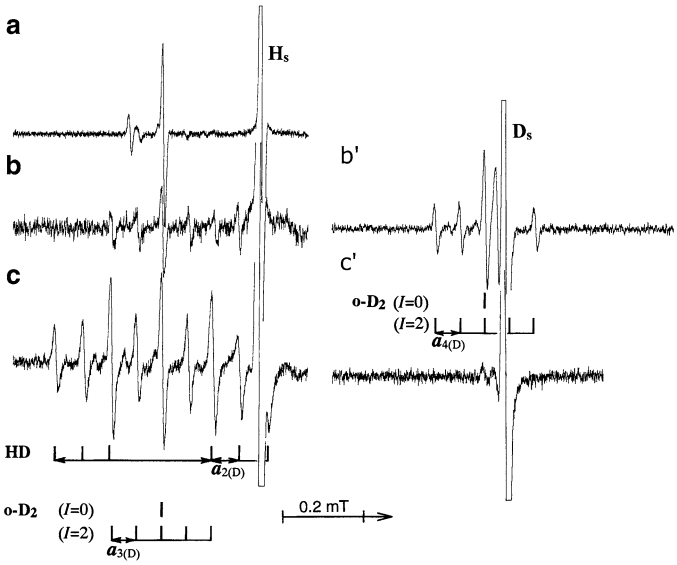

Fig. 4.5 Low-field components of the EPR spectra observed for H-atoms (*left column*) and D-atoms (*right column*) in a solid Ar matrix containing (**a**) 1.0 mol% H_2, (**b**) 1.0 mol% D_2, and (**c**) 3.3 mol% HD at 20 K; $a_1(H) = 0.386$ mT, $a_2(D) = 0.068$ mT and $a_3(D) = a_4(D) = 0.062$ mT. The H- and D-atoms were produced by X-ray radiolysis of the samples at 4.2 K (Adapted from Ref. [23] with kind permission of © Elsevier 1997)

were observed for the newly appeared D-atoms generated in the irradiated Ar matrix containing D_2 (Fig. 4.5b′) No super-*hf* signals were observed for the newly appeared D-atoms in the irradiated Ar matrix containing HD (see Fig. 4.5c′).

4.3.2 H···H_2 Complex Formation via Tunneling Reaction

During the migration of hydrogen atoms in the solid Ar containing HD, the H- and D-atoms may independently encounter an HD molecule isolated in a substitutional site (H_s). Reaction (4.1) is an exothermic process, whereas reaction (4.2) is an endothermic process [23, 44, 74, 75]. Then the D-atoms are expected to react with HD *via* a tunneling reaction (4.1) to produce an H-atom, which is trapped near the D_2 molecule. On the other hand the H-atom is expected to be merely trapped in the neighborhood of the HD molecule without producing a D-atom:

$$HD + D \rightarrow H + D_2 \tag{4.1}$$

$$HD + H \rightarrow D + H_2 \tag{4.2}$$

The super-*hf* structure with the apparent nine isotropic lines observed for the H-atom in the Ar matrix containing HD can be reasonably attributed to a superposition of two complexes, H···D_2 (products) and H···HD (reactants). The EPR spectrum expected for the latter complex is a double triplet with super-*hf* couplings of a_1(H) and a_2(D) as shown by the stick diagrams in Fig. 4.5c: a_1(H) being expected to be 6.514 times larger than a_2(D).

Now we concentrate on the H···D_2 complex. *Para*-D_2 (*p*-D_2) and *ortho*-D_2 (*o*-D_2) should be considered as a partner hydrogen molecule possibly forming a complex with the H-atom. The *p*-D_2 and *o*-D_2 can take rotational levels of $J = $ odd and $J = $ even, respectively, because deuterons are *bosons* with integral nuclear spin ($I = 1$) so that *o*-D_2 ($J = 0$) is more stable by *ca.* 85 K than *p*-D_2 ($J = 1$) in the ground state [25]. The conversion between *o*-D_2 and *p*-D_2 is expected to be forbidden without any magnetic interaction. The H and D-atoms can serve as magnetic perturbations to allow the adjacent *p*-D_2 to convert into *o*-D_2 in the lowest rotational level, $J = 0$, at low temperatures. As a result, the total nuclear spin quantum numbers, $I = 0$ and 2, can be allowed for the *o*-D_2 ($J = 0$) to give five isotropic lines of peak intensity 1:1:2:1:1 with a_3(D) for the H···D_2 complex; for the super-*hf* structure, a singlet due to *o*-D_2 ($I = 0$) and each of five lines due to *o*-D_2 ($I = 2$) are equal in intensity.

The above explanation is rationalized by the experimental result showing no super-*hf* structure being observed for the H···H_2 complex. This suggests that the *o*-H_2 molecule ($I = 1$) paired with an H-atom is converted into *p*-H_2 ($I = 0$). Furthermore the same super-*hf* pattern as that for the H···D_2 complex was observed for the D···D_2 complex (Fig. 4.5b′). We conclude that applying D-labeling in an EPR study of the solid H_2/Ar system, the complex formation between a hydrogen atom and a hydrogen molecule in the low temperature solid Ar matrix could be clearly demonstrated by observing the super-*hf* structure of the hydrogen atom, where the complex is in the lowest rotational state.

In the end we note that the unpaired electron spin density on each of the three H-atoms of the complex has been theoretically calculated as a function of distance between the H-atom and the H_2 molecule [23]. By comparing the observed super-*hf* coupling constants with the theoretical ones, the mean distance between the atom and the molecule was evaluated to be 0.173 nm. In the temperature range of 24.4–29.3 K, the complex decayed *via* a thermal activation process. The potential energy of 3.5 kJ mol^{-1} was experimentally evaluated for the complex in the solid Ar. The value is one-half of that for hydrogen atoms (6–7 kJ mol^{-1}) trapped in octahedral interstitial sites in the solid Ar at 16.2–17.2 K [76].

4.4 *Para*-H_2 Matrix and High-Resolution EPR Spectra

The solid hydrogen molecule is a well-known quantum solid [77] because of its large vibrational amplitude at zero-point energy level. Normal hydrogen (*n*-H_2) molecules consist of 25% *para*-hydrogen (*p*-H_2) and 75% *ortho*-hydrogen (*o*-H_2)

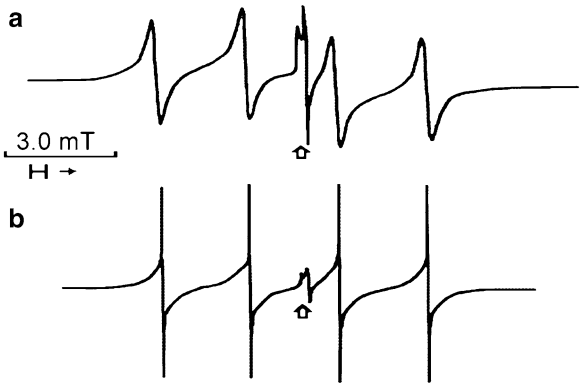

Fig. 4.6 EPR spectra of CH_3 radicals produced in the UV-illuminated H_2 and CH_3I (0.06 mol%) mixtures at 4.2 K. CH_3 radicals in n-H_2 (**a**) and in p-H_2 (**b**) (Adapted from Ref. [24] with kind permission of © Elsevier 1994)

molecules. The p-H_2 has a rotational quantum number of $J = 0$ at 4.2 K, whereas the o-H_2 has $J = 1$; as a result, the n-H_2 molecules are in rotational quantum states, $J = 0$ and 1, at 4.2 K. Interestingly, the abundance of the non-magnetic p-H_2 with I (total nuclear spin quantum number) = 0 can be enhanced by the conversion of the nuclear spin state of the magnetic o-H_2 with $I = 1$. For radicals trapped in the p-H_2 no intermolecular dipolar interaction can be expected between the electron spin and nuclear spin, *i.e.* no hyperfine interaction. Thus, the solid p-H_2 is potentially useful as a low temperature matrix for high-resolution EPR spectroscopy [24].

4.4.1 High-Resolution EPR Spectra of Small Organic Radicals in Solid p-H_2

Miyazaki and his co-workers first demonstrated that the EPR line width (0.011 mT) of H-atoms (H_t) trapped in the solid p-H_2 at 4.2 K is *ca.* three times narrower than that (0.034 mT) of H_t in the n-H_2 [78]. The difference in the line width originates from that in the dipolar *hf* interactions in the two matrices. As the nuclear spin I of p-H_2 is zero, no dipolar interaction between the electron spin (S) of H_t and the nuclear spins of the surrounding p-H_2 molecules can be expected. Thus the p-H_2 matrix can give rise to a narrow EPR linewidth. On the other hand, the o-H_2 molecules with $I = 1$ located near H_t in the n-H_2 matrix can cause linewidth broadening due to non-vanishing dipolar interaction.

The same group has further reported high-resolution EPR spectra of some small alkyl radicals, such as methyl and ethyl radicals, trapped in solid H_2 matrices [24, 79]. Figure 4.6 shows the spectra of CH_3 radicals generated by the UV photolysis of CH_3I in the n-H_2 and p-H_2 matrices at 4.2 K. The quartet spectrum of CH_3 in the solid p-H_2 matrix is much narrower (0.03 mT) than that in the n-H_2 (0.26 mT) similar to the case of the trapped hydrogen-atom (H_t) in the H_2 matrices. Ethyl radicals (C_2H_5) were also generated by UV photolysis of C_2H_5I isolated in solid p-H_2 [79]. Although the *hf* anisotropies due to α-H($-CH_2$) and

β-H($-CH_3$) partially remain in the EPR spectra of C_2H_5 in the temperature range between 3.1 and 6.7 K, the linewidth was as narrow as 0.02 mT, which is close to that (0.01 mT) of the isotropic spectrum in liquid ethane reported by Fessenden [80]. Small splittings attributable to the "*A*" and "*E*" transitions (refer to Sect. 4.2.1) were resolved in the spectrum; the former and latter stand for the lowest and second lowest rotational energy levels of the CH_3 group in C_2H_5 radicals, respectively. Based on the temperature dependence of the *E/A* intensity ratio, the rotational energy splitting between the *A* and *E* levels was evaluated to be 5.3 ± 0.7 K in the *p*-H_2 matrix. The narrower EPR line-width of C_2H_5 in *p*-H_2 is consistent with the absence of the dipolar *hf* interactions of the electron spin of a CH_3 radical with the nuclear magnetic moments of the matrix molecules.

4.4.2 H_6^+ Cation Formation in Irradiated Solid p-H_2

In a series of the pregnant research on solid H_2, Kumada and Kumagai, et al., have succeeded to observe EPR spectra of the H_6^+ radical cation which was generated and stabilized in irradiated solid *p*-H_2 matrix [46, 47, 81, 82]. The observed H_6^+ cation is better described as a $[H_2(H_2)H_2]^+$ ion with a D_{2d} symmetry, where the central H_2 is H_2^+-core, and the two H_2 molecules at both ends are side-on H_2 molecules, as described below. Theoretical calculations as well as D-labeling studies played an indispensable role for the spectral identification and dynamics of the radical cation.

Figure 4.7 shows EPR spectra observed at 4.2 K for a pure *p*-H_2 solid irradiated at the same temperature. The quartet *hf* lines separated by 20.44 mT marked as B_i (*i*: 1–4) in the figure were observed and attributed to the ^{1}H *hf* splitting due to two magnetically equivalent ^{1}H-atoms, which are clearly suggested by the second-order *hf* splittings [80] at the central two lines due to the two different nuclear states of $[I = 1, m_I = 0]$ and $[I = 0, m_I = 0]$. By comparing the experimental *hf* values with the theoretical ones the magnetically equivalent two ^{1}H-atoms with 20.44 mT *hf* splittings were attributed to the H_2^+-core of the H_6^+ cation ion [46, 81]. That is, the calculations predict that the most stable molecular ion complex of H_6^+ is a H_2^+-core with $[H_2(H_2)H_2]^+$ type of structure as depicted in Fig. 4.8. In the $[H_2(H_2)H_2]^+$ ion the central H_2^+-core is collinearly bound by two side-on H_2 molecules so as to be stabilized by charge-transfer interaction with the binding energy of 2.12 eV. Isotropic ^{1}H *hf* splittings of 20.08 and 10.26 mT were computed for the two equivalent H_2^+ core protons and for the four protons of the two side-on H_2, respectively, at the B3LYP/6-311+G(3df,3pd) level of calculations. The observed ^{1}H *hf* splitting (20.44 mT) is in good agreement with the theoretical one calculated for the H_2^+-core protons.

The ^{1}H *hf* splittings due to the two side-on H_2 molecules is, however, missing although a splitting of *ca.* 10 mT has been predicted by the calculations. This can be rationalized as follows. The rotational constant of H_2 (*ca.* 8 meV) is much larger

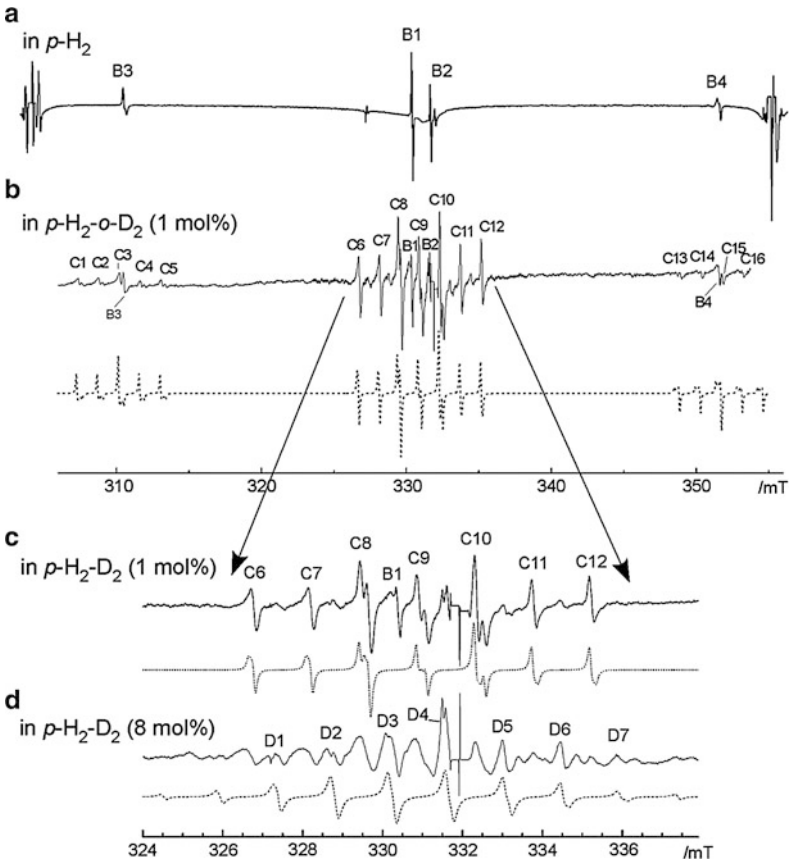

Fig. 4.7 EPR spectra of γ-ray irradiated solid p-H_2 (**a**), p-H_2 containing 1 mol% o-D_2 (**b**, **c**), and p-H_2 containing 8 mol% o-D_2 (**d**), together with simulated ones (*dotted lines*). The central part is expanded in (**c**) and (**d**) (The spectra were obtained from Drs. J. Kumagai and T. Kumada)

than the rotational barrier (1.4 meV) calculated for side-on H_2 along the main axis of H_6^+ and the thermal energy at 4 K (0.4 meV). Thus, almost all side-on H_2 molecules can rotate freely and only the $J = 0$ rotational state is possibly populated at 4.2 K [25]. In this case, like for the p-H_2 molecule, the side-on H_2 at $J_{sid}(H_2) = 0$ rotational level can be exclusively at the $I_{sid}(H_2) = 0$ state due to the parity conservation rule on exchanging the ^1H (*fermion*) species.

D-substitution of the side-on H_2 molecules could be much informative because the *hf* interactions with side-on D_2 or HD nuclei in $H_4D_2^+$ or H_5D^+ are possibly observed due to the parity conservation rule even if side-on D_2 or HD nuclei in $H_4D_2^+$ or H_5D^+ are in free rotational states [13, 81]. When o-D_2 (1 mol%) was added to the p-H_2 matrix, multiplets were visible at each B-line after γ-irradiation at 4.2 K (Fig. 4.7b, c). The spectrum was attributed to $[H_2(H_2)D_2]^+$ where one

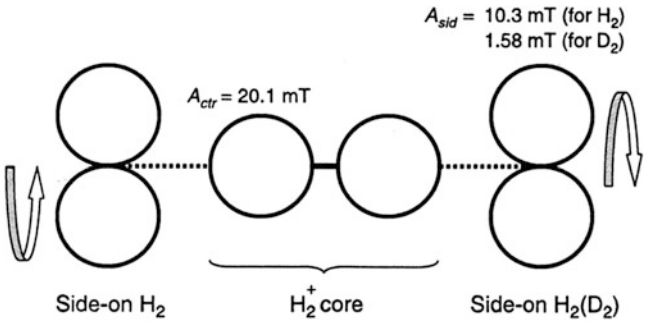

Fig. 4.8 Schematic representation of the molecular structure of H_2^+-core H_6^+ ($H_4D_2^+$). The structure is composed of the H_2^+-core sandwiched between two side-on H_2 (D_2) rotors directed perpendicular to the core axis (Reproduced from Ref. [46] with kind permission of © Elsevier 2006)

side-on H_2 is substituted isotopically by D_2. A further addition of *o*-D_2 (8 mol%) to the matrix led to an additional change in the super-*hf* structure, in accordance with the simulation of the spectra for $[D_2(H_2)D_2]^+$, *i.e.* a preferential formation of $[D_2(H_2)D_2]^+$ rather than $[H_2(H_2)D_2]^+$ (Fig. 4.7d). No trace of EPR signals due to $[H_2(D_2)H_2]^+$, $[H_2(D_2)D_2]^+$ and $[D_2(D_2)D_2]^+$ species was detected in the systems. The observed regioselective substitution of a side-on H_2 molecule by D_2 can be explained in terms of the difference in ZPVE between the reactant and product. The reaction (4.3), for example, is an exothermic process by 17 meV, while the substitution for the core-H_2 by D_2 is endothermic [47], being consistent with the observations.

$$[H_2\,(H_2)\,H_2]^+ + D_2 \rightarrow H_2 + [H_2\,(H_2)\,D_2]^+ + 17\,\text{meV} \tag{4.3}$$

$$[H_2\,(H_2)\,D_2]^+ + D_2 \rightarrow H_2 + [D_2\,(H_2)\,D_2]^+ + 18\,\text{meV} \tag{4.4}$$

Furthermore, the decay rate for H_6^+ at 4.2 K decreased depending on the number of D_2 introduced in the side-on position; $[H_2(H_2)H_2]^+$ decays much faster than $[D_2(H_2)D_2]^+$. In contrast, $[H_2(H_2)HD]^+$ and $[H_2(HD)H_2]^+$ were also observed in *p*-H_2–HD, suggesting that reaction energies for the HD substitutions are comparable to the thermal energy of 4 K (0.4 meV) in accordance with theoretical calculations [47, 81].

More noteworthy is that a small *hf* anisotropy was visible in the EPR spectra of $[H_2(H_2)H_2]^+$ and $[H_2(H_2)D_2]^+$ radical cations. The anisotropic splitting is *ca.* –0.06 mT for both species at 4.2 K, but the value is much smaller than the theoretical ones, 1.17–1.25 mT. On decreasing the temperature to 1.7 K, however, the anisotropic coupling increased to be 1.17 mT for $[H_2(H_2)D_2]^+$; the value is fairly close to the theoretical ones. Any change in the anisotropic *hf* splitting was not observed for $[H_2(H_2)H_2]^+$. The experimental results have been discussed in

terms of a precession motion of the H_6^+ ion in the *p*-H_2 matrix, where the H_6^+ ion is trapped in a single substitutional *hcp* cage consisting of eight triangular and six square planes of crystalline *p*-H_2 [82].

There are still some unsettled questions for the H_6^+ species in irradiated solid *p*-H_2 systems. However, the formation of $[H_2(H_2)H_2]^+$ in *p*-H_2 is a highly important and attractive finding, especially, for people working in the field of matrix isolation spectroscopy and molecular science of interstellar materials.

4.4.3 Partial Orientation and Dynamics of NO_2 in Solid H_2

NO_2 is one of few stable gaseous molecular radicals with one unpaired electron and is well established to have large anisotropy of both *A* and *g* tensors whose principal axes are coincident with the molecular ones [83, 84]. Thus NO_2 can be potentially useful as a spin probe to study motional dynamics of molecules in matrices. High-resolution EPR spectra of NO_2 trapped in the solid H_2 permitted us to discuss both on preferential orientation and rotational diffusion of NO_2 in the matrix [45].

A gaseous sample of *p*-H_2 molecules containing a small amount of NO_2 was prepared in a *Suprasil* EPR sample tube. The sample tip was cooled down to 4.2 K to condense the mixture gas for EPR measurements. EPR spectra of NO_2 observed in the solid *p*-H_2 matrix are shown in Fig. 4.9. The spectral lineshape at 4.2 K is analyzed in terms of an axial symmetric *A* and *g* tensor components: $g_{/\!/} = 2.0022$, $g_\perp = 1.9920$, and $A_{/\!/} = 5.85$ mT, $A_\perp = 5.04$ mT. The observed axial symmetric values are well correlated with the non-overall symmetric values of the rigid state NO_2 observed in a Ne matrix as follows: $g_{/\!/} \approx g_z$, $g_\perp \approx (g_x + g_y)/2$, and $A_{/\!/} \approx A_z$, $A_\perp \approx (A_x + A_y)/2$. This suggests that the NO_2 molecule rotates about the molecular z-axis with a frequency high enough to completely average out the *x* and *y* components ($\nu \gg |g_x - g_y| \approx 2$ MHz).

The spectral peak intensity was found to depend on the orientation of the sample cell to the external magnetic field (B_0). The orientation dependence was much enhanced when a flat sample tube was used. When the flat plane was parallel to B_0, the maximum and minimum intensities were obtained for the $A_\perp$ and $A_{/\!/}$ components, respectively. When the plane was perpendicular to B_0, the opposite orientation dependence was observed. The results suggest that the NO_2 molecule partially orients in the H_2 matrix to make its z-axis perpendicular to the flat plane of the cell even at a low temperature of 4.2 K. On increasing the temperature to 5.5 K, the NO_2 spectra disappeared irreversibly.

We propose the following model for the observed partial orientation and rotation of NO_2 in the solid hydrogen matrix. The NO_2 orients its C_2-axis to be parallel to the direction of the *c*-axis direction of the *hcp* crystalline lattice, to which the crystal preferentially grows during the sample cooling process to 4.2 K from room temperature. The N-atom of NO_2 may be favorably held by three H_2 molecules in the β-plane of the *hcp* crystalline lattice so as to allow NO_2 to rotate freely about the C_2-axis.

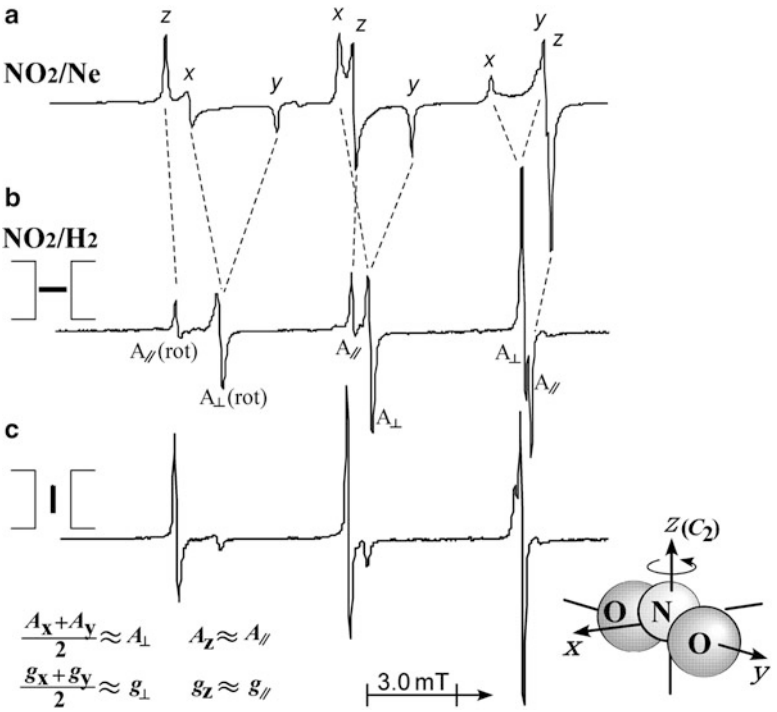

Fig. 4.9 EPR spectra of NO_2 (*ca.* 0.1 mol%) in (**a**) Ne and (**b** and **c**) *p*-H_2 matrices. Spectra (**b**) and (**c**) were recorded at the orientation of the flat sample plane parallel and perpendicular to the magnetic field, respectively. The molecular axes of NO_2 coincide with the principal directions of the *A* and *g* tensors

4.5 Jahn-Teller Distortion of T_d and D_{3h} Molecules and D-Isotope Effects

Tetrahedral molecules in T_d symmetry have a threefold degenerate t_2 highest occupied molecular orbital (HOMO). When they release one electron from the molecules, the degeneracy is lifted and the associated radical cations are formed having a lower symmetry of either C_{3v}, C_{2v} or D_{2d} due to the so called static Jahn-Teller (*J*-*T*) distortion [1, 2, 30–33]. In this section we deal with a C_{2v} structure distortion of methane [34, 35] and tetramethylsilane (TMS) [31, 36, 48, 49] radical cations from an original T_d symmetry. As for a C_{3v} distortion from T_d, the neopentane radical cation, $C(CH_3)_4^+$, can be a typical example [1–4, 85]. That is, the unpaired electron in $C(CH_3)_4^+$ is mainly located in one of the four C−C bonds. Three hydrogens, one at each of the other three methyl groups, in the trans position with respect to the C−C bond with the unpaired electron, gave large couplings of 4.2 mT. Furthermore, we deal with a structural distortion of the trimethylenemethane

Table 4.1 Experimental isotropic *hf* values of a_{iso} (mT) for ^{1}H and D in selectively D-labeled methane radical cations in neon at 4 K [35]. The experimental values of $a_{iso}(^1H)$ and $a_{iso}(D)$ were converted to $a_{iso}(D)^a$ and $a_{iso}(^1H)^b$*hf* "scales" by dividing and multiplying by the ratio of the ^{1}H and D nuclear *g*-factor, $g_H/g_D = 6.514$, respectively

	CH_4^+	CDH_3^+	$CD_2H_2^+$	CD_3H^+	CD_4^+
$a_{iso}(^1H)$	5.43	7.64	12.2	12.5	–
$a_{iso}(D)^a$: $a_{iso}(^1H)/(g_H/g_D)$	0.83	1.2	1.9	1.9	–
$a_{iso}(D)$	–	(−)0.22	(−)0.22	0.45	0.81
$a_{iso}(^1H)^b$: $a_{iso}(D)\cdot(g_H/g_D)$	–	(−)1.4	(−)1.4	2.9	5.3

radical cation (TMM^+) [13, 86, 87]. A precursor of TMM^+ is the neutral TMM biradical with a D_{3h} symmetry, which is in a triplet state with a doubly degenerate e'' HOMO in the ground state [88–90].

4.5.1 *Methane Radical Cations: CH_4^+, CDH_3^+, $CD_2H_2^+$, CD_3H^+ and CD_4^+*

Knight et al. observed EPR spectra of a series of selectively deuterated methane radical cations, CH_4^+, CDH_3^+, $CD_2H_2^+$, CD_3H^+ and CD_4^+, generated and stabilized in a neon matrix at 4 K [34, 35]. The observed isotropic *hf* coupling constants (a_{iso}) are summarized in Table 4.1. The $a_{iso}(^1H)$ value of 5.43 mT for ^{1}H in CH_4^+, divided by the ratio of the ^{1}H and D nuclear *g* factors, $g_H/g_D = 6.514$, yields an equivalent deuterium $a_{iso}(D)$ value of 0.83 mT. This value agrees well with the observed $a_{iso}(D)$ value of 0.81 mT for CD_4^+, in which all the ^{1}H-atoms are replaced with D-atoms. No unusual characteristics are evident. However, for the methane radical cations containing a mixture of ^{1}H- and D-atoms, *i.e.* CDH_3^+, $CD_2H_2^+$ and CD_3H^+, the simple conversion from the ^{1}H *hf* scale to the D *hf* scale using the appropriate ratio of *g*-factors does not account for the observed *hf* values. For example, in CDH_3^+ the observed $a_{iso}(^1H)$ value of 7.64 mT predicts a deuterium $a_{iso}(D)$ value of 1.2 mT which is considerably larger than the directly observed deuterium $a_{iso}(D)$ value of −0.22 mT. Furthermore the value of $a_{iso}(^1H) = 7.64$ mT observed for CDH_3^+ differs substantially from that observed for CH_4^+ (5.43 mT).

In order to account for the observed isotropic *hf* values of ^{1}H- and D-atoms, $a_{iso}(^1H)$ and $a_{iso}(D)$, the following rules (a)-(d) were proposed for the location of ^{1}H- and D-atoms in the radical cation [35]. (a) The methane radical cation possesses a C_{2v} type geometrical structure with two distinctly different electronic sites, *i.e.* apical "*a*" site and equatorial "*e*" site, see Fig. 4.10. (b) Site "*a*" can accommodate two ^{1}H- or D-atoms and is coplanar with the carbon *p*-orbital with an unpaired electron, whereas site "*e*" can accommodate two atoms and lies in the nodal plane of this same carbon *p*-orbital. (c) D-atoms prefer the nodal plane site "*e*" and ^{1}H-atoms prefer the co-planar site "*a*". (d) ^{1}H-atoms can exchange with other ^{1}H-atoms

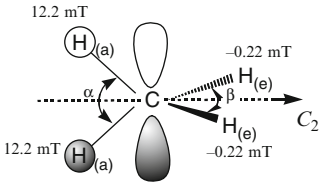

Fig. 4.10 Schematics of the C_{2v} geometrical structure in the CH_4^+ cation with the $^2B_1$ state. Sites marked as "*a*" are coplanar with the carbon *p*-orbital with an unpaired electron and sites "*e*" lie in the nodal plane of the *p*-orbital. ^{1}H-atoms prefer the co-planar "*a*" site and D-atoms favor the nodal plane site "*e*" [94]

even between the different sites, "*a*" and "*e*", but not with D-atoms, and D-atoms will likewise exchange with other D-atoms but not with ^{1}H-atoms in a different electronic environment. The orbitals of atoms that occupy the nodal plane site "*e*" cannot efficiently mix with the *p*-orbital. The *hf* interaction is dominated by a spin polarization mechanism so as to produce a small negative a_{iso} value. The 1*s* orbitals of the ^{1}H- and D-atoms in the co-planar site "*a*" can mix with this carbon *p*-orbital and yield a large positive a_{iso} value.

Based on the rules outlined above, the a_{iso}(D) values observed for D in CDH_3^+ and $CD_2H_2^+$ are almost the same and equal to −0.22 mT. There are two equivalent positions in the nodal plane site "*e*", which are strongly preferred by the D-atoms. Likewise for $CD_2H_2^+$ and CD_3H^+, the first two ^{1}H-atoms can occupy their preferred co-planar site "*a*" and exhibit a large *hf* coupling of 12.2 and 12.5 mT, respectively. Thus we can determine that $a_{iso}(^1H)$ for site "*a*" has a value of *ca.* 12.2 mT and $a_{iso}(^1H)$ for site "*e*" has a hydrogen equivalent value of −1.4 mT (−0.22 mT for D). A weighted average of these two basic a_{iso} values can account for the observed *hf* splittings. For CH_4^+, where H-atoms exchange with those in different sites, we have 5.39 mT $[(2 \times 12.2 - 2 \times 1.43)/4]$ *vs.* the experimental value of 5.43 mT. Furthermore, for CDH_3^+ such H-atom exchanges also occur and we have 7.66 mT $[(2 \times 12.2 - 1.43)/3]$ *vs.* the experimental value of 7.64 mT. However, for $CD_2H_2^+$ and CD_3H^+, the ^{1}H-atoms do not exchange their positions with the D-atoms in site "*e*" and the observed hydrogen $a_{iso}(^1H)$ values are almost the same (12.2 and 12.5 mT).

The C_{2v} structure of the CH_4^+ cation has been theoretically supported by calculations with several different methods [91–94]. For example, the calculations by the LSD(BP)-DFT/DZP method [94] resulted in two longer C−H bonds (1.208 Å) and two shorter C−H bonds (1.104 Å) lying in mutually orthogonal planes: the angle "α" between the longer bonds and the angle "β" between the shorter bonds are 58.6° and 124.5°, respectively. The experimental ^{1}H *hf* splittings have been well reproduced by the theoretical calculations: for two equivalent ^{1}H-atoms at "*a*" sites, 12.2 (*exp*) *vs.* 12.11 mT (*cal*), and for two equivalent ^{1}H-atoms at "*e*" sites, −1.43 (*exp*) *vs.* −1.63 mT (*cal*) [94].

The D-isotope effects observed for the selectively D-labeled methane radical cations can be interpreted in terms of a zero-point vibrational energy (ZPVE) of

a C−H bond stretching vibration, see Sect. 4.6 and Refs. [26, 28, 29]. In short, the singly occupied molecular orbital (SOMO) is delocalised from the centre carbon to the hydrogens making the corresponding C−H bond weaker and longer. The ZPVE is proportional to $(k/m)^{1/2}$ as the first approximation, where k is the force constant and m is the mass of the hydrogen nucleus. The decrease in ZPVE upon deuteration is greater for bonds having larger force constants. Thus, the deuterium atoms can preferentially occupy positions with a larger force constant, *i.e.* the nodal plane positions with a short bond distance.

Readers can refer to [35] for more detailed analysis of the EPR spectroscopic data of D-labeled methane radical cations on the basis of dynamic *J-T* distortions.

4.5.2 *Tetramethylsilane Radical Cations: $Si(CH_3)_4^+$, $Si(CH_3)_3(CD_3)^+$ and $Si(CH_3)_2(CD_3)_2^+$*

Tetramethylsilane (TMS) has a degenerate t_2 HOMO with a T_d symmetry similar to CH_4. As an extension of the C_{2v} structural distortion and ^{1}H/D isotope effects of methane radical cations, here we present the deuterium (D) substitution effects on the static and dynamic structures (conformations) of the TMS^+ radical cation. The EPR spectra of $Si(CH_3)_4^+$ in a C_{2v} symmetry were first observed in halocarbon matrices by Williams *et al.*, although incorrect EPR parameters were extracted from the insufficiently resolved spectra [95]. Better resolved spectra of $Si(CH_3)_4^+$ were obtained together with $Ge(CH_3)_4^+$ and $Sn(CH_3)_4^+$ by Bonazzola using $SiCl_4$, $GeCl_4$, $TeCl_4$ and $SnCl_4$ as matrices [48, 49].

Well-resolved isotropic EPR spectra were observed for selectively D-labeled radical cations of $Si(CH_3)_4^+$ (TMS^+), $Si(CH_3)_3CD_3^+$ (TMS-d_3^+), and $Si(CH_3)_2(CD_3)_2^+$ (TMS-d_6^+), which were generated in $SnCl_4$ matrices by ionizing radiation at 77 K [36]. The spectrum of TMS^+ was well reproduced by a computer simulation using $g_{iso} = 2.0049$ and isotropic *hf* couplings of $|a_{iso}(a; 6\ H)| = 0.95$ mT and $|a_{iso}(e; 6\ H)| = 0.47$ mT; the EPR parameters are very close to the reported ones [48, 49]. On the other hand, the *ab initio* MO calculations [36] predicted that TMS^+ has a C_{2v} structure having two apical ("*a*") methyl groups with a long Si−C bond distance of 2.014 Å and a small bond angle of 88.6° and two equatorial ("*e*") methyl groups with a short Si–C bond distance of 1.858 Å and a large bond angle of 115.6°, as shown in Fig. 4.11. The carbon atoms of the "*e*" methyl groups are in the nodal plane of the Si *p*-orbital containing a relatively large spin density. The ^{1}H-nuclei of the "*a*" methyl groups were calculated to have an average *hf* value of (−)0.4 mT, whereas those of the "*e*" methyl groups had an average value of (+)0.21 mT. Referring to the calculated ^{1}H *hf* couplings one can attribute the larger experimental *hf* coupling of 0.95 mT to the ^{1}H nuclei of the "*a*" methyl groups with the longer Si–C bonds and the smaller one of 0.47 mT to those of the "*e*" methyl groups with the shorter Si–C bonds.

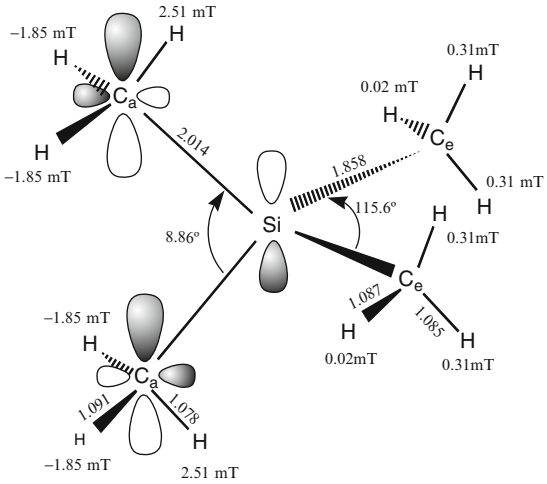

Fig. 4.11 Geometrical structure of TMS^+ and schematics of the singly occupied molecular orbital (SOMO) calculated at the UHF/6-31+G(d,p) level. The ^1H *hf* couplings were evaluated for the structure by the DFT (B3LYP/6-31+G(d,p)) method. Letters "C_a" and "C_e" stand for the carbon atoms at apical ("*a*") and equatorial ("*e*") positions, respectively (Adapted from Ref. [36] with kind permission of © The Royal Society of Chemistry 2001)

The EPR spectra of TMS-d_3^+ and TMS-d_6^+ consist of the multiple lines of 0.47 mT splitting; the value is the same as the ^1H *hf* splitting of the equatorial CH_3 groups in the C_{2v} structure of TMS^+ [36]. This suggests that the C_{2v} structure is retained for these D-labeled TMS radical cations. If the CD_3 group in TMS-d_3^+ occupies either the apical ("*a*") site and or the equatorial ("*e*") site at random (or statistically), the TMS-d_3^+ cation can be observed with a mixture of the two conformations. The observed spectra could not be reproduced by simulation for the mixed two conformations, but well simulated for a single conformation only with the "*e*" CD_3 group (model (a) *A* in Fig. 4.12).

For TMS-d_6^+, simulated spectra were calculated for three different C_{2v}-like species: two CD_3 groups at the "*a*" and "*e*" positions at random (model (b) *A*), two single-conformation models with two "*e*" CD_3 groups (model (b) *B*), and with two "*a*" CD_3 groups (model (b) *C*). Only for model (b) *A* the simulation satisfactorily reproduced the experimental spectrum. This is in clear contrast with the results for $CH_2D_2^+$, where the heavier D-nuclei occupy "*e*" sites, and the TMS-d_6^+ cation was concluded to have one CD_3 group at "*a*" site and the other CD_3 group at "*e*" site in a C_{2v}-like structure. One can expect asymmetrical displacements in TMS^+, which form two pairs of unequal Si–C bonds, *i.e.* elongated and compressed bonds, corresponding to "*a*" and "*e*" carbons, respectively; similar asymmetrically distorted structures have been observed for a series of radical cations of alkyl-substituted cycloalkanes [28, 37–40, 96], silacycloalkanes [5, 27, 41] and diethylsilanes [42]. Lighter methyl groups, CH_3, would be more advantageous for such simultaneous displacements. For TMS-d_6^+, the first pair of asymmetric bonds may be simultaneously utilized by two lighter CH_3 groups and the last pair by two CD_3 groups. In the case of TMS-d_3, the first pair of asymmetric bonds may be occupied by two CH_3 groups and the last pair of bonds by one CD_3 group and one CH_3 group. The CD_3 group may prefer the "*e*" site in the nodal plane, because this site needs a smaller displacement after releasing one electron to form the radical cation. Thus, model (a) *A* is plausible for TMS-d_3^+, in accord with the observation.

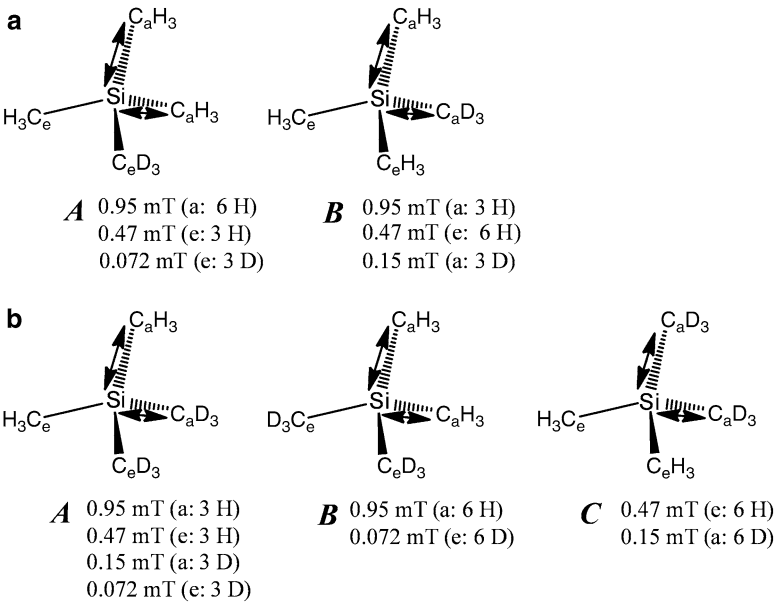

Fig. 4.12 (**a**) Two possible C_{2v} structures of TMS-d_3^+ with one CD_3 group at equatorial ("*e*") site (model (**a**) *A*) and at apical ("*a*") site (model (**a**) *B*). (**b**) Three possible C_{2v} structures of TMS-d_6^+ with one CD_3 group at the "*e*" and one CD_3 group at the "*a*" sites (model (**b**) *A*), both CD_3 groups at the "*e*" sites (model (**b**) *B*), and both CD_3 groups at the "*a*" sites (model (**b**) *C*). Letters "C_a" and "C_e" stand for the carbon atoms at the "*a*" and "*e*" sites, respectively, and the *arrow* denotes the elongated Si—C bond. The numerical values are isotropic ^{1}H or D *hf* splittings expected for each conformation (Adapted from Ref. [36] with kind permission of © The Royal Society of Chemistry 2001)

4.5.3 Trimethylenemethane Radical Cation (TMM$^+$)

Neutral trimethylenemethane (TMM) is one of the most attractive organic molecules for investigating the electronic structure because of the simplest known 4π-electron system of a D_{3h} symmetry. Here we shortly discuss *J-T* structural distortion of trimethylenemethane radical cation (TMM$^+$). Several EPR studies have shown that the ground electronic state of neutral TMM is a triplet with a doubly degenerate nonbonding π-MO ("*e*" orbitals in D_{3h}) singly occupied by the two unpaired electrons [88–90]. DFT computations predict that in TMM$^+$ the D_{3h} structure of TMM is expected to be distorted to a lower symmetry of C_{2v} due to the *J-T* effect, so as to split the original degenerate "*e*" orbitals into a_2 and b_1 orbitals ($^2A_2$ and $^2B_1$ states), see Fig. 4.13 [13].

The TMM$^+$ radical cation was generated by ionizing radiation in a CF_2ClCF_2Cl matrix [86]. The EPR spectrum observed at 4.2 K consists of a septet of *hf* lines with $a_{iso}(H) = 0.93$ mT splitting with relative intensity close to a binomial one, attributed to six magnetically equivalent ^{1}H-atoms of TMM$^+$. The EPR spectral lineshape did not change appreciably between 4 and 125 K. In contrast to the prediction the

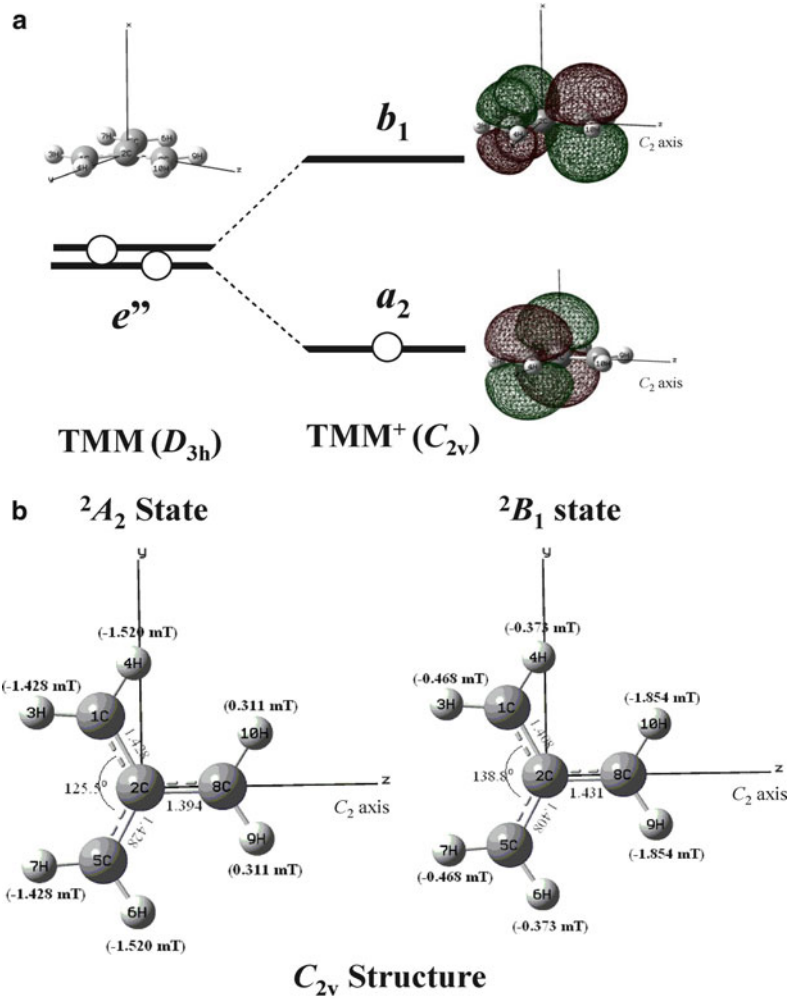

Fig. 4.13 (**a**) Schematic representation showing that the original D_{3h} symmetry of TMM is reduced to a lower one of C_{2v} due to *J-T* effect for TMM$^+$ so as to split the doubly degenerate SOMOs of "*e*" into a_2 and b_1 orbitals, together with plots of the latter two orbitals projected to the x-z plane. The computations of a_2 and b_1 MOs were performed using DFT at the B3LYP/6-31+G(d,p) level. (**b**) Optimized geometrical structures corresponding to the $^2A_2$ and $^2B_1$ states of TMM$^+$ with C_{2v} symmetry calculated at the B3LYP/6-31+G(d, p) level. The bond lengths are in Å. The isotropic ^{1}H *hf* splittings (*in parentheses*) were computed at the B3LYP/6-311+G(2d, p) level for the two geometry optimized structures (Adapted from Ref. [13] with kind permission of © Springer 2011)

experimental results suggest that the TMM^+ cation in the fluorocarbon matrix has an apparent D_{3h} structure. The experimental result was discussed in terms of an intra-molecular dynamics of TMM^+ among the three equivalent C_{2v} structures with $^2A_2$ ground state, depending on which of the three C–C bonds is the elongated one along the C_2 symmetry axis, so as to average the structural distortion (dynamic *J-T* effect) [13, 86].

The "*e*" orbital degeneracy of TMM can be removed by methyl substitution. The radical cation of 1,1,2,2-tetramethyltrimethylenemethane (TMM-Me_4^+; C_{2v} symmetry) gave rise to *hf* couplings characteristic of a SOMO that closely resembles the b_1 orbital in TMM^+ [87].

4.6 D-Isotope Effects on Methyl Hydrogen Conformation

In this section, we present deuterium (D) isotope effects on the methyl group conformation in D-labeled dimethylether (DME) radical cations studied by EPR spectroscopy in combination with *ab initio* and density functional theory (DFT) calculations [26]. The temperature-dependent EPR spectra show strong D-isotope effects on the ^1H *hf* splittings which were revealed for selectively D-labeled cations of $CD_3OCH_3^+$, $CD_3OCH_2D^+$ and $CD_3OCHD_2^+$. The D-isotope effects and temperature-dependent ^1H *hf* splittings can be interpreted in terms of a zero-point vibrational energy (ZPVE) of a C–H bond stretching vibration by incorporating the mass difference of the two hydrogen isotopes in addition to that of their magnetic properties. A similar D-isotope effect on the methyl hydrogen conformation has been reported for the partially deuterated monofluoromethane radical cation of $CFDH_2^+$ by Knight et al. [50].

4.6.1 Dimethylether Radical Cations: $CH_3OCH_3^+$, $CH_3OCH_2D^+$ $CD_3OCH_3^+$, $CD_3OCH_2D^+$, $CD_3OCHD_2^+$ and $CD_3OCD_3^+$

4.6.1.1 EPR Results

Six selectively D-labeled DME radical cations were generated and stabilized in a halocarbon matrix by ionising radiation at 77 K; they are $CH_3OCH_3^+$, $CH_3OCH_2D^+$, $CD_3OCH_3^+$, $CD_3OCH_2D^+$, $CD_3OCHD_2^+$ and $CD_3OCD_3^+$, see Fig. 4.14 [26]. In the EPR spectra of the $CD_3OCH_3^+$, $CD_3OCH_2D^+$ and $CD_3OCHD_2^+$ radical cations, the number of ^1H *hf* lines decreases from four to three and two depending on the number of light hydrogens (^1H), respectively. Interestingly the ^1H *hf* splitting increases with increasing number of D-atoms substituted from 4.3 mT for the CH_3 group to 5.2 mT for the CH_2D group and 6.2 mT for the CHD_2 group at 77 K (Table 4.2). Furthermore, strong temperature-

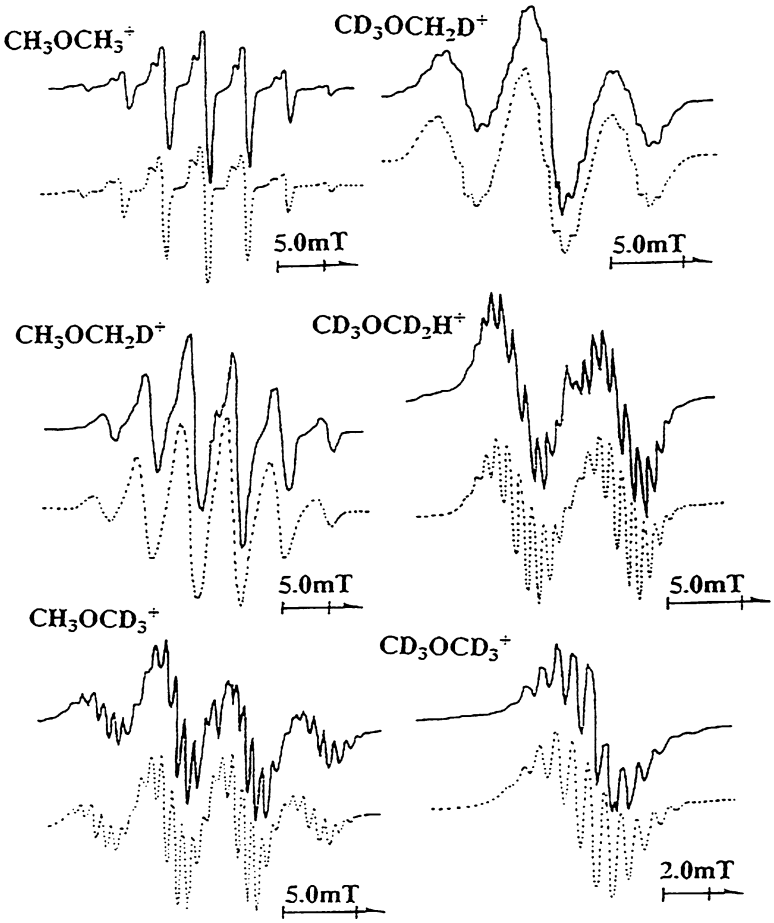

Fig. 4.14 EPR spectra of six different D-labeled DME^+ in CCl_3F matrix at 77 K. The simulation spectra (*dotted lines*) were calculated using ^1H and D *hf* splittings listed in Table 4.2 (Adapted from Ref. [26] with kind permission of © The American Chemical Society (2000))

dependent ^1H *hf* splittings were observed for $CD_3OCH_2D^+$ and $CD_3OCHD_2^+$ in the temperature range from 4 to 100 K at which temperature the radical cations undergo changes to neutral radicals. For example, the ^1H *hf* splitting of $CD_3OCHD_2^+$ decreases with increasing temperature from 8.8 mT at 4 K to 6.2 mT at 80 K; above this temperature the *hf* splitting becomes almost constant up to 100 K. On the other hand, no appreciable temperature dependence was observed for the ^1H *hf* splitting of the CH_3 group in $CD_3OCH_3^+$; the observed splitting of 4.3 mT corresponds to the rotationally averaged value for the CH_3 groups in $CH_3OCH_3^+$ and remained unchanged. These results lead us to conclude that the ^1H-atoms of the CH_2D and CHD_2 groups in $CD_3OCH_2D^+$ and $CD_3OCHD_2^+$ take fixed positions at 4 K and that the associated ^1H and D *hf* splittings cannot be completely averaged out even at higher temperatures up to 100 K.

Table 4.2 Experimental ^{1}H and D *hf* splittings of selectively D-labeled dimethyl ether radical cations in halocarbon matrix [26]

Radical cation	^{1}H and D *hf* splittings (mT)	*T*(K)
$CH_3OCH_3^+$	4.3 ($6H_\beta$)	10[a]
$CH_3OCH_2D^+$	4.3 ($3H_\beta$), 5.2 ($2H_\beta$), 0.5 ($1D_\beta$)	77[a]
$CH_3OCD_3^+$	4.3($3H_\beta$), 0.6 ($3D_\beta$)	10[a]
	4.3($3H_\beta$), 0.6 ($3D_\beta$)	77[b]
$CD_3OCH_2D^+$	8.4 ($1H_\beta$), 4.2 ($1H_\beta$), 0.6 ($4D_\beta$)	4.2[a]
	5.2 ($2H_\beta$), 0.6 ($4D_\beta$)	77[b]
$CD_3OCHD_2^+$	8.8 ($1H_\beta$), 0.6 ($5D_\beta$)	10[a]
	6.2 ($1H_\beta$), 0.6 ($5D_\beta$)	77[b]
$CD_3OCD_3^+$	0.6 ($6D_\beta$)	77[b]

[a]In CCl_3F matrix

[b]In all halocarbon matrixes used: CCl_3F, CCl_2FCClF_2, CCl_3CF_3, $CClF_2CClF_2$, $CBrF_2CBrF_2$, $c-C_6F_{12}$ and CF_3-$c-C_6F_{11}$

4.6.1.2 D-Isotope Effects on Methyl Hydrogens Conformation

Using the McConnell type of equation for β-protons [97], $a_H{}^\beta = B_0 cos^2\theta$, and the experimental splitting of 4.3 mT for the rotationally averaging, $<a_H{}^\beta> = (1/2)B_0$, we obtain 8.6 mT for the proportional constant, B_0. Comparing with the experimental value of 8.8 mT for the ^{1}H splitting of CHD_2 group, we can conclude that the light hydrogen (^{1}H) preferentially occupies the $\theta = 0°$ position which is parallel to the unpaired electron orbital of the oxygen in $CD_3OCHD_2^+$, see Fig. 4.15. The preference of the light hydrogen (^{1}H) to occupy the $\theta = 0°$ position can be explained as follows. Through the hyperconjugation effect, which is at a maximum around the $\theta = 0°$ position, the singly occupied molecular orbital (SOMO) is delocalised from the oxygen atom to the hydrogen atom, making the corresponding C–H bond weaker and longer. Note that the effect is, however, partially countered by the nonbonding, repulsive interaction between the C–H bond(s), which offsets the equilibrium from the perfectly eclipsed conformation [26]. Since the ZPVE of a C–H stretching vibration is proportional to $(k/m)^{1/2}$ in the first approximation, where k is the force constant and m is the mass of the hydrogen nucleus, the decrease in the ZPVE upon deuteration can be larger for bonds having higher force constants. Thus, the deuterium atoms can preferentially occupy positions with a larger force constant, *i.e.* the nodal plane positions with a short bond distance, refer to Sect. 4.5.1.

4.6.1.3 Temperature-Dependent ^{1}H *hf* Splittings

The observed temperature-dependency of ^{1}H *hf* splittings is successfully analysed using the following model [26]. That is, if molecular radical cations can exist in several forms, *i.e.* as rotational or geometrical isomers, an interchanging possibly occurs among the isomers so as to average the associated *hf* splittings. In this case a mean total *hf* splitting, $<\Sigma a_i>$, can be obtained by Eq. (4.5):

$$<\Sigma a_i> = p_I \Sigma a_I + p_{II} \Sigma a_{II} + p_{III} \Sigma a_{III} \ldots \quad (4.5)$$

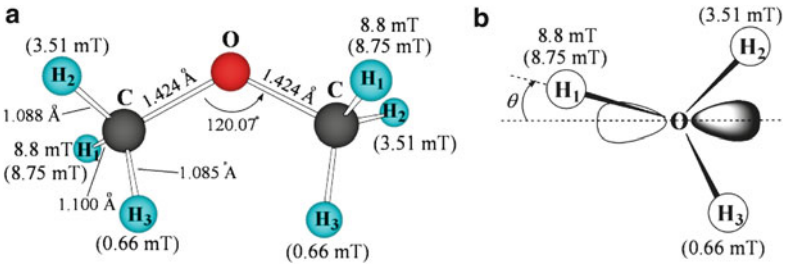

Fig. 4.15 The experimental isotropic ^{1}H *hf* splitting (8.8 mT) of $CD_3OCHD_2^+$ is compared with the theoretical ones computed for $CH_3OCH_3^+$. Optimized geometrical structure (**a**) was calculated by the *ab initio* MO method at the MP2/6-31+G(d,p) level. The values in parentheses are the ^{1}H *hf* splittings evaluated for the structure using the DFT method at the BLYP/6-31 G(d,p) level [26]. In the methyl hydrogen conformation (**b**) of DME radical cation the light hydrogen (^{1}H) of the CHD_2 group preferentially occupies the position which is parallel to the unpaired electron orbital of the oxygen in $CD_3CHD_2^+$

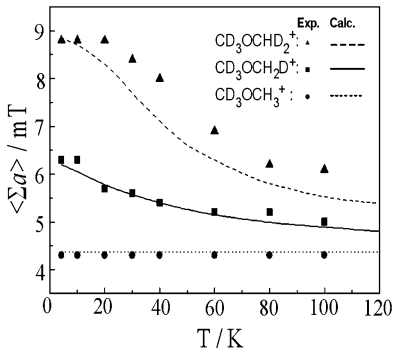

Fig. 4.16 The temperature dependencies of total ^{1}H *hf* splitting, $<\Sigma a_i>$, are compared with the theoretical ones for $CD_3OCHD_2^+$, $CD_3OCH_2D^+$ and $CD_3OCH_3^+$ (Adapted from Ref. [26] with kind permission of © The American Chemical Society of Chemistry 2000)

where p_i (i = I, II, ...) are the probabilities of finding the different forms and Σa_i the total ^{1}H *hf* splittings of the corresponding form [98]. As already mentioned, the D-atoms in selectively deuterated methyl groups preferentially occupy the sites with the larger C–X (X: ^{1}H or D) force constant to minimize the ZPVE. Thus, the ZPVEs of D-labeled DME^+ depend both on how many sites and which positions the D-atoms occupy.

Figure 4.16 shows the (mean) total ^{1}H *hf* splittings, $<\Sigma a_i>$, observed for $CD_3OCHD_2^+$, $CD_3OCH_2D^+$ and $CD_3OCH_3^+$ as a function of temperature [26]. The theoretical values of $<\Sigma a_i>$ in the figure were calculated according to Eq. (4.5), using a Boltzmann distribution to evaluate the probability of finding the different rotational isomers. The ZPVEs were obtained from the frequency calculations at the MP2/6-31+G(d,p) level and the ^{1}H *hf* splittings of a_i (i = I, II, ...) were calculated at the BLYP/6-311+G(2df,p) level for the MP2 calculated structures.

Table 4.3 Experimental *hf* splittings of the isotopically labeled methylfluoride and methanol radical cations determined by EPR measurements in neon matrices at 4 K [50, 99]

Hyperfine Splittings (MHz)[a, b]					
Radical cation[c]	Nucleus	A_X	A_Y	A_Z	a_{iso}
$^{13}CH_3F^+$	^{1}H	317	323	312	317
	^{19}F	919	−127	−156	211
	^{13}C [d]	48	–	54	–
CH_2DF^+	^{1}H	483	476	483	481
	D [e]	$\|A_X\|$: 5.0	$\|A_Y\|$ <3	$\|A_Z\|$: 7.1	$\|a_{iso}\|$: 5
	^{19}F	965	−130	−166	223
$^{13}CH_3OH^+$	^{1}H (CH_3)	230	230	230	230
	^{13}C [d]	40	–	29	–
	^{1}H (OH)	±55	–	±80	–
CH_2DOH^+	^{1}H	330	–	328	–
	D [e]	$\|A_X\|$: 4.3	–	$\|A_Z\|$: 3.9	$\|a_{iso}\|$: 5
	^{1}H (OH)	±60	–	75	–

[a]The MHz unit can be converted to the mT unit using the following relation: A_i (mT) = 0.07144771 A_i (MHz)/g_i (i = X, Y, Z)
[b]The experimental uncertainty for all of these values is ±(1–3) MHz
[c]The g-tensors observed are $g_X = 2.0032(5)$, $g_Y = 2.0106(8)$, $g_Z = 2.0120(5)$ for CH_3F^+ and $g_X = 2.0042(4)$, $g_Z = 2.010(1)$ for CH_2DOH^+
[d]The signs of ^{13}C *hf* tensors cannot be determined from the experimental results alone, however, theory indicates that $A_X > 0$ and $A_Z < 0$
[e]The signs of a_{iso}(D) cannot be determined from the experimental results alone, but theory predicts a negative value

4.6.2 *Methylfluoride Cations: CH_3F^+ vs. CH_2DF^+*

Methylfluoride (CH_3F) has a doubly degenerate HOMO and, similar to the methane cation, the associated radical cation of CH_3F^+ [50] is expected to show drastic static and dynamic *J-T* effects as has been theoretically discussed [51]. Furthermore, the structure of CH_3F^+ is of interest since the cation is isoelectronic with the neutral methoxy radical (CH_3O) and with radical cations such as CH_3OH^+ [99], $CH_3NH_2^+$, $CH_3CH_3^+$[1–7].

Knight and his collaborators reported an EPR study on three different isotope combinations of methylfluoride radical cation, $^{12}CH_3F^+$, $^{13}CH_3F^+$ and $^{12}CH_2DF^+$, which were generated by photoionization at 16.8 eV and other methods in neon matrices [50]. The experimentally determined *hf* (A) tensors are summarized in Table 4.3. The EPR spectrum of CH_3F^+ at 4 K shows that three ^{1}H-atoms are magnetically equivalent with an averaged large *hf* splitting of 317 MHz on the EPR time scale. Furthermore, the observed values of ^{19}F and ^{13}C *hf* tensors suggest that a considerably large amount of unpaired electron is in the F $2p_x$ orbital, but significant spin density also resides in the carbon $2p_x$ orbital. The results can be explained in terms of a static C_s conformation with a $^2A''$ state (Fig. 4.17). In this conformation the two H-atoms are connected to the central C-atom by the dashed lines in the figure

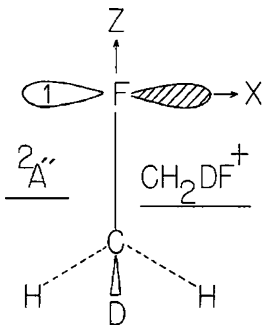

Fig. 4.17 The coordinate system of CH_3F^+ used to define the observed EPR parameters assigned to the X, Y and Z direction. The unpaired electron is shown here in the F $2p_x$ orbital but significant spin density also resides on the H-atoms and the carbon $2p_x$ as shown by $^{13}CH_3F^+$ experiments. In the CH_2DF^+ case shown, the D-atom lies in the YZ plane – the nodal plane of the F $2p_x$ orbital which is the molecular symmetry plane (Adapted from Ref. [50] with kind permission of © The American Institute of Physics 1991)

and have a significant amount of the spin density, *i.e*. a large isotropic *hf* value, due to a hyperconjugation mechanism; a similar conformation has been reported for some planar radicals such as H_2CO^+ [100], H_2CN [101], and H_2BO [101]. The unique H-atom (occupying a site of the D-atom in Fig. 4.17) located in the nodal plane of the ^{19}F $2p_x$ orbital should have a very small or negative a_{iso} value. These large differences in the H-atom environments must be undergoing some type of averaging giving the clear quartet ^1H *hf* structure for the CH_3 group of CH_3F^+ with $a_{iso} = 317$ MHz.

The presence of a single D-atom in the methylfluoride radical cation drastically changes the EPR *hf* pattern and confirms the averaging conformation mentioned above for CH_3F^+. That is, the D-atom in CH_2DF^+ acts to prevent the averaging process yielding two ^1H-atoms with an unusually large a_{iso} value of 481 MHz and one with a_{iso}(D) value of −5 MHz (or −34 MHz on the ^1H-atom scale). A weighted average of the a_{iso} values for CH_2DF^+ is 309 MHz [(2 x 481–34)/3)], which is very close to the value of $a_{iso} = 317$ MHz observed for CH_3F^+. One suggested mechanism for this averaging is a combination of dynamic *J-T* distortion and tunnelling interchange of the H-atoms [50]. The ZPVE difference between ^1H- and D-atoms can be responsible for restricting the averaging or interchange phenomenon as described in the preceding sections of this chapter for the selectively deuterated methane radical cations (CH_4^+, CH_3D^+, $CH_2D_2^+$, CHD_3^+ and CD_4^+) [34] and dimethylether radical cations ($CD_3OCH_3^+$, $CD_3OCH_2D^+$, $CD_3OCHD_2^+$ and $CD_3OCD_3^+$) [26].

In the end we add to note that Knight *et al*. have also reported an EPR study of the radical cations of four different isotope combinations of the methanol cation (CH_3OH^+) generated in neon matrices at 4 K [99], see EPR parameters in Table 4.3. Similar to the methylfluoride radical cation the observed *hf* splittings for CH_2DOH^+ again indicate an unusually large deuterium effects with $a_{iso} = 329$ MHz for the CH_2 protons and $|a_{iso}| = 4.1$ MHz for the D-atom.

4.7 Static and Dynamic Structures of Radical Cations of Cyclohexane and Related Molecules

The radical cations of small saturated hydrocarbons have been of interest because they are fundamentally important chemical species with σ-electron system and generally have degenerate or nearly degenerate HOMOs [1–5, 33]. Ionization can be followed by a geometrical distortion due to instability of the degenerate orbitals, *i.e. Jahn-Teller* (*J-T*) or *pseudo J-T distortion* [37–42, 102–115]. In this section we deal with three topics on static and dynamic structural distortions of cyclohexane (*c*C6) and related radical cations in low temperature matrices. The first topic deals with the *J-T* split HOMO of the radical cations of selectively alkyl-substituted cyclohexanes [39, 40]. The second topic deals with deuterium isotope effects on static and dynamic structures of the cyclohexane radical cation itself [5, 28, 29]. The third topic is on the radical cations of silacyclohexane (*c*SiC5), in which the Si-atom can be regarded to play a role as a "probe" to detect an asymmetrically distorted geometrical structure (^2A state in C_1 symmetry) with one of the two Si—C bonds being elongated [5, 27, 41].

4.7.1 Jahn-Teller Distorted Structures of Cyclohexane Cation

The radical cation of cyclohexane (*c*C6) is of particular interest because of its high molecular symmetry, D_{3d}, with a degenerate highest occupied molecular orbital (HOMO). The introduction of substituents to cyclohexane in a certain symmetrical or asymmetrical manner is a chemically intuitive way to remove orbital degeneracy; therefore electronic states similar to those predicted by the *J-T* theorem could be studied. Thus, a series of EPR studies were carried out on structural distortions and dynamics in the radical cations of selectively alkyl-substituted cyclohexanes and related molecules [1, 5, 37–42, 102–108]. The radical cations were classified as ^2A_g-like (in an elongated C_{2h} structure), ^2B_g-like (in a compressed C_{2h} structure), and $^2A''$-like (in a C_s structure) with structural resemblance to the *c*C6 cation, see Fig. 4.18 [39]. Furthermore, the radical cations of methylcyclohexane (Me-*c*C6) and 1,1-dimethylcyclohexane (1,1-Me_2-*c*C6) were concluded to take an asymmetrically distorted C_1 geometrical structure with one elongated C–C bond of which one carbon is attached to the methyl group(s) [37, 38]. The temperature-dependent EPR spectra were analysed in terms of a selective bond length alternation between the two adjacent C–C bonds and their structures were concluded to be averaged by intra-molecular dynamics so as to give an apparently symmetric C_s structure with increasing temperature.

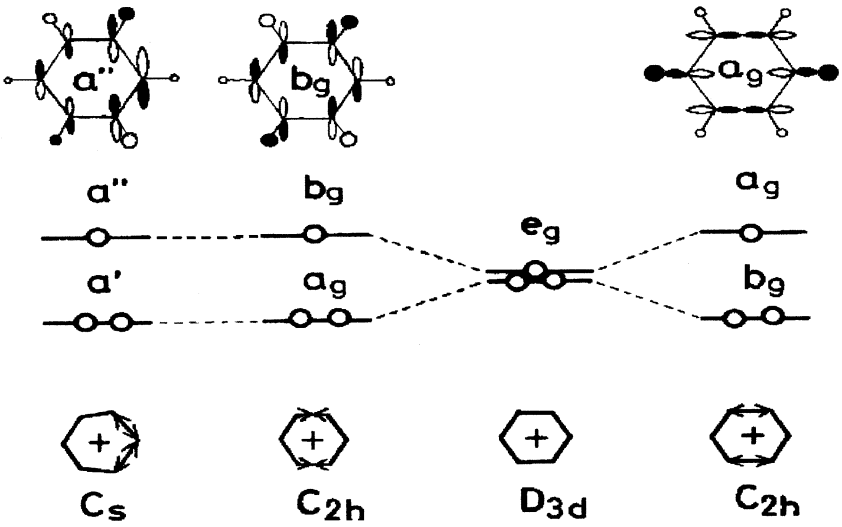

Fig. 4.18 Schematic representation showing how the $4e_g$ degenerate HOMOs in cyclohexane radical cation (cC6$^+$) are lifted by a structural distortion from the original D_{3d} to either C_{2h} or C_s symmetry: the *arrows* ($\leftrightarrow$ and $\rightarrow\ \leftarrow$) stand for the elongated and compressed C–C bonds, respectively. The unpaired electron in the cation occupies either the a_g (^2A_g state in C_{2h}), b_g (^2B_g state in C_{2h}) or "a" ($^2A''$ state in C_s) orbital (Adapted from Ref. [39] with kind permission of © The American Chemical Society of Chemistry 1990)

4.7.2 D-Isotope Effects on the Structure of Cyclohexane Cation

D-labeling is another way of obtaining information about the static and dynamic *Jahn-Teller* (*J-T*) effects of the cyclohexane radical cation (cC6$^+$) [1–5]. Thus the following selectively deuterated cC6$^+$s were radiolytically generated in a cC$_6$F$_{12}$ or CF$_3$-cC$_6$F$_{11}$ matrix at low temperatures and subjected to EPR studies combined with *ab initio* and density functional theory (DFT) calculations. They were cC6$^+$, cC6-1,1-$d_2$$^+$, cC6-1,1,3,3-$d_4$$^+$ [28], cC6-1,1,4,4-$d_4$$^+$ [29], cC6-1,1,2,2,3,3-$d_6$$^+$ and cC6-$d_{12}$$^+$. Here our attention is focused on cC6-1,1,3,3-$d_4$$^+$ as a prototype of the deuterated cyclohexane cations.

4.7.2.1 EPR Spectrum and C_{2h} Distorted Structure

The 4.2 K spectrum consists of essentially a triple triplet with isotropic ^{1}H *hf* splittings of $a_1 = 8.4$ ($\pm$0.5) mT and $a_2 = 2.2$ mT ($\pm$0.5). Assuming a C_{2h} distorted structure with both the C(3)–C(4) and the C(6)–C(1) bonds elongated, the larger (a_1) and smaller (a_2) triplets are attributable to two sets of two equatorial ^{1}H-atoms at the C(2) and C(5) positions and at the C(4) and C(6) positions, respectively (Fig. 4.19).

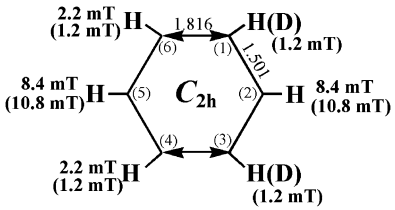

Fig. 4.19 Assignment of the experimental ^{1}H *hf* splittings (error limit: ±0.5 mT) of *c*C6-1,1,3,3-d_4^+ in cC_6F_{12} matrix at 4.2 K. The values in parentheses are the theoretical *hf* splittings calculated for the equatorial ^{1}H-atoms in a C_{2h} structure. The *arrows* (↔) stand for the elongated C–C bonds: the theoretical C–C bond lengths (Å) are given in the figure (Adapted from Ref. [28] with kind permission of © Elsevier 1998)

The *ab initio* MO calculations of *c*C6$^+$ at the MP2/6-31+G(d,p) level resulted in a C_{2h} structure whose total energy was lower by 1.20 kcal·mol^{-1} (5.02 kJ·mol^{-1}) than the C_s structure (next stable structure). The theoretical ^{1}H *hf* splittings were evaluated by the DFT method for the optimized structure and are shown in Fig. 4.19. Based on the assumption of the C_{2h} distorted structure with both C(3)−C(4) and C(6)−C(1) bonds elongated, the larger ^{1}H *hf* splitting of 10.8 mT (a_1) and smaller splitting of 1.2 mT (a_2) were calculated for two equatorial ^{1}H-atoms at the C(2) and C(5) positions and four equatorial ^{1}H-atoms at the C(1), C(3), C(4) and C(6) positions, respectively. The theoretical *hf* values of 10.8 mT and 1.2 mT, correspond rather well to the experimentally observed values of 8.4 and 2.2 mT. Thus, it was concluded that the geometrical structure of *c*C6-1,1,3,3-d_4^+ was distorted into the C_{2h} structure from the original D_{3d} structure. The possible *J-T* distortion mode is illustrated in Fig. 4.18 together with a schematic representation of SOMO (a_g) and next lower SOMO (b_g) in the C_{2h} structure.

4.7.2.2 Zero-Point Vibrational Energy (ZPVE)

Depending on the sites which the D-atoms occupy, three C_{2h} distorted forms, *P*, *Q* and *Q′*, are possible for *c*C6-1,1,3,3-d_4^+ (Fig. 4.20). The theoretical calculations (DFT/6-31+G(d,p) level) suggest that ZPVE of the *P* form is lower by 0.204 kcal·mol^{-1} (0.846 kJ·mol^{-1}) than that of the *Q* form. The *Q* and *Q′* forms are mirror images with an identical ZPVE. The probability of finding the different forms (p_P, p_Q, $p_{Q'}$) can be assumed to follow a Boltzmann distribution, the same as for the D-labeled dimethylether (DME) radical cations in Sect. 4.6.1. Using the calculated ZPVE values the following probabilities are evaluated for the *P*, *Q* and *Q′* forms: for example, $p_P : p_Q : p_{Q'} = 0.998 : 0.001 : 0.001$ at 4.2 K and 0.478: 0.261: 0.261 at 170 K. At 4.2 K, the p_Q (and $p_{Q'}$) value is essentially zero so that the *P* form dominates the EPR spectrum.

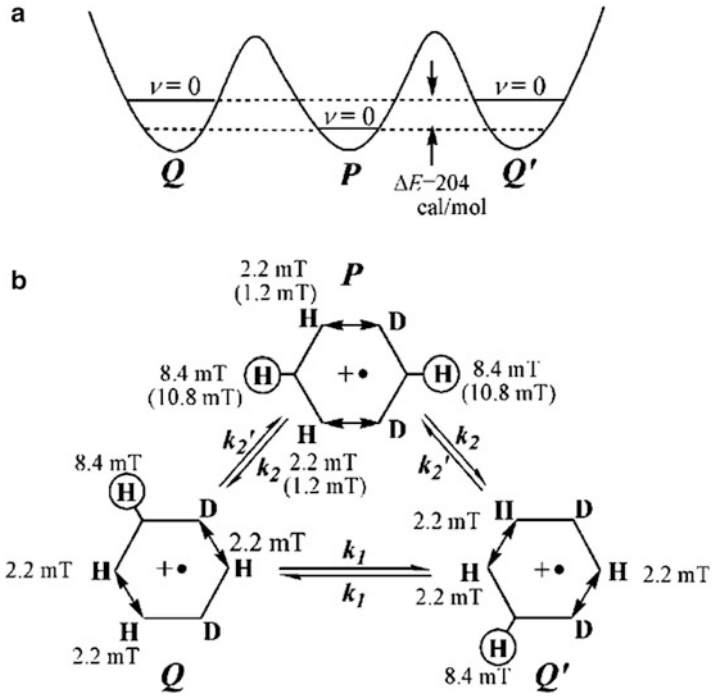

Fig. 4.20 (**a**) Potential energy curve with zero-point vibrational energies (ZPVEs) calculated for three C_{2h} geometrical structures (P, Q and Q') of *c*C6-1,1,3,3-d_4^+. (**b**) Schematics showing three site exchange (or jump) among one C_{2h} (P) and two C_{2h} (Q and Q') structures (Adapted from Ref. [28] with kind permission of © Elsevier 1998)

4.7.2.3 Temperature-Dependent EPR Spectra and Total ^{1}H *hf* Splittings

The EPR spectral lineshapes of *c*C6-1,1,3,3-d_4^+ depended strongly on temperature. With increasing temperature from 4.2 K the original triple triplet changes into a septet with an averaged *hf* splitting of 6.2 (±0.5) mT (2H) and 3.1 (±0.5) mT (2H) at 77 K, and an apparent quintet at 170 K as shown in Fig. 4.21.

The total ^{1}H *hf* splitting, Σa_i, was found to decrease with increasing temperature from 21.2 (±0.5) mT (4.2 K) to 17.8 (±0.5) mT (170 K) (Fig. 4.22). When the three forms are interchanged with rates faster than 1.7×10^8 sec^{-1}, which corresponds to the ^{1}H *hf* difference between the 8.4 (±0.5) mT and 2.2 (±0.5) mT splittings (Fig. 4.20), a mean total ^{1}H *hf* splitting, $<\Sigma a_i>$, can be obtained by Eqs. (4.6) and (4.7) in a similar manner to the case of the selectively D-labeled DME cations [26] mentioned in Sect. 4.6.1:

$$< \Sigma a_i >= p_P \Sigma a_P + p_Q \Sigma a_Q + p_{Q'} \Sigma a_Q \tag{4.6}$$

$$p_P + p_Q + p_{Q'} = 1 \tag{4.7}$$

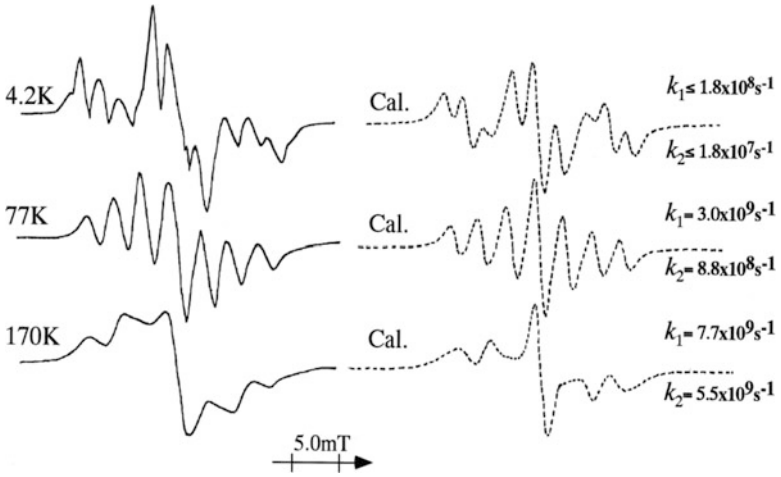

Fig. 4.21 Temperature-dependent EPR spectra of *c*C6-1,1,3,3-d_4^+ in a *c*C_6F_{12} matrix. The simulated spectra are shown with the *dotted lines* together with the exchange rates k_1 and k_2 employed in the calculations (Adapted from Ref. [28] with kind permission of © Elsevier 1998)

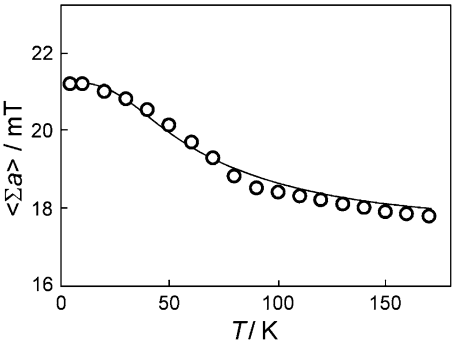

Fig. 4.22 The experimental total ^{1}H *hf* splittings (∘), $\sum a$ (error limit: ±0.5 mT), are plotted against temperature for *c*C6-1,1,3,3-d_4^+ together with the calculated ones (*solid line*) (Adapted from Ref. [28] with kind permission of © Elsevier 1998)

Using the theoretical values of p_P, p_Q (= $p_{Q'}$) and the experimental ones $\Sigma a_P = 2 \times (8.4 + 2.2) = 21.2$ mT, and Σa_Q (=$\Sigma a_{Q'}$) $= 8.4 + 3 \times 2.2 = 15.0$ mT, the temperature dependency of $<\Sigma a_i>$ was calculated and compared well with the experimental values in Fig. 4.22.

Then, based on the assumption of an exchange (or jump) mode shown in Fig. 4.20, the temperature-dependent EPR spectra were successfully reproduced by the simulations using the experimental ^{1}H *hf* splittings of 8.4 mT (2H) and 2.2 mT (2H) as the rigid limit values and the exchange rates, k_1 between the Q and Q' forms and k_2 between the Q (Q') and P forms, as adjustable parameters [28].

An EPR study was also carried out for other D-labeled cyclohexane radical cations, namely *c*C6-1,1-d_2, *c*C6-1,1,4,4-d_4^+ [29], and *c*C6-1,1,2,2,3,3-d_6^+. The observed temperature-dependent EPR spectra were successfully analyzed by employing the same method as for *c*C6-1,1,3,3-d_4^+. For example, in contrast to the

*c*C6-1,1,3,3-d_4^+ cation the theoretical calculations for *c*C6-1,1,4,4-d_4^+ resulted in a *Q* form whose ZPVE was lower by 1.71 kJ·mol^{-1} than that of the *P* form. Assuming a Boltzmann distribution, the p_Q value approaches unity with decreasing temperature so that the *Q* (and Q′) form will dominate at 4.2 K: at this temperature any interchange is improbable between the *P* and *Q* (or *Q*′) forms. With increasing temperature, the three forms (one *P* form and two *Q* forms) start to interchange.

We summarize the D-isotope effects on the structure of *c*C6$^+$as follows. (a) Three equivalent C_{2h} structures are possible for *c*C6$^+$. (b) The value of ZPVE can be shifted by the number and position of the substituted D-atoms due to the mass effect. (c) By changing the temperature the population of each ZPVE level can be shifted under the assumption of a Boltzmann distribution, which is reflected by the temperature-dependent EPR spectra. The readers can refer to the original papers [28, 29] for further details.

4.7.3 Asymmetrically Distorted Structure and Dynamics of Silacyclohexane Cation

We have first reported in 1988 that Me-*c*C6$^+$ and 1,1-Me$_2$-*c*C6$^+$ take an asymmetrically distorted geometrical structure (^2A electronic state in C_1 symmetry) with one elongated C-C bond, of which one carbon is attached to the methyl group(s) [37, 38, 40, 96] as mentioned in Sect. 4.7.1. Since then, a number of radical cations with a similar asymmetrical structural distortion have been reported. They include the following cycloalkane and related alkane radical cations: *c*SiC3$^+$ [5, 106], 1-Me-*c*SiC3$^+$, 1,1-Me$_2$-*c*SiC3$^+$ [5], *c*C5$^+$ [5, 108], Me-*c*C5$^+$, 1,1-Me$_2$-*c*C5$^+$, *c*SiC4$^+$ [5], *c*SiC5$^+$ [5, 27, 107], 1-Me-*c*SiC5$^+$, 1,1-Me$_2$-*c*SiC5$^+$ [27, 107], 1,*c*2,*c*3-Me$_3$-*c*C6$^+$, 1,*t*2,*c*3-Me$_3$-*c*C6$^+$ [39], Et$_2$Si$^+$ [42], Et$_2$SiMe$^+$, Et$_2$SiMe$_2{}^+$ and Et$_4$Si$^+$, see Fig. 4.23. Based on the experimental results combined with *ab initio* and DFT calculations, it is concluded that the decrease in symmetry upon one-electron oxidation is an intrinsic property of alkane radical cations when the geometrical structure of the parent molecules has certain symmetrical elements such as C_s, C_2, and C_{2v} in, even though they are not Jahn-Teller (*J*-*T*) active species.

Here, we focus on the asymmetrical structural distortion and dynamics of silacyclohexane (*c*SiC5) radical cation [27, 107]. The *c*SiC5 molecule contains one Si-atom in the ring; the ionisation potential (I_p) of the Si-atom is considerably lower than that of the C-atom: $I_{p1} = 8.15$ eV (Si) *vs.* 11.26 (C) [116]. In the radical cation of *c*SiC5$^+$ the unpaired electron is expected to favourably reside on a particular Si–C bond or on the two Si–C bonds equally. Thus the Si-atom can be regarded as a "probe" to observe whether *c*SiC5$^+$ takes either an asymmetrically distorted C_1 structure or a symmetrical C_s structure. The EPR spectra were observed at 4.2 K for methyl-substituted silacyclohexane radical cations such as *c*SiC5$^+$, 1-Me-*c*SiC5$^+$, 1,1-Me$_2$-*c*SiC5$^+$, 4,4-Me$_2$-*c*SiC5$^+$, which were radiolytically generated in *c*C_6F_{12} and CF_3-*c*C_6F_{11} matrices. The three selectively D-labeled compounds, *c*SiC5-2,2,6,6-d_4, 1-Me-*c*SiC5-2,2-d_2 and 1-Me-*c*SiC5-2,2,6,6-d_4, were used to unambiguously assign the ^{1}H *hf* splittings.

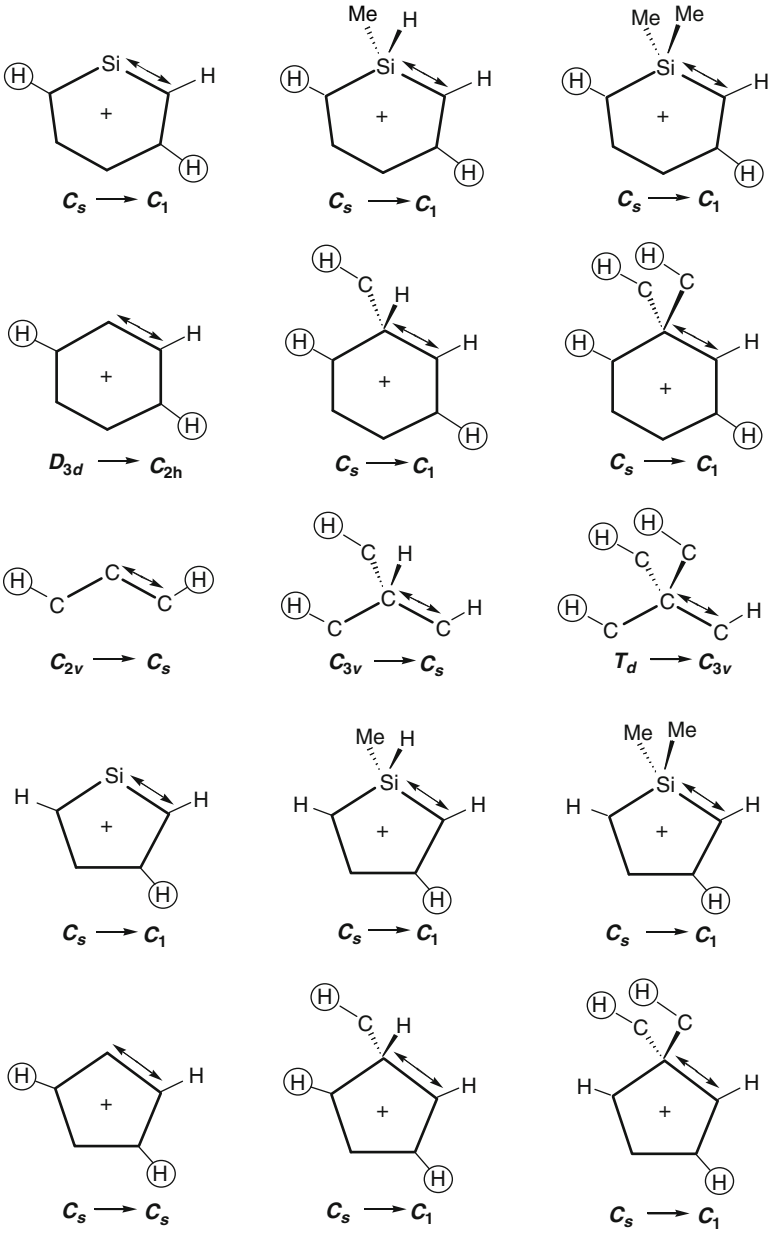

Fig. 4.23 Schematic presentation showing structural distortions in the radical cations of saturated hydrocarbons and those with one Si-atom substituent. The *arrow* (↔) indicates a σ–bond in which the unpaired electron mainly resides so as to asymmetrically elongate the corresponding bond length. The encircled hydrogen atoms are located in the trans position with respect to the elongated σ–bond with a large unpaired electron density and give rise to a large ^{1}H *hf* splitting detectable by EPR

Table 4.4 Experimental *hf* splittings and their assignments for the D-labeled radical cations of silacyclohexane (*c*SiC5$^+$) and 1-methyl-silacyclohexane (1-Me-*c*SiC5$^+$) in CF_3-*c*C_6F_{11} matrix at 4.2 K [27]

		Hyperfine splittings (mT)			
Radical cation[a]	Nucleus	Equatorial at C(2)[b]	Equatorial at C(3)	Equatorial at C(5)	Equatorial at C(6)
*c*SiC5$^+$	^{1}H	2.60	7.55	2.85	3.45
*c*SiC5-2,2,6,6-$d_4$$^+$	^{1}H	2.60	7.55	2.85	3.45
	D	2.60	–	–	3.45
1-Me-*c*SiC5$^+$	^{1}H	2.0	7.3	2.4	3.0
1-Me-*c*SiC5-2,2,6,6-$d_4$$^+$	^{1}H	–	7.3	2.4	–
	D	2.0	–	–	3.0

[a]See Figs. 4.24 and 4.26 for the numbering
[b]"Equatorial at C(2)" stands for equatorial ^{1}H-atom (or D-atom) at carbon (2) position of the radical cations, as the case may be

4.7.3.1 EPR Results

The 4.2 K EPR spectra of *c*SiC5$^+$ and 1-Me-*c*SiC5$^+$ in *c*C_6F_{12} and CF_3-*c*C_6F_{11} matrices were successfully analyzed using the ^{1}H *hf* splittings given in Table 4.4 by the spectral simulation method. The 4.2 K spectrum of *c*SiC5-2,2,6,6-$d_4$$^+$ consists of a doublet of doublets with *hf* splittings of 7.55 mT (1H) and 2.85 mT (1H) and that of 1-Me-*c*SiC5$^+$ consists of a double doublet with 3.0 and 2.0 mT splittings in addition to the splittings of 1-Me-*c*SiC5-2,2,6,6-$d_4$$^+$. Here we assume an asymmetrically distorted C_1 structure of *c*SiC5 in a static structure, in which the unpaired electron is predominately in one of the two Si–C bonds, Si–C(2). The Si–C bond with higher spin density is expected to be weaker and elongated. Based on this assumption the ^{1}H *hf* splittings of 7.3 mT and 2.4 mT observed for 1-Me-*c*SiC5 $^+$ are reasonably attributed to the two equatorial hydrogens, H_{3e} and H_{5e} and the 2.0 and 3.0 mT splittings to two equatorial 1-Me-*c*SiC5$^+$ hydrogens at C(2) and C(6), *i.e.* H_{2e} and H_{6e}. The asymmetrically distorted C_1 structure has been fully supported theoretically by the MO calculations, see Fig. 4.24.

4.7.3.2 Origin of the Structural Distortion

The structural distortion can originate from the second-order *J*-*T* theory (pseudo *J*-*T* effect) [27, 117]. Based on the theory, the energy of the radical cation in the ground electronic state is expressed by Eq. (4.8):

$$E = E_0 + Q\left\langle \psi_0 \left| \frac{\partial U}{\partial Q} \right| \psi_0 \right\rangle + \frac{Q^2}{2}\left\langle \psi_0 \left| \frac{\partial^2 U}{\partial Q^2} \right| \psi_0 \right\rangle + \sum_k \frac{\left[Q \left\langle \psi_0 \left| \frac{\partial U}{\partial Q} \right| \psi_k \right\rangle \right]^2}{(E_0 - E_k)} \tag{4.8}$$

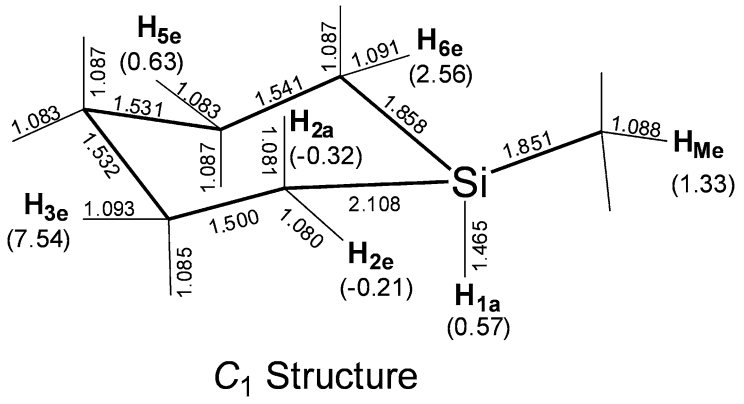

Fig. 4.24 Optimised C_1 geometrical structure of 1-Me-*c*SiC5$^+$ calculated by using *ab initio* MO method at the UHF/6-311+G(d) level of Gaussian 09. The values in parentheses are the isotropic ^{1}H *hf* splittings (in mT) evaluated at the B3LYP/6-311+G(d) level for the structure and the bond lengths in Å

Where E_0 is the energy without distortion, Q is the displacement of the normal coordinate, U is the nuclear-nuclear and nuclear-electronic potential energy, Ψ_0 and Ψ_k are the electronic wave functions for the ground and excited states. For an asymmetric distortion the second term is zero because it is an odd function with respect to Q. The third and the fourth terms are always positive and negative, respectively. Thus, the asymmetrical structure can be energetically preferable when the sum of the latter two terms is negative. The fourth term is inversely proportional to the energy difference between the electronic ground and lower lying electronic excited states. In the case that the energy difference is smaller than several electron volts (eV), as for the present alkane radical cations, the fourth term predominates over the third term so as to make the asymmetrical C_1 structure the most stable.

4.7.3.3 Temperature-Dependent EPR Spectra

Here we consider the temperature-dependent EPR spectra of 1-Me-*c*SiC5-2,2,6,6-$d_4$$^+$ as an example, see Fig. 4.25. The 4.2 K spectrum consists of a doublet of doublets with ^{1}H *hf* splittings of 7.3 mT and 2.4 mT with the inner doublet less intense than the outer one. With increasing temperature a new singlet appeared at the central position and its intensity increased with temperature. At 140 K the spectrum became a triplet of 4.9 mT with a relative intensity close to a binomial one. The EPR spectra can be explained by an interchange of the two H-atoms, *i.e.*, H_{3e} and H_{5e}. The 1-Me-*c*SiC5$^+$ has two energetically equivalent mirror image structures, one with the Si–C(2) bond elongated and the other with the Si–C(6) bond elongated (Fig. 4.26). The figure schematically presents how ^{1}H *hf* splittings of 7.3 and 2.4 mT are averaged by such intramolecular exchange process with the rate k (s^{-1}).

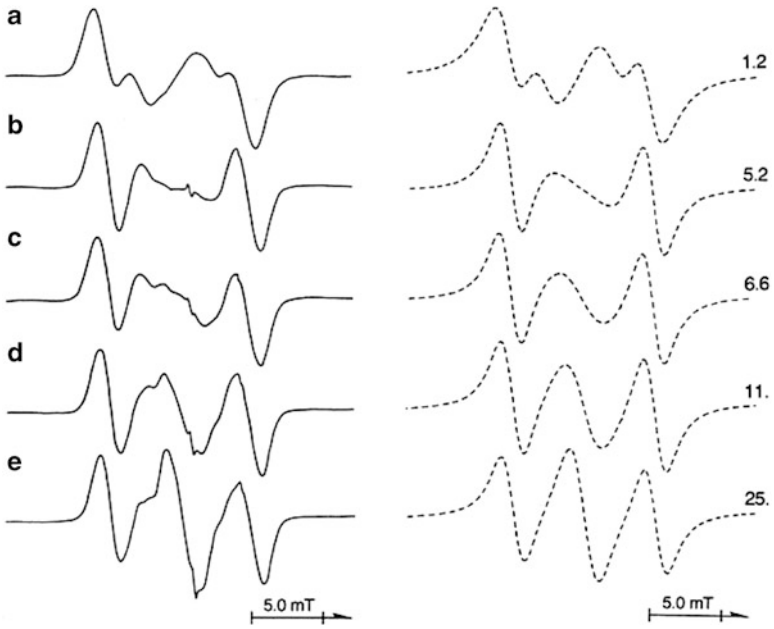

Fig. 4.25 Temperature-dependent EPR spectra of 1-Me-*c*SiC5-2,2,6,6-$d_4$$^+$ observed in CF_3-cC_6F_{11} matrix: (**a**) 4.2 K, (**b**) 77 K, (**c**) 110 K, (**d**) 130 K, (**e**) 140 K. The *dotted lines* in the *right column* are the simulated spectra together with the exchange rate constant, k (in $10^7\ s^{-1}$), employed in the calculations (Adapted from Ref. [27] with kind permission of © The American Chemical Society 1997)

The weaker inner doublet of the 4.2 K spectrum of 1-Me-*c*SiC5-2,2,6,6-$d_4$$^+$ was explained by assuming that the isotropic *hf* splittings of H_{3e} and H_{5e} have been partially averaged by the exchange process with a slightly smaller rate constant, k (s^{-1}) than the *hf* splitting difference in the two hydrogens, $|a(H_{3e}) - a(H_{5e})| = 1.3 \times 10^7\ (s^{-1})$. With a k value nearly equal to the difference in the two *hf* splittings the inner doublet should disappear as observed at *ca*. 40 K. On further increasing the temperature a new singlet appears at the central position and its intensity grows, suggesting a further increase in the rate constant. Arrhenius plots of the rate constants, k (s^{-1}), show a non-linear relationship over the temperature range of 4.2–130 K for all silacyclohexane radical cations studied. Assuming a linear relationship in the higher temperature region between 60 and 130 K, an activation energy of *ca.* 0.3 kcal mol^{-1} was evaluated for both *c*SiC5$^+$ and 1-Me-*c*SiC5$^+$ in the CF_3-cC_6F_{11} matrix. Furthermore, below 40 K, the rate constants were almost independent of temperature: $k = 3.6 \times 10^7\ s^{-1}$ for *c*SiC5$^+$ and $k = 1.2 \times 10^7\ s^{-1}$ for 1-Me-*c*SiC5$^+$.

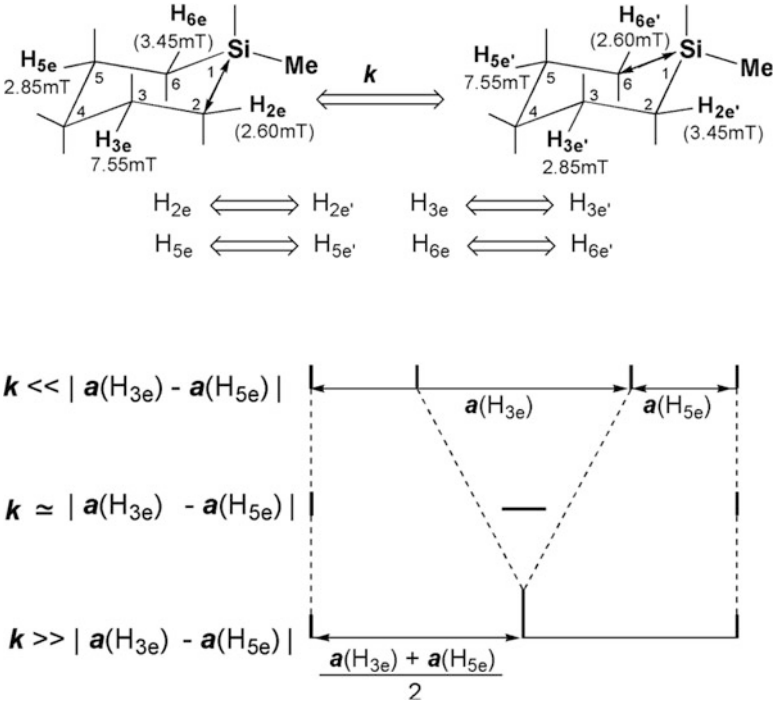

Fig. 4.26 A diagram showing how the EPR lineshapes of 1-Me-*c*SiC5^{+} depend on the intramolecular hydrogen exchange rate k (s^{-1}) between the two asymmetrically distorted C_1 structures, see text for more details (Adapted from Ref. [27] with kind permission of © The American Chemical Society 1997)

4.8 D-Labeling Study on S_H2 Reactions of Methyl Radicals in Solid Methylsilane

Bimolecular homolytic substitution (S_H2) reactions [118–121] play an important role in radical chemistry and have been regarded as a useful tool in synthesis [122] because of the elemental steps available for free radicals (R_1) to generate a new radical (R_2) as expressed in reaction (4.9):

$$R_1 + A{-}R_2 \rightarrow [R_1{-}{-}{-}A{-}{-}{-}R_2]^{\#} \rightarrow R_1{-}A + R_2 \qquad (4.9)$$

The most common reactions of S_H2 type are the abstraction reactions of hydrogen (A: H) or halogen (A: X) at monovalent centers. It is known that more complex S_H2 reactions generally proceed at multivalent centers, which include Si-, Ge- and Sn-atoms, having low-lying unfilled orbitals. The reaction can proceed

favorably only when it is exothermic and/or the temperature is high enough to give the reactants sufficient kinetic energy. Thus the S_H2 reactions have been experimentally studied mainly in the gas phase by means of mass spectroscopy [123], whereas studies in condensed phase, especially in solids at low temperature, are quite limited [52–54, 124].

Here we present our recent D-labeling study on the S_H2 reactions by methyl radicals in the solid methylsilane (CH_3SiH_3) at cryogenic temperatures [52–54]. The CH_3SiH_3 molecule, the simplest alkylsilane, is composed of a CH_3 group and a SiH_3 group, which are expected to show remarkably different reactivity from each other; *i.e.* the Si–H bond length of Si with sp^3 hybridization is *ca.* 0.149 nm, which is *ca.* 36% longer than the corresponding C–H bond (*ca.* 0.110 nm) [116]. In addition, the dissociation energy of the Si-H bond is *ca*. 40 kJ mol^{-1} smaller than the C–H bond. These properties may significantly contribute to either classical or non-classical (or tunnel) reaction kinetics, or both. Thus, the CH_3SiH_3 molecule was chosen as a candidate molecule for studying the S_H2 reactions including the hydrogen abstraction reaction. The EPR study shows a selective H-atom abstraction reaction from the Si–H bond of CH_3SiH_3, which competes with a S_H2 reaction of the CH_3 radical with CH_3SiH_3.

4.8.1 Direct EPR Evidence for S_H2 Reaction of CH_3 Radical with CH_3SiH_3

An EPR study was carried out for a solid solution containing a small amount of methyl iodide in solid methylsilane in a temperature range of 3–115 K [52–54]. Figure 4.27 shows the EPR spectra of (a) CH_3I/CH_3SiH_3, (b) CD_3I/CH_3SiD_3, and (c) CH_3I/CH_3SiD_3 systems observed immediately after UV photolysis at 77 K. For (a) the CH_3I/CH_3SiH_3 system the CH_3SiH_2 radical dominates the spectrum and the CH_3 radical is a minor component. The result suggests that the CH_3 radical generated by UV (reaction (4.10)) selectively abstracts an H-atom from the SiH_3 group of CH_3SiH_3 to yield the CH_3SiH_2 radical, reaction (4.11). Well resolved EPR spectra due to ^{127}I-atom were observed after UV photolysis below 60 K, supporting the photolytic C–I bond scission of CH_3I to form the CH_3 radical in solid CH_3SiH_3. No appreciable amount of CH_2SiH_3 radicals was observed. This suggests negligible contribution of competitive reaction (4.12) .

$$CH_3I \text{ (or } CD_3I) \rightarrow CH_3 \text{ (or } CD_3) + I \tag{4.10}$$

$$CH_3 \text{ (or } CD_3) + SiH_3CH_3 \rightarrow CH_4 \text{ (or } CD_3H) + SiH_2CH_3 \tag{4.11}$$

$$CH_3 \text{ (or } CD_3) + SiH_3CH_3 \rightarrow CH_4 \text{ (or } CD_3H) + SiH_3CH_2 \tag{4.12}$$

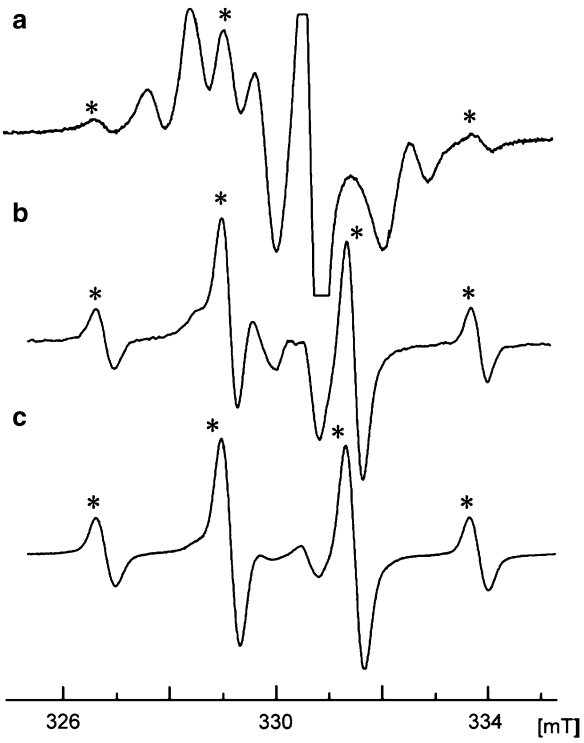

Fig. 4.27 EPR spectra observed at 77 K for solid methylsilanes containing iodomethane (1 mol%) immediately after UV-light exposure at 77 K. (**a**) CH_3I/CH_3SiH_3, (**b**) CD_3I/CH_3SiD_3, and (**c**) CH_3I/CH_3SiD_3 systems. The peaks due to the CH_3 radical are denoted by an asterisk (*) (Adapted from Ref. [53] with kind permission of © Elsevier 2005)

On the other hand, for (b) the CD_3I/CH_3SiD_3 system the CD_3 radical generated by UV is not visible in the spectrum; instead, the CH_3 radical was observed as a major component. CH_3SiD_3 used as a solid matrix is the only possible precursor of the CH_3 radical. Thus it is suggested that the CD_3 radicals formed are converted into CH_3 radicals by a S_H2 type of reaction (4.13):

$$CD_3 + SiD_3CH_3 \rightarrow [CD_3 \cdots SiD_3 \cdots CH_3]^{\#} \rightarrow CD_3SiD_3 + CH_3 \qquad (4.13)$$

The failure to observe CD_3 radicals in the CD_3I/CH_3SiD_3 system further suggests that the reverse reaction of reaction (4.13) does not occur.

For (c) the CH_3I/CH_3SiD_3 system the CH_3 radical again predominates the spectrum over the other radicals. In this system the CH_3 radical can come either from solute CH_3I as a 'primary' radical or from matrix CH_3SiD_3 as a 'secondary' radical, or both. Thus, it is possible to experimentally observe that the methyl radical reacts with methylsilane *via* the S_H2 reaction to yield a new methyl radical only when the CD_3 radical and selectively deuterated CH_3SiD_3 molecule are used as reactants. A similar S_H2 reaction was observed for the low temperature CD_3I/CH_3GeD_3 solid system [53].

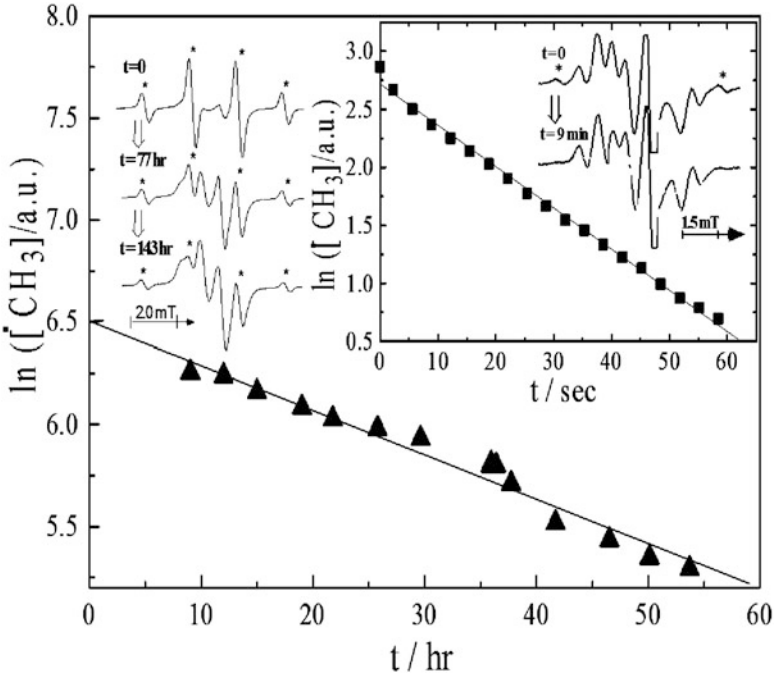

Fig. 4.28 First-order plots of CH_3 radicals decaying in the CH_3I/CH_3SiH_3 (■) and CH_3I/CH_3SiD_3 (▲) systems at 77 K in dark. The CH_3 radicals were generated by the UV-photolysis of the two different methylsilanes containing 1 mol% of CH_3I at 77 K (Adapted from Ref. [52] with kind permission of © The Royal Society of Chemistry 2002)

4.8.2 Enormously Large D-Isotope Effects on H-Atom Abstraction by CH_3 Radicals in Solid CH_3SiH_3

As described in the foregoing section, the EPR spectra observed immediately after UV-photolysis of the CH_3I/CH_3SiH_3 system are dominated by the SiH_2CH_3 radical, but with a small amount of CH_3 radical. When SiD_3CH_3 is employed, on the contrary, the major radical turns out to be CH_3, but with a small amount of CH_3SiD_2. The experimental results suggest that hydrogen atom abstraction by the CH_3 radical occurs preferentially at the Si–H bond of CH_3SiH_3, but not at the C–H bond.

The CH_3 radicals decayed by following the first order reaction kinetics with a concomitant formation of the SiH_2CH_3 (SiD_2CH_3) radical in the solid SiH_3CH_3 (SiD_3CH_3) system as shown in Fig. 4.28. The associated decaying reaction rates of CH_3, k, show an anomalously large isotope effect; *i.e.*, for example, $k_{(Si\text{-}H)} \approx 4 \times 10^{-2}$ s^{-1} and $k_{(Si\text{-}D)} \approx 7 \times 10^{-6}$ s^{-1} (*i.e.*, $k_{(Si\text{-}H)}/k_{(Si\text{-}D)} \approx 5 \times 10^3$) at 77 K. Furthermore, a non-linear Arrhenius plot was obtained for the reaction rates so as to become almost independent of the temperature below 20 K. Assuming a linear Arrhenius plot above 20 K, an apparent activation energy for

the reaction is evaluated to be $E_{a(\mathrm{Si\text{-}H})} \approx 1$ kJ mol^{-1} and $E_{a(\mathrm{Si\text{-}D})} \approx 9$ kJ mol^{-1} (*i.e.*, $E_{a(\mathrm{Si\text{-}H})}/E_{a(\mathrm{Si\text{-}D})} \approx 1/10$). The observed large D-isotope effect on the rates and the non-linear Arrhenius plot strongly suggest that quantum mechanical tunnelling effects [125–130] dominate the H-atom abstraction reaction from the Si–H bond of the SiH_3 group, especially below 20 K.

Hiraoka et al. have reported that amorphous silicon thin films have been formed by successive H-atom abstraction from the silane (SiH_4) molecule by H-atoms at a low temperature of 10 K [131]. They could not provide, however, any direct experimental evidences of radical species as reaction intermediates, because the reactions were monitored by in situ IR spectroscopy. The present EPR study on the H-atom abstraction from the Si–H bond of methylsilane strongly supports that the quantum mechanical tunnelling reaction can play an important role, too, for the formation of amorphous silicon from SiH_4.

We have investigated the cause of the observed S_H2 reaction between the methyl radical and methylsilane by means of quantum chemical calculations [54]. In particular, an extensive search was undertaken for various SiH_3CH_3/CH_3I complexes. The computational data for the S_H2 reaction coupled with the structural and energetic properties of SiH_3CH_3/CH_3I complexes formed prior to photolysis of methyl iodide, are very useful to understand detailed mechanisms of the S_H2 reaction proceeded in solid state.

References

1. Shiotani M (1987) ESR studies of radical cations. Magn Reson Rev 12:333–381
2. Lund A, Shiotani M (eds) (1991) Radical ionic systems: properties in condensed phases. Kluwer Academic Publishers, Dordrecht
3. Lindgren M, Shiotani M (1991) ESR studies of radical cations of cycloalkanes and saturated heterocycles. In: Lund A, Shiotani M (eds) Radical ionic systems: properties in condensed phases. Kluwer Academic Publishers, Dordrecht
4. Shiotani M, Lund A (1991) Deuterium labeling studies of cation radicals. In: Lund A, Shiotani M (eds) Radical ionic systems: properties in condensed phases. Kluwer Academic Publishers, Dordrecht
5. Shiotani M, Komaguchi K (1998) ESR studies on structural distortion and dynamics of saturated hydrocarbon radical cations: recent development. Houshasen Kagaku (Radiat Chem Jpn) 65:2–15
6. Shiotani M (1991) ESR. In: Tabata Y (ed) CRC handbook of radiation chemistry. CRC Press, Boca Raton, pp 139–144
7. Shiotani M, Yoshida H (1991) ESR of radical ions. In: Tabata Y (ed) CRC handbook of radiation chemistry. CRC Press, Boca Raton, pp 440–467
8. Shiotani M (1991) ESR spectra of free radicals generated by ionizing radiations. In: Tabata Y (ed) CRC handbook of radiation chemistry. CRC Press, Boca Raton, pp 544–567
9. Shiotani M, Lindgren M (1994) Radicals on surfaces formed by ionizing radiation. In: Lund A, Rhodes CJ (eds) Radicals on surfaces. Kluwer Academic Publishers, Dordrecht
10. Willard JE (1988) Chemical kinetics of small organic radicals in organic and rare gas matrices at cryogenic temperatures. In: Alfassi ZB (ed) Chemical kinetics of small organic radicals, vol IV. CRC Press, Boca Raton

11. Benderskii VA, Makarov DE, Wight CA (1994) Chemical dynamics at low temperatures, vol 8, Advances in chemical physics. Wiley, New York
12. Lund A, Shiotani M (eds) (2003) EPR of free radicals in solids. Kluwer Academic Publishers, Dordrecht
13. Lund A, Shiotani M, Shimada S (2011) Principles and applications of ESR spectroscopy. Springer, Dordrecht, pp 211–271
14. Yamada T, Komaguchi K, Shiotani M, Benetis NP, Sϕrnes AR (1999) High resolution EPR and quantum effects on CH_3, CH_2D, CHD_2 and CD_3 radicals under argon-matrix isolation conditions. J Phys Chem A 103:4823–4829
15. McConnell HM (1958) Free rotation in solids at 4.2°K. J Chem Phys 29:1422
16. Freed JH (1965) Quantum effects of methyl-group rotations in magnetic resonance: ESR splittings and linewidths. J Chem Phys 43:1710–1720
17. Clough S, Poldy F (1969) Study of tunneling rotation of methyl groups by electron spin resonance and electron nuclear double resonance. J Chem Phys 51:2076–2084
18. Davidson RB, Miyagawa I (1970) ESR study of quantum tunneling of a methyl group: a simple tunneling model. J Chem Phys 52:1727–1732
19. Clough S, Hill JR (1974) Temperature dependence of methyl group tunneling rotation frequency. J Phys C Solid State Phys 7:L20–L21
20. Geoffroy M, Kispert LD, Hwang JS (1979) An ESR, ENDOR, and ELDOR study of tunneling rotation of a hindered methyl group in x-irradiated 2,2,5-trimethyl-1,3-dioxane-4,6-dione crystals. J Chem Phys 70:4238–4242
21. Matsushita M, Momose T, Shida T (1990) Internal rotation of the methyl group in the radical cation of dimethyl ether. J Chem Phys 92:4749–4758
22. Kubota S, Matsushita M, Shida T, Abu-Raqabah A, Symons MCR, Wyatt JL (1995) Internal rotation of the methyl groups in the *t*-butyl radical as studied by ESR. Bull Chem Soc Jpn 68:140–145
23. Komaguchi K, Kumada T, Aratono Y, Miyazaki T (1997) Evaluation of the distance between the hydrogen atom and hydrogen molecule in the tunneling reaction $HD + D \rightarrow H + D_2$ in an argon matrix at 20 K. Chem Phys Lett 268:493–497
24. Miyazaki T, Yamamoto K, Arai J (1994) Effect of rotational quantum states ($J = 0$, 1) of matrix H_2 molecules on ESR spectra of radicals at 4.2 K. Chem Phys Lett 219:405–408
25. Silvera IF (1980) The solid molecular hydrogens in the condensed phase: fundamentals and static properties. Rev Mod Phys 52:393–452
26. Shiotani M, Isamoto N, Hayashi M, Fängström T, Lunell S (2000) Deuterium isotope effects on rotation of methyl hydrogens: a study of the dimethyl ether radical cation by ESR spectroscopy and ab initio and density functional theory. J Am Chem Soc 122:12281–12288
27. Komaguchi K, Shiotani M (1997) Asymmetrically distorted structure, selective bond length alternation, and reactions of radical cations of silacyclohexanes: an ESR and ab-initio MO study. J Phys Chem 101:6983–6990
28. Wang P, Shiotani M, Lunell S (1998) Structure and dynamics of radical cations of selectively deuteriated cyclohexanes: an ESR and ab initio study. Chem Phys Lett 292:110–114
29. Shiotani M, Wang P, Komaguchi K (1999) Static and dynamic structural distortion of cyclohexane radical cations in low temperature matrices: an ESR study. Bull Polish Acad Sci Chem 47:89–102
30. Coulson CA, Strauss HL (1962) Static Jahn-Teller distortions in the small molecules: CH_4^+, CF_4^+, NH_3^+ (excited state) and NH_3 (excited state). Proc R Soc Lond Ser A 269:443–455
31. Dixon RN (1971) On the Jahn-Teller distortion of CH_4^+. Mol Phys 20:113–126
32. Grimm FA, Gody J (1970) A calculation on the geometry of CH_4^+. Chem Phys Lett 6:336–338
33. Shchegoleva LN, Schastnev PV (1995) Molecular distortions in ionic and excited states. CRC Press, New York
34. Knight LB Jr, Steadman J, Feller D, Davidson ER (1984) Experimental evidence for a C_{2v} ($^2B_1$) ground-state structure of the methane cation radical: ESR and ab initio CI investigations of CH_4^+ and $CD_2H_2^+$ in neon matrices at 4 K. J Am Chem Soc 106:3700–3701

35. Knight LB Jr, King GM, Petty JT, Matsushita M, Momose M, Shida T (1995) Electron spin resonance studies of the methane radical cations ($^{12,13}CH_4^+$, $^{12,13}CDH_3^+$, $^{12}CD_2H_2^+$, $^{12}CD_3H^+$, $^{12}CD_4^+$) in solid neon matrices between 2.5 and 11 K: analysis of tunneling. J Chem Phys 103:3377–3385
36. Komaguchi K, Marutani T, Shiotani M, Hasegawa A (2001) Isotope effects in partially deuterated tetramethylsilane cations studied by EPR spectroscopy. Phys Chem Chem Phys 3:3536–3540
37. Shiotani M, Ohta N, Ichikawa T (1988) Structure and reaction of methylcyclohexane radical cation: ESR studies. Chem Phys Lett 149:185–190
38. Lindgren M, Shiotani M, Ohta N, Ichikawa T, Sjöqvst L (1989) ESR evidence of a distorted ^2A_g electronic structure for the methylcyclohexane radical cation. Chem Phys Lett 161:127–130
39. Shiotani M, Lindgren M, Ichikawa T (1990) The Jahn-Teller split HOMO of the cyclohexane cation in selectively alkyl-substituted cyclohexanes: an ESR and MNDO/INDO MO study. J Am Chem Soc 112:967–973
40. Shiotani M, Lindgren M, Ohta N (1991) Ichikawa T (1991) Radical cations of cyclohexanes alkyl-substituted on one carbon: an ESR study of the Jahn-Teller distorted HOMO of cyclohexane. J Chem Soc Perkin Trans 2:711–719
41. Fängström T, Lunell S, Engles B, Eriksson L, Shiotani M, Komaguchi K (1997) Structure and dynamics of the silacyclobutane radical cation, studies by ab initio and density functional theory and electron spin resonance spectroscopy. J Chem Phys 107:297–306
42. Komaguchi K, Marutani T, Shiotani M, Hasegawa A (1999) Asymmetrically distorted structure of radical cations of ethylsilanes, studied by electron resonance spectroscopy, ab initio and density functional theories. Phys Chem Chem Phys 1:4549–4554
43. Komaguchi K, Nomura K, Shiotani M (2007) High-resolution ESR study of the $H\cdots CH_3$, $H\cdots CHD_2$, $D\cdots CH_2D$, and $D\cdots CD_3$ radical pairs in solid argon. J Phys Chem A111:726–733
44. Komaguchi K, Kumada T, Takayanagi T, Aratono Y, Shiotani M, Miyazaki T (1999) H atom-H_2 molecule van der Waals complexes in solid argon matrix by high-resolution ESR spectroscopy. Chem Phys Lett 300:257–261
45. Komaguchi K, Yamada S, Shiotani M, Kasai PH (1999) Partial orientation and dynamics of NO_2 in solid hydrogen: a high resolution ESR study. In: Proceeding of 3rd international conference on low temp chem, Nagoya
46. Kumada T, Yakayanagi T, Kumagai J (2006) ESR study of H_6^+ and $H_4D_2^+$ produced in irradiated solid hydrogen. J Mol Struct 786:130–133
47. Kumagai J, Inagaki H, Kariya S, Ushida T, Shimizu Y, Kumada T (2007) Electron spin resonance study on H_6^+, H_5D^+, $H_4D_2^+$, and $H_2D_4^+$ in solid hydrogen. J Chem Phys 127(024505):1–13
48. Bonazzola L, Michaut JP, Roncin J (1991) Structure of $Si(CH_3)_4^+$ radical cation: an ESR and theoretical study. J Phys Chem 95:3132–3135
49. Bonazzola L, Michaut JP, Roncin J (1992) Structure of $X(CH_3)_4^+$ and $(CH_3)_3XX(CH_3)_3^+$ radical cations. (X = Si, Ge, Sn). New J Chem 16:489–496
50. Knight LB Jr, Gregory BW, Hill DW, Arrington CA, Momose T, Shida T (1991) Electron-spin-resonance studies of $^{12}CH_3F^+$, $^{13}CH_3F^+$, and $^{12}CH_2DF^+$ in neon matrices at 4 K: comparison with theoretical calculations. J Chem Phys 94:67–79
51. Yates BF, Bouma WJ, Radon L (1987) Ylides and ylidions: a comparative study of unusual gas-phase structures. J Am Chem Soc 109:2250–2263
52. Komaguchi K, Ishiguri Y, Tachikawa H, Shiotani M (2002) Selectivity and enormous H/D isotope effects on H atom abstraction by CH_3 radicals in solid methylsilane at 3.0 K-115 K. Phys Chem Chem Phys 4:5276–5280
53. Komaguchi K, Norberg D, Nakazawa N, Shiotani M, Persson P, Lunell S (2005) Direct ESR evidence for S_H2 reaction of methyl radical with methylsilane and methylgermane in a low temperature solid phase: a deuterium labeling study. Chem Phys Lett 410:1–5

54. Norberg N, Shiotani M, Lunell S (2008) S_H2 reaction vs. hydrogen abstraction/expulsion in methyl radical-methylsilane reactions: effects of prereactive complex formation. J Phys Chem A 112:1330–1338
55. Jen CK, Foner SN, Cochran EL, Bowers VA (1958) Electron spin resonance of atomic and molecular free radicals trapped at liquid helium temperature. Phys Rev 112:1169–1182
56. Morehouse RL, Christiansen JJ, Gordy W (1966) ESR of free radicals trapped in inert matrices at low temperature: CH_3, SiH_3, GeH_3, and SnH_3. J Chem Phys 45:1751–1758
57. Kasai PH, McLeod D Jr (1972) Electron spin resonance study of pyrolysis and photolysis of 2-iodoacetic acid and 2-iodoacetamide. J Am Chem Soc 94:7975–7981
58. Cirelli G, Russu A, Wolf R, Rudin M, Schweiger A, Günthard HH (1982) Detection of endor spectra of paramagnetic species isolated in solid argon. Chem Phys Lett 92:223–224
59. Fujimoto M, Gesser HD, Garbutt B, Cohen A (1966) Electron paramagnetic resonance of methyl radicals on porous glass surface. Science 154:381–382
60. Shiotani M, Yuasa F, Sohma J (1975) Electron spin resonance studies of methyl radicals trapped on 4A type zeolite. J Phys Chem 79:2669–2674
61. Fessenden RW (1967) Electron spin resonance spectra of some isotopically substituted hydrocarbon radicals. J Phys Chem 71:74–83
62. Kubota S, Iwaizumi M, Ikegami Y, Shimokoshi K (1979) Anisotropic hyperfine interaction in the electron spin resonance spectrum of the methyl radical trapped in $CH_3COONa{\cdot}3D_2O$ crystal at low temperatures. J Chem Phys 71:4771–4776
63. Sϕrnes AR, Benetis NP, Erickson R, Mahgoub AS, Eberson L, Lund A (1997) Effect of isotopic substitution on the electron spin dynamics of the $CH_3C(COOH)_2$ radical in x-irradiated methyl malonic acid powder: intrinsic potentials and activation energies. J Phys Chem A 101:8987–8994
64. Kurita Y (1964) Electron spin resonance study of radical pairs trapped in irradiated single crystals of dimethylglyoxime at liquid-nitrogen temperature. J Chem Phys 41:3926–3927
65. Gordy W, Morehouse R (1966) Triplet-state electron spin resonance of an H-atom – methyl radical complex in a solid matrix. Phys Rev 151:207–210
66. Toriyama K, Iwasaki M, Nunome K (1979) ESR studies of irradiated methane and ethane at 4.2 K and mechanism of pairwise trapping of radicals in irradiated alkanes. J Chem Phys 71:1698–1705
67. Atherton NM (1973) Electron spin resonance: theory and applications. Wiley, New York
68. Foner SN, Cochran EL, Bowers VA, Jen CK (1960) Multiple trapping sites for hydrogen atoms in rare gas matrices. J Chem Phys 32:963–971
69. Adrian FJ (1960) Matrix effects on the electron spin resonance spectra of trapped hydrogen atoms. J Chem Phys 32:972–981
70. VanZee RJ, Williams AP, Weltner W Jr (1997) Electron spin resonance of the $H\cdots NH_2$ radical pair. J Phys Chem 101:2917–2920
71. Knight LB Jr, Rice WE, Moore L, Davidson ER (1995) ESR observation of the $H\cdots H$, $H\cdots D$, and $D\cdots D$ spin-pair radicals in rare gas matrices. J Chem Phys 103:5275–5278
72. Knight LB Jr, Rice WE, Moore L, Davidson ER, Dailey RS (1998) Theoretical and electron spin resonance studies of the $H\cdots H$, $H\cdots D$, and $D\cdots D$ spin-pair radicals in rare gas matrices: a case of extreme singlet-triplet mixing. J Chem Phys 109:1409–1424
73. Knight LB Jr, Bell BA, Cobranchi DP, Davidson ER (1999) Electron spin resonance and theoretical studies of the $^{14}N\cdots{}^{14}N$ spin pair radicals in neon matrices: the effects of mixing among the $^1\Sigma_g{}^+$, $^3\Sigma_u{}^+$, $^5\Sigma_g{}^+$, and $^7\Sigma_u{}^+$ electronic states. J Chem Phys 111:3145–3154
74. Hancock GC, Mead CA, Truhlar DG, Varandas AJC (1989) Reaction rates of $H(H_2)$, $D(H_2)$, and $H(D_2)$ van der Waals molecules and the threshold behavior of the bimolecular gas-phase rate coefficient. J Chem Phys 91:3492–3503
75. Takayanagi T, Sato S (1990) The bending-corrected-rotating-linear-model calculations of the rate constants for the $H + H_2$ reaction and its isotopic variants at low temperatures: the effect of van der Waals well. J Chem Phys 92:2862–2868
76. Vaskonen K, Eloranta J, Kiljunen T, Kunttu H (1999) Thermal mobility of atomic hydrogen in solid argon and krypton matrices. J Chem Phys 110:2122–2128

77. Van Kranendonk J (1983) Solid parahydrogen. Plenum Press, New York
78. Miyazaki T, Hiraku T, Fueki K, Tsuchihashi Y (1991) Effect of rotational quantum states ($J = 0, 1$) on the tunneting reaction $H_2 + H \rightarrow H + H_2$, in parahydrogen solid at 4.2 K. J Phys Chem 95:26–29
79. Kumada T, Kumagai J, Miyazaki T (2001) High-resolution electron spin resonance spectroscopy of ethyl radicals in solid parahydrogen. J Chem Phys 114:10024–10030
80. Fessenden RW (1962) Second-order splittings in the ESR spectra of organic radicals. J Chem Phys 37:747–750
81. Kumada T, Tachikawa H, Takayanagi T (2005) H_6^+ in irradiated solid para-hydrogen and its decay dynamics: reinvestigation of quartet electron paramagnetic resonance lines assigned to H_2^-. Phys Chem Chem Phys 7:776–784
82. Shinizu Y, Kumada T, Kumagai J (2008) Electron spin resonance spectroscopy of molecules in large precessional motion: a case of H_6^+ and $H_4D_2^+$ in solid parahydrogen. J Magn Reson 194:76–80
83. Shiotani M, Freed JH (1981) ESR studies of NO_2 adsorbed on surfaces. Analysis of motional dynamics. J Phys Chem 85:3873–3883
84. Kasai PH, Weltner W Jr, Whipple EB (1965) Orientation of NO_2 and other molecules in neon matrices at 4°K. J Chem Phys 42:1120–1121
85. Iwasaki M, Toriyama K, Nunome K (1981) Electron spin resonance study of electronic and geometrical structures of $C_2H_6^+$ and other simple alkane cations at 4.2 K: possible evidence for Jahn-Teller distortion. J Am Chem Soc 103:3591–3592
86. Komaguchi K, Shiotani M, Lund A (1997) An ESR study of trimethylenemethane radical cation. Chem Phys Lett 265:217–223
87. Bally T, Maltsev A, Gerson F, Frank D, de Meijere A (2005) Radical cation of a trimethylenemethane with a nondegenerate ground state. J Am Chem Soc 127:1984–1988
88. Dowd P (1972) Trimethylenemethane. Acc Chem Res 5:242
89. Claesson O, Lund A, Gillbro T, Ichikawa T, Edlund O, Yoshida H (1980) A single crystal EPR study of ground state triplet trimethylenemethane. J Chem Phys 72:1463–1470
90. Slipchenko LV, Krylova AI (2003) Electronic structure of the trimethylenemethane diradical in its ground and electronically excited states: bonding, equilibrium geometries, and vibrational frequencies. J Chem Phys 118:6874–6883
91. Meyer W (1973) PNO-CI studies of electron correlation effects. I. Configuration expansion by means of nonorthogonal orbitals, and application to the ground state and ionized states of methane. J Chem Phys 58:1017–1035
92. Paddon-Raw MN, Fox DJ, Pople JA, Houk KN, Pratt DW (1985) Dynamic Jahn-Teller effects in CH_4^+. Location of the transition structures for hydrogen scrambling and inversion. J Am Chem Soc 107:7696–7700
93. Frey RF, Davidson ER (1988) Potential energy surfaces of CH_4^+. J Chem Phys 88:1775–1785
94. Eriksson LA, Lunell S, Boyd RJ (1993) Electronic structure calculations of hydrocarbon radical cations: a density functional study. J Am Chem Soc 115:6896–6900
95. Walther BW, Williams F (1982) ESR spectra and structure of the tetramethylsilane and tetramethylgermaneradical cations. J Chem Soc Chem Commun 1982:270–272
96. Sjöqvst L, Lindgren M, Lund A, Shiotani M (1990) Mirror inversion of the low-symmetry ground-state structures of the methylcyclohexane and 1, l-dimethylcyclohexane radical cations. J Chem Soc Faraday Trans 86:3377–3382
97. Heller C, McConnell HM (1960) Radiation damage in organic crystals. II. Electron spin resonance of $(CO_2H)CH_2CH(CO_2H)$ in β-succinic acid. J Chem Phys 32:1535–1539
98. Frankel GK (1967) Line widths and frequency shifts in electron spin resonance spectra. J Phys Chem 71:139–171
99. Knight LB Jr, Kerr K, Villanueva M, Mckinley AJ (1992) Theoretical and neon matrix electron spin resonance studies of the methanol cation: CH_3OH^+, CH_3OD^+, CH_2DOH^+ and $^{13}CH_3OH^+$. J Chem Phys 97:5363–5376

100. Knight LB Jr, Steadman J (1984) An ESR investigation of the formaldehyde cation radicals ($H_2{}^{12}CO^+$ and $H_2{}^{13}CO^+$) in neon matrices at 4 K. J Chem Phys 80:1018–1025
101. Weltner W Jr (1983) Magnetic atoms and molecules. Van Nostrand, New York
102. Iwasaki M, Toriyama K (1984) Electron spin resonance studies of structures and reactions of radical cations of a series of cycloalkanes in low-temperature matrices. Faraday Discuss Chem Soc 78:19–33
103. Lunell S, Huang MB, Claesson O, Lund A (1985) Theoretical ab initio and low-temperature ESR study of the cyclohexane cation. J Chem Phys 82:5121–5126
104. Lindgren M, Matsumoto M (1992) Shiotani M (1992) Radical cations of cis- and trans-1,3-di- and 1,3,5-trimethylcyclohexanes: matrix influence on two nearly degenerate SOMOs. J Chem Soc Perkin Trans 2:1397–1402
105. Shiotani M, Matsumoto M, Lindgren M (1993) Electronic structure, methyl group reorientation and reactions of radical cations of 1,2,4-trimethylcyclohexanes: an EPR study. J Chem Soc Perkin Trans 2:1995–2002
106. Komaguchi K, Shiotani M, Ishikawa M, Sasaki K (1992) Structure and ring puckering motion of the σ-localized silacyclobutane radical cation: ESR evidence. Chem Phys Lett 200:580–586
107. Shiotani M, Komaguchi K, Ohshita J, Ishikawa M, Sjöqvist L (1992) An asymmetrically distorted structure of the 1-methylsilacyclohexane radical cation: ESR evidence. Chem Phys Lett 188:93–99
108. Lindgren M, Komaguchi K, Shiotani M, Sasaki K (1994) Upon the structure of c-$C_5H_{10}{}^+$: asymmetrical SOMO of methylsubstituted cyclopentane cation radicals. J Phys Chem 98:8331–8338
109. Ito Y, Mohamed HFM, Shiotani M (1996) Vacancies in the solids of low molecular weight organic compounds observed by positron annihilation. J Phys Chem 100:14161–14165
110. Itagaki Y, Shiotani M, Tachikawa H (1997) Electronic structure of methylacetylene radical anion: an EPR and MO study. Acta Chem Scand 51:220–223
111. Hasegawa A, Itagaki Y, Shiotani M (1997) EPR spectra and structure of the radical cations of fluorinated benzenes. J Chem Soc Perkin Trans 2:1625–1631
112. Kadam RM, Erickson R, Komaguchi K, Shiotani M, Lund A (1998) The static Jahn-Teller distortion of the monomer and geometry of the dimer cation. Chem Phys Lett 290:371–378
113. Itagaki Y, Shiotani M, Hasegawa A, Kawazoe H (1998) EPR spectra and structure of the radical cations of fluorinated ethylenes and propenes. Bull Chem Soc Jpn 71:2547–2554
114. Sakurai H, Shiotani M, Ichikawa T (1999) Hydrogen molecule detachment in irradiated 1,2-dimethyl cyclohexane: stereo-selective reaction. Radiat Phys Chem 54:235–240
115. Itagaki Y, Shiotani M (1999) Photoinduced isomerization of trans-acetylene radical anion to vinylidene radical anion in 2-methyltetrahydrofuran. J Phys Chem A 103:5189–5195
116. Lide DR (ed) (2001) CRC handbook of chemistry and physics, 82nd edn. CRC Press, Boca Raton
117. (a) Pearson RG (1969) A symmetry rule for predicting molecular structure and reactivity. J Am Chem Soc 91:1252–1254; (b) A symmetry rule for predicting molecular structures. J Am Chem Soc 91:4947–4955
118. Ingold KU, Roberts BP (1973) Free-radical substitution reactions. Wiley-Interscience, New York
119. Davies AG, Roberts BP (1973) Bimolecular homolytic substitution at metal centers. In: Kochi JK (ed) Free radicals, vol 1. Wiley-Interscience, New York, pp 547–587
120. Fossey J, Lefort D, Sorba J (1995) Free radicals in organic chemistry. Wiley, Chichester, pp 123–137
121. Walton JC (1998) Homolytic substitution – a molecular ménage à trois. Acc Chem Res 31:99–107
122. Schiesser CH, Wild LM (1996) Tetrahedron 52:13265–13314
123. Turecek F (2003) Transient intermediates of chemical reactions by neutralization-reionization mass spectroscopy. In: Schalley CA (ed) Modern mass spectroscopy – topics in current chemistry 225. Springer, Berlin

124. Wisniowski P, Bobrowski K, Carmichael I, Hug GL (2004) Bimolecular homolytic substitution (S_H2) reactions with hydrogen atoms. Time-resolved electron spin resonance detection in the pulse radiolysis of α-(Methylthio)acetamide. J Am Chem Soc 126:14468–14474
125. Sullivan PJ, Koski WS (1963) An electron spin resonance study of the relative stabilities of free radicals trapped in irradiated methanol at 77°K. J Am Chem Soc 85:384–387
126. French WG, Willard JE (1968) Radical decay kinetics in organic glasses. Spatial effects and isotope effects. J Phys Chem 72:4604–4608
127. Williams F, Sprague ED (1971) Evidence for hydrogen atom abstraction by methyl radicals in the solid state at 77°K. J Am Chem Soc 93:787–788
128. Sprague ED (1973) Hydrogen atom abstraction by methyl radicals in 3-methylpentane glass at 77 K. J Phys Chem 77:2066–2070
129. Miyazaki T (1991) Reaction of hydrogen atoms produced by radiolysis and photolysis in solid phase at 4 and 77 K. Radiat Phys Chem 37:635–642
130. Hadson RL, Shiotani M, Williams F (1977) Hydrogen atom abstraction by methyl radicals in methanol glasses at 15–100 K: evidence for a limiting rate constant below 40 K by quantum-mechanical tunneling. Chem Phys Lett 48:193–196
131. Hiraoka K, Sato T, Sato S, Hishiki S, Suzuki K, Takahashi Y, Yokoyama T, Kitagawa S (2001) Formation of amorphous silicon by the low-temperature tunneling reaction of H atoms with solid thin film of SiH_4 at 10 K. J Phys Chem B 105:6950–6955

Chapter 5
XSophe – Sophe – XeprView and Molecular Sophe: Computer Simulation Software Suites for the Analysis of Continuous Wave and Pulsed EPR and ENDOR Spectra

Graeme R. Hanson, Christopher J. Noble, and Simon Benson

Abstract Herein we provide a description of the XSophe-Sophe-XeprView and Molecular Sophe computer simulation software suites for the analysis of continuous wave (CW) and pulsed EPR spectra. While the XSophe-Sophe-XeprView computer simulation software suite employs a traditional structural approach through calculation of the spin Hamiltonian parameters which are then compared with other compounds or parameters obtained from computational chemistry calculations, Molecular Sophe utlizes an integrated molecular structure approach. Both computer simulation suites are completely general, employ matrix diagonalization, the mosaic misorientation linewidth model and provide additional tools (calculation of energy level diagrams, transition roadmaps and transition surfaces) aiding scientists in their analysis of complex CW or pulsed EPR spectra. Molecular Sophe enables the computer simulation of continuous wave and orientation selective pulsed EPR and electron nuclear double resonance (ENDOR) spectra. The molecular structure approach employed within Molecular Sophe, promises to revolutionize the 3-dimensional molecular (geometric and electronic) characterization of paramagnetic species using a combination of high resolution EPR spectroscopy and quantum chemistry calculations.

5.1 Introduction

Multifrequency continuous wave electron paramagnetic resonance (CW EPR), pulsed EPR spectroscopy and electron nuclear double (triple) resonance (END(T)OR) [1–17] have been shown to be powerful tools for structurally (geometric and electronic) characterising paramagnetic molecules or centers within

G.R. Hanson (✉) • C.J. Noble • S. Benson
Centre for Advanced Imaging, The University of Queensland, Brisbane, QLD 4072, Australia
e-mail: Graeme.Hanson@cai.uq.edu.au

A. Lund and M. Shiotani (eds.), *EPR of Free Radicals in Solids I*, Progress in Theoretical Chemistry and Physics 24, DOI 10.1007/978-94-007-4893-4_5,

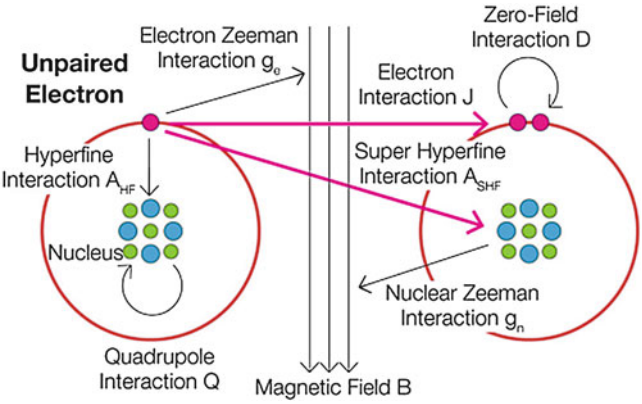

Fig. 5.1 Spin Hamiltonian interactions [35]

molecules that contain one or more unpaired electrons. Computer simulation of the experimental randomly orientated CW EPR, single crystal CW EPR, orientation selective pulsed EPR and ENDOR spectra from isolated or coupled paramagnetic centers is often the only means available for accurately extracting the spin Hamiltonian parameters required for the determination of structural information [1, 2, 18–35]. EPR spectra are often complex and arise through a range of interactions involving one or more unpaired electrons, the external magnetic field and one or more nuclei.

Pictorially, these interactions are shown in Fig. 5.1 and in summary [1, 2, 5, 18, 19] the:

- electron Zeeman interaction involves the interaction of the magnetic dipole moment associated with the spin and orbital angular momentum of the unpaired electron with an externally applied magnetic field. The magnitude of this interaction is described by the 3×3 g matrix. ($\mathbf{B}\cdot g\cdot\mathbf{S}$);
- fine structure interaction involves the interaction between the magnetic dipole moments of electrons on an atom containing more than one unpaired electron. The magnitude of this interaction is described by the second rank D tensor. Second order terms, D and E/D correspond to the axial zero field splitting (D) and the asymmetry parameter E/D which varies from 0 (axial symmetry) to 1/3 (rhombic symmetry) ($\mathbf{S}\cdot D\cdot\mathbf{S}$). Fourth and sixth order corrections to the fine structure interaction tensor D, may also be necessary to adequately interpret the spectrum;
- hyperfine interaction involves the interaction between the magnetic dipole moments of the unpaired electron(s) and the nucleus of the same atom. The magnitude of this interaction is described by the hyperfine (A) 3×3 matrix. ($\mathbf{S}\cdot A\cdot\mathbf{I}$);
- superhyperfine interaction involves the interaction between the magnetic dipole moments of the unpaired electron and the nucleus of different atoms. The

magnitude of this interaction is described by the hyperfine (A) 3×3 matrix. (**S**·A·**I**). The hyperfine matrix can be utilized to determine the distance and orientation of the nuclear spin from the electron spin;

- quadrupole interaction requires the existence of a quadrupole moment which arises from an inhomogeneous electric field gradient at the nucleus. By necessity, the nuclear spin must be greater than ½ and the nucleus must experience a symmetry lower than cubic. The magnitude of this interaction is described by a second rank tensor Q or P, both of which are used interchangeably in the literature and throughout this chapter (**I**·Q·**I**) or (**I**·P·**I**);
- nuclear Zeeman interaction involves the interaction of the magnetic dipole moment arising from the nuclear spin with an externally applied magnetic field (γ $(1 - \sigma)$ **B**·**I**) and
- exchange interaction involves the interaction of magnetic dipole moments of unpaired electrons on different atoms. There are three contributions to the exchange interaction, (i) isotropic exchange (J **S**·**S**) which results from the interaction of the two unpaired electrons on different atoms through molecular orbitals (ii) antisymmetric exchange (**G**·**S**x**S**) and (iii) anisotropic exchange (**S**·J·**S**) which has contributions from the dipole-dipole through space interaction and spin orbit coupling.

Mathematically these interactions can be written using the spin Hamiltonian formalism. For an isolated paramagnetic center (A) a general spin Hamiltonian (H) [1, 2, 5, 18] is:

$$H_A = \boldsymbol{S} \cdot D \cdot \boldsymbol{S} + \beta \boldsymbol{B} \cdot g \cdot \boldsymbol{S} + \sum_{k=1}^{AllNuclei} \left[\boldsymbol{S} \cdot A_k \cdot \boldsymbol{I}_k + \boldsymbol{I}_k \cdot Q_k \cdot \boldsymbol{I}_k - \gamma_k (1 - \sigma) \boldsymbol{B} \cdot \boldsymbol{I}_k \right] \tag{5.1}$$

where **S** and **I** are the electron and nuclear spin operators respectively, D the zero field splitting tensor, g and A are the electron Zeeman and hyperfine coupling matrices respectively, Q the quadrupole tensor, γ the nuclear gyromagnetic ratio, σ the chemical shift tensor, β the Bohr magneton and **B** the applied magnetic field. Additional hyperfine, quadrupole and nuclear Zeeman interactions will be required when superhyperfine splitting is resolved in the experimental EPR spectrum. When two or more paramagnetic centers (A_{ij} i, j = 1, ..., N; i ≠ j) interact, the EPR spectrum is described by a total spin Hamiltonian (H_{Total}) which is the sum of the individual spin Hamiltonians (H_{Ai}, Eq. 5.1) for the isolated centers (A_i) and the interaction Hamiltonian (H_{Aij}) which accounts for the isotropic exchange ($J_{i,j}\mathbf{S_i}$. $\mathbf{S_j}$), antisymmetric exchange (V_{ij} . $\mathbf{S_i} \times \mathbf{S_j}$) and the anisotropic exchange ($\mathbf{S_i}$. J_{ij} . $\mathbf{S_j}$) interactions between a pair of paramagnetic centers [1, 19, 20]. The anisotropic exchange interaction has contributions from the dipole-dipole and spin-orbit interactions.

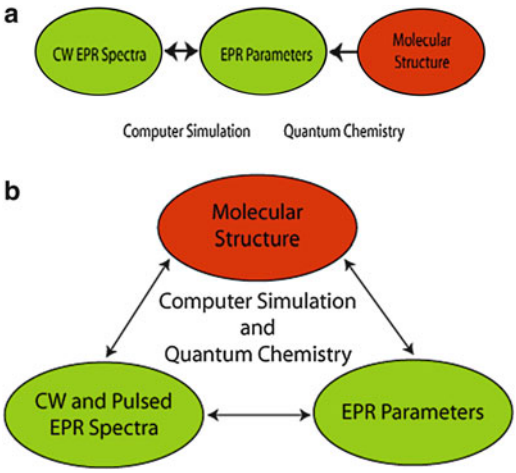

Fig. 5.2 (**a**) Traditional and (**b**) Structure based approaches to determining geometric and electronic structure of paramagnetic centers from CW and pulsed EPR [35]

$$H_{Tot} = \sum_{i=1}^{N} H_{A_i} + \sum_{i,j=1, i \neq j}^{N} H_{A_{ij}}$$
$$H_{A_{ij}} = J_{A_{ij}} \boldsymbol{S}_{A_i} \cdot \boldsymbol{S}_{A_j} + V_{A_{ij}} \boldsymbol{S}_{A_i} \times \boldsymbol{S}_{A_j} + \boldsymbol{S}_{A_i} \cdot J_{A_{ij}} \cdot \boldsymbol{S}_{A_j} \quad (5.2)$$

Computer simulation of randomly oriented or single crystal EPR spectra from isolated or coupled paramagnetic centers is required to accurately determine the spin Hamiltonian parameters (Eqs. 5.1 and 5.2) and the electronic and geometric structure of the paramagnetic center.

Elucidation of the three dimensional geometric and electronic structural information of redox active cofactors within a metalloenzyme relies on the observation of hyperfine coupling between nuclei and the electron spin which is often unresolved in randomly orientated CW EPR spectra. Consequently, the traditional approach to interpreting CW EPR spectra is to: (i) simulate the CW EPR spectrum to determine the spin Hamiltonian parameters, (ii) compare these to parameters from well characterized molecules to determine molecular structure and/or perform quantum chemistry calculations to reproduce the EPR parameters (Fig. 5.2a). The XSophe-Sophe-XeprView computer simulation software suite (Sect. 5.2) can and has been extensively utilized to determine the spin Hamiltonian parameters from CW EPR spectra utilizing this traditional approach [29–33].

The advent of multidimensional pulsed EPR and electron nuclear double (triple) resonance (END(T)OR) spectroscopy in conjunction with orientation selective experiments and computer simulation overcomes this problem and allows three dimensional structures (electronic and geometric) of paramagnetic centers to be determined. While electron spin echo envelope modulation (ESEEM) experiments are particularly sensitive for extremely weak couplings from 4 to 6 Å away from the paramagnetic center, the ENDOR experiment is far more sensitive to strongly coupled nuclei 2–4 Å away from the paramagnetic center [12]. Two dimensional

correlation experiments can be applied to ESEEM or ENDOR pulse sequences, yielding detailed structural information on the number and type of nuclei present and their distance and relative orientation from the paramagnetic center. For example, the complete structural characterization of the spin density distribution and consequently the structure of the photosynthetic reaction center (PS I) has been ascertained through careful two dimensional ESEEM and END(T)OR spectroscopy by Lubitz et al. [13]. Pulse sequences based on pulsed ENTOR have been developed for directly determining crystallographic information (internuclear separations between nuclei and the paramagnetic center and their relative orientation with respect to the paramagnetic center) directly through the dipole-dipole interaction [14]. Elucidation of three dimensional crystallographic information (distance and orientation) of multiple paramagnetic centers within a metalloenzyme relies on the observation of anisotropic exchange (dipole-dipole) coupling between the multiple electron spins. While CW EPR can be used to measure the distance and orientation of redox active centers up to about 8 Å apart and power saturation studies can be used to infer slightly larger distances, pulsed ELDOR allows distances up to 80 Å and their distributions to be measured directly from a Pake doublet [36].

Herein we describe the XSophe-Sophe-XeprView and the Molecular Sophe computer simulation software suites for the analysis of continuous wave and pulsed EPR and END(T)OR spectra, energy level diagrams, transition roadmaps and transition surfaces. The integrated approach employed in Molecular Sophe is based on molecular structure (Fig. 5.2b) and has the potential to revolutionize the 3-dimensional molecular (geometric and electronic) characterization of paramagnetic centers using high resolution EPR spectroscopy and quantum chemistry calculations. Until now the analysis of complex CW and pulsed EPR spectra has been based on a spin system rather than molecular structure and the analysis of pulsed EPR spectra has mainly relied upon analytical expressions involving perturbation theory.

5.2 XSophe-Sophe-Xeprview Computer Simulation Software Suite

The XSophe-Sophe-XeprView computer simulation software suite [29–33] (Fig. 5.3) for the analysis of isotropic, randomly oriented and single crystal CW EPR spectra consists of: XSophe, an X-windows graphical user interface; the Sophe authentication and Common Object Request Broker Architecture (CORBA) daemons; Sophe, a state-of-the-art computational programme for simulating CW EPR spectra and XeprView®, Bruker Biospin's programme for visualizing and comparing experimental and simulated spectra.

The software suite is supported on the latest versions of openSuSE (11.2, 11.3, 11.4) and Mandriva (2007.[0,1], 2008.[0,1], 2009.[0,1], 2010.[0,1,2], 2011.0). Older versions of the Linux operating system including RedHat (6.2, 7.1, 7.2, 7.3, 8.0) and Mandrake (8.1, 8.2, 9.0) are also available. The SGI IRIX platform is no longer actively supported. Use of the latest versions of the operating systems is strongly recommended from both feature and security perspectives [33].

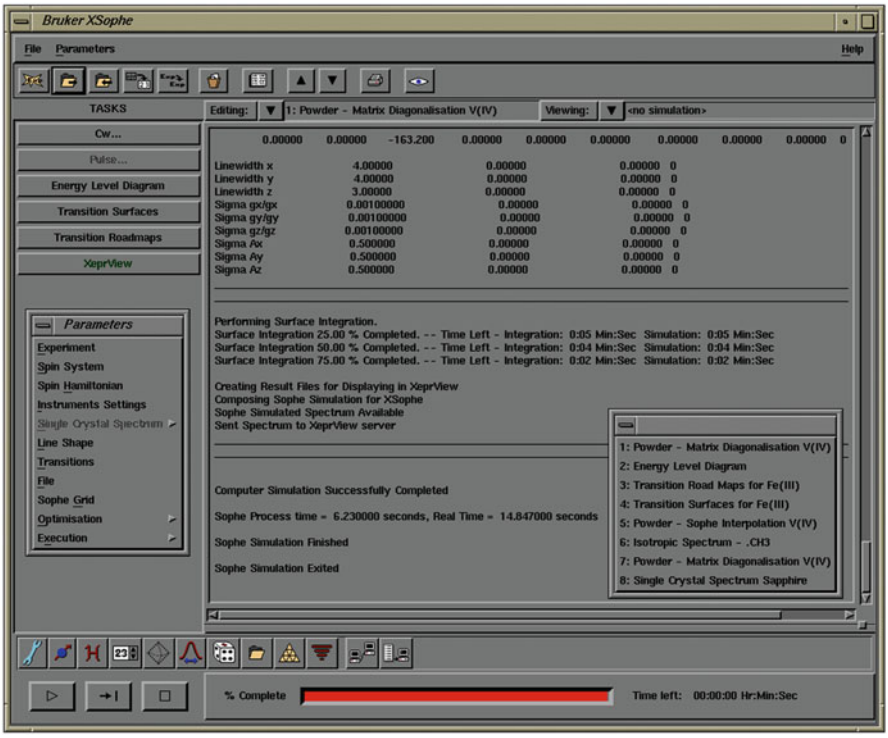

Fig. 5.3 The XSophe (v 1.1.4) graphical user interface. The interface allows the creation and execution of multiple input files on local or remote hosts. There are macro task buttons to guide the novice through the various menus and two button bars to allow easy access to the menus. For example the bottom bar (*left* to *right*), Experimental Parameters, Spin System, Spin Hamiltonian, Instrumental Parameters, Single Crystal Settings, Lineshape Parameters, Transition Labels/Probabilities, File Parameters, Sophe Grid Parameters, Optimisation Parameters, Execution Parameters and Batch Parameters

5.2.1 The XSophe X-windows Graphical User Interface

XSophe-Sophe-XeprView computer simulation software suite provides scientists with an easy-to-use research tool for the analysis of isotropic, randomly orientated and single crystal continuous wave (CW) EPR spectra. XSophe provides an X-Windows graphical user interface (Fig. 5.3) to the Sophe program allowing; the creation of multiple input files, the local and remote execution of Sophe and display of sophelog (output from Sophe) and input parameters/files.

XSophe allows transparent transfer of EPR spectra and spectral parameters between XSophe, Sophe and XeprView®, using state-of-the-art platform-independent Corba libraries. This interactivity (Fig. 5.4) allows the interaction of the XSophe interface with Sophe and its execution on the same computer or a remote host through a simple change of the hostname. XSophe contacts the Sophe Corba

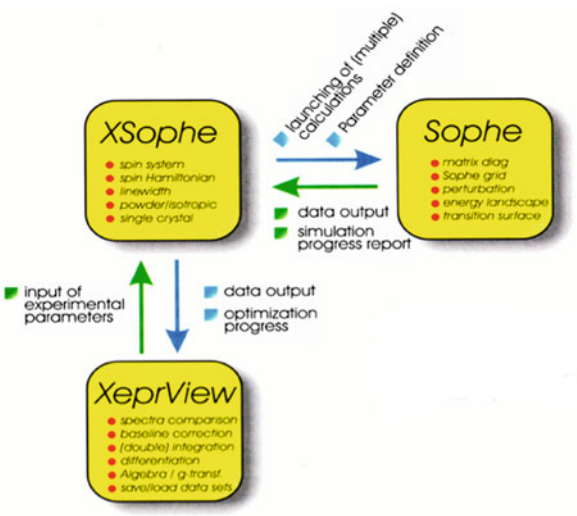

Fig. 5.4 A schematic showing the interactivity of the XSophe, Sophe and XeprView® software components

daemon, which then interacts with the Sophe authentication daemon *via* a socket to validate the username and password which is encrypted with 128 bit encryption and embedded in a Corba string. Once validated the Sophe authentication daemon forks the Sophe computational program which performs the simulation. The output of CW EPR spectra (1D and 2D) from the Sophe program can be visualized in conjunction with the experimental spectrum in XeprView® or Xepr®.

Computer simulation of single crystal EPR spectra measured in a plane perpendicular to a rotation axis can be performed by defining the rotation axis and the beginning and end angles in a plane perpendicular to this axis. Energy level diagrams, transition roadmaps and transition surfaces aid interpretation of complicated randomly orientated EPR spectra and can be viewed with a web browser, for example Mozilla Firefox® and an OpenInventor scene graph viewer.

5.2.2 Sophe

Sophe is a sophisticated computer simulation software programme written in C++ employing a number of innovative technologies including; the SOPHE partition and interpolation schemes, a field segmentation algorithm, the mosaic misorientation line width model and spectral optimisation. In conjunction with the SOPHE partition scheme and the field segmentation algorithm, the SOPHE interpolation scheme [31, 37] and mosaic misorientation linewidth model [35] greatly increase the speed of simulations for most spin systems. The optimisation algorithms in the suite provide the experimentalist with the possibility of finding the spin Hamiltonian parameters in a systematic manner rather than a trial-and-error process. The functionality of Sophe is described below [29–33]:

Experiments
Continuous Wave EPR Spectra displayed in XeprView®.
Energy level diagrams, transition surfaces and transition roadmaps displayed in a web browser, for example Mozilla Firefox®.
Homotopy is available in the Sophe computational program.

Spin Systems
Isolated and magnetically coupled spin systems.
An unlimited number of electron and nuclear spins is supported with nuclei having multiple isotopes.

Spin Hamiltonian Interactions
Fine Structure Interaction, 2nd, 4th and 6th order contributions [$\mathbf{S}\cdot D\cdot\mathbf{S}$, B4, B6].[8]
Isotropic and Anisotropic Electron Zeeman [$g\beta\mathbf{B}\cdot\mathbf{S}$, $\beta\ \mathbf{B}\cdot g\cdot\mathbf{S}$].
Isotropic and Anisotropic Hyperfine [$a\mathbf{S}\cdot\mathbf{I}$, $\mathbf{S}\cdot A\cdot\mathbf{I}$].
Nuclear Zeeman Interaction [$g_N\ \beta_N\mathbf{B}\cdot\mathbf{I}$].
Quadrupole [$\mathbf{I}\cdot P\cdot\mathbf{I}$].
Isotropic Exchange [$J_{iso}\mathbf{S_i}\cdot\mathbf{S_j}$].
Anisotropic Exchange (dipole dipole coupling) [$\mathbf{S_i}\cdot J\cdot\mathbf{S_j}$].

Continuous Wave EPR Spectra
Spectra types:

Solution, randomly orientated and single crystal.

Symmetries:

Isotropic, axial, orthorhombic, monoclinic and triclinic.

Multidimensional spectra:

Variable temperature, multifrequency and the simulation of single crystal spectra in a plane.

Methods
Matrix diagonalization – mosaic misorientation linewidth model.
Sophe Interpolation.

Optimisation (Direct Methods)
Methods:

Hooke and Jeeves.
Quadratic variation of Hooke and Jeeves.
Simplex.
Two Simulated Annealing methods.

Spectral Comparison:

Raw data and Fourier transform.

For nuclear superhyperfine interactions Sophe offers two different approaches; full matrix diagonalization and first order perturbation theory. If all the interactions were to be treated exactly, a Mn(II) ($S = 5/2$, $I = 5/2$) coupled to four ^{14}N nuclei would span an energy matrix of 2,916 by 2,916. To fully diagonalize a Hermitian matrix of this size would be numerically intensive and require substantial memory requirements (~68 MB for a single matrix of this size with double precision). In fact, in most systems the electronic spin interacts strongly with one or two nuclei but weakly with other nuclei and first order perturbation theory may be a satisfactory treatment, which will ease the computational burden for large spin systems.

The specification of transition labels is not necessary in Sophe. In the absence of labels a threshold value for the transition probability is required. The program will then perform a search for all transitions, which have a transition probability above this threshold value at a range of selected orientations. For a single octant the following orientations (θ,$\boldsymbol{\phi}$) are chosen: (0°,0°), (45°,0°), (90°,0°), (45°,90°), (90°,45°), (90°,90°). The transitions found then act as "input" transitions.

The program is designed to simulate CW EPR spectra measured in either the perpendicular ($B_0 \perp B_1$) or parallel ($B_0 \,||\, B_1$) modes, where B_0 and B_1 are the steady and oscillating magnetic fields, respectively. It can also easily generate single crystal EPR spectra for any given orientation of B_0 and B_1 with respect to a reference axis system, which is normally either the laboratory axis system or the principal axis system of a chosen interaction tensor or matrix in the spin Hamiltonian.

5.3 Molecular Sophe Computer Simulation Software Suite

The Molecular Sophe (MoSophe) computer simulation software suite [35, 38] consists of a graphical user interface, the computational programme Sophe and a variety of software tools (XeprView®, Gnuplot, ivview and Ghostview and a web browser) for visualizing and comparing simulations and experimental EPR spectra. A complete description of the graphical user interface is given in the user manual [38]. This provides scientists with powerful research tools for determining the geometric and electronic structure of magnetically isolated and coupled paramagnetic centers within metalloproteins and other paramagnetic molecules. Molecular Sophe is Project oriented. Each project can contain a number of simulations, each of which contains a sample with one or molecules consisting of atoms and bonds (interactions). The scientist can then choose a range of experiments to be applied to that sample to elucidate the geometric and electronic structure of the molecule(s). Upon starting Molecular Sophe (mosophe) a splash screen is displayed showing the progress in loading the software and finally allows the user to choose a project (Default if none available) from the Project list to load into the graphical user interface. The list of projects is stored in the user's home directory (/home/user/.mosophe/projects).

Pressing the Load button displays the graphical user interface for MoSophe (Fig. 5.5). The graphical user interface incorporates a Menu, Tool Bar, Explorer

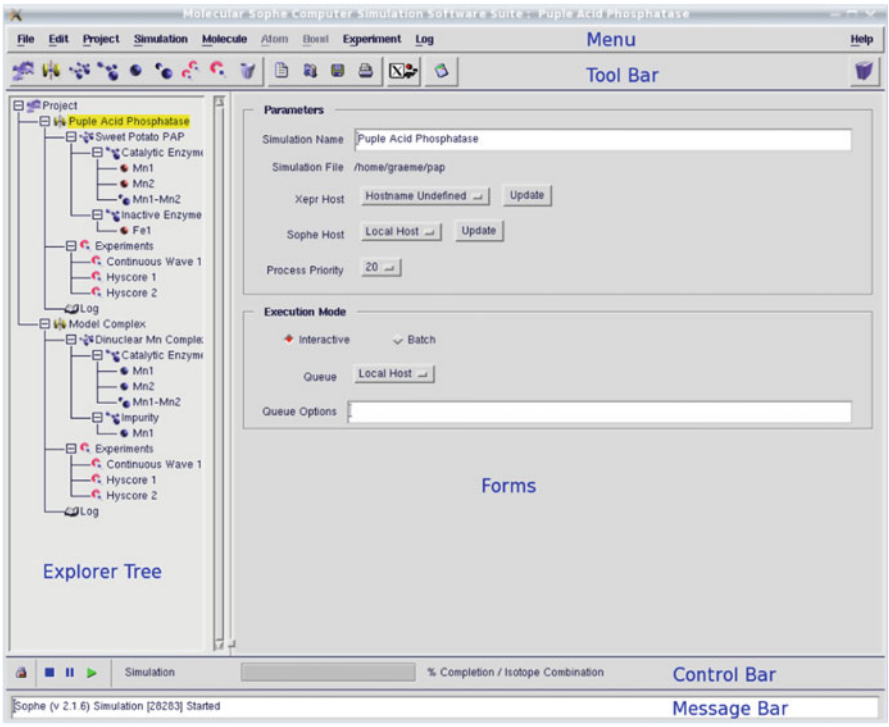

Fig. 5.5 Molecular Sophe graphical user interface showing the Simulation form

Tree, Forms, Control Bar and Message Bar (Fig. 5.5). The main menu provides access to all functions while the toolbar contains some of the commonly used functions in creating a sample, adding experiments and running external programmes (XeprView®, printing and a units calculator). The choice of external programmes and CORBA settings (for transferring spectra between MoSophe and XeprView®) should be set through the Preferences window which can be accessed from the menu (Edit, Edit Preferences) and saved to disk so that in future runs of Molecular Sophe, the settings are loaded automatically upon startup. All of the Buttons, Fields, Tree Nodes have context sensitive help which can be accessed by moving the mouse over the desired widget. In addition, the user manual can be accessed by selecting the book icon on the right hand side of the Toolbar.

The Project Form (top node within the explorer tree) displays the status of the multiple simulations through timing bars for each simulation. The timing bars are colour coded: grey – simulation has not been started; green – simulation running; and red – simulation finished. A right mouse click on the Project Node displays a menu enabling the user to add and load a simulation, create a new project, load a project, save and delete a project.

The Simulation Form is displayed by a left mouse click on the Simulation Node (entitled 'Purple Acid Phosphatase' and coloured yellow in Fig. 5.5) in the

Explorer Tree and allows the choice of Host on which to execute the computational programme Sophe (currently only localhost), the process priority, whether to run it interactively or in a batch queue (currently only interactively) and the host running the XeprView® programme in which to display the resultant spectra. The name of the simulation can also be modified through the Simulation Form. A right mouse click on the Simulation Node displays a menu enabling the user to save, delete, copy, print and run a simulation.

The Sample Node (entitled 'Sample' or 'Sweet Potato PAP' in Fig. 5.5) is the next level of the Explorer Tree. The sample can consist of multiple molecules (added through the Molecule menu (top toolbar or right mouse click) in different proportions which itself will be able to be optimized. This is important for many paramagnetic samples, for example the manganese enriched sweet potatoe purple acid phosphatase contains a catalytically active dinuclear Mn(II) active site and a small proportion of an inactive dinuclear Fe(III)Zn(II) active site (Fig. 5.5) [39b]. Metalloproteins can also have more than a single paramagnetic prosthetic group producing multicomponent EPR spectra. Inclusion or exclusion of a particular molecule//molecular fragment can be toggled with the radio button adjacent to the Molecule name in the Molecule Form.

The state of the sample (Crystal, Powder, Frozen Solution, Liquid, Gas or Glass) may also be chosen which will govern various aspects of the computational programme, Sophe. If the Crystal state is chosen, the user can then select the Point Group for the host crystal.

The name of the molecule can be changed in the Molecule Form and a comment added if desired. The units for the atom's positional coordinates within the molecule and the lineshape function for all of the experiments (simulations) can be defined in the Molecule Form. Once a molecule has been added at the sample Node, the user can add atoms and subsequently bonds through the Molecule menu or by a right mouse click on the Molecule Node. Adding an atom displays a Periodic Table from which the user can select an atom by clicking (left mouse button) on the appropriate element. The atom is then added to the Molecule in the Explorer.

A left mouse click on the atom (Explorer Tree) displays the atom forms: Electron Zeeman, Hyperfine, Fine Structure (Fig. 5.6), Quadrupole, Linewidth, Isotopes and Position. Each Tab also has a three state button (colour coded tick) associated with it which may be changed by a middle mouse click. The three states are: Red Tick – *Active and Valid*; Blue Tick – *Inactive and Valid* and No Tick – *Inactive and Invalid*. A right mouse click on the value, minimum, maximum fields enables the user to set the range of the parameter to be varied using the toggle up and down arrows to the right of the parameter field. Currently the Sophe computational code does not have any optimization algorithms present as a new method is being developed for the global optimization of all spin Hamiltonian, linewidth and geometric parameters from multiple experiments.

The value of the electron spin can be selected and if greater than zero, the atom in the Explorer Tree is colored orange (Fig. 5.6) and the Electron Zeeman Tab now has a Red Tick. The symmetry of the various interactions can be chosen by selecting the appropriate Representation (Orthorhombic, Axial and Isotropic for the Electron

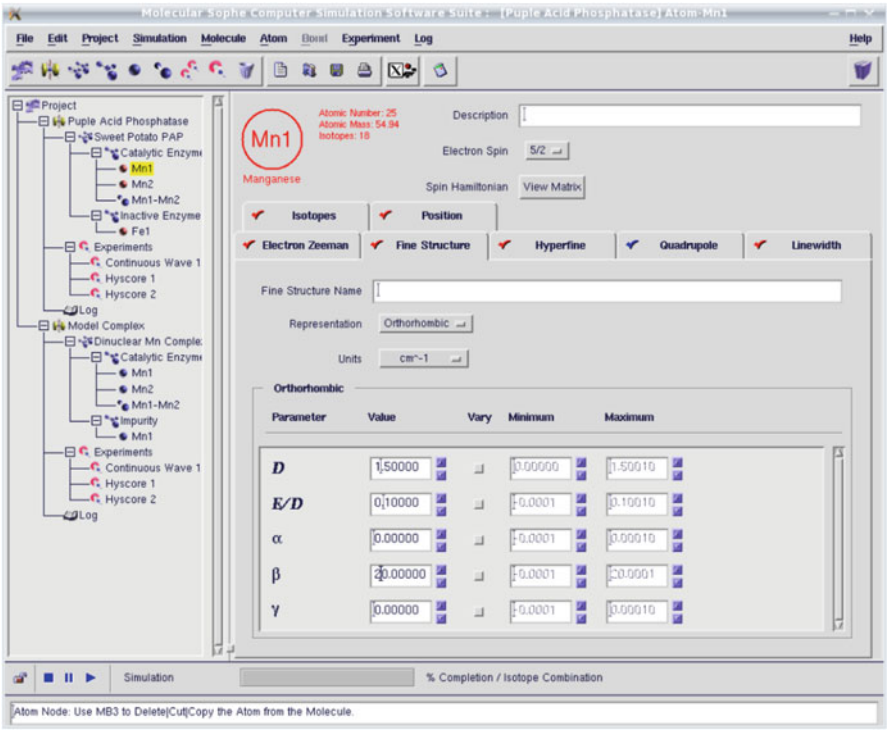

Fig. 5.6 Molecular Sophe graphical user interface showing the Atom form with an orthorhombic zero field splitting tensor

Zeeman and Hyperfine Interactions. Other interactions have different options). An Orthorhombic Fine Structure Representation is shown in Fig. 5.6.

For site symmetries lower than orthorhombic, one or more of the three Euler angles α, β and γ will be greater than zero. α ($\beta = \gamma = 0$) greater than zero rotates (about the Z axis) g_x, g_y away from the X and Y axes, corresponding to C_{2h} monoclinic sites. A rotation of β ($\alpha = \gamma = 0$) rotates (about X) the g_y and g_z axes away from the Y and Z axes corresponds to C_s symmetric sites. In randomly oriented samples containing a single unpaired electron the g matrix is assumed to be coincident with the internal coordinate system and the hyperfine matrix is rotated from away from the g matrix. The symmetry can be further lowered to triclinic symmetry (C1) by making α, β and γ greater than zero. The angle α rotates g_x and g_y about Z, β rotates g_y and g_z about g_x and γ rotates g_x and g_y about the new g_z. There are two Euler angles available for an axially symmetric site and none for an isotropic or cubic site.

Additional atoms with or without electron spins can be added (duplicated) by a right mouse click on the Molecule node within the Explorer Tree and selecting the appropriate menu item. Interactions or "bonds" can also be created in a similar

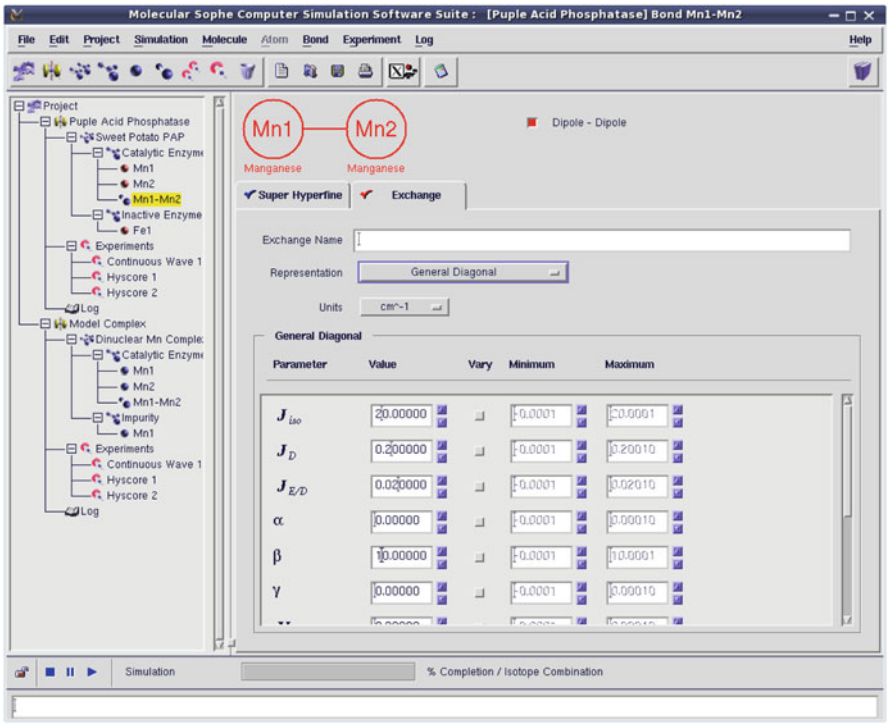

Fig. 5.7 Molecular Sophe graphical user interface showing a Mn—Mn bond form with a general diagonal form of the exchange interaction. Given the spin Hamiltonian in Eq. 5.2, a positive value of J_{iso} corresponds to antiferromagnetic coupling between the two atoms and for inorganic chemists who are used to working with the Hamiltonian ($H = -2J_{iso}{}^{*}\ S_1.S_2$, * is used here to distinguish the two values), $J_{iso}{}^{*} = -J_{iso}/2$

manner. It is important in the bond dialog, that at least the atom on the left hand side contains one or more unpaired electrons. In this context, the term bond is loosely defined to include not only bonds but also interactions between electron spins and either nuclear spins (superhyperfine interaction) or other electron spins (exchange interaction).

Once the bond is created in the Explorer Tree then a left mouse click on the bond opens up either the Superhyperfine or Exchange Interaction Form, dependent upon whether or not both atoms have non zero electron spins. The superhyperfine interaction can be toggled off//on by clicking (middle mouse button) on the red//blue tick radio button on the superhyperfine tab.

The exchange interaction involves the interaction of two or more paramagnetic centers, for example the dinuclear Mn(II) center in manganese enriched purple acid phosphatase (Fig. 5.7) [39]. The total spin Hamiltonian for an exchange coupled system is given by the sum of the individual spin Hamiltonians and the interaction Hamiltonian (Eqs. 5.1 and 5.2 respectively). The interaction Hamiltonian

is comprised of three components, namely isotropic exchange, anisotropic exchange interaction (dipole-dipole and spin orbit coupling) and antisymmetric exchange. Within the Exchange Tab of the Bond form there are eight representations (Isotropic, Anisotropic (Axial, Axial Diagonal, Orthorhombic, Orthorhombic Diagonal, Antisymmetric, General and General Diagonal). The General Diagonal representation is shown in Fig. 5.7.

The anisotropic exchange parameters (dipole-dipole and spin orbit contributions) can either be added through the Anisotropic (Axial, Orthorhombic) or General Representations and Diagonal variants (Fig. 5.7) of these. If the positional coordinates have been supplied for both atoms, then the dipole-dipole interaction can be automatically calculated by the MoSophe through toggling the Dipole-Dipole check box (red is enabled).

The antisymmetric exchange term (Eq. 5.2, V_{ab} $S_a \times S_b$) can be included by selecting the Antisymmetric or General exchange representations, the latter also includes isotropic and anisotropic interactions. Dipole-dipole terms can also be included by selecting the Dipole-Dipole check box (red is enabled) [38]. The antisymmetric exchange interaction has been found to be important for di- and trinuclear copper(II) systems where the orbitals containing the unpaired electrons partially overlap [40, 41].

Once the sample has been created, the user can now perform a range of experiments. The choice of experiment is accessed through the Experiment Menu or by a right mouse click on the Experiment Node and selecting an Experiment Type. The range of experiments include CW-EPR, Pulsed EPR (FID, 2 Pulse ESEEM, 3-Pulse ESEEM, SECSY, HYSCORE, 2 Pulse Echo, MIMS and Davies ENDOR) and Reports (Energy Level Diagrams, Transition Roadmaps and Transition Surfaces). Multidimensional experiments can also be performed by adding additional abscissas (Temperature, Microwave Frequency, Goniometer Angle and Magnetic Field). Examples of the Continuous Wave EPR (Fig. 5.8) and HYSCORE (Fig. 5.9) forms are described below.

The Continuous Wave EPR Experiment Form has Continuous Wave, Sophe, Spectra and Configuration tabs with the latter three tabs being common to all experiments. The Continuous Wave EPR Form (Fig. 5.8) allows the user to enter values concerning the field sweep (center field, sweep width and the number of data points), microwave frequency, detection mode and temperature. The units for the field sweep parameters include Gauss, mTesla and Tesla and those for the microwave frequency are MHz, GHz and THz. The harmonic corresponds to the nth derivative spectrum, where $n = 0$, 1 and 2, the first derivative being the normal mode acquired on an EPR spectrometer using phase sensitive detection. While experimentally the phase of the EPR spectrum can vary anywhere between 0° and 180°, only the limits are really useful at present. Setting the phase to 180° inverts the spectrum. Boltzmann populations for each energy level are automatically included and consequently the temperature will affect the intensity of the EPR transition between two different energy levels. For exchange coupled systems the magnitude and sign of J_{iso} may be obtained from a variable temperature spectrum/simulation

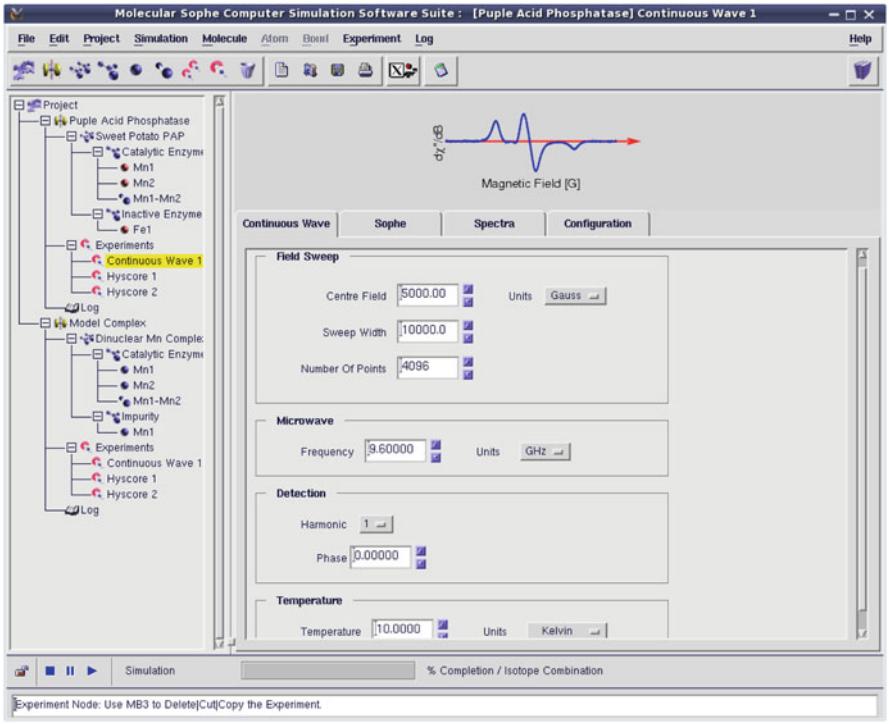

Fig. 5.8 Molecular Sophe graphical user interface showing a CW EPR experiment form

(Sect. 5.8.3). Similarly, if the zero field splitting is larger than the microwave quantum, then a variable temperature spectrum/simulation can provide the sign and magnitude of the axial zero field splitting (D) (Sect. 5.8.2).

If the user selects a multidimensional CW EPR spectrum, for example multi-frequency, variable temperature or single crystal experiment then additional tabs are added to the CW EPR Experiment Form, namely, Frequency, Temperature and Goniometer Angle. These tabs allow the user to define the start and increment values for the particular parameter and the number of data points in the additional dimension. The parameters in this tab, for example the temperature tab, overrides the temperature setting in the Continuous Wave tab. This also applies to the microwave frequency and Goniometer Angle.

The Sophe tab allows the user to input various parameters required for the computational calculation, define the SOPHE Grid (Sect. 5.4.2) and determine the transition probability (selection rules to be used). In the Calculation Panel, matrix diagonalization is currently the only method available for performing continuous wave and pulsed EPR simulations. The field segmentation algorithm employed in the computational program (Sophe) requires the user to define the number of field segments where matrix diagonalization will be employed. While the number of field segments can usually be set to one or two, sometimes sharp features (vertical lines)

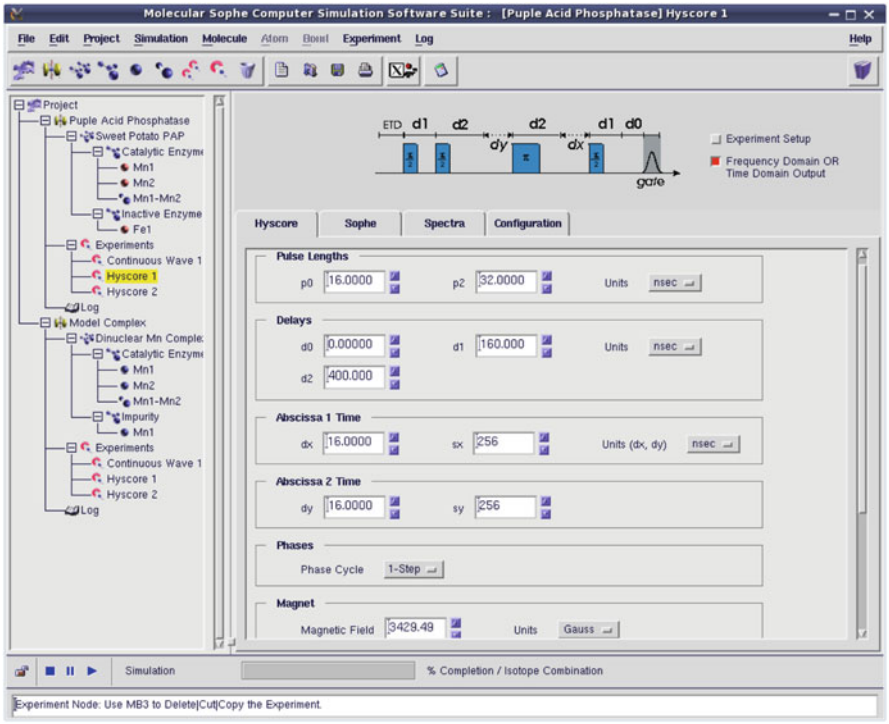

Fig. 5.9 Molecular Sophe graphical user interface showing a HYSCORE experiment form

may be apparent in the spectrum and these arise from the presence of multiple transitions within a segment. If this occurs then the number of segments should be increased.

Floquet Theory [42] is often used to describe the evolution of a periodic time dependent semiclassical spin Hamiltonian in magnetic resonance. The number of Floquet Segments and Floquet Harmonics are only used in the simulation of Pulsed EPR experiments (Sect. 5.5). The number of Floquet Segments refers to the number of segments microwave pulses are divided into so that within each segment the time dependent spin Hamiltonian is 'assumed' to be time independent. These segments are used to calculate the average Hamiltonian for the pulse. When the number of Floquet Segments is set to zero, the representation is reduced to the rotating frame which is only appropriate for species in which there is no significant electron spin state mixing, for example species containing only a single unpaired electron. For high spin and exchange coupled molecules, the number of Floquet Segments should be greater than zero.

The SOPHE grid (Sect. 5.4.2) is defined by the number of orientations between the 'z' and 'x' global coordinate system [37]. The number of gamma steps, used in the simulation of pulsed EPR experiments, is used to calculate the transition probabilities of the echo intensities.

The Selection Rules are used to define the transition threshold for inclusion of transitions in the simulation. Setting the selection rules to 'ALL' sets the transition threshold to zero, 'None' sets it to one and 'Some' is somewhere in between, which the user can define to only observe forbidden or allowed transitions. In principle the Selection Rules should always be set to 'ALL'.

Molecular Sophe employs a data directory to store all of the information associated with a particular simulation, including the input file for the computational programme, Sophe, and all of the input and output spectra. This simplifies the organization of simulations. The Spectra Form allows the import of an experimental spectrum into the Molecular Sophe data directory and the export of simulated spectra from this directory. A title for the experiment can also be added which is added to the resultant simulation spectrum. The user can also choose the filetype (Be3st and ESP Bruker formats) of the spectrum to import into the data directory and the output file format (Be3st and ESP Bruker formats, GNUPlot, Image Plot, Postscript and OpenInventor).

Apart from the OpenInventor file format which is specifically used for the visualization of transition surfaces, ALL of the other file formats are generated when you run a simulation. You can change the output file type and select View spectrum to see the results in a different format. Both the Bruker Be3st and ESP format files are displayed within Bruker's XeprView® and the gnuplot file is displayed in a gnuplot X11 terminal window. The Image (portable network graphics 'xxx.png' format) and postscript files are displayed in an appropriate viewer defined in the preferences window. Typically the default viewers are the web browser Mozilla Firefox® and ghostview, respectively. Representative examples showing all displays can be found in Sects. 5.6 and 5.8.

The resonator Configuration Form allows the user to choose: the Bruker spectrometer resonator type; the orientation of the microwave magnetic field with respect to the external applied magnetic field (B_0); the microwave magnetic field strength (B_1) at 0 dB; the radio frequency (RF) magnetic field strength (B_2) at 0 dB. Apart from the dual mode resonator (ER4116DM) which may have B_1 either parallel or perpendicular to B_0, all of the other resonators have B_1 perpendicular to B_0.

The second example is the HYSCORE Experiment [43] which can be added to the Experiment Node in the Explorer Tree (Fig. 5.9). The HYSCORE Experiment form (Fig. 5.9) shows the pulse sequence and contains the HYSCORE, Sophe, Spectra and Resonator Configuration tabs. Within the HYSCORE tab the user can define the Pulse Length of the $\pi/2$ and π pulses, (po and p2 respectively), Delay times (d0, d1 and d2), Abscissa Times, Phase cycle, static Magnetic Field, the Microwave Frequency, Attenuation and the Temperature of the experiment. Creation of the $\pi/2$ and π pulses is dependent upon, the pulse length (p0 and p2), the microwave attenuation and the microwave magnetic field strength (B_1) at 0 dB. The latter is defined in the Resonator Configuration Tab. The attenuation required to obtain a $\pi/2$ flip angle with the $\pi/2$ pulse length and B_1 can be obtained by selecting the Experiment Setup Toggle Button and running the experiment. The number of bands can be set to one for this setup experiment. This will produce a

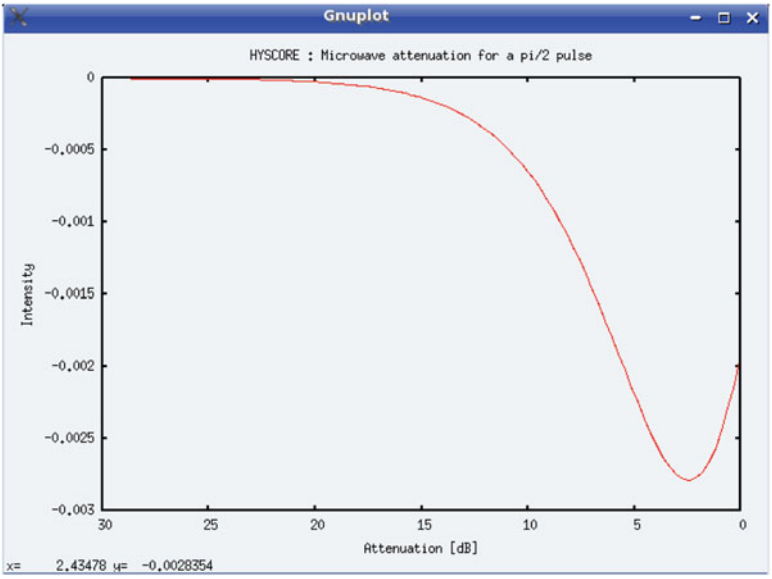

Fig. 5.10 Gnuplot output showing the result of a typical pulse setup experiment. The attenuation of a π/2 pulse is 2.4 dB

plot of attenuation versus echo intensity (Fig. 5.10). The Position Qualifier within XeprView® or gnuplot can be used to determine the power associated with the maximum echo intensity. Alternatively, the MoSophe calculator can be used to determine the attenuation from the pulse length and B_1 at 0 dB (Sect. 5.7).

Currently the HYSCORE is monitored at a single point (detection gate delay d0), rather than integrating over a detection gate. 'dx' and 'dy' define the time increments in the two dimensions and 'sx' and 'sy' correspond to the number of data (time) points calculated. Whilst the pulse sequence assumes 'dx' and 'dy' are identical as is often the case experimentally, this condition is not strictly required in the Sophe software. The units for both 'dx' and 'dy' are selected from the Units Menu for 'dx'. The HYSCORE tab is a scrollable window and as such all of the parameters may not be visible upon selecting the tab. The remaining parameters (magnetic field and temperature) and the parameters in the other tabs have been defined previously in the CW EPR Experiment Form. The HYSCORE simulation can be output in either frequency or time domain by selecting (red) or deselecting (blue) the check box labelled 'Frequency Domain OR Time Domain'.

Orientation selective experiments involve performing a pulsed EPR experiment, such as HYSCORE as a function of orientation (magnetic field). The orientation selective HYSCORE Experiment will provide a four dimensional data set from which the complete hyperfine matrix for the remote nucleus can be determined. Subsequently the internuclear distance and orientation of the nucleus from the electron spin can be extracted from the anisotropic components of the hyperfine

matrix, assuming the dipole-dipole interaction is valid. Computer simulation of an orientation selective HYSCORE (or any other pulsed) experiment involves adding a pulsed experiment and choosing Magnetic Field as the second abscissa. Unfortunately, Xepr® cannot currently visualize one or more four dimensional data sets. This can be overcome by duplicating (copying) the HYSCORE experiment and changing the static magnetic field position. Remember to change the output filename as all simulations will be saved in the same directory.

5.4 Theory for the Computer Simulation of Randomly Orientated CW EPR Spectra

Computer simulation of the experimental randomly orientated or single crystal EPR spectra from isolated or coupled paramagnetic centers is required to accurately determine the spin Hamiltonian parameters (Eqs. 5.1, 5.2) and the electronic and geometric structure of the paramagnetic center. Simulation of randomly orientated EPR spectra is performed in frequency space through the following integration [1, 44]:

$$S\left(B,\,\nu_c\right) = \sum_{i=0}^{N}\sum_{j=i+1}^{N} C \int_{\theta=0}^{\pi}\int_{\phi=0}^{\pi} \left|\mu_{ij}\right|^2 f\left[\nu_c - \nu_0(B), \sigma_\nu\right] d\cos\theta\, d\phi \qquad (5.3)$$

where S(B, υ_c) denotes the spectral intensity, $|\mu_{ij}|^2$ is the transition probability, υ_c the microwave frequency, υ_o(B) the resonant frequency, σ_v the spectral line width, $f[\upsilon_c - \upsilon_o(B), \sigma_\upsilon]$ a spectral lineshape function which normally takes the form of either Gaussian or Lorentzian, and C a constant which incorporates various experimental parameters. The summation is performed over all the transitions (i, j) contributing to the spectrum and the integrations, performed numerically (Sect. 5.4.2), are performed over half of the unit sphere (for ions possessing triclinic symmetry), a consequence of time reversal symmetry [1, 18]. For paramagnetic centers exhibiting orthorhombic or monoclinic symmetry, the integrations in Eq. 5.3 need only be performed over one or two octants respectively. Whilst centers exhibiting axial symmetry only require integration over θ, those possessing cubic symmetry require only a single orientation.

5.4.1 Field Versus Frequency Swept CW EPR

In practice the CW EPR experiment is a field swept experiment in which the microwave frequency (υ_c) is kept constant and the magnetic field varied. Computer simulations performed in field space assume a symmetric lineshape function f

in Eq. 5.3 ($f(B-B_{res})$, σ_B) which must be multiplied by $d\upsilon/dB$ and a constant transition probability across a given resonance [1, 44, 45]. Pilbrow has described the limitations of this approach in relation to asymmetric lineshapes observed in high spin Cr(III) spectra and the presence of a distribution of g-values (or g-strain broadening) [44, 45]. The following approach has been employed by Pilbrow et al. in implementing Eq. 5.3 (frequency swept) into computer simulation programmes based on perturbation theory [1, 45]. Firstly, at a given orientation of (θ, $\boldsymbol{\phi}$), the resonant field positions (B_{res}) are calculated with perturbation theory and then transformed into frequency space ($\upsilon_0(B)$). Secondly, the lineshape ($f(\upsilon_c-\upsilon_0$ (B), σ_υ) and transition probability are calculated in frequency space across a give resonance and the intensity at each frequency stored. Finally, the frequency swept spectrum is transformed back into field space. Performing computer simulations in frequency space produces assymmetric lineshapes (without having to artificially use an asymmetric lineshape function) and secondly, in the presence of large distributions of g-values will correctly reproduce the downfield shifts of resonant field positions [45].

Unfortunately, the above approach cannot be used in conjunction with matrix diagonalization as an increased number of matrix diagonalizations would be required to calculate f and the transition probability across a particular resonance. However, Homotopy [46, 47] which is in general three to five times faster than brute force matrix diagonalization allows the simulations to be performed in frequency space. Homotopy has been incorporated into the computational programme Sophe, a component of the XSophe-Sophe-XeprView computer simulation software suite.

5.4.2 Numerical Integration – Choice of Angular Grid

The simulation of a randomly orientated EPR spectrum involves integration over a unit sphere (Eq. 5.3) which is perfomed numerically by partitioning a unit sphere and calculating the resonant field positions and transition probabilities at all of the vertex points. The simplest and most popular partition scheme is that of using the geophysical locations on the surface of the Earth for the presentation of world maps. However, the solid angle subtended by the grid points is uneven and alternative schemes have been invented and used in the simulation of magnetic resonance spectra. For example, in order to reduce computational times involved in numerical integration over the surface of the unit sphere, the igloo [48], triangular [49], spiral [50] and SCVT [51] methods have been invented for numerical investigations of spatial anisotropy. In 1995, we described the SOPHE partition scheme in which any portion of the unit sphere ($\theta\in[0, \pi/2]$, $\phi\in[\phi_1, \phi_2)$ or $\theta\in[\pi/2, \pi]$, $\phi\in[\phi_1, \phi_2]$) can be partitioned into triangular convexes[37]. For a single octant ($\theta\in[0, \pi/2]$, $\phi\in[0, \pi/2]$) the triangular convexes can be defined by three sets of curves

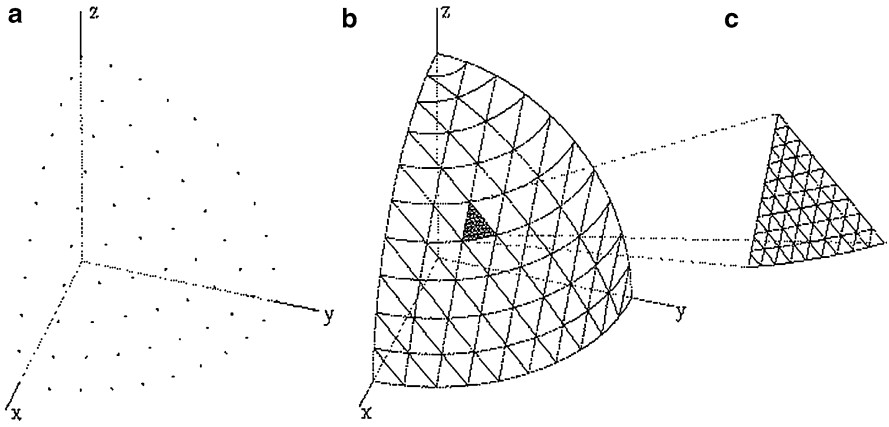

Fig. 5.11 A schematic representation of the SOPHE partition scheme. (**a**) Vertex points with a SOPHE partition number N = 10; (**b**) the SOPHE partition grid in which the three sets of *curves* are described by Eq. 5.4. (**c**) Subpartitioning into *smaller triangles* can be performed by using either Eq. 5.4 or alternatively the points along the edge of the *triangle* are interpolated by a cubic spline interpolation [37] and each point inside the *triangle* is either linearly (or with a cubic spline) interpolated three times and an average is taken (Reproduced from reference [37] with kind permission of © Elsevier (1995))

$$\begin{aligned} \theta &= \frac{\pi}{2}\frac{i}{N} \\ \theta \quad \phi &= \frac{\pi}{2}\frac{i-1}{N}(\phi_2 - \phi_1) \\ \theta \quad \phi = \theta \quad (\phi_2 - \phi_1) &- \frac{\pi}{2}\frac{i-1}{N}(\phi_2 - \phi_1), \quad (i = 1, 2, \ldots, N) \end{aligned} \tag{5.4}$$

where N is defined as the partition number and gives rise to N + 1 values of θ. Similar expressions can be easily obtained for θ∈[π/2, π], ϕ∈[ϕ_1, ϕ_2]. A three dimensional visualisation of the SOPHE partition scheme is given in Fig. 5.11b.

As can be seen this method partitions the surface of the unit sphere into triangular convexes which resemble the roof of the famous **S**ydney **Op**era **H**ous**e** (SOPHE). In the SOPHE grid there are N curves in each set with the number of grid points varying from 2 to N + 1 in steps of 1. In order to produce simulated spectra of high quality, the unit sphere is often required to be finely partitioned, in other words, a large number of vertex points are required to reduce computational noise which is often observed when the spin Hamiltonian parameters are highly anisotropic and the linewidths are small. Each triangle in Fig. 5.11b can be easily subpartitioned into smaller triangles, referred to as tiny triangles. In Fig. 5.11c, a selected triangle is further partitioned into 81 tiny triangles with a subpartion number N = 10. The grid formed in such a subpartition can still be described by Eq. 5.4. In this particular case, θ is stepped in a smaller step of π/(2(N−1)*(M−1)) from θ = 45° to θ = 54°, the

two corresponding curves which bound the triangle (Fig. 5.11c). A similar process is applied to curves in sets 2 and 3. Alternatively, various interpolation schemes may be used to generate finer grids for simulating randomly orientated EPR spectra [25, 49, 50, 52, 53]. In 1995 we described a highly efficient interpolation scheme, the SOPHE interpolation scheme (Sect. 5.4.3.2) [37].

5.4.3 Calculation of Resonant Field Positions

The very nature of EPR spectroscopy as a field-swept technique imposes a computational challenge to computer simulation of randomly orientated spectra. In essence, during an EPR experiment, the spin system under investigation is constantly modified through the Zeeman interactions as the magnetic field is swept. In a general situation where two or more interactions have comparable energies, the search for resonant field positions is not a trivial task as the dependence of the energies of the spin states on field strength (B_0) can be very complex. The complication involved is best manifested by the presence of multiple transitions between a given pair of energy levels.

5.4.3.1 Brute Force – Matrix Diagonalization and Field Segmentation Algorithms

A number of search schemes have been used in the full matrix diagonalization approach for locating resonant field positions [25, 52, 54–56]. Generally, they can be grouped into two categories. In category I, the resonant field position is searched independently for every transition. Among the schemes belonging to this category, the so-called iterative bisection method is the safest but probably the most inefficient method [25]. Other more efficient methods such as the Newton-Raphson method have also been used [25]. In general, these search schemes are time-consuming as a large number of diagonalizations are normally required. The search schemes belonging to category II may be called segmentation methods. In these schemes, the field sweep range is divided equally into k segments and for each segment, the whole energy matrix is diagonalized once for the center field value of that segment. Thus only k diagonalizations are performed for each orientation. A perturbation theory is then employed for determining the presence of a transition in each segment. This search scheme is still limited to situations where in each segment there is no more than one possible transition. However, if k is not too small, the chance of having two resonances in a single segment is rare. Reijerse et al. [52] use a first-order perturbation approach for exploring transitions in each segment. However, from our experience, first-order perturbation theory cannot be guaranteed to produce resonant field positions with satisfactory precision. In Sophe we have adopted the second-order eigenfield perturbation theory (described below) originally developed by Belford et al. [57]. This method has also been used by other groups [55].

In Eigenfield perturbation theory [57] the Hamiltonian is first diagonalized at an arbitrary field point X_0. A series of adjustments are then made to the magnetic field strength, the eigenvalues and eigenvectors until the resonant field position can be approximated to sufficient accuracy by B_0.

The initial Hamiltonian $H_0 = H_{FI} + X_0\, H_{FD}$ (H_{FI} and H_{FD} are the field independent and dependent Hamiltonians) is diagonalized to determine the required pair of eigenvalues ($E_{u,0}$ and $E_{v,0}$) and eigenvectors (U_0 and V_0). The difference between these eigenvalues is called W_0, and the required microwave frequency is given by $W_0 + \delta W$. The magnetic field strength is then adjusted by a factor:

$$X_1 = \frac{\delta W}{A_{vv} - A_{uu}} \tag{5.5}$$

where $A_{uu} = <U_0 \mid H_{FD} \mid U_0>$ and $A_{vv} = <V_0 \mid H_{FD} \mid V_0>$. The Hamiltonian is adjusted by the term $H_j = X_j\, H_{FD}$, where H_{FD} is the field dependent Hamiltonian. The equations:

$$\begin{gathered}\sum_{j=0}^{n}(H_j - E_{u,j})U_{n-j} = 0 \\ (H_0 - E_{v,0} - W_0)V_n + (H_1 - E_{v,1} - \delta W)V_{n-1} \\ + \sum_{j=2}^{n}(H_j - E_{v,j})V_{n-j} = 0\end{gathered} \tag{5.6}$$

are then used to obtain the corresponding change to the eigenvalues and eigenvectors given by $E_{u,n}$ and $E_{v,n}$ and U_n and V_n respectively. The magnetic field strength is then re-adjusted according to:

$$X_n = \sum_{j=1}^{n-1} \frac{X_j\, A_{vv(n-j)} - A_{uu(n-j)}}{A_{uu} - A_{vv}} \tag{5.7}$$

where $A_{uu(n-j)} = <U_n|\ \hat{A}\ |U_{(n-j)}>$. The magnetic field strength, eigenvalues and eigenvectors are iteratively adjusted in this manner until the resonant field position has been determined to sufficient accuracy. The final solutions for the magnetic field strength, eigenvalues (E) and eigenvectors (q) are given by:

$$\begin{gathered}B_0 = \sum_{k=0}^{n} X_k \\ E_i = \sum_{k=0}^{n} E_{u,k} \qquad\qquad E_j = \sum_{k=0}^{n} E_{v,k} \\ q_i = \sum_{k=0}^{n} U_k \qquad\qquad q_j = \sum_{k=0}^{n} V_k\end{gathered} \tag{5.8}$$

This procedure has been incorporated into the Sophe computational programme [30], where for each orientation over the SOPHE grid the field range is divided into a number of intervals, *k*. Matrix diagonalization is performed once in each interval, and the above perturbations are then employed to locate the resonant field positions within the interval. The segment number, *k*, is a user-input parameter. We have found that second-order eigenfield perturbation theory used in conjunction with our segmentation scheme can deal with complicated situations such as multiple transitions and has also proved to be efficient and reliable for locating the resonant field positions in field-swept EPR spectra.

A saving factor in the segmentation method lies in the fact that full matrix diagonalization is only performed *k* times irrespective of the number of transitions involved. By contrast, in the other schemes, a few diagonalizations are required for each transition and for large spin systems this number can become very large. The precision of the resonant field positions normally depends on the segment number *k* as well as on the spin system. How large the segment number should be depends on the nature of the system under study. However, simulations can be performed with different segmentation numbers providing an easy test of precision.

5.4.3.2 SOPHE Interpolation Method

The SOPHE interpolation scheme is divided into two levels of interpolation, a global interpolation using cubic splines [58] and a local interpolation using simple linear interpolation. Given the function values which may represent the resonant field position or the transition probability at the vertex points (Fig. 5.11a), we use the cubic spline interpolation method to interpolate the function values at all other points on the curves described by Eq. 5.4 (Fig. 5.11b). This is actually carried out in three different sets. In each set, there are N interpolations with the number of knots (vertex points) varying from 2 to N + 1. Although in two of the three sets (Eq. 5.4b and c) both variables θ and ϕ are involved, variable ϕ can be treated as a parameter [37]. First derivative boundary conditions [58] have been employed in our program which has been proved to produce high-quality interpolated data [37].

After the global interpolation, the integration over the unit sphere can be viewed as integrating through individual triangularly shaped convexes. A second level of interpolation is carried out based on the values globally interpolated and this is schematically shown in Fig. 5.11c. The resonant field position and transition probability are calculated at the vertices (tiny triangles) formed by linear interpolation (up to version 1.0.2 of XSophe) of the points on adjacent sides of the triangular convex. This is repeated for the other two pairs of sides of the triangular convex and the results averaged. Linear interpolation is based on a subpartition scheme and each triangular convex can be subpartitioned differently [37]. Intuitively speaking, the global cubic spline interpolation can be viewed as building up a "skeleton" based on the SOPHE grid and the local linear interpolation can be viewed as a "*tile filling process*". Up until version 1.1 of XSophe we assumed that all of the

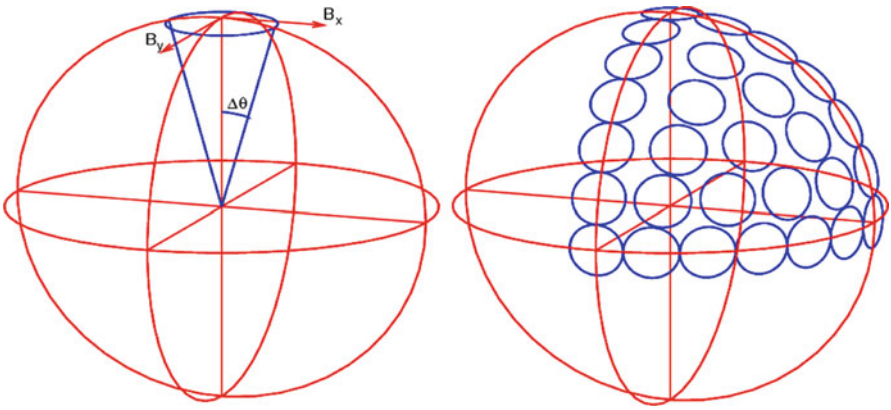

Fig. 5.12 Mosaic misorientation model

tiny triangles in a given triangle subtended the same solid angle. In version 1.1 of XSophe and all versions of Molecular Sophe we calculate the exact areas and use cubic spline interpolation for the *tile filling process*.

The use of the SOPHE interpolation scheme significantly reduces the time-consuming process of locating the resonant field positions and evaluation of the transition probabilities in the brute force matrix diagonalization (Sect. 5.4.3.4). The disadvantage of the SOPHE interpolation scheme is that it will fail when there are multiple resonant field positions present at a given orientation (θ, $\boldsymbol{\phi}$) or when looping transitions are present. The mosaic misorientation line width model (Sect. 5.4.3.3) [30] or homotopy (Sect. 5.4.4) [46, 47] are two alternative approaches to solving these problems. While the mosaic misorientation line width model is implemented in both the XSophe-Sophe-XeprView and Molecular Sophe computer simulation software suites, Homotopy is only implemeted in the former.

5.4.3.3 Mosaic Misorientation [30]

When the line width is small compared to the anisotropy of the system it is necessary to integrate over a large number of orientations to avoid simulation noise in the simulated spectrum. This increases the computational time considerably. The SOPHE grid and Interpolation schemes were developed as a way to overcome this problem. An alternative approach based on the mosaic misorientation linewidth model [59] was developed by our group. In the mosaic misorientation model (Fig. 5.12) a Gaussian distribution of molecular geometry axes about an average crystal c-axis is assumed. In the current implementation the partial derivatives of the eigenvalues with respect to a rotation about the x and y axes are calculated using first order perturbation theory.

The contribution of a Gaussian distribution, of half-width $\Delta\theta$, to the linewidth can then be calculated with the following equation.

$$\sigma_m^2 = \left(\Delta\theta \frac{\partial E_{ij}}{\partial \theta_x}\right)^2 + \left(\Delta\theta \frac{\partial E_{ij}}{\partial \theta_y}\right)^2, \quad E_{ij} = E_i - E_j \tag{5.9}$$

In the simulation of powder spectra each point in the SOPHE grid is considered to be a microcrystallite with a Gaussian distribution of orientations, $\Delta\theta$ (Fig. 5.12), such that there is an overlap between adjacent grid points (Fig. 5.12).

$$\Delta\theta = \frac{\pi}{4(N-1)} \tag{5.10}$$

At turning points in the spectrum the partial derivatives of the eigenvalues and hence σ_m are zero and the linewidths are determined by other contributions. At other orientations where the resonant field varies strongly with orientation the line widths will be broadened (smoothed). This model simulates an EPR spectrum where the important features, the turning points, are resolved in a significantly reduced time. Increasing N, the number of bands in the SOPHE grid, will lead to a convergence to the 'true' spectrum. For a large number of spin systems, N can be set to 20. The mosiac misorientation linewidth model can be contrasted to interpolation schemes by considering it as an extrapolation method.

5.4.3.4 A Comparison of Brute Force Matrix Diagonalization, SOPHE Interpolation and Mosaic Misorientation

An example demonstrating the efficiency of the SOPHE partition and interpolation schemes and the mosaic misorientation linewidth model is shown in Fig. 5.13 where we have calculated a randomly orientated spectrum for a high spin rhombically distorted Cr(III) ion for which an appropriate spin Hamiltonian is:

$$\begin{aligned} H = {} & g_e \boldsymbol{B} \cdot \boldsymbol{S} + D\left[\boldsymbol{S}_z^2 - \frac{1}{3}\boldsymbol{S}(\boldsymbol{S}+1)\right] + E(\boldsymbol{S}_x^2 - \boldsymbol{S}_y^2) \\ & + \boldsymbol{S} \cdot \boldsymbol{A} \cdot \boldsymbol{I} - g_n \beta \boldsymbol{B} \cdot \boldsymbol{I} \end{aligned} \tag{5.11}$$

The spin Hamiltonian parameters employed were $g_e = 1.990$, $D = 0.10$ (cm^{-1}), $E/D = 0.25$, $g_n = 1.50$, $A_x = 120$, $A_y = 120$, $A_z = 240$ (10^{-4} cm^{-1}). A narrow line width was chosen (30 MHz) in order to demonstrate the high efficiency of these approaches. The unit sphere has to be partitioned very finely in order to produce simulated spectra with high signal-to-noise ratios when there is large anisotropy and the spectral linewidths are narrow. The simulated spectra employing brute force matrix diagonalization with $N = 18$ and $N = 400$ are shown in Fig. 5.13a, b repectively. Including the SOPHE interpolation scheme with a partition number $N = 18$

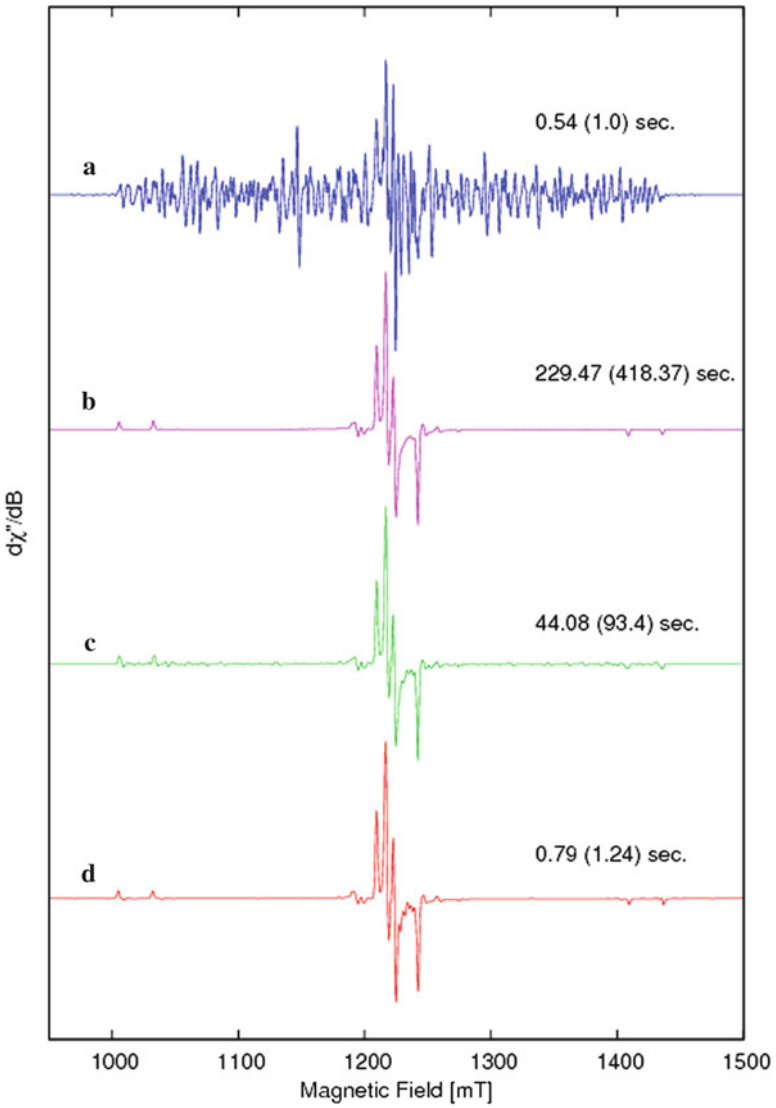

Fig. 5.13 Computer simulations of the powder EPR spectrum from a fictitious spin system (S = 3/2; I = 3/2) which demonstrates the efficiency of the SOPHE partition and interpolation schemes and the mosaic misorientation linewidth model. (**a**) Without the SOPHE interpolation scheme, N = 18, (**b**) Without the SOPHE interpolation scheme, N = 400, (**c**) With the SOPHE interpolation scheme, N = 18 and (**d**) With the mosaic misorientation linewidth model, N = 18. The computational times were obtained on a SGI O2 R5K (180 MHz). $\upsilon = 34$ GHz; field axis resolution: 4096 points; an isotropic Gaussian lineshape with a half width at half maximum of 30 MHz was used in the simulations

(Fig. 5.13c) dramatically improves the signal to noise ratio with a considerable reduction in computational time. Application of the mosaic misorientation line width model (Fig. 5.13d) also dramatically improves the signal to noise ratio and is computationally faster than the SOPHE interpolation method as interpolation has many overheads. Clearly the mosaic misorientation linewidth model is the fastest approach and now replaces the brute force matrix diagonalization approach within the computational programme Sophe and is also preferred over SOPHE interpolation.

5.4.4 Homotopy Segmentation Algorithm

Methods such as the brute force technique employ full matrix diagonalization to calculate the complete set of eigenvalues and eigenvectors as a function of orientation. However the simulation process generally makes use of only the pair of eigenvalues and eigenvectors directly involved in the current transition. The computational time involved in determining these eigenpairs can be improved through the use of alternative numerical methods such as Homotopy [46, 47]. Our group has developed a number of simulation techniques based on the Homotopy algorithm (the Methods of Unresolved Edges [47], Unmatched Segments [47] and the Homotopy Segmentation Method [47]).

After an initial matrix diagonalization of the spin Hamiltonian and the determination of the resonant field positions at an arbitrary orientation (Fig. 5.14), the Homotopy Segmentation method determines the resonant field positions at each orientation independently (in a similar manner to the Eigenfield method). This is achieved by generating a set of splines which approximate the transition level energies as a function of the magnetic field.

The resonant field positions (*i.e.* where $F_{i,j}$ equals zero, Eq. 5.12) and the turning points of $F_{i,j}$ with respect to B can be determined directly from these splines.

$$\boldsymbol{F}_{ij} = \left(E_i - E_j\right) - h\nu \tag{5.12}$$

EPR spectra can be simulated through either evaluating the resonant field positions at a given set of orientations exactly, or by evaluating the resonant fields at a small number of orientations and then interpolating over the transition surfaces (Fig. 5.15) to produce an approximation for the resonant field positions at the remaining set of orientations. If interpolation is being employed, it is necessary to connect the resonant field positions from adjacent orientations into a fully-connected surface. This is considered in Sect. 5.4.4.2. Each resonant field position irrespective of whether it was determined exactly or is an approximation then contributes a transition lineshape to the final EPR spectrum.

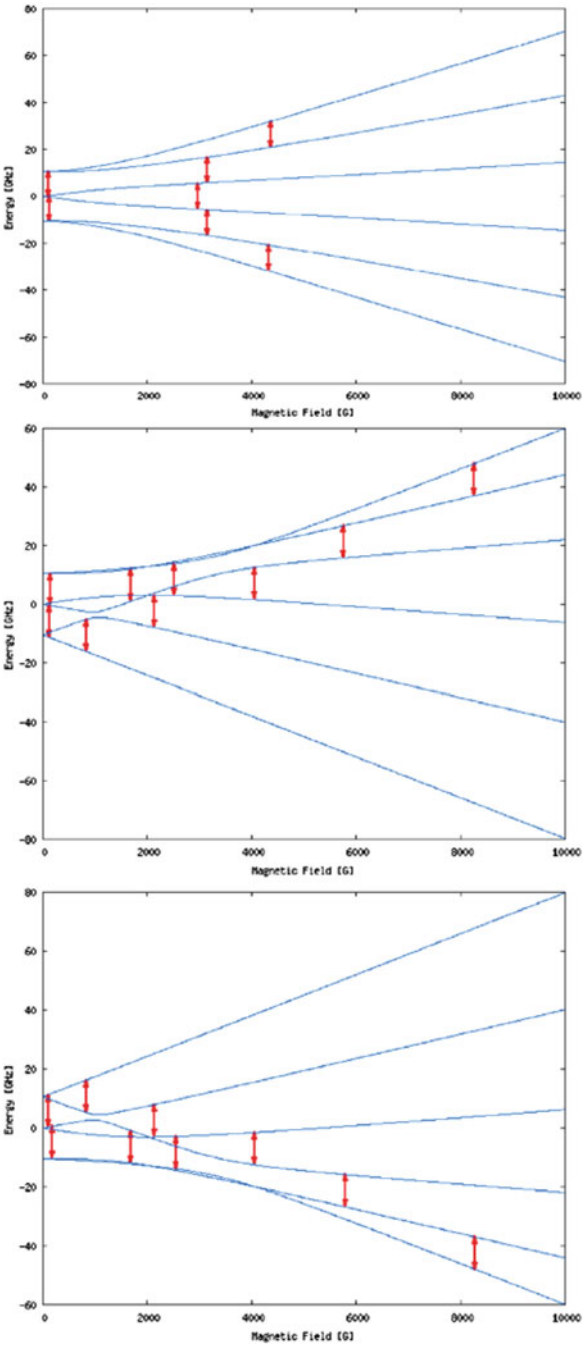

Fig. 5.14 Energy level diagrams with B_0 parallel to the X, Y and Z axes (*top-bottom*) showing the EPR transitions for a high spin Fe(III) center with $D = 0.1\ cm^{-1}$, $E/D = 0.25$, $g = 1.99$, $\theta = 0^o$, $\phi = 0^o$ and $\upsilon = 11$ GHz

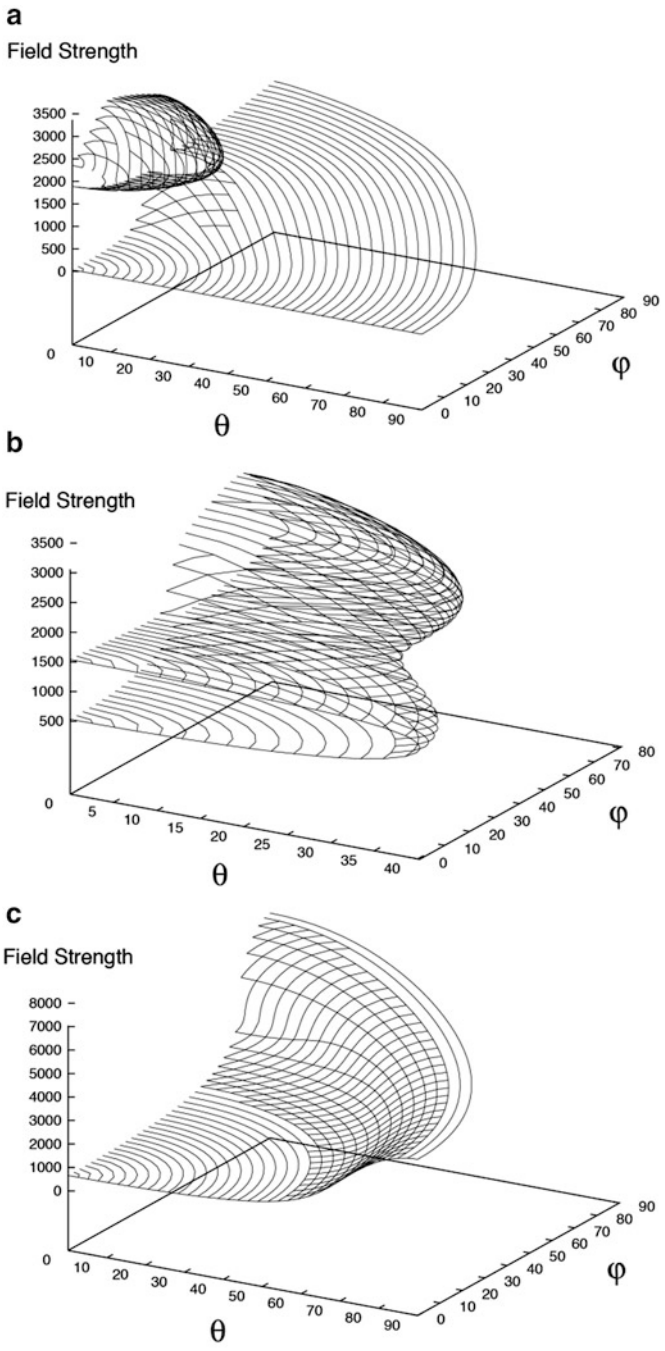

Fig. 5.15 Transition surfaces for the high spin Fe(III) center described in Fig. 5.14, $\upsilon = 9$ GHz. (**a**) between levels 2 and 4, (**b**) between levels 3 and 5 and (**c**) between levels 5 and 6 (Reproduced from reference [46] with kind permission of © Elsevier (1995))

5.4.4.1 Locating the Resonant Field Positions at a Single Orientation

As with the Eigenfield method, the Homotopy Segmentation method determines the resonant field positions at each orientation independently. The field range over the spectrum is divided into a distribution of points (where the number of points required is significantly smaller than that required by the Eigenfield method). Matrix diagonalization is then employed to compute all of the eigenvalues at each field point. To improve computational time, a variant of matrix diagonalization is employed at this stage which only computes the complete set of eigenvalues. A set of splines can then be produced which model each eigenvalue as a function of the magnetic field strength. The resonant field positions at the given orientation are predicted by the points where the distance between any two splines matches the microwave frequency.

The initial set of splines were defined from an even distribution of field points. Homotopy is then employed to determine additional eigenvalues in the regions of predicted resonant field positions. These new field points are added to the splines until each of the resonant field positions has been determined to sufficient accuracy.

No eigenvectors have so far been determined at the current orientation. The transition probability and linewidth are a function of the two eigenvectors contributing to each resonant field position. The required eigenvectors, and the resulting transition probability and linewidth, are determined at three points on the spline in the vicinity of each resonant field position. A quadratic function is then produced which describes these values as a function of field, and is used to approximate the transition probability and linewidth at the resonant field position.

This procedure determines all of the resonant field positions present at a single orientation. The resonant field positions are located to a required level of accuracy (as required by the numerical integration of the resonant field position as a function of orientation). If interpolation is employed within the simulation or the surfaces are to be visualized, then adjacent resonant fields need to be matched and the turns traced. These additional procedures employ the turning points of the F_{ij} functions (ie. the local maxima and minima of F_{ij} as a function of magnetic field, see Sect. 5.4.4.2). These turning points are not used in the numerical integration, and hence no new points are added to the splines to improve the accuracy of the turning points.

5.4.4.2 Comparing Adjacent Orientations

In general, adjacent orientations will contain the same number of resonant field positions and turning points, in which case these points can be matched directly. This however is not the case if:

- a resonant field position or turning point move so they are inside the field range at one orientation, and outside the field range at another,
- two resonant field positions merge, causing a turn in the transition surface,
- or if two turning points merge and cancel each other out.

These phenomena only occur at a few select orientations, and it is unlikely that more than one of these phenomena will occur between any two grid points.

When there are the same number of resonant field positions at two adjacent orientations these resonant field positions are simply matched up one to one. If the number of resonant fields changes by one between adjacent orientations, then the resonant field positions can still be simply matched one to one. It is assumed that the new resonant field was produced from a field moving from outside the field range at one orientation to inside the range at the other orientation, and so either the first or last resonant field at a given orientation will have no neighbour. The slope of F_{ij} at each resonant field will either be positive or negative, and will be the same at two adjacent points. Hence by matching the sign of the slope at the endpoints, the extra field point can be determined. If there are two extra points at one orientation, the field points might still be matched one to one. The two points might both have moved in from the ends of the field range. This is assumed to have occurred if the sign of the slope does not match at either end of the field range.

When the resonant field positions cannot be matched one to one (such as when there is a turn in the transition surface), turning points are considered. In most cases there will be the same number of turning points at adjacent orientations, and between any two turning points there will be at most one resonant field position. Hence if two turning points are matched and they both contain a resonant field position between them, then the two resonant field positions can also be matched. If two turning points are matched, but there is a resonant field position at only one orientation, then a turn in the surface has been encountered. In this case the turning point at one orientation will be positive, the turning point at the other orientation will be negative, and there will be a turn in the surface between these two turning points. Turning points might have moved in from the ends of the field range, in a similar way to the resonant field positions. The turning points may still be matched up if there are one or two more turning points between adjacent orientations.

A turn in the surface is encountered if the turning point at one orientation is positive, and the turning point at an adjacent orientation is negative. The surface will turn at an intermediate orientation where the value of F (B,θ) at the turning point is zero. Homotopy is used to trace a line between the two turning points until the turn is resolved to sufficient accuracy.

In highly complex regions of the transition surfaces, the number of resonant field positions and turning points may vary significantly between adjacent orientations in the numerical grid. In these regions it is no longer possible to simply match the orientations point for point, and hence the above procedures are employed to determine the complete set of resonant field positions and turning points at intermediate orientations between these points.

5.4.5 Linewidth Models

A number of linewidth models originally developed for magnetically isolated paramagnetic species have been incorporated into the XSophe-Sophe-XeprView

computer simulation software suite. For all the linewidth models discussed below the linewidth parameter, σ_υ, is given in energy units. In Sophe (field space version), σ_υ is converted to a field-domain linewidth parameter σ_B through $\sigma_B = |dB/dE_{ij}|\sigma_\upsilon$ (where B is the magnetic field and $E_{ij} = E_i - E_j$)[1, 44]. $|dB/dE_{ij}|$ is calculated for each transition by using eigenfield perturbation theory [57]. The linewidth models incorporated into Sophe include:

- Kivelson's linewidth model [60] for isotropic spectra

$$\sigma_v = \alpha + \beta M_I + \gamma M_I^2 + \delta M_I^3 \tag{5.13}$$

  The coefficients α, β, γ and δ can be related to the solvent viscosity, correlation time, molecular hydrodynamics radius and the anisotropy of the spin system under study [60].
- Angular variation of the g-values [1].

$$\sigma_v^2 = \left(\sigma_x^2 g_x^2 l_x^2 + \sigma_y^2 g_y^2 l_y^2 + \sigma_z^2 g_z^2 l_z^2\right)/g^2 \tag{5.14}$$

  where $g^2 = g_x{}^2\ l_x{}^2 + g_y{}^2\ l_y{}^2 + g_z{}^2\ l_z{}^2$, σ_i's (i = x,y,z) are the input linewidth parameters and l_i's (i = x,y,z) are the direction cosines of the magnetic field with respect to the principal axes of the g matrix.
- A correlated distribution of g and A values.

  A correlated distribution of g and A values also termed g and A strain was originally developed by Froncisz and Hyde [61] and has been used successfully to account for the linewidth variations encountered in spin S = 1/2 systems particularly in copper, low spin cobalt, molybdenum(V) and tungsten(V) complexes.[1, 8, 62–66] When expressed in the frequency-domain, [1, 44] the linewidth in this model is based on the formula

$$\sigma_v^2 = \left(\sum_{i=x,y,z}\left\{\sigma_{R_i}^2 + \left[\frac{\sigma g_i}{g_i}\nu_0(B) + \sigma A_i M_I\right]^2\right\} g_i^2 l_i^2\right)/g^2 \tag{5.15}$$

  where the σR_i (i = x, y, z) are the residual linewidths due to unresolved metal and/or ligand hyperfine splitting, homogeneous linewidth broadening, and other sources, σg_i's and σA_i's are the half widths of the Gaussian distributions of the g and A values. The g-A strain model involves nine parameters for a rhombically distorted metal ion site.
- A statistical distribution of D and E.

  Wenzel and Kim [67] have described a statistical D-E strain model. In their model, the distributions of D and E are assumed to be Gaussian and independent of each other with the resulting full width at maximum slope due only to strain is given by

$$\sigma_{DE}^2 = \sigma_D^2 \left\{ < \psi_i \left| \boldsymbol{S}_z^2 \right| \psi_i > - < \psi_j \left| \boldsymbol{S}_z^2 \right| \psi_j > \right\}^2 + \sigma_E^2 \left\{ < \psi_i \left| \boldsymbol{S}_x^2 - \boldsymbol{S}_y^2 \right| \psi_i > - < \psi_j \left| \boldsymbol{S}_x^2 - \boldsymbol{S}_y^2 \right| \psi_j > \right\}^2 \quad (5.16)$$

where σ_D and σ_E are the half-widths at maximum slope of the distributions of D and E in energy units, respectively, and ψ_i and ψ_j are the wavefunctions associated with transition i $\leftrightarrow$ j. A residual linewidth, σ_R, is convoluted with the D-E strain effects

$$\sigma_v^2 = \sigma_{DE}^2 + \sigma_R^2 \quad (5.17)$$

While the released version of Molecular Sophe only contains one linewidth model, namely the linewidth variation of the g-values, our development version provides a linewidth model similar to the distribution of D and E values, but extended to all spin Hamiltonian and geometric parameters. This has been used to analyse multifrequency EPR spectra of low spin Co(II) complexes and dinuclear Cu(II) complexes [65b, 68b, c].

5.4.6 Parallelization

With the advent of multiprocessor computers and the new algorithms described above, the simulation of EPR spectra from complex spin systems consisting of multiple electron and or nuclear spins becomes feasible with Sophe. Optimisation of the spin Hamiltonian parameters by the computer will also be possible for these spin systems. Parallelization of the matrix diagonalization method has been performed at the level of the vertices in the Sophe grid using OpenMP. For example, if a computer has eight processors then the number of Sophe grid points is divided into groups of eight and each group is then processed by one of the processors with the resultant spectra being added to an array shared by the eight processors. For the hypothetical Cr(III) spin system shown in Fig. 5.13 a threefold reduction in computational time utilising the XSophe-Sophe-XeprView computer simulation software suite and three CPUs is observed. Greater reductions are observed for more complex spin systems.

5.4.7 Optimization Algorithms

A unique set of spin Hamiltonian parameters for an experimental EPR spectrum is obtained through minimising the goodness of fit parameter (GF)

$$GF = \left(\sum^{N} \left(Y_{\exp} - S(B, V_c) * \alpha \right)^2 \right)^{1/2} / (N * \sigma) \quad (5.18)$$

where the experimental spectrum (Y_{exp}) has been baseline corrected assuming a linear baseline and the simulated spectrum has been scaled by α to Y_{exp}. N is the number of points in common between the experimental and simulated spectra and σ is the magnitude of noise in the spectrum. In the past minimising GF has been performed through a process of trial-and-error by visually comparing the simulated and experimental spectra until a close match was found. Recent progress in reducing computational times for computer simulations (Sect. 5.4.3.3) and the improved speed of workstations allows the use of computer-based optimisation procedures to find the correct set of spin Hamiltonian parameters from a given EPR spectrum.

The most appropriate technique for optimising a set of spin Hamiltonian parameters is nonlinear least squares [69]. This method has the advantage that the differences ($Y_{exp}-S(B, \upsilon_c)$, Eq. 5.18) associated with the more extreme positive or negative values are exaggerated, which emphasizes genuine peak mis-matching whilst tending to reduce the impact of noise. Unfortunately, evaluation of $S(B, \upsilon_c)$ can take a long time and as there is no analytic derivative information available, this method is not really an option for general spin systems. Direct search methods are characterized by evaluating the function at several points within the spin Hamiltonian parameter space (H_p-space) [70] and then using the knowledge gained during the last few evaluations in an attempt to choose a more promising point. These methods have lost popularity over time, and have been largely superseded by methods using derivative information, although they are still used in places where noise is prevalent. They suffer only two drawbacks: the algorithms are particularly susceptible to becoming trapped in local minima; and they tend to be fairly inefficient in their use of function evaluations (at least in comparison with derivative-based methods on functions where derivatives are available). Three of these direct methods were considered particularly promising, the Hooke and Jeeve's [71], Simplex [72] and a Quadratic variation of the Hooke and Jeeves method. We have also implemented two simulated annealing approaches [73] in Sophe as part of the XSophe-Sophe-XeprView computer simulation software suite [30].

In addition there are several problems which need to be addressed, including (i) the sensitivity of scaling the various spin Hamiltonian parameters and the method chosen for comparing the experimental simulated spectra [31]. In XSophe we allow the user to control the sensitivity of parameter adjustment throughout the optimisation procedure and secondly the user can compare the spectra directly or the Fourier transformed spectra. The latter method provides increased resolution through separating the high and low frequency components [74]. As an aid to optimising the computer simulation XSophe-Sophe-XeprView has the capability of displaying intermediate spectra (Magnetic Field vs. Intensity vs. Iteration Number) and the corresponding spin Hamiltonian parameters. Ideally, you would like to optimize a set of multifrequency EPR spectra with a single set of spin Hamiltonian parameters. Although this can be achieved in the current version of XSophe, the methodology is not straight forward.

5.4.7.1 Hooke and Jeeves Method

The Hooke and Jeeve's method [71] was first publicized in 1961 and has been widely used for some time. The method starts with an "exploratory" move. Each parameter is considered in turn, and checks are made to see how changes made to the parameter affect the error. A fixed step is made in the positive direction, and it is observed whether the error increases or decreases. If no improvement is made, then a fixed step is made in the negative direction. Again it is observed whether the error is improved. Based upon which fixed steps improved the error (but ignoring how much the error changes), a direction for "pattern" moves is then determined. Fixed steps are then made along the "pattern" direction until no further progress is made, at which stage another exploratory move is made [71].

5.4.7.2 Quadratic Variation of the Hooke and Jeeves Method

One of the problems observed while using the Hooke and Jeeve's method is that fixed steps are made simply based on whether the error is increasing or decreasing, but ignoring how much each parameter affects the error. During the "exploratory" move, three points are typically evaluated with respect to each parameter. A quadratic can be drawn through these three points and a prediction can be made for the value of each parameter which minimizes the error. Consequently a quadratic variation of the Hooke and Jeeve's method [30] was developed in which a quadratic function with respect to each parameter replaced the fixed steps in the Hooke and Jeeve's method.

5.4.7.3 Simplex Method

The Spendley, Hext and Himsworth (or Simplex) method [72] has a very geometrical interpretation. It works by taking an $H_P + 1$ vertex simplex (i.e. a regular $H_P + 1$ sided figure in H_P-space) and evaluating GF at each of the vertices. It then takes the vertex point with the largest value of GF (subject to a few restrictions) and replaces it with its reflection in the hyper-plane formed by the other H_P points.

The elegant nature of this algorithm is apparent in considering the case where $H_P = 2$. The problem can now be visualized by a three dimensional surface (i.e. GF vs. the two H_P parameters) whose lowest point (valley/well) we aim to find. The simplex in this case is an equilateral triangle which 'rests' upon the three dimensional surface. The algorithm, simply dictates that the highest of the three points will lift over the other two, causing the triangle to 'flip' over (so the highest point now points down hill). This process is repeated, and the triangle 'flips' its way down to bottom of a nearby minimum. If the triangle cannot flip to a new minimum, the size of the triangle is contracted and termination takes place when the number of contractions reaches a defined limit.

The simplex method has two advantages over the Hooke and Jeeve's method. The first is its use of $H_P + 1$ evaluations of GF in determining the next point at which to evaluate S(B, υ_c) compared with the Hooke and Jeeve's method which uses at most two points (and then only during the pattern step, it normally uses only one). The second advantage is that the simplex method is somewhat more resilient to local minima. If one of the points is very close and if the simplex is still large enough, the simplex may well 'flip out' of the well. Unfortunately, in some circumstances, the simplex method can fail. To take a two-dimensional case, it is susceptible to becoming trapped in a deep, narrow 'valley' if one of the points lands very close to the bottom and the other two points are on different walls. Having reached this stage, no progress can be made except along the valley (the sides are too steep to allow any climbing). If the point near the bottom is on the down-hill side of the valley, then no movement can be made as the triangle cannot flip over a point, only a line. Consequently, improvement is only possible with contractions occurring about the lowest point which will result in early termination in a local minimum. A possible way to overcome this difficulty, is to combine the standard simplex algorithm described above with a stochastic process (such as simulated annealing). This method would hopefully 'break-out' of such minima.

5.4.7.4 Simulated Annealing

Simulated annealing is one of a class of methods known as Monte-Carlo methods [73]. The simplest Monte-Carlo method starts at a point $H_p{}^0$ and makes a random step of length *l* in H_p space to the new point $H_p{}'^0$. If GF ($H_p{}'^0$) is less than $H_p{}^0$ then the step is accepted and $H_p{}^1$ is set to $H_p{}'^0$ at which point the process is repeated by taking a step from $H_p{}^1$. However if GF increases, then the step is rejected and another step is taken from $H_p{}^0$. This process gradually forms a sequence of $H_p{}^s$ with decreasing values of GF. The algorithm terminates with answer $H_p{}^k$ when no more progress is being made. At this point the algorithm may be restarted from this answer with a decreased step size.

The concept of simulated annealing comes (somewhat loosely) from the annealing (solidifying) of liquids (especially molten metals). The molecules in their liquid state have a high kinetic energy, which allows (indeed, forces) them to change their location and orientation. By cooling, their energy is depleted and so they gradually 'settle down' into what eventually becomes their fixed location. The 'structure' which results, differs significantly depending upon the rate of cooling.

Simulated annealing attempts to emulate the slow cooling process by using one very significant change from the standard Monte-Carlo method [73]. Rather than rejecting all function-increasing steps, it accepts the 'uphill' k*th* step with probability $P(H_p{}^k, T)$ where P satisfies $\lim_k (P = 0)$. The value T is known as the temperature of the system and decreases as k increases in accordance with a cooling schedule. The hope is that the acceptance of a detrimental step will have long-term benefits by allowing the sequence of $H_p{}^s$ to 'escape' from a local minimum.

Two approaches for choosing a random point have been implemented into Sophe. In the first method, a random jump is performed by choosing a random point on a hypershere of radius r about the current point. Both the temperature and the radius are decreased periodically throughout the search. The benefit of this approach is that all H_p dimensions are searched simultaneously. In the second approach, each of the H_p axes are searched in turn.

5.4.7.5 Parameter and Spectral Scaling

An important part of practical multi-variable optimisation is the sensitivity of scaling the various spin Hamiltonian parameters. Since the Hooke and Jeeves and Simplex algorithms take finite steps along various co-ordinate axes, there must be some uniformity in the rate of change in GF in each of these directions. Since a change of δ in one of the g values would have significantly less effect on $S(B, \upsilon_c)$ than a step of δ in one of the A values, then, without scaling, for any given step size, only some of the variables will be usefully optimized. To solve this problem, the H_p-space formed by the parameters to be varied is transformed to one where a given step length will have a more uniform effect on GF in each of the H_p directions. Given the necessity of avoiding costly evaluations of $S(B, \upsilon_c)$ and derivative information this can be done by performing a linear transformation by multiplying each of the spin Hamiltonian parameters by h_i. The h_i's are manually chosen to keep fluctuations in GF to approximately the same order of magnitude. Parameter scaling is not required in the quadratic and simulated annealing approaches as the step size is dynamically adjusted.

The simulated spectrum is multiplied by α (Eq. 5.18) so that it can be directly compared to the experimental spectrum, Y_{exp}. In Sophe we have three methods for scaling, double integration (for derivative EPR spectra), peak to peak extrema and optimisation of the scaling factor.

5.4.7.6 Spectral Comparison

Many complex randomly orientated EPR spectra contain overlapping resonances with complex lineshapes. Optimisation of such spectra often leads to the computer broadening (increase in linewidth) of one of the resonances to reduce the error. Although we do not profess to have the ultimate solution to this problem, we have employed two approaches to help solve this problem. The first approach involves the ability to control the sensitivity of parameter adjustment throughout the optimisation procedure, whilst the second involves the comparison of the Fourier transformed experimental and simulated spectra. The latter method provides increased resolution through separating the high and low frequency components [66, 74]. As an aid to optimising the computer simulation, XSophe/Xepr has the capability of displaying intermediate spectra (Magnetic Field vs. Intensity vs. Iteration Number) and the corresponding spin Hamiltonian parameters.

5.4.7.7 Molecular Sophe

While the graphical user interface of the released version of Molecular Sophe incorporates the functionality for the optimization of the spin Hamiltonian parameters, the computational programme Sophe does not have the required functionality. In our development version we have incorporated non-linear least squares optimization of all spin Hamiltonian, linewidth and geometric parameters and allow the optimization of multi-component, multiple derivatives, multifrequency CW and pulsed EPR spectra simultaneously [75]. We have exploited this development version to analyse the multifrequency EPR spectra of low spin Co(II) complexes and dinuclear Cu(II) complexes [65b, 68b, c].

5.5 Computer Simulation of Pulsed EPR Spectra

The simulation of pulsed EPR spectra involves calculating the evolution of an observable ($\bar{O}$; Eq. 5.19) during the microwave pulses, radiofrequency pulses and free evolution periods that comprise the pulse sequence. The signal in an arbitrary pulsed EPR experiment can be simply described in superoperator notation [12, 42].

$$\langle \bar{O} \rangle = \left\langle \rho_0 \left| \hat{R}_1 \hat{R}_2 \ldots \hat{R}_3 \right| \hat{O}_n \right\rangle \tag{5.19}$$

In most experiments the initial density matrix (ρ_0) is the equilibrium density matrix (ρ) with diagonal elements given by the Boltzmann population of the energy levels in the eigenbasis of the static Hamiltonian:

$$\rho_{ii} = \frac{e^{\frac{-E_i}{kT}}}{\sum_{j=1}^{n} e^{\frac{-E_j}{kT}}} \tag{5.20}$$

The density matrix for a two level spin system (S = 1/2) is :

$$\rho = \begin{bmatrix} \rho_{11} & \rho_{12} \\ \rho_{21} & \rho_{22} \end{bmatrix} \tag{5.21}$$

and the corresponding superbra is:

$$\langle \rho | = \begin{bmatrix} \rho_{11} & \rho_{12} & \rho_{21} & \rho_{22} \end{bmatrix} \tag{5.22}$$

The detection operator (observable) in Eq. 5.19 is given by:

$$O = \begin{bmatrix} O_{11} & O_{12} \\ O_{21} & O_{22} \end{bmatrix} \tag{5.23}$$

and the corresponding superket is:

$$|O\rangle = \begin{bmatrix} O_{11} \\ O_{21} \\ O_{12} \\ O_{22} \end{bmatrix} \tag{5.24}$$

The transverse magnetization (M_x, M_y) are proportional to S_x, S_y, respectively and are determined by the g value in the x-y plane, the microwave power and other experimental factors.

In general a pulse sequence is comprised of one or more microwave pulses, free evolution periods and possibly radio frequency pulses, see for example the HYSCORE pulse sequence shown in Fig. 5.9. Each of these components can be mathematically described by a superpropagator (R) (Eq. 5.25), which in turn is derived from a direct product of the propagators:

$$\hat{R} = R \otimes R^{-1}$$

$$\hat{R} = \begin{bmatrix} R_{11} & R_{12} \\ R_{21} & R_{22} \end{bmatrix} \otimes \begin{bmatrix} R_{11}^* & R_{21}^* \\ R_{12}^* & R_{22}^* \end{bmatrix} = \begin{bmatrix} R_{11}R_{11}^* & R_{11}R_{21}^* & R_{12}R_{11}^* & R_{12}R_{21}^* \\ R_{11}R_{12}^* & R_{11}R_{22}^* & R_{12}R_{12}^* & R_{12}R_{22}^* \\ R_{21}R_{11}^* & R_{21}R_{21}^* & R_{22}R_{11}^* & R_{22}R_{21}^* \\ R_{12}R_{12}^* & R_{12}R_{22}^* & R_{22}R_{12}^* & R_{22}R_{22}^* \end{bmatrix} \tag{5.25}$$

Coherence transfer pathways provide a way of visualizing the transfer of magnetization during a pulse sequence and in general an element of the density matrix undergoes the following transformation:

$$\rho_{ij} \xrightarrow{\boldsymbol{R}} \sum_{l=0}^{n} \sum_{k=0}^{n} R_{ik} R_{lj}^* \rho_{kl} \tag{5.26}$$

In the eigenbasis of the static Hamiltonian the superpropagator for each free evolution period is diagonal. The time dependence of each element in the density matrix (ρ) is simply given by:

$$\rho_{ij} \xrightarrow{Et} e^{-2i\pi E_{ij} t} \rho_{ij} \tag{5.27}$$

During the microwave pulses the Hamiltonian is no longer time-independent and contains a term oscillating at the microwave frequency. Using Floquet theory [42] the superpropagators for the microwave pulses can be expressed as a Fourier series. For many spin systems the series converges rapidly and can be truncated at a low number of harmonics.

$$\hat{R}(t) = \sum_{m=-n}^{n} \hat{R}_m e^{-im\omega_{mw}t} \tag{5.28}$$

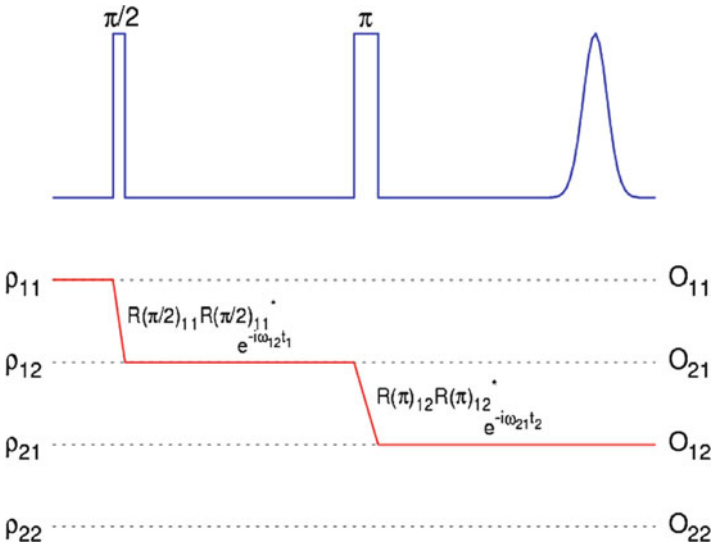

Fig. 5.16 A schematic diagram showing a pulsed EPR sequence and the evolution of the equilibrium density matrix through the microwave pulses and free evolution periods to the detection operator. One coherence pathway is shown

Pulsed EPR experiments typically involve phase cycling where the experiment is repeated with different combinations of the phases of the microwave pulses. It can be seen that for a single pulse the phase cycle $[0, \pi]$ filters out all odd Floquet harmonics while the phase cycle $[0, -\pi]$ filters out all even Floquet harmonics.

$$\hat{R}_n e^{-in(\omega_{mw}t+\pi)} = (-1)^n \hat{R}_n e^{-in\omega_{mw}t} \tag{5.29}$$

The use of phase cycling reduces the number of coherence pathways that must be followed. This can be further reduced if we include the condition that the initial Fourier index is 0 at equilibrium and at the time of detection must be given by $p = \pm 1$. This is shown in Fig. 5.16 for a two pulse sequence. The first pulse has $p = +1$ the second pulse $p = -2$. One pathway through the density matrix (in superbra notation) is shown in Fig. 5.16. Each coherence pathway yields a peak which is then added to the spectrum. The spectrum may have one or more frequency dimensions depending on how the time periods are incremented in the experiment. The final spectrum is obtained by averaging over all pathways. For powder spectra integration over three dimensional space (orientation) using the SOPHE grid is also performed [37].

The above approach to the simulation of pulsed EPR spectra allows the simulation of pulsed EPR spectra from not only isolated paramagnetic samples containing a single unpaired electron but also from samples containing multiple unpaired electrons, for example high spin Fe(III) centers found in cytochromes and non heme iron proteins and coupled centers, such as the type III copper containing enzymes and the binuclear metallohydrolyases.

5.6 Visual Aids for Analysing Complex CW EPR Spectra

XSophe-Sophe-XeprView and Molecular Sophe provide three tools (Energy level Diagrams, Transition Roadmaps and Transition Surfaces) for aiding the analysis of complex CW EPR spectra. Both computational suites output a web page (html) describing the spin system and various experimental parameters in conjunction with Portable Network Graphics (png) and postscript (ps) files which can be viewed with a Mozilla Firefox® browser and Ghostview or an another postscript viewer. Both the Portable Network Graphics (png) and postscript (ps) files can be incorporated into OpenOffice.org, Microsoft Office or other wordprocessing and graphics programmes.

5.6.1 Energy Level Diagrams

The XSophe-Sophe-XeprView and Molecular Sophe programmes employ matrix diagonalization to calculate energy level diagrams and EPR transitions along the x, y and z principal directions. An example of such a calculation is shown in Fig. 5.17.

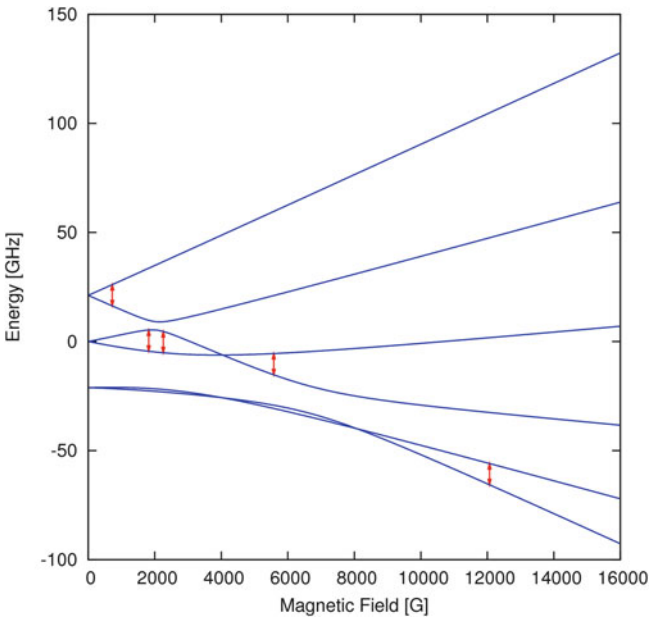

Fig. 5.17 An Energy level Diagram for a hypothetical high spin Fe(III), S = 5/2 spin system (D = 6 GHz, E/D = 1/3, g = 2, ν_c = 9.75 GHz, N = 1, Field Steps = 100, T = 4 K) (Produced by the XSophe-Sophe-XeprView computer simulation software suite [30] using the default Eenergy level default.sph data file)

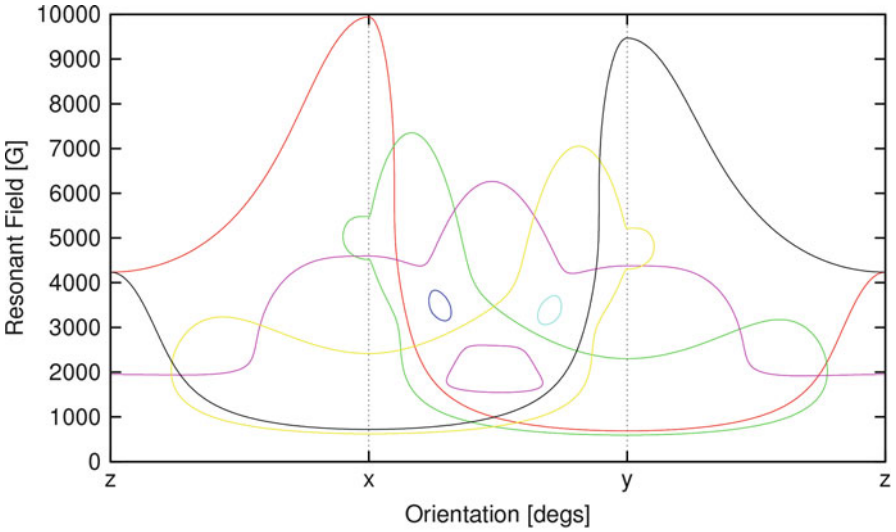

Fig. 5.18 A Transition Roadmap for a hypothetical high spin Fe(III), S = 5/2 spin system (D = 4.5 GHz, E/D = 1/3, g = 2, χ, ρ, τ = 90°, υ_c = 9.75 GHz, N = 100, Field Steps = 100, T = 4 K) (Produced from XSophe [30] using the default TransitionRoadmap_default.sph data file)

5.6.2 *Transition Roadmaps*

The XSophe-Sophe-XeprView and Molecular Sophe programmes employ matrix diagonalization to calculate transition roadmaps which can be viewed using a Mozilla Firefox® web browser (Fig. 5.18).

5.6.3 *Transition Surfaces*

The XSophe-Sophe-XeprView and Molecular Sophe programmes employ matrix diagonalization to calculate transition surfaces producing an output spectrum file (html) and an OpenInventor (iv) file which can be viewed using an OpenInventor viewer (ivview in conjunction with a web browser Firefox®) on a personal computer running Linux (Fig. 5.19) [33]. The scene graphs are plotted using cartesian coordinates, which is extremely useful for highly anisotropic spin systems such as high spin systems. This requires the minimum field to be set to zero which is defined as the origin. In contrast, for nearly isotropic systems, it is important to examine a single transition at a time. The choice of transitions can be made through the Transition Labels/Probabilities window and either setting the transition threshold or defining the transitions.

In high spin systems looping transitions can often be observed and these are seen as bubbles in the surface (Fig. 5.20).

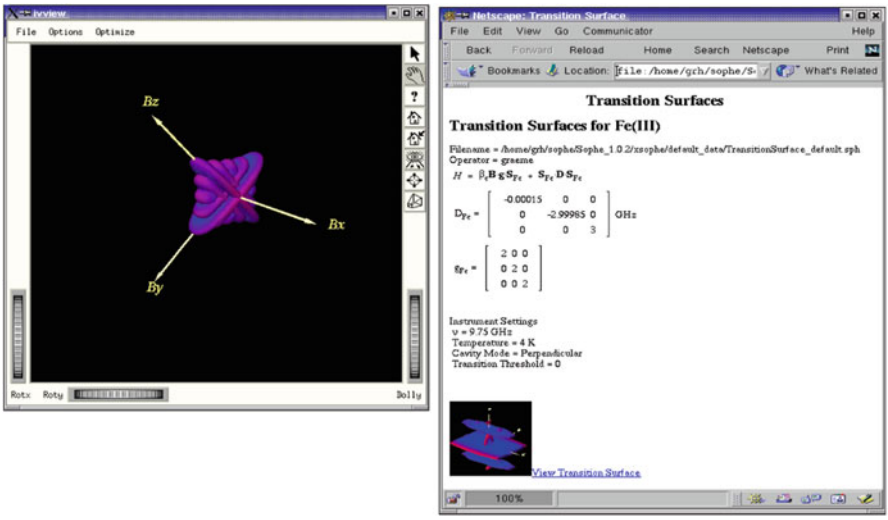

Fig. 5.19 A Transition Surface for a hypothetical high spin Fe(III), S = 5/2 spin system (D = 4.5 GHz, E/D = 1/3, g = 2, υ_c = 9.75 GHz, N = 1, Field Steps = 30, T = 4 K) (Produced from XSophe [30] using the default TransitionSurface_default.sph data file). Results are displayed within a netscape browser and the OpenInventor scene graph viewer ivview on computers running Linux

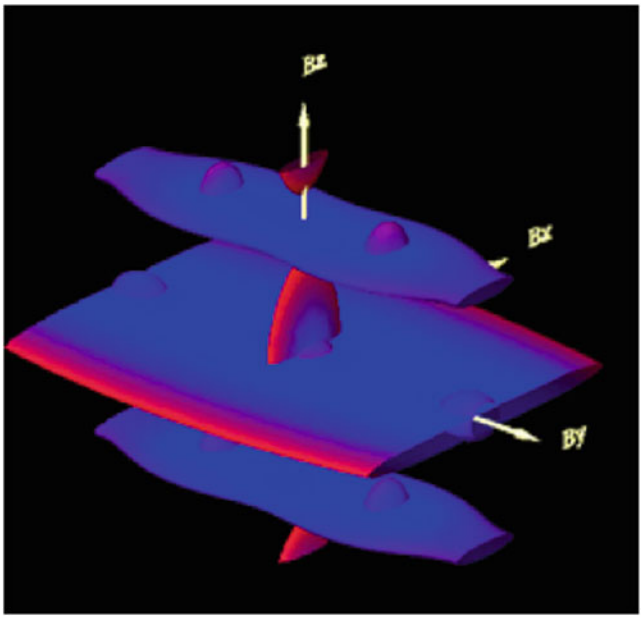

Fig. 5.20 A transition surface for a high spin Fe(III) spin center found in sweet potato purple acid phosphatase (D = −0.88 cm^{-1}, E/D = 0.1925, g = 2, υ_c = 9.5784 GHz, N = 1, Field Steps = 100, T = 4 K) revealing looping transitions [39]

5.7 Molecular Sophe Calculator

The MoSophe calculator [38] (Fig. 5.21) is based upon html and javascript and requires a java enabled web browser such as Mozilla Firefox®. The calculator can be either started from the calculator button in the Molecular Sophe toolbar or can be started from within a browser by loading the following file on a personal computer running Linux with Molecular Sophe installed. The software is platform independent and can be installed on Mac OSX, and Windows operating systems, though the location of the file (eprcalculator.html) will be different.

/usr/bin/firefox/usr/mosophe/utils/eprcalculator.html

Selecting the calculator button in the toolbar starts the MoSophe calculator and the initial screen displays a menu with seven items:

- Electron Zeeman Interaction,
- Nuclear Zeeman Interaction,
- Flip Angle: MW pulse,
- Flip Angle: RF pulse,
- Dipole-Dipole: electron-electron,
- Dipole-Dipole: electron-nucleus and
- Energy Equivalents.

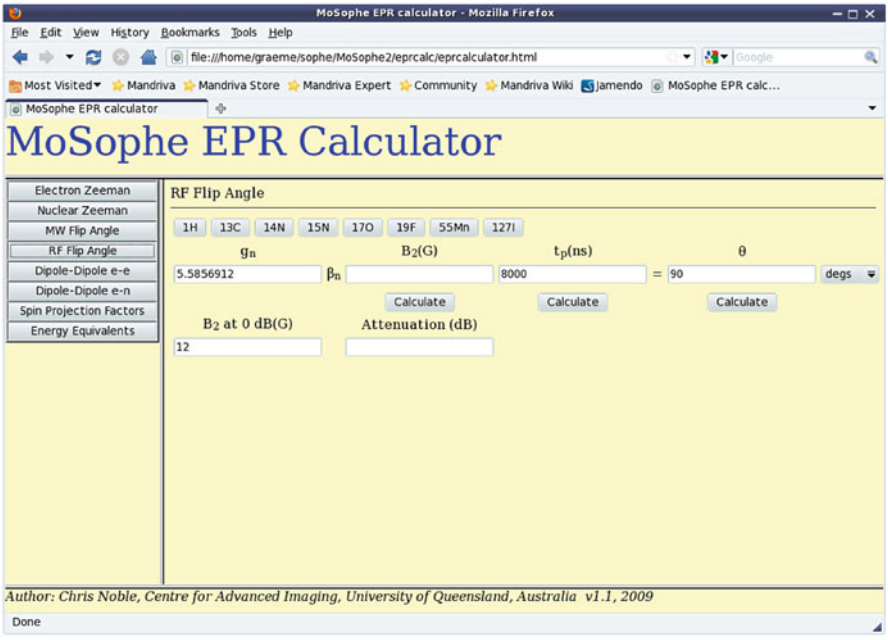

Fig. 5.21 MoSophe Calculator showing the RF pulse flip angle screen [38]

The electron Zeeman option allows the determination of g-values (enter a microwave frequency and resonant field position), resonant field positions (enter a g-value and a microwave frequency) or the conversion of hyperfine coupling constants from gauss to frequency units ($10^{-4}\,cm^{-1}$ or MHz) (enter a g-value and hyperfine coupling constant).

Selecting the Nuclear Zeeman Interaction allows the calculation of the Larmor frequency, by first selecting a nucleus (or alternatively manually adding a nuclear g-value, for a list of these see the isotope forms in MoSophe, enter a magnetic field (B_0) and select the Frequency Calculate button. Alternatively, you can calculate the resonant field position given a nuclear g-value and frequency by selecting the Calculate button below B_0. The nuclear g-value can also be calculated from a value of B_0 and a frequency.

Selecting MW Flip Angle from the main menu enables the microwave flip angles, pulse lengths and B_1 attenuation to be calculated. The user can calculate the B_1 field strength and attenuation for a microwave $\pi/2$ pulse given a g-value, pulse length (ns), B_1 field strength at 0 dB and setting $\theta = 90°$. Alternatively, the turn angle can be calculated by entering a g-value, pulse length (ns) and either a value for B_1 or the B_1 field strength at 0 dB and an attenuation. Similarly, the pulse length can be calculated by entering a g-value, turn angle and either a B_1 field strength at 0 dB and an attenuation or simply a value for B_1.

Selecting RF Flip Angle from the main menu produces the calculator shown in Fig. 5.21 for determining radio frequency flip angle, pulse lengths and B_2 attenuations. The user can calculate the B_2 field strength and attenuation for a radio frequency π pulse given a nuclear g_n-value, pulse length (ns), B_2 field strength at 0 dB and setting $\theta = 90°$. Alternatively, the turn angle can be calculated by entering a nuclear g_n-value, pulse length(ns) and either a value for B_2 or the B_2 field strength at 0 dB and an attenuation. Similarly, the pulse length can be calculated by entering a nuclear g_n-value, flip angle and either a B_2 field strength at 0 dB and an attenuation or simply a value for B_2.

Selecting Dipole-Dipole electron-electron (e-e) Exchange from the main menu produces the calculator shown in Fig. 5.22. The anisotropic electron-electron exchange coupling constant can be calculated from the g-values (g_A, g_B) for the two paramagnetic centers and an internuclear distance (r). Alternatively, the distance can be determined by entering a value for J_{AB}. When the two paramagnetic centers are strongly exchange coupled, the zero field splitting for each ion (D_A, D_B) and the internuclear anisotropic exchange (D_{AB}) interactions can be treated as perturbations to the isotropic exchange interaction and D_{AB} can be calculated from J_{AB} using the appropriate numerical coefficient (d_{AB}) of the projector operator for a particular spin system. For example when $S_A = S_B = 5/2$, and the resonances arise from an $S_T = 3$ spin state the numerical coefficient is 47/90 and D_{AB} is automatically calculated from the value of J_{AB}.

Selecting Dipole-Dipole electron-nuclear (e-n) from the main menu produces the calculator shown in Fig. 5.23. The anisotropic hyperfine coupling constant (A_{dd}) can be calculated from the principal components of the hyperfine matrix using the equations given within the Notes for this calculator (Fig. 5.23). Given a value of

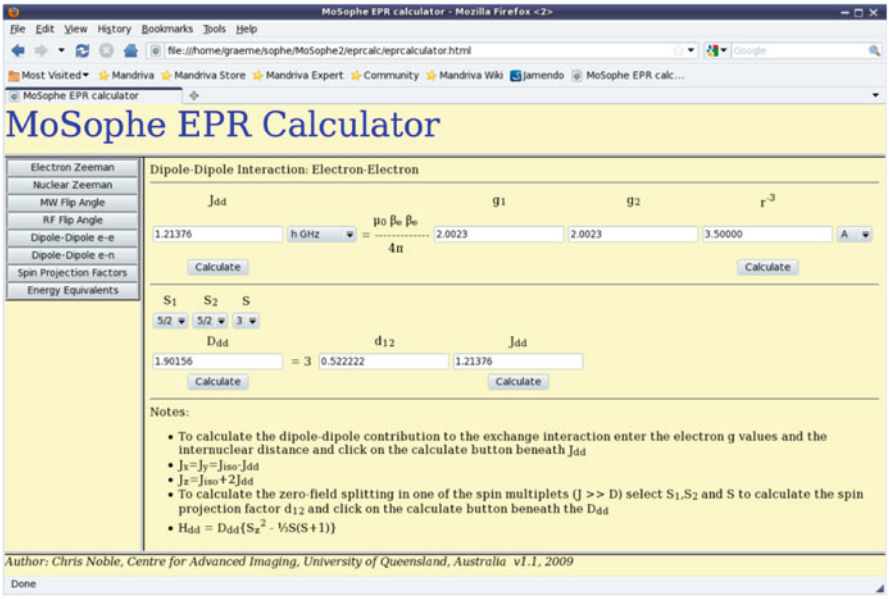

Fig. 5.22 MoSophe Calculator [38] showing the electron electron (e-e) dipole-dipole calculator screen. In the calculator, the subscripts *1*, *2* are equivalent to A and B in Eq. 5.1

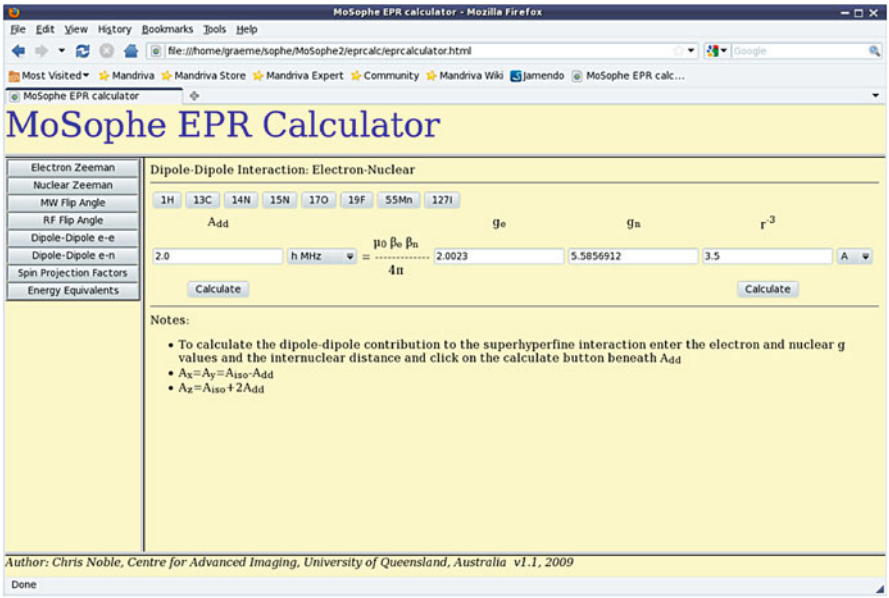

Fig. 5.23 MoSophe Calculator [38] showing the electron-nuclear (e-n) dipole-dipole calculator screen

A_{dd} and the electron and nuclear g-values (g_A, g_n) for the atoms containing the unpaired electron(s) and nuclear spin an internuclear distance (r) can be calculated. Alternatively, entering an internuclear distance and the electron and nuclear g-values (g_A, g_n) for the atoms containing the unpaired electron(s) and nuclear spin allows the calculation of A_{dd}.

Selecting Energy Equivalents from the main menu enables the user to quickly convert energies to different units commonly used by EPR scientists.

5.8 Role of Frequency (and Temperature) in Extracting Spin Hamiltonian Parameters

Often X-band randomly orientated CW EPR spectra are complex consisting of many overlapping resonances and the only means of extracting a unique set of spin Hamiltonian parameters is to perform a multifrequency CW EPR experiment. The most common microwave frequencies employed for such experiments are listed in Table 5.1.

The use of microwave frequencies higher than X-band can improve spectral resolution (g-value resolution, Sect. 5.8.1) and simplify spectra by eliminating state mixing, energy level crossings and anticrossings and looping transitions (Sect. 5.8.4). However, if there is a large distribution of parameters (g, A and D) as is the case in many Jahn Teller distorted copper(II) complexes and low symmetry high spin Fe(III) centers, increasing the microwave frequency can lead to significant broadening of the resonances which can cancel out the gain in spectral resolution (Sect. 5.8.5).

5.8.1 Electron Zeeman and Hyperfine Interactions

The resonant magnetic field positions for an $S = 1/2$, $I = 0$ axially symmetric spin system are given by:

Table 5.1 List of the most common microwave frequency bands for CW EPR experiments

Microwave band	Microwave frequencies (GHz)	Common frequency (GHz)
L	1–2	~1
S	2–4	~4
C	4–8	6
X	8–12	9.2–9.7
K	18–26	~24
Q	26–40	~35
W	75–110	~95
D	110–170	

$$B_{\parallel} = \frac{h\nu_c}{\beta g_{\parallel}} \; B_{\perp} = \frac{h\nu_c}{\beta g_{\perp}} \tag{5.30}$$

The magnetic field separation (resolution) between these two resonances is:

$$B_{\parallel} - B_{\perp} = \frac{h\nu_c}{\beta\left(g_{\parallel} - g_{\perp}\right)} = K\nu_c \tag{5.31}$$

Clearly, increasing the microwave frequency increases the g value resolution, though the spectral linewidth also increases (Eq. 5.15, Fig. 5.24). While Q-band is often satisfactory for transition metal ion sites with a single unpaired electron, radicals often require frequencies greater than or equal to 95 GHz to completely resolve the three components of the g-matrix [4].

Another application of high frequency EPR is to separate field independent resonances from those which are field dependent. Often the preparation and purification of magnetically coupled species (eg. dinuclear copper(II) complexes) results in the presence of a small amount (<5%) of monomeric (S = 1/2) impurity and at X-band frequencies the allowed $\Delta M_S = \pm 1$ resonances overlap with those from the dipole-dipole coupled species [68]. Increasing the microwave frequency to at least 35 GHz allows the resolution of the spectra from both species, though the formally forbidden $\Delta M_S = \pm 2$ resonances are significantly less intense than at X-band frequencies. Higher frequencies such as Q- and W-band have also been exploited to resolve multiple species present in chemical equilibria.

5.8.2 The Fine Structure Interaction

For many high spin Fe(III) centers found in biological systems, the axial zero field splitting (D) is greater than the X-band microwave quantum (0.3 cm^{-1}) and thus transitions are only observed within Kramers' doublets rather than between them. Consequently, the only method for determining D is to either increase the microwave frequency or perform a variable temperature measurement. In either case computer simulation is required to extract the value of D. An example of a variable temperature computer simulation for a high spin Fe(III) center is shown in Fig. 5.25 with the temperature dependence (slices along the temperature axis at a specific magnetic field) shown in Fig. 5.25 for both negative and positive values of D respectively.

Metalloproteins containing high spin Ni(II) (S = 1), Mn(III) (S = 2) and Fe(II) (S = 2) often appear to be EPR silent at X-band frequencies as there is insufficient energy to produce a transition between energy levels. Sometimes, the Fe(II) spin systems contain a significant distribution of zero field splittings which allows the observation of $\Delta M_S = \pm 4$ forbidden transitions whose lineshapes are quite 'strange'.

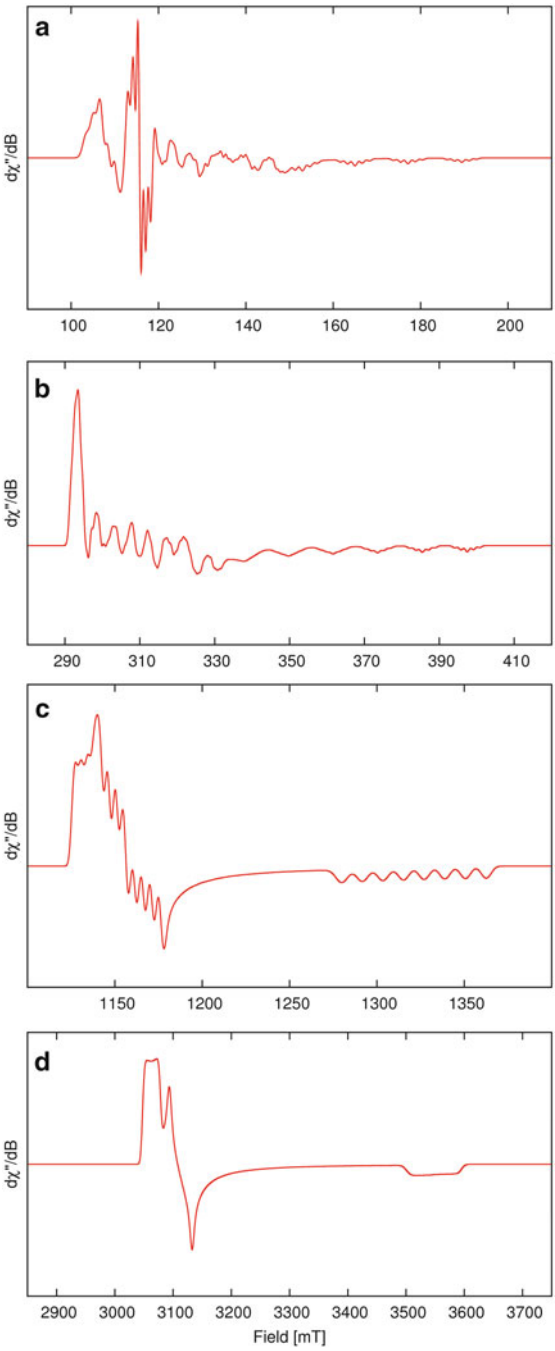

Fig. 5.24 Multifrequency computer simulation of CW EPR spectra from a low spin Co(II) center ligated by two magnetically equivalent nitrogen atoms. Spin Hamiltonian and linewidth parameters are: $g_{x,y,z}$, 2.194. 2.230, 1.925; $A_{x,y,z}$ (Co), 50.0, 40.0, 106.0×10^{-4} cm^{-1}; $A_{x,y,z}$ (N), 10.0, 10.0, 15.0×10^{-4} cm^{-1}; $\sigma_{Rx,y,z}$, 5.0, 5.0, 5.0×10^{-4} cm^{-1}; $(\sigma g/g)_{x,y,z}$, 0.001, 0.001, 0.002; $\sigma A_{x,y,z}$, 0.2, 0.2, 1.2×10^{-4} cm^{-1}. (**a**) $\upsilon_c = 4.0$ GHz, (**b**) 9.6 GHz, (**c**) $\upsilon_c = 35.6$ GHz, (**d**) $\upsilon_c = 95.6$ GHz

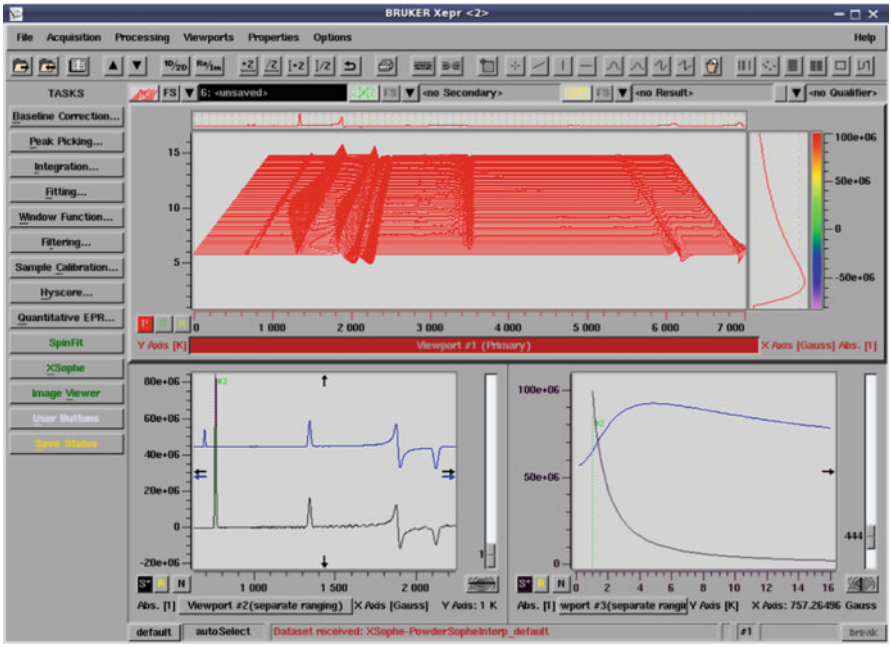

Fig. 5.25 Variable temperature computer simulation of the Fe(III) center found in sweet potato purple acid phosphatase, $\upsilon_c = 9.6$ GHz. (*Red*, *Blue*) Spin Hamiltonian parameters are $D = -0.88$ cm^{-1}, $E/D = 0.1925$ and $g = 2$, (*Black*) Spin Hamiltonian parameters are $D = 0.88$ cm^{-1}, $E/D = 0.1925$ and $g = 2$, (lower right handside display) Temperature dependence of the resonance at $B = 134.188$ (*Blue*), 75.726496 (*Black*) mT

5.8.3 *Isotropic and Anisotropic Exchange Interactions*

Variable temperature EPR spectroscopy is often employed to extract the isotropic exchange coupling constant, J_{iso}. An example of an antiferromagnetically coupled spin system is a nitroxide biradical [76] which can be described by the following spin Hamiltonian:

$$H = \boldsymbol{J}_{iso}\boldsymbol{S}_1 \cdot \boldsymbol{S}_2 + \sum_{i=1}^{2} (g\ \beta \boldsymbol{B} \cdot \boldsymbol{S}_i + A_{iso}\, \boldsymbol{S}_i \cdot \boldsymbol{I}_i[N] - g_n \cdot \beta_n \cdot \boldsymbol{B} \cdot \boldsymbol{I}_i[N]) \tag{5.32}$$

where $g = 2.00585$, $A_{iso}(^{14}N) = 13.5 \times 10^{-4}$ cm^{-1} and $J_{iso} = 40$ cm^{-1}. A variable temperature simulation (Fig. 5.26) of the experimental variable temperature spectrum can be used to extract the isotropic exchange coupling constant. However, if J is large, then a combination of higher frequencies and/or higher temperatures is required to extract the exchange coupling constant.

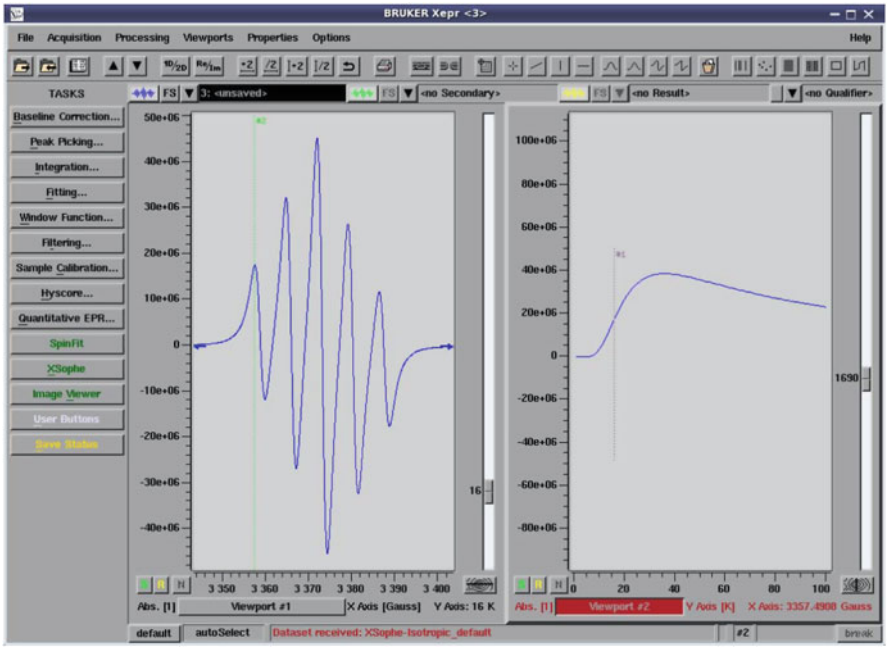

Fig. 5.26 Variable temperature computer simulation of the nitroxide diradical. EPR parameters are given in the text. $\upsilon_c = 9.5962$ GHz. The spectrum on the *right hand* side is a slice along the temperature axis at B = 335.74908 mT

5.8.4 *State Mixing and the Existence of Energy Level Crossings, Anticrossings and Looping Transitions*

State Mixing occurs when one or more of the spin Hamiltonian interactions are of similar magnitude. This leads to energy level crossings and anticrossings. When the Nuclear Hyperfine and Quadrupole Interactions are of a similar magnitude state mixing can lead to the observation of formally forbidden $\Delta M_I = \pm 2$ and 3 transitions. Computer simulation of these forbidden resonances allows the accurate determination of the quadrupolar coupling constants. At very low frequencies the Nuclear Hyperfine and Electron Zeeman Interactions become comparable leading to state mixing and complex spectra resulting in the apparent unequal spacings (A/gβ) between the hyperfine resonances. Conversely, state mixing can also occur for high spin systems when the zero field splitting or exchange interactions are of a similar magnitude to the electron Zeeman interaction. This not only leads to energy level crossings and anticrossings but also looping transitions (Fig. 5.27a, b). Increasing the microwave frequency (magnetic field) to Q- and W-band frequencies (Fig. 5.27c, d) leads to simpler spectra where the Electron Zeeman interaction dominates the Fine Structure interaction.

State mixing also allows the observation of $\Delta M_S = \pm 2$ transitions in dipole-dipole coupled systems, for example binuclear copper(II) complexes. Analysis of

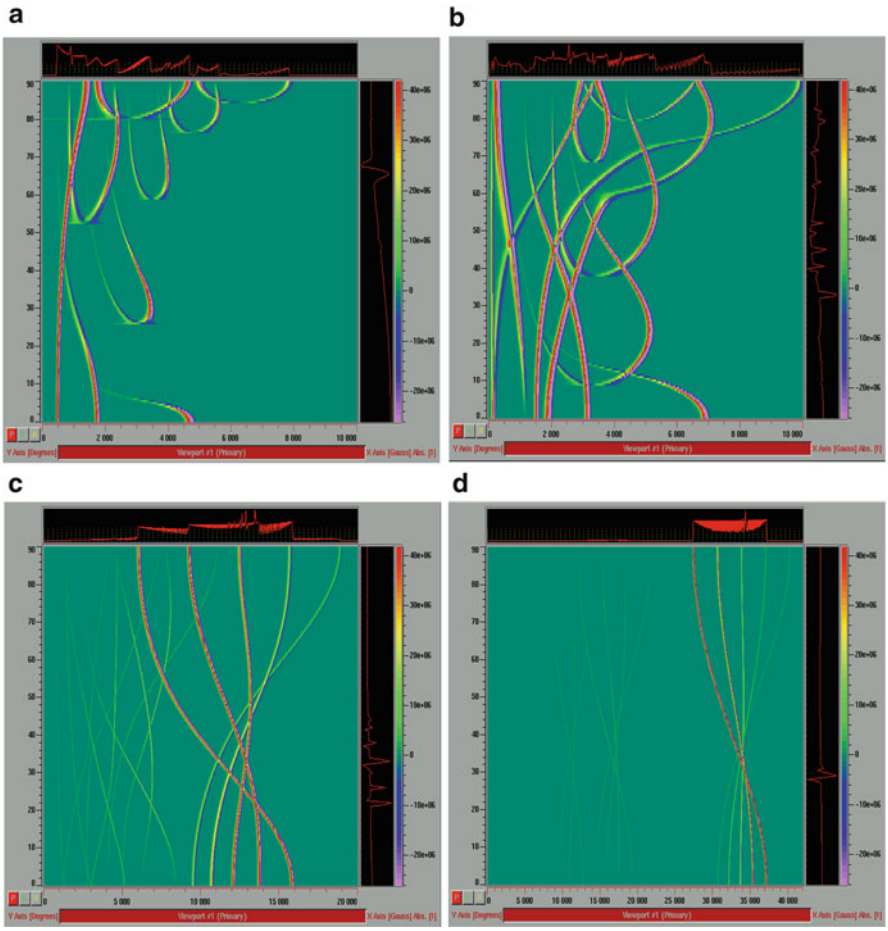

Fig. 5.27 Single Crystal EPR spectra of a high spin Fe(III) spin system with D = −4.5 GHz, E/D = 0, and g = 2.0. (**a**) S-band spectrum, υ_c = 4.0 GHz, (**b**) X-band spectrum, υ_c = 9.75 GHz, (**c**) Q-band spectrum, υ_c = 35.0 GHz, (**d**) W-band spectrum, υ_c = 95.0 GHz

CW EPR spectra containing these resonances allows the distance and orientation of the two copper(II) centers to be determined. The transition probability for these resonances is inversely proportional to frequency and consequently their intensity is maximized at lower microwave frequencies, such as S-band.

5.8.5 Distributions of Parameters

Often metal centers in metalloproteins, transition metal complexes and glasses exist as a distribution of structures which can arise from interactions with solvents, poorly

formed glasses in frozen solution samples and completely different coordination geometries/symmetries. These distributions of structures lead to distributions of various spin Hamiltonian parameters causing frequency dependent linewidth broadening. A correlated *g-A* strain model, originally developed by Froncisz and Hyde [61] and expressed in the frequency-domain (Eq. 5.15) has been incorporated into XSophe (Sect. 5.4.5) to account for the linewidth variations encountered in $S = 1/2$ spin systems particularly in copper, low spin cobalt and molybdenum(V) complexes [1, 61–66]. As the frequency is increased g value resolution increases (Eq. 5.31) but the linewidth also increases (Fig. 5.24, Eq. 5.31). Conversely, lowering the frequency from X-band to S-band decreases g-value resolution but reduces the linewidth allowing the observation of superhyperfine coupling to ligating nuclei (Fig. 5.24a). S-band EPR spectroscopy has been exploited in identifying ligating nuclei to copper(II) ions in Type II copper proteins [61, 66], oxomolybdenum(V) complexes [62, 64] and mononuclear molybdenum enzymes [63] and low spin cobalt(II) complexes [65]. Importantly, the angular variation of this linewidth model (Eq. 5.15) does not accurately reproduce the linewidth of angular anomalies or off axis extrema [45a]. This has been overcome in our development version where we have incorporated distributions of all spin Hamiltonian, linewidth and geometric parameters.

5.9 Pulsed EPR Simulations

The Molecular Sophe computer simulation software suite [38] contains a number of standard (default) experiments which have been optimized and are stored in/usr/mosophe/examples. Over time the number of examples will increase. Shown in the figures below are some of the results. Proton and nitrogen HYSCORE simulated spectra are shown in Fig. 5.28 and a SECSY experiment in Fig. 5.29.

5.10 Conclusions

The XSophe-Sophe-XeprView computer simulation software suite provides scientists with an easy-to-use research tool for determining the spin Hamiltonian parameters from isotropic, randomly orientated and single crystal CW EPR spectra. These spin Hamiltonian parameters can then be used to determine the electronic and geometric structure of the paramagnetic center. In the past scientists have compared the spin Hamiltonian parameters derived from computer simulation studies with well defined structures in the literature. More recently, scientists are utilizing quantum chemistry calculations to determine the electronic and geometric structures of paramagnetic species and comparing the calculated spin Hamiltonian parameters with those determined experimentally.

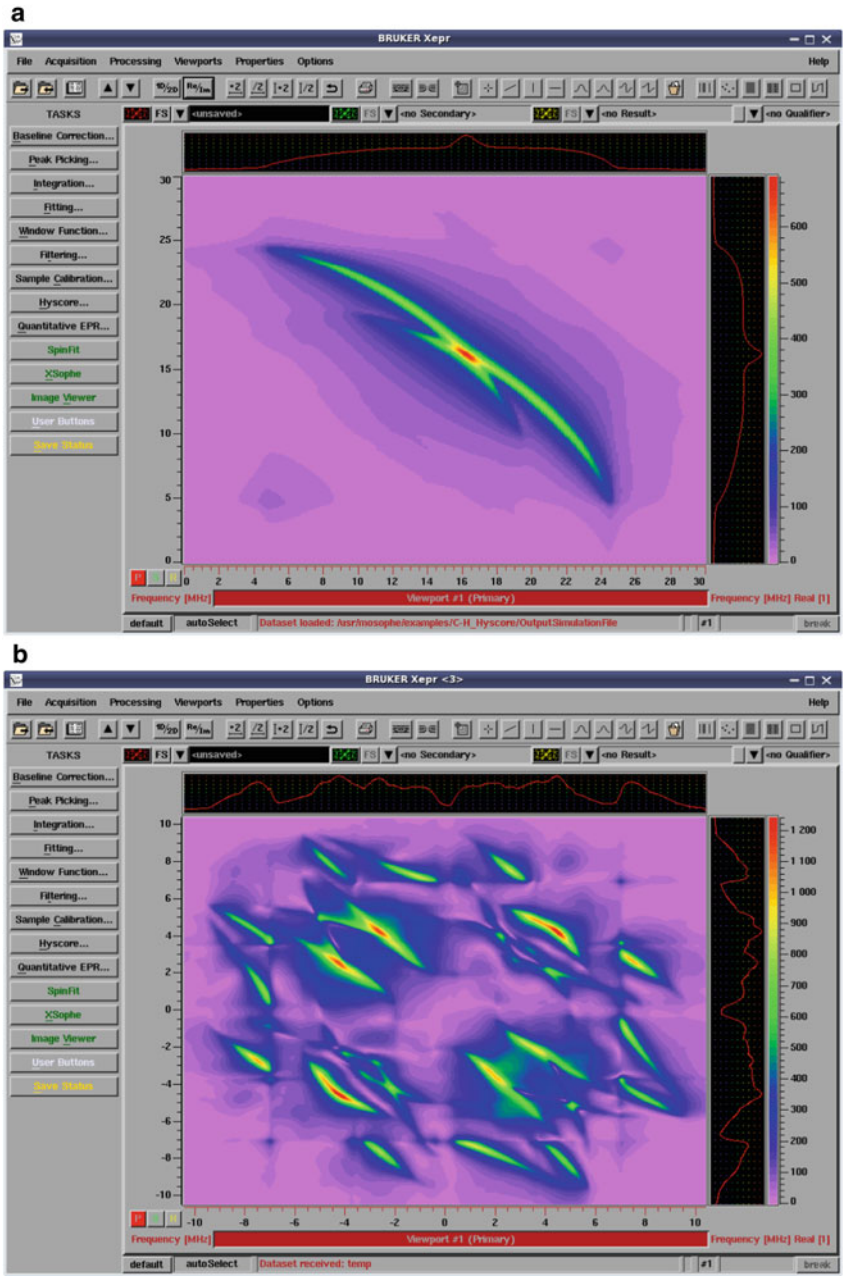

Fig. 5.28 Computer simulated (MoSophe) HYSCORE spectra showing coupling to a single proton (**a**) and nitrogen (**b**) nuclei. (**a**) g = 2.0; $A_{x,y,z}$ (^{14}N) = 20.0, 20.0, −10.0 MHz; C, (H) $_{x,y,z}$ 0.0,0.0,0.0, (0.0,0.0,0.0) Å; π/2 pulse = 16.0 nsec, π pulse = 32 nsec, d0,d1,d2 = 10,20,16 nsec, B = 342.949 mT, υ_c = 9.6 GHz. (**b**) C-N fragment. g = 2.0; $A_{x,y,z}$ (^{14}N) = 4.0, 4.0, 8.0 MHz; P = −1.0 MHz; C, (N) $_{x,y,z}$ 0.0,0.0,0.0, (0.0,0.0,3.0) Å; π/2 pulse =16.0 nsec, π pulse = 32 nsec, d0,d1,d2 = 0,160,0 nsec, B = 342.949 mT, υ_c = 9.6 GHz

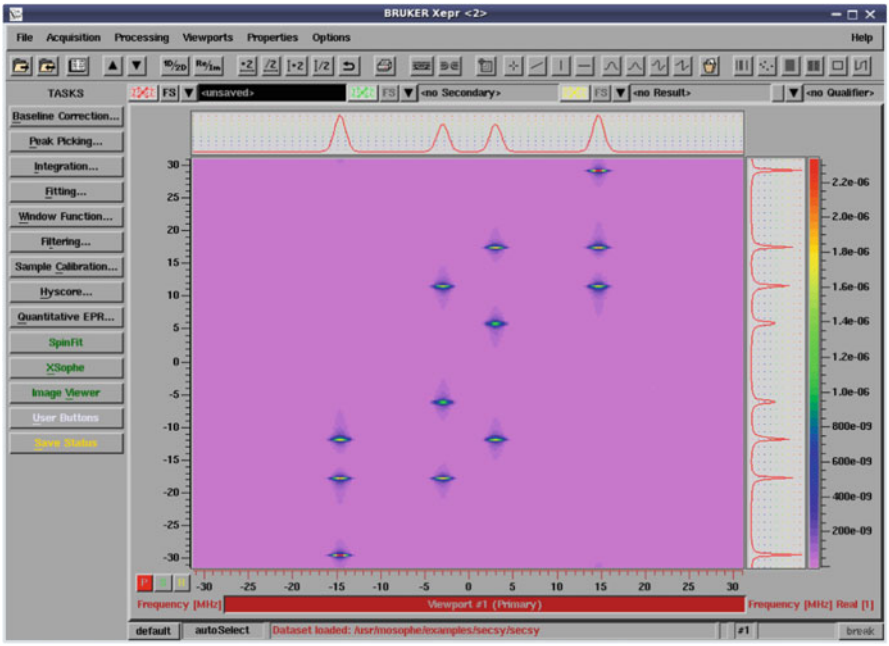

Fig. 5.29 Computer simulated (MoSophe) proton SECSY spectrum. g = 2.0; $A_{x,y,z}$ (^{1}H) = 8.0, 8.0, 4.0 MHz; C, (H) $_{x,y,z}$ 0.0,0.0,0.0, (0.0,0.0,2.0) Å; π/2 pulse = 16.0 nsec, π pulse = 32 nsec, d0,d1 = 0,100 nsec, B = 342.949 mT, υ_c = 9.6 GHz

The output of one- and two-dimensional CW EPR spectra from the Sophe programme can be visualized in conjunction with the experimental spectrum in XeprView® or Xepr®. Computer simulation of single crystal spectra measured in a plane perpendicular to a rotation axis can be performed by defining the rotation axis and the beginning and end angles in the plane perpendicular to this axis. Energy level diagrams, transition roadmaps and transition surfaces aid interpretation of complicated randomly orientated EPR spectra and can be viewed with a Mozilla Firefox® browser and an OpenInventor scene graph viewer for transition surfaces. The XSophe-Sophe-XeprView computer simulation software suite is available through the EPR Division of Bruker Biospin (http://www.bruker-biospin.com).

Molecular Sophe incorporates an integrated approach, based upon molecular structure for the analysis of CW and pulsed EPR and pulsed ENDOR spectra. The ultimate aim of this approach is to optimize the spin Hamiltonian parameters from a variety of EPR experiments and utilize the dipole-dipole interaction to extract geometric (distance and orientation) information on the three dimensional structure of the paramagnetic center in a noncrystalline environment. Molecular Sophe represents the first step towards this goal, and we are currently developing iResonanz in conjunction with our development version of the Sophe computational programme from the Molecular Sophe computer simulation suite to enhance the

functionality of the current released version of Sophe. The software suite, apart from the lack of optimization and variety of lineshape functions has all of the functionality of the XSophe-Sophe-XeprView computer simulation software suite and many new features including: a more intuitive graphical user interface, multiple components, multiple experiments for each sample, the use of representations, transfer of the interactions principal components and Euler angles to Sophe (rather than the matrix in XSophe-Sophe-XeprView), inclusion of antisymmetric exchange and its various representations, inclusion of dipole-dipole coupling, user defined external programs and a complete user manual [35, 38]. The development version of Sophe enables the use of non-linear squares optimization of all spin Hamiltonian, linewidth and geometric parameters from multifrequency, multiderivative CW EPR and pulsed EPR experiments. Several papers have appeared using this software and we are refining/tuning the functionality of this software [65b, 68b, c]. The approach utilized within this version of Sophe will be reported elsewhere.

In summary, the XSophe-Sophe-XeprView and Molecular Sophe computer simulation software suites have been used by a large number of laboratories to gain invaluable insights into the three dimensional geometric and electronic structure of paramagnetic molecules.

Acknowledgments We would like to thank past members of the Sophe group, including Dr. Kevin Gates, Dr. Mark Griffin, Dr. Anthony Mitchell, Andrae Muys, Dr. Deming Wang for their contributions to the computer simulation software suites described herein.

References

1. Pilbrow JR (1990) Transition ion electron paramagnetic resonance. Clarendon, Oxford
2. Mabbs FE, Collison DC (1992) Electron paramagnetic resonance of transition metal compounds. Elsevier, Amsterdam
3. Basosi R, Antholine WE, Hyde JS (1993) Multifrequency ESR of copper biophysical applications. In: Berliner LJ, Reuben J (eds) Biological magnetic resonance, vol 13. Plenum Press, New York
4. Moebius K, Savitsky A (2008) High field EPR spectroscopy of proteins and their model systems: characterization of transient paramagnetic states. Royal Society of Chemistry, Cambridge
5. Misra S (2011) Multifrequency electron paramagnetic resonance: theory and applications. Wiley-VCH, Weinheim
6. Sarker B (2005) Electrochemistry spectroelectrochemistry and multifrequency EPR of dinuclear transition metal complexes containing nitrogen-rich bridging ligands. Logos, Berlin
7. Grinberg O, Berliner LJ (eds) (2004) Very high frequency (VHF) ESR/EPR in biological magnetic resonance, vol 22. Kluwer Academic/Plenum, New York
8. Hanson GR, Brunette AA, McDonell AC, Murray KS, Wedd AG (1981) Electronic properties of thiolate compounds of oxomolybdenum (V) and their tungsten and selenium analogues. Effects of 17-O, 98-Mo and 95-Mo isotope substitution upon ESR spectra. J Am Chem Soc 103:1953–1959
9. Lebedev YS (1994) Very-high-field EPR and its applications. Appl Magn Reson 7:339–369
10. Brunel LC (1996) Recent developments in high frequency/high magnetic field CW EPR. Applications in chemistry and biology. Appl Magn Reson 11:417–423

11. Reijerse EJ, VanDam PJ, Klaassen AAK, Hagen WR, VanBentum PJM, Smith GM (1998) Concepts in high-frequency EPR—applications to bio-inorganic systems. Appl Magn Reson 14:153–167
12. Schweiger A, Jeschke G (2001) Principles of pulse electron paramagnetic resonance. Oxford University Press, Oxford
13. (a) Kaess H, Rautter J, Zweygart W, Struck A, Scheer H, Lubitz W (1994) EPR, ENDOR, and TRIPLE resonance studies of modified bacteriochlorophyll cation radicals. J Phys Chem 98:354–363; (b) Kaess H, Rautter J, Boenigk B, Hoefer P, Lubitz W (1995) 2D ESEEM of the 15N-Labeled radical cations of bacteriochlorophyll a and of the primary donor in reaction centers of rhodobacter sphaeroides. J Phys Chem 99:436–448; (c) Lendzian F, Huber M, Isaacson RA, Endeward B, Plato M, Bonigk B, Mobius K, Lubitz W, Feher G (1993) The electronic structure of the primary donor cation radical in rhodobacter sphaeroides R-26: ENDOR and TRIPLE resonance studies in single crystals of reaction centers. Biochim Biophys Acta 1183:139–160; (d) Käβ H, Bittersmann-Weidlich E, Andréasson L-E, Bönigk B, Lubitz W (1995) ENDOR and ESEEM of the 15N labelled radical cations of chlorophyll a and the primary donor P700 in photosystem I. Chem Phys 194:419–432
14. Thomann H, Bernardo M (2007) Electron–nuclear multiple resonance spectroscopy. Encyclopedia of magnetic resonance. Wiley, pp 1–17. onlinelibrary.wiley.com/doi/10.1002/9780470034590.emrstm0153/full
15. Feher G (1956) Observation of nuclear magnetic resonances via the electron spin resonance line. Phys Rev 103:834–835
16. Kevan L, Kispert LD (eds) (1979) Electron spin double resonance spectroscopy. Wiley-Interscience, New York
17. Dorio MM, Freed JH (eds) (1979) Multiple electron spectroscopy. Plenum Press, New York
18. Abragam A, Bleaney B (1970) Electron paramagnetic resonance of transition ions. Clarendon, Oxford
19. Bencini A, Gatteschi D (1990) EPR of exchange coupled systems. Springer, Berlin
20. Smith TD, Pilbrow JR (1974) The determination of structural properties of dimeric transition metal ion complexes from EPR spectra. Coord Chem Rev 13:173–278
21. Taylor PC, Baugher JF, Kriz HM (1975) Magnetic resonance spectra in polycrystalline solids. Chem Rev 75:203–240
22. Swalen JD, Gladney HM (1964) Computer analysis of electron paramagnetic resonance spectra. IBM J Res Dev 8:515–526
23. Swalen JD, Lusebrink TRL, Ziessow D (1973) Computer applications in magnetic resonance. Magn Reson Rev 2:165–184
24. Vancamp HL, Heiss AH (1981) Computer applications in electron paramagnetic resonance. Magn Reson Rev 7:1–40
25. Gaffney BJ, Silverstone HJ (1993) Simulation of the EMR spectra of the high-spin iron in proteins. In: Berliner LJ, Reuben J (eds) Biological magnetic resonance. Plenum Press, New York, pp 1–101
26. Brumby S (1980) Numerical analysis of EPR spectra. 3. Iterative least-squares analysis of significance plots. J Magn Reson 39:1–9
27. Brumby S (1980) Numerical analysis of EPR spectra. 4. Spectra of 1- and 2-methylnaphthalene anions. J Magn Reson 40:157–165
28. Wang D, Hanson GR (1996) New methodologies for computer simulation of paramagnetic resonance spectra. Appl Magn Reson 11:401–415
29. Hanson GR, Gates KE, Noble CJ, Mitchell A, Benson S, Griffin M, Burrage K (2003) XSophe - Sophe - XeprView a computer simulation software suite for the analysis of continuous wave EPR spectra. In: Shiotani M, Lund A (eds) EPR of free radicals in solids: trends in methods and applications. Kluwer Press, Dordrecht, pp 197–237
30. Hanson GR, Gates KE, Noble CJ, Griffin M, Mitchell A, Benson S (2004) XSophe-Sophe-XeprView. A computer simulation software suite (v. 1.1.3) for the analysis of continuous wave EPR spectra. J Inorg Biochem 98:903–916

31. Griffin M, Muys A, Noble C, Wang D, Eldershaw C, Gates KE, Burrage K, Hanson GR (1999) XSophe, a computer simulation software suite for the analysis of electron paramagnetic resonance spectra. Mol Phys Rep 26:60–84
32. Heichel M, Höfer P, Kamlowski A, Griffin M, Muys A, Noble C, Wang D, Hanson GR, Eldershaw C, Gates KE, Burrage K (2000) XSophe-Sophe-XeprView Bruker's professional CW-EPR simulation suite. Bruker Rep 148:6–9
33. Hanson GR (2005) XSophe release notes, 1.1.4.1. Bruker Biospin, Germany, pp 1–79. www.cai.uq.edu.au/epr/simulation/XSophe
34. Stoll S, Schweiger A (2006) EasySpin, a comprehensive software package for spectral simulation and analysis in EPR. J Magn Reson 178:42–55
35. Hanson GR, Noble CJ, Benson S (2009) Molecular Sophe, an integrated approach to the structural characterization of metalloproteins, the next generation of computer simulation software in high resolution EPR: applications to metalloenzymes and metals in medicine. In Hanson GR, Berliner LJ (eds) Biol Magn Reson 28:105–173
36. (a) Berliner LJ, Eaton SS, Eaton GR (eds) (2001) Distance measurements in biological systems by EPR. Biological magnetic resonance, vol 19. Kluwer Academic Press, New York; (b) Jeschke G, Pannier M, Spiess HW (2001) Double electron-electron resonance methodical advances and application to disordered systems, pp 493–512, ibid
37. Wang D, Hanson GR (1995) A new method for simulating randomly oriented powder spectra in magnetic resonance: the *S*ydney *Op*era *H*ous*e* (SOPHE) method. J Magn Reson A 117:1–8
38. Hanson GR, Noble CJ, Benson S (2010) Molecular Sophe. An integrated computer simulation software suite for the analysis of CW and pulsed EPR spectra user manual v 2.1.6, pp 1–152. www.cai.uq.edu.au/epr/simulation/MoSophe
39. (a) Schenk G, Boutchard CL, Carrington LE, Noble CJ, Moubaraki B, de Jersey BJ, Hanson GR, Hamilton S (2001) A purple acid phosphatase from sweet potato contains an antiferromagnetically coupled binuclear Fe-Mn center. J Biol Chem 276:19084–19088; (b) Mitić N, Noble CJ, Gahan LR, Hanson GR, Schenk G (2009) Metal ion mutagenesis – conversion of a purple acid phosphatase from sweet potato to a neutral phosphatase with the formation of an unprecedented catalytically competent $Mn^{II}Mn^{II}$ active site. J Am Chem Soc 131:8173–8179
40. Yoon J, Mirica LM, Stack TD, Solomon EI (2004) Spectroscopic demonstration of a large antisymmetric exchange contribution to the spin-frustrated ground state of a D3 symmetric hydroxy-bridged trinuclear Cu(II) complex: ground-to-excited state superexchange pathways. J Am Chem Soc 126:12586–12595
41. Atanasov M, Comba P, Hanson GR, Hausberg S, Helmle S, Wadepohl H (2011) Cyano-bridged homodinuclear copper(II) complexes. Inorg Chem 50:6890–6901
42. Jeener J (1982) Superoperators in magnetic resonance. Adv Magn Reson 10:1–51
43. Hofer P (1994) Distortion-free electron-spin-echo envelope-modulation spectra of disordered solids obtained from two-dimensional and three-dimensional HYSCORE experiments. J Magn Reson A 111:77–86
44. Pilbrow JR (1984) Lineshapes in frequency-swept and field-swept epr for spin 1/2*. J Magn Reson 58:186–203
45. (a) Sinclair GR (1988) Modelling strain broadened EPR spectra. PhD thesis, Monash University, Victoria, Australia; (b) Pilbrow JR, Sinclair GR, Hutton DR, Troup GJ (1983) Asymmetric lines in field-swept EPR: Cr^{3+} looping transitions in ruby. J Magn Reson 52:386–399
46. Gates KE, Griffin M, Hanson GR, Burrage K (1998) Computer simulation of magnetic resonance spectra employing homotopy. J Magn Reson 135:104–112
47. Griffin M (2002) The computer simulation of electron paramagnetic resonance spectra employing homotopy. PhD thesis, The University of Queensland, Queensland, Australia
48. (a) Belford RL, Nilges MJ (1979) EPR symposium 21st Rocky mountain conference, Denver, CO; (b) Maurice AM (1980) Acquisition of anisotropic information by computational analysis of isotropic EPR spectra. PhD thesis, University of Illinois, Urbana, IL; (c) Nilges MJ (1979) Electron paramagnetic resonance studies of low symmetry nickel(I) and molybdenum(V) complexes. PhD thesis, University of Illinois, Urbana, IL

49. Alderman DW, Solum MS, Grant DM (1986) Methods for analyzing spectroscopic line shapes. NMR solid powder patterns. J Chem Phys 84:3717–3725
50. Mombourquette MJ, Weil JA (1992) Simulation of magnetic resonance powder spectra. J Magn Reson 99:37–44
51. Craciun C (2010) Application of the SCVT orientation grid to the simulation of CW EPR powder spectra. Appl Magn Reson 38:279–293
52. Gribnau MCM, van Tits JLC, Reijerse EJ (1990) An efficient general algorithm for the simulation of magnetic resonance spectra of orientationally disordered solids. J Magn Reson 90:474–485
53. van Veen G (1969) Simulation and analysis of EPR spectra of paramagnetic ions in powders. J Magn Reson 38:91–109
54. Nettar D, Villafranca NI (1985) A program for EPR powder spectra simulation. J Magn Reson 64:61–65
55. Scullane MI, White LK, Chasteen ND (1982) An efficient approach to computer simulation of EPR spectra of high-spin Fe(III) in rhombic ligand fields. J Magn Reson 47:383–397
56. McGavin DG, Mombourquette MJ, Weil JA (1993) EPR ENDOR user's manual. University of Saskatchewan, Saskatchewan
57. Belford GG, Belford RL, Burkhalter JF (1973) Eigenfields: a practical direct calculation of resonance fields and intensities for field-swept fixed-frequency spectrometers. J Magn Reson 11:251–265
58. Su BQ, Liu DY (1989) Computational geometry – curves and surface modelling. Academic, Singapore
59. Shaltiel D, Low W (1961) Anisotropic broadening of linewidth in the paramagnetic resonance spectra of magnetically dilute crystals. Phys Rev 124:1062–1067
60. (a) Kivelson D, (1960) Theory of ESR linewidths of free radicals. J Chem Phys 33:1094–1106; (b) Wilson R, Kivelson D (1966) ESR linewidths in solution. I. Experiments on anisotropic and spin—rotational effects. J Chem Phys 44:154–168; (c) Wilson R, Kivelson D (1966) ESR linewidths in solution. III. Experimental study of the solvent dependence of anisotropic and spin—rotational effects. J Chem Phys 44:4440–4444; (d) Atkins PW, Kivelson D (1966) ESR linewidths in solution. II. Analysis of spin—rotational relaxation data. J Chem Phys 44: 169–174
61. (a) Froncisz W, Hyde JS (1980) Broadening by strains of lines in the g-parallel region of Cu^{2+} EPR spectra. J Chem Phys 73:3123–3131; (b) Hyde JS, Froncisz W (1982) The role of microwave frequency in EPR spectroscopy of copper complexes. Ann Rev Biophys Bioeng 11:391–417
62. (a) Drew SC, Hill JP, Lane I, Hanson GR, Gable RW, Young CG (2007) Synthesis, structural characterization and multifrequency electron paramagnetic resonance studies of mononuclear thiomolybdenyl complexes. Inorg Chem 46:2373–2387; (b) Drew SC, Young CG, Hanson GR (2007) A density functional study of the electronic structure and spin Hamiltonian parameters of mononuclear thiomolybdenyl complexes. Inorg Chem 46:2388–2397
63. Sproules S, Banerjee P, Weyhermüller T, Yan Y, Donahue JP, Wieghardt K (2011) Monoanionic molybdenum and tungsten tris(dithiolene) complexes: a multifrequency EPR study. Inorg Chem 50:7106–7122
64. (a) Wilson GL, Greenwood RJ, Pilbrow JR, Spence JT, Wedd AG (1991) Molybdenum(V) sites in xanthine oxidase and relevant analog complexes: comparison of molybdenum-95 and sulfur-33 hyperfine coupling. J Am Chem Soc 113:6803–6812; (b) Greenwood RJ, Wilson GL, Pilbrow JR, Wedd AG (1993) Molybdenum(V) sites in xanthine oxidase and relevant analog complexes: comparison of oxygen-17 hyperfine coupling. J Am Chem Soc 115:5385–5392
65. (a) Oliver SW, Smith TD, Hanson GR, Lahey N, Pilbrow JR, Sinclair GR (1987) Electron spin resonance study of the copper (II) and cobalt (II) chelates of 2,3;7,8;12,13;17,18-tetrakis-(9,10-dihydroanthracene-9,10-diyl)porphyrazine. J Chem Soc Faraday Trans 1(84):1475–1489; (b)

Nielsen P, Toftlund H, Bond AD, Boas JF, Pilbrow JR, Hanson GR, Noble CJ, Riley MJ, Neville SM, Moubaraki B, Murray KS (2009) Systematic study of spin crossover and structure in $[Co(terpyRX)_2](Y)_2$ systems, (terpyRX = 4′-alkoxy-2,2′:6′,2″-terpyridine, X = 4, 8, 12, $Y = BF_4^-$, ClO_4^-, PF_6^-, BPh_4^-). Inorg Chem 48:7033–7047

66. Antholine WE, Bennett B, Hanson GR (2011) Copper coordination environments. In: Misra SK (ed) Mutltifrequency electron paramagnetic resonance. Wiley-VCH/Verlag/GmbH, Berlin, pp 647–718
67. Wenzel RF, Kim YW (1965) Linewidth of the electron paramagnetic resonance of $(Al_2O_3)1\text{-}x(Cr_2O_3)_x$. Phys Rev 140:A1592–A1598
68. (a) Comba P, Dovalil N, Haberhauer G, Hanson GR, Kato Y, Taura T (2010) Complex formation and stability of westiellamide derivatives with copper(II). J Biol Inorg Chem 15:1129–1135; (b) Comba P, Dovalil N, Hanson GR, Linti G (2011) Synthesis and CuII coordination chemistry of a patellamide derivative – consequences of the change from the natural thiazole/oxazoline to the artificial imidazole heterocycles. Inorg Chem 50:5165–5174; (c) Comba P, Dovalil N, Gahan LR, Haberhauer G, Hanson GR, Noble CJ, Seibold B, Vadivelu P (2012) Cu^{II} coordination chemistry of patellamide derivatives. Possible biological functions of cyclic pseudo-peptides. Chem Eur J 18:2578–2590
69. (a) Misra SK (1976) Evaluation of spin-Hamiltonian parameters from EPR data by the method of least-squares fitting. J Magn Reson 23:403–410; (b) Misra SK (1986) Evaluation of spin Hamiltonian parameters from ESR data of single crystals. Mag Reson Rev 10:285–331; (c) Misra SK (1983) Evaluated of spin Hamiltonian parameters of electron-nuclear spin-coupled systems from EPR data by the method of least-squares fitting. Physica 121B:193–201; (d) Misra SK, Subramanian S (1982) Calculation of parameter errors in the analysis of electron paramagnetic resonance data. J Phys C 15:7199–7207
70. Spin Hamiltonian parameters are constrained to a portion of P-space as this will prevent the generation of a NULL spectrum
71. Hooke R, Jeeves TA (1961) 'Direct search' solution of numerical and statistical problems. J Assoc Comput Mach 8:212–229
72. Spendley W, Hext GR, Himsworth FR (1962) Sequential application of simplex designs in optimisation and evolutionary operation. Technometrics 4:441–461
73. (a) Nicholson DM, Chowdhary A, Schwartz L (1984) Monte Carlo optimization of pair distribution functions: application to the electronic structure of disordered metals. Phys Rev B 29:1633–1637; (b) Bohachevsky IO, Johnson ME, Myron LS (1986) Generalized simulated annealing for function optimization. Technometrics 28:209–217; (c) Corana A, Marchesi M, Martini C, Ridella S (1987) Minimizing multimodal functions of continuous variables with the "simulated annealing" algorithm. ACM Trans Math Software 13:262–280; (d) Heynderickx H, De Raedt H, Schoemaker D (1986) Simulated anneal method for the determination of spin Hamiltonian parameters from ESR data. J Magn Reson 70:134–139
74. Basosi R, Della Lunga G, Pogni R (1996) Resolution enhancement of nitrogen hyperfine patterns in the EPR spectra of Cu(II) complexes: FT analysis of $Cu(II)(His\text{-}Gly)_2$. Appl Magn Reson 11:437–442
75. Noble CJ, Hanson GR (2011) Personal communication
76. Micallef A, Hanson GR (2011) Personal communication

Chapter 6
The Calculation of the Hyperfine Coupling Tensors of Biological Radicals

Fuqiang Ban, James W. Gauld, Stacey D. Wetmore, and Russell J. Boyd

Abstract This chapter reviews the performance of density functional theory for the calculation of hyperfine coupling tensors and the development of computational methodology for biological radicals. Remarkable advances in density functional theory (DFT) have made it possible to study biological radicals as straightforwardly as closed-shell molecules. The conformational and charge dependence of the observed hyperfine coupling tensors can therefore be explored by employing reliable computational procedures. Although, hyperfine coupling tensors are highly dependent on the structure of the radical, temperature and environmental effects are typically smaller than 10 %. As a consequence, hyperfine coupling tensor calculations on isolated biological radicals (at zero kelvin) closely reproduce the hyperfine coupling tensors of most radicals observed in condensed phases (at higher temperatures), and are appropriate for the purpose of theoretical assignment and interpretation. Often, precise identification of unknown radicals can be made by systematic comparison of observed experimental values with hyperfine coupling tensors calculated for all possible conformations of a radical and its protonated or deprotonated derivatives. The aim of this chapter is to review the ability of DFT methods to account for the hyperfine coupling tensors of a variety of biological radicals.

F. Ban • R.J. Boyd (✉)
Department of Chemistry, Dalhousie University, Halifax, NS, Canada B3H 4R2
e-mail: russell.boyd@dal.ca

J.W. Gauld
Department of Chemistry and Biochemistry, University of Windsor, Windsor, ON, Canada N9B 3P4

S.D. Wetmore
Department of Chemistry and Biochemistry, University of Lethbridge, Lethbridge, Alberta, Canada T1K 3M4

A. Lund and M. Shiotani (eds.), *EPR of Free Radicals in Solids I*, Progress in Theoretical Chemistry and Physics 24, DOI 10.1007/978-94-007-4893-4_6,

6.1 Introduction

DNA and protein oxidation is associated with various pathological conditions such as cancer, Alzheimer's, and many other diseases; thus, the study of the relevant biological radicals has become one of the most exciting topics in molecular biology [1–4]. It is also noteworthy that biological radicals play important roles in enzymatic catalysis [1] and in the mechanisms of many toxins [5] and hypoxia-selective antitumor drugs [6–8]. ESR spectroscopy and related techniques are powerful tools for investigating such radical species [9]. The key quantities measured by electron spin resonance spectroscopy are the g-tensors and the hyperfine coupling tensors, from which valuable information about the identity, the chemical environment and the spin density distribution of a radical can be deduced.

A general feature of radical species is their high reactivity and, therefore, short life-times. Indeed, many radicals live only long enough to be characterized by ESR spectroscopy at very low temperatures. Fundamental ESR experiments have concentrated on the identification of the products generated upon irradiation of model biological systems such as amino acids [10] or the components of DNA [11]. Due to the fact that experiments can often obtain the hyperfine coupling tensors for only some of the magnetic nuclei (such as protons) in biological radicals, ambiguous assignments of the observed hyperfine coupling tensors may occur. In addition, the conformational complexity of protein radicals and DNA radicals creates further difficulties for interpreting their ESR spectra. However, the characterization of new radicals may be assisted by comparisons of observed and computed hyperfine coupling tensors. Indeed, the increasing popularity of ESR techniques in probing the functionality of biological radicals *in vivo* demands reliable theoretical predictions on the relationship between hyperfine coupling tensors and molecular structure.

ESR experiments provide only indirect geometrical and electronic information. A more complete description of the molecular and electronic structures, and therefore the full spin density distribution and the associated hyperfine coupling tensors, is often provided by theory. In recent years, remarkable progress has been made in the calculations of hyperfine coupling tensors [12–20a, b]. While accurate hyperfine coupling constants can be predicted by the highest levels of electron correlation theory (such as QCI, MRCI and CC methods) for small radical species [21], comparable results can often be obtained from the methods based on density functional theory, DFT (such as B3LYP and PWP86) [14, 16, 18, 22–24]. Since the computational cost and memory requirements of DFT methods are considerably less than those of conventional correlated *ab initio* procedures, the number of basis functions, and hence atoms, is not nearly as limiting a factor at the DFT level. Furthermore, because of their ability to treat larger systems, DFT methods may be used to obtain more realistic descriptions of the interactions between radical systems and their surroundings by explicit consideration of the latter [25–27a, b]. In addition to earlier assessments of DFT methods in combination with various basis sets, the performance of the SVWN, BLYP, B3LYP, BP86 and B3P86 methods and the

Pople basis sets have recently been evaluated on the basis of gas-phase calculations performed on small radicals by Gauld et al. [18]. Furthermore, the strategies for including environmental effects using current density functional theory methods have been reviewed by Barone and coworkers [20a]. In summary, DFT methods are now a serious alternative to conventional *ab initio* techniques for the computation of hyperfine coupling tensors.

Calculated hyperfine coupling tensors have been utilized as a probe for understanding the molecular structures and other properties of biological radicals. The hyperfine coupling tensors of peroxyl radicals [22], the phenoxyl radical [26], quinone radicals [27a, b], the radical cation and anion of chlorophyll [27c], the bacteriopheophytin *a* radical anion [27d], the β-carotene radical cation [28], amino acid radicals [29], radicals derived from various DNA components [30a–e] and radicals involved in B_{12}-dependent reactions [30f, g] have been extensively studied at various levels of density functional theory. The results have shown that DFT methods work well, particularly for large organic radicals.

In this chapter, the relative performance of various levels of theory for the calculation of hyperfine coupling tensors is briefly reviewed. Methods based on density functional theory are highlighted, and the appropriateness of these techniques for investigating the hyperfine coupling tensors of biological radicals is discussed. Practical computational procedures of hyperfine coupling tensor calculations for biological radicals are illustrated using examples from our recent work on amino acid-derived radicals.

6.2 Theoretical Background

The hyperfine splittings displayed in an electron spin resonance (ESR) spectrum are the fingerprints for radical species and can be reproduced by accurate theoretical calculations. Practical applications of theory, however, are limited by computer resources. The accuracy of hyperfine coupling calculations at a certain level of theory depends on the cancellation of errors arising from the deviation of geometrical structures from experiment, the truncation of electron correlation effects, and the neglect of environmental, temperature, and relativistic effects. Thus, it is critical to employ reliable computational procedures to obtain an unambiguous theoretical interpretation of experimental data. In this section, the theoretical description of hyperfine coupling tensors is briefly introduced and available theoretical methods are reviewed. The observed performance of various levels of theory on the basis of gas-phase calculations and the current methodologies for incorporation of environmental effects are also overviewed. Finally, a computational scheme of combined levels of theory is highlighted as being suitable for the hyperfine coupling calculations of large radical species.

6.2.1 Theoretical Description of Hyperfine Coupling Tensors

All radicals have one or more unpaired electrons with intrinsic spin. As the unpaired electron is delocalized in a radical, there is a non-zero probability that the unpaired electron exists at each nucleus. Hence, the magnetic moment of the electron can interact with the magnetic moment of each nucleus, and give rise to the hyperfine interaction, an intrinsic and unique property of radical species. Since the magnetic moment is a vector, the hyperfine interaction of two magnetic moments is described by a tensor, the so-called hyperfine coupling tensor. Experimentally, the hyperfine coupling tensors are determined by measuring the hyperfine structures detected by electron spin or paramagnetic resonance (ESR or EPR) spectroscopy.

For a given nucleus, the hyperfine interaction can be described by the hyperfine coupling tensor (A) in the Hamiltonian of the hyperfine interaction:

$$\hat{H}_{hf} = \hat{I} \bullet A \bullet \hat{S} \tag{6.1}$$

where $\hat{I}$ and $\hat{S}$ are the nuclear and electronic spin operators, and

$$A = \begin{bmatrix} A_{XX} & 0 & 0 \\ 0 & A_{YY} & 0 \\ 0 & 0 & A_{ZZ} \end{bmatrix} \tag{6.2}$$

The A_{ii} ($i = X$, Y and Z) are called the principal components of the hyperfine coupling tensor. The A tensor can be separated into two parts:

$$A = A_{iso} \bullet \begin{bmatrix} 1 & 0 & 0 \\ 0 & 1 & 0 \\ 0 & 0 & 1 \end{bmatrix} + \begin{bmatrix} T_{XX} & 0 & 0 \\ 0 & T_{YY} & 0 \\ 0 & 0 & T_{ZZ} \end{bmatrix} \tag{6.3}$$

where A_{iso} is the isotropic hyperfine coupling constant (HFCC), which describes the magnitude of the hyperfine interaction, and T_{XX}, T_{YY} and T_{ZZ} ($T_{XX} + T_{YY} + T_{ZZ} = 0$) are the anisotropic hyperfine coupling constants, which reflect the asymmetry of the spin density about the nucleus.

For radicals with N magnetic nuclei, the hyperfine interaction Hamiltonian is given by:

$$\hat{H}_{hf} = \sum_{i=1}^{N} \hat{I}_i \bullet A_i \bullet \hat{S} \tag{6.4}$$

where the sum extends over all magnetic nuclei.

The isotropic hyperfine coupling constant of a given nucleus in a radical arises from a quantum mechanical contact of the unpaired electron and the nucleus, and can be calculated [9c] in hertz (Hz) by:

$$A_{iso} = \frac{2\mu_0}{3h} g\beta_e g_N \beta_N \rho^{\alpha-\beta}(0) \tag{6.5}$$

where $\rho^{\alpha-\beta}(0)$ is the spin density at the nucleus, μ_0 is the permeability constant in vacuum, h is Planck's constant, g is the electronic g factor, g_N is the nuclear g factor, β_e is the Bohr magneton, and β_N is the nuclear magneton. In many radicals, $g \approx g_e = 2.0023$ where g_e is the Zeeman splitting constant for the free electron. It should be noted that the "spin density" at a nucleus is often confused with the "Mulliken spin population" of the nucleus, as pointed out independently by Chipman [15] and Barone [16].

The anisotropic hyperfine coupling constants result from the electron-nuclear magnetic-dipole interactions. The ij^{th} component of the anisotropic coupling (in Hz) can be computed from:

$$T_{ij} = \frac{\mu_0}{4\pi h} g\beta_e g_N \beta_N \sum_{\mu\nu} \rho_{\mu\nu}^{\alpha-\beta} \left\langle \phi_\mu \left| r_{kN}^{-5} (r_{kN}^2 \delta_{ij} - 3 r_{kN,i} r_{kN,j}) \right| \phi_\nu \right\rangle \tag{6.6}$$

where $\rho_{\mu\nu}^{\alpha-\beta}$ is an element of the spin density matrix.

The hyperfine coupling constant is a field-independent property, while the isotropic coupling constant measures the difference of two resonance frequencies of the unpaired electron in magnetic atoms and molecules. Thus, the SI unit for hyperfine coupling constants is the hertz. However, hyperfine couplings have to be observed in an applied magnetic field B in ESR spectroscopy. In order to induce the electronic spin resonance of free electrons in EPR experiments, the resonance frequency and the applied magnetic field must be tuned to meet the requirement

$$h\nu = g_e \beta_e B \tag{6.7}$$

where ν is the resonance frequency. EPR spectroscopists often give hyperfine coupling constants in gauss (G) or tesla (T) [1G $=10^{-4}$ T], of the magnetic field. According to Eq. (6.7), the conversion factor from G to MHz is 2.8025.

6.2.2 *A Survey of Available Theoretical Methods*

Before undertaking a hyperfine coupling tensor calculation, it is important to carefully consider the levels of theory available, and their relative performance. In the present section, we survey the levels of theory currently available to calculate electronic properties. Subsequently, Sect. 6.2.3 provides a discussion of the relative success of these techniques for the calculation of HFCCs.

The Hartree-Fock (HF) method is the simplest *ab initio* model that can be employed for studying chemical problems. Inherent in the accuracy of Hartree-Fock calculations is the choice of the basis set used to describe the molecular orbitals.

There are a number of different types of basis sets developed as a combination of Slater-type functions (orbitals) or Gaussian-type functions (orbitals). Slater functions ($e^{-\zeta r}$) closely resemble atomic orbitals; however, Gaussian functions ($e^{-\alpha r^2}$) are more computationally efficient. Therefore, typical basis sets use linear combinations of Gaussian functions to obtain the accuracy of Slater functions, but yet maintain the computational advantage of Gaussian functions. The smallest possible basis sets (minimal basis sets) use only one function to describe each occupied atomic orbital (*i.e.*, STO-3G). Improvements upon minimal basis sets are achieved by using a double-zeta (triple-zeta) split-valence basis set (denoted as DZ (TZ)), which distinguishes between the core and valence regions and uses twice (triple) the number of functions to describe the chemically important valence region (*i.e.*, 3-21G and 6-31G (DZ basis sets) or 6-311G (TZ basis set)). Further improvements to the basis set include the addition of polarization functions (often denoted as *), which are functions with higher angular momentum that allow orbitals to distort within the molecular environment. These functions can be added to only the heavy atoms (*i.e.*, 6-31G* or 6-31G(d)) or also to hydrogen (*i.e.*, 6-31G** or 6-31G(d,p)). Diffuse functions (denoted as +), which are functions with small exponents (*i.e.*, very large orbitals), can also be added to heavy atoms (*i.e.*, 6-31 + G(d,p)) or to all atoms including hydrogen (*i.e.*, 6-31++G(d,p)) in order to improve the description of systems with loosely bound electrons (*i.e.*, anions or hydrogen bonded systems). Pople and coworkers developed the basis sets mentioned thus far, however similar systematically designed basis sets developed by Dunning and coworkers (*i.e.*, cc-pVDZ, aug-cc-pVTZ) are also popular. Many other basis sets have also been designed to specifically calculate different properties to a high degree of accuracy.

There are two main methods based on HF theory used for open-shell molecules such as radicals. The first method, restricted open-shell HF (ROHF), uses a combination of doubly and singly occupied orbitals to describe the system. The second method, unrestricted HF (UHF), accounts for different interactions between an unpaired electron and the two paired electrons by using two different molecular orbital expansions which allow the paired electrons to occupy different regions in space. UHF generally provides a more accurate description of open-shell molecules than ROHF. However, a major drawback of UHF is that the wavefunction is not a pure spin state, a deficiency referred to as spin contamination.

The Hartree-Fock limit represents the best that can be done with a single electron configuration (*i.e.*, a HF calculation with an infinitely large basis set). However, quantitative predictions often require going beyond the Hartree-Fock level. The major deficiency of Hartree-Fock theory is its incomplete description of electron correlation. That is, Hartree-Fock theory predicts that the probability of finding two electrons in the same region of space is equal to the product of the individual probabilities. Clearly, this approximation does not hold for electrons of parallel spin since it is energetically favourable for these electrons to be far from each other (*i.e.*, the motion of electrons is correlated). Conventional electron correlation methods and methods based on density functional theory [31] are the two main approaches for incorporation of the effects of electron correlation.

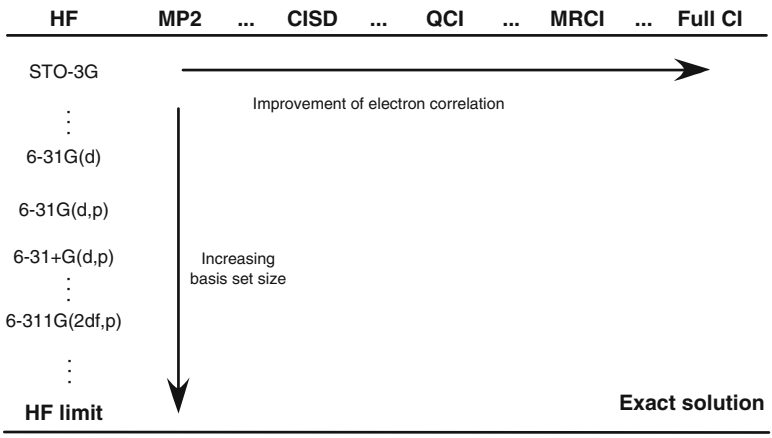

Fig. 6.1 Hierarchy of conventional *ab initio* methods (Adapted from Ref. [32])

A hierarchy of the conventional electron correlation methods, as well as a hierarchy of basis sets, is best illustrated by a Pople diagram [32], such as shown in Fig. 6.1.

Following the hierarchy, the exact solution of the non-relativistic Schrödinger equation, and thus the exact spin density distribution for evaluation of hyperfine coupling tensors, may be approached in a systematic manner. Methods that approach the exact solution (*i.e.*, MRCI or Full CI with very large basis sets) may be highly accurate. However, they are often too computationally expensive, and therefore they are limited to small radicals (*i.e.*, less than five heavy atoms).

In comparison to the conventional correlated methods, density functional theory attempts to obtain all information, including the wave function, from the electron density of the system. In current DFT methods, the electron correlation is incorporated into the Hamiltonian by means of the exchange-correlation energy functional (E_{XC}). Unfortunately, the exact form of E_{XC} is unknown. Thus, various models, including the local spin density approximation (LSDA) [31c] and generalized gradient approximations (GGA) [33a–d], have to be employed for practical calculations. In the LSDA approximation, the explicit form of E_{XC} depends only on the electron density and is obtained on the assumption that E_{XC} can be separated into an exchange functional (E_X) and a correlation functional (E_C). One such functional combination is SVWN, which is constructed as a linear combination of the Slater exchange term [34] and the correlation functional fitted by Vosko, Wilk and Nusair [35]. In the GGA approximation, the spin gradients are introduced to correct for the non-uniformity of the electron density neglected by LSDA. The GGA-corrected exchange functionals PW86 [33a] (Perdew and Wang) and B88 [36a] (Becke), and the GGA-corrected correlation functionals P86 [33b, c] (Perdew), LYP [37] (Lee, Yang, and Parr), and PW91[33d] (Perdew and Wang) are in common use. To further correct for the deficiencies of GGA functionals, Becke developed hybrid functionals that combine DFT and Hartree-Fock methods. These functionals are written as

a linear combination of Hartree-Fock, LSDA and B88 exchange contributions, together with LSDA and non-local correlation contributions (usually P86, PW91 or LYP). Three coefficients are used to fit the functional form to experimental data (atomization energies, ionization potentials and proton affinities). Indeed, Becke's three-parameter hybrid exchange functional combined with the LYP correlation functional (B3LYP) [36b, c, 37] has become the most popular E_{XC} functional. Basis sets typically used in Hartree-Fock based calculations (*i.e*. Pople or Dunning basis sets) are also employed in DFT calculations.

Since each DFT functional is constructed in a unique manner, the accuracy of density functional methods depends upon both the exchange-correlation functional and the basis set implemented. Furthermore, it is not possible to construct a hierarchical diagram for DFT methods. Therefore, there is no systematic way to study the convergence of DFT-based methods as in the conventional methods [21], other than improving the basis set used. However, GGA functionals generally behave better than LSDA functionals for most properties. Extensive tests have shown that functionals like B3LYP can achieve chemical accuracy with some exceptions. Another important feature of well-behaved DFT methods for large molecules, such as B3LYP, is that the results are often less dependent on the size of the basis set compared with conventional techniques. Specific to open shell systems, spin contamination is less of a concern with DFT methods compared with conventional correlation techniques.

All DFT methods account for some of the effects of electron correlation and therefore DFT procedures are superior to HF methods. The principal advantages of DFT methods over more conventional *ab initio* electron correlation techniques are computational efficiency and small disk requirements. For example, the computational time required for QCISD(T) or CCSD(T) calculations scales roughly as N^7, where N is the number of orbitals, but typical DFT calculations scale approximately as N^3, which can be further reduced for very large molecules to N with modern linear scaling algorithms. Hence, DFT methods are the preferred choice for molecular systems that are too large to be treated by conventional electron correlation methods, such as biologically relevant systems.

6.2.3 An Overview of the Relative Performance of Various Theoretical Methods for HFCC Calculations

Isotropic HFCCs are calculated by evaluating the spin density at the nucleus in question, a property that has been proven to be very difficult to calculate accurately. Since the anisotropic HFCCs are integrated over all space, rather than being evaluated at a single point, they are less sensitive to the quality of the method employed. Therefore, accurate anisotropic hyperfine coupling constants are also obtained when a level of theory suitable for the calculation of isotropic hyperfine coupling constants is implemented.

The performance of various levels of conventional theory for the calculation of isotropic hyperfine coupling constants has been summarized in reviews by Feller and Davidson [13], Chipman [15], Barone [16], Engels et al. [17] and Eriksson [19]. Importantly, Chipman's spin polarization model [38] has made it possible to understand the factors involved in computing hyperfine coupling constants. As introduced in Sect. 6.2.2, the theoretical method and the basis set are the two variables that determine the quality of the calculated hyperfine coupling tensors. In summary, high recovery of electron correlation and the use of a well-balanced basis set, which accurately describe the spin density at the nucleus of interest (see, for example, Refs. [13, 15, 38]), are both generally important for the quantitative prediction of isotropic HFCCs.

Basis set requirements for accurate HFCCs are much more involved than those for the accurate calculation of other electronic properties. Both the core and the valence space must be very well described for hyperfine coupling calculations (*i.e.*, a well-balanced basis set). In general, basis sets no smaller than triple zeta quality should be used to calculate HFCCs. In some instances, diffuse functions are very important; however, these drastically increase the computational cost.

Since the weight of electron correlation effects on A_{iso} varies from atom to atom, as well as with the electronic structures of different families of radicals, good results may be obtained for some radicals at the ROHF, UHF, and CIS levels of theory in conjunction with tailored basis sets due to fortuitous cancellation of errors. Therefore, these methods should not be relied upon if accurate data is desired. Among conventional *ab initio* approaches, it is essentially only multireference configuration interaction (MRCI), quadratic configuration interaction (QCI), and coupled-cluster (CC) techniques, in conjunction with large basis sets, that consistently generate HFCCs of high accuracy [15, 21, 39–44]. Basis sets of double-zeta plus polarization (DZP) quality or lower are found to be inadequate [13–15, 38], except for special cases where fortuitous cancellation of errors occurs. One problem with such approaches is that they are computationally quite expensive, even for moderately sized systems, and hence studies using these methods are restricted to relatively small systems.

As discussed in Sect. 6.2.2, an alternative approach for calculating hyperfine coupling tensors is represented by density functional theory (DFT). We must once again stress that the major deficiency of DFT is that a lower energy from one method does not guarantee that the functional leads to more accurate properties, and therefore all functional combinations must be carefully tested to determine the best DFT method for a particular property for a chosen class of molecules. In general, LSDA yields unacceptable isotropic HFCCs since the density is not localized, but GGA functionals lead to an improved description since an improved description of the core density is obtained. In particular, extensive assessments have shown that combinations of certain gradient-corrected functionals with appropriate basis sets such as (PBE0[45]/EPR-III[16]) [20a], (B3LYP/EPR-III and B3LYP/EPR-II) [16], (PWP86[33a–c]/IGLO-III[46]) [16, 47], (PWP86/6-311G(2d,p)) [24] and (B3LYP/6-311 + G(2df,p)) [18], can provide

reasonably accurate results. Noticeably, PWP86/6-311G(2d,p), B3LYP/EPR-III and B3LYP/EPR-II have been applied extensively to study the hyperfine coupling tensors of biological radicals [27, 29, 30].

Since hyperfine coupling tensors are measured at a temperature above absolute zero (*i.e.*, the temperature routinely used for gas-phase calculations), the excitation of vibrational motions at higher temperatures may have effects on the molecular structure of the radical, and therefore on hyperfine coupling tensors. The features and applicability of theoretical methods for incorporating temperature or vibrational effects by means of vibronic coupling, vibrational averaging, and molecular dynamics have been summarized by Eriksson [19]. Barone and coworkers [20a] have more recently reviewed the procedures for including the vibrational averaging correction to hyperfine coupling tensors in detail. It should be noted that temperature effects on the hyperfine coupling constants are generally less than 10 %, and therefore they are not included in our applied computational procedure.

6.2.4 Methodologies for Incorporating Environmental Effects

One common feature of biomolecules in condensed phases is the existence of hydrogen bonding interactions with surrounding molecules. Inclusion of such interactions in calculations is important for a better understanding of environmental effects on the hyperfine coupling tensors. Static models for approximating surrounding molecules are (a) a finite supermolecular model, (b) a continuum with a dielectric constant characteristic of the solvent, and (c) a hybrid model in which the environment is represented by the combination of a few important surrounding molecules with a continuum for the remaining molecules. Currently it is often an overwhelming challenge to perform calculations on large supermolecular models (a) at reliable levels of theory (*i.e.*, including both the radical of interest and surrounding molecules in the geometry optimization and single-point calculations). However, calculations using models (b) and (c) can be routinely carried out using the self-consistent reaction field (SCRF) methods [48], in which the target radicals of model (b), as well as some of the nearest neighbor molecules in model (c), are embedded in a cavity of the continuum of a dielectric. The advantage of model (c) over model (b) is the inclusion of specific solvent effects on the radical structure and therefore, on the hyperfine coupling tensors.

In the last 10 years, tremendous progress has been made in the SCRF approach, for which the Onsager model [49, 50] and a family of polarized continuum models (PCM) are currently available. The Onsager model and PCM models differ in how they define the cavity and the electric field [48], where the PCM models use a more elaborate representation of the cavity. It has been shown that the Onsager model is very efficient for geometry optimizations [50d], while PCM based methods, such as the self-consistent isodensity PCM (SCIPCM) often have convergence problems for geometry optimizations. Recently, Barone's group has implemented

the conducter-like polarized continuum method (CPCM) [51] to describe the solvent effects on the hyperfine coupling tensors [29i, 52]. Their results have shown that the CPCM method is very promising.

6.2.5 *A Practical Computational Scheme for the HFCCs in Biological Radicals*

In principle, accurate hyperfine coupling tensors of all magnetic nuclei in a radical can be obtained at reliable levels of theory using a sufficiently large supermolecular model. However, as discussed in Sect. 6.2.4, such a supermolecular model is generally too expensive for geometry optimizations. On the basis of the fact that environmental effects on gas-phase optimized structures for radicals are typically minor, the use of isolated radicals for hyperfine coupling tensor calculations is widely employed in the literature. Indeed, since the major contribution to the hyperfine coupling constants arises due to spin delocalization and spin polarization within (isolated) radicals, calculations on isolated radicals often provide satisfactory results.

Predicting hyperfine coupling tensors for biological radicals begins with a conformational search that is generally extremely time-consuming and, therefore, computationally expensive. Since the molecular geometry depends only upon the first derivatives of the energy, reasonably accurate geometries can often be obtained at quite modest levels of theory (*i.e.*, MP2 or DFT with a small basis set). However, properties such as hyperfine coupling constants converge only at a very high level of theory. Thus, optimizing the geometry at a lower level of theory followed by a higher-level single-point calculation on the optimized structures represents a cheaper, yet reliable, computational scheme for hyperfine coupling tensor calculations.

It should be noted that there are cases where environmental effects must be considered to obtain the correct structures of certain radicals, for example, the zwitterionic forms of amino acid radicals in solution or in single crystals. In these instances, one must choose a suitable approach from those discussed in Sect. 6.2.4 on a case-by-case basis.

We have performed hyperfine coupling tensor calculations [29a–c] on a variety of isolated amino acid radicals derived from glycine, alanine and hydroxyproline (Scheme 6.1) at the PWP86/6-311G(2d,p)//B3LYP/6-31 + G(d,p) level of theory. For zwitterionic forms of the amino acid radicals, the geometry optimizations were performed using the Onsager model at the B3LYP/6-31 + G(d,p) level of theory (denoted by Onsager-B3LYP/6-31 + G(d,p)). Thus, the hyperfine coupling tensor calculations were obtained from the PWP86/6-311G(2d,p)//Onsager-B3LYP/6-31 + G(d,p) level. We note that the 6-31 + G(d,p) basis set was chosen for the geometry optimizations in order to ensure that an accurate description is obtained for anions (*i.e.*, the diffuse functions) and hydrogen bonds (*i.e.*, the diffuse and polarization functions).

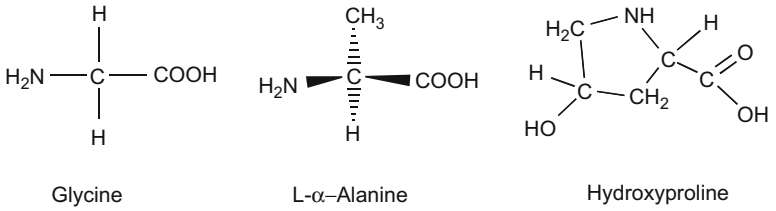

Glycine L-α–Alanine Hydroxyproline

Scheme 6.1 Schematic illustration of the structures of glycine, L-α-alanine and hydroxyproline

In the following section, we illustrate the procedures that have been employed in our studies of the relationship between conformations and hyperfine coupling tensors of amino acid radicals. For a complementary discussion of the radicals formed by radiation damage to the constituents of DNA, the reader is referred to a recent review [20b].

6.3 Theoretical Studies of Amino Acid Radicals

6.3.1 Calculations on Isolated Amino Acid Radicals

The structures of some amino acid radicals are scarcely affected by the environment of single crystals and solvents, and therefore can be readily obtained by gas-phase geometry optimizations. Comparison of the calculated hyperfine coupling tensors for each conformer of the isolated amino acid radicals with available experimental data may identify the specific conformations of the radical(s) that give rise to the observed hyperfine coupling tensors. For the first example, we illustrate how two observed (average) proton tensors (Table 6.1) of the $–CH_3$ moiety in the L-α-alanine radical R1: NH_2-C$^{\bullet}$(CH_3)-COOH in the single crystals were assigned and interpreted by our calculations.

A B3LYP/6-31 + G(d,p) conformational search found four possible conformers of R1 (Fig. 6.2).

The average of the calculated methyl proton isotropic HFCCs in the four conformers of R1 separates the conformers into two groups (Table 6.1). One group contains only R1-I with an averaged methyl proton isotropic HFCC ($H_{\beta(ave)}$) equal to 41.3 MHz, which is in excellent agreement with one of the experimental values (39.5 MHz). The second group consists of R1-II, R1-III, and R1-IV with an averaged methyl proton isotropic HFCC ($H_{\beta(ave)}$) of approximately 35 MHz, which is in excellent agreement with the second experimental value (33.1 MHz). In addition, all of the anisotropic components for both groups are in nearly perfect agreement with the corresponding experimental values. This leads to the conclusion that at least two conformers of R1 exist in the irradiated L-α-alanine crystals at 295 K. R1-I could be one conformer and the second conformer could be R1-II, R1-III or R1-IV.

Table 6.1 Comparison of calculated and experimental [10b] hyperfine couplings (MHz) of the R1 radical of L-α-alanine

Tensor	HFCC	R1-I	R1-II	R1-III	R1-IV	Exptl	
$H_{\beta1}$	A_{iso}	1.5	2.0	46.9	19.0		
	T_{xx}	−3.9	−3.4	−3.7	−3.5		
	T_{yy}	−2.7	−3.2	−2.7	−3.2		
	T_{zz}	6.6	6.6	6.4	6.6		
$H_{\beta2}$	A_{iso}	61.1	61.2	56.0	71.7		
	T_{xx}	−3.5	−3.3	−3.5	−3.5		
	T_{yy}	−3.2	−3.0	−2.8	−2.9		
	T_{zz}	6.7	6.4	6.3	6.4		
$H_{\beta3}$	A_{iso}	60.5	43.7	1.4	15.7		
	T_{xx}	−3.6	−3.5	−3.5	−3.3		
	T_{yy}	−2.9	−2.8	−2.7	−2.8		
	T_{zz}	6.6	6.3	6.2	6.1		
$H_{\beta(ave)}$	A_{iso}	41.3	35.6	34.8	35.4	39.5	33.1
	T_{xx}	−3.7	−3.4	−3.6	−3.4	−2.7	−2.3
	T_{yy}	−3.2	−3.0	−2.7	−3.0	−2.2	−2.3
	T_{zz}	6.6	6.3	6.3	6.4	5.0	4.6

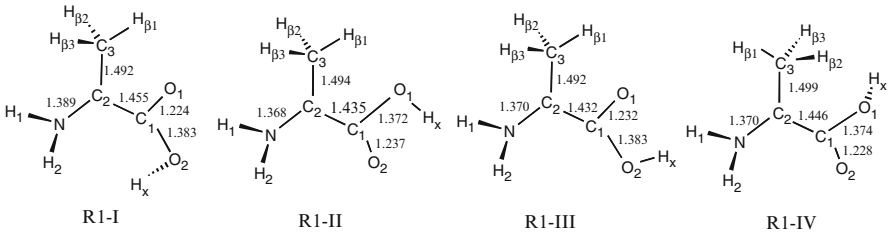

Fig. 6.2 The optimized structures for the four conformations of the R1 radical of L-α-alanine

The above theoretical assignment is supported by the correlation between the isotropic HFCCs and the structures. When the coplanarity of H_1, H_2, N and C_2 of R1 is examined by considering the magnitude of the sum of the three bond angles of the amino group (Table 6.2), the four conformers can be separated into the same two groups as isolated by examining $H_{\beta(ave)}$. The sum of the three bond angles in R1-I is at least 6.8° less than that of the second group. Thus, the N centre in R1-I is more pyramidal than those of the other three conformations, which is likely due to the specific repulsion between the amino group and the hydroxyl group in R1-I. The structural difference of the two groups of conformers results in distinct atomic spin populations (Table 6.3) and explains the difference in their proton isotropic HFCCs. More specifically, the more planar the amino group, the more easily the β spin electron of the lone pair of the N atom can be polarized by the unpaired α electron spin at the C_2 atom. As a consequence, the greater the spin polarization across the C_2—N bond, the lower the α (positive) spin population on the C_2 atom, and therefore the larger the α spin population on the N atom (Table 6.3), or the

Table 6.2 The three bond angles (degrees) and their sum of the amino group in the R1 radical of L-α-alanine

Structure	$\angle H_1NC_2$	$\angle H_2NC_2$	$\angle H_1NH_2$	Sum
R1-I	116.1	117.4	112.4	345.9
R1-II	120.1	116.8	117.8	354.7
R1-III	119.6	117.1	117.1	355.4
R1-IV	119.9	117.3	117.3	352.7

Table 6.3 The PWP86/6-311G(2d,p) calculated spin populations of the C_2 and N atoms in the R1 radical of L-α-alanine

Atom	R1-I	R1-II	R1-III	R1-IV
C_2	0.597	0.519	0.521	0.537
N	0.162	0.232	0.222	0.235

smaller the methyl proton isotropic HFCCs. Hence, the structural features of the two groups of conformers support the conclusion that R1-I possesses a larger spin population on the C_2 atom and therefore a larger methyl proton isotropic HFCC than R1-II, R1-III, and R1-IV.

In summary, the above example shows the dependence of HFCCs on spin polarization. Specifically, the H_β isotropic hyperfine coupling constants in an L-α-alanine derived radical depends on the extent of spin polarization across the N—C bond. Next, we will illustrate how theory may offer interpretations for observed differences in hyperfine coupling tensors of an amino acid radical based on a conformational study. In particular, we find that a radical derived from hydroxyproline leads to different HFCCs due to the conformational difference caused by intramolecular hydrogen-bonding interactions.

The hyperfine couplings of two hydroxyproline-derived radicals have been observed experimentally. These have been assigned to different conformations of the radical R2 (shown in Fig. 6.3), which is formed upon deamination of the hydroxyproline radical anion. One conformation was observed at 77 K [10c], denoted as exptl I (Table 6.4), while the second conformer was observed at 125 K [10c], denoted as exptl II (Table 6.4). For temperatures between 77 and 125 K, a mixture of conformations was observed [10c]. Our calculations [29b] concluded that the observed radical is in a neutral form. Eight possible conformers R2-I to R2-VIII were found and are shown schematically in Fig. 6.3. The conformers may be divided into two groups depending on whether or not they contain an intramolecular hydrogen bond between the carboxylic group and the $–NH_2$ moiety. The conformers R2-I, R2-II, R2-III, R2-V and R2-VI, hereafter referred to as group I, contain a slightly shortened hydrogen bond between O_2 of the carboxylic group and H_4 of the $–NH_2$ moiety (2.316 Å $< r_{O\ldots H} <$ 2.431 Å). The conformers R2-IV, R2-VII and R2-VIII, hereafter referred to as group II, contain no such hydrogen bond ($r_{O\ldots H} > 3.661$ Å). Consequently, the structures of the group II conformers are more open than those of group I.

As can be seen in Table 6.4, these differences in the structures are also reflected in the calculated hyperfine coupling tensors. For the conformers in group I, the

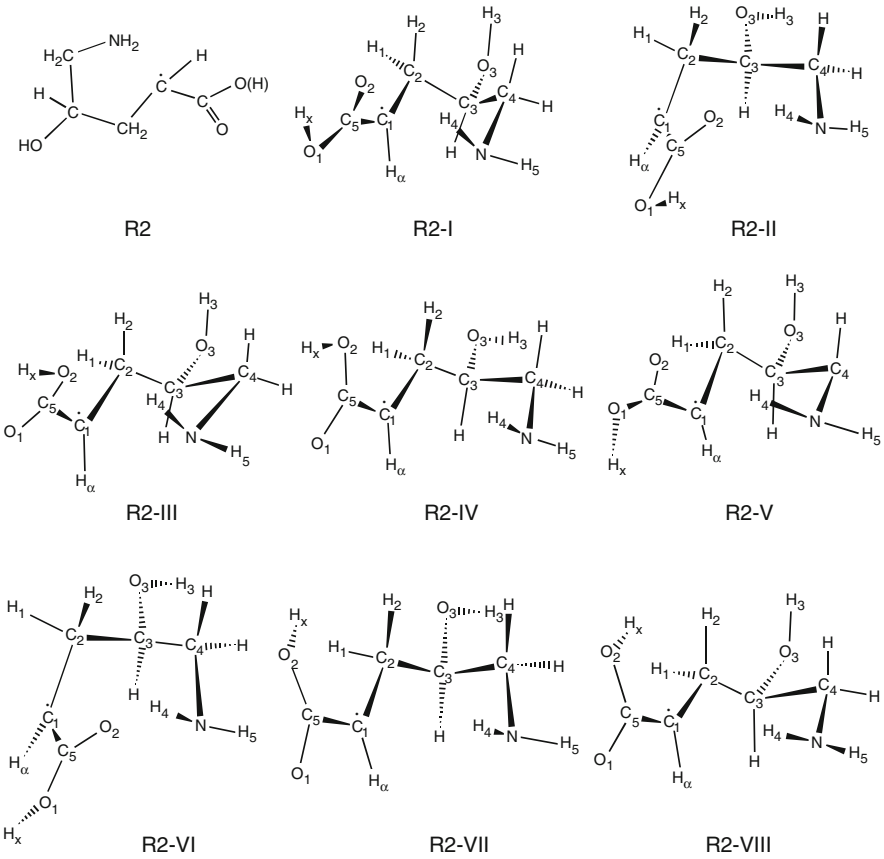

Fig. 6.3 Optimized structures for the eight conformers of the R2 radical of hydroxyproline

Table 6.4 PWP86/6-311G(2d,p) calculated and experimental [10c] HFCCs (MHz) for eight conformers of the R2 hydroxyproline-derived radical

	H_α				H_1				H_2			
System	A_{iso}	T_{xx}	T_{yy}	T_{zz}	A_{iso}	T_{xx}	T_{yy}	T_{zz}	A_{iso}	T_{xx}	T_{yy}	T_{zz}
R2-I	−47.5	−29.8	−1.9	31.6	72.4	−4.4	−3.2	7.6	3.7	−3.7	−2.8	6.5
R2-II	−49.0	−30.6	−1.9	32.6	79.1	−4.6	−3.2	7.8	3.3	−4.0	−2.8	6.8
R2-III	−47.0	−28.9	−2.3	31.2	78.3	−4.4	−3.2	7.6	2.5	−3.4	−3.3	6.7
R2-IV	−50.9	−30.5	−2.2	32.7	139.5	−5.4	−2.5	7.9	22.2	−3.9	−3.2	7.1
R2-V	−46.3	−29.8	−1.5	31.3	71.6	−4.4	−3.1	7.5	3.5	−3.7	−2.7	6.4
R2-VI	−47.5	−30.6	−1.6	32.2	80.2	−4.6	−3.1	7.7	2.9	−3.8	−2.8	6.7
R2-VII	−52.8	−30.8	−1.9	32.7	136.8	−5.2	−2.5	7.7	34.1	−3.9	−3.3	7.3
R2-VIII	−50.5	−30.4	−2.5	32.9	130.6	−5.1	−2.6	7.7	21.4	−3.7	−3.3	7.1
Exptl I	−57.2	−32.4	1.9	30.6	78.0	−4.8	−3.4	8.3				
Exptl II	−56.5	−32.4	1.3	31.1	123.1	−5.1	−2.2	7.4	21.4	−4.3	−3.2	7.6

calculated H_α, H_1 and H_2 isotropic HFCCs range approximately from −46 to −49, from 70 to 80 and from 2 to 4 MHz, respectively. These coupling constants are in close agreement with those measured experimentally at 77 K (*i.e.*, exptl I). The small calculated coupling constants of H_2 support the experimental suggestion that the second β-hydrogen coupling may have been too small to be observed. Since the calculated hyperfine coupling tensors of the group I conformers are very similar to each other, it is not possible to determine if exptl I is due to one conformer or a mixture of the group I conformers. For conformers in group II, the H_α, H_1 and H_2 isotropic HFCCs range approximately from −50 to −53, from 130 to 140 and from 21 to 34 MHz, respectively. These coupling constants are in good agreement with the conformer observed at 125 K, i.e., exptl II, with those of R2-VIII in closest agreement. These results clearly show that differences in HFCCs at the two temperatures arise due to a change in conformation, where intramolecular hydrogen-bonding interactions are present at lower temperatures.

Through the above examples, it should be noted that the hyperfine coupling tensors for a particular radical significantly depend on its conformation. Therefore, a simple HFCC study based solely on the global minimum structure will not necessarily help the assignment of the experimentally observed hyperfine coupling tensors. Hyperfine coupling tensor calculations on the complete conformational space of the proposed radicals and its derivatives are required for the unambiguous assignment of the experimental data.

6.3.2 *Calculations on the Zwitterionic Form of Isolated Amino Acid Radicals*

Amino acids can exist as zwitterionic species in the crystalline state and in solution. Therefore, when irradiated, radicals in a zwitterionic form, such as R3: $^{+}NH_3{}^{\bullet}CHCOO^{-}$ (from glycine), can be formed. The zwitterionic structure of amino acids and their derived radicals has been a challenge for theoretical chemistry. *Ab initio* calculations on glycine [53] and its radical [29i, j] have shown that their zwitterionic structures do not correspond to energy minima in the gas phase. Thus, environmental effects must be accounted for in order to explore the zwitterionic structures.

We have shown that the observed hyperfine coupling tensors of zwitterionic isomers of the amino acid radicals of glycine [29b], alanine [29a] and hydroxyproline [29c] can be reproduced by PWP86/6-311(2d,p) single point calculations on the zwitterionic structures obtained by Onsager-B3LYP/6-31 + G(d,p) optimizations. For example, the structure of R3 (Fig. 6.4) was optimized using the Onsager model with an estimated cavity radius of 3.24 Å and the dielectric constant of water ($\varepsilon = 78.39$). The resulting geometry possesses C_s symmetry with a planar radical centre. Thus, R3 is a typical π-radical. The computed full hyperfine tensors of R3, as well as the experimental values and other previously calculated values, are listed in Table 6.5.

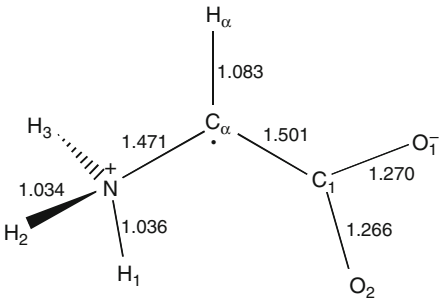

Fig. 6.4 The optimized structure for the zwitterionic radical R3 of glycine

Table 6.5 PWP86/6-311G(2d,p) calculated and experimental HFCCs (MHz) of the R3 of glycine

Tensor	A_{iso}	T_{xx}	T_{yy}	T_{zz}	A_{iso}^{exp}	T_{xx}^{exp}	T_{yy}^{exp}	T_{zz}^{exp}	A_{iso}^{e}
H_α	−58.96	−36.06	−1.46	37.51	−63.72[a]	−33.80[a]	1.85[a]	31.94[a]	−60.3
H_1	2.33	−5.39	−4.66	10.05	3.3[b]	−7.3[b]	−1.8[b]	9.2[b]	
H_2	77.06	−5.47	−4.52	9.99	62.91[a]	−6.60[a]	−4.07[a]	10.66[a]	
H_3	77.06	−5.47	−4.52	9.99	83.05[a]	−5.86[a]	−4.80[a]	10.65[a]	
H_{ave}	52.15	−5.44	−4.57	10.01	49.07[a]	−2.93[a]	−2.05[a]	4.97[a]	52.1
C_α	98.73	−76.29	−74.57	150.87	126.7[c]	−90.0[c]	−36.7[c]	126.8[c]	95.3
N	−6.96	−0.43	0.20	0.22	−8.72[d]	−0.98[d]	−0.76[d]	1.71[d]	−9.0

[a]Ref. [10a]
[b]Ref. [54]
[c]Ref. [55]
[d]Ref. [56]
[e]Ref. [29i] (B3LYP/EPR-II calculated values)

The H_α isotropic and anisotropic HFCCs are in good agreement with the experimental values. The anisotropic components of the hyperfine tensors of the three amino hydrogens (H_1, H_2 and H_3) are also in good agreement with the experimental values. The isotropic HFCCs of H_1, H_2 and H_3 are of similar magnitude as the experimental values with the largest differences of 14.15 and 5.99 MHz being observed for H_2 and H_3, respectively. The isotropic HFCC and anisotropic components of the nitrogen are in good agreement with the experimental values. It can be seen that the calculated C_α HFCC at the PWP86/6-311(2d,p) level is in fair agreement with the experimental value and slightly better than a previous B3LYP/EPR-II calculated value [29i]. The B3LYP/EPR-II study [29i] has shown that the deviation of C_α HFCC based on the optimized zwitterionic structure can be significantly corrected by including the effect of vibrational averaging. The HFCCs of H_α and N, however, are not sensitive to vibrational averaging.

The average (52.15 MHz) of the isotropic HFCCs of the three amino protons is in good agreement with the experimentally observed value of 49.07 MHz at 280 K, suggesting that the amino group rotates freely at this temperature. Furthermore, the results also suggest that at 100 K the orientation of the amino group in glycine crystals is constrained, giving rise to the three distinct hyperfine coupling tensors of the amino protons. Therefore, a further investigation was undertaken on the effects on the isotropic HFCCs of H_1, H_2, H_3, H_α, C_α and N of rotating the amino

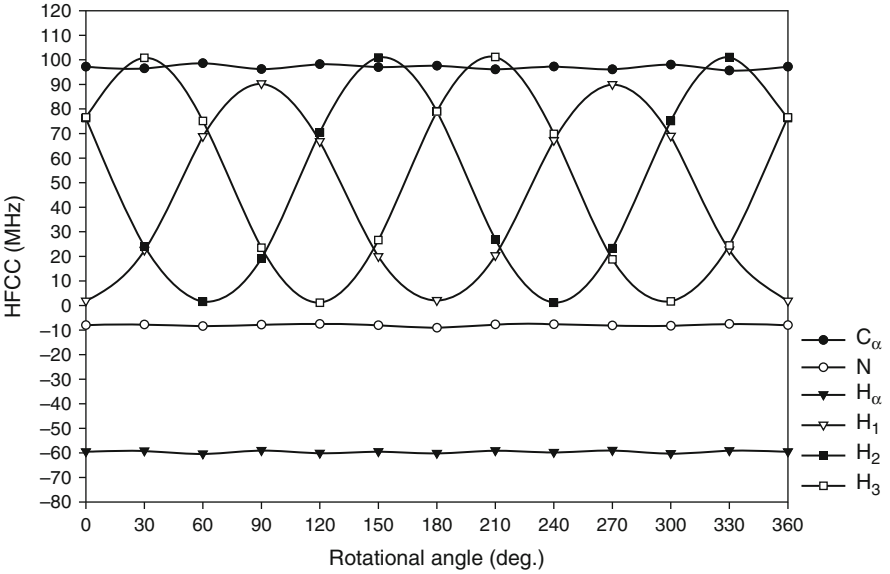

Fig. 6.5 Variation of H_α, H_1, H_2, H_3, C_α, and N isotropic HFCCs with rotational angle of the amino group of the R3 radical of glycine

group about the N—C_α bond in R3. The rotation of the amino group was carried out by incrementally increasing the dihedral angle $\angle H_1NC_\alpha C_1$ by 30°, starting from $\angle H_1NC_\alpha C_1 = 0°$. The variation of the isotropic HFCCs as a function of the rotational angle is shown in Fig. 6.5. From Fig. 6.5 it can be seen that the isotropic HFCCs of H_1, H_2 and H_3 change dramatically, while the isotropic couplings of H_α, C_α and N are almost constant. It is noted that the difference in amplitude of the variation of the HFCC of H_1 and those of H_2 and H_3 is due to the fact that the geometrical parameters of the amino group have been constrained during rotation.

When the amino group is rotated by approximately 5°, the isotropic HFCCs of H_2 and H_3 are in good agreement with the experimental values of 62.91 and 83.05 MHz at 100 K, while the isotropic HFCC of H_1 is still less than 5 MHz. These results support the fact that only the hyperfine splittings of two of the three constrained amino protons are easily observed; while the third remains too small to be distinguished from the many lines observed in the ENDOR spectrum [10a, i]. Thus, from the hyperfine coupling tensor calculations on the isolated R3 radical it can be concluded that the crystalline environment has little direct effect on the ESR spectra of R3, similar to the conclusion of a previous study [29i].

In summary, from the above example, it is clear that the PWP86/6-311G(2d,p)//Onsager-B3LYP/6-31 + G(d,p) method provides a useful tool to study zwitterionic amino acid radicals. Furthermore, this example once again emphasizes the benefits of comparing theoretical and experimental HFCCs to obtain information about molecular structure.

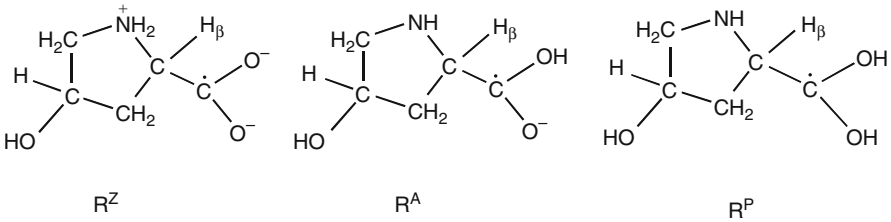

Scheme 6.2 Schematic illustration of the structures of the R^Z, R^A and R^P radicals of hydroxyproline

6.3.3 Theoretical Assignments Versus Experimental Observations

We have shown in Sects. 6.3.1 and 6.3.2 that the PWP86/6-311G(2df,p)//B3LYP/6-31 + G(d,p) calculations on isolated amino acid radicals of both neutral and zwitterionic forms can reproduce the observed hyperfine coupling tensors. Thus, this validates our chosen computational scheme, and our procedure can now be used to study, and hopefully solve, more complex problems, in particular cases where experimental assignment is difficult.

To illustrate the usefulness of theory to understand experimental spectra and to aid spectral assignments, we will consider a hydroxyproline-derived radical. Upon irradiation of hydroxyproline, two H_β hyperfine coupling tensors were observed (the isotropic HFCCs (A_{iso}) are 23.9 and 61.0 MHz) which were assigned to two different conformations of the zwitterionic radical R^Z (Scheme 6.2), since no carboxylate hydrogen interactions were detected [10c]. However, our calculations suggest that this assignment is inaccurate [29c].

Since proton-transfer may be involved in the formation of a radical in an irradiated hydroxyproline single crystal, we systematically examined the zwitterionic radical anion R^Z, its non-zwitterionic radical anion R^A and the protonated neutral radical R^P (Scheme 6.2). Two possible conformers of R^Z were found at the Onsager-B3LYP/6-31 + G(d,p) level, and four conformers of R^A and four conformers of R^P were found during a conformational search at the B3LYP/6-31 + G(d,p) level.

The PWP86/6-311G(2d,p) calculated isotropic H_β HFCCs of R^Z, R^A and R^P are significantly different in magnitude. The calculated H_β isotropic HFCCs of R^Z are smaller than 5 MHz, which are very different from either of the two observed A_{iso}. The calculated H_β isotropic HFCCs of two of the four conformers of R^A are approximately 20 MHz, while the calculated H_β isotropic HFCCs for all four conformers of R^P are approximately 60 MHz.

Thus, the DFT calculations clearly illustrate that the two observed hyperfine coupling tensors are given by R^A and R^P and *not*, as previously proposed, by two conformations of R^Z. This example shows how theory can be used to aid experimental assignment in difficult cases.

6.4 Concluding Remarks

The present chapter has briefly reviewed the performance of theoretical methods available to predict the hyperfine coupling tensors for (bio)organic radicals. The computation of accurate isotropic hyperfine coupling constants requires levels of theory that recover a large portion of the total electron correlation and well-balanced basis sets. Suitable methods include conventional correlation theories, such as QCI, MRCI, CC, and density functional methods, such as B3LYP and PWP86. However, although QCI, MRCI, CC (in conjunction with appropriate basis sets) can provide accurate results for small radicals, they are prohibitively expensive for systematic studies of large biological radicals. In contrast, B3LYP and PWP86 methods in combination with Pople basis sets show promising accuracy with a dramatic reduction in computational time, and have been applied successfully to a range of large biological radicals.

It is noteworthy that the spin density distribution, and therefore the hyperfine coupling constants, correlates with the conformations of the radical, and the correlation has been widely employed to rationalize the identity of the predominant biological radicals. Since many biological radicals are studied experimentally in solution or in the solid state, the environment can modify the gas-phase structure of the radicals. However, since modelling the conformation of biological systems with inclusion of the environmental effects arising from hydrogen bonding, van der Waals and steric interactions remains an overwhelming task (even for contemporary DFT levels of theory), isolated radicals are commonly used in hyperfine coupling tensor calculations under the assumption that the environmental and electronic effects of surrounding molecules on molecular structures and the hyperfine coupling tensor are minor.

By means of a few examples from our recent research on amino acid radicals, gas-phase PWP86/6-311(2d,p)//B3LYP6-31 + G(d,p) hyperfine coupling tensor calculations have proven to be sufficiently accurate to complement experiment for the purpose of unambiguous characterization of most radical species. There are cases, however, for which the environmental effects can be large enough to transform the (gas-phase) structures of amino acids, and therefore their derived radicals, into different isomers (such as into the zwitterionic form) or to modify the coplanarity of the $–NH_2$ moiety [29i]. For zwitterionic amino acid radicals, we have shown that the Onsager model can account for the most dominant environmental effects, and reliable zwitterionic structures can be obtained using the Onsager-B3LYP/6-31 + G(d,p) level of theory. Subsequently, PWP86/6-311(2d,p) gas-phase single-point calculations on the isolated zwitterionic structures of amino acid radicals appear to provide accurate proton hyperfine coupling constants. The results imply that the electronic effects of the environments on radical properties, such as HFCCs, are small.

Of course, the most accurate and reliable calculations of biological radicals should include the structural and electronic effects due to both the environment and the temperature. Although many practical calculations of hyperfine coupling constants of large biological radicals are heavily dependent on a cancellation of

errors, considerable effort has been made by research groups, such as Barone and coworkers [52], to examine the limit of current density functional theory in the prediction of hyperfine coupling constants. It can be expected that with further development of efficient algorithms and more powerful computers, more elaborate computational schemes will be able to provide more reliable descriptions of the relationship between structure and hyperfine coupling tensors. We are convinced that theoretical calculations will play an even more important role in identifying important biological radicals in the future.

Acknowledgements We gratefully acknowledge the Natural Sciences and Engineering Research Council of Canada (NSERC) and the Killam Trusts for financial support. In addition, we thank Dr. Leif A. Eriksson for fruitful discussions and collaborations.

References

1. Stubbe J, van der Donk WA (1998) Protein radicals in enzyme catalysis. Chem Rev 98:705–762
2. Garrison WM (1987) Reaction mechanisms in the radiolysis of peptides, polypeptides, and proteins. Chem Rev 87:381–98
3. Pogozelski WK, Tullius TD (1998) Oxidative strand scission of nucleic acids: routes initiated by hydrogen abstraction from the sugar moiety. Chem Rev 98:1089–1107
4. (a) Stubbe J (1989) Protein radical involvement in biological catalysis? Annu Rev Biochem 58:257–285; (b) Stubbe J (1988) Radicals in biological catalysis. J Biochem 27:3893–3900
5. Halliwell B, Gutteridge JMC (1999) Free radicals in biology and medicine. Oxford University Press Inc, New York
6. Denny WA, Wilson WR (2000) Tirapazamine: a bioreductive anticancer drug that exploits tumour hypoxia. Exp Opin Invest Drugs 9:2889–2901
7. Brown JM (1999) The hypoxic cell: a target for selective cancer therapy-eighteenth Bruce F. Cain memorial award lecture. Cancer Res 59:5863–5870
8. Brown JM (1993) SR 4233 (tirapazamine): a new anticancer drug exploiting hypoxia in solid tumors. Br J Cancer 67:1163–70
9. (a) Weltner W Jr (1983) Magnetic atoms and molecules. Van Nostrand, New York; (b) Atherton NM (1993) Principles of electron spin resonance. Ellis Horwood Limited, Chichester
10. (a) Glycine: Sanderud A, Sagstuen E (1998) EPR and ENDOR studies of single crystals of α-glycine x-ray irradiated at 295 K. J Phys Chem B 102:9353–9361 and references therein; (b) Alanine: Sagstuen E, Hole EO, Haugedal SR, Nelson WH (1997) Alanine radicals: structure determination by EPR and ENDOR of single crystals X-Irradiated at 295 K. J Phys Chem A 101:9763–9772 and references therein; (c) Hydroxyproline: Nelson WH (1981) ESR and ENDOR studies of radicals produced in hydroxyproline single crystals by x-irradiation at low temperature. J Chem Phys 74:2710–2716 and references therein; (d) Tyrosine (in frozen solution): Hulsebosch RJ, van der Brink JS,. Nieuwenhuis SAM, Gast P, Raap J, Lugtenburg J, Hoff A (1997) Electronic structure of the neutral tyrosine radical in frozen solution. selective 2 H-, 13 C-, and 17O-isotope labeling and EPR spectroscopy at 9 and 35 GHz. J Am Chem Soc 119:8685–8694
11. (a) Uracil: Sagstuen E, Hole EO, Nelson WH, Close DM (1998) Radiation damage to DNA base pairs. II. Paramagnetic resonance studies of 1-methyluracil·9-ethyladenine complex crystals x-irradiated at 10 K. Radiat Res 149:120–127; Herak JN, McDowell CA (1974) ENDOR study of long range spin interactions in molecular crystals. I. 1-Methyl uracil. J Chem Phys 61:1129–1135; (b) Thymine: Sagstuen E, Hole EO, Nelson WH, Close DM (1992) Radiation-induced free-radical formation in thymine derivatives: EPR/ENDOR of anhydrous thymine single crystals x-irradiated at 10 K. J Phys Chem 96:1121–1126; Hole EO, Sagstuen

E, Nelson WH, Close DM (1991) Primary reduction and oxidation of thymine derivatives: ESR/ENDOR of thymidine and 1-methylthymine x-irradiated at 10 K. J Phys Chem 95:1494–1503; (c) Adenine: Nelson WH, Sagstuen E, Hole EO, Close DM (1998) Electron spin resonance and electron nuclear double resonance study of X-irradiated deoxyadenosine: proton transfer behavior of primary ionic radicals. Radiat Res 149:75–86 and references therein; (d) Cytosine: Sagstuen E, Hole EO, Nelson WH, Close DM (1992) Protonation state of radiation-produced cytosine anions and cations in the solid state – EPR/ENDOR of cytosine monohydrate single crystals X-irradiated at 10 K. J Phys Chem 96:8269–8276 and references therein; (e) Guanine: Hole EO, Nelson WH, Sagstuen E, Close DM (1992) Free radical formation in single crystals of 2′-deoxyguanosine 5′-monophosphate tetrahydrate disodium salt: an EPR/ENDOR study. Radiat Res 129:119–138 and references therein; (f) Sugar: Close DM, Nelson WH, Sagstuen E, Hole EO (1994) ESR and ENDOR study of single crystals of deoxyadenosine monohydrate x-irradiated at 10 K. Radiat Res 137:300–309 and references therein; Hole EO, Sagstuen E (1987) Free radical formation in crystals of 2′-deoxyguanosine 5′-monophosphate irradiated at 15 K: an ESR study. Radiat Res 109:190–205; Sagstuen E (1980) Radiation damage to nucleosides and nucleotides. III. AC4′-centered radical in the ribose moiety of uridine-5′-phosphate single crystals. Radiat Res 84:164–70; Sagstuen E (1981) Radiation damage to nucleosides and nucleotides. II. EPR of uridine single crystals at 295 K. J Magn Reson 44:518–530

12. Lund A, Lindgren M, Lunell S, Maruani J (1989) Hydrocarbon radical cations in condensed phases. In: Maruani J (ed) Molecules in physics, chemistry and biology, vol 3. Kluwer Academic Publishers, Dordrecht, pp 259–300
13. Feller D, Davidson ER (1991) Theoretical approaches to ESR spectroscopy. In: Maksić ZB (ed) Theoretical models of chemical bonding part 3. Molecular spectroscopy, electronic structure and intermolecular interactions. Springer, Berlin
14. Malkin VG, Malkina OL, Salahub DR, Eriksson LA (1995) The calculation of NMR and ESR spectroscopy parameters using density functional theory. In: Politzer P, Seminario JM (eds) Theoretical and computational chemistry, vol 2. Elsevier, Amsterdam, pp 273–347
15. Chipman DM (1995) Magnetic hyperfine coupling constants in free radicals. In: Langhoff SR (ed) Quantum mechanical electronic structure calculations with chemical accuracy. Kluwer Academic Publishers, Dordrecht
16. Barone V (1996) Structure, magnetic properties and reactivities of open-shell species from density functional and self-consistent hybrid methods. In: Chong DP (ed) Recent advances in computational chemistry, vol 1, Recent advances in density functional methods part I. World Scientific Publishing Co. Pte. Ltd, Singapore
17. Engels B, Eriksson LA, Lunell S (1996) Recent developments in configuration interaction and density functional theory calculations of radical hyperfine structure. Adv Quantum Chem 27:297–369
18. Gauld JW, Eriksson LA, Radom L (1997) Assessment of procedures for calculating radical hyperfine structures. J Phys Chem A 101:1352–1359
19. Eriksson LA (1998) Encyclopedia of computational chemistry. Wiley, Chichester
20. (a) Adamo C, Cossi M, Rega N, Barone V, p 467; (b) Wetmore SD, Eriksson LA, Boyd RJ, p 409 (2001) In: Eriksson LA (ed) Theoretical and computational chemistry, vol 9, Theoretical biochemistry-processes and properties of biological systems. Elsevier, The Netherlands
21. (a) Kong J, Boyd RJ (1997) The convergence of basis set contractions: a case study of the molecular hyperfine structure of $^{14}NH_2$. J Chem Phys 107:6270–6274; (b) Kong J, Boyd RJ, Eriksson LA (1995) Re-examination of the hyperfine structure of $^{14}NH_2$. J Chem Phys 102:3674–3678; (c) Funken K, Engels B, Peyerimhoff SD, Grein F (1990) Study of the hyperfine coupling constants of the amidogen molecules NH_2, NHD, and ND_2. Chem Phys Lett 172:180–186; (d) Engels B, Peric M, Reuter W, Peyerimhoff SD (1992) Study of the hyperfine coupling constants (nitrogen-14 and hydrogen) of amidogen (NH_2) molecules in the X^2B_1 ground state and the A^2A_1 excited state. J Chem Phys 96:4526–4535
22. Wetmore SD, Boyd RJ, Eriksson LA (1997) Density functional theory investigation of hyperfine coupling constants in peroxy radicals. J Chem Phys 106:7738–7748

23. Barone V, Bencini A, Di Matteo A (1997) Intrinsic and environmental effects in the structure and magnetic properties of organic molecular magnets: bis(imino)nitroxide. J Am Chem Soc 119:10831–10837
24. Eriksson LA (1997) Evaluation of the performance of non-local and hybrid density functional theory methods for π-radical hyperfine structures. Mol Phys 91:827–833
25. Pauwels E, van Speybroeck V, Lahorte P, Waroquier M (2001) Density functional calculations on alanine-derived radicals: influence of molecular environment on EPR hyperfine coupling constants. J Phys Chem A 105:8794–8804
26. (a) Chipman DM (1999) Structure and properties of p-aminophenoxyl radical. J Phys Chem A 103:11181–11187; (b) Chipman DM (2000) Hydrogen-bonding effects on free-radical properties. J Phys Chem A 104:11816–11821
27. (a) O'Malley PJ (1997) A hybrid density functional study of the p-benzosemiquinone anion radical: the influence of hydrogen bonding on geometry and hyperfine couplings. J Phys Chem A 101:6334–6338; (b) O'Malley PJ (1998) B3LYP, hybrid density functional studies of the durosemiquinone radical: the effect of symmetrical and asymmetrical hydrogen bonding on spin densities and hyperfine couplings. J Phys Chem A 102:248–253; (c) O'Malley PJ (1999) The electronic structure of the bacteriopheophytin a anion radical, in vivo. J Am Chem Soc 121:3185–3192; (d) O'Malley PJ (2000) The effect of oxidation and reduction of chlorophyll a on its geometry, vibrational and spin density properties as revealed by hybrid density functional methods. J Am Chem Soc 122:7798–7801
28. Himo F (2001) Density functional theory study of the β-carotene radical cation. J Phys Chem A 105:7933–7937
29. (a) Ban F, Gauld JW, Boyd RJ (2000) A density functional theory study of the radiation products of glycine. J Phys Chem A 104:5080–5086; (b) Ban F, Gauld JW, Boyd RJ (2000) Theoretical studies of the radiation products of hydroxyproline. J Phys Chem A 104:8583–8592; (c) Ban F, Wetmore SD, Boyd RJ (1999) A density-functional theory investigation of the radiation products of L-α-alanine. J Phys Chem A 103:4303–4308; (d) Himo F, Gräslund A, Eriksson LA (1997) Density functional calculations on model tyrosyl radicals. Biophys J 72:1556–1567; (e) Himo F, Eriksson LA (1997) Theoretical study of model tryptophan radicals and radical cations: comparison with experimental data of DNA photolyase, cytochrome c peroxidase, and ribonucleotide reductase. J Phys Chem B 101:9811–9819; (f) Himo F, Babcock GT, Eriksson LA (1999) Tyrosyl radical in galactose oxidase not strongly perturbed by cysteine cross-link. Chem Phys Lett 313:374–378; (g) Himo F, Eriksson LA, Blomberg MRA, Siegbahn PEM (2000) Substituent effects on OH bond strength and hyperfine properties of phenol, as model for modified tyrosyl radicals in proteins. Int J Quantum Chem 76:714–723; (h) Himo F (2000) Stability of protein-bound glycyl radical: a density functional theory study. Chem Phys Lett 328:270–276; (i) Rega N, Cossi M, Barone V (1998) Structure and magnetic properties of glycine radical in aqueous solution at different pH values. J Am Chem Soc 120:5723–5732; (j) Barone V, Adamo C, Grand A, Subra R (1995) Structure and ESR features of glycine radical in its zwitterionic form. Chem Phys Lett 242:351–354
30. (a) Wetmore SD, Boyd RJ, Eriksson LA (1998) Radiation products of thymine, 1-methylthymine, and uracil investigated by density functional theory. J Phys Chem B 102:5369–5377; (b) Wetmore SD, Himo F, Boyd RJ, Eriksson LA (1998) Effects of ionizing radiation on crystalline cytosine monohydrate. J Phys Chem B 102:7484–7491; (c) Wetmore SD, Boyd RJ, Eriksson LA (1998) Comparison of experimental and calculated hyperfine coupling constants. Which radicals are formed in irradiated guanine? J Phys Chem B 102:9332–9343; (d) Wetmore SD, Boyd RJ, Eriksson LA (1998) Theoretical investigation of adenine radicals generated in irradiated DNA components. J Phys Chem B 102:10602–10614; (e) Wetmore SD, Boyd RJ, Eriksson LA (1998) A comprehensive study of sugar radicals in irradiated DNA. J Phys Chem B 102:7674–7686; (f) Wetmore SD, Smith DM, Radom (2001) Enzyme catalysis of 1,2-amino shifts: the cooperative action of B6, B12, and aminomutases. J Am Chem Soc 123:8678–8689; (g) Wetmore SD, Smith DM, Goldling BT, Radom L (2001) Interconversion of (S)-glutamate and (2S,3S)-3-methylaspartate: a distinctive B_{12}-dependent carbon-skeleton rearrangement. J Am Chem Soc 123:7963–7972

31. (a) Hohenberg P, Kohn W (1964) Inhomogeneous electron gas. Phys Rev B 136:864–871; (b) Kohn W, Sham LJ (1965) Self-consistent equations including exchange and correlation effects. Phys Rev A 140:1133–1138; (c) Parr RG, Yang W (1989) Density-functional theory of atoms and molecules. Oxford University Press, Oxford; (d) Koch W, Holthausen MC (1999) A chemist's guide to density functional theory, 2nd edn. Wiley-VCH, Weinheim
32. Hehre WJ, Radom L, Schleyer PvR, Pople JA (1986) Ab initio molecular orbital theory. Wiley, New York
33. (a) Perdew JP, Yue W (1986) Accurate and simple density functional for the electronic exchange energy – generalized gradient approximation. Phys Rev B 33:8800–8802; (b) Perdew JP (1986) Density-functional approximation for the correlation-energy of the inhomogeneous electron-gas. Phys Rev B 33:8822–8824; (c) Perdew JP (1986) Correction. Phys Rev B 34:7406; (d) Perdew JP, Wang Y (1992) Accurate and simple analytic representation of the electron-gas correlation-energy. Phys Rev B 45:13244–13249
34. Slater JC (1974) Quantum theory of molecules and solids. McGraw Hill, New York
35. Vosko SH, Wilk L, Nusair M (1980) Accurate spin-dependent electron liquid correlation energies for local spin density calculations: a critical analysis. Can J Phys 58:1200–11
36. (a) Becke AD (1988) Density-functional exchange-energy approximation with correct asymptotic behaviour. Phys Rev A 38:3098–3100; (b) Becke AD (1993) Density-functional thermochemistry. III. The role of exact exchange. J Chem Phys 98:5648–5652; (c) Stephens PJ, Devlin FJ, Frisch MJ, Chabalowski CF (1994) Ab initio calculation of vibrational absorption and circular dichroism spectra using density functional force fields. J Phys Chem 98:11623–11627
37. Lee C, Yang W, Parr RG (1988) Development of the Colle-Salvetti correlation-energy formula into a functional of the electron density. Phys Rev B 37:785–9
38. Chipman DM (1992) The spin polarization model for hyperfine coupling constants. Theor Chim Acta 82:93–115
39. (a) Engels B (1991) Estimation of the influence of the configurations neglected within truncated multireference CI wave functions on molecular properties. Chem Phys Lett 179:398–404; (b) Engels B, Peyerimhoff SD (1989) The hyperfine coupling constants of the $X^3\Sigma^-$ states of imidogen (NH). Influence of polarization functions and configuration space on the description of spin polarization. Mol Phys 67:583–600; (c) Karna SP, Grein F, Engels B, Peyerimhoff SD (1989) The hyperfine coupling constants of fluoride diatomic ion(1-) ($^{19}F_2^-$): an ab initio MRD-CI basis set study. Int J Quantum Chem 36:255–263; (d) Karna SP, Grein F, Engels B, Peyerimhoff SD (1990) Ab initio configuration-interaction studies of the ground state potential energy and hyperfine coupling constants of the chlorine molecular ion(1-) ($^{35}Cl_2^-$). Mol Phys 69:549–557; (e) Funken K, Engels B, Peyerimhoff SD, Grein F (1990) Study of the hyperfine coupling constants of the amidogen molecules NH_2, NHD, and ND2. Chem Phys Lett 172:180–186; (f) Feller D, Davidson ER (1988) A multireference-CI determination of the isotropic hyperfine constants for first row atoms boron to fluorine. J Chem Phys 88:7580–7587; (g) Engels B, Peyerimhoff SD, Davidson ER (1987) Calculation of hyperfine coupling constants. An ab initio MRD-CI study for nitrogen to analyze the effects of basis sets and CI parameters. Mol Phys 62:109–127; (h) Engels B, Peyerimhoff SD (1988) Study of the 1s and 2s shell contributions to the isotropic hyperfine coupling constant in nitrogen. J Phys B 21:3459–3471
40. (a) Feller D (1990) An ab initio study of the magnetic hyperfine properties of difluoride ion ($F_2^-(^2\Sigma_u^+)$). J Chem Phys 93:579–589; (b) Feller D, Glendening E, McCullough EA Jr, Miller RJ (1993) A comparison of unrestricted Hartree-Fock- and restricted open-shell Hartree-Fock-based methods for determining the magnetic hyperfine parameters of nitric oxide (X 2Π). J Chem Phys 99:2829–2840
41. Barone V, Adamo C, Grand A, Subra R (1995) Structure and ESR features of glycine radical in its zwitterionic form. Chem Phys Lett 242:351–4
42. (a) Carmichael I (1991) Ab initio quadratic configuration interaction calculation of the isotropic hyperfine coupling constants in the ethyl radical. J Phys Chem 95:6198–6201; (b) Carmichael I (1991) Ab initio quadratic configuration interaction calculations of isotropic hyperfine coupling constants. J Phys Chem 95:108–111; (c) Carmichael I (1990) Isotropic coupling constant for

the nitrogen atom from correlated calculations based on spin-unrestricted wave functions. J Chem Phys 93:863–864; (d) Chipman DM, Carmichael I, Feller D (1991) Molecular orbital studies of hyperfine coupling constants in the H2CN and H(HO)CN radicals. J Phys Chem 95:4702–4708; (e) Carmichael I (1994) Hyperfine splitting in N4+ from ab Initio Calculation. J Phys Chem 98:5044–5048; (f) Carmichael I (1995) Correlation effects on the hyperfine splitting in HNCN. J Phys Chem 99:6832–6835

43. Sekino H, Bartlett RJ (1985) Spin density of radicals by finite field many-body methods. J Chem Phys 82:4225–9
44. Perera SA, Watts JD, Bartlett RJ (1994) A theoretical study of hyperfine coupling constants. J Chem Phys 100:1425–34
45. (a) Perdew JP, Burke K, Ernzerhof M (1996) Generalized gradient approximation made simple. Phys Rev Lett 77:3865–3868; (b) Perdew JP, Burke K, Ernzerhof M (1997) Generalized gradient approximation made simple. [Erratum to document cited in CA126:51093]. Phys Rev Lett 78:1396; (c) Adamo C, Barone V (1998) Toward chemical accuracy in the computation of NMR shieldings: the PBE0 model. Chem Phys Lett 298:113–119
46. (a) Kutzelnigg W, Fleischer U, Schindler M (1990) In: NMR-basic principles and progress, vol 23. Springer, Heidelberg. The IGLO-III basis set consists of an (11s7p2d/6s2p) primitive set contracted to [7s6p2d/4s2p]
47. (a) Eriksson LA, Malkina OL, Malkin VG, Salahub DR (1994) The hyperfine structures of small radicals from density functional calculations. J Chem Phys 100:5066–5075; (b) Austen MA, Eriksson LA, Boyd RJ (1994) A density functional theory study of the free radicals NH_2, NF_2, NCl_2, PH_2, PF_2, and PCl_2. Can J Chem 72:695–704; (c) Eriksson LA, Wang J, Boyd RJ, Lunell S (1994) A comparative study of the hyperfine structures of neutral nitrogen oxides: DFT vs CISD results. J Phys Chem 98:792–799; (d) Martell JM, Eriksson LA, Boyd RJ (1995) Hyperfine structures of the series $C_2H_nF_{5-n}$, $n = 0–5$: a density functional theory study. J Phys Chem 99:623–629; (e) Eriksson LA, Wang J, Boyd RJ (1995) The interactions between alkali metals and C_2H_2. Density functional theory as an analytic tool. Chem Phys Lett 235:422–429; (f) Kong J, Eriksson LA, Boyd RJ (1994) A density functional theory study of the hyperfine structures of the atoms B to O and the species NH_2 and NH_3^+. Chem Phys Lett 217:24–30
48. Foresman JB, Frisch Æ (1996) Exploring chemistry with electronic structure methods. Gaussian, Inc., Pittsburgh
49. Onsager L (1936) Electric moments of molecules in liquids. J Am Chem Soc 58:1486–93
50. (a) Wong MW, Frisch MJ, Wiberg KB (1991) Solvent effects. 1. The mediation of electrostatic effects by solvents. J Am Chem Soc 113:4776–4782; (b) Wong MW, Wiberg KB, Frisch MJ (1992) Solvent effects. 2. Medium effect on the structure, energy, charge density, and vibrational frequencies of sulfamic acid. J Am Chem Soc 114:523–529; (c) Wong MW, Wiberg KB, Frisch MJ (1992) Solvent effects. 3. Tautomeric equilibria of formamide and 2-pyridone in the gas phase and solution: an ab initio SCRF study. J Am Chem Soc 114:1645–1652; (d) Wong MW, Wiberg KB, Frisch MJ (1991) Hartree-Fock second derivatives and electric field properties in a solvent reaction field: theory and application. J Chem Phys 95:8991–8998
51. Barone V, Cossi M (1998) Quantum calculation of molecular energies and energy gradients in solution by a conductor solvent model. J Phys Chem A 102:1995–2001
52. Adamo C, Heitzmann M, Meilleur F, Rega N, Scalmani G, Grand A, Cadet J, Barone V (2001) Interplay of intrinsic and environmental effects on the magnetic properties of free radicals issuing from H-Atom addition to cytosine. J Am Chem Soc 123:7113–7117
53. Ding Y, Krogh-Jespersen K (1992) The glycine zwitterion does not exist in the gas phase: results from a detailed, ab initio, electronic structure study. Chem Phys Lett 199:261–6
54. Collins MA, Whiffen DH (1966) Electron spin resonance of irradiated glycine at 77°K. Mol Phys 10:317–25
55. Morton JR (1964) Electron spin resonance in irradiated glycine crystals. J Am Chem Soc 86:2325–9
56. Hedberg A, Ehrenberg A (1968) Resolution enhancement of electron spin resonance spectra from irradiated single crystals of glycine. J Chem Phys 48:4822–8

Addition: Update from the Original Version

A6.1 Introduction

Over the last decade, driven in part by a desire to apply computational chemistry to important biologically-relevant systems, there have been tremendous efforts made to computationally investigate ever larger and more complete chemical systems. This has presented a particular challenge for the calculation of electron paramagnetic resonance (EPR) parameters, specifically hyperfine coupling constants (HFCCs), which are well-known to often be highly sensitive to the environmental nuances in which the radical site resides and choice of computational method. That is, their ability to act as a highly insightful diagnostic tool of a radical's nature also means that they are often computationally challenging to determine reliably and accurately. Traditionally, for small radical systems, high-level conventional *ab initio* electron correlation methods (*e.g.*, QCISD) coupled with large extensive basis sets selected principally on their ability to accurately describe the core electrons, were used. Unfortunately, such approaches are not computationally tractable for the necessarily large chemical models usually required in, for example, investigations on protein- or DNA-based radicals.

Density functional theory (DFT) has established itself as the contemporary quantum mechanical method of choice for the study of biochemical systems. This is due to the fact that it is often able to provide accurate and reliable structures at a significantly reduced computational cost compared to *ab initio* wave function-based electron correlation methods. For example, the DFT methods B3LYP and PBE0 are now widely used for calculations of magnetic properties as they are able to describe the differential variations in spin polarization of a different shell on balance [1–3]. Indeed, one can now routinely use such approaches to examine large chemical models of up to 200 atoms; and this number will only increase with the advent of faster and more powerful computers. However, as large as these models may seem, they are still relatively modest given that, for example, a protein is composed of thousands of atoms.

Despite the limitations outlined above, several computational protocols have been devised, and are increasingly being applied, that enable one to reliably and accurately model a range of effects arising from the larger environment including stereo-electronic, polarity, pH and hydrogen bonding, as well as dynamic effects [4]. For instance, using hybrid quantum mechanic/molecular mechanic (QM/MM) methods, one can divide a larger chemical system into two or more "layers", with each one being treated at a different level of theory. Furthermore, this approach can be applied on its own or coupled with molecular dynamics (MD), *i.e.* QM/MM-MD.

In the previous edition of this book, we reviewed the application of quantum mechanical methods, and DFT in particular, for the accurate and reliable calculation of HFCCs of small radicals. In this update we present our perspectives on a number of related recent methodological developments for simulating HFCCs of large systems in condensed phases. More specifically, we highlight relevant new

developments in basis sets, use of "composite approaches", and computational approaches that integrate Car-Parrinello molecular dynamics/classical molecular dynamics with quantum mechanical calculations, or combine classical molecular dynamic simulations with hybrid QM/MM methods.

A6.2 Recent Developments in Basis Set Choices for Calculating HFCCs

When employing hybrid density functionals or performing ab initio dynamics, it is generally true that the smallest basis sets that enable semi-quantitative evaluations, without large errors due to basis set incompleteness, are split valence basis sets augmented by diffuse functions [5, 6], such as aug-cc-pVDZ or 6-31 + G(d,p). While these are suitable for the computation of electric and magnetic properties, they often perform poorly for HFCCs due to an inadequate description of the core-valence region [7, 8]. Instead, as outlined in our original chapter, either highly specialized basis sets, such as IGLO-X, or decontraction of more standard basis sets, such as 6-311 + G(2df,p), were used in the previous literature.

More recently, the group of Barone has developed a modified Pople 6-31G split-valence basis set that contains a reduced number of polarization and diffuse functions, which is commonly referred to as N07D [1, 2]. Barone et al. have performed an extensive assessment of the utility of this basis set for HFCCs on a large set of free radicals containing second and third row atoms. Importantly, they showed that when used in combination with the B3LYP and PBE0 methods (*i.e.*, the B3LYP/N07D and PBE0/N07D levels of theory), it is able to provide remarkably accurate structural parameters and HFCC tensors are obtained at reasonable computational costs. The excellent performance of these models lies in the optimization of core-valence *s* functions for hyperfine coupling constants, while retaining/improving the good performances of the parent 6-31 + G(d,p) basis set for valence properties through re-optimization of polarization and diffuse *p* functions [1, 2]. Unfortunately, however, the N07D basis set must be re-optimized for each atom and for each choice of density functional.

A6.3 Computational Strategies to Simulate Radicals in a Chemical Environment

For radicals within a polar chemical environment, especially a solvent such as water, the calculation of HFCCs still presents a significant computational challenge. However, a number of protocols have now been developed and applied that enable one to model the steric and/or electronic effects of the environment, as well as the effect of explicit radical solvent interactions. Such current strategies can be illustrated by considering, for example, the HFCCs of nitroxides.

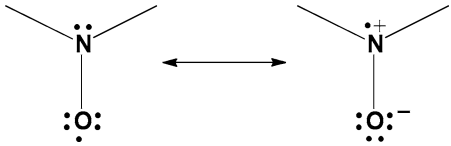

Fig. 6.6 The two resonance structures for the dimethyl nitroxide radical

Nitroxides are common radicals in biology, biochemistry, and biophysics. In particular, they are widely used to investigate the conformational changes related to the motion of biomolecules and different nanostructures by EPR spectroscopy [9–11]. Due to the possibility of resonance within the nitroxide functionality itself, their radical nature can be thought of as a mixture of a formal neutral oxygen centered radical and a zwitterionic nitrogen centered radical (Fig. 6.6). In more polar environments, the latter zwitterionic form is favoured and thus the spin density is more localized on the nitrogen (N) centre; hence, the N HFCC increases. Consequently, these molecules are also good models for examining the ability of a particular computational protocol to adequately and accurately model general (*e.g.*, polarity) or specific (*e.g.*, hydrogen bonding) environmental effects.

A6.3.1 Composite Approaches: The Use of QCISD and DFT to Achieve Higher Accuracy with Computational Feasibility

The use of composite computational methods to approximate the results of higher more accurate levels of theory, but at reduced costs, is well known and widely applied in determining thermochemical values of chemical systems, *e.g.*, the G1/2/3 and CBS-X methods. Related approaches can also be used for determining HFCCs of radicals. In particular, the quadratic configuration interaction, singles and doubles (QCISD) method coupled with appropriately tailored basis sets [12] provides highly accurate HFCCs for most radicals [13, 14]. At present, QCISD-level computations are generally only computationally feasible for the most modest of systems, *e.g.*, a few heavy atoms. In contrast, while DFT-based approaches are "cheaper" and can be applied to significantly larger systems, they are known to underestimate the absolute value of the nitrogen HFCC for nitroxides [15–21]. However, they do give quite reliable geometries.

Building upon this fact, Improta and Barone proposed a composite approach to compute the HFCC of the nitroxide's N centre in the same spirit as the ONIOM family of methods [22]. More specifically, they proposed the procedure shown in Eq. (6.8):

$$A_{iso} = \left(A_{iso}^{DFT}\right) \text{big system} + \left(A_{iso}^{QCISD} - A_{iso}^{DFT}\right) \textit{small} \text{ system} \tag{6.8}$$

in which "big system" refers to the complete real radical system of interest; and "small system" to a suitable reduced model whose geometry is frozen to that of

the corresponding fragment in the "big system". A number of studies have shown that this procedure does indeed provide reliable results for the nitrogen HFCCs in nitroxides [17–21]. In such cases, the latter "small system" was chosen to be the dimethyl nitroxide moiety, while the former "big system" was the whole nitroxide containing molecule plus solvent molecules strongly hydrogen bonded to the solute. When such a composite approach is employed, attention must be paid both to the size of the model system and to the quality of the computational method used in the calculation on the complete, "big" system.

A6.3.2 Computational Approaches Integrating Car-Parrinello Molecular Dynamics/Classical Molecular Dynamics with Quantum Mechanical Calculations that Involve Discrete-Continuum Embedding

The accuracy of computed spectroscopic data for small-to-medium sized molecules in the gas phase has long been comparable to that of the experiments [23, 24]. In contrast, the physics and the chemistry of aqueous solutions have presented a considerable challenge to theoretical and computational chemists for the last two decades [25, 26]. Indeed, reliable and accurate computational methods for spectroscopic properties in solution have only become validated and popular in recent years. For instance, recent developments in the polarizable continuum model (PCM), e.g., the integral equation formalism (IEF)-PCM, have proven to be highly successful and are now widely applied [27]. However, many studies have also shown the limits of PCM-based methods in reproducing strong solute-solvent interactions related to intermolecular hydrogen bonding [28]. In particular, these observations highlight the fact that solute-solvent hydrogen bonding plays a key role in protic solvents and cannot be neglected or approximated within a dielectric-dependent approach.

Combining a cluster chemical model that includes the solute and its closest solvent molecules, with a PCM-based description of the polarity of the surrounding bulk solvent could effectively solve this problem [28]. Unfortunately, the cluster or supramolecular frame needs to be sampled onto the configuration space of the solute-solvent system. This means that the geometries of the solute and its closest solvent molecules must be statistically averaged among the energetically accessible configurations of the system. Thus, the efficiency of the sampling methods becomes crucial for the accuracy of the quantum chemical calculations.

Quantum molecular dynamics simulation within the Car–Parrinello (CP) framework [29], and conventional molecular dynamics simulations based on a classical treatment of the nuclei motion are techniques that can account for the intrinsic dynamics of solvent molecules in the first solvation shell of a radical. Within the framework of density functional theory, the Car-Parrinello (CP) extended-Lagrangian scheme [30] provides an approach for classical molecular dynamics

simulation and first-principles electronic structure calculations. Indeed, it has become the method of choice for investigating the dynamics of condensed phases [31]. Barone and coworkers have proposed that HFCCs can be computed using suitable quantum mechanical methods on a statistical basis; the statistical ensemble is generated by regularly extracting frames from the trajectories of the MD simulations. Only the solute (nitroxide) and the solvent molecules of its first hydration shell are explicitly considered; the remaining solvent molecules of the bulk are accounted for by means of a PCM-based approach or by the electrostatic potential fitted (ESPF) method [32].

Recently Pavone et al., by means of an integrated computational approach combining Car-Parrinello molecular dynamics with quantum mechanical calculations involving discrete-continuum embedding, investigated the prototypical spin probe di-tert-butyl nitroxide (DTBN) in aqueous solution. For the DTBN system in aqueous solution, the initial configuration was obtained by replacing six water molecules with a DTBN molecule in an equilibrated cubic supercell including 64 water molecules at a density of 1.00 g/cm^3. The simulation in a vacuum was performed starting from the optimized structure of DTBN. After equilibration, the simulations were performed for a total time of 4.0 ps, during which statistical averages were taken. The dynamical effect on the HFCC was computed at the PBE0 level of theory by averaging the values obtained along the CPMD trajectories. Equal time-spaced structures of DTBN (for the gas phase) and DTBN-$(H_2O)_2$ (for the aqueous solution) were extracted along the CPMD trajectories, a calculation of the N HFCC was repeated on each of these frames. Notably, quantitative agreement between computed and experimental parameters was achieved [33]. Their results also further showed that 200 frames along the trajectories are sufficient to obtain a well-converged average.

In 2004, Improta and Barone [3] suggested that no density functional at that time was able to provide quantitative A_{iso} values for the N centre of nitroxides. Building upon their "ONIOM-like approach" described above, they suggested an expanded related approach that also included corrections for dynamic and bulk solvent effects as summarized in Eq. (6.9).

$$A_{iso} = \left(A_{iso}^{DFT}\right) big + \left(A_{iso}^{QCID} - A_{iso}^{DFT}\right) small + \Delta\,(\text{dynamics}) + \Delta\,(\text{solvent}) \tag{6.9}$$

More specifically, they employed the composite approach of QCISD/Chipman and PBE0/EPR-II to calculate the HFCC of the N atom using the "big" and "small" systems shown in Fig. 6.7. As the number of water-nitroxide hydrogen bonds in individual CPMD frames ranged from zero to two, clusters containing the solute plus the two water molecules closest to the nitroxide oxygen were extracted from the aqueous solution trajectory, the rest of the solvent was then described using a PCM method. Using the PBE0/6-311++G(3df,2pd) energy minimum as the gas-phase reference structure of DTBN, the model system was extracted (dimethyl nitroxide kept frozen at the structure of DTBN) for the QCISD/Chipman calculation. The

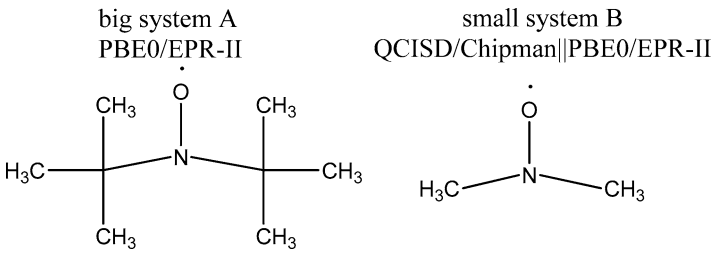

Fig. 6.7 Illustration of the "big" and "small" nitroxide solute systems used

Table 6.6 Calculated HFCC (in gauss) of the N atom of DTBN with corrections from dynamic and bulk solvent effects

	QCISD/DFT	Δ(dynamics)	Δ(solvent)	Total	Exp [34]
A_{iso}	15.5	0.1	1.6	17.2	17.17

effect of the intramolecular dynamics of DTBN on the HFCC was quantified as the difference between the HFCC of the PBE gas-phase minimum and that averaged over the PBE CPMD gas-phase trajectory (denoted as Δ(dynamics) in Eq. (6.9)). The effect of the bulk solvent, Δ(solvent), was taken into account as the difference between the HFCC obtained from the gas-phase and the aqueous-solution dynamics. The calculated corrections to the DFT calculated HFCC of the N atom of the nitroxide (A_{iso}(A)DFT) are summarized in Table 6.6. Combining the computed data using Eq. (6.9) gives a calculated HFCC of the nitroxide's N centre in very good quantitative agreement with the experimental value.

This example of computing HFCCs of a radical within a solvent shows that the coupling of an effective treatment of electronic variables by state-of-the-art quantum chemistry calculations and the sampling of nuclear configurational space by first-principles atomistic simulations can provide both a qualitative understanding of the underlying physicochemical processes and quantitative agreement of computed and experimental HFCC values. Thus, an integrated computational approach consisting of accurate conventional correlated methods, reliable HF-GGA hybrid density functionals, mixed discrete-continuum solvent models, and averaging from molecular dynamics simulations can be a valuable complementary computational approach to experiment.

A6.3.3 A Combined Approach of Classical Molecular Dynamic Simulations and QM/MM Methods

Tryptophan radicals play essential roles as intermediates in electron, proton or hydrogen atom transfer in DNA photolyase [35], *Escherichia coli* Y177W mutant of RNR [36], azurin [37], and cytochrome c peroxidase [38, 39]. In order to better understand the roles of such radicals in these systems and the associated electron

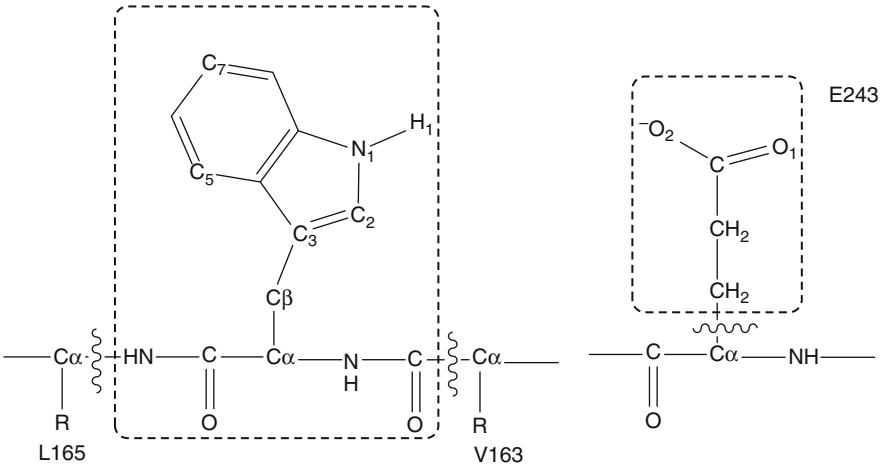

Fig. 6.8 The chemical model consisting of W164 hydrogen bonded to the R-group of E243 used by Bernini et al. [44] for the QM region is denoted within the dashed-line boxes

transfer processes, considerable experimental effort has focused on the assignment of the observed spectral data to a neutral deprotonated or cationic protonated species. The experimental EPR spectra of tryptophan radicals show signals that are not obscured in the class of heme enzymes referred to as versatile peroxidases (VPs) [40–42]. In particular, EPR/ENDOR studies unambiguously demonstrate the involvement of a solvent exposed neutral tryptophan radical in the mechanistic catalytic cycle of VP [40, 41].

EPR magnetic parameters of tryptophan radicals are influenced by the protein environment. Hence, a realistic model should include the entire protein together with the surrounding solvent cage. In recent years, QM/MM methods [43] have been used to calculate HFCCs and g tensors of protein radicals [44]. Within this approach, a reactive part of the system containing the radical is treated with accurate QM methods, while the environment (the protein matrix and the solvent) is modelled at a lower level of theory such as molecular mechanics (MM). Importantly, however, the use of such an approach ensures that the influence of the protein geometry and hydrogen bonds on the radical are adequately included in the calculations. Consequently, this approach has the potential to provide reliable EPR parameters for radicals that lie within large biochemical systems, e.g., protein-based radicals.

Bernini et al. [44] have modeled the (W164) tryptophan radical of the VP enzyme (PDB ID: 2BOQ) using a combined approach of classical molecular dynamics simulation and QM/MM. The QM region was defined as in Fig. 6.8. A 10 ns constrained molecular dynamic simulation (only side chains and solvent molecules were free to move) was performed after initial equilibration using NAMD2.6 [45]. The snap shot at 10 ns was then used as a starting structure to obtain a QM/MM optimized geometry. The latter geometry optimizations were performed using the B3LYP functional for the QM layer while the CHARMM27 force field [46] was

employed for the MM part. A mixed basis set, hereafter called 6-31G(d,p)$^{\#}$ was used, which is the 6-31G(d,p) basis set for all atoms except for the indolic H_1 and N_1, and carboxylic oxygen O_2 of E243 for which the 6-311++G(d,p) basis set was used.

The tryptophan radical was studied both in its cationic form (VP_Trp-cat) and neutral form (VP_Trp-neu). The latter was obtained by transferring the H_1 proton to the O_2 oxygen of the carboxylic group of the glutamyl residue E243. The calculated HFCCs at the B3LYP/TZVP level of theory obtained using the software package ORCA [47] are shown in Table 6.7. It is noted that the MM point charges are taken into account by using the 'orca_pc' module, which adds the MM point charge contribution to the one-electron matrix and the nuclear repulsion.

It was concluded to be impossible to discriminate between the neutral and cationic radical derivatives of W164 on the basis of only g-tensor values [40, 41]. Instead, it is more useful to inspect the computed Mulliken spin densities of these two species that are known to be different [48]. The calculated spin density distribution on the benzene ring is large and similar (Table 6.8). However, there is a quantitatively different spin density on N_1 and C_3 (see Table 6.8) between the neutral and cationic forms because the pyrrole ring is significantly affected by the retention or loss of the H_1 hydrogen at N_1. More specifically, the tryptophan radical cation is predicted to have a smaller spin density on C_3 and N_1, a larger and more positive spin density on C_2, and a larger isotropic HFCC for H_1. As can be seen in Table 6.8, the tryptophan radical cation does not explain the experimentally observed N_1 and C_2 spin densities and H_1 HFCC.

In contrast, the computed HFCCs and Mulliken spin densities of the N-deprotonated neutral tryptophan radical hydrogen-bonded to the R-group of E243 fits the experimental data. This suggests that the QM/MM optimized structure of VP containing a neutral tryptophan radical is correct and, furthermore should be used to study the associated proton-coupled electron transfer reaction.

The results obtained using the synergistic combination of MD and QM/MM methods are clearly a notable improvement over those previously calculated, especially the HFCC values for the β-methylene protons $H_{\beta 1}$ and $H_{\beta 2}$ (see Table 6.7). More specifically, previous computations used a chemical model consisting of a neutral tryptophan radical (N-deprotonated 3-ethylindole) hydrogen bonded to a single water either *in vacuo* (Tables 6.7 and 6.8: *in vacuo* Trp + H_2O) or in bulk (PCM) solvent (Tables 6.7 and 6.8: PCM Trp + H_2O) [41]. Thus, modern DFT-based QM/MM approaches are suitable for the calculations of the HFCCs of amino acid radicals in proteins.

A6.4 Conclusions

From a methodological point of view, methods rooted in density functional theory, although not always as accurate as desired, have become very effective tools. Indeed, DFT methods couple a remarkable reliability in the computation of the geometric

Table 6.7 Calculated (B3LYP/TZVP) HFCC (mT) of tryptophan neutral and cationic radicals using the QM/MM optimized geometry of VP (see text)

					In vacuo [40, 41]	PCM [40, 41]
Tensor	HFCC	Exp [40]	VP_Trp-neu	VP_Trp-cat	Trp + H_2O	Trp + H_2O
$H_{\beta 1}$	A_{iso}	2.6	2.59	2.33	2.86	3.14
	x	2.35	2.47	2.22	2.73	3.01
	y	2.75	2.78	2.5	3.06	3.33
	z	2.7	2.53	2.27	2.79	3.08
$H_{\beta 2}$	A_{iso}	1.15	1.01	0.89	1.19	1.31
	x	1.13	0.95	0.84	1.07	1.19
	y	1.13	0.9	0.78	1.12	1.25
	z	1.18	1.19	1.05	1.38	1.49
H_1	A_{iso}	0.01	0.06	0.35	0.01	0.01
	x	0.1	0.22	0.65	0.08	0.08
	y	0.19	0.2	0.08	0.18	0.17
	z	0.07	0.17	0.49	0.06	0.07
H_2	A_{iso}	0.04	0.19	0.34	0.01	0.05
	x	0.28	0.34	0.45	0.17	0.14
	y	0.04	0.07	0.01	0.03	0.12
	z	0.11	0.31	0.57	0.13	0.18
H_5	A_{iso}		0.51	0.55	0.42	0.44
	x	0.64	0.75	0.81	0.6	0.63
	y	$\leq\|0.15\|$	0.22	0.23	0.18	0.2
	z	0.49	0.57	0.6	0.47	0.5
H_7	A_{iso}		0.42	0.44	0.34	0.36
	x	$\leq\|0.15\|$	0.14	0.14	0.1	0.11
	y	0.62	0.66	0.69	0.56	0.57
	z	0.46	0.45	0.47	0.37	0.39
N	A_{iso}		0.23	0.17	0.31	0.34
	x	$\leq\|0.15\|$	0.08	0.08	0.13	0.07
	y	$\leq\|0.15\|$	0.09	0.1	0.12	0.06
	z	1.00	0.88	0.74	1.19	1.15

parameters and HFCCs of organic free radicals given a very favorable scaling with the number of active electrons. Hybrid functionals such as the B3LYP or the parameter-free PBE0 model are able to treat the differential spin polarization of different shells in a balanced way. They provide a good description of the HFCCs of many classes of compounds. With optimized medium-sized basis sets, such as the N07D basis set, B3LYP or PBE0 can effectively treat large systems of biological significance. A combined PBE0 or B3LYP/QCISD approach can further extend the reliability of the computational model to species such as nitroxides for which conventional and hybrid density functionals are not sufficiently accurate. The coupling of effective dynamical treatments with quantum mechanical evaluations of HFCC for a statistically significant number of configurations is one of the most promising approaches for quantitative prediction of HFCCs. Coupling classical

Table 6.8 Calculated (B3LYP/TZVP) Mulliken spin densities of the tryptophan neutral and cationic radicals obtained by using the QM/MM optimized geometry of VP (see text)

				In vacuo [40, 41]	PCM [40, 41]
Atom	Exp [40]	VP_trp-neu	VP_Trp-cat	Trp + H_2O	Trp + H_2O
N_1	0.2	0.19	0.15	0.28	0.25
C_2	$\leq\|0.05\|$	0.01	0.08	0.10	0.04
C_3	0.52	0.56	0.48	0.61	0.53
C_4		0.19	0.18		
C_5	0.17	0.26	0.27	0.22	0.18
C_6		0.09	0.10		
C_7	0.15	0.19	0.19	0.16	0.14
C_8		0.02	0.05		
C_9		0.06	0.04		
C_β		0.03	0.03		

molecular dynamics simulation with the hybrid quantum-mechanical/molecular mechanical (QM/MM) method provides a realistic strategy to study amino acid radicals in protein environments.

References

1. Vincenzo B, Paola C, Emiliano S (2008) Development and validation of the B3LYP/N07D computational model for structural parameter and magnetic tensors of large free radicals. J Chem Theory Comput 4:751–764
2. Barone V, Paola C (2008) Accurate and feasible computations of structural and magnetic properties of large free radicals: the PBE0/N07D model. Chem Phys Lett 454:139–143
3. (a) Improta R, Barone V (2004) Interplay of electronic, environmental, and vibrational effects in determining the hyperfine coupling constants of organic free radicals. Chem Rev 104:1231–544; (b) Barone V, Paola C, Alfonso P (2010) An integrated computational protocol for the accurate prediction of EPR and PNMR parameters of aminoxyl radicals in solution. Magn Reson Chem 48(S1):S11–S22
4. Barone V, Paola C, Alfonso P (2010) An integrated computational protocol for the accurate prediction of EPR and PNMR parameters of aminoxyl radicals in solution. Magn Reson Chem 48(S1):S11–S22
5. Iyengar SS, Frisch MJ (2004) Effect of time-dependent basis functions and their superposition error on atom-centered density matrix propagation (ADMP): connections to wavelet theory of multiresolution analysis. J Chem Phys 121:5061–5070
6. Improta R, Barone V, Kudin KN, Scuseria GE (2001) Structure and conformational behavior of biopolymers by density functional calculations employing periodic boundary conditions. I. The case of polyglycine, polyalanine, and poly-alpha-aminoisobutyric acid in vacuo. J Am Chem Soc 123:3311
7. Chipman DM (1989) Spin densities of first-row atoms calculated from polarization wave functions with accurate numerical methods Phys ReV A 39:475–480
8. Barone V (1995) Structure, EPR parameters, and reactivity of organic free radicals from a density functional approach. Theor Chim Acta 91:113

9. Altenbach C, Marti T, Khorana HG, Hubbell WL (1990) Transmembrane protein structure: spin labeling of bacteriorhodopsin mutants. Science 248:1088–1092
10. Mchaourab HS, Lietzow MA, Hideg K, Hubbell WL (1996) Motion of spin-labeled side chains in T4 lysozyme. Correlation with protein structure and dynamics. Biochemistry 35(24):7692–7704
11. Lucarini M, Franchi, P, Pedulli GF, Pengo P, Scrimin P, Pasquato L (2004) EPR study of dialkyl nitroxides as probes to investigate the exchange of solutes between the ligand shell of monolayers of protected gold nanoparticles and aqueous solutions. J Am Chem Soc 126:9326–9329
12. Chipman DM (1989) Gaussian basis sets for calculation of spin densities in first-row atoms. Theor Chim Acta 76:73–84
13. Carmichael I (1997) Atomic spin densities from correlation-consistent basis sets. J Phys Chem A 101:4633–4636
14. Barone V, Grand A, Minichino C, Subra R (1993) Theoretical approach to the structure and hyperfine coupling constants of nonrigid radicals: the case of dihydronitrosyl radical. J Phys Chem 97:6355–6361
15. Barone V, Bencini A, Cossi M, di Matteo A, Mattesini M, Totti F (1998) Assessment of a combined QM/MM approach for the study of large nitroxide systems in vacuo and in condensed phases. J Am Chem Soc 120:7069–7078
16. Adamo C, di Matteo A, Rey P, Barone V (1999) Tuning of structural and magnetic properties of nitronyl nitroxides by the environment. A combined experimental and computational study. J Phys Chem A 103(18):3481–3488
17. Barone V, Bencini A., Matteo di A (1997) Intrinsic and environmental effects in the structure and magnetic properties of organic molecular magnets: bis(imino)nitroxide. J Am Chem Soc 119:10831–10837
18. Improta R, Scalmani G, Barone V (2001) Quantum mechanical prediction of the magnetic titration curve of a nitroxide 'spin probe'. Chem Phys Lett 336:349–356
19. Tedeschi AM, D'Errico G, Busi E, Basosi R, Barone V (2002) Micellar aggregation of sulfonate surfactants studied by electron paramagnetic resonance of a cationic nitroxide: an experimental and computational approach. Phys Chem Chem Phys 4:2180–2188
20. Improta R, Di MA, Barone V (2000) Effective modeling of intrinsic and environmental effects on the structure and electron paramagnetic resonance parameters of nitroxides by an integrated quantum mechanical/molecular mechanics/polarizable continuum model approach. Theor Chem Acc 104:273–279
21. Saracino GAA, Tedeschi A, D'Errico G, Improta R, Franco L, Ruzzi M, Corvaia C, Barone V (2002) Solvent polarity and pH effects on the magnetic properties of ionizable nitroxide radicals: a combined computational and experimental study of 2,2,5,5-tetramethyl-3-carboxypyrrolidine and 2,2,6,6-tetramethyl-4-carboxypiperidine nitroxides. J Phys Chem A 106:10700–10706
22. Dapprich S, Komiromi I, Byun KS, Morokuma K, Frisch MJ (1999) A new ONIOM implementation in Gaussian98. Part I. The calculation of energies, gradients, vibrational frequencies and electric field derivatives. THEOCHEM 461–462:1–21
23. Roos BO (1999) Theoretical studies of electronically excited states of molecular systems using multiconfigurational perturbation theory. Acc Chem Res 32:137–144
24. Helgaker T, Jaszunski M, Ruud K (1999) Ab initio methods for the calculation of NMR shielding and indirect spin-spin coupling constants. Chem Rev 99:293–352
25. Garrett BC, Dixon DA, Camaioni DM, Chipman DM, Johnson MA, Jonah CD, Kimmel GA, Miller JH, Rescigno TN, Rossky PJ (2005) Role of water in electron-initiated processes and radical chemistry: issues and scientific advances. Chem Rev 105:355–389
26. Wernet P, Nordlund D, Bergmann U, Cavalleri M, Odelius M, Ogasawara H, Naeslund LA, Hirsch TK, Ojamaee L, Glatzel P (2004) The structure of the first coordination shell in liquid water. Science 304:995–999

27. Scalmani G, Barone V, Kudin KN, Pomelli CS, Scuseria GE, Frisch MJ (2004) Achieving linear-scaling computational cost for the polarizable continuum model of solvation. Theor Chem Acc 111:90–100
28. (a) Cossi M, Barone V (2000) Solvent effect on vertical electronic transitions by the polarizable continuum model. J Chem Phys 112:2427–2435; (b) Cossi M, Barone V (2001) Time-dependent density functional theory for molecules in liquid solutions. J Chem Phys 115:4708–4717; (c) Aquilante F, Roos B, Barone V (2003) A theoretical investigation of valence and Rydberg electronic states of acrolein. J Phys Chem 119:12323–12324; (d) Koch A, Thomas S, Kleinpeter E (1997) Ab initio study, semiempirical calculation and NMR spectroscopy of keto-enol tautomerism of triazolopyrimidines. THEOCHEM 401:1–14; (e) Saracino GA, Tedeschi A, D'Errico G, Improta R, Barone V (2002) Solvent polarity and pH effects on the magnetic properties of ionizable nitroxide radicals: a combined computational and experimental study of 2,2,5,5-tetramethyl-3-carboxypyrrolidine and 2,2,6,6-tetramethyl-4-carboxypiperidine nitroxides. J Phys Chem A 106:10700–10706
29. Car R, Parrinello M (1985) Unified approach for molecular dynamics and density-functional theory. Phys Rev Lett 55:2471–2474
30. Tedeschi AM, D'Errico G, Busi E, Basosi R, Barone V (2002) Micellar aggregation of sulfonate surfactants studied by electron paramagnetic resonance of a cationic nitroxide: an experimental and computational approach. Phys Chem Chem Phys 4:2180–2188
31. (a) Kanai Y, Cicero G, Selloni A, Car R, Galli G (2005) A theoretical study of biotin chemisorption on Si-SiC(001) surfaces. J Phys Chem B 109:13656; (b) Fischer D, Curioni A, Billeter SR, Andreoni W (2004) Effects of nitridation on the characteristics of silicon dioxide. Dielectric and structural properties from ab initio calculations. Phys Rev Lett 92:236405; (c) Gleich D, Hutter J (2004) Computational approaches to activity in rhodium-catalysed hydroformylation. Chem Eur J 10:2435–2444
32. Ferré N, Ángyán JG (2002) Approximate electrostatic interaction operator for QM/MM calculations. Chem Phys Lett 356:331–339
33. Pavone M, Cimino P, De Angelis F, Barone V (2006) Interplay of stereoelectronic and environmental effects in tuning the structural and magnetic properties of a prototypical spin probe: further insights from a first principle dynamical approach. J Am Chem Soc 128:4338–4347
34. (a) Kawamura T, Matsunami S, Yonezawa T (1967) Solvent effects on the g-value of di-tert-butyl nitric oxide. Bull Chem Soc Jpn 40:1111–1115; (b) Mukerjee P, Ramachandran C, Pyter RA (1982) Solvent effects on the visible spectra of nitroxides and relation to nitrogen hyperfine splitting constants. Nonempirical polarity scales for aprotic and hydroxylic solvents. J Phys Chem 86:3189; (c) Owenius R, Engstrom M, Lindgren M, Huber M (2001) Influence of solvent polarity and hydrogen bonding on the EPR parameters of a nitroxide spin label studied by 9-GHz and 95-GHz EPR spectroscopy and DFT calculations. J Phys Chem A 105:10967–10977
35. Bleifuss G, Kolberg M, Potsch S, Hofbauer W, Bittl R, Lubitz W, Graslund A, Lassmann G, Lendzian F (2001) Tryptophan and tyrosine radicals in ribonucleotide reductase: a comparative high-field EPR study at 94 GHz. Biochemistry 40:15362–15368
36. Pötsch S, Lendzian F, Ingemarson R, Hörnberg A, Thelander L, Lubitz W, Lassmann G, Gräslund A (1999) The iron-oxygen reconstitution reaction in protein R2-Tyr-177 mutants of mouse ribonucleotide reductase: EPR and electron nuclear double resonance studies on a new transient tryptophan radical. J Biol Chem 274:17696–17704
37. Miller JE, Gradinaru C, Crane BC, Di Bilio AJ, Wehbi WA, Un S, Winkler JR, Gray HB (2003) Spectroscopy and reactivity of a photogenerated tryptophan radical in a structurally defined protein environment. J Am Chem Soc 125:14220–14221
38. Pelletier H, Kraut J (1992) Crystal structure of a complex between electron transfer partners, cytochrome c peroxidase and cytochrome c. Science 258:1748–1755
39. Barrows TP, Bhaskar B, Thomas LP (2004) Electrostatic control of the tryptophan radical in cytochrome c peroxidase. Biochemistry 43:8826–8834

40. Pogni R, Baratto MC, Teutloff C, Giansanti S, Ruiz-Duenas FJ, Choinowski T, Piontek K, Martinez AT, Lendzian F, Basosi R (2006) A tryptophan neutral radical in the oxidized state of versatile peroxidase from Pleurotus eryngii: a combined multifrequency EPR and density functional theory study. J Biol Chem 281:9517–9526
41. Pogni R, Teutloff C, Lendzian F, Basosi R (2007) Tryptophan radicals as reaction intermediates in versatile peroxidases: multifrequency EPR, ENDOR and density functional theory studies. Appl Magn Reson 31:509–526
42. Perez-Boada M, Ruiz-Duenas FJ, Pogni R, Basosi R, Choinowski T, Martinez MJ, Piontek K, Martinez AT (2005) Versatile peroxidase oxidation of high redox potential aromatic compounds: site-directed mutagenesis, spectroscopic and crystallographic investigation of three long-range electron transfer pathways. J Mol Biol 354:385–402
43. Senn HM, Thiel W (2009) QM/MM methods for biomolecular systems. Angew Chem Int Ed 48:1198
44. Bernini C, Pogni R, Ruiz-Duenas FJ, Martinez AT, Basosi R, Sinicropi A (2011) EPR parameters of amino acid radicals in P. eryngii versatile peroxidase and its W164Y variant computed at the QM/MM level. Phys Chem Chem Phys 13:5078–5098
45. Phillips JC, Braun R, Wang W, Gumbart J, Tajkhorshid E, Villa E, Chipot C, Skeel RD, Kale L (2005) Scalable molecular dynamics with NAMD. J Comput Chem 26:1781
46. MacKerell AD Jr, Bashford D, Bellott M, Dunbrack RL Jr, Evanseck JD, Field MJ, Fischer S, Gao J, Guo H, Ha S, Joseph-McCarthy D, Kuchnir L, Kuczera K, Lau FTK, Mattos C, Michnick S, Ngo T, Nguyen DT, Prodhom B, Reiher III WE, Roux B, Schlenkrich M, Smith JC, Stote R, Straub J, Watanabe M, Wiórkiewicz-Kuczera J, Yin D, Karplus M (1998) All-atom empirical potential for molecular modeling and dynamics studies of proteins. J Phys Chem B 102:3586–3616
47. Neese F (2009) ORCA, an ab initio, density functional and semi-empirical program package, University of Bonn, Germany, version 2.7
48. Connor HD, Bradley ES, Carolyn M, Herbert JS Jr, Mason RP (2008) L-tryptophan radical cation electron spin resonance studies: connecting solution-derived hyperfine coupling constants with protein spectral interpretations. J Am Chem Soc 130:6381–6387

Chapter 7
Ab Initio and Density Functional Calculations of Electronic g-Tensors for Organic Radicals

Martin Kaupp

Abstract Recent development and validation of quantum chemical methods for the calculation of electronic g-tensors is reviewed. The emphasis is on ab initio and density functional methods, whereas semi-empirical methods are covered only briefly. Methodological differences and the relative performance of various approaches are discussed critically, in particular regarding the treatment of spin-orbit coupling and of electron correlation. First applications to biologically relevant radicals are reviewed. Examples range from phenoxyl radicals via semiquinone radical anions to more demanding amino acid radicals.

7.1 Introduction

While hyperfine coupling tensors provide information about the detailed interactions between electronic spin density and certain nuclei within a given radical, the electronic g-tensor is a property of the entire molecule. It reflects the general spin density distribution and often is characteristically influenced by certain bonding features, and by interactions with the environment, e.g. in a protein binding site or in the cavities of a zeolite. It thus provides important spectroscopic information that may help in characterizing paramagnetic species in solids [1, 2].

In routine X-band (9 GHz) EPR of organic radicals, it is difficult to resolve accurately the individual components of the g-tensor, unless single-crystal data are available. The appearance of the spectra is usually dominated by partly resolved hyperfine interactions. Increased spin-orbit interactions lead to a larger spread of the tensor and thus allow closer analysis at low magnetic fields only when significant spin density is located onto heavier atoms, or when very low-lying

M. Kaupp (✉)
Institut für Chemie, Theoretische Chemie, Technische Universität Berlin, Sekr. C 7, Strasse des 17. Juni 135, D-10623 Berlin, Germany
e-mail: martin.kaupp@tu-berlin.de

A. Lund and M. Shiotani (eds.), *EPR of Free Radicals in Solids I*, Progress in Theoretical Chemistry and Physics 24, DOI 10.1007/978-94-007-4893-4_7,

excited states exist. During the past 10 years, however, the development of high-field high-frequency EPR spectroscopy (HF-EPR) has provided an increasing amount of accurate g-tensors of organic radicals, in particular regarding species of biological relevance [3–5]. At higher magnetic fields, the g-tensor anisotropy frequently dominates the solid-state spectra and may thus be resolved.

The g-tensors measured may hold key information about structure and bonding of radicals, and on their specific environment. Due to the relatively complicated nature of the g-tensor, its analysis by quantum chemical means is indispensable if we want to relate it to structure and bonding. Detailed models to rationalize the measured g-tensors have been developed early on in EPR history, for transition metal complexes [6], and for organic π-radicals [7, 8] (cf. below). Given the improved spectral information available from HF-EPR experiments, it has become increasingly desirable to be able to calculate g-tensors more quantitatively. Significantly enhanced interest in g-tensors of organic radicals by EPR spectroscopists, combined with improvements in reliable quantum chemical programs and computer hardware, have contributed to a tremendous development in quantitative calculation.

This chapter focusses mainly on this progress since the mid 1990s on the side of ab initio and density functional methods. Previous semi-empirical approaches will be touched upon relatively briefly. Compared to the initial edition of this chapter 2003, we consider further methodological developments regarding better treatments of electron correlation, refined spin-orbit operators, new density functionals, treatments of solvent effects and molecular dynamics, as well as extensions to calculations on extended systems using periodic boundary conditions. We have also included some more recent application examples, for example on more difficult types of amino acid radicals.

Additional reviews of material related to this chapter have appeared since its 2003 edition. A 2004 book on the quantum-chemical calculation of NMR and EPR parameters [9] contains several chapters related to g-tensors [10]. Another book chapter by Cimino et al. discusses various methodological aspects of g-tensor calculations, in particular regarding an integrated approach to include dynamical effects at various time scales (see below), and applications mainly to nitroxide spin labels [11]. Both g- and hyperfine tensor calculations on organic radicals have been reviewed in Ref. [12].

7.2 The Hamiltonian

The link between the quantum chemical treatment and the actual EPR spectrum is provided by the effective spin Hamiltonian approach. In particular, the g-tensor parameterizes the Zeeman interaction between external magnetic field **B** and an effective spin **S** of the molecule [2]:

$$\hat{\mathbf{H}}_{spin} = \mu_B \mathbf{B} \mathbf{g} \mathbf{S}, \tag{7.1}$$

(where $\mu_B = e\hbar/2m_e$ is the Bohr magneton). Actually, the EPR experiment does not measure the unsymmetric tensor $\boldsymbol{g}$, but the diagonal elements of the symmetric tensor $\boldsymbol{G} = \boldsymbol{g}.\boldsymbol{g}^{\mathbf{T}}$. We will in the following concentrate on spatially non-degenerate Kramers doublet states, although the perturbation theoretical treatment is also applicable to higher spin multiplicities (see below). Other spin-Hamiltonian terms like zero-field splittings or $\Delta M_S = \pm 2$ transitions will not be covered here [1, 6].

It is necessary to identify in our quantum chemical treatment those terms that are represented by the spin Hamiltonian for the Zeeman interaction. The g-tensor is dominated by spin-orbit (SO) coupling and is thus intrinsically a relativistic property. Therefore, the relativistic four-component Dirac equation in the presence of an external magnetic field provides a suitable starting point for the derivation of the relevant terms in the Hamiltonian [2, 7, 13]. Initially, all practical calculations of g-tensors have used either (a) nonrelativistic (or scalar relativistic) wave functions, with SO coupling and other relativistic terms, as well as the influence of the external magnetic field, added by perturbation theory ("one-component approach"), or (b) "two-component methods", in which SO coupling is treated variationally, but the positronic degrees of freedom (which are also described by the Dirac equation) have been eliminated. More recently, also fully relativistic four-component Dirac-Kohn-Sham approaches have been added to the arsenal of methods.

In this review, we focus on organic radicals that contain only relatively light atoms. Then a perturbation theoretical treatment of SO coupling (one-component approach) is expected to be sufficient in most cases, and the following brief exposition of the theoretical background of quantum chemical g-tensor calculations will concentrate on the perturbation approach, based on the Breit-Pauli (BP) Hamiltonian (we will, however, discuss below the cysteine radical as an example, where the leading-order perturbational SO treatment is insufficient). The derivation of the terms that occur in the BP Hamiltonian of an open-shell system in the presence of an external magnetic field, starting from the Dirac equation, may be found, e.g., in the book of Harriman [2] and will not be described here in detail. Briefly, the derivation requires transformation from the four-component Dirac equation to two- or one-component form, e.g. by the free-particle Foldy-Wouthuysen transformation [2]. Due to singularities in this transformation for systems in the presence of a Coulomb potential (electron–electron repulsion and electron-nucleus attraction), application of the BP Hamiltonian is only appropriate to first order in SO coupling (i.e. in a one-component approach with perturbational treatment of SO coupling), and for compounds containing only relatively light atoms. However, regularized transformations like the "zero-order regular approximation" (ZORA) method [14] or the Douglas-Kroll-Hess (DKH) transformation [15] are available that allow a variational, two-component treatment. A two-component DFT-ZORA implementation of g-tensor calculations is already in wide use (see below; cf. Ref. [16] for more details). Interestingly, the earlier derivation by Harriman [2] is closely related to the ZORA method [16]. The DKH-Hamiltonian is also available for DFT calculations of g-tensors [17, 18], and most recently it has been demonstrated that even fully relativistic DFT approaches may be implemented efficiently for systems of appreciable size [19, 20].

We will in the following refer to g-shift tensors, $\Delta \boldsymbol{g}$, defined by

$$\boldsymbol{g} = g_e 1 + \Delta \boldsymbol{g} \tag{7.2}$$

i.e. deviations from the free-electron value, $g_e = 2.002319$. The g-shifts will often be given in ppm, i.e. in units of 10^{-6}. Restricting the Breit-Pauli Hamiltonian to those terms that are linear or bilinear in **B** and **S**, and employing Rayleigh-Schrödinger perturbation theory up to second order, we end up with the relevant terms contributing to $\Delta \boldsymbol{g}$ [2]:

$$\Delta \boldsymbol{g} = \Delta \boldsymbol{g}_{so/oz} + \Delta \boldsymbol{g}_{GC} + \Delta \boldsymbol{g}_{RMC} \tag{7.3}$$

The "paramagnetic" second-order spin-orbit/orbital Zeeman cross term, $\Delta \boldsymbol{g}_{SO/OZ}$ (Eq. 7.4), dominates the g-shift tensor, except for the smallest Δg-values. It has already been introduced in Pryce's classical perturbation treatment [21] and arises from the joint action of the external magnetic field (orbital Zeeman operator, Eq. 7.5) and the SO operator (BP SO Hamiltonian in Eq. 7.6) in second-order perturbation theory [2, 22]:

$$\Delta g_{SO/OZ,uv} = \frac{g_e \alpha^2}{2S} \left[\sum_n \frac{\left\langle \Psi_0^{(0)} \middle| H_{SO,v} \middle| \Psi_n^{(0)} \right\rangle \left\langle \Psi_n^{(0)} \middle| H_{OZ} \middle| \Psi_0^{(0)} \right\rangle}{E_0^{(0)} - E_n^{(0)}} + c.c \right] \tag{7.4}$$

$$H_{OZ,u} = -\sum_i \mathbf{l}_{iO,u}, \tag{7.5}$$

$$H_{SO,v} = \sum_i \left(\sum_N \frac{Z_N \mathbf{L}_{iNv}}{r_{iN}^3} - \sum_{j \neq i} \frac{L_{jv}^i}{r_{ij}^3} - 2 \sum_{j \neq i} \frac{\mathbf{L}_{iv}^j}{r_{ij}^3} \right) s_i \tag{7.6}$$

In Eqs. 7.4, 7.5, and 7.6 (which are in atomic units), α denotes the fine structure constant, u and v are Cartesian coordinates, $\Psi_o^{(0)}$ the unperturbed ground-state wavefunction, and $\Psi_n^{(0)}$ the unperturbed wavefunction of the n'th excited state (with eigenenergies $E_o^{(0)}$ and $E_n^{(0)}$, respectively). $\mathbf{l}_{io}$ represents orbital angular momentum, and S is the magnitude of total spin of the molecule (it has been introduced to make Eqs. 7.4, 7.7, and 7.8 suitable also for high-spin systems [23, 24]). Within the SO operator H_{SO} (Eq. 7.6), Z_N is the charge of nucleus N, $\mathbf{L}_{iN}$ the angular momentum of electron i relative to the position of nucleus N, L_j^i the angular momentum of electron i relative to the position of electron j, $\mathbf{r}_{iN}$ and $\mathbf{r}_{ij}$ are relative electron-nucleus and electron–electron position vectors, and $\boldsymbol{s}_\mathbf{i}$ is a spin operator for electron i. The first term in Eq. 7.6 is the one-electron SO operator, in which the interaction between spin and angular momentum of an electron is mediated by the potential due to the charge of the nuclei. The second term is the two-electron SO operator (largely due to the screening of nuclear charge around nucleus N by the core electrons), and the third term is the so-called spin-other-orbit (SOO) term (see Sect. 7.3.3).

The "diamagnetic" spin-Zeeman gauge correction terms, $\Delta \boldsymbol{g}_{GC}$ (Eq. 7.7), reflect the magnetic-field dependence of the SO operators. They have been considered first by Stone to obtain a properly gauge-invariant theory of the g-tensor [7], but they are usually much smaller than the $\Delta \boldsymbol{g}_{SO/OZ}$ contributions (claims that the SOO part of $\Delta \boldsymbol{g}_{GC}$ could be larger than previously assumed were based on a rather approximate treatment [25] and have not been confirmed so far). In most implementations, the two-electron contributions to $\Delta \boldsymbol{g}_{GC}$ are either neglected or taken into account only approximately.

$$\Delta g_{GC,uv} = -\frac{\alpha^2 g_e}{4S} \left\langle \Psi_o^{(0)} \right| \left(\sum_N Z_N \sum_i \frac{\mathbf{r}_{iN} \cdot \mathbf{r}_i \delta_{uv} - r_{iNu} r_{iv}}{r_{iN}^3} \right) s_i + \left(\sum_{ij} \frac{\mathbf{r}_{ij} \cdot (2\mathbf{r}_j - \mathbf{r}_i)\delta_{uv} - (2\mathbf{r}_j - \mathbf{r}_i)_v (\mathbf{r}_{ij})_u}{r_{ij}^3} \right) s_i \left| \Psi_o^{(0)} \right\rangle \tag{7.7}$$

Finally, the relativistic mass correction to the spin-Zeeman term, $\Delta \boldsymbol{g}_{RMC}$ (Eq. 7.8), arises from field-dependent kinematic relativistic effects and provides another relatively small, isotropic contribution to the Δg-value [2, 26]:

$$\Delta g_{RMC-SZ,uv} = -\frac{\alpha^2 g_e}{2S} \delta_{uv} \left\langle \Psi_o^{(0)} \right| \sum_i \left(-\frac{1}{2} \nabla_i^2 \right) s_i \left| \Psi_o^{(0)} \right\rangle \tag{7.8}$$

Without this contribution, it would be impossible to explain the frequently negative Δg_{zz} contributions in organic π-radicals [26]. $\Delta \boldsymbol{g}_{GC}$ and $\Delta \boldsymbol{g}_{RMC}$ may be calculated in a relatively straightforward manner as expectation values of the unperturbed ground state wave function. Note that, in contrast to a two-component approach, in the perturbation theoretical one-component treatment S is still considered to be a good quantum number.

7.3 Quantum Chemical Approaches

While the calculation of hyperfine tensors does already have a much longer history of first-principles theoretical treatments [27], the massive development of methods to calculate electronic g-tensors by ab initio quantum chemistry, and by modern approaches of density-functional theory (DFT), started only in the mid 1990s (earlier, approximate DFT implementations have already been reported in the 1980s [28], and very early ab initio calculations date back even further [29]). In spite of this relatively short period of time, the variety of alternative approaches available is already appreciable and may appear confusing to the non-expert interested in applications of such quantum chemical calculations. We will in the following attempt to mark the main distinguishing features of various methods. Before turning to ab initio methods, we briefly summarize the main points of the earlier semiempirical approaches.

7.3.1 Semi-empirical Calculations

Semiempirical MO treatments use the orbitals and orbital energies obtained in approximate semiempirical calculations (originally at the simple Hückel level [7, 8], later at extended-Hückel [30], CNDO [31], INDO [26, 32–38] or NDDO [39–41] levels of approximation) to evaluate the dominant $\Delta \boldsymbol{g}_{SO/OZ}$ terms in Eq. 7.4. At the simplest level, the energy denominator was simply replaced by the energy differences between occupied and virtual MOs. This would correspond to an uncoupled Hartree-Fock approach. However, Hartree-Fock orbital energies (also in semi-empirical variants) are not well suited to describe excited states, as the virtual MOs are too diffuse and experience shielding due to all occupied MOs. As a next step, Coulomb-shift terms have been added (this corresponds to the use of configuration-state energies rather than orbital energies) [32]. Due to the presence of Hartree-Fock exchange terms at CNDO, INDO, or NDDO levels, a full variational perturbation theory treatment would require the iterative solution of the coupled-perturbed Hartree-Fock equations (see below).

Further approximations were often applied in the semi-empirical approaches. In particular, the matrix elements in Eq. 7.4 were usually restricted to their one-center contributions. While this appears to be a reasonable approximation for the matrix elements of the very short-ranged SO operator (Stone's first approximation [7]), the OZ operator is less localized, and the one-center approximation is doubtful in this case (Stone's second approximation [7]). Later calculations thus dropped the second approximation. It should be noted, however, that the minimal basis sets employed in semi-empirical MO approaches, and the often ill-suited nature of the virtual MOs, do already severely limit the accuracy achievable in such calculations. A further potential source of uncertainty stems from the semiempirical, effective one-electron SO operators employed (but see below [29]).

7.3.2 Ab Initio Approaches

Early Hartree-Fock calculations of g-tensors by Moores and McWeeny [29] still suffered from the small basis sets and limited wave functions available at the time (see also Ref. [32]). The first modern ab initio calculations are due to Lushington et al., who developed restricted-open-shell Hartree-Fock (ROHF) [42] and multi-reference configuration-interaction (MRCI) approaches [22, 43]. They used explicitly a sum-over-states (SOS) approach (over a limited number of states) to calculate the $\Delta g_{SO/OZ}$ terms of Eq. 7.4, and they included the other two terms in Eq. 7.3 as well. The lack of electron correlation and spin polarization in the ROHF calculations is corrected for at the MRCI level, where the ground-state wavefunction consists already of a superposition of multiple configuration-state functions. Lushington et al. calculated explicitly all matrix elements of the full Breit-Pauli SO Hamiltonian (Eq. 7.6). This, and the effort involved in the configuration-interaction approach,

limited the initial calculations to small molecules, providing benchmark results of high accuracy (cf. Sect. 7.4), provided the SOS expansion is sufficiently long. More recently, SOS-based MRCI calculations were extended to medium-sized systems by a more efficient implementation that uses also approximate meanfield spin-orbit operators [44].

Alternative approaches are based on linear-response theory or, equivalently, on untruncated SOS. Initial linear-response approaches at the ROHF and multi-configuration self-consistent field (MCSCF) levels of ab initio theory are due to Vahtras et al. [45]. The initial implementation calculated explicitly the full set of one- and two-electron integrals over the Breit-Pauli SO Hamiltonian. Meanwhile, the more economic atomic-meanfield approximation (AMFI, cf. below) has been implemented into the code [46]. Perturbation theoretical treatments of dynamical electron correlation within the CASPT2 ansatz, and coupled-cluster wavefunctions were initially reported for doublet states [47]. MRCI calculations for triplet states were reported in Ref. [48]. More recently, derivative theory for g-tensors has also been implemented up to MRCI [49] and coupled-cluster [50] levels by Neese, Gauss and coworkers, in the latter case even using distributed gauge origins (see below).

The advantage of the ab initio treatments is that their accuracy regarding electron correlation may in principle be improved systematically towards the exact result (for a given Hamiltonian and level of perturbation theory), by extending the one-particle basis set and the number of configurations included in the CI or MCSCF treatment. In spite of remarkable improvements in efficiency over the last few years, these ab initio approaches are still most suitable for somewhat smaller molecules, and apart from selected applications serve best as methods to benchmark more economic, approximate treatments like those based on DFT, which have become the workhorse for g-tensor calculations of organic radicals.

7.3.3 Approaches Based on Density Functional Theory

DFT implicitly includes electron-correlation effects at much lower cost than the abovementioned post-Hartree-Fock methods [51]. A principal disadvantage of DFT is the lack of a way for systematic improvement towards an exact limit, as the exact exchange-correlation functional is not known. DFT calculations of properties like g-tensors thus require careful validation for a given functional. A further general, as yet unsolved question in DFT calculations of magnetic response properties is the dependence of the exchange-correlation potential on the paramagnetic currents induced by the magnetic field. The problems related to the current dependence have been discussed in detail in the field of NMR chemical shift calculations [52], but the problem applies equally to calculations of g-tensors. As appropriate and reliable current-density functionals are so far lacking, all implementations presently neglect the current dependence. Some open questions pertain also to the proper treatment of SO coupling within a DFT framework (see below). In spite of a significant

number of open basic theoretical questions, DFT methods have become increasingly important in g-tensor calculations. This is mainly due to the overall high quality of the results combined with computational efficiency.

One of the two first modern DFT approaches (see below; cf. Ref. [28] for more approximate, older implementations at the X_α level) has been reported by van Lenthe et al. [16] and is implemented in the widely used ADF code [53]. It differs fundamentally from most of the other methods discussed below, as it is a two-component method. The zero-order regular approximation (ZORA [14]) is employed, a regularized version of the elimination-of-the-small-component-method for the transformation of the Dirac equation. The main advantage of the approach is the variational treatment of SO coupling which is important mostly for compounds of heavier elements, or for systems with very close-lying excited states. A limitation of that implementation has been the use of a spin-restricted treatment, due to the difficulty of describing spin polarization within a two-component DFT approach. The approximate SO operators used are a further potential source of error (cf. discussion below). The two-component DKH-DFT approach of Neyman et al. [17] also has been based on a spin-restricted formalism and approximate SO operators. More recently, two-component g-tensor calculations, based on a non-collinear spin-density functional DKH-DFT approach, were shown to account well for spin polarization within a two-component framework and to thus solve this previous dilemma [18]. The implementation uses AMFI SO operators at DKH level and thus can account for the SOO contributions as well. Meanwhile, such non-collinear DFT calculations of g-tensors can even be performed efficiently at four-component Dirac-Kohn-Sham level for sizeable molecules [19] (in particular also transition-metal complexes [20]), so far still with some limitations regarding the SO operators.

The first modern one-component DFT approach reported by Schreckenbach and Ziegler (SZ) [54] in the ADF code was followed by two alternative but related molecular DFT g-tensor implementations, by us, initially in the deMon [55], then in the ReSpect code [56], and by Neese in the ORCA code [57] (the more recent implementation in the commercial Gaussian program is based on Neese's initial derivation, using semi-empirical SO operators). These three approaches do all employ second-order perturbation theory based on unrestricted Kohn-Sham calculations. Differences between these implementations are mainly in the SO operators used in Eq. 7.4 (see below). A further linear response implementation at ZORA level is due to Autschbach and coworkers [58]. We mention also approaches that include second-order SO effects within the framework of quadratic response theory [59].

Due to the presence of an external magnetic field in the perturbation expressions (cf. Eq. 7.1), g-tensor calculations are in principle subject to the so-called "gauge problem", that has hampered NMR chemical shift calculations for a long time. In calculations with a finite basis set, the result depends on the choice of gauge origin of the magnetic vector potential. In the field of NMR chemical shifts, distributed-gauge methods like gauge-including-atomic-orbitals (GIAO [60]) or individual-gauges-for-localized-orbitals (IGLO [61]) have been developed, which allow the gauge- and basis-set-dependence to be minimized. These and other related approaches have

also been extended to g-tensor calculations [16, 54, 55, 62, 65, 68]. Fortunately, g-tensors are much less gauge-dependent than chemical shifts. Thus, calculations with a common gauge origin, e.g. at the center of charge or center of nuclear charges of the molecule, often do already provide sufficiently accurate results. Exceptions occur when the g-shifts are very small, and/or SO contributions from atoms in different parts of the molecule are of similar magnitude. Examples will be discussed further below.

A very notable recent development is the implementation of codes for DFT g-tensor calculations on extended systems using periodic boundary conditions, allowing calculations on solids or surfaces. The first implementation by Pickard and Mauri [62] used augmented plane wave basis sets and the "gauge-including projector augmented wave method" (GIPAW) to deal with the gauge problem (implemented in the PARATEC code [63]). A second PAW-based approach with a somewhat different treatment of the gauge (following Sebastiani and Parrinello [64]) is due to Declerck et al. [65], using the CPMD code [66]. The projector augmented wave method allows to correct for deficiencies (present in spite of the fact that the g-tensor is in principle a valence property) of the underlying pseudopotential approximation. An even better starting point is the intrinsically all-electron "Gaussian augmented-plane-wave ansatz" of Lippert et al. [67], which has recently been extended to g-tensor calculations by Weber et al. [68] within the CP2K code [69] (using yet another set of approaches for the gauge). Last, but not least, Kadantsev and Ziegler [70] used the solid-state version of the ADF code with a mix of Slater and numerical basis functions and GIAOs for a g-tensor implementation with periodic boundary conditions. The difference of this latter implementation compared to the others is, that it is based on the two-component ZORA ansatz of van Lenthe described above and thus includes spin-orbit coupling variationally (albeit so far only in a spin-restricted fashion).

A proper relativistic DFT treatment of SO coupling requires relativistic density functionals that include, among other things, the Breit interaction (transverse interaction), which derives from relativistic corrections to electron–electron repulsion. However, none of the existing implementations uses relativistic functionals, which introduce additional complications. The traditional DFT implementations, exemplified by those of Schreckenbach and Ziegler [54] or van Lenthe et al. [16], approximate the SO contributions in the following way: In addition to the potential due to the charge of the nuclei (one-electron SO term in Eq. 7.6), the electrons experience shielding due to the other electrons, mainly due to the core electrons (two-electron SO term in Eq. 7.6). Within Kohn-Sham theory, this shielding is represented by the relevant contributions from an approximate effective Kohn-Sham potential (Coulomb and X_α-exchange terms). The Breit interaction is not included in this treatment, and the so-called "spin-other-orbit" (SOO) terms are thus lacking. As the SOO terms are of opposite sign than the dominant one-electron SO terms, their lack leads overall to an overestimate of the SO/OZ contributions (see Sect. 7.4).

In our own implementations [55, 56], we stepped outside the conventional Kohn-Sham treatment and used three different types of approaches to the SO matrix elements: The full treatment of all one- and two-electron integrals over the full BP

SO operator (using explicitly the Kohn-Sham determinant as approximation to the wavefunction), as done in the abovementioned ab initio methods. This approach includes the SOO terms (as well as some exact-exchange-type SO contributions [56]). While the initial implementation was prohibitively expensive for larger molecules, our more recent implementation allows straightforward application also to larger systems like amino-acid radicals [71, 72]. The atomic meanfield approximation [73] (as implemented in the AMFI code [74]) replaces the explicit treatment of the integrals by integrals over a sum of effective atomic SO operators (replacing the full molecular density matrix by a superposition of one-center density matrices). This reduces the computational effort significantly relative to the full BP treatment, with very little loss of accuracy [55]. The AMFI approximation provides thus a very powerful means of treating the SO matrix elements in Eq. 7.4 (including the SOO terms) accurately for larger molecules. It has also been used successfully in many other types of applications, ranging all the way from SO-effects on NMR chemical shifts [75] to photophysical transition probabilities [76]. SO pseudopotentials (SO-ECPs) treat only the valence electrons explicitly. SO-ECPs are used in conjunction with scalar relativistic pseudopotentials inserted at the Kohn-Sham stage of the calculation [55, 77]. This approximation is well-suited for g-tensor calculations and becomes particularly useful for compounds of heavy elements [55]. We will not discuss it further here.

Neese and coworkers used initially [57] semi-empirical, effective one-electron SO operators (by introducing effective nuclear charges due to Koseki et al. [78], as done in all semi-empirical and early ab initio or DFT treatments) in their ORCA program. This is still the only possibility in the Gaussian program. More recently [79], Neese implemented a "spin-orbit meanfield" (SOMF) approximation intermediate between AMFI and the full treatment, which is based on a mean-field approach (using in practice a resolution of the identity) but without the one-center approximation of AMFI. Pickard and Mauri apparently include an approximate treatment of the SOO terms [62]. However, the data reported as yet are very close to those of SZ, suggesting that the SOO contributions are underestimated. Yet another approximation to the SOO terms is currently used in the GAPW implementation of Weber et al. [68].

All initial DFT implementations used the local density approximation (LDA) or the generalized gradient approximation (GGA) [51]. For these "pure" DFT approaches, the local exchange operators and lack of a current dependence of the functional (see above) make any coupling terms in the second-order perturbation theory treatment vanish. We thus end up with an uncoupled set of equations (uncoupled DFT approach, UDFT [80]), in which the energy denominator in Eq. 7.4 may be replaced by the occupied and virtual Kohn-Sham orbital energies (and the sum over excited states is replaced by a double sum over all occupied and virtual orbitals). Fortunately, the Kohn-Sham orbitals include electron correlation effects implicitly. This is also reflected in the orbital energies. The UDFT approach is therefore a much better approximation than one might expect from what was said further above about the poor quality of uncoupled Hartree-Fock methods. In particular, the virtual Kohn-Sham MOs experience the field of only n-1 electrons

and are thus a much better basis for perturbation theory (and for the description of electronically excited states) than are virtual Hartree-Fock MOs [51, 80, 81]. The one-component DFT perturbation approach with LDA or GGA functionals is thus particularly easy to implement, computationally very efficient, and surprisingly accurate (see Sect. 7.4). This is a major reason for its successful application to larger molecules.

The UDFT approach with currently available LDA or GGA functionals is less successful in the calculation of g-tensors for transition metal complexes [54, 55]. Therefore, our and Neese's implementations (subsequently the commercial Gaussian implementation, and most recently the ADF implementation) were extended to allow the use of so-called hybrid functionals that include a part of exact Hartree-Fock exchange [56, 57]. This "exact-exchange mixing" requires the iterative solution of coupled-perturbed Kohn-Sham (CPKS) equations. Still more recently, we have demonstrated that a corresponding CPKS scheme may also be derived and implemented for local hybrid functionals with position-dependent exact-exchange admixture [82]. While global or local hybrid functionals depending on the occupied orbitals have indeed been shown to provide a possibility to improve the performance for transition metal systems, they do not appear to lead to significantly improved g-tensors for organic radicals (albeit in a recent survey, the B3LYP hybrid has been favored over some other functionals in calculations on small radicals [50]). So-called meta-GGA functionals give no significant improvements for transition-metal complexes [83] and only slightly smaller g-shifts for main-group radicals compared to GGA functionals [83]. We will in the following restrict our comparisons to the simple BP86 GGA functional, keeping in mind the relatively minor variations of the quality of computed g-tensors for organic radicals with the functional.

An active recent area of development by us and others has been the inclusion of solvent and dynamical effects in g-tensor calculations. In particular the dynamics of solvation on EPR-parameters have been in the focus of interest, by combining ab initio molecular dynamics (MD) simulations with calculations of g- and hyperfine tensors for snapshots along an MD trajectory [84, 85]. Examples include in particular semiquinone radical anions and nitroxide spin labels in aqueous solution. While the ps time frame available in the ab initio MD does not allow slower motions of the solute to be included, it has been shown that a more realistic description of solvation in protic solvents than with continuum models (cf. below) is possible, but of course at the price of substantial computational effort. Apart from solvation, also environmental effects in solids on radical g-tensors have been evaluated in this way [86]. To include also dynamical effects on longer time scales, Barone and coworkers have proposed an integrated approach in which regular (ab initio) MD is used for the fast motions, whereas more phenomenological, stochastic descriptions based on the solution of the stochastic Liouville equation are used for the slower motions [87, 88] (see also review in Ref. [11]).

A less costly way to include solvation are polarizable continuum models (PCM), which assume an isotropic polarizable solvent environment, most suitable for systems with little specific and dominant long-range dielectric solvation. In the field of g-tensor calculations, we initiated this by comparing PCM and specific cluster

solvation, as well as combinations of the two, for benzosemiquinone radical anion in different solvents [89]. More refined implementations that account for coupling terms with the PCM solvation in the linear response approach (needed particularly for hybrid DFT calculations and/or GIAOs) have also been reported [90, 91]. The latter implementation by Neese and coworkers interestingly extends beyond PCM-type models by utilizing also Klamt's COSMO-RS approach [92]. This provides a means to model even protic solvents without explicit supermolecular cluster or periodic-boundary-condition approaches. Yet another possibility to include environmental effects are mixed quantum-mechanics/molecular-mechanics (QM/MM) approaches. Regarding g-tensor calculations, in the simplest case this requires just the inclusion of point charges for the (solvent, protein, ...) environment, often following a QM/MM structure optimization [93]. A yet more realistic description may require multipole expansions and polarizability terms [94].

7.4 Performance of Ab Initio and DFT Methods, Validation Studies

Initial validation studies of ab initio methods focussed on small main group radicals, for which either gas-phase microwave data or EPR spectra in inert matrices were available. This is expected to minimize environmental effects and to allow the evaluation of the intrinsic accuracy of the quantum chemical methods. The first studies were carried out at ROHF and MRCI levels by Lushington et al. [22, 42, 43]. Subsequently developed methods have often been gauged initially for similar sets of small radicals. Table 7.1 shows a collection of results for some of these systems with Lushington's MRCI results and a range of different DFT methods (all using the BP86 GGA functional for better comparison). The comparison has been taken from the recent work of Neese [57], except for a few corrections, and for missing entries with our own approach (AMFI), which we have added. We focus only on methods that incorporate electron correlation. Results at the overall less reliable Hartree-Fock level of theory may be found in the comparative study of Neese [57].

It should be noted that only part of the experimental data are from gas-phase microwave measurements, where $\Delta g_{\perp}$ is estimated from spin-rotation constants, via Curl's equation [95]. The other data are matrix-isolation EPR results. In the latter case, some of the smaller values (in particular $\Delta g_{||}$ for some linear radicals, and some values for charged species) may be influenced significantly by environmental effects and should thus be viewed with caution. In general, very small values also tend to have significant relative contributions from first-order terms. We disregard in the following the $\Delta g_{||}$ values for linear radicals. But even the more reliable data may easily exhibit error ranges of ± 500 ppm.

Keeping these restrictions in the experimental data base in mind, it is clear that the MRCI approach provides rather accurate results, except for Δg_x in H_2CO^+, where it differs both from experiment and from all DFT methods. As ROHF and UHF calculations give ca. 3,000 ppm for this value [57], it appears possible that the

Table 7.1 Comparison of different DFT approaches for the calculation of g-shift components (in ppm) for small radicals (BP86-UDFT results)[a]

Molecule		Expt.	AMFI	SZ	Neese	ZORA	MRCI
CO^+	$\Delta g_\perp$	−2,400[b]	−2,458	−3,129	−2,622	−3,464	−2,674
CN	$\Delta g_\perp$	−2,000[b]	−1,939	−2,514	−2,033	−2,701	
BO	$\Delta g_\perp$	−1,700[b]	−1,796	−2,298	−1,924	−2,455	−1,899
BS	$\Delta g_\perp$	−8,100, −8,900	−9,043	−9,974	−9,928	−11,743	−8,449
MgF	$\Delta g_\perp$	−1,300	−1,869	−2,178	−2,433	−1,967	−1,809
AlO	$\Delta g_\perp$	−1,800 to −1,900[b]	−1,991	−222	−2,920	855	−2,284
H_2O^+[c]	Δg_x	200	−142	103	−185	−780	−292
	Δg_y	18,800	10,205	13,824	11,475	46,527	16,019
	Δg_z	4,800	3,702	5,126	4,412	7,765	4,217
HCO[c]	Δg_x	1,500	2,275	2,749	2,183	3,095	
	Δg_y	0	−224	−270	−307	−175	
	Δg_z	−7,500	−7,476	−9,468	−7,891	−12,196	
NF_2[c]	Δg_x	−100	−617	−738	−636	−318	
	Δg_y	6,200	6,288	7,619	6,970	10,576	
	Δg_z	2,800	3,928	4,678	4,264	6,254	
NO_2[c]	Δg_x	3,900	3,400	4,158	3,281	5,000	3,806
	Δg_y	−11,300	−11,229	−13,717	−11,270	−16,000	−10,322
	Δg_z	−300	−688	−760	−706	−600	−235
O_2H[c]	Δg_x	−800	−221		−305	−2150	
	Δg_y	39,720	22,629		24,300	85,158	
	Δg_z	5,580	4,879		5,120	5,127	
CO_2^-[c]	Δg_x	700	1,086	1,522	490	2,236	
	Δg_y	−4,800	−5,420	−7,210	−5,151	−8,056	
	Δg_z	−500	−769	−803	−969	−624	
O_3^-[c]	Δg_x	200, 1,300	−429	−554	−476	−439	
	Δg_y	16,400, 14,700	15,312	19,380	15,323	22,475	
	Δg_z	10,000, 9,700	8,552	10,542	8,736	12,710	
H_2CO^+[c]	Δg_x	200	62	76	18	−286	1296
	Δg_y	−800	−1,067	−1,220	−678	−1,131	−30
	Δg_z	4,600	4,837	6,231	5,507	8,046	5,510
C_3H_5[c]	Δg_x	0	−65	−115	−79	−152	
	Δg_y	400	497	769	634	854	
	Δg_z	800	603	660	731	1,023	

[a]Cf. Ref. [57] for more data and further discussions

[b]Best gas phase estimate [96]

[c]Allyl radical. For C_{2v} symmetrical triatomic radicals, g_x is perpendicular to the molecular plane, g_z is parallel to the bisector of the B-A-B angle, and g_y is in-plane tangential. The orientation for the C_s symmetrical triatomic radicals is analogous. In H_2CO^+, g_x is oriented in-plane, perpendicular to the C–O bond, g_y is parallel to the C–O bond, and g_z is out-of-plane. In C_3H_5, g_x is in-plane, perpendicular to the central C–H bond, g_x is out-of-plane, and g_z is parallel to the C–H bond

limited CI treatment in this case was not able to correct for the severe Hartree-Fock errors. More recent post-HF approaches give rather variable results for Δg_x and Δg_y [44, 50], so that more work will be needed before definite statements can be made on the reliability of theoretical and experimental values for this radical cation.

Table 7.2 Results of linear regression analyses for comparisons between theory and experiment for selected g-shift tensor components of first-row radicals[a]

	AMFI	SZ	Neese	ZORA
Intercept B[a]	−1	4	73	359
Slope A[a]	1.039	1.264	1.094	1.553
Regression coefficient	0.996	0.995	0.992	0.995
Standard deviation (in ppm)	489	603	680	808

[a] $\Delta g_{ii}(\text{calc.}) = A\ \Delta g_{ii}(\text{exp.}) + B$ (A and B in ppm). The data include the 16 presumably most reliable values: $\Delta g_{\perp}$ of CO^+, CN, BO, BS, MgF, as well as Δg_x and Δg_z of HCO, Δg_y and Δg_z of NF_2, H_2CO^+, and C_2H_5, Δg_x and Δg_y of NO_2, and Δg_y of CO_2^-. All calculations used the BP86 GGA functional and extended basis sets

In most cases, however, different post-HF approaches agree well, and we may take the MRCI data as good benchmark data to gauge the DFT results. When doing so, it becomes clear that in the majority of the relevant components, DFT results with atomic meanfield SO operators (AMFI) tend to be in reasonable agreement with MRCI or experiment, or their magnitude is slightly too large. Exceptions are Δg_y in H_2O^+, and in O_2H. In these two, somewhat unusual cases, DFT results with gradient-corrected functionals (BP86) tend to significantly underestimate the corresponding g-shift. Interestingly, local density functionals provide larger values for these systems [56, 57]. In the case of H_2O^+, this has been traced back to an unusually large dependence of the HOMO and SOMO energies on the functional, due to extremely pronounced spin polarization [56] (B3LYP results for this radical are larger than the BP86 data but lower than the LSDA data [50]).

To obtain a meaningful statistical comparison that allows us to judge the influence of the different SO operators and treatment of spin polarization, we select in the following the larger, presumably more reliable components of a number of first- and second-row radicals. We exclude H_2O^+ and O_2H, due to their exceptional behavior (cf. above). AlO is also excluded, as here the data of SZ are very different from all other DFT results, for unknown reasons. Table 7.2 shows the resulting statistical analysis of the correlation between the different DFT methods and experiment. Figure 7.1 shows the corresponding plot for the AMFI results. It should be kept in mind, that a different selection of examples could lead to somewhat larger or smaller slope or scatter, and neither the current experimental accuracy nor the current status of post-HF approaches allows a better or more detailed benchmarking at this point in time.

We argue that the AMFI SO operator is usually an excellent approximation to the full Breit-Pauli SO Hamiltonian (see further below for exceptions), and thus the remaining errors reflect the intrinsic deficiencies of the given exchange-correlation functional [55, 56]. If we thus take the AMFI data as reference DFT values, we may obtain estimates of the influence of technical differences of the other three DFT methods. Neese's initial GTO implementation differs from our method mainly in the use of semi-empirical Koseki-style SO operators [57]. The g-shifts are close to

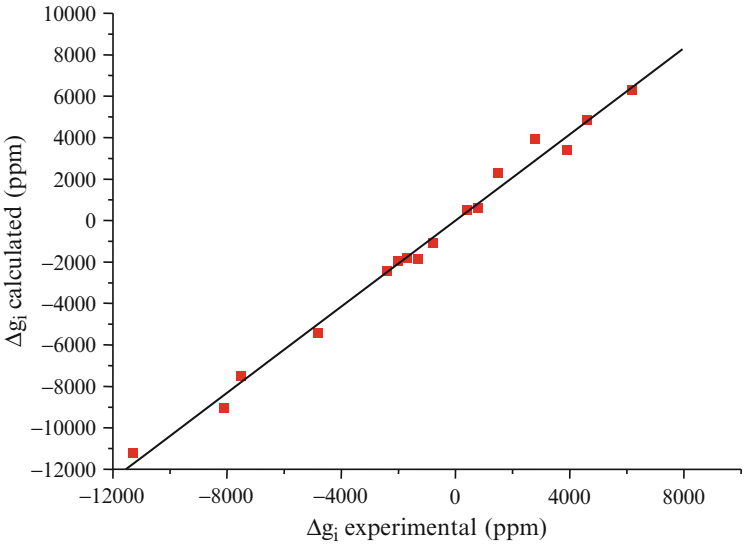

Fig. 7.1 Comparison of DFT results with AMFI SO operators for selected g-tensor components of main group radicals (UDFT-BP86 data, cf. Tables 7.1 and 7.2)

the AMFI results in most cases, with a tendency to be somewhat higher (at most a few percent). The more recent SOMF implementation (data not shown) gives values even closer to the AMFI data [79], confirming the validity of the latter (a full BPMF treatment gives very similar results, data not shown). The STO implementation of SZ [54] uses the abovementioned effective Kohn-Sham-potential approach to the two-electron SO contributions. It gives consistently ca. 25% larger g-shifts than the AMFI results, and thus somewhat inferior agreement with experiment or MRCI results for these light main group radicals (except for systems like H_2O^+ or O_3^-). About half of the discrepancy between AMFI and SZ results has been attributed to the lack of SOO contributions for the latter [55]. Another part is accounted for by exact-exchange-type SO integrals that appear in the AMFI (or full Breit-Pauli) implementation [56] but not in SZ's method. The good correlation coefficient suggests that the larger SO values are systematic. However, the relative magnitude of the different SO contributions changes for systems with atoms from other parts of the periodic table [55].

The ZORA approach is a two-component method that includes SO coupling variationally and thus differs from the other three methods [16]. However, the two-component treatment is not expected to lead to major differences for the present light-atom radicals, as SO effects are small. The ZORA method and the SZ method are both implemented in the ADF code [53]. They use the same types of STO basis sets and very similar SO operators. The major difference is the spin-restricted nature of the current ZORA implementation. This appears to lead to significantly larger g-shifts in most cases, i.e. the ZORA values typically overestimate experiment or

MRCI results by ca. 55%. One notable exception is $\Delta g_\perp$ in the MgF radical, where the ZORA result is in the same range as the AMFI or SZ data. The SOMO in MgF is a magnesium 3 s-orbital with slight $3p_z$ admixture, which polarizes the orbital away from the fluorine ligand. Spin polarization effects in this radical are known to be very small, and thus the spin-restricted approach gives close agreement with the spin-unrestricted methods. Consequently, the ZORA calculations overestimate Δg_y by more than 100% for systems like H_2O^+ and O_2H, where spin polarization is very large (cf. above). In a number of calculations, van Lenthe et al. used the one-component approach of SZ in a spin-restricted way for comparison to the ZORA calculations [16]. Then the agreement between ZORA and perturbational results was good, whereas the g-shift were generally larger than in an unrestricted treatment. This suggests that spin polarization tends to reduce g-shifts in general. This is confirmed also by recent two-component spin-polarized DKH calculations (using DKH AMFI SO operators) [18], which agree well with the one-component AMFI results in Table 7.1 and differ from the one-component results only for radicals containing heavier atoms (due to higher-order SO effects). We identify thus spin polarization and treatment of the spin-orbit matrix elements as crucial factors determining the accuracy of the computed g-anisotropy.

The above discussion used data obtained only with the BP86 GGA functional. However, available calculations with other GGA functionals gave very similar results. LDA functionals tend to provide somewhat larger g-shifts, which leads to overall inferior agreement with experiment for light main-group radicals (but to slightly improved agreement for many transition-metal complexes). The few available calculations with hybrid functionals indicate similar results as obtained at the GGA level [50]. Our first test calculations with meta-GGA functionals (which include dependencies on the Laplacian of the density or on local kinetic energy density) provided somewhat smaller g-shifts than GGA functionals [83].

Calculations on larger organic π-radicals (see also Sect. 7.5) confirm the small-radical results discussed here. UDFT calculations with GGA functionals and AMFI SO operators tend to provide good correlation with experimental data but apparently overestimate the largest g-shift components systematically by ca. 5–10% [55, 97]. Correlated ab initio data are scarce in this case and consist essentially of some MCSCF calculations on the simplest aromatic π-radicals [98–100]. As these calculations had to be limited to relatively small basis sets and active orbital spaces, they are probably not suitable as high-level benchmark data. More recent MRCI results for some organic triplet radicals are also not yet at a level, where they provide definite benchmark values [48]. DFT results thus so far have to be judged mostly against experiment. This requires usually an adequate treatment of environmental effects (hydrogen bonding, dielectric effects, etc. . . .). Moreover, low-energy vibrational or rotational motion may also have to be considered for the larger systems. Examples will be mentioned in Sect. 7.5.

Fortunately, it has been found that the basis-set requirements of DFT g-tensor calculations are moderate [54, 55]. Typically, polarized valence double-zeta basis sets do already provide quite reasonable results, and further basis-set extension gives only small effects. However, it should be noted that in aromatic π-radicals

polarization *p*-functions on the ring hydrogen atoms have been found necessary [55]. Many DFT programs improve the scaling of computational cost with system size by using auxiliary basis sets to fit the charge density (and sometimes the exchange-correlation potential). This introduces a further approximation that needs to be controlled carefully.

We should finally mention a few cases, where complications arise with the standard DFT approaches, and other measures have to be taken. The first example are thiolate-substituted phenoxyl radicals used as good models for the special cysteine-substituted tyrosyl radical in *galactose oxidase* [101]. Here it turned out that the orientation of the g-tensor components within the molecular plane depends dramatically on the position of the origin of a common gauge. This was the first example, where a more refined gauge treatment (in that case of GIAOs) was essential for the quality of the results. The large gauge dependence is due to the fact, that SO contributions from the sulfur atom of the thiolate substituent and from the phenoxyl oxygen atom are of similar magnitude, in a low-symmetry situation [101]. The second type of examples are radicals derived from glycine (like N-acetyl-glycine in a single-crystal environment [71] or protein-glycyl radicals [72]). Here the extremely small g-shift components, again with SO contributions of similar magnitude from several atoms in the molecule, also led to a large gauge dependence (now even for the magnitude of the g-shifts), and GIAOs had to be used. Here the AMFI approximation was also at its limits (it is not strictly compatible with GIAOs), and a full treatment of the BP SO Hamiltonian was preferred. Finally, the cysteine radical should be mentioned, but for different reasons: Due to a near-degeneracy of the singly occupied molecular orbital with a doubly occupied sulfur-type nonbonding MO, the leading-order perturbation treatment of SO effects turned out to be insufficient to reproduce the perpendicular components of the g-tensor correctly [102]. A third-order perturbation correction derived from a coupling between the sulfur 3p-orbitals was employed by the authors to correct for these deficiencies. A spin-polarized two-component DKH treatment provides the necessary higher-order SO terms in a more complete way [18].

7.5 Applications to Biologically Relevant Radicals

Since the 2003 edition of this chapter, where the number of application examples had been rather limited, substantially more applications have appeared. To be able to add some more recent examples to this section without extending the size of this chapter too much compared to the 2003 edition, we have deleted a few examples and shortened the description somewhat for others. In particular, we neglect work on nitroxide spin labels, as this has been reviewed recently in some detail [11]. The strong development of the field does not allow anymore a comprehensive discussion of the many other new applications within the scope of this article, and we had to make a selection. Among the persistent radicals of importance in biological electron transfer processes [103], tyrosyl radicals, and in particular semiquinone radical

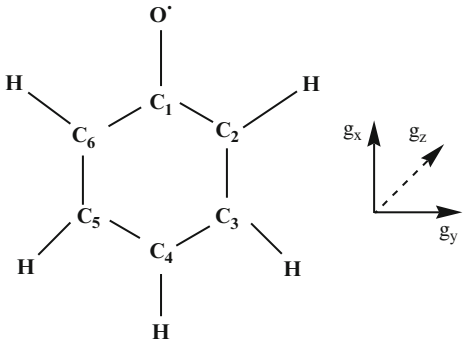

Fig. 7.2 Conventional g-tensor orientation for phenoxyl radicals, and atom labelling

anions have been the primary targets of the first g-tensor calculations by ab initio or DFT methods. Recently, the study of further amino-acid-based radicals and of some other radical intermediates in important biological reactions has also been initiated, and we report on selected examples.

7.5.1 Phenoxyl Radicals

The tyrosyl radical, a substituted phenoxyl radical derived from the amino acid tyrosine, is of central importance in many single-electron transfer processes in living organisms, from photosynthesis to cell replication. It has been investigated by HF-EPR in a considerable variety of proteins, and in vitro [39, 104, 105]. Its g-tensor and that of related phenoxyls have thus also been studied quantum chemically, initially by semi-empirical calculations [39, 105], more recently also by ab initio [98–100] and DFT [55, 106–108] methods.

Stone's perturbation model [7, 8] predicts positive Δg_x and Δg_y components for the phenoxyl radical, with the largest (Δg_x) oriented parallel to the carbonyl C–O bond (Fig. 7.2). The second largest component, Δg_y, is expected to be oriented within in the phenoxyl plane, perpendicular to the C–O bond. Essentially no $\Delta g_{SO/OZ}$ contributions are predicted for Δg_z, perpendicular to the plane (Fig. 7.2). These expectations have been confirmed experimentally [39, 104, 105], by semi-empirical MO calculations [39, 105], and by recent, more quantitative calculations [55, 98–100]. The Δg_x component is dominated by a $^2B_1 \rightarrow {}^2B_2$ SO/OZ contribution (excitation from the n(b_2)-HOMO to the $\pi(b_1)$-SOMO), whereas Δg_y arises mainly from interaction between the π^2B_1 ground state and the σ^2A_1 excited state [98].

It has been shown [98] that quantitative calculations of phenoxyl g-tensors require an adequate treatment of nondynamical electron correlation effects. Ab initio ROHF results overestimate both Δg_x and Δg_y dramatically. MCSCF calculations provided much better results, but due to their large computational requirements these could only be applied to small models like unsubstituted phenoxyl [98]. A significant dependence of the g-shift components on the C–O bond length has

also been noted. Good agreement with experiment has been obtained in UDFT calculations with AMFI SO operators and GGA functionals [55]. Typically, Δg_x is overestimated by ca. 5–10% at this computational level. This has been shown by comparison with experimental data for the tyrosyl radical (in the absence of hydrogen bonding), and for the 2,4,6-tris-*t*-butyl-phenoxyl radical (no experimental data are available for phenoxyl itself).

It had always been assumed that the g-tensor of phenoxyl radicals is dominated by the large spin density and SO coupling constant of the carbonyl oxygen atom. This was later confirmed by the MCSCF and DFT studies. However, our UDFT study, which used the AMFI approximation and thus allowed a break-down of the g-shift components into atomic contributions, showed that the *ortho* carbon atoms (C_2, C_6) provide small but nonnegligible negative contributions (ca. –360 ppm) to Δg_x and positive contributions (ca. +280 ppm) to Δg_y [55]. The *para* carbon atom (C_4) contributes another ca. +150 ppm to both Δg_x and Δg_y.

Substituents in 2- or 6-position of the phenoxyl radical have a rather significant influence on the g-tensor, in particular on Δg_x. For example, Δg_x in the 2,4,6-tris-*t*-butyl-phenoxyl is reduced by ca. 35% (Δg_y by ca. 15%) compared to phenoxyl [55]. This is due to hyperconjugation of the alkyl substituents with the delocalized π-system of phenoxyl, which reduces the spin density on oxygen. Similar substituent effects have been computed for semiquinones (see below). In contrast, differences between tyrosyl and unsubstituted phenoxyl are below 5%. This indicates that the "alanyl" substituent in 4-position of the tyrosyl radical has only a small influence on the g-tensor, and thus phenoxyl (or even better 4-methyl-phenoxyl) is a reasonable model for g-tensor calculations on the tyrosyl radical [55].

Effects of thioether substituents in tyrosyl radicals have been of interest in the context of the function of *galactose oxidase* (GO). In this enzyme complex, which catalyzes the two-electron oxidation of primary alcohols to aldehydes [103, 109], a tyrosine residue is covalently cross-linked in *ortho*-position to the thioether function of a cysteine residue [110]. Whether this link has a crucial effect on spin-density distributions and g-tensors of the tyrosyl radical created, has been discussed controversially, from the experimental [111, 112] and theoretical [100, 112] side. EPR measurements indicate a reduced Δg_x (by ca. 25%) and enhanced Δg_y (by ca. 100%) compared to unsubstituted tyrosyl, leading to an almost axially symmetrical tensor [111, 112]. Gerfen et al. [112] used Kohn-Sham orbitals obtained in LDA calculations to compute the $\Delta g_{SO/OZ}$ contributions to g-shifts for cresyl and 2-methylthiocresyl model radicals and found very large differences between the two systems. However, these calculations involved severe approximations, in particular the one-center approximation for both SO and OZ matrix elements in Eq. 7.4 (Stone's first and second approximation [7], cf. Sect. 7.3.1) and did therefore not provide quantitatively correct results. Subsequent MCSCF calculations of the g-tensor for the *ortho*-SH substituted phenoxyl radical [100] instead provided very small substituent effects, a ca. 13% decrease in Δg_x but only a 7% increase in Δg_y (the principal axis of g_x was rotated by ca. 9° from the C—O bond, compared to 23° in the DFT calculations [112]). Our own DFT calculations [101] on systems like 2-methylthiophenoxyl provide a more accurate picture, which is intermediate

Table 7.3 Comparison of contributions to Δg principal components of phenoxyl and 2-methylthiophenoxyl (in ppm)[a]

Phenoxyl	Δg_x	Δg_y	Δg_z
Δg_{GC}(1el)	188	273	194
Δg_{RMC}	−206	−206	−206
$\Delta g_{SO/OZ}$	8,808	2,220	−8
Total	8,790	2,286	−20
2-Methylthiophenoxyl	Δg_x	Δg_y	Δg_z
Δg_{GC}(1el)	240	260	202
Δg_{RMC}	−207	−207	−207
$\Delta g_{SO/OZ}$	6,109	4,792	−56
Total	6,142	4,845	−61

[a]UDFT/BP86 results with DZVP basis set, AMFI SO approximation, and common gauge origin at the center of mass [101]

Table 7.4 Fragment analysis of $\Delta g_{SO/OZ}$ contributions (in ppm) in *ortho*-SCH_3-phenoxyl[a]

Fragment	Δg_{xx}	Δg_{xy}	Δg_{xz}	Δg_{yx}	Δg_{yy}	Δg_{yz}	Δg_{zx}	Δg_{zy}	Δg_{zz}
Phenoxyl	4,721	127	−1	−1	1,658	−1	−1	0	−10
S	1,312	−519	−1	−212	3,201	−1	0	−1	−45
CH_3	6	7	0	6	3	0	0	0	−2
Σ	6,037	−385	−2	−205	4,862	−2	−1	−1	−57
$\Delta g_{SO/OZ}$	6,039	−386	−2	−206	4,861	−3	−1	−1	−56

[a]Contributions in general axis system, as shown in Fig. 7.2. Fragment contributions are obtained by separate perturbation calculations, in which only the AMFI-SO operators on a given fragment are employed [101]

between these extreme viewpoints: Compared to unsubstituted phenoxyl, Δg_x is reduced by ca. 30%, and Δg_y is increased by ca. 110%, in reasonable agreement with the experimental observation of a nearly axial tensor (Table 7.3). Probably, the active space in the MCSCF calculations was insufficient to provide quantitative results. The break-down of the DFT g-tensor results into atomic contributions (Table 7.4) indicates that (a) substitution reduces the contribution from the phenoxyl fragment to both Δg_x and Δg_y, due to withdrawal of spin density from the phenoxyl oxygen atom, and (b) the sulfur SO contribution is significant. It increases Δg_x somewhat and Δg_y dramatically (Table 7.4). A relatively small amount of spin density on the heavy sulfur atom (ca. 0.13 a.u.) is sufficient to produce significant SO contributions to the g-tensor of the radical. The comparably small substituent effect on Δg_x is due to a partial compensation between changes in the phenoxyl contribution and the direct sulfur contribution. Our systematic DFT studies indicate furthermore an influence of hydrogen bonding on the g-tensor of the modified tyrosyl radical in apo-GO, and even much larger effects of heavier substituent atoms like selenium or tellurium [101]. Further studies performed on a synthetic model for apo-GO confirmed the importance of hydrogen bonding for the g-tensor [107].

Indeed, both g_x and g_y of the tyrosyl radical are also reduced by hydrogen bonding to the phenoxyl oxygen atom. A reduction of g_x from ca. 2.0087–2.0089 in systems without significant hydrogen bonding to ca. 2.0066–2.0076 by hydrogen

bonding is usually taken as characteristic probe of the nature of the protein environment [39, 104, 105]. Very similar behavior holds for semiquinones and for nitroxide radicals (see below). The reduced Δg_x is mainly due both to an increased energy denominator (stabilization of the "in-plane" b_1 HOMO by hydrogen bonding) and reduced SO and OZ matrix elements for the decisive $^2B_2 \rightarrow {}^2B_1$ excitation. As the electrostatic interactions are optimal for a direct alignment of the hydrogen bond with the HOMO, the reduction of Δg_x is expected to be most pronounced for an in-plane coordination. Δg_y is somewhat less affected by hydrogen bonding.

The qualitative features of these effects of hydrogen bonding have early on been accounted for within Stone's model [8]. Sun et al. used semi-empirical (PM3-MNDO) calculations to model the electrostatic influence of hydrogen bonding on the g-tensors [39, 105]. Both point charge models and an explicit treatment of hydrogen bonding by water or acetic-acid complexes were employed. A Taylor expansion of the electrostatic interactions was used to evaluate the dependence of the effect on g_x on the distance to the hydrogen bond donor or to a positively charged metal center. From the comparison between models for the tyrosyl radical in ribonucleotide reductase (which does not exhibit hydrogen bonding), the one in photosystem II (Tyr-D^0), and tyrosyl in solid tyrosine hydrochloride, a structural model for hydrogen bonding to the Tyr-D^0 radical was suggested [39]. While the earliest calculations used relatively crude estimates for bond lengths, later studies employed fully DFT optimized structures for the model complexes [105]. Applications have also been extended to Tyr_Z [113] and to synthetic analogues of Tyr_D of photosystem II [106], to QM/MM studies of a tyrosyl radical in *versatile peroxidase* [114], to a general screening of substituent and hydrogen-bonding effects on the g-tensor of phenoxyl radicals [115], as well as to fluorinated phenoxyl radicals possibly occurring during degradation of fuel-cell membranes [116]. The results of quantum chemical calculations have also been used to calibrate empirical incremental schemes [108].

7.5.2 Semiquinone Radical Anions

The electronic structures of semiquinone radical anions are closely related to those of phenoxyl radicals, and the qualitative features of the g-tensor have been accounted for by the Stone model [8]. As for phenoxyls, Δg_x is dominated by the coupling between the in-plane n-type HOMO and the out-of-plane π-type SOMO (similarly, Δg_y arises again mainly from a $\sigma \rightarrow \pi^*$ transition). However, the spin density is distributed more symmetrically, and both carbonyl oxygen atoms contribute to the SO/OZ terms. Due to the larger energy gap between HOMO and SOMO, Δg_x is less positive than for phenoxyl. In contrast, Δg_y is more positive than for phenoxyl. Due to the resulting smaller difference between Δg_x and Δg_y, the resolution of g_x and g_y in EPR experiments is more demanding for semiquinones than for the tyrosyl radical.

The role of semiquinones in biological electron transfer processes is probably even more remarkable than that of tyrosyl radicals. Typically, quinones are reduced in one-electron steps, leading first to the semiquinones (either as radical anion or protonated as neutral radical), and often ultimately in a second step (accompanied by protonation) to the hydroquinones [117]. The intermediately produced semiquinone radical anions are essential spin probes in EPR experiments. This holds, e.g., for photosynthetic reaction centers, and for several processes in respiration [118]. Some of the most important quinones involved in such processes are ubiquinone-10 (in reaction centers of purple bacteria, and in many other processes), plastoquinone-9 (in photosystem II, PS-II), and phylloquinone (Vitamin K_1; in PS-I). Similar to the discussion above for tyrosyl radicals, the g-tensors of semiquinones are influenced both by substituent effects and by hydrogen bonding. They are therefore often characteristic for the type of quinone involved in a given electron transfer process, as well as for the protein environment around the semiquinone. Semiquinones in proteins have thus been central targets of HF-EPR studies [119]. In addition, a considerable number of semiquinone radical anions have also been studied in isotropic solution. In particular, W-band (95 GHz) experiments on a large variety of semiquinones in frozen isopropanol, and some studies in other solvents, have provided a valuable database against which theoretical approaches can be validated [120, 121].

Semi-empirical calculations by Knüpling et al. [40] used a UHF-PM3 *ansatz* and modelled the solute-solvent interactions either by point charges or by explicit inclusion of two or four methanol molecules hydrogen-bonded to the semiquinone oxygen atoms. Given the rather severe approximations inherent in these calculations, as well as significant uncertainties in the structures employed, the final results with four methanol molecules are in surprisingly good agreement with experiment. However, these calculations would predict hydrogen bonding to reduce Δg_x only by ca. 200–400 ppm, i.e. only ca. 4–9% relative to the results for the free radical anions. This is much less than the ca. 20–30% obtained in DFT calculations [97] (see below). The good agreement of the PM3 results with experiment thus appears to be partly due to cancellation of rather large errors. Due to their very approximate nature, these types of calculations are probably better suited for qualitative modelling than for quantitative predictions.

We have subsequently studied [97] the g-tensors of a very similar series of semiquinones by our DFT approach [55], using gradient-corrected functionals (BP86), DZVP basis sets, and accurate AMFI SO operators. Hydrogen-bonding interactions with the solvent were modelled by explicit coordination with a varying number of water or isopropanol molecules. The structures were fully optimized at DFT level. The calculations suggested complexes with two hydrogen bonds to each of the carbonyl oxygen atoms to provide the most likely model for the first solvation shell, augmented by one additional hydrogen bond to each of the two methoxy groups in models for ubisemiquinone-10 (Fig. 7.3) [97]. The calculations indicated a nonnegligible dependence of Δg_x (also partly of Δg_y) on the orientation of the hydrogen bonds, as well as on the conformation of substituents in the substituted

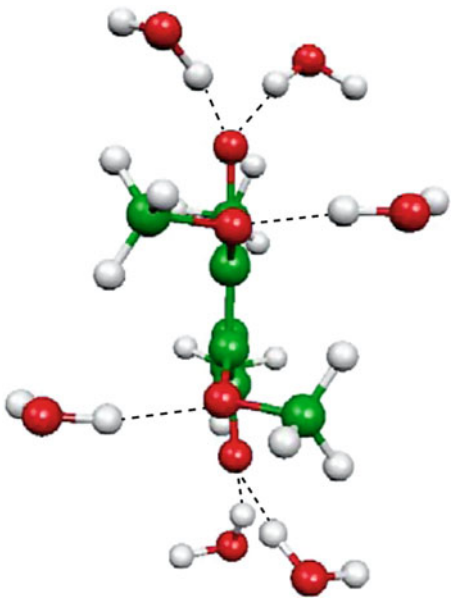

Fig. 7.3 UQ-$M^{-}\cdot(H_2O)_6$ model for solvation of ubisemiquinone in isotropic protic solution [97]. Note the extra two hydrogen bonds to the methoxy substituents. The structure of the UQ-$M^{-}\cdot(i\text{PrOH})_6$ model complex is similar [97]

semiquinones (again in particular of methoxy substituents in UQ-M). Moreover, the two types of motion appear to proceed along very shallow potential energy surfaces, and they are coupled to each other. This constitutes one of the major limitations in the accuracy achievable in the g-tensor calculations. In the absence of accurate molecular dynamics information, a reasonable selection of low-lying configurations is required [97].

When taking this into account and using appropriate hydrogen-bonded model complexes $Q^{-}\cdot(i\text{PrOH})_4$ (and UQ-$M^{-}\cdot(i\text{PrOH})_6$), a remarkable correlation with experimental W-band data in frozen 2-propanol was obtained (Fig. 7.4) [97]. After scaling of the computed Δg_x values by a factor of 0.92, all results were within ca. ± 130 ppm of experiment. Given the estimated experimental uncertainties of at least ca. ± 100 ppm, this means quantitative agreement between theory and experiment. Quantitative agreement, even without the need of scaling, was found for Δg_y [97]. Given the accuracy of the SO operators employed, it is thought that the systematic overestimate of Δg_x reflects inherent deficiencies in the currently used exchange-correlation functionals. Improved functionals may well eliminate the need for scaling. However, even at the present level of accuracy, the results allow quantitative predictions, making DFT calculations of g-tensors of semiquinone radical anions an extremely valuable tool to be used in conjunction with HF-EPR studies. We note in passing that unsolvated semiquinone models provide much too large g-shifts and poor correlation with the experimental data in protic solution. However, these values are good estimates for the results expected in the absence of hydrogen bonding or other solvent interactions [97]. Other DFT studies of semiquinones in protic or protein environment have been performed by Lubitz and coworkers [122].

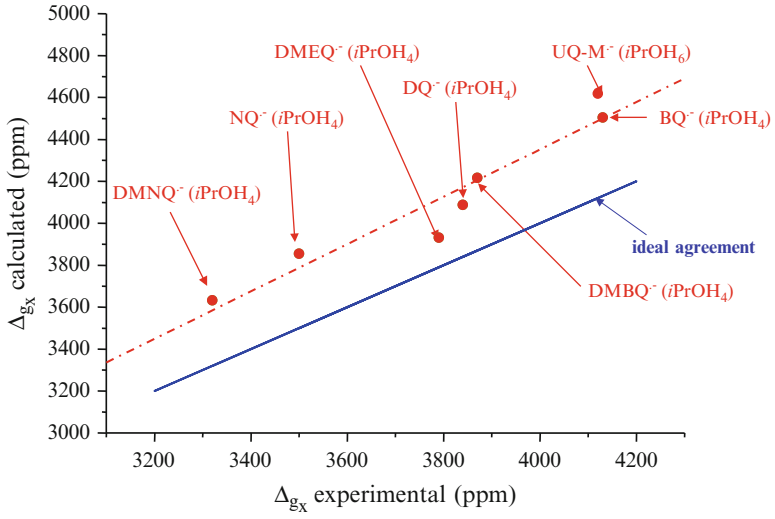

Fig. 7.4 Comparison of DFT calculations (UDFT-BP86 results with AMFI SO operators) of explicitly solvated semiquinone model complexes with experimental Δg_x values in frozen 2-propanol [97]. Abbreviations: *BQ* (1,4-benzoquinone), *DMBQ* (2,3-dimethyl-1,4-benzoquinone), *DMEQ* (2,3-dimethyl-5-ethyl-1,4-benzoquinone), *DQ* (duroquinone: 2,3,5,6-tetramethyl-1,4-benzoquinone), *TMQ* (2,3,5-trimethyl-1,4-benzoquinone), *UQ-M* (2,3-dimethoxy-5,6-dimethyl-1,4-benzoquinone), *NQ* (1,4-naphthoquinone), *DMNQ* (2,3-dimethyl-1,4-naphthoquinone)

The obtained accuracy suggested that DFT methods should also be useful for studies on semiquinones in protein environments. Our first application [123] focussed on the A_1 semiquinone binding site of PS-I in cases when insufficient structural information is available. The unusual g-tensors of so-called "reconstituted" preparations of PS-I [124] caught our attention, where smaller quinones like DQ or NQ replace the native phylloquinone. HF-EPR data have indicated a different orientation of the semiquinone than in native PS-I. Moreover, both g_x *and* g_y were significantly larger than measured in protic solvents, or when reconstituted into reaction centers of purple bacteria (bRC) [124]. Our calculations had indicated that even in the complete absence of hydrogen bonds (i.e. in the free gas-phase radical anions), Δg_y in $DQ^{-\cdot}$ or $NQ^{-\cdot}$ should never be significantly larger than ca. 3,000 ppm (Table 7.5). In contrast, the reconstituted PS-I preparations exhibited values of ca. 4,000 ppm with $DQ^{-\cdot}$, and of ca. 3,700 ppm with $NQ^{-\cdot}$ [124]. Thus, it seemed likely that previously neglected interactions could be responsible for the unusual g-tensors in these systems.

We therefore started to investigate interactions of quinones and semiquinones with tryptophan (Trp) residues [123]. A variety of evidence had pointed to π-π interactions between phylloquinone and a Trp residue in the A_1 binding site. In the course of our computational study, the X-ray crystallographic analysis of the

Table 7.5 Calculated g-shift tensors (in ppm) for various model systems of duro- and naphthosemiquinone compared to experimental data in different environments[a]

	Δg_{iso}	Δg_{xx}	Δg_{yy}	Δg_{zz}
$DQ^{-\cdot}$				
Free	2,785	5,347	3,021	−14
$+(H_2O)_4$	2,270	4,200	2807	−195
$+(iPrOH)_4$	2,071	3,932	2,549	−267
exp. (in iPrOH) [117, 118]	2,160	3,790	2,800	−100
exp. (in MTHF) [117, 118]	2,380	4,380	2,910	−140
exp. (in Zn-bRC)[b]	2,200	3,800	2,800	0
exp. (in PS-I) [121]	3,000	5,000	4,000	0
$NQ^{-\cdot}$				
Free	2,795	5,464	2,896	−25
$+(H_2O)_4$	2,233	4,064	2,632	3
$+(iPrOH)_4$	2,167	3,856	2,617	29
exp. (in iPrOH) [117, 118]	2,060	3,500	2,730	−40
exp. (in Zn-bRC)[b]	2,100	3,500	2,800	0
exp. (in PS-I) [121]	2,700	4,400	3,700	0

[a]Cf. Ref. [97]
[b]In zinc-substituted reaction centers of purple bacteria [124]

PS-I complex of *S. elongatus* at 2.5 Å resolution confirmed a π-stacked interaction between Q_K-A and Trp A697 (as well as a very similar one between Q_K-B and Trp B677 in the B-branch) [125].

Interestingly, our extensive structure optimizations of semiquinone-indole model complexes at the MP2 level of theory (this ab initio level was used to account for potential dispersion contributions to the π-stacking interactions) indicated that π-stacked arrangements are actually rather *unfavorable* for the anionic complex, and the optimizations converged to a T-stacked arrangement (Fig. 7.5a) with significant hydrogen bonding from the indole N–H hydrogen to the π-system of the semiquinone. In contrast, the π-stacked arrangement (Fig. 7.5b) was confirmed to provide the most favorable interaction for the neutral quinone-indole complexes [123].

Subsequent DFT calculations of the g-tensors for the free semiquinones, their indole complexes in various structural arrangements, and models incorporating an additional hydrogen bond (to account for hydrogen bonding to the Leu A722 residue indicated by X-ray analysis), provided interesting insights: π-stacked semiquinone-indole interactions do not alter g_x or g_y noticeably and certainly cannot account for the large g_y values of $DQ^{-\cdot}$ or $NQ^{-\cdot}$ reconstituted into PS-I. Interestingly, the only interactions we found to enhance *both* g_x *and* g_y relative to the free semiquinones were T-stacked hydrogen bonds to the semiquinone π-system [123].

This suggested the following situation: Small quinones without extended side chain like DQ or NQ may reorient within the reconstituted A_1 site upon reduction to the semiquinone. This leads to a significant stabilization of the semiquinone relative to the neutral quinone, and thus to an increased redox potential. In these reconstituted preparations, the semiquinone should not be able to transfer its excess

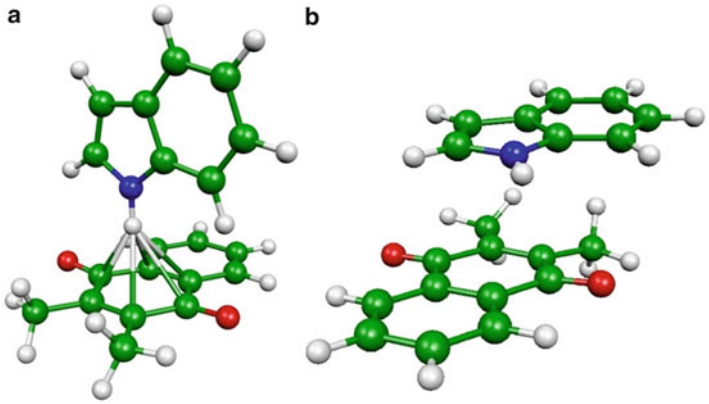

Fig. 7.5 (**a**) Fully MP2-optimized structure of the complex between 2,3-dimethylnaphthosemiquinone and indole. Note the T-stacked arrangement [123]. (**b**) Fully MP2-optimized structure of the complex between neutral 2,3-dimethylnaphthoquinone and indole. Note the π-stacked arrangement [123]

electron to the next acceptor (the iron-sulfur cluster F_x) within the electron transfer chain of PS-I, and thus photoreduction of $NADP^+$ will be interrupted. This agrees with experimental observation. In contrast, the native phylloquinone (Q_K) acceptor has an extended side chain in 3-position of the semiquinone, which prohibits reorientation of the semiquinone. In the enforced π-stacked orientation relative to the Trp residue, the semiquinone is destabilized relative to the quinone, and the redox potential is tuned more negative, as needed for forward electron transfer.

The increase of g_y in various T-stacked semiquinone model complexes was smaller than the observed enhancement in the reconstituted reaction centers, suggesting more than one T-stacked hydrogen bond to the semiquinone. It appears likely, that this type of T-stacked hydrogen bonding to semiquinone radical anions may generally be an important ingredient in biological electron transfer processes involving quinones.

Excellent accuracy of modelled g-tensors at the same level was also obtained for quinone binding sites of bacterial reaction centers [126]. This experience suggested applications to situations where experimental structural data are lacking. A first example, that was directly motivated by the PS-I results discussed above, were computationally constructed cyclophane-type dyads between a semiquinone and another aromatic system [127]. The idea was that the abovementioned reorientation upon reduction of the quinone could be used to construct an electrochemically driven molecular motor. The computational results suggested that indeed a modified g-tensor should provide a spectroscopic probe to such a reorientation from a π- to a T-stacked arrangement [127].

Better modelling of solvation in protic environments requires molecular dynamics, as the hydrogen bonds exchange on a short time scale. To see how well the static models simulate this, and to get a more realistic picture of the hydrogen bonding, we

carried out ab initio molecular dynamics simulations followed by EPR parameter calculations of semiquinone radical anions in aqueous solution. Initially, the g-tensor of the simplest semiquinone, benzosemiquinone, was studied, whereas later studies extended to various hyperfine tensors, as well as to the more biologically relevant ubisemiquinone radical anion [84]. A variety of insights on the time scale of the motions, on both regular and T-stacked hydrogen bonding (cf. above), on conformation and hydrogen bonding of methoxy substituents in ubisemiquinone, and on the influence of these motions on the various EPR parameters were obtained. We refer the reader to the original publications [84].

A further application to biological semiquinone sites, where no conclusive structural information on the H-bond environment was available, used DFT calculations of g- and hyperfine tensors for models of the strong (Q_H) quinol binding site of *quinol oxidase* (QOX), the terminal enzyme in the respiratory chain of certain bacteria [128]. Based on a protein X-ray structure without bound quinone/semiquinone/quinol, as well as site-directed mutagenesis studies, a putative binding site had been suggested. Various EPR studies (see, e.g. Ref. [129]) culminated initially in the suggestion of a completely asymmetrical environment for the anionic semiquinone radical, with hydrogen bonds only to one of the two semiquinone oxygen atoms O1 but not to O4. This conclusion was mainly based on the very different ^{13}C hyperfine tensors for the two ipso carbon atoms (semiquinone carbonyl groups). However, based on our previous experience and analyses [97, 123, 126, 127], the very low Δg_x component of the g-tensor seemed incompatible with such a completely asymmetrical environment. The subsequent computations of g- and various hyperfine tensors confirmed this and strongly suggested an asymmetrical but not single-sided 2:1 or 3:2 hydrogen-bonding environment for the binding site [128]. However, this was not the end of the story. Based on ESEEM and ENDOR studies of both non-exchangeable (methyl) and exchangeable protons, Yap et al. suggested a neutral protonated radical to account for the EPR signals, rather than the anionic semiquinones used in our studies [130]. As some initial DFT comparisons by Boesch and Wheeler [131] did not provide conclusive evidence for one or the other hypothesis, we carried out extended studies of g- and hyperfine tensors of both neutral and anionic models [132]. While some neutral models provided indeed excellent agreement with experimental g-tensor and methyl ^1H hyperfine data, none of them could account for the ^{13}C carbonyl hyperfine tensors. This supports strongly the anionic semiquinone hypothesis for the Q_H binding site of QOX and rules out essentially the protonated neutral variant [132].

While these examples all pertained to *para*-semiquinone radicals, g-tensors of *ortho*-semiquinone radical anions have recently been studied by DFT methods by Witwicki and coworkers, initially by spin-restricted two-component ZORA calculations on Mg or Pb complexes [133] more recently by one-component CPKS calculations on various protonation and solvation situations [134]. The interest of these studies was mainly fuelled by the occurrence of *o*-semiquinone structural motives in humic acid derivatives (in equilibrium with phenolic and quinonoid structural elements), an important part of the composition of natural soil or sediments.

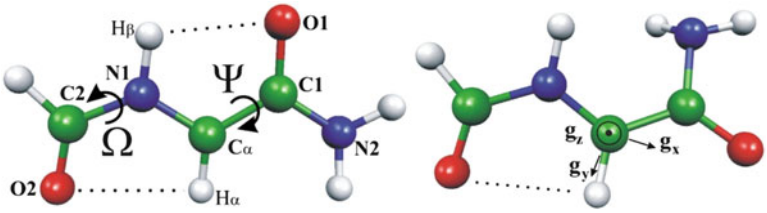

Fig. 7.6 Two conformations of a peptide glycyl radical. *Left*: *trans-trans*-conformation with indication of the relevant dihedral angles. This conformation appears to be the most likely for the ARNR glycyl radical. *Right*: *trans-cis*-conformation with orientation of g-tensor components. This appears to be the conformation of the PFL and BSS glycyl radicals (Reproduced from Ref. [72]. With kind permission of © The American Chemical Society 2007)

7.5.3 Other Amino-Acid Derived Radicals

While tyrosyl radicals (or semiquinones and nitroxides) exhibit a g-anisotropy that is typically accessible in W-band experiments, other amino-acid-based radicals like glycyl or tryptophanyl have even smaller anisotropies that may require even higher frequencies and magnetic fields. At the same time, such small g-shifts are a challenge to the computational methodology (e.g. regarding the gauge origin or the SO operators), as has been discussed further above [71, 72]. The most difficult cases so far are due to radicals derived from the amino acid glycine. An initial study by Ciofini et al. provided rather reasonable agreement of computed g-tensors with experiment when using the Gaussian implementation, Koseki-style semi-empirical SO operators, and a cluster + continuum dipeptide model [135]. Another study by Un looked at a different conformer of the dipeptide model by similar methods and gave conflicting results [112]. To be able to obtain an accuracy that will allow conformational and environmental questions to be answered meaningfully, we thus carried out a detailed calibration study of essentially all important influences on the g-tensor, initially for the N-acetyl-glycine radical (NAG) in a single-crystal environment (for which comprehensive structural information was available) [71], and later for models of glycine radicals in protein environment [72]. Apart from the strong sensitivity to the gauge question and SO operators discussed above, it turned out that conformation is the single most important factor that determines the g-tensor of protein glycyl radicals, whereas the hydrogen-bonding environment was less important than in other cases (due to a compensation between intra- and intermolecular hydrogen bonding). Based on the detailed calibration of computed g-tensors against experiment for the NAG case [71], it was subsequently possible to identify a different conformation of the radical as the most likely reason for differences in the g-tensor of the glycyl radical observed in an anaerobic *ribonucleotide reductase*(ARNR) compared to two other experimentally observed radicals [70]. More specifically, it appears that the ARNR glycyl radical has the extended *trans-trans*-conformation (Fig. 7.6, left), whereas radicals observed in *pyruvate formate lyase* (PFL) and in *benzylsuccinate synthase* (BSS) exhibit a

trans-cis-conformation (Fig. 7.6, right). Dynamical and environmental effects have recently been studied also for the case of glycine radical in an irradiated glycine single crystal, based on extensive ab initio molecular dynamics simulation [86]. Here the most important issue was, whether cluster models or extended solid-state calculations of g-tensors are preferable. Both approaches had their pros and cons, and it was shown that care has to be taken in constructing the cluster models to take into account hydrogen bonding and electrostatics of the crystal environment in a balanced way [86].

The tryptophanyl radical has also received increased attention recently, in particular regarding the question if EPR parameters allow the distinction between the neutral or protonated cationic forms of the radical in different protein environments [114, 115, 136, 137]. It turned out that the g-tensor calculations alone give probably not sufficient information, but combined with the comparison between computed and experimental hyperfine tensors, an unambiguous assignment to a neutral or cationic tryptophan radical could be made.

A different situation pertains to cysteinyl radicals, where much larger g-anisotropies make life easier for theoreticians on one side, but where higher-order SO effects have to be included to account for the perpendicular components of the g-tensor, as discussed further above [18, 102].

7.5.4 Miscellaneous Radicals

Another type of important cofactor radicals in photosystems are chlorophyll and bacteriochlorophyll radical cations. Due to their size and low g-anisotropies, they are a challenge to quantum chemistry, that has so far not been solved, in spite of some preliminary calculations [138]. A related set of species with small g-shifts are radicals derived from the biliverdin chromophore, for which calculations give at least some insight into possible protonation states [139]. More related to semiquinones are radicals derived from the flavin or pterin chromophores [140–142], for which calculations have also proven useful. We note in particular the elaborate QM/MM study of a flavoprotein radical in *glucose oxidase* by Pauwels et al. [140], which combined sophisticated ab initio MD and EPR parameter calculations to unravel the influence of the protein and hydrogen-bonding environment on the g-tensor, and to provide also orientational information. The same group used periodic DFT g-tensor calculations also in applications to radiation-induced alkoxy radical in α-L-rhamnose [143] and α-L-sorbose.

An interesting puzzle for DFT calculations of g- and hyperfine tensors resulted recently for a nucleotide radical formed during a site-directed mutagenesis and high-field EPR study of E. coli *ribonucleotide reductase* [144]. In close collaboration between two theory and several experimental groups, it was found, that the signal observed experimentally is due to an unexpected semidionenucleotide radical of cytidine 5′-diphosphate. This assignment was strongly influenced by the relatively large g-anisotropy that could not be reproduced by other structural suggestions. Last but not least we mention further studies on thiazolyl and thiothymine radicals [145].

7.6 Conclusions and Outlook

In the first edition of this chapter in 2003, we emphasized how since the mid 1990s, for the first time reliable ab initio and DFT methods for the computation of electronic g-tensors of organic radicals had become available, and how this is expected to transform the field of EPR work on biological radicals. Some first applications of such calculations were reviewed, and due to the novelty of such computations this could still be done rather comprehensively. Since then, methodology has developed further. But the most striking observation is, that in only 8 years g-tensor computations for bioradicals and related systems by DFT methods have matured from a testing field to a more or less routine task that accompanies many (in particular high-field) EPR works. It has thus not been possible to review all application studies in detail, and we have selected examples that illustrate the general direction the field is moving to, emphasizing our own application work.

The availability of standard methodology for g-tensor calculations in freely or commercially available codes has spurred this remarkable, widespread use by both computational chemists and spectroscopists. This bears of course also the danger that a too black-box-type uncritical application may lead to errors and/or misleading results. In particular, it is often overlooked that the g-tensor is essentially a spin-orbit property, and thus the way the spin-orbit operators and their matrix elements are approximated in practice (see Sect. 7.3) is essential. A discussion of the spin-orbit treatment should thus be an integral part of the methodology discussion in any publication using g-tensor calculations. To some extent this holds also for the gauge question, albeit this is often a less critical aspect. It is furthermore important to indicate if restricted or unrestricted calculations have been done in a DFT application.

Meanwhile a bewildering variety of different methods ranging from simple one-component perturbational DFT via high-level multireference-CI, CASPT2 or coupled-cluster approaches to relativistic two- or four-component treatments have been implemented and tested. It is one of the goals of this article to make the reader aware of these many different possibilities and of their advantages and disadvantages.

We have not discussed here transition-metal complexes, for which the achievable accuracy in g-tensor calculations is currently lower, but where a significant amount of applications have been made recently (in particular for bioinorganic chemistry and catalysis). Another field, which will benefit greatly from quantitative g-tensor calculations and has seen tremendous progress, but which we have not been able to cover here, are paramagnetic defects in solids. These can be treated by cluster models or by the more recent periodic-solid calculations described above.

We have also tried to indicate the importance of dynamical effects and the ways how they have recently been incorporated in computational studies of g-tensors. For more information on this topic, and for applications to nitroxide spin labels and related systems, we refer the reader to the original papers and reviews cited.

Acknowledgments I am very grateful for the important contributions by J. Vaara, O. L. Malkina, V. G. Malkin, and B. Schimmmelpfennig to our own entry into the field of g-tensor calculations, with further contributions due to S. Kacprzak, A. Arbouznikov, R. Reviakine, I. Ciofini, M. Munzarová, J. Asher, C. Remenyi, F. MacMillan, S. Schinzel, I. Malkin, P. Hrobárik, M. Repiský, S. Komorovský, V. Hrobáriková, C. Urban, T. Gress, and S. Schlund. Helpful comments on the 2003 version of the manuscript are due to I. Ciofini, J. Vaara, A. Arbuznikov, and V. G. Malkin. Funding over the years from Deutsche Forschungsgemeinschaft of our own research in this field is also gratefully acknowledged.

References

1. See, e.g.: Weil JA, Bolton JR (1994) Electron paramagnetic resonance: elementary theory and practical applications. Wiley, New York; Weltner W Jr (1983) Magnetic atoms and molecules. Van Nostrand, New York
2. Harriman JE (1978) Theoretical foundations of electron spin resonance. Academic, New York
3. Möbius K (1993) In: Berliner LJ, Reuben J (eds) Biological magnetic resonance, vol 13. Plenum Press, New York, pp 253–274
4. Prisner TF (1997) In: Warren W (ed) Advances in magnetic and optical resonance, vol 20. Academic, New York, pp 245–299
5. Un S, Dorlet P, Rutherford AW (2001) A high-field EPR tour of radicals in photosystems I and II. Appl Magn Reson 21:341–361
6. Cf., e.g.: Abragam A, Bleaney B (1970) Electron paramagnetic resonance of transition ions. Clarendon Press, Oxford; Symons MCR (1978) Chemical and biochemical aspects of electron-spin resonance spectroscopy. Van Nostrand, New York; Atherton NM (1993) Principles of electron spin resonance. Prentice Hall, New York
7. Stone AJ (1963) Gauge invariance of the g tensor. Proc R Soc A 271:424–434
8. Stone AJ (a) (1963) g Factors of aromatic free radicals. Mol Phys 6:509–515; (b) (1964) g tensors of aromatic hydrocarbons. Mol Phys 7:311–316
9. Kaupp M, Bühl M, Malkin VG (eds) (2004) Calculation of NMR and EPR parameters. Theory and application. Wiley-VCH, Weinheim
10. Lushington GH (2004) Ab initio calculations of g-tensors. In Ref. [9], Ch. 33, pp 533–540; Patchkovskii S, Schreckenbach G (2004) Calculation of EPR g-tensors with density functional theory. In Ref. [9], Ch. 32, pp 505–532
11. Cimino P, Neese F, Barone V (2010) Computational spectroscopy. In: Grunenberg J (ed) Methods, experiments and applications. Wiley-VCH, Weinheim, pp 63–104
12. Vahtras O, Engstroem M, Agren H (2003) Quantum chemical calculations of molecular g-tensors of biological radicals. In Braendas EJ, Kryachko ES (eds) Fundamental world of quantum chemistry, vol 2, pp 483–524. Kluwer, Dordrecht
13. McWeeny R (1992) Methods of molecular quantum mechanics. Academic, London
14. van Lenthe E, Baerends EJ, Snijders JG (1993) Relativistic regular two-component Hamiltonians. J Chem Phys 99:4597–4610
15. Samzow R, Hess BA, Jansen G (1992) The two-electron terms of the no-pair Hamiltonian. J Chem Phys 96:1227–1231
16. van Lenthe E, Wormer PES, van der Avoird A (1997) Density functional calculations of molecular g-tensors in the zero-order regular approximation for relativistic effects. J Chem Phys 107:2488–2498
17. Neyman KM, Ganyushin DI, Matveev AV, Nasluzov VA (2002) Calculation of electronic g-tensors using a relativistic density functional Douglas-Kroll method. J Phys Chem A 106:5022–5030
18. Malkin I, Malkina OL, Malkin VG, Kaupp M (2005) Relativistic two-component calculations of electronic g-tensors that include spin polarization. J Chem Phys 123:244103/1-16

19. Komorovský S, Repiský M, Malkina OL, Malkin VG, Malkin I, Kaupp M (2006) Resolution of identity Dirac-Kohn-Sham method using the large component only: calculations of g-tensor and hyperfine tensor. J Chem Phys 124:084108/1-8
20. Hrobárik P, Repiský M, Komorovský S, Hrobáriková V, Kaupp M (2011) Assessment of higher-order spin-orbit effects on electronic g-tensors of d^1 transition-metal complexes by relativistic two- and four-component methods. Theor Chem Acc 129:715–725
21. Pryce MH (1950) A modified perturbation procedure for a problem in paramagnetism. Proc Phys Soc 63:25–29
22. Lushington GH (1996) PhD thesis, The University of New Brunswick, Canada
23. Patchkovskii S, Ziegler T (2001) Calculation of the EPR g-tensors of high-spin radicals with density functional theory. J Phys Chem A 105:5490
24. Engström M, Minaev B, Vahtras O, Ågren H (1998) Linear response calculations of electronic *g*-factors and spin-rotational coupling constants for diatomic molecules with a triplet ground state. Chem Phys 237:149–158
25. Patchkovskii S, Strong RT, Pickard CJ, Un Gauge S (2005) Invariance of the spin-other-orbit contribution to the g-tensors of electron paramagnetic resonance. J Chem Phys 122: 214101/1-9
26. Angstl R (1989) Contribution of the relativistic mass correction to the *g* tensor of molecules. Chem Phys 132:435–442
27. See, e.g.: Engels B, Eriksson LA, Lunell S (1996) Recent developments in conzuration interaction and density functional theory calculations of radical hyperfine structure. Adv Quantum Chem 27:297–369
28. See, e.g.: Geurts PJ, Bouten PCP, van der Avoird AJ (1997) Hartree–Fock–Slater–LCAO calculations on the Cu(II) bis(dithiocarbamate) complex; Magnetic coupling parameters and optical spectrum. J Chem Phys 73:1306–1312; Belanzoni P, Baerends EJ, van Asselt S, Langewen PB (1995) Density functional study of magnetic coupling parameters. Reconciling theory and experiment for the TiF_3 complex. J Phys Chem 99:13094–13102; Swann J, Westmoreland TD (1997) density functional calculations of *g* values and molybdenum hyperfine coupling constants for a series of molybdenum(V) oxyhalide anions. Inorg Chem 36:5348–5357
29. Moores WH, McWeeny R (1973) The calculation of spin-orbit splitting and g tensors for small molecules and radicals. Proc R Soc A 332:365–384. See also: Ishii M, Morihashi K, Kikuchi O (1991) Ab initio calculations of g values of free radicals by finite perturbation theory. J Mol Struct Theochem 235:39–49
30. See, e.g.: Keijzers CP, de Vries HHM, van der Avoird A (1972) Extended Hueckel calculation of the electron paramagnetic resonance parameters of copper(II) bis(dithiocarbamate). Inorg Chem 11:1338–1343; Dalgård E, Linderberg J (1975) Energy weighted maximum overlap in magnetic fields, applications to electron spin resonance problems. Int J Quantum Chem S9:269–277; Mishra KC, Mishra SK, Roy JN, Ahmad S, Das TP (1985) g-Tensor in a low-spin heme system using molecular orbital theory – ferricytochrome c and nitrosylhemoglobin. J Am Chem Soc 107:7898–7904; Roy JN, Mishra KC, Mishra SK, Das TP (1989) Variational theory for g tensor in electron paramagnetic resonance experiments: application to ferricytochrome c and azidomyoglobin. J Phys Chem 93:194–200
31. Chuvylkin ND, Zhidomirov GM (1973) CNDO/SP calculation of *g*-tensors of free radicals. Mol Phys 25:1233–1235
32. Angstl R (1990) Calculation of molecular g tensors. Comparison of Rayleigh-Schroedinger and Hartree-Fock perturbation theory. Chem Phys 145:413–426
33. Morikawa T, Kikuchi O (1971) SCF MO INDO calculation of g-tensors of some σ-type radicals. Theor Chim Acta 22:224–228; McCain DC, Hayden DW (1973) Theory of electron spin g-values for carbonyl radicals. J Magn Reson 12:312–330
34. Plato M, Möbius K, Lubitz W (1991) Molecular orbital calculations on chlorophyll radical ions. In Scheer H (ed) Chlorophylls. CRC Press, Boca Raton, pp 1015–1046; Hales BJ (1975) Immobilized radicals. I. Principal electron spin resonance parameters of the benzosemiquinone radical benzosemiquinone radical. J Am Chem Soc 97:5993–5997

35. Hsiao Y-W, Zerner MC (1999) Calculating ESR g tensors of doublet radicals by the semiempirical INDO/S method. Int J Quantum Chem 75:577–584
36. Plakhutin BN, Zhidomirov GM, Zamaraev KI (1983) INDO calculations of spin Hamiltonian constants in transition metal complexes. Effect of structural distortions and adduct formation on the g-tensor of copper(II) bis(acetylacetonate.). J Struct Chem 24:3–11
37. For an INDO-CI approach, see: Neese F (2001) Configuration interaction calculation of electronic g tensors in transition metal complexes. Int J Quantum Chem 83:104–114; Neese F, Solomon EI (1998) Calculation of zero-field splittings, g-values, and the relativistic nephelauxetic effect in transition metal complexes. Application to high-spin ferric complexes. Inorg Chem 37:6568–6582
38. Mustafaev SA, Malkin VG, Schastnev PV (1987) Application of finite perturbation method in calculating g-factors of free-radicals. J Struct Chem 28:667–673
39. Un S, Atta M, Fontcave M, Rutherford AW (1995) g-Values as a probe of the local protein environment: high-field EPR of tyrosyl radicals in ribonucleotide reductase and photosystem II environment: high-field EPR of tyrosyl radicals in ribonucleotide reductase and photosystem II. J Am Chem Soc 117:10713–10719
40. Knüpling M, Törring JT, Un S (1996) The relationship between the molecular structure of semiquinone radicals and their g-values. Chem Phys 219:291–304
41. Törring JT, Un S, Knüpling M, Plato M, Möbius K (1997) On the calculation of G tensors of organic radicals. J Chem Phys 107:3905–3913
42. Lushington GH, Grein F (1996) Complete to second-order ab initio level calculations of electronic g-tensors. Theor Chim Acta 93:259–267
43. Bruna P, Lushington GH, Grein F (1997) Stability, properties and electronic g-tensors of H_2CO- as stabilized in $H_2CO{\cdot}Na$ complexes. Chem Phys 225:1–15
44. Brownridge S, Grein F, Tatchen J, Kleinschmidt M, Marian CM (2003) Efficient calculation of electron paramagnetic resonance g-tensors by multireference configuration interaction sum-over-state expansions, using the atomic mean-field spin-orbit method. J Chem Phys 118:9552–9562
45. Vahtras O, Minaev B, Ågren H (1997) Ab initio calculations of electronic g-factors by means of multiconfiguration response theory. Chem Phys Lett 281:186–192
46. Vahtras O, Engström M, Schimmelpfennig B (2002) Electronic *g*-tensors obtained with the mean-field spin–orbit Hamiltonian. Chem Phys Lett 351:424–430
47. Bolvin H (2006) An alternative approach to the g-matrix: theory and applications. ChemPhysChem 7:1575–1589
48. Tatchen J, Kleinschmidt M, Marian CM (2009) Calculating electron paramagnetic resonance g-matrices for triplet state molecules from multireference spin-orbit configuration interaction wave functions. J Chem Phys 130:154106/1-17
49. Neese F (2007) Analytic derivative calculation of electronic g-tensors based on multireference configuration interaction wavefunctions. Mol Phys 105:2507–2514
50. Gauss J, Kallay M, Neese F (2009) Calculation of electronic g-tensors using coupled cluster theory. J Phys Chem A 113:11541–11549
51. See, e.g.: Koch W, Holthausen MC (2000) A chemist's guide to density functional theory. Wiley-VCH, Weinheim
52. See, e.g.: van Wüllen C (1995) Density functional calculation of nuclear magnetic resonance chemical shifts. J Chem Phys 102:2806–2811; Lee AM, Handy NC, Colwell SM (1995) The density functional calculation of nuclear shielding constants using London atomic orbitals. J Chem Phys 103:10095–10109, and references therein
53. See, e.g.: Te Velde G, Bickelhaupt FM, Baerends EJ, Fonseca Guerra C, van Gisbergen SJA, Snijders JG, Ziegler T (2001) Chemistry with ADF. J Comput Chem 22:931–967, and references therein
54. Schreckenbach G, Ziegler T (1997) Calculation of the g-tensor of electron paramagnetic resonance spectroscopy using gauge-including atomic orbitals and density functional theory. J Phys Chem A 101:3388–3399

55. Malkina OL, Vaara J, Schimmelpfennig B, Munzarová ML, Malkin VG, Kaupp M (2000) Density functional calculations of electronic g-tensors using spin-orbit pseudopotentials and mean-field all-electron spin-orbit operators. J Am Chem Soc 122:9206–9218
56. Kaupp M, Reviakine R, Malkina OL, Arbuznikov A, Schimmelpfennig B, Malkin VG (2002) Calculation of electronic g-tensors for transition metal complexes using hybrid density functionals and atomic meanfield spin-orbit operators. J Comput Chem 23:794–803
57. Neese F (2001) Prediction of electron paramagnetic resonance g values using coupled perturbed Hartree-Fock and Kohn-Sham theory. J Chem Phys 115:11080–11096
58. Autschbach J, Pritchard B (2011) Calculation of molecular g-tensors using the zeroth-order regular approximation and density functional theory: expectation value versus linear response approaches. Theor Chem Acc 129:453–466
59. Manninen P, Vaara J, Ruud K (2004) Perturbational relativistic theory of electron spin resonance g-tensor. J Chem Phys 121:1258–1265; Rinkevicius Z, de Almeida KJ, Oprea CI, Vahtras O, Ågren H (2008) Degenerate perturbation theory for electronic g-tensors: leading-order relativistic effects. J Chem Theory Comput 4:1810–1828
60. See, e.g.: Ditchfield R (1974) Self-consistent perturbation theory of diamagnetism. I. A gauge-invariant LCAO method for NMR chemical shifts. Mol Phys 27:789–807; Wolinski K, Hinton JF, Pulay P (1990) Efficient implementation of the gauge-independent atomic orbital method for NMR chemical shift calculations. J Am Chem Soc 112:8251–8260
61. Kutzelnigg W, Fleischer U, Schindler M (1990) The IGLO-Method: Ab-initio calculation and interpretation of NMR chemical shifts and magnetic susceptibilities. In: NMR-basic principles and progress, vol 23. Springer, Heidelberg, pp 165–262
62. Pickard CJ, Mauri F (2002) First-principles theory of the EPR g-tensor in solids: defects in quartz. Phys Rev Lett 88:086403/1-4
63. Canning A et al. (2003) Paratec, PARAllel Total Energy Code. http://www.nersc.gov/projects/paratec
64. Sebastiani D, Parrinello M (2001) A new ab-initio approach for NMR chemical shifts in periodic systems. J Phys Chem A 105:1951–1958
65. Declerck R, Van Speybroeck V, Waroquier M (2006) First-principles calculation of the EPR g tensor in extended periodic systems. Phys Rev B 73:115113/1-8
66. CPMD V3.11, Copyright IBM Corp 1990–2006. Copyright MPI für Festkörperforschung Stuttgart 1997–2001
67. Lippert G, Hutter J, Parrinello M (1999) The Gaussian and augmented-plane-wave density functional method for ab initio molecular dynamics simulations. Theor Chem Acc 103:124–140
68. Weber V, Iannuzzi M, Giani S, Hutter J, Declerck R, Waroquier M (2009) Magnetic linear response properties calculations with the Gaussian and augmented-plane-wave method. J Chem Phys 131:014106/1-11
69. CP2K. http://cp2k.berlios.de
70. Kadantsev ES, Ziegler T (2009) Implementation of a DFT-based method for the calculation of the Zeeman g-tensor in periodic systems with the use of numerical and Slater-type atomic orbitals. J Phys Chem A 113:1327–1334
71. Kacprzak S, Reviakine R, Kaupp M (2007) Understanding the EPR parameters of glycine-derived radicals: the case of N-Acetylglycyl in the N-Acetylglycine single-crystal environment. J Phys Chem B 111:811–819
72. Kacprzak S, Reviakine R, Kaupp M (2007) Understanding the electron paramagnetic resonance parameters of protein-bound glycyl radicals. J Phys Chem B 111:820–831
73. Hess BA, Marian C, Wahlgren U, Gropen O (1996) A mean-field spin-orbit method applicable to correlated wavefunctions. Chem Phys Lett 251:365–371
74. Schimmelpfennig B (1996) Atomic spin-orbit meanfield integral program. Stockholms Universitet, Sweden
75. Malkina OL, Schimmelpfennig B, Kaupp M, Hess BA, Chandra P, Wahlgren U, Malkin VG (1998) Spin-orbit corrections to NMR shielding constants from density functional theory. How important are the two-electron terms? Chem Phys Lett 296:93–104

76. Ruud K, Schimmelpfennig B, Ågren H (1990) Internal and external heavy-atom effects on phosphorescence radiative lifetimes calculated using a mean-field spin-orbit Hamiltonian. Chem Phys Lett 310:215–221
77. Vaara J, Malkina OL, Stoll H, Malkin VG, Kaupp M (2001) Study of relativistic effects on nuclear shieldings using density-functional theory and spin-orbit pseudopotentials. J Chem Phys 114:61–71
78. Koseki S, Schmidt MW, Gordon MS (1992) MCSCF/6–31 G(D, P) Calculations of one-electron spin-orbit-coupling constants in diatomic-molecules. J Chem Phys 96:10768–10772
79. Neese F (2005) Efficient and accurate approximations to the molecular spin-orbit coupling operator and their use in molecular g-tensor calculations. J Chem Phys 122:034107/1-13
80. See, e.g.: Malkin VG, Malkina OL, Casida ME, Salahub DR (1994) Nuclear magnetic resonance shielding tensors calculated with a sum-over-states density functional perturbation theory. J Am Chem Soc 116:5898–5908
81. Malkin VG, Malkina OL, Eriksson LA, Salahub DR (1995) The calculation of NMR and ESR spectroscopy parameters using density functional theory. In: Seminario JM, Politzer P (eds) Modern density functional theory: a tool for chemistry; theoretical and computational chemistry, vol 2. Elsevier, Amsterdam, pp 273–347
82. Arbuznikov AV, Kaupp M (2009) Coupled-perturbed scheme for the calculation of electronic g-tensors with local hybrid functionals. J Chem Theory Comput 5:2985–2995
83. Arbuznikov A, Kaupp M, Reviakine R, Malkina OL, Malkin VG (2002) Validation study of meta-GGA functionals and of a model exchange-correlation potential in density functional calculations of EPR parameters. Phys Chem Chem Phys 4:5467–5474
84. Asher JR, Kaupp M (2008) Car-Parrinello molecular dynamics simulations and EPR property calculations on aqueous ubisemiquinone radical anion. Theor Chem Acc 119:477–487; Asher JR, Kaupp M (2007) Hyperfine coupling tensors of the benzosemiquinone radical anion from Car-Parrinello molecular dynamics. ChemPhysChem 8:69–79; Asher JR, Doltsinis NL, Kaupp M (2005) Extended Car-Parrinello molecular dynamics and electronic g-tensors study of benzosemiquinone radical anion. Magn Reson Chem 43:237–247; Asher JR, Doltsinis NL, Kaupp M (2004) Ab initio molecular dynamics simulations and g-tensor calculations of aqueous benzosemiquinone radical anion: effects of regular and "T-Stacked" hydrogen bonds. J Am Chem Soc 126:9854–9861
85. Pavone M, Cimino P, De Angelis F, Barone V (2006) Interplay of stereoelectronic and environmental effects in tuning the structural and magnetic properties of a prototypical spin probe: further insights from a first principle dynamical approach. J Am Chem Soc 128:4338–4347; Brancato G, Regia N, Barone V (2007) Unraveling the role of stereo-electronic, dynamical, and environmental effects in tuning the structure and magnetic properties of glycine radical in aqueous solution at different pH values. J Am Chem Soc 129:15380–15390; Barone V, Carbonniere P, Pouchan C (2005) Accurate vibrational spectra and magnetic properties of organic free radicals: the case of H_2CN. J Chem Phys 122:224308/1-8; Pavone M, Silllanpaa A, Cimino P, Crescenzi O, Barone V (2006) Evidence of variable H-bond network for nitroxide radicals in protic solvents. J Phys Chem B 110:16189–16192; Pavone M, Biczysko M, Rega N, Barone V (2010) Magnetic properties of nitroxide spin probes: reliable account of molecular motions and nonspecific solvent effects by time-dependent and time-independent approaches. J Phys Chem B 114:11509–11514
86. Pauwels E, Asher J, Kaupp M, Waroquier M (2011) Cluster or periodic, static or dynamic – the challenge of calculating the g tensor of the solid-state glycine radical. Phys Chem Chem Phys 13:18638–18646. doi:10.1039/C1CP21452G
87. Barone V, Polimeno A (2006) Toward an integrated computational approach to CW-ESR spectra of free radicals. Phys Chem Chem Phys 8:4609–4629
88. Pavone M, Biczysko M, Rega N, Barone V (2010) Magnetic properties of nitroxide spin probes: reliable account of molecular motions and nonspecific solvent effects by time-dependent and time-independent approaches. J Phys Chem B 114:11509–11514; Barone V, Cimino P, Pedone A (2010) An integrated computational protocol for the accurate prediction of EPR and PNMR parameters of aminoxyl radicals in solution. Magn Res Chem S1:11–22

89. Ciofini I, Reviakine R, Arbuznikov A, Kaupp M (2004) Solvent effects on g-tensors of semiquinone radical anions: polarizable continuum versus cluster models. Theor Chem Acc 111:132–140
90. Rinkevicius Z, Telyatnyk L, Vahtras O, Ruud K (2004) Electronic g-tensors of solvated molecules using the polarizable continuum model. J Chem Phys 121:5051–5060
91. Sinnecker S, Rajendran A, Klamt A, Diedenhofen M, Neese F (2006) Calculation of solvent shifts on electronic g-tensors with the conductor-like screening model (COSMO) and its self-consistent generalization to real solvents (Direct COSMO-RS). J Phys Chem A 110:2235–2245
92. Klamt A, Jonas V, Bürger T, Lohrenz JC (1998) Refinement and parametrization of COSMO-RS. J Phys Chem A 102:5074–5085
93. Sinnecker S, Neese F (2006) QM/MM calculations with DFT for taking into account protein effects on the EPR and optical spectra of metalloproteins. Plastocyanin as a case study. J Comput Chem 27:1463–1475
94. Rinkevicius Z, Murugan NA, Kongsted J, Aidas K, Steindal AH, Agren H (2011) Density functional theory/molecular mechanics approach for electronic g-tensors of solvated molecules. J Phys Chem B 115:4350–4358
95. Curl RF (1965) Relation between electron spin rotation coupling constants and g-tensor components. Mol Phys 9:585–597; Knight LB, Weltner WJ (1970) Spin-coupling constant, γ, and g tensor in $^2\Sigma$ molecules. J Chem Phys 53:4111–4112
96. Bruna PJ, Grein F (2000) Comparing electron-spin g-tensor results of first-row radicals with those of higher rows. Int J Quantum Chem 77:324–335; Bruna PJ, Grein F (2001) Electron-spin magnetic moment (g Factor) of $X^2\Sigma^+$ diatomic radicals $MX^{(\pm)}$ with nine valence electrons (M = Be, B, Mg, Al; X = N, O, F, P, S, Cl), An ab initio study. J Phys Chem A 105:3328–3339
97. Kaupp M, Remenyi C, Vaara J, Malkina OL, Malkin VG (2002) Density functional calculations of electronic g-tensors for semiquinone radical anions, the role of hydrogen bonding and substituent effects. J Am Chem Soc 124:2709–2722
98. Engström M, Vahtras O, Ågren H (1999) Hartree-Fock linear response calculations of g-tensors of substituted benzene radicals. Chem Phys 243:263–271
99. Engström M, Himo F, Gräslund A, Minaev B, Vahtras O, Ågren H (2000) Hydrogen bonding to tyrosyl radical analyzed by ab initio g-tensor calculations. J Phys Chem A 104:5149–5153
100. Engström M, Himo F, Ågren H (2000) Ab initio g-tensor calculations of the thioether substituted tyrosyl radical in galactose oxidase. Chem Phys Lett 319:191–196
101. Kaupp M, Gress T, Reviakine R, Malkina OL, Malkin VG (2003) g-Tensor and spin density of the modified tyrosyl radical in galactose oxidase: a density functional study. J Phys Chem B 107:331–337
102. van Gastel M, Lubitz W, Lassmann G, Neese F (2004) Electronic structure of the cysteine thiyl radical: a DFT and correlated ab initio study. J Am Chem Soc 126:2237–2246
103. See, e.g.: Stubbe J, van der Donk WA (1998) Protein radicals in enzyme catalysis. Chem Rev 98:705–762
104. See, e.g.: Allard P, Barra AL, Andersson KK, Schmidt PP, Atta M, Gräslund A (1996) Characterization of a new tyrosyl free radical in salmonella typhimurium ribonucleotide reductase with EPR at 9.45 and 245 GHz. J Am Chem Soc 118:895–896; van Dam PJ, Willems J-P, Schmidt PP, Pötsch S, Barra A-L, Hagen WR, Hoffman BM, Andersson KK, Gräslund A (1998) High-frequency EPR and pulsed Q-Band ENDOR studies on the origin of the hydrogen bond in tyrosyl radicals of ribonucleotide reductase R2 proteins from mouse and herpes simplex virus type 1. J Am Chem Soc 120:5080–5085; Un S, Gerez C, Elleingard E, Fontecave M (2001) Sensitivity of tyrosyl radical g-values to changes in protein structure: a high-field EPR study of mutants of ribonucleotide reductase. J Am Chem Soc 123:3048–3054; Ivancich A, Dorlet P, Goodin DB, Un S (2001) Multifrequency high-field EPR study of the tryptophanyl and tyrosyl radical intermediates in wild-type and the W191G mutant of cytochrome c peroxidase. J Am Chem Soc 123:5050–5058, and references cited in these works

105. Ivancich A, Mattioli TA, Un S (1999) Effect of protein microenvironment on tyrosyl radicals. A high-field (285 GHz) EPR, resonance Raman, and hybrid density functional study. J Am Chem Soc 121:5743–5753
106. Benisvy L, Bittl R, Bothe E, Garner CD, McMaster J, Ross S, Teutloff C, Neese F (2005) Phenoxyl radicals hydrogen-bonded to imidazolium: analogues of tyrosyl D of photosystem II: High-field EPR and DFT studies. Angew Chem Int Ed Engl 44:5314–5317; Brynda M, Britt RD (2007) Density functional theory calculations on the magnetic properties of the model tyrosine radical-histidine complex mimicking tyrosyl radical Y_D· bul. In Photosystem II. Res Chem Intermed 33:863–883
107. Benisvy L, Hammond D, Parker DJ, Davies ES, Garner CD, McMaster J, Wilson C, Neese F, Bothe E, Bittl R, Teutloff C (2007) Insights into the nature of the hydrogen bonding of Tyr272 in apo-galactose oxidase. J Inorg Biochem 101:1859–1864
108. Svistunenko DA, Jones TGA (2009) Radicals in proteins: a comparison of empirical and density functional calculated EPR parameters. Phys Chem Chem Phys 11:6600–6613
109. Klinman JP (1996) Mechanisms whereby mononuclear copper proteins functionalize organic substrates. Chem Rev 96:2541–2561
110. Ito N, Phillips SEV, Stevens C, Ogel ZB, McPherson MJ, Keen JN, Yadaf KDS, Knowles PF (1991) Novel thioether bond revealed by a 1.7 Angstrom label crystal structure of galactose oxidase. Nature 350:87–90
111. Babcock GT, El-Deeb MK, Sandusky PO, Whittaker MM, Whittaker JW (1992) Electron paramagnetic resonance and electron nuclear double resonance spectroscopies of the radical site in galactose oxidase and of thioether-substituted phenol model compounds. J Am Chem Soc 114:3727–3734
112. Gerfen GJ, Bellew BF, Griffin RG, Singel DJ, Ekberg CA, Whittaker JW (1996) High-frequency electron paramagnetic resonance spectroscopy of the apogalactose oxidase radical. J Phys Chem 100:16739–16748
113. Un S, Boussac A, Sugiura M (2007) Characterization of the tyrosine-Z radical and its environment in the spin-coupled S_2Tyr_Z· bul. State of photosystem II from thermosynechococcus elongates. Biochemistry 46:3138–3150
114. Bernini C, Pogni R, Ruiz-Duenas FJ, Martinez AT, Basosi R, Sinicropi A (2011) EPR parameters of amino acid radicals in *P. eryngii* versatile peroxidase and its W164Y variant computed at the QM/MM level. Phys Chem Chem Phys 13:5078–5098
115. Un S (2005) The g-values and hyperfine coupling of amino acid radicals in proteins: comparison of experimental measurements with ab initio calculations. Magn Reson Chem 43:229–236
116. Schoenberger F, Kerres J, Dilger H, Roduner E (2009) EPR spectroscopic investigation of radical-induced degradation of partially fluorinated aromatic model compounds for fuel cell membranes. Phys Chem Chem Phys 11:5782–5795
117. See, e.g.: Patai S (1974) Chemistry of quinoid compounds. Interscience, New York; Trumpower BL (ed) (1982) Function of quinones in energy conserving systems. Academic Press, New York; Morton RA (1965) Biochemistry of quinones. Academic Press, New York
118. See, e.g.: Pedersen JA (1985) EPR spectra from natural and synthetic quinones and quinoids. CRC Press, Boca Raton
119. See, e.g.: Lubitz W, Feher G (1999) The primary and secondary acceptors in bacterial photosynthesis. Part 3. Characterization of the quinone radicals Q_A· and Q_B· by EPR and ENDOR. Appl Magn Reson 17:1–48; Levanon H, Möbius K (1997) Advanced EPR spectroscopy on electron transfer processes in photosynthesis and biomimetic model systems. Annu Rev Biophys Biomol Struct 26:495–540
120. Burghaus O, Plato M, Rohrer M, Möbius K, MacMillan F, Lubitz W (1993) 3-mm high-field EPR on semiquinone radical anions $Q^{\cdot-}$ related to photosynthesis and on the primary donor $P^{\cdot+}$ and acceptor $Q_A^{\cdot-}$ in reaction centers of Rhodobacter sphaeroides R-26. J Phys Chem 97:7639–7647; Rohrer M, Plato M, MacMillan F, Grishin Y, Lubitz W, Möbius K (1995) Orientation-selected 95 GHz high-field ENDOR spectroscopy of randomly oriented plastoquinone anion radicals. J Magn Reson 116:59–66

121. Nimz O, Lendzian F, Boullais C, Lubitz W (1998) Influence of hydrogen bonds on the electronic g-tensor and ^{13}C-hyperfine tensors of ^{13}C-labeled ubiquinones. EPR and ENDOR study. Appl Magn Reson 14:255–274
122. Epel B, Sinnecker S, Zimmermann H, Lubitz W (2006) Phylloquinone and related radical anions studied by pulse electron nuclear double resonance spectroscopy at 34 GHz and density functional theory. J Phys Chem B 110:11549–11560; Sinnecker S, Reijerse E, Neese F, Lubitz W (2004) Hydrogen bond geometries from electron paramagnetic resonance and electron-nuclear double resonance parameters: density functional study of quinone radical anion-solvent interactions. J Am Chem Soc 126:3280–3290; Niklas J, Epel B, Antonkine ML, Sinnecker S, Pandelia M-E, Lubitz W (2009) Electronic structure of the quinone radical anion $A_1^{\cdot -}$ of photosystem I investigated by advanced pulse EPR and ENDOR techniques. J Phys Chem B 113:10367–10379
123. Kaupp M (2002) The function of photosystem I. quantum chemical insight into the role of tryptophan-quinone interactions. Biochemistry 41:2895–2900
124. Sieckmann I, van der Est A, Bottin H, Sétif P, Stehlik D (1991) Nanosecond electron transfer kinetics in photosystem I following substitution of quinones for vitamin K_1 as studied by time resolved EPR. FEBS Lett 284:98–102; van der Est A, Sieckmann I, Lubitz W, Stehlik D (1995) Differences in the binding of the primary quinone acceptor in Photosystem I and reaction centers of Rhodobacter sphaeroides-R26 studied with transient EPR spectroscopy. Chem Phys 194:349–359
125. Jordan P, Fromme P, Witt HT, Klukas O, Saenger W, Krauß N (2001) Three-dimensional structure of cyanobacterial photosystem I at 2.5 Å resolution. Nature 411:909–917
126. Kacprzak S, Kaupp M (2004) Electronic g-tensors of semiquinones in photosynthetic reaction centers. A density functional study. J Phys Chem B 108:2464–2469
127. Kacprzak S, Kaupp M (2006) Molecular mechanical devices based on quinone-pyrrole and quinone-indole dyads: a computational study. J Phys Chem B 110:8158–8165
128. Kacprzak S, Kaupp M, MacMillan F (2006) Protein-cofactor interactions and EPR parameters for the Q_H quinone binding site of quinol oxidase. A density functional study. J Am Chem Soc 128:5659–5671
129. Grimaldi S, Ostermann T, Weiden N, Mog T, Miyoshi H, Ludwig B, Michel H, Prisner TF, MacMillan F (2003) Asymmetric binding of the high-affinity $Q_H^{\cdot -}$ ubisemiquinone in quinol oxidase (bo3) from Escherichia coli studied by multifrequency electron paramagnetic resonance spectroscopy. Biochemistry 42:5632–5639
130. Yap LL, Samoilova RI, Gennis RB, Dikanov SA (2007) Characterization of mutants that change the hydrogen bonding of the semiquinone radical at the Q_H site of the cytochrome bo3 from Escherichia coli. J Biol Chem 282:8777–8785
131. Boesch SE, Wheeler RA (2009) Isotropic ^{13}C hyperfine coupling constants distinguish neutral from anionic ubiquinone-derived radicals and tell which oxygen is protonated in the neutral. ChemPhysChem 10:3187–3189
132. MacMillan F, Kacprzak S, Hellwig P, Michel H, Kaupp M (2010) Elucidating mechanisms in haem copper oxidases: the high-affinity Q_H binding site in quinol oxidase as studied by DONUT-HYSCORE spectroscopy and density functional theory. J Chem Soc Faraday Trans 148:315–344
133. Witwicki M, Jezierska J (2011) Effects of solvents, ligand aromaticity, and coordination sphere on the g-tensor of anionic *o*-semiquinone radicals complexed by Mg^{2+} ions: DFT studies. J Phys Chem B 115:3172–3184; Witwicki M, Jerzykiewicz M, Jaszewski AR, Jezierska J, Ozarowski A (2009) Influence of Pb(II) ions on the EPR properties of the semiquinone radicals of humic acids and model compounds: high field EPR and relativistic DFT studies. J Phys Chem A 113:14115–14122
134. Witwicki M, Jezierska J (2010) Protic and aprotic solvent effect on molecular properties and g-tensors of *o*-semiquinones with various aromaticity and heteroatoms: a DFT study. Chem Phys Lett 493:364–370; Witwicki M, Jezierska J, Ozarowski A (2009) Solvent effect on EPR, molecular and electronic properties of semiquinone radical derived from 3,4-dihydroxybenzoic acid as model for humic acid transient radicals: high-field EPR and DFT

studies. Chem Phys Lett 473:160–166; Witwicki M, Jaszewski AR, Jezierska J, Jerzykiewicz M, Jezierski A (2008) The pH-induced shift in the g-tensor components of semiquinone-type radicals in humic acids – DFT and EPR studies. Chem Phys Lett 462:300–306

135. Ciofini I, Adamo C, Barone V (2004) Complete structural and magnetic characterization of biological radicals in solution by an integrated quantum mechanical approach: glycyl radical as a case study. J Chem Phys 121:6710–6718
136. Pogni R, Teutloff C, Lendzian F, Basosi R (2007) Tryptophan radicals as reaction intermediates in versatile peroxidases: multifrequency EPR, ENDOR and density functional theory studies. Appl Magn Reson 31:509–526
137. Bleifuss G, Kolberg M, Pötsch S, Hofbauer W, Bittl R, Lubitz W, Gräslund A, Lassmann G, Lendzia F (2001) Tryptophan and tyrosine radicals in ribonucleotide reductase: a comparative high-field EPR study at 94 GHz. Biochemistry 40:15362–15368
138. Teutloff C, Hofbauer W, Zech SG, Stein M, Bittl R, Lubitz W (2001) High-frequency EPR studies on cofactor radicals in photosystem I. Appl Magn Reson 21:363–379; Petrenko A, Redding K, Kispert LD (2005) The influence of the structure of the radical cation dimer pair of aromatic molecules on the principal values of a g-tensor: DFT predictions. Chem Phys Lett 406:327–331
139. Stoll S, Gunn A, Brynda M, Sughrue W, Kohler A, Ozarowski A, Fisher A, Lagarias JC, Britt RD (2009) Structure of the biliverdin radical intermediate in phycocyanobilin: ferredoxin oxidoreductase identified by high-field EPR and DFT. J Am Chem Soc 13:1986–1995
140. Pauwels E, Declerck R, Verstraelen T, De Sterck B, Kay CWM, Van Speybroeck V, Waroquier M (2010) Influence of protein environment on the electron paramagnetic resonance properties of flavoprotein radicals: A QM/MM study. J Phys Chem B 114:16655–16665
141. Fuchs MR, Schleicher E, Schnegg A, Kay CWM, Törring JT, Bittl R, Bacher A, Richter G, Möbius K, Weber S (2002) g-Tensor of the neutral flavin radical cofactor of DNA photolyase revealed by 360-GHz electron paramagnetic resonance spectroscopy. J Phys Chem B 106:8885–8890
142. Stoll S, Jahromi YN, Woodward JJ, Ozarowski A, Marletta MA, Britt RD (2010) Nitric oxide synthase stabilizes the tetrahydrobiopterin cofactor radical by controlling its protonation state. J Am Chem Soc 132:11812–11823
143. Pauwels E, Declerck R, Van Speybroeck V, Waroquier M (2008) Evidence for a Grotthuss-like mechanism in the formation of the rhamnose alkoxy radical based on periodic DFT calculations. Rad Res 169:8–18
144. Zipse H, Artin E, Wnuk S, Lohman GJS, Martino D, Griffin RG, Kacprzak S, Kaupp M, Hoffman B, Bennati M, Stubbe J, Lees N (2009) Structure of the nucleotide radical formed during reaction of CDP/TTP with the E441Q-$\alpha 2\beta 2$ of *E. coli* ribonucleotide reductase. J Am Chem Soc 131:200–211
145. Tanaka A, Nakashima K-I (2011) DFT studies of ESR parameters for N-O centered radicals, N-alkoxyaminyl and aminoxyl radicals. Magn Reson Chem 49:603–610; Tanaka A, Nakashima K-I, Miura Y (2010) DFT studies of N-alkoxyaminyl radicals: ESR parameters, UV–vis absorptions and generations. Tetrahed 67:2260–2268; Gomzi V (2008) Radicals formed in cytosine-hydrochloride(thiocytosine) single crystals: insights from a DFT study. J Mol Struct Theochem 860:137–140; Gomzi V (2007) Dependence of the radical g-tensor on the molecular environment. Sulfur-centered radicals of thiocytosine in the cytosine crystal matrices. Chem Phys 333:112–118

Chapter 8
Quantum Chemical Calculations of the Zero-Field Splitting Tensors for Organic Spin Multiplets

Kenji Sugisaki, Kazuo Toyota, Kazunobu Sato, Daisuke Shiomi, Masahiro Kitagawa, and Takeji Takui

Abstract In this chapter the state-of-the-art quantum chemical methods for zero-field splitting (ZFS) tensors (**D** tensors) of organic high spin multiplets are reviewed. Both spin–spin dipolar ($\mathbf{D}^{SS}$) and spin–orbit ($\mathbf{D}^{SO}$) coupling terms appearing in the first and second order, respectively, in the perturbation theory starting from the non-relativistic Schrödinger equation are focused on. Theoretical frameworks for the $\mathbf{D}^{SS}$ and $\mathbf{D}^{SO}$ tensors in terms of ab initio molecular orbital theory and density functional theory (DFT) are outlined, and several examples of the $\mathbf{D}^{SS}$ and $\mathbf{D}^{SO}$ tensor calculations including spin–orbit coupling dominant systems ($D^{SO} \gg D^{SS}$), electronic ground states of organic high-spin systems (spin-quintet and septet species), excited triplet states of closed-shell molecules, and a thermally accessible excited triplet state of quinonoidal dinitrene are given, emphasizing that they all have given testing grounds for the theoretical treatment of **D** tensors.

8.1 Introduction

The last decades have witnessed that nowadays computational methods for most of the spin-Hamiltonian parameters such as hyperfine (**A**) tensors, **g** tensors, exchange coupling parameters J, and nuclear quadrupole (**Q**) tensors are well established [1], and we can routinely calculate these spin-Hamiltonian parameters by utilizing published or available quantum chemistry program packages, except for reliable quantum chemical computations for J in unlimited constraints.

K. Sugisaki • K. Toyota • K. Sato • D. Shiomi • T. Takui (✉)
Department of Chemistry and Molecular Materials Science, Graduate School of Science, Osaka City University, 3-3-138 Sugimoto, Osaka 558-8585, Japan
e-mail: takui@sci.osaka-cu.ac.jp

M. Kitagawa
Department of System Innovation, Graduate School of Engineering Science, Osaka University, 1-3 Machikaneyama, Toyonaka, Osaka 560-8531, Japan

A. Lund and M. Shiotani (eds.), *EPR of Free Radicals in Solids I*, Progress in Theoretical Chemistry and Physics 24, DOI 10.1007/978-94-007-4893-4_8,

By contrast, the exploitation of theoretical methods for zero-field splitting (ZFS) tensors [2] (**D** tensors) is still a developing field and it is one of the currently important issues in the field of electron spin science and technology as well as in quantum chemistry. Anisotropic interactions between unpaired electrons can break the degeneracy of electron spin sublevels even in the absence of external magnetic field. The fact that ZFS originates in interactions between electron spins implies the relativistic nature of ZFS phenomena. Because the **D** tensors are parameters reflecting relative orientations of unpaired electrons in the molecular framework, accurate determinations of the **D** tensors of organic spin multiplets are essentially important tasks not only to understand their electronic structures but also to establish a quantum chemistry-based rationale for molecular designs of open-shell organic systems with novel functionalities [3]. Studies of organic high-spin systems have been motivated from the standpoint of molecular magnetisms and magnetics, and spintronics in earlier days [4–6], and recently they take part in the field of quantum computing and quantum information processing [7], which are entirely new concepts of computations and information technologies based on quantum mechanical principles such as the superposition of states and quantum entanglement [8]. Stable organic ground-triplet or high spins ($S > 1$), in ensemble in the solid state, with sizable ZFS parameters can afford implementation of quantum information processors, such as quantum memories, coupled with superconducting qubits (quantum bits).

ESR spectroscopy is widely used for the detections and characterizations of organic spin multiplets. The major advantages of ESR are its high sensitivity and selectivity. Pulse-based electron spin transient nutation (ESTN) spectroscopy [9] can afford a straightforward identification of spin multiplicities even in the mixture of high-spin multiplets, oriented or non-oriented media. Technical advances in synthetic chemistry and progresses in matrix isolation techniques [10] allow us to observe clean continuous-wave (cw-) ESR spectra, and a hybrid eigenfield method [11] for calculating exact resonance fields and transition probabilities enables us to derive accurate ZFS parameters by simulating the fine-structure ESR spectra. The determination of the directions of the principal axes of **D** with respect to molecular skeletons is also important, but it generally requires angular dependence experiments using oriented samples such as magnetically diluted single crystals, liquid crystals and thin films.

In principle, quantum chemical calculations can afford to give **D** tensors without a priori knowledge of the spin structures of chemical systems. We note that the strength of spin–orbit couplings which appear as the second-order contribution to **D** is hard to predict from molecular formulas. In organic molecules consisting of only light atoms the spin–orbit couplings are conceived of as being weak, and historically spin–orbit coupling contributions to the **D** tensors of organic open-shell species have often been ignored in the theoretical model. However, recent sophisticated considerations of the spin–orbit coupling terms of the **D** tensors have revealed the importance of the spin–orbit couplings for the quantitative understanding of the **D** tensors [12].

This chapter is organized as follows. In the Sect. 8.2, we give a brief introduction of ZFS phenomena and explain theoretical backgrounds of ZFS. Theoretical approaches to **D** tensors based on ab initio post-SCF and density functional theory (DFT) are summarized. In the Sect. 8.3, we provide some examples of theoretical calculations of **D** tensors. Electronically ground and thermally accessible excited states of mono-, di-, and tri-nitrenes, and excited triplet states of closed-shell diazabenzenes are considered. Spin-mediated carbene chemistry is important, but not included in the examples because of space limitations. Group-16 diatomic molecules (O_2-analogs) are also treated as prototypical examples that the spin–orbit couplings dominantly contribute to their **D** tensors. In the Sect. 8.4, summary and future perspectives of the **D** tensor calculations are given.

8.2 Theoretical Background

ZFS effects can be observed in spin multiplet systems, and ZFS is often a leading contribution in the spin-Hamiltonian of the system with the spin quantum number $S > 1/2$. Since ZFS arises from interactions between electron spins, quantum chemical understanding of the **D** tensors is important, particularly in quest for molecular spin devices or new molecular functionalities relevant to spin structures of open shell compounds. In this section, general characteristics of the **D** tensors are briefly outlined. Then, physical origins of the ZFS and theoretical approaches to the **D** tensors are summarized. Some examples of the calculations will be provided in the Sect. 8.3.

8.2.1 Zero-Field Splitting Tensors

In the phenomenological spin-Hamiltonian, the ZFS term is described as follows:

$$H^{ZFS} = \mathbf{S} \cdot \mathbf{D} \cdot \mathbf{S} \tag{8.1}$$

where **S** denotes an electron spin operator, and **D** is a traceless tensor of rank two:

$$\mathbf{D} \doteq \begin{pmatrix} D_{xx} & D_{xy} & D_{xz} \\ D_{yx} & D_{yy} & D_{yz} \\ D_{zx} & D_{zy} & D_{zz} \end{pmatrix} \tag{8.2}$$

$$D_{xx} + D_{yy} + D_{zz} = 0 \tag{8.3}$$

By using the traceless condition, the **D** tensor can be characterized by only two scalar parameters D and E, termed ZFS parameters or fine-structure parameters, and

by three principal axes due to the nature of the tensor. The D and E values are related to the three principal values in the following equations:

$$D = D_{ZZ} - (D_{XX} + D_{YY})/2 \tag{8.4}$$

$$E = (D_{XX} - D_{YY})/2 \tag{8.5}$$

Throughout this chapter we use x, y, and z in subscript for computational Cartesian coordinates (or experimental coordinates) and X, Y, and Z for the principal axes coordinates in which the **D** tensor is in a diagonal form.

$$D_{XY} = D_{XZ} = D_{YX} = D_{YZ} = D_{ZX} = D_{ZY} = 0 \tag{8.6}$$

By convention, if the **D** tensor has an axial symmetry, the D_{ZZ} axis is chosen to be parallel to the symmetric axis with vanishing E value. Otherwise, the D_{ZZ} axis is chosen to satisfy the following relationship

$$|E/D| \leqslant 1/3. \tag{8.7}$$

These definitions are convenient for qualitative understanding of the **D** tensor, because in particular organic biradical systems the D value is roughly proportional to $1/{r_{12}}^3$, where r_{12} is the distance between two unpaired electrons, and the E value reflects the deviation of the **D** tensor from the axial symmetry. These interpretations can be easily understood from the definition of the spin–spin dipolar coupling Hamiltonian. The absolute sign of D enables us to roughly extract the mode of unpaired electron distributions. In spin-triplet systems, if two unpaired electrons are spatially localized, a negative D value is expected and the D_{ZZ} axis is along the direction connecting the two unpaired electrons. By contrast, if two unpaired electrons are delocalized onto the same π systems like the $\pi\pi^*$ excited triplet state of benzene, the D_{ZZ} axis is perpendicular to the π conjugation and a positive D value is anticipated. These interpretations are convenient and useful for the qualitative understanding, but they are sometimes too simple to describe real systems or to provide new insights into electronic spin structures. For example, which absolute sign is expected in three-dimensionally spin-delocalized molecular systems like an excited triplet state of fullerene or a triplet ground state of dianionic fullerene? Putative answers based on naïve pictures are not correct. Quantum chemical calculations are potentially capable of giving right answers to the questions.

It should be noted that the conventional definitions of the principal axes are sometimes inconvenient in order to discuss substituent effects and geometry dependence of the **D** tensor, when the direction of the D_{ZZ} axis with respect to the molecular frame is changed by perturbations. In such cases, a coordinate system fixed to the molecular axis can often be used, e.g., a molecular long axis for D_{xx}, a short axis for D_{yy}, and perpendicular to the molecular plane for D_{zz} in planar π-conjugated hydrocarbons.

8.2.2 The First Order Contribution from Spin–Spin Dipolar Couplings

As already stated, ZFS originates in the relativistic effect. In organic molecules, the D values are typically less than 1 cm^{-1} and a perturbation approach starting from the non-relativistic Schrödinger equation and Breit–Pauli Hamiltonian is suitable for the calculation of the **D** tensors. In the well-known Breit–Pauli Hamiltonian, spin–spin dipolar coupling and spin–orbit coupling terms contain spin operators and thus have contributions to the **D** tensors [2].

The theoretical Hamiltonian of the spin–spin dipolar coupling is represented as follows:

$$H^{SS} = \alpha^2 \sum_{i<j} \left[\frac{\mathbf{s}_i \cdot \mathbf{s}_j}{r_{ij}^3} - \frac{3\left(\mathbf{s}_i \cdot \mathbf{r}_{ij}\right)\left(\mathbf{s}_i \cdot \mathbf{r}_{ij}\right)}{r_{ij}^5} \right] \tag{8.8}$$

Here, α is a fine-structure constant, $\mathbf{r}_{ij} = \mathbf{r}_i - \mathbf{r}_j$ and $r_{ij} = |r_i - r_j|$ for electrons i and j at positions $\mathbf{r}_i$ and $\mathbf{r}_j$, and $\mathbf{s}_i$ and $\mathbf{s}_j$ are spin operators acting on electrons i and j, respectively. In H^{SS}, two spin operators are involved and therefore it appears as the first order term in the perturbation expansion of the **D** tensor. Thus, the spin–spin dipolar term of the **D** tensor (denoted the $\mathbf{D}^{SS}$ tensor) can be calculated as an expectation value by using the unperturbed (zeroth order) wavefunction.

$$D_{ab}^{SS} = \frac{\alpha^2}{S\left(2S-1\right)} \left\langle \Psi_{n,S,Ms=S} \left| \sum_{i<j} \frac{r_{ij}^2 \delta_{ab} - 3\left(r_{ij}\right)_a \left(r_{ij}\right)_b}{r_{ij}^5} \right. \right.$$
$$\left. \left. \times \left(2s_{iz}s_{jz} - s_{ix}s_{jx} - s_{iy}s_{jy}\right) \right| \Psi_{n,S,Ms=S} \right\rangle \tag{8.9}$$

Here a and b run over x, y, and z, and the subscripts of Ψ represent the n'th eigenstate with the spin quantum number S and corresponding magnetic quantum number $M_S = S$.

After the second quantization of the right hand side of Eq. (8.9) and summing over spins we obtain the following equation.

$$D_{ab}^{SS} = \frac{\alpha^2}{2S\left(2S-1\right)}$$
$$\times \sum_{pqrs} \int p^*\left(\mathbf{r}_1\right) q^*\left(\mathbf{r}_2\right) \frac{r_{12}^2 \delta_{ab} - 3r_{12a}r_{12b}}{r_{12}^5} r\left(\mathbf{r}_1\right) s\left(\mathbf{r}_2\right) d\mathbf{r}_1 d\mathbf{r}_2 \Gamma_{pqrs}^{SS} \tag{8.10}$$

Here, Γ^{SS} is a two-particle spin density matrix.

$$\Gamma^{SS}_{pqrs} = \frac{1}{2}\left\langle \Psi_{n,S,Ms=S} \middle| \left(a^{\dagger}_{p\alpha} a^{\dagger}_{q\alpha} a_{s\alpha} a_{r\alpha} \; - a^{\dagger}_{p\beta} a^{\dagger}_{q\alpha} a_{s\alpha} a_{r\beta} \right.\right.$$
$$- a^{\dagger}_{p\alpha} a^{\dagger}_{q\beta} a_{s\alpha} a_{r\beta} - a^{\dagger}_{p\beta} a^{\dagger}_{q\alpha} a_{s\beta} a_{r\alpha} - a^{\dagger}_{p\alpha} a^{\dagger}_{q\beta} a_{s\beta} a_{r\alpha}$$
$$\left.\left. + a^{\dagger}_{p\beta} a^{\dagger}_{q\beta} a_{s\beta} a_{r\beta} \right) \middle| \Psi_{n,S,Ms=S} \right\rangle \tag{8.11}$$

When the wavefunction consists of a single determinant, such as a Hartree–Fock wavefunction, two-particle spin density matrices can be constructed in a sufficient manner from the spin density matrices. Mathematical transformation along this line leads to the following equation of $\mathbf{D}^{\mathrm{SS}}$, which have been derived by McWeeny and Mizuno [13]:

$$D^{SS}_{ab} = \frac{\alpha^2}{4S\,(2S-1)} \sum_{pqrs} \left(\rho^{\alpha-\beta}_{pr} \rho^{\alpha-\beta}_{qs} - \rho^{\alpha-\beta}_{ps} \rho^{\alpha-\beta}_{qr} \right)$$
$$\times \int p^{*}\,(\mathbf{r}_1)\, q^{*}\,(\mathbf{r}_2)\, \frac{r^2_{12}\delta_{ab} - 3r_{12a}r_{12b}}{r^5_{12}} r\,(\mathbf{r}_1)\, s\,(\mathbf{r}_2)\, d\mathbf{r}_1 d\mathbf{r}_2 \tag{8.12}$$

Recently, Eq. (8.12) has been adopted to calculate $\mathbf{D}^{\mathrm{SS}}$ tensors in terms of density functional theory (DFT) in which the Kohn–Sham determinant is used for the spin density constructions by several groups [12b, c, 14–20]. It should be noted that if Eq. (8.12) is combined with the DFT spin density the obtained $\mathbf{D}^{\mathrm{SS}}$ tensor is not for the real system but for the non-interacting reference system. In this context, the insertion of the DFT-based spin densities into Eq. (8.12) should be referred to as a "mean-field approximation" or a "no interaction approximation". Behaviors of "no interaction approximation" in the $\mathbf{D}^{\mathrm{SS}}$ tensor will be discussed in the Sect. 8.3.

For the post-HF approaches to the calculation of the $\mathbf{D}^{\mathrm{SS}}$ tensors, configuration interaction (CI) [21–23], multiconfiguration self-consistent field (MCSCF) [22, 24–26], and multireference CI (MRCI) [27], etc., have been reported. It has been shown that single excitation CI (CIS or SECI) tends to overestimate the D^{SS} value in triplet-state methylene [22, 23], but the inclusion of double and higher excitation operators systematically improves the D^{SS} value [22]. The MCSCF method has been mainly adapted to the excited triplet states of aromatic systems and triplet ground-state carbenes and nitrenes, and it can afford to reproduce D^{SS} values in a quantitative or semiquantitative manner. Computational codes for the calculations of $\mathbf{D}^{\mathrm{SS}}$ tensors at the CASSCF and RASSCF levels are available in the Dalton program package [28]. The MRCI method has been applied to the $\mathbf{D}^{\mathrm{SS}}$ tensor of dioxygen O_2 by Gilka et al. [27] and they pointed out the importance of the doubly excited configurations on the D^{SS} value. Also, they found that the correlation energy and D^{SS} value exhibit different behaviors with respect to the number of reference configurations.

It should be noted that the spin–spin contact Hamiltonian also contains two electron spin operators and thus it can contribute to **D** tensors at the first order, but the spin–spin contact term is just a constant contribution which does not depend on M_S and therefore it is isotropic. This corresponds to a shift of the energy origin, having no effects on the energy separations among spin sublevels. ESR is the spectroscopy that involves magnetic transitions between the spin sublevels and therefore isotropic term of **D** cannot be measured. Thus the isotropic spin–spin contact term of the **D** tensors is normally neglected.

8.2.3 *The Second Order Contribution from Spin–Orbit Couplings*

The Breit–Pauli spin–orbit coupling Hamiltonian is written in the form

$$H^{SO} = \frac{\alpha^2}{2}\left[\sum_{i,A}\frac{Z_A}{r_{iA}^3}\mathbf{l}_{iA}\cdot\mathbf{s}_i - \sum_{i\neq j}\frac{1}{r_{ij}^3}\mathbf{l}_{ij}\cdot\left(\mathbf{s}_i + 2\mathbf{s}_j\right)\right] \tag{8.13}$$

where Z_A is the charge of a nucleus A. The first term of Eq. (8.13) contains one electron and one nuclear index, and it is referred to as a one-electron spin–orbit term. The second and the third terms of Eq. (8.13), on the contrary, include two electron spin indices. These terms are usually called as spin–same-orbit and spin–other-orbit terms, respectively. Because the two electron terms in the Breit–Pauli spin–orbit Hamiltonian grow slowly as the nuclear charge Z increases, but the one-electron term grows rapidly with increasing Z (roughly scaled by Z^4), empirical one-electron operators described in Eq. (8.14) are sometimes utilized for molecules containing heavy atoms.

$$H_{eff}^{SO} = \frac{\alpha^2}{2}\left[\sum_{i,A}\frac{Z_A^{eff}}{r_{iA}^3}\mathbf{l}_{iA}\cdot\mathbf{s}_i\right] \tag{8.14}$$

where $Z_A{}^{eff}$ denotes an empirical effective charge of a nucleus A. In the framework of DFT, this approximated Hamiltonian is sometimes used. However, it should be emphasized that this approximation is not always appropriate because in organic molecules composed of only light atoms the one-electron and the two-electron terms are comparable in magnitude. More sophisticated treatments of the approximated spin–orbit Hamiltonian are summarized by Marian [29].

Because the spin–orbit coupling Hamiltonian (Eq. 8.13) contains one spin operator, the spin–orbit contribution to the **D** tensor (the $\mathbf{D}^{SO}$ term) appears in the second order in the perturbation theory. Therefore, the $\mathbf{D}^{SO}$ tensor can be computed by utilizing the following sum-over-states (SOS) equations [12b, 30]:

$$D_{ab}^{SO} = \sum_{n,\sigma} C\,(\sigma)\,\frac{\left\langle \Psi_{0,S,M} \left| H_a^{SO} \right| \Psi_{n,S+\sigma,M} \right\rangle \left\langle \Psi_{n,S+\sigma,M} \left| H_b^{SO} \right| \Psi_{0,S,M} \right\rangle}{E_{n,S+\sigma} - E_{0,S}} \tag{8.15}$$

$$C\,(\sigma = -1) = -\frac{1}{2S-1}, \quad C\,(\sigma = 0) = \frac{1}{S^2}, \quad C\,(\sigma = +1) = -\frac{1}{2S+1} \tag{8.16}$$

Here, σ runs over −1, 0, and +1. Note that the coefficients $C(\sigma)$ (Eq. 8.16) depend on the choice of the intermediate states in regard to the M_S value. This is the reason why $C(\sigma)$'s appearing in references [12b] and [30] are different (see Ref. 12b for the details). This SOS equation has a very simple form and it is easily implemented in quantum chemistry programs. The SOS approaches to $\mathbf{D}^{SO}$ tensors have been adopted in wavefunction-based methods such as CI [21a, c] and MCSCF [22, 24, 25]. The difficulty in the calculation of the $\mathbf{D}^{SO}$ tensor in terms of the SOS formula is that sophisticated and balanced descriptions of wavefunctions of electronically excited states of different spin multiplicities as well as the ground state are required to obtain quantitative results. This requirement is sometimes very severe, and in case the target state is surrounded by nearby electronic states, it is very hard to obtain the $\mathbf{D}^{SO}$ tensor of organic high spins even qualitatively. Complete active space (CAS)-SCF wavefunctions are frequently used for the calculation of $\mathbf{D}^{SO}$ tensors with Eq. (8.15), but it is known that the CASSCF energy difference is in general not directly comparable to the experimental ΔE, due to the apparent lack of dynamical electron correlation effects. Thus, the $\mathbf{D}^{SO}$ tensor calculated by conventional SOS-CASSCF approach suffers from an uncertainty arising from inaccurate CASSCF energy differences and in some cases the calculated $\mathbf{D}^{SO}$ tensor is far from the experimentally obtained one. This difficulty can be circumvented by using the second-order multireference Møller–Plesset (MRMP2) method [31] for the calculation of the zeroth order energies to take into account dynamical electron correlation effects, as recently proposed by us [12].

In the hybrid CASSCF/MRMP2 approach, spin–orbit coupling matrices appearing in the numerator of Eq. (8.15) are calculated at the CASSCF level, and energy differences in the denominator are computed at the MRMP2 level. This approach allows us to calculate $\mathbf{D}^{SO}$ tensors in the presence of dynamical electron correlation effects, and as discussed in the Sect. 8.3, this approach enables us to predict $\mathbf{D}^{SO}$ tensors quantitatively, regardless of the spin multiplicity of the target state and whether the target state is a ground or an excited state, if the appropriate CASSCF active space is chosen.

Another approach to $\mathbf{D}^{SO}$ tensor calculations by CI or MCSCF methods is a method based on the spin–orbit CI (SO-CI). In the SO-CI approach [32], the spin–orbit CI Hamiltonian matrix expanded into a matrix corresponding to all M_S values for a pair of multiplicities is generated as the sum of unperturbed spin-free Hamiltonian and spin–orbit Hamiltonian matrices. In the state basis, the spin-free Hamiltonian is of course diagonal, and only the spin–orbit Hamiltonian has off-diagonal elements. Then, the Hamiltonian matrix is diagonalized to obtain spin-mixed wavefunctions and eigenenergies. In the SO-CI approach, principal

values of the **D** tensor is obtainable directly from the energy differences between spin sublevels. In the SO-CI with the MCSCF wavefunction, substituting CASPT2 [33] energies for the diagonal elements of the spin–orbit CI Hamiltonian is efficient to account for dynamical electron correlation effects [34, 35]. This approach is termed a spin–orbit state interaction (SO-SI) method. Note that in the framework of ab initio methods for the $\mathbf{D}^{SO}$ tensor calculations without the SOS formula, there is also a generalized unrestricted Møller–Plesset approach. This approach is based on two-component SCF procedures with the second-order Douglas–Kroll–Hess Hamiltonian, and it has been applied to triplet diatomic systems [36].

The SOS approach to $\mathbf{D}^{SO}$ tensors is straightforward and it is easy to carry out theoretical analyses, but this approach is not always suitable for large systems from the viewpoint of computational costs. For the $\mathbf{D}^{SO}$ tensor calculations of large systems only the DFT-based approaches are still realistic choices. To date, several approaches to $\mathbf{D}^{SO}$ tensor calculations by DFT have been proposed [37–42], but here we refer to only three methods very briefly: coupled-perturbed (CP) [37], Pederson–Khanna (PK) [38], and quasi-restricted orbital (QRO) methods [39], all of them are equipped in the ORCA program package [43]. The CP method is based on the analytic derivatives of the SCF energy and a set of coupled-perturbed equations are to be solved. The PK method solves sum-over orbital pair equations that resemble the SOS equation (8.15). This approach is valid only in the absence of non-local exchange potentials, namely for pure exchange–correlation functionals, but it has been applied in conjunction with hybrid functionals. The QRO method is quite similar to the PK approach, but natural orbitals constructed from the unrestricted HF or KS orbitals are used for the expansion of sum-over orbital pair equations. The relationships among these methods are recently analyzed in detail [44], and the performance of these methods is briefly discussed in the next section.

8.3 Applications

In this section, some examples of quantum chemical calculations for the **D** tensors of open shell molecular systems are given. Again, it should be emphasized that the computational methods for the **D** tensors have not fully been established yet, and therefore conclusive discussions are sometimes difficult, especially in the spin–spin part. We have noted that this point has not seriously been examined in spite of the fact that the theoretical fine-structure parameters of extensively π-delocalized hydrocarbons greatly depart from the experimental ones. Since electron correlation plays a significant role in the spin–spin dipolar term $\mathbf{D}^{SS}$, high-level ab initio methods such as MRCI or coupled-cluster are required to obtain genuinely accurate $\mathbf{D}^{SS}$ tensors. As discussed below, the RO-DFT method generally can give practically quantitative $\mathbf{D}^{SS}$ tensors when less than two unpaired electrons are delocalized onto π-conjugations, as a result of some kind of systematical cancellation of errors. However, as discussed in Sect. 8.3.5, RO-DFT fails to predict correct $\mathbf{D}^{SS}$ tensors when the static electron correlation plays an important role in the wavefunction, even if the unpaired electrons are spatially localized.

Table 8.1 Theoretical and experimental fine-structure parameter D (in unit of cm^{-1}) of group-16 triplet diatomics

	B3LYP [42]	BP86 [42]	BP86 [42]	BP86 [42]	BP86 [42]	BP86 [42]	CASSCF	Exptl. [45]
H^{SO}[a]	SOMF	SOMF	SOMF	SOMF	AMFI	AMFI	Full BP	
ZFS[b]	CP	CP	QRO	PK	PK	2comp	SOS	
O_2	+3.2	+3.1	+3.3	+2.4			+2.5	4.0
SO	+9.0	+8.5	+7.9	+4.5	+4.1	+4.1	+8.7	10.6
S_2	+18.9	+18.0	+18.0	+9.3	+9.2	+9.6	+19.7	23.6
SeO	+146.8	+141.6	+103.4	+65.1	+69.5	+70.3	+121.2	165.9
SeS	+171.5	+165.1	+137.4	+78.4	+83.0	+83.7	+161.7	205.0
Se_2	+488.5	+429.9	+411.0	+217.7	+232.7	+223.9	+469.5	510.0

[a]Theoretical Hamiltonian used for the evaluation of spin–orbit coupling. SOMF is an effective one electron spin–orbit Hamiltonian, AMFI is an atomic mean-field spin–orbit operator, and full BP is a full Breit–Pauli Hamiltonian

[b]Theoretical models for the $\mathbf{D}^{SO}$ tensor calculation. *CP* coupled-perturbed, *QRO* quasi-restricted orbital, *PK* Pederson–Khanna, *2comp* two component noncolinear spin-density-functional method, *SOS* sum-over-states approach

8.3.1 Group-16 Triplet Diatomics

At first, we discuss performances of the $\mathbf{D}^{SO}$ tensor calculations, because the theoretical method for the $\mathbf{D}^{SO}$ tensor is more advanced and sophisticated than those for $\mathbf{D}^{SS}$. Here we treat group-16 triplet diatomics, namely O_2 and O_2-analogs. It is well known that the spin–orbit coupling becomes strong as the row of the periodic table goes down. Group-16 diatomic molecules have spin-triplet ground states, and their fine-structure parameters have been determined experimentally [45]. Indeed, these molecules are inorganic, but they are suitable for a benchmark study.

Table 8.1 summarizes the theoretical and experimental fine-structure parameter D of group-16 homo- and hetero-diatomics up to fourth row.

Vahtras et al. reported the theoretical D^{SS} value of O_2 to be 1.44 cm^{-1} at the CASSCF/aug-cc-pCVTZ level [25a]. Ganyushin and Neese reported the D^{SS} values of O_2, SO, and S_2 to be 1.56, 0.65, and 0.27 cm^{-1}, respectively, at the CASSCF level with a "mean-field approximation" [46]. At the MRCI/cc-pVTZ level with a reference space of 250 configurations the theoretical D^{SS} value is 1.54 cm^{-1}. The SOS-CASSCF calculations for $\mathbf{D}^{SO}$ in Table 8.1 are carried out using (12,8) active space which includes all valence s and p orbitals, with def2-TZVPP basis set. Here, (n,m) represents n active electrons in the m chosen orbitals. The CASSCF/MRMP2 calculations are carried out by using GAMESS software [47]. As shown in Table 8.1, all methods reproduce tendencies of the D value. The PK and the two-component SDFT approaches tend to underestimate the D value to be about one half. In heavier molecules the CP approach gives the best agreements with the experiment, but the CP method overestimates the D^{SO} value in dioxygen O_2 to some extent. It should

be noted that the CP method does not always give quantitative $\mathbf{D}^{SO}$ tensors; it is regarded that the PK method gives better $\mathbf{D}^{SO}$ tensors than the CP approach [18a, 39, 48].

The SOS-CASSCF method tends to underestimate the D value in heavier molecules. Deviations of the D^{SO} values from experimental ones are ca. 10 and 20% for homo- and hetero-diatomics, respectively. Applying energy denominator corrections by MRMP2 do not improve significantly the theoretical D^{SO} value in these molecules: the D^{SO} values calculated at the hybrid CASSCF/MRMP2 level are +2.4, +8.4, +20.0, +129.6, +160.4, and +473.4 cm^{-1} for O_2, SO, S_2, SeO, SeS, and Se_2, respectively.

One of the great advantages of the SOS approach is the easiness of theoretical analyses. Here, we pick up Se_2 as an example. The ground state of Se_2 is $1\ ^3B_{1g}$ state in the largest Abelian (D_{2h}) symmetry ($1\ ^3\Sigma_g^-$ in $D_{\infty h}$), in which the unpaired electrons occupy $4b_{2g}$ and $4b_{3g}$ orbitals of 4p–4p antibonding nature. Applying the SOS approach gives the following $\mathbf{D}^{SO}$ tensor:

$$D^{SO}\ (\text{Calcd.}) = \begin{pmatrix} -2.9669 & 0 & 0 \\ 0 & -2.8656 & 0 \\ 0 & 0 & 466.5986 \end{pmatrix} \tag{8.17}$$

Note that the $\mathbf{D}^{SO}$ tensor is already diagonal in the computational coordinates from molecular symmetry. The *XX*, *YY*, and *ZZ* components are the results of spin–orbit coupling to excited states of B_{2g}, B_{3g}, and A_g symmetries, respectively. It is clear that the large D^{SO} value of Se_2 originates from strong spin–orbit coupling between the $1\ ^3B_{1g}$ ground state and the A_g excited states. Equations (8.18) and (8.19) specify contributions from the singlet and triplet excited states, respectively.

$$D^{SO}\ (\text{Singlet}) = \begin{pmatrix} 18.0053 & 0 & 0 \\ 0 & 18.2480 & 0 \\ 0 & 0 & 467.5344 \end{pmatrix} \tag{8.18}$$

$$D^{SO}\ (\text{Triplet}) = \begin{pmatrix} -20.9722 & 0 & 0 \\ 0 & -21.1136 & 0 \\ 0 & 0 & -0.9358 \end{pmatrix} \tag{8.19}$$

Interestingly, most of the $D^{SO}{}_{ZZ}$ value arises from couplings with the singlet A_g excited states, and contributions from the triplet A_g excited states are negligibly small, although contributions from the singlet and triplet states are in the same magnitude, but the sign is different in the $D^{SO}{}_{XX}$ and $D^{SO}{}_{YY}$ terms.

Important electronic states for the $\mathbf{D}^{SO}$ calculations of Se_2 are summarized in Table 8.2, and selected molecular orbitals of Se_2 are illustrated in Fig. 8.1.

The $1\ ^1A_g$ and $2\ ^1A_g$ states are described by the linear combination of SOMO → SOMO spin flip excitations. Because of the degeneracy of the two

Table 8.2 Selected electronic states of Se_2 calculated at the CASSCF(12,8)/def2-TZVPP

State	Main configurations	$\Delta E_{CASSCF}/cm^{-1}$	SOCC[a]/cm^{-1}
$1\ ^1B_{1g}$	Ground state		
$1\ ^1A_g$	0.71 ($4b_{2g} \rightarrow 4b_{3g}$) −0.64 ($4b_{3g} \rightarrow 4b_{2g}$)	4,836	91.2465
$2\ ^1A_g$	−0.69 ($4b_{3g} \rightarrow 4b_{2g}$) −0.63 ($4b_{2g} \rightarrow 4b_{3g}$)	7,125	1819.4923
$1\ ^3B_{2g}$	0.99 ($9a_g \rightarrow 4b_{3g}$)	36,231	867.9534
$1\ ^3B_{3g}$	−0.99 ($9a_g \rightarrow 4b_{2g}$)	36,546	874.0933
$1\ ^1B_{2g}$	−0.99 ($9a_g \rightarrow 4b_{3g}$)	42,905	871.9180
$1\ ^1B_{3g}$	0.99 ($9a_g \rightarrow 4b_{2g}$)	42,990	878.6036

[a]Spin–orbit coupling constants ($|<\Psi_g|H^{SO}|\Psi_e>|$)

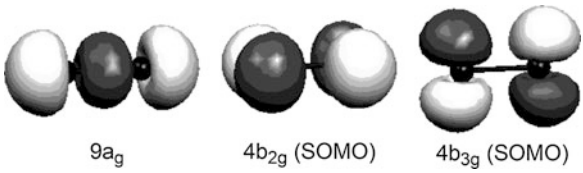

Fig. 8.1 Selected CASSCF canonical orbitals of Se_2

SOMOs these excited states have small excitation energies. The $2\ ^1A_g$ state has a very large spin–orbit coupling constant, which is the major origin of the large D value. This result is consistent with the well known El-Sayed's rule [49] for spin–orbit coupling. By contrast, both the $1\ ^3B_{2g}$ and $1\ ^1B_{2g}$ states are represented as electron promotion from the $9a_g$ orbital (valence Si–Si σ bond/sp lone pairs of Si) to the $4b_{3g}$ SOMO. Because the same orbitals are participated in the singlet and triplet excitations, these excited states have the same magnitude of spin–orbit coupling constants. Excitation energies of singlet and triplet excited states are a bit different, due to the existence of exchange coupling in the triplet excited states. As a result, similar magnitudes of $\mathbf{D}^{SO}$ contributions are obtained in the singlet and triplet B_{2g} and B_{3g} excited states. The difference of the absolute sign between the singlet and triplet states arises from the spin multiplicity dependent coefficients (see Eq. 8.13). Note that such cancellation between the singlet and triplet excited states does not appear in the A_g excited state, because SOMO → SOMO excitation does not occur without flipping of the spin.

8.3.2 Electronic Ground States of Triplet Arylnitrenes

Nitrenes are isoelectronic chemical entities of carbenes, and they have two unpaired electrons on the univalent nitrogen atom [50] while carbenes do on the divalent carbon atom. In general, nitrenes have high-spin ground states and their singlet–triplet energy gaps are larger than in the corresponding carbenes. Because of the short spin–spin distance, both nitrenes and carbenes have considerably large D values. For example, experimental D values of imidogen NH [51] and methylene

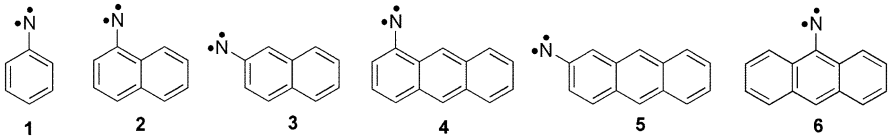

Scheme. 8.1 Molecular structures of the studied arylnitrenes

Table 8.3 Theoretical and experimental ZFS parameters of triplet arylnitrenes **1–6**

Molecule	D^{SS}/cm^{-1} [a]	D^{SO}/cm^{-1} [b]	D^{SS+SO}/cm^{-1}	$\|D$(Exptl.)$\|$/cm^{-1}
1	+0.8820	+0.1118	+0.9938	0.9978 [51]
2	+0.6642	+0.0809	+0.7451	0.793 [53]
3	+0.7925	+0.0965	+0.8890	0.925 [53]
4	+0.5254	+0.0682	+0.5936	0.6625 [51]
5	+0.6451	+0.0838	+0.7289	0.7779 [51]
6	+0.3476	+0.0487	+0.3963	0.47 [54]

[a]The $\mathbf{D}^{SS}$ tensors are calculated by using RO-HCTH/407/EPR-II spin densities
[b]The $\mathbf{D}^{SO}$ tensors are calculated at the hybrid CASSCF/MRMP2 level with cc-pVDZ basis set. Active space for CASSCF is (10,9), (12,12), and (12,12) for phenyl-, naphthyl-, and anthryl-nitrenes, respectively. Figures of the active space are provided elsewhere [12c]

CH_2 [52] are 1.86 and 0.6881 cm^{-1}, respectively. On the other hand, aryl-substituted nitrenes and carbenes have smaller D values than bare imidogen and methylene due to spin delocalization onto aryl rings [51]. Because arylnitrenes have very different D values depending on the size of the aryl ring and substituted position of nitrene, systematical investigations of the **D** tensors are interesting and provide new insights into the electronic spin structures. We also emphasize that such systematical study is necessary to understand behaviors of a "no interaction approximation" or a "mean-field approximation" in the $\mathbf{D}^{SS}$ tensor calculations by DFT. As firstly pointed out by Sinnecker and Neese [16a], a good correlation with the experimental values is obtained if RO-DFT spin density is used for the $\mathbf{D}^{SS}$ tensor calculations, but distinctly larger deviations are obtained in the U-DFT spin density-based $\mathbf{D}^{SS}$ tensor calculations. At first glance, this seems to be strange, because the U-DFT spin density is much more realistic than the RO-DFT ones. In fact, observed good correlations in RO-DFT are due to a result of systematical cancellation of errors, but the origins of errors are not completely disclosed even now.

The theoretical and experimental ZFS parameters of triplet phenyl-, naphthyl-, and anthryl-nitrenes **1–6** (see Scheme 8.1) are summarized in Table 8.3.

Note that there is no necessity that the principal axes of $\mathbf{D}^{SS}$ coincide with those of $\mathbf{D}^{SO}$. In arylnitrenes under study, the $\mathbf{D}^{SS}$ and $\mathbf{D}^{SO}$ tensors can be regarded to be approximately coaxial. As shown in Table 8.3, theory can predict the D^{SS+SO} value of **1** very accurately. Deviation of the D^{SS+SO} value from the experimental one becomes large as the D value decreases. Interestingly, the ratio of D^{SO} and D(Exptl.) is about 1:10 and almost constant among nitrenes under study.

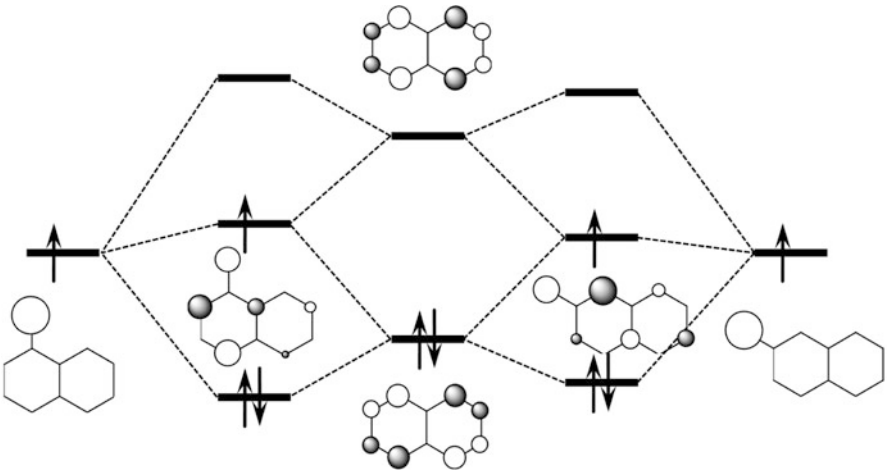

Fig. 8.2 Orbital interaction diagram of naphthylnitrenes **2** (*left*) and **3** (*right*)

Analyses of the excited states of **1**–**6** revealed that the most important excited states in respect of the $\mathbf{D}^{\mathrm{SO}}$ contributions are the $1\ ^1\mathrm{A}'$ and $2\ ^1\mathrm{A}'$, and $1\ ^1\mathrm{A}_1$ and $2\ ^1\mathrm{A}_1$ states, for C_s and C_{2v} molecules, respectively. These excited states are described mainly by the SOMO → SOMO spin flip excitations. Considering the fact that the in-plane SOMO is well localized on the nitrene nitrogen atom, the perturbation of the $\mathbf{D}^{\mathrm{SO}}$ tensor can be understood by the modulation of the energy level and spatial distribution of the SOMO of π nature. In fact, trends of the D^{SO} value with respect to the aryl ring size and nitrene substituted position can be explained with the help of the concept of orbital interactions [55, 56] between the $2\mathrm{p}_\pi$ orbital of the nitrene nitrogen atom and the frontier MOs of the aryl ring, as illustrated in Fig. 8.2 in case of naphthylnitrenes.

Orbital energy levels and spatial distributions of SOMO in naphthylnitrenes are mainly controlled by the strengths of orbital interactions between the $2\mathrm{p}_\pi$ orbital of nitrene nitrogen and the frontier MOs of naphthalene. The order of the atomic orbital coefficients of both the HOMO and LUMO is C1 > C2 in naphthalene, and C9 > C1 > C2 in anthracene, where the numbering of atoms obeys the IUPAC nomenclature. Therefore, the strength of the orbital interactions between the $2\mathrm{p}_\pi$ orbital of the nitrene nitrogen atom and the frontier MOs of the aryl group is in the order **2** > **3**, and **6** > **4** > **5**, for naphthyl- and anthryl-nitrenes, respectively. Strong orbital interaction causes overflow of spin density from the nitrogen atom to the aryl ring, and destabilization of SOMO. Both of the two mechanisms work to decrease the D^{SO} value.

Trends of the $\mathbf{D}^{SS}$ tensors calculated by using the DFT spin density can be extracted by introducing the $D(\mathrm{Exptl.}) - D^{\mathrm{SO}}$ as reference data. Figure 8.3 illustrates deviations of the calculated D^{SS} values from the $D_{\mathrm{Ref}}{}^{\mathrm{SS}}$ values as well as the $\langle S^2 \rangle$ expectation values at U-DFT.

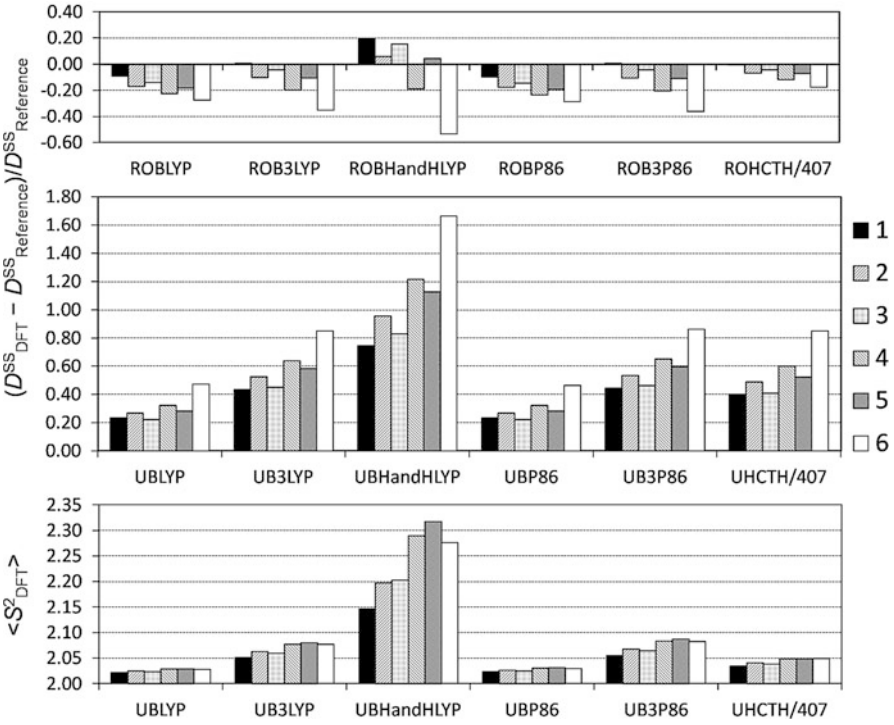

Fig. 8.3 The $(D_{DFT}{}^{SS} - D_{Ref}{}^{SS})/D_{Ref}{}^{SS}$ values and $<S^2>$ values. $D_{Ref}{}^{SS}$ are taken from the D(Exptl.)–D^{SO}

Clearly the U-DFT approach tends to overestimate the D^{SS} value, especially when hybrid exchange–correlation functional is used. Even when pure functionals are adopted, the calculated D^{SS} values largely exceed the references. In the U-DFT calculations good correlation between the calculated D^{SS} and $<S^2>$ values is seen. However, the symmetry-adapted cluster-configuration interaction (SAC-CI) [57] spin density-based calculations also overestimate the D^{SS} value ($D_{SAC\text{-}CI}{}^{SS} = +1.1840, +0.9180, +1.0490, +0.8271, +0.9365$, and $+0.5604\ cm^{-1}$ for **1**, **2**, **3**, **4**, **5**, and **6**, respectively). The SAC-CI wavefunction is an eigenfunction of the $\mathbf{S}^2$ operator and therefore the SAC-CI spin density is spin contamination free. Hence we can conclude that spin contamination is not the only root of overestimation. By contrast, the RO-DFT approach has a tendency to underestimate the D^{SS} value. The deviation becomes large as the D value decreases, but the magnitude of errors is smaller compared with the U-DFT calculations.

These tendencies can be explained by the following mechanisms. (1) The "no interaction approximation" tends to overestimate the D^{SS} value for nitrenes. (2) Spin polarization in the U-DFT calculations induces the larger atomic spin density on the nitrene nitrogen atom, especially spin delocalized systems like **6**, resulting in the overestimation of D^{SS}. (3) In the RO-DFT calculations less spin density is

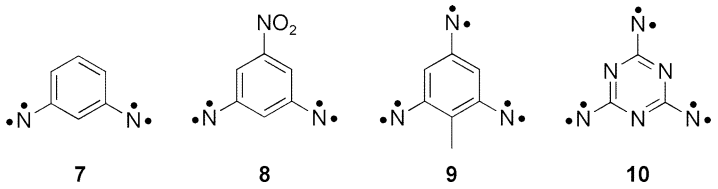

Scheme. 8.2 Spin-quintet dinitrenes and septet trinitrenes

distributed on the nitrene site, because RO-DFT cannot describe spin polarization by definition. This negative error and positive error from the "no interaction approximation" may cancel each other out, fortuitously.

It should be noted that these tendencies might be specific in (n,π)-type triplets. In fact, the "mean-field approximation" in CASSCF tends to underestimate the D^{SS} value in the ππ* excited triplet state of polyacenes [16a]. Behaviors of the "mean-field approximation" equation in (π,π)-systems can also be seen in the next section.

8.3.3 High-Spin Dinitrenes and Trinitrenes

One of the fundamental and important questions in high-spin chemistry is relevant to the electronic structures of organic high-spin molecules which are designed by invoking topologically controlled robust π spin polarizations [5]. Organic molecule-based magnetism dates back to the first experimental detection of quintet ground state *m*-phenylenebis(phenylcarbene) and phenylene-1,3-dinitrene in 1967 [4]. Since then, ESR spectra of dozens of quintet dinitrenes and septet trinitrenes have been observed [58]. Spectral simulations of the ESR spectra of oligonitrenes based on the eigenfield method can afford to give very accurate **D** tensors. Experimentally determined **D** tensors have been frequently analyzed in terms of a semiempirical model [59–61] in which the **D** tensor of oligonitrenes is described as the sum of the **D** tensor of the mononitrene unit $\mathbf{D}^{i}$ and an interaction tensor term $\mathbf{D}^{ij}$, where *i* and *j* labels the mononitrene unit. Quantitative evaluation of the interaction tensors is in general difficult and the point-dipole approximation has been often used. The only exception is found in the single crystal ESR work on biphenyl-3,3′-bis(phenylmethylene) in the thermally accessible triplet and quintet states [61b, c], in which the interaction tensor $\mathbf{D}^{ij}$ has experimentally been derived.

The $\mathbf{D}^{SS}$ and $\mathbf{D}^{SO}$ tensors of spin-quintet phenylene-1,3-dinitrene **7** and 5-nitrophenylene-1,3-dinitrene **8**, and spin-septet 2-methyl-1,3,5-trinitrenobenzene **9** and 2,4,6-trinitreno-1,3,5-triazine **10** (see Scheme 8.2) are typically calculated in terms of hybrid CASSCF/MRMP2 and the RO-B3LYP spin densities, respectively. The results are summarized in Table 8.4.

The D_{ZZ} axes of quintet dinitrenes **7** and **8** are parallel to the axis connecting two nitrene sites, and those of septet trinitrenes **9** and **10** are perpendicular to the π conjugation. Trinitrene **10** has threefold symmetry and thus the *E* value

Table 8.4 Theoretical and experimental ZFS parameters of oligonitrenes **7–10**

Molecule	D^{SS}/cm^{-1}	D^{SO}/cm^{-1}	D^{SS+SO}/cm^{-1}	$\lvert D(\text{Exptl.})\rvert/cm^{-1}$
7	+0.1580	+0.0250	+0.1830	0.205 [17]
8	+0.1686	+0.0257	+0.1943	0.224 [58c]
9	−0.0635	−0.0117	−0.0752	0.0938 [58s]
10	−0.0968	−0.0140	−0.1108	0.123 [58k]

is exactly equal to zero. Contributions from the spin–orbit coupling amount to more than 10%, indicating the importance of the spin–orbit coupling effects in the ground state of oligonitrenes. The $|D^{SS+SO}/D(\text{Exptl.})|$ value is less than unity and is smaller in septet trinitrenes than in quintet dinitrenes. Considering the fact that the $|D^{SS+SO}/D(\text{Exptl.})|$ value of triplet phenylnitrene **1** is 0.996 (see Table 8.3), it can be said that the error in the **D** tensor calculation becomes large as the number of the spin site increases. Indeed, this is relevant to the contribution from the interaction tensor terms. As discussed below, the underestimations of the D value in oligonitrenes originate from inaccurate descriptions of the interaction tensor term of $\mathbf{D}^{SS}$.

The localized MO analysis for the excited states revealed that the most important excited states in the $\mathbf{D}^{SO}$ tensor are intra-nitrene-site SOMO → SOMO spin flip excited low-spin states. For example, the spin–orbit couplings with the $2\ ^3B_1$ and $2\ ^3A_1$ excited states of spin-quintet **7** result in large contributions of 0.0288 cm^{-1} to D_{ZZ} and 0.0096 cm^{-1} to D_{YY}, respectively. The D^{SO} value estimated from spin–orbit coupling with these only two states is 0.0240 cm^{-1}, and this is 96% of the theoretical D^{SO} value in Table 8.4. With regard to the intra-site excitations, the π → n-SOMO and n-SOMO → π* (here n-SOMO specifies in-plane SOMOs) excited states have non-negligible spin–orbit coupling constants (∼30 cm^{-1}). By contrast, the spin–orbit coupling constants of inter-site SOMO → SOMO spin flip excited states are ten times smaller. Contributions to the $\mathbf{D}^{SO}$ tensor are approximately proportional to the square of the spin–orbit coupling constant (see Eq. 8.15), and therefore non-local SOMO → SOMO excitations are roughly hundred times less important than the π → n-SOMO and n-SOMO → π* excited states.

By comparing the **D** tensors obtained from quantum chemical calculations and constructed from a semiempirical model without considering interaction tensors $\mathbf{D}^{ij}$, the amounts of site–site interaction terms in the **D** tensor can be extracted. In the semiempirical model of dominant one-center spin–spin interactions the **D** tensors of quintet dinitrenes and septet trinitrenes are expressed as follows.

$$\mathbf{D}_{S=2} = \left(\mathbf{D}^{i}_{S=1} + \mathbf{D}^{j}_{S=1}\right)/6 \tag{8.20}$$

$$\mathbf{D}_{S=3} = \left(\mathbf{D}^{i}_{S=1} + \mathbf{D}^{j}_{S=1} + \mathbf{D}^{k}_{S=1}\right)/15 \tag{8.21}$$

Here, $\mathbf{D}^i$, $\mathbf{D}^j$ and $\mathbf{D}^k$ denote the **D** tensors of the triplet nitrene units. Using theoretical $\mathbf{D}^{SS}$ and $\mathbf{D}^{SO}$ tensors of triplet phenylnitrene **1** for the **D** tensors of the mononitrene unit and applying vector angles between the two C–N bond at

the optimized geometry to define relative orientations of $\mathbf{D}^i$, $\mathbf{D}^j$, and $\mathbf{D}^k$, the ZFS parameters of the semiempirical model are calculated to be $D^{SS} = +0.1868\ cm^{-1}$, $E^{SS} = -0.0368\ cm^{-1}$, $D^{SO} = +0.0234\ cm^{-1}$, $E^{SO} = -0.0046\ cm^{-1}$ for quintet **7**, and $D^{SS} = -0.0882\ cm^{-1}$, $D^{SO} = -0.0112\ cm^{-1}$, $E^{SS} = E^{SO} = 0.0000\ cm^{-1}$ for septet **9**. From these results, we can determine the interaction tensor contributions in $\mathbf{D}^{SO}$ to be 4–7%. By contrast, the interaction tensors of $\mathbf{D}^{SS}$ amount to 18 and 40% in **7** and **9**, respectively, and these values are abnormally large. It is interesting that much better agreement with the experimental data is obtainable if the $\mathbf{D}^{SS}$ tensors for the model systems with neglecting the mononitrene site–site interactions are added to $\mathbf{D}^{SO}$ for the real systems. These results suggest that the descriptions of the interaction tensor terms of $\mathbf{D}^{SS}$ may be insufficient in the RO-DFT spin density-based calculations. This is consistent with the fact that the "mean-field approximation" provides large errors in (π,π)-type electronic structure systems. In fact, if we adopted the CASSCF method for the calculation of the $\mathbf{D}^{SS}$ tensors, the interaction terms of $\mathbf{D}^{SS}$ are estimated to be ca. 7 and 14% for di- and tri-nitrenes, respectively [26].

8.3.4 Electronically Excited States of Diazabenzenes

So far, **D** tensors of open-shell molecules in their ground state have been discussed. As well known, ZFS can be observed in the excited triplet states of closed shell molecules [62]. In fact, earlier theoretical studies of **D** tensors have been mainly focused on the excited triplet states of aromatic hydrocarbons [63]. For the theoretical study of the **D** tensor of excited states, the ab initio MO method can be applied in a straightforward manner. Excited triplet state is in general surrounded by nearby electronic states, and therefore a conventional SOS-CASSCF approach for the $\mathbf{D}^{SO}$ tensor sometimes suffers from errors arising from inaccurate CASSCF energy denominators in Eq. (8.15). Usage of the hybrid CASSCF/MRMP2 method is encouraged to obtain quantitative $\mathbf{D}^{SO}$ tensors of excited states.

It is known that nπ* excited states exhibit strong spin–orbit coupling with the closed-shell ground state [49]. Therefore, a sophisticated treatment of the $\mathbf{D}^{SO}$ tensors is important for quantitative discussions of relevant electronic structures. With regard to the spin–spin part, Eq. (8.12)-based calculations give acceptably accurate $\mathbf{D}^{SS}$ tensors in nπ* excited states, because one of the electron spins is localized onto the lone-pair orbital [23].

The lowest excited triplet state of diazabenzenes, namely pyrazine (**11**), pyrimidine (**12**), and pyridazine (**13**) have nπ* character and their ZFS parameters were determined experimentally [64–66]. Several theoretical calculations of the **D** tensor have been reported, but geometry relaxation effects in the excited states have rarely been discussed.

The $\mathbf{D}^{SS}$ and $\mathbf{D}^{SO}$ tensors of **11**–**13** calculated at both the ground and excited states geometry are summarized in Table 8.5. In these molecules, the $\mathbf{D}^{SS}$ tensors are calculated using Eq. (8.12) with the SAC-CI spin densities. Note that the $D^{SS}{}_{ZZ}$ axis

Table 8.5 Experimental and theoretical D values of **11**–**13** in their $n\pi^*$ excited triplet state

Molecule	Geom	D^{SS}/cm^{-1}	$D^{SO}(\Delta E_{CASSCF})$ /cm^{-1}	$D^{SO}(\Delta E_{MRMP2})$ /cm^{-1}	D^{SS+SO} /cm^{-1}	D(Exptl.) /cm^{-1}
11	S_0	+0.502	+2.045	−0.055	+0.447	+0.345 [64]
	T_1	+0.383	+0.237	−0.063	+0.320	
12	S_0	+0.165	+0.046	−0.020	+0.170[a]	0.1653 [65]
	T_1	+0.197	−0.021	+0.012	+0.196[a]	
13	S_0	+0.453	+0.012	−0.018	+0.435	+0.261 [66]
	T_1	+0.347	−0.018	−0.030	+0.317	

[a]The D_{ZZ} axis of $\mathbf{D}^{SO}$ tensor does not coincide with that of the $\mathbf{D}^{SS}$ tensor
[b]Absolute sign of D is not determined experimentally

Table 8.6 Vertical excitation energies of pyrazine at the CASSCF(10,8)/cc-pVDZ and the MRMP2/cc-pVDZ levels of theory

State	ΔE(CASSCF)/eV	ΔE(MRMP2)/eV	ΔE(Exptl. [67])/eV
$1\,^3B_{3u}$	4.13	3.21	3.42
$1\,^3B_{1u}$	4.11	4.29	4.0
$1\,^3A_u$	5.96	4.35	4.2
$1\,^3B_{2u}$	5.21	4.40	4.5
$1\,^1B_{2u}$	5.33	4.92	4.81
$2\,^3B_{1u}$	5.37	5.05	5.70
$1\,^1B_{1u}$	8.77	6.54	6.51
$2\,^1B_{1u}$	10.77	7.20	7.67
$2\,^1B_{2u}$	10.24	7.14	7.67

of **12** is parallel to the C_2 axis, but the $D^{SO}{}_{ZZ}$ axis is along the direction connecting the two nitrogen atoms. Thus, the D^{SS+SO} value of **12** is not a simple sum of the D^{SS} and D^{SO} values.

It is clear that using CASSCF energies in the SOS formula (Eq. 8.12) is problematic in **11**. The D^{SO} value obtained from conventional SOS-CASSCF is too large to compare with the experimental D value. In Table 8.6, excitation energies of selected excited states calculated at the ground-state geometry are summarized. At the CASSCF level the $1\,^3B_{1u}$ state of $\pi\pi^*$ character has lower energy than the $1\,^3B_{3u}$ state of $n\pi^*$ nature, and the energy separation between the two states are quite small compared to the experimental value. By applying MRMP2 correction, the excitation energy of the $1\,^3B_{3u}$ state is significantly improved and becomes comparable to the experimental one.

The D^{SS+SO} values calculated at the S_0 geometry are overestimated compared with experiments, especially in **11** and **13**. Large deviations between theory and experiment can be improved by considering geometry relaxation in the excited state. Geometry optimization of the lowest $n\pi^*$ excited triplet state of **11**–**13** at the CIS/cc-pVDZ level revealed that out-of-plane atom displacements occur in **11** and **13**. The D^{SS} values of **11** and **13** decrease about 25% in the T_1 geometry, and the D^{SS+SO} value agrees with the experimental one within ca. 20% of error. Pyrimidine **12** possesses planar C_{2v} geometry in the $n\pi^*$ excited state, and the D^{SS+SO} value does not change drastically. Entirely, the spin–orbit contributions amount to 5–20% of the D value in the $n\pi^*$ excited triplet state of diazabenzenes.

8.3.5 The Lowest Spin-Triplet State of Phenylene-1,4-Dinitrene

In the last part of this section, we present a clear-cut proof that electron correlations play an essential role in the spin structure and the **D** tensor, of organic open-shell molecules. Phenylene-1,4-dinitrene (**14**) has a singlet ground state with a quinonoidal electronic structure [68–70], but ESR of a thermally excited triplet state can be observed [68]. In the lowest triplet state of **14**, the unpaired electron is well localized onto the in-plane 2p orbitals of the nitrogen atom, and if we apply the point-dipole approximation to evaluate the D^{SS} value by using the N$\cdots$N distance as the spin–spin distance, the D^{SS} value is calculated to be -0.0162 cm^{-1}. However, the experimentally determined $|D|$ value of **14** in the triplet state is 0.169 cm^{-1}, which is about ten times larger than the D^{SS} value of point-dipole approximation. Historically, this extraordinarily large $|D|$ value has been explained by the π-spin polarization mechanism [68c]. The $\mathbf{D}^{SO}$ term is conceived of as being small, but no reliable quantum chemical calculations of the $\mathbf{D}^{SO}$ tensor have been reported.

The $\mathbf{D}^{SO}$ calculations are carried out using the hybrid CASSCF/MRMP2 method. The obtained D^{SO} value is -0.0149 cm^{-1}, which is about 8% of the experimental $|D|$ value. The D_{ZZ} principal axis of the $\mathbf{D}^{SO}$ tensor is parallel to the molecular long-axis. This result suggests that the large $|D|$ value should originate from the spin–spin dipolar term.

The D^{SS} value calculated at the RO-B3LYP/cc-pVDZ level is -0.0246 cm^{-1}. This is larger than that the value estimated from the point-dipole approximation, but still quite smaller than the experimental $|D|$ value. The RO-B3LYP spin density is dominantly localized onto the in-plane 2p orbital of nitrogen atoms, and the induced π-spin density is negligibly small. By contrast, if we adopt the CASSCF method for the $\mathbf{D}^{SS}$ tensor calculation, the D^{SS} value of -0.1533 cm^{-1} is obtained. Hence, the D^{SS+SO} value is -0.1682 cm^{-1} (the ${D^{SS}}_{ZZ}$ axis coincides with the ${D^{SO}}_{ZZ}$ axis), which is surprisingly close to the experimental $|D|$ value.

What does the difference of the resultant $\mathbf{D}^{SS}$ tensor among the point-dipole approximation, RO-DFT and CASSCF arise from? The point-dipole and RO-DFT use information on the spin density only, but in the CASSCF method, the two-particle spin density matrices Γ^{SS} are explicitly calculated. Then, what is the effect that the two-particle spin density matrix contains but is not included in the spin-density based approaches? The wavefunction analysis can make this difference clear. The CAS-CI main configuration of the $1\ ^3B_{1u}$ state is (inactive)$^{40}(7b_{1u})^2(8a_g)^2(1b_{3u})^2(1b_{2g})^2(1b_{1g})^2(2b_{3u})^2\ (4b_{3g})^1(1b_{2u})^1$ (see Fig. 8.4 for the active orbitals of **14**). The CI coefficient of this electron configuration is -0.89. The CAS-CI configuration having the second largest CI coefficient ($C = 0.17$) is described by two electron transitions from $2b_{3u}$ to $2b_{2g}$ orbitals. Combination of these two major configurations can be interpreted as the open-shell singlet diradicaloid electron configuration in the π orbitals in addition to the two localized unpaired electrons onto the in-plane 2p orbitals, by applying the concept of the localized molecular orbital. Therefore, the existence of the two- electron ($2b_{3u} \rightarrow 2b_{2g}$, $2b_{3u} \rightarrow 2b_{2g}$) excitation configuration insists on the presence of the

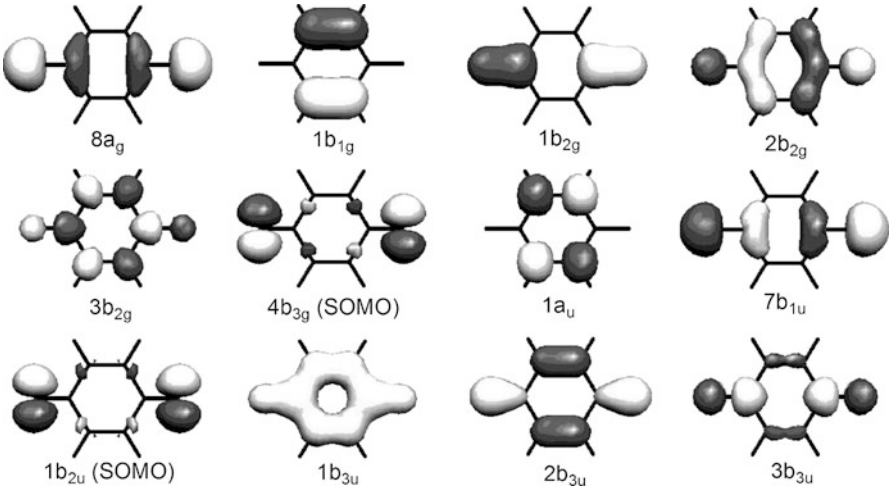

Fig. 8.4 CASSCF active space of **14**. $4b_{3g}$ and $1b_{2u}$ orbitals are singly occupied in the main configuration of the $1\ ^3B_{1g}$ state

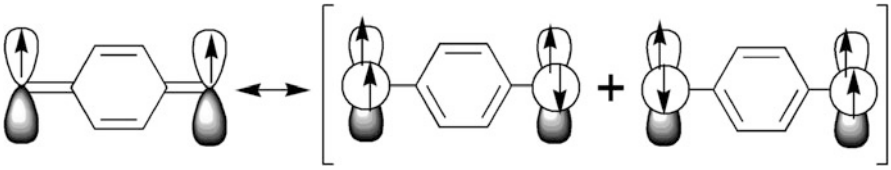

Fig. 8.5 Resonance structures of phenylene-1,4-dinitrene **14**

triplet-nitrene–singlet-nitrene resonance structures, as illustrated in Fig. 8.5. Note that these nitrene-like resonance structures do not contribute to the π spin density, because the π orbitals are either doubly occupied or unoccupied in the two major configurations. Therefore, correct $\mathbf{D}^{SS}$ tensors cannot be obtained by the spin density-based approaches such as the point-dipole approximation and RO-DFT. In other words, the spin-triplet state of **14** is a very representative system that static electron correlation plays an essentially important role in the **D** tensor.

8.4 Summary and Outlook

Theoretical calculations of the **D** tensors for organic molecules in their spin-triplet and higher spin multiplet states can date back to pioneering papers reported in 1950s [63]. Since then, many theoretical works with regard to the **D** tensors have been documented, but genuinely quantitative calculations of chemically interesting large systems are still difficult. During this half century, computational chemistry

becomes popular even among experimentalists, especially owing to the remarkable development of the DFT framework. DFT-based approaches for the **D** tensors have many difficulties to be circumvented, but it is true that the most realistic choice for the **D** tensor calculations of large chemical systems is DFT-based. In this context, we believe that the identification of the origin of its intrinsic errors in the **D** tensor calculation is very important.

With regard to ab initio MO methods starting from Hartree–Fock, it is proved that sophisticated treatments with highly electron correlated wavefunctions can reproduce both the $\mathbf{D}^{\mathrm{SS}}$ and $\mathbf{D}^{\mathrm{SO}}$ tensors accurately. A bottleneck in the high-level ab initio calculations is their computational costs relevant to computational resource. The dimension of the Hamiltonian matrix to be diagonalized strongly depends on the size of active space in CASSCF, and on the number of basis functions in CI. Also, the number of low-lying excited states generally increases as the number of electrons grows. As seen in the Sect. 8.3, the hybrid CASSCF/MRMP2 method is one of the best approaches for the $\mathbf{D}^{\mathrm{SO}}$ tensor calculations at present. For the calculations of large chemical systems by the hybrid method, utilizing the perturbation theory to select important excited states in the viewpoint of excitation energy and spin–orbit coupling constants, prior to the MRMP2 calculations, might be useful. In this philosophy, the energy correction scheme is adopted only to the target and important excited states.

Even though the high-level ab initio calculations of the **D** tensors of relatively large systems are difficult to perform, the establishment of theoretical methods for the **D** tensor based on state-of-the-art ab initio MO formalism is essentially important in order to construct reference theoretical values of the ZFS parameters and to elucidate the behaviors of various approximations and the electronic structures of open-shell systems. Discussions of the DFT-based $\mathbf{D}^{\mathrm{SS}}$ tensor calculations in the Sect. 8.3.2 never hold without reliable theoretical $\mathbf{D}^{\mathrm{SO}}$ tensors. As shown in phenylene-1,4-dinitrene (**14**), when the static electron correlation plays a crucially important role in determining its ZFS parameters, ab initio post-SCF approaches are essential to obtain the theoretical $\mathbf{D}^{\mathrm{SS}}$ tensor even qualitatively.

Another important task for the thorough understanding of the **D** tensor of real chemical systems is the calculations of the **D** tensors with environmental effects taken into account, such as matrices and counterions. Although the ESR measurement of spin-multiplet states is generally carried out in the solid state, matrix molecules can affect molecular geometries and electronic structures [17]. Also, counterions can perturb spin density distributions in magnetic molecules via coulomb interactions, as is well known in triplet dianions of π-conjugated hydrocarbons [71, 72]. The existence of counterions also influences energy preferences of the molecular conformations of high spin entities in solution [73]. These environmental effects can be taken into account by several approaches, such as using a polarizable continuum model (PCM), running molecular dynamics simulations, utilizing QM/MM or ONIOM methods, and doing geometry optimization with environments (matrix host molecules, counterions, etc.).

The quantum chemical calculation is a powerful tool for the investigations of novel open-shell spin multiplet systems. In quest of novel spin-based functionality

materials, sophisticated synthetic chemistry for open shell compounds and spin technology for manipulating quantum spin states of electron spin qubits are emerging. Extremely stable nitroxide biradicals with the isoelectronic structure of trimethylenemethane have been isolated [74], serving as ensemble molecular memory devices, which couple with macroscopic spin qubits. In such a new application of the ground-state triplet species, the coupling mode can be analyzed by differentiating between any contributions of spin–orbit terms and those of spin–spin interactions. We emphasize that the **D** tensor calculations reviewed here can serve to develop further attempts to elucidate electronic and molecular structures for open-shell spin multiplets in quest for novel spin functionalities from both the theoretical and experimental sides.

Acknowledgments This work has been supported by Grants-in-Aid for Scientific Research (B) and Scientific Research on Innovative Areas, "Quantum Cybernetics" from MEXT, Japan. The support by JST through Core Research for Evolutional Science and Technology (CREST) project, "Implementation of Molecular Spin Quantum Computers" and the support by the Funding Program for World-Leading Innovative R&D on Science and Technology (FIRST) project on "Quantum Information Processing", JSPS, Japan are also acknowledged.

References

1. Kaupp M, Bühl M, Malkin VG (2005) Calculation of NMR and EPR parameters: theory and applications. Wiley-VCH, Weinheim
2. Harriman JE (1978) Theoretical foundations of electron spin resonance. Academic, New York
3. (a) Morita Y, Suzuki S, Fukui K, Nakazawa S, Kitagawa H, Kishida H, Okamoto H, Naito A, Sekine A, Ohashi Y, Shiro M, Sasaki K, Shiomi D, Sato K, Takui T, Nakasuji K (2008) Thermochromism in an organic crystal based on the co-existence of σ- and π-dimers. Nat Mater 7:48–51; (b) Morita Y, Yakiyama Y, Nakazawa S, Murata T, Ise T, Hashizume D, Shiomi D, Sato K, Kitagawa M, Nakasuji H, Takui T (2010) Triple-stranded metallo-helicates addressable as Lloyd's electron spin qubits. J Am Chem Soc 132:6944–6946; (c) Morita Y, Suzuki S, Sato K, Takui T (2011) Synthetic organic-spin chemistry for structurally well-defined open-shell graphene fragments. Nat Chem 3:197–204; (d) Morita Y, Nishida S, Murata T, Moriguchi M, Ueda A, Satoh M, Arifuku K, Sato K, Takui T (2011) Organic tailored batteries materials using stable open-shell molecules with degenerate frontier orbitals. Nat Mater 10:947–951
4. (a) Itoh K (1967) Electron spin resonance of an aromatic hydrocarbon in its quintet ground state. Chem Phys Lett 1:235–238; (b) Wasserman E, Murray RW, Yager WA, Trozzoro AM, Smolinsky G (1967) Quintet ground states of *m*-dicarbene and *m*-dinitrene compounds. J Am Chem Soc 89:5076–5078
5. (a) Murahashi S, Yoshimura Y, Yamamoto Y, Moritani I (1972) Quintet carbenes: *m*-Phenylenebis(phenylmethylene) and *m*-phenylenebis(methylene). Tetrahedron 28:1485–1496; (b) Takui T, Itoh K (1973) Detection of an aromatic hydrocarbon in its septet electronic ground state by electron spin resonance. Chem Phys Lett 19:120–124; (c) Itoh K (1978) Electronic structures of aromatic hydrocarbons with high spin multiplicities in the electronic ground state. Pure Appl Chem 50:1251–1259; (d) Teki Y, Takui T, Itoh K, Iwamura H, Kobayashi K (1983) Design, preparation and ESR detection of a ground-state nonet hydrocarbon as a model for one-dimensional organic ferromagnets. J Am Chem Soc 105:3722–3723; (e) Sugawara T, Bandow S, Kimura K, Iwamura H, Itoh K (1984) Magnetic behavior of nonet tetracarbene,

m-phenylenebis((diphenylmethylen-3-yl)methylene). J Am Chem Soc 106:6449–6450; (f) Fujita I, Teki Y, Takui T, Kinoshita T, Itoh K, Miko F, Sawaki Y, Iwamura H, Izuoka A, Sugawara T (1990) Design, preparation, and electron spin resonance detection of a ground-state undecet (S = 5) hydrocarbon. J Am Chem Soc 112:4074–4075

6. (a) Lahti PM (1999) Magnetic properties of organic materials. Marcel Dekker; (b) Itoh K, Kinoshita M (2000) Molecular magnetism: new magnetic materials. Gordon and Breach, Amsterdam; (c) Itoh K, Takui T (2004) High spin chemistry underlying organic molecular magnetism topological symmetry rule as the first principle of spin alignment in organic open-shell systems of π-conjugation and their ions. Proc Jpn Acad Ser B 80:29–40
7. (a) Rahimi R, Sato K, Furukawa K, Toyota K, Shiomi D, Nakamura T, Kitagawa M, Takui T (2005) Pulsed ENDOR-based quantum information processing. Int J Quantum Info 3:197–204; (b) Sato K, Rahimi R, Mori N, Nishida S, Toyota K, Shiomi D, Morita Y, Ueda A, Suzuki S, Furukawa K, Nakamura T, Kitagawa M, Nakasuji K, Nakahara M, Hara H, Carl P, Höfer P, Takui T (2007) Implementation of molecular spin quantum computing by pulsed ENDOR technique: direct observation of quantum entanglement and spinor. Physica E 40:363–366; (c) Sato K, Nakazawa S, Rahimi R, Ise T, Nishida S, Yoshino T, Mori N, Toyota K, Shiomi D, Yakiyama Y, Morita Y, Kitagawa M, Nakasuji K, Nakahara M, Hara H, Carl P, Höfer P, Takui T (2009) Molecular electron-spin quantum computers and quantum information processing: pulse-based electron magnetic resonance spin technology applied to matter spin-qubits. J Mater Chem 19:3739–3754; (d) Yoshino T, Nishida S, Sato K, Nakazawa S, Rahimi R, Toyota K, Shiomi D, Morita Y, Kitagawa M, Takui T (2011) ESR and ^{1}H-, ^{19}F-ENDOR/TRIPLE study of fluorinated diphenylnitroxides as synthetic bus spin-qubit radicals with client qubits in solution. J Phys Chem Lett 2:449–453
8. Nielsen MA, Chuang IL (2000) Quantum computation and quantum information. Cambridge University Press, Cambridge
9. (a) Sato K, Shiomi D, Takui T, Itoh K, Kaneko T, Tsuchida E, Nishide H (1994) FT pulsed EPR/transient quantum spin nutation spectroscopy applied to inorganic high-spin systems and a high-spin polymer as models for organic ferromagnets. J Spectrosc Soc Jpn 43:280–291; (b) Sato K, Yano M, Furuichi M, Shiomi D, Takui T, Abe K, Itoh K, Higuchi A, Katsuma K, Shirota Y (1997) Polycationic high-spin states of one- and two-dimensional (diarylamino)benzenes, prototypical model units for purely organic ferromagnetic metals as studied by pulsed ESR/electron spin transient nutation spectroscopy. J Am Chem Soc 119:6607–6613; (c) Tomioka H, Watanabe T, Hirai K, Furukawa K, Takui T, Itoh K (1995) 2,2′,4,4′,6,6′-Hexabromodiphenylcarbene. The first stable triplet carbene in fluid solution at low temperature and in the crystal state at room temperature. J Am Chem Soc 117:6376–6377; (d) Shohoji MCBL, Franco MLTMB, Lazana CRLR, Nakazawa S, Sato K, Shiomi D, Takui T (2000) Electronic quartet and triplet states of polyanionic C_{60} fullerene and their anomalous spin relaxation as studied by cw-ESR/2D-electron spin transient nutation spectroscopy. J Am Chem Soc 122:2962–2963; (e) Sawai T, Sato K, Ise T, Shiomi D, Toyota K, Morita Y, Takui T (2008) Macrocyclic high-spin (S = 2) molecule: spin identification of a sterically rigid metacyclophane-based nitroxide tetraradical by two-dimensional electron spin transient nutation spectroscopy. Angew Chem Int Ed 47:3988–3990
10. Bally T (2004) Matrix isolation. In: Moss RA, Platz MS, Jones M Jr (eds) Reactive intermediates chemistry. Wiley Interscience, New Jersey
11. (a) Sato K (1994) Dr thesis. Osaka City University; (b) Banwell CN, Primas H (1963) On the analysis of high-resolution nuclear magnetic resonance spectra I. Methods of calculating N.M.R. spectra. Mol Phys 6:225–256; (c) Belford GG, Belford RL, Burkhalter JF (1973) Eigenfields: a practical direct calculation of resonance fields and intensities for field-swept fixed-frequency spectrometers. J Magn Reson 11:251–265; (d) McGregor KT, Scaringe RP, Hatfield WE (1975) E.P.R. calculations by the eigenfield method. Mol Phys 30:1925–1933
12. (a) Sugisaki K, Toyota K, Sato K, Shiomi D, Kitagawa M, Takui T (2009) Ab initio calculations of spin–orbit contribution to the zero-field splitting tensors of $n\pi^*$ excited states by the CASSCF method with MRMP2 energy correction. Chem Phys Lett 477:369–373; (b) Sugisaki K, Toyota K, Sato K, Shiomi D, Kitagawa M, Takui T (2010) Spin–orbit contributions in

high-spin nitrenes/carbenes: A hybrid CASSCF/MRMP2 study of the zero-field splitting tensors. ChemPhysChem 11:3146–3151; (c) Sugisaki K, Toyota K, Sato K, Shiomi D, Kitagawa M, Takui T (2011) Ab initio and DFT studies of the spin–orbit and spin–spin contributions to the zero-field splitting tensors of triplet nitrenes with aryl scaffolds. Phys Chem Chem Phys 13:6970–6980

13. McWeeny R, Mizuno Y (1961) The density matrix in many-electron quantum mechanics II. Separation of space and spin variables; spin coupling problems. Proc R Soc Lond Ser A 259:554–577
14. Petrenko TT, Petrenko TL, Bratus VY (2002) The carbon <100> split interstitial in SiC. J Phys Condens Matter 14:12433–12440
15. Shoji M, Koizumi K, Hamamoto T, Taniguchi T, Takeda R, Kitagawa Y, Kawakami T, Okumura M, Yamanaka S, Yamaguchi K (2005) A theoretical study of zero-field splitting of organic biradicals. Polyhedron 24:2708–2715
16. (a) Sinnecker S, Neese F (2006) Spin–spin contributions to the zero-field splitting tensor in organic triplets, carbenes and biradicals—a density functional and ab initio study. J Phys Chem A 110:12267–12275; (b) Sander W, Grote D, Kossmann S, Neese F (2008) 2,3,5,6-Tetrafluorophenylnitren-4-yl: electron paramagnetic resonance spectroscopic characterization of a quartet-ground-state nitreno radical. J Am Chem Soc 130:4396–4403; (c) Grote D, Finke C, Kossmann S, Neese F, Sander W (2010) 3,4,5,6-Tetrafluorophenylnitren-2-yl: a ground-state quartet triradical. Chem Eur J 16:4496–4506; (d) Neuhaus P, Winkler M, Sander W (2011) EPR spectroscopic and computational characterization of the 2-dehydro-*m*-xylylene and 4-dehydro-*m*-xylylene triradicals. J Phys Org Chem 24:976–992
17. Koto T, Sugisaki K, Sato K, Shiomi D, Toyota K, Itoh K, Wasserman E, Lahti PM, Takui T (2010) High-spin nitrene fine-structure ESR spectroscopy in frozen rigid glasses: exact analytical expressions for the canonical peaks and a D-tensor gradient method for line broadening. Appl Magn Reson 37:703–736
18. (a) Misochko EY, Korchagin DV, Bozhenko KV, Chapyshev SV, Aldoshin SM (2010) A density functional theory study of the zero-field splitting in high-spin nitrenes. J Chem Phys 133:064101 (b) Chapyshev SV, Korchagin DV, Budyka MF, Gavrishova TN, Neuhaus P, Sander W (2011) Strain effects in electron spin resonance spectroscopy of quintet 2,6-bis(4′-nitrenophenyl)-4-phenylpyridine. J Phys Chem A 115:8419–8425
19. van Gastel M (2010) Zero-field splitting of the lowest excited triplet states of C_{60} and C_{70} and benzene. J Phys Chem A 114:10864–10870
20. Perumal SSRR (2011) Zero-field splitting of compact trimethylenemethane analogue radicals with density functional theory. Chem Phys Lett 501:608–611
21. (a) Langhoff SR (1974) Ab initio evaluation of the fine structure of the oxygen molecule. J Chem Phys 61:1708–1716; (b) Langhoff SR, Davidson ER, William Kern C (1975) Ab initio study of the zero-field splitting parameters of $^3B_{1u}$ benzene. J Chem Phys 63:4800–4807; (c) Davidson ER, Ellenbogen JC (1980) An ab initio calculation of the zero-field splitting parameters of the $^3A''$ state of formaldehyde. J Chem Phys 73:865–869; (d) Feller D, Borden WT, Davidson ER (1981) Calculation of zero field splitting parameters for trimethylenemethane. J Chem Phys 74:2256–2259; (e) Motten AG, Davidson ER, Kwiram AL (1981) Calculations of zero-field splittings in pyridine derivatives. J Chem Phys 75:2603–2607
22. Havlas Z, Downing JW, Michl J (1998) Spin–orbit coupling in biradicals. 2. Ab initio methodology and application to 1,1-biradicals: carbene and silylene. J Phys Chem A 102:5681–5692
23. Sugisaki K, Toyota K, Sato K, Shiomi D, Kitagawa M, Takui T unpublished results
24. (a) Havlas Z, Michl J (1999) Ab initio calculation of zero-field splitting and spin–orbit coupling in ground and excited triplets of *m*-xylylene. J Chem Soc Perkin Trans 2 2299–2303; (b) Havlas Z, Kývala M, Michl J (2003) Spin–orbit coupling in biradicals. 4. Zero-field splitting in triplet nitrenes, phosphinidenes, and arsinidenes. Collect Czech Chem Commun 68:2335–2342; (c) Havlas Z, Kývala M, Michl J (2005) Spin–orbit coupling in biradicals. 5. Zero-field splitting in triplet dimethylnitrenium, dimethylphosphenium and dimethylarsenium cations. Mol Phys 103:407–411

25. (a) Vahtras O, Loboda O, Minaev B, Ågren H, Ruud K (2002) Ab initio calculations of zero-field splitting parameters. Chem Phys 279:133–142; (b) Loboda O, Minaev B, Vahtras O, Schimmelphennig B, Ågren H, Ruud K, Jonsson D (2003) Ab initio calculations of zero-field splitting parameters in linear polyacenes. Chem Phys 286:127–137; (c) Loboda O, Minaev B, Vahtras O, Ruud K, Ågren H (2003) Ab initio study of nonhomogeneous broadening of the zero-field splitting of triplet guest molecules in diluted glasses. J Chem Phys 119:3120–3129; (d) Rubio-Pons O, Loboda O, Minaev B, Schimmelpfennig B, Vahtras O, Ågren H (2003) CASSCF calculations of triplet state properties: applications to benzene derivatives. Mol Phys 101:2103–2114; (e) Minaev B, Loboda O, Rinkevicius Z, Vahtras O, Ågren H (2003) Fine- and hyperfine- structure in three low-lying $^3\Sigma^+$ states of molecular hydrogen. Mol Phys 101:2335–2346; (f) Minaev B, Loboda O, Vahtras O, Ruud K, Ågren H (2004) Solvent effects on optically detected magnetic resonance in triplet spin labels. Theor Chem Acc 111:168–175; (g) Rubio-Pons O, Minaev B, Loboda O, Ågren H (2005) Ab initio calculations of vibronic activity in phosphorescence microwave double resonance spectra of *p*-dichlorobenzene. Theor Chem Acc 113:15–27; (h) Minaev BF, Khomenko EM, Bilan EA, Yashchuk LB (2005) Calculation of the fine structure of the triplet state $\tilde{a}^3A_2$ of the ozone molecule by the method of multiconfiguration self-consistent field. Opt Spectrosc 98:209–213; (i) Loboda O, Tunell I, Minaev B, Ågren H (2005) Theoretical study of triplet state properties of free-base porphin. Chem Phys 312:299–309
26. Sugisaki K, Toyota K, Sato K, Shiomi D, Kitagawa M, Takui T unpublished results
27. Gilka N, Taylor PR, Marian CM (2008) Electron spin–spin coupling from multireference configuration interaction wave functions. J Chem Phys 129:044102
28. Dalton, a molecular electronic structure program, Release Dalton2011 (2011). see http://daltonprogram.org/
29. Marian CM (2001) Spin–orbit coupling in molecules. In: Lipkowitz KB, Boyd DB (eds) Reviews in computational chemistry, vol 17. Wiley-VCH, New York
30. Neese F, Solomon EI (1998) Calculation of zero-field splittings, g-values, and the relativistic nephelauxetic effect in transition metal complexes. Application to high-spin ferric complexes. Inorg Chem 37:6568–6582
31. (a) Hirao K (1992) Multireference Møller–Plesset method. Chem Phys Lett 190:374–380; (b) Hirao K (1992) Multireference Møller–Plesset perturbation theory for high-spin open-shell systems. 196:397–403; (c) Hirao K (1993) State-specific multireference Møller–Plesset perturbation treatment for singlet and triplet excited states, ionized states and electron attached states of H_2O. Chem Phys Lett 201:59–66
32. (a) Ribbing C, Odelius M, Laaksonen A, Kowalewski J, Roos B (1990) Simple nonempirical calculations of the zero-field splitting in transition metal systems: I. The Ni(II)-water complexes. Int J Quantum Chem Quantum Chem Symp 24:295–309; (b) Ribbing C, Odelius M (1993) Normal coordinate analysis of the zero-field splitting in octahedral NiF_6^{4-}. I. Ab initio calculations. Mol Phys 78:1259–1266; (c) Buenker RJ, Alekseyev AB, Liebermann HP, Lingott R, Hirsch G (1998) Comparison of spin–orbit configuration interaction methods employing relativistic effective core potentials for the calculation of zero-field splittings of heavy atoms with a $^2P^O$ ground state. J Chem Phys 108:3400–3408; (d) Chattopadhyay A, Das KK (2004) Electronic states of TlX (X = As, Sb, Bi): a configuration interaction study. J Phys Chem A 108:7306–7317; (e) Kleinschmidt M, Tatchen J, Marian CM (2006) SPOCK.CI: a multireference spin–orbit configuration interaction method for large molecules. J Chem Phys 124:124101
33. (a) Andersson K, Malmqvist PÅ, Roos BO, Sadlej AJ, Wolinski K (1990) Second-order perturbation theory with a CASSCF reference function. J Phys Chem 94:5483–5488; (b) Andersson K, Malmqvist PÅ, Roos BO (1992) Second-order perturbation theory with a complete active space self-consistent field reference function. J Chem Phys 96:1218–1226; (c) Roos BO, Andersson K, Fulscher MP, Malmqvist PÅ, Serrano-Andres L, Pierloot K, Merchán M (1996) Multiconfigurational perturbation theory: Applications in electronic spectroscopy. In Prigogine I, Rice SA (eds) Advances in chemical physics: new methods in computational quantum mechanics, vol XCIII. Wiley-VCH, New York

34. Roos BO, Malmqvist PÅ (2004) Relativistic quantum chemistry: the multiconfigurational approach. Phys Chem Chem Phys 6:2919–2927
35. (a) de Graaf C, Sousa C (2006) Assessing the zero-field splitting in magnetic molecules by wave function-based methods. Int J Quantum Chem 106:2470–2478; (b) Maurice R, Bastardis R, de Graaf C, Suaud N, Mallah T, Guihéry N (2009) Universal theoretical approach to exact anisotropic spin Hamiltonians. J Chem Theory Comput 5:2977–2984; (c) Maurice A, Pradipto AM, Guihéry N, Broer R, de Graaf C (2010) Antisymmetric magnetic interactions in oxo-bridged Copper(II) bimetallic systems. J Chem Theory Comput 6:3092–3101
36. Yoshizawa T, Nakajima T (2011) Second-order generalized unrestricted Møller–Plesset perturbation theory for the spin–orbit part of zero-field splitting tensors. Chem Phys Lett 515:296–301
37. Neese F (2007) Calculation of the zero-field splitting tensor on the basis of hybrid density functional and Hartree–Fock theory. J Chem Phys 127:164112
38. Pederson MR, Khanna SN (1999) Magnetic anisotropy barrier for spin tunneling in $Mn_{12}O_{12}$ molecules. Phys Rev B 60:9566–9572
39. Neese F (2006) Importance of direct spin–spin coupling and spin-flip excitations for the zero-field splittings of transition metal complexes: a case study. J Am Chem Soc 128:10213–10222
40. (a) Takeda R, Shoji M, Yamanaka S, Yamaguchi K (2005) Density functional study of zero-field splitting. Polyhedron 24:2238–2241; (b) Takeda R, Koizumi K, Shoji M, Nitta H, Yamanaka S, Okumura M, Yamaguchi K (2007) Ab initio studies on the zero-field splitting parameters of manganese porphyrin complexes. Polyhedron 26:2309–2312
41. Aquino F, Rodriguez JH (2005) First-principle computation of zero-field splittings: application to a high valent Fe(IV)-oxo model of nonheme iron proteins. J Chem Phys 123:204902
42. Reviakine R, Arvuznikov AV, Tremblay JC, Remenyi C, Malkina OL, Malkin VG, Kaupp M (2006) Calculation of zero-field splitting parameters: comparison of a two-component noncolinear spin-density-functional method and a one-component perturbational approach. J Chem Phys 125:054110
43. Neese F ORCA, an ab initio, density functional and semiempirical program package, University of Bonn, Germany
44. Schmitt S, Jost P, van Wüllen C (2011) Zero-field splittings from density functional calculations: analysis and improvement of known methods. J Chem Phys 134:194113
45. Huber KP, Herzberg G (1979) Molecular spectra and molecular structure IV. Constants of diatomic molecules. Van Nostrand Reinhold, New York
46. Ganyushin D, Neese F (2006) First-principle calculations of zero-field splitting parameters. J Chem Phys 125:024103
47. Schmidt MW, Baldridge KK, Boatz JA, Elbert ST, Gordon MS, Jensen JH, Koseki S, Matsunaga N, Nguyen KA, Su SJ, Windus TL, Dupuis M, Montgomery JA (1993) General atomic and molecular electronic structure system. J Comput Chem 14:1347–1363
48. Zein S, Duboc C, Lubitz W, Neese F (2008) A systematic density functional study of the zero-field splitting in Mn(II) coordination compounds. Inorg Chem 47:134–142
49. El-Sayed MA (1963) Spin–orbit coupling and the radiationless processes in nitrogen heterocyclics. J Chem Phys 38:2834–2838
50. Lwowski W (1970) Nitrenes. Wiley, New York
51. Wasserman E (1971) Electron spin resonance of nitrene. Prog Phys Org Chem 8:319–336
52. Wasserman E, Yager WA, Kuck VJ (1970) EPR of CH_2: a substantially bent and partially rotating ground state triplet. Chem Phys Lett 7:409–413
53. Kuzaj M, Lüerssen H, Wentrup C (1986) ESR observation of thermally produced triplet nitrenes and photochemically produced triplet cycloheptatrienylidenes. Angew Chem Int Ed Engl 25:480–482
54. Alverado R, Grivet JP, Igier C, Barcelo J, Rigaudy J (1977) Spectroscopic studies of azides and nitrenes derived from anthracene. J Chem Soc Faraday Trans 2(73):844–857
55. Whangbo MH (2005) Concepts of perturbation, orbital interaction, orbital mixing and orbital occupation. In: Dykstra CE, Frenking G, Kim KS, Scuseria GE (eds) Theory and applications of computational chemistry The first forty years. Elsevier, Amsterdam

56. Sugisaki K, Toyota K, Sato K, Shiomi D, Takui T (2006) Ab initio MO analysis of the excited electronic states of high-spin quintet 2-methylphenylene-1,3-dinitrene. Angew Chem Int Ed 45:2257–2261
57. (a) Nakatsuji H, Hirao K (1978) Cluster expansion of the wavefunction. Symmetry-adapted-cluster expansion, its variational determination, and extension of open-shell orbital theory. J Chem Phys 68:2053–2065; (b) Nakatsuji H (1978) Cluster expansion of the wavefunction. Excited states. Chem Phys Lett 59:362–364; (c) Nakatsuji H (1979) Cluster expansion of the wavefunction. Electron correlations in ground and excited states by SAC (symmetry-adapted-cluster) and SAC CI theories. Chem Phys Lett 67:329–331; (d) Nakatsuji H (1991) Description of two- and many-electron processes by the SAC-CI method. Chem Phys Lett 177:331–337; (e) Ehara M, Ishida M, Toyota K, Nakatsuji H (2002) SAC-CI general-*R* method: theory and applications to the multi-electron processes. In Sen KD (ed) Reviews in modern quantum chemistry, vol 2. World scientific, Singapore
58. (a) Wasserman E, Schueller K, Yager WA (1968) EPR detection of the septet ground state of a trinitrene. Chem Phys Lett 2:259–260; (b) Haider K, Soundararajan N, Shaffer M, Platz MS (1989) EPR spectroscopy of a diaza derivative of meta-xylylene. Tetrahedron Lett 30:1225–1228; (c) Fukuzawa TA, Sato K, Ichimura AS, Kinoshita T, Takui T, Itoh K, Lahti PM (1996) Electronic and molecular structures of quintet bisnitrenes as studied by fine-structure ESR spectra from random orientation: all the documented ZFS constant correct? Mol Cryst Liq Cryst 278:253–260; (d) Nakai T, Sato K, Shiomi D, Takui T, Itoh K, Kozaki M, Okada K (1999) High-spin nitrenes with *s*-triazine skeleton. Mol Cryst Liq Cryst 334:157–166; (e) Nakai T, Sato K, Shiomi D, Takui T, Itoh K, Kozaki M, Okada K (1999) ESR study of high-spin nitrenes with *s*-triazine skeleton. Synth Met 103:2265–2266; (f) Chapyshev SV, Walton R, Lahti PM (2000) Effect of substitution on the yield of high-spin nitrenes in the photolysis of 2,6-diazopyridines. Mendeleev Commun 10:114–115; (g) Chapyshev SV, Walton R, Lahti PM (2000) Orbital control in the selective photolysis of azido groups of 2,4,6-triazido-3,6-dichloropyridine. Mendeleev Commun 10:187–188; (h) Chapyshev SV, Walton R, Sanborn JA, Lahti PM (2000) Quintet and septet state systems based on pyridylnitrenes: effects of substitution on open-shell high-spin states. J Am Chem Soc 122:1580–1588; (i) Chapyshev SV, Tomioka H (2003) Photochemical transformations of quintet *m*-phenylenedinitrenes. Bull Chem Soc Jpn 76:2075–2089; (j) Chapyshev SV, Walton R, Serwinski PR, Lahti PM (2004) Quintet state electron spin resonance spectra of pyridyldinitrenes. J Phys Chem A 108:6643–6649; (k) Sato T, Narazaki A, Kawaguchi Y, Niino H, Bucher G, Grote D, Wolff JJ, Wenk HH, Sander W (2004) Generation and photoreactions of 2,4,6-trinitreno-1,3,5-triazine, a septet trinitrene. J Am Chem Soc 126:7846–7852; (l) Chapyshev SV (2006) Photochemical synthesis and ESR spectra of quintet *meta*-phenylenedinitrene. Russ Chem Bull Int Ed 55:1126–1131; (m) Chapyshev SV (2006) Photochemical synthesis and properties of quintet pyridyl-2,6-dinitrenes. Russ Chem Bull Int Ed 55:1593–1597; (n) Chapyshev SV, Lahti PM (2006) Zero-field splitting parameters of quintet 2,6-dinitrenopyridines. J Phys Org Chem 19:637–641; (o) Kuzina SI, Mikhailov AI, Chapyshev SV (2007) Radiolysis and photolysis of crystalline 2,4,6-triazido-3,5-dichloropyridine: generation of quintet dinitrenes. High Ener Chem 41:245–250; (p) Misochko EY, Akimov AV, Chapyshev SV (2008) High resolution electron paramagnetic resonance spectroscopy of quintet pyridyl-2,6-dinitrene in solid argon: magnetic properties and molecular structure. J Chem Phys 128:124504; (q) Misochko EY, Akimov AV, Chapyshev SV (2008) High resolution electron paramagnetic resonance spectroscopy of septet pyridyl-2,4,6-trinitrene in solid argon: fine-structure parameters of six electron-spin cluster. J Chem Phys 129:174510; (r) Chapyshev SV, Grote D, Finke C, Sander W (2008) Matrix isolation and EPR spectroscopy of septet 3,5-difluoropyridyl-2,4,6-trinitrene. J Org Chem 73:7045–7051; (s) Chapyshev SV, Misochko EY, Akimov AV, Dorokhov VG, Neuhaus P, Grote D, Sander W (2009) Molecular structure and magnetic parameters of septet 2,4,6-trinitrenotoluene. J Org Chem 74:7238–7244; (t) Chapyshev SV, Neuhaus P, Grote D, Sander W (2010) Matrix isolation and magnetic parameters of septet 3,5-dicyanopyridyl-2,4,6-trinitrene. J Phys Org Chem 23:340–346

59. Tsukada H, Mukai K, Iwamura H (1987) (3-Nitrenophenyl)methylene: a ground state quintet molecule having both carbenic and nitrenic atoms. J Chem Soc Chem Commun 1159–1160
60. Koto T, Sato K, Shiomi D, Toyota T, Itoh K, Wasserman E, Takui T (2009) Random-orientation high-spin electron spin resonance spectroscopy and comprehensive spectral analyses of the quintet dicarbene and dinitrene with meta-topological linkers: origins of peculiar line-broadening in fine-structure ESR spectra in organic rigid glasses. J Phys Chem A 113: 9521–9526
61. (a) Nakazawa S, Sato K, Shiomi D, Franco MLTMB, Lazana CRLR, Shohoji MCBL, Itoh K, Takui T (2008) Electronic and molecular structures of C_{60}-based polyanionic high-spin molecular clusters: direct spin identification and electron spin transient nutation spectroscopy for high-spin chemistry. Inorg Chim Acta 361:4031–4037; (b) Takui T (1973) Dr thesis, Osaka University, Osaka; (c) Asano M (1973) Master thesis, Osaka University, Osaka
62. (a) McGlynn SP, Azumi T, Kinoshita M (1969) Molecular spectroscopy of the triplet state. Prentice-Hall, New Jersey (b) van del Waals JH (2001) EPR of photo-excited triplet states: a personal account. Appl Magn Reson 20:545–561
63. (a) Hameka HF (1959) Theory of the electron spin resonance of benzene in the triplet state. J Chem Phys 31:315–321; (b) Gouterman M, Moffitt W (1959) Origin of zero-field splittings in triplet states of aromatic hydrocarbons. J Chem Phys 31:1107–1108b; (c) Gouterman M (1959) Calculations on the zero-field splittings in triplet states of various aromatic hydrocarbons. II. J Chem Phys 31:1369–1371; (d) Boorstein SA, Gouterman M (1963) Theory for zero-field splittings in aromatic hydrocarbons. III. J Chem Phys 39:2443–2452; (e) Chiu YN (1963) Zero-field splittings in some triplet-state aromatic molecules. J Chem Phys 39:2736–2748; (f) Chiu YN (1963) Carbon $2p_z$ multiple-center dipolar interaction integrals in the matrix element over LCAO molecular orbitals. J Chem Phys 39: 2749–2756; (g) van del Waals JH, ter Maten G (1964) Zero-field splitting of the lowest triplet state of some aromatic hydrocarbons: calculation and comparison with experiment. Mol Phys 8:301–318; (h) Amos T, Snyder LC (1965) Unrestricted Hartree–Fock calculations. III. Zero-field splittings in triplet state of naphthalene, anthracene, and phenanthrene. J Chem Phys 43:2146–2147; (i) Godfrey M, Kern CW, Karplus M (1966) Studies of zero-field splittings in aromatic molecules. J Chem Phys 44:4459–4469
64. Burland DM, Schmidt J (1971) The dynamic properties of the lowest triplet states of pyrazine and pyrimidine in zero magnetic field. Mol Phys 22:19–31
65. Hochstrasser RM, Lin T (1970) Optical and magnetic field studies of the lowest triplet state of the pyrazine crystal. J Chem Phys 53:2676–2680
66. Terajima M, Yamauchi S, Hirota N (1986) Properties of the short-lived triplet states of pyridazine and 3,6-dichloropyridazine studied by a time-resolved EPR method. J Chem Phys 84:3679–3687
67. Weber P, Reimers JR (1999) Ab initio and density functional calculations of the energies of the singlet and triplet valence excited states of pyrazine. J Phys Chem A 103:9821–9829
68. (a) Singh B, Brinen JS (1971) Low-temperature photochemistry of *p*-diazidobenzene and 4,4′-diazidoazobenzene. J Am Chem Soc 93:540–542; (b) Nimura S, Kikuchi O, Ohana T, Yabe A, Kaise M (1996) Singlet–triplet energy gaps of quinonoidal dinitrenes. Chem Lett 125; (c) Minato M, Lahti PM (1997) Characterizing triplet states of quinonoidal dinitrenes as a function of conjugation length. J Am Chem Soc 119:2187–2195
69. Ichimura AS, Lahti PM (1993) Meta- and para-phenylenedinitrene; an ab initio computational study. Mol Cryst Liq Cryst 233:33–40
70. Nicolaides A, Tomioka H, Murata S (1998) Direct observation and characterization of *p*-phenylenebisnitrene. A labile quinonoidal diradical. J Am Chem Soc 120:11530–11531
71. (a) Sommerdijk JL, de Boer E (1969) Calculation of the zero-field-splitting parameters of the triplet dianion of triphenylene and its ion triple. J Chem Phys 50:4771–4775; (b) Sommerdijk JL, van Broekhoven JAM, van Willigen H, de Boer E (1969) Interpretation of ESR experiments on the triplet dianions of 1,3,5-triphenylbenzene and triphenylene. J Chem Phys 51: 2006–2010

72. (a) Ebata K, Setaka W, Inoue T, Kabuto C, Kira M, Sakurai H (1998) Planar hexasilylbenzene dianion with thermally accessible triplet state. J Am Chem Soc 120:1335–1336; (b) Setaka W, Ebata K, Sakurai H, Kira M (2000) Multiplicity of planar hexasilylbenzene dianions: effects of substituents and counterions. J Am Chem Soc 122:7781–7786
73. Suzuki S, Nagata A, Kuratsu M, Kozaki M, Tanaka R, Shiomi D, Sugisaki K, Toyota K, Sato K, Takui T (2012) Trinitroxide-trioxytriphenylamine: spin-state conversion from triradical doublet to diradical cation triplet by oxidative modulation of a π-conjugated system. Angew Chem Int Ed 51:3193–3197
74. Suzuki S, Furui T, Kuratsu M, Kozaki M, Shiomi D, Sato K, Takui T, Okada K (2010) Nitroxide-substituted nitronyl nitroxide and iminonitroxide. J Am Chem Soc 132: 15908–15910

General Appendices

Tables G1–G5 and G7 below were adapted from the Appendix in [Anders Lund, Masaru Shiotani and Shigetaka Shimada: Principles and Applications of ESR Spectroscopy (Springer, 2011)] with permission from Springer.

Table G1 Fundamental constants[a]

Quantity	Symbol	Value	SI unit
Speed of light	c	$2.997\,924\,58 \times 10^{8}$	$\mathrm{m\ s^{-1}}$
Elementary charge	e	$1.602\,176 \times 10^{-19}$	C
Faraday constant	$F = N_{\mathrm{A}}e$	$9.648\,456 \times 10^{4}$	$\mathrm{C\ mol^{-1}}$
Boltzmann constant	k	$1.380\,65 \times 10^{-23}$	$\mathrm{J\ K^{-1}}$
Gas constant	$R = N_{\mathrm{A}}k$	8.314 47	$\mathrm{J\ K^{-1}\ mol^{-1}}$
Planck constant	h	$6.626\,068 \times 10^{-34}$	J s
	$\hbar = h/2\pi$	$1.054\,571 \times 10^{-34}$	J s
Avogadro constant	N_{A}	$6.022\,14 \times 10^{-23}$	$\mathrm{mol^{-1}}$
Atomic mass unit	u	$1.660\,54 \times 10^{-27}$	kg
Mass			
Electron	m_{e}	$9.109\,38 \times 10^{-31}$	kg
Proton	m_{p}	$1.672\,62 \times 10^{-27}$	kg
Neutron	m_{n}	$1.674\,93 \times 10^{-27}$	kg
Vacuum permittivity	$\varepsilon_0 = 1/c^2\mu_0$	$8.854\,188 \times 10^{-12}$	$\mathrm{F\ m^{-1}}$

[a]CODATA recommended values of the fundamental physical constants 2006, National Institute of Standards and Technology, Gaithersburg, Maryland 20899–8420, USA; http://physics.nist.gov/cuu/Constants/

A. Lund and M. Shiotani (eds.), *EPR of Free Radicals in Solids I*, Progress in Theoretical Chemistry and Physics 24, DOI 10.1007/978-94-007-4893-4,

Table G2 Magnetic constants in SI units[a]

Quantity	Symbol	Numerical value	Unit
Magnetic constant	$\mu_0 = 4\pi \times 10^{-7}$	$12.566\,370 \times 10^{-7}$	$N\,A^{-2}$
Bohr magneton	μ_B (β_e)	$927.400\,915\,(23) \times 10^{-26}$	$J\,T^{-1}$
Nuclear magneton	μ_N (β_N)	$5.050\,783\,24(13) \times 10^{-27}$	$J\,T^{-1}$
Electron *g*-factor	g_e	2.002 319 304 361 7(15)	
Electron gyromagnetic ratio	γ_e	$1.760\,859\,770\,(44) \times 10^{11}$	$s^{-1}\,T^{-1}$
μ_B/h	μ_B/h	$13.996\,246\,4(35) \times 10^{9}$	$Hz\,T^{-1}$
μ_B/hc	μ_B/hc	46.686 451 5(12)	$m^{-1}\,T^{-1}$
μ_N/h	μ_N/h	7.622 593 84(19)	$MHz\,T^{-1}$

[a]CODATA recommended values of the fundamental physical constants 2006, National Institute of Standards and Technology, Gaithersburg, Maryland 20899–8420, USA; http://physics.nist.gov/cuu/Constants/

Table G3 Conversion factors for EPR (ESR) coupling constants[a, b]

Unit	MHz	mT	cm^{-1}
MHz	1	0.071 447 66/g	$0.333\,564\,095 \times 10^{-4}$
mT	13.996 25·g	1	$4.668\,645 \times 10^{-4}$ ·g
cm^{-1}	$2.997\,924\,58 \times 10^{4}$	$0.214\,194\,9 \times 10^{4}$/g	1

A coupling given in a unit of the 1st column is calculated in other units by multiplication with the factor in the corresponding row.
Calculations of g from measured values of microwave frequency ν_e (GHz) and resonance field B (T), of resonance field, and of nuclear frequency ν_N (MHz):

$$g = \frac{h}{\mu_B} \cdot \frac{\nu_e}{B} = 0.071447656 \frac{\nu_e(GHz)}{B(T)},\ B(T) = \frac{h}{\mu_B} \cdot \frac{\nu_e}{g} = 0.071447656 \frac{\nu_e(GHz)}{g}$$

$$\nu_N(MHz) = \frac{\mu_N}{h} \cdot g_N B = 7.62259384 \cdot g_N B(T)$$

[a]The factors were obtained from CODATA recommended values of the constants in Table G1; http://physics.nist.gov/cuu/Constants/
[b]Mohr PJ, Taylor BN, Newell DB (2008) Rev Mod Phys 80:633; J Phys Chem Ref. Data 37:1187

Table G4 Other useful conversion factors

1 eV	$1.602\,18 \times 10^{-23}$ J
	96.485 kJ mol^{-1}
	8065.5 cm^{-1}
1 cal	4.184 J
1 atm	101.325 kPa
1 cm^{-1}	$1.986\,4 \times 10^{-23}$ J
1 D (Debye)	$3.335\,64 \times 10^{-30}$ C m
1 Å	10^{-10} m
1 T	10^{-4} G (or gauss)
1 L atm	= 101.325 J
θ/°C	= T/K − 273.15

Table G5 Symbols, variables and units in EPR (ESR)

Symbol	Name or description	Unit and/or value
A, a	Hyperfine coupling (splitting) constant	MHz, mT (milli-Tesla)
D	Zero-field splitting, Fine structure	cm^{-1}, MHz, mT
B (H)	External magnetic field	T (Tesla)
e	Electron charge	$1.602\ 177 \times 10^{-19}$ A·s
g	g-factor	Dimensionless
G	Radiation yield	$\mu mol \cdot J^{-1}$
h	Planck constant	$6.626\ 068 \times 10^{-34}$ J·s
I	Nuclear spin angular momentum	J·s
I	Nuclear spin quantum number	Dimensionless
J	Heisenberg exchange coupling	cm^{-1}, MHz, mT
k	Boltzmann constant	1.380658×10^{-23} $J \cdot K^{-1}$
L	Orbital angular momentum	J·s
l	Orbital quantum number	Dimensionless
m_e	Electron mass	0.910939×10^{-30} kg
m_I	Nuclear magnetic quantum number	Dimensionless
m_S	Electron magnetic quantum number	Dimensionless
P	Microwave power	$J \cdot s^{-1}$
Q	Nuclear quadrupole coupling	cm^{-1}, MHz, mT
S	Electron spin angular momentum	J·s
S, s	Electron spin quantum number	Dimensionless
v	Speed	$m \cdot s^{-1}$
λ	Spin-orbit coupling constant	cm^{-1}
μ	Magnetic moment	A·s
μ_B, (β_e)	Bohr magneton	9.274015×10^{-24} $J \cdot T^{-1}$
μ_N, (β_N)	Nuclear magneton	5.050787×10^{-27} $J \cdot T^{-1}$
ν	Frequency	Hz

Table G6 Abbreviations

Abbreviation	Name or description
Magnetic resonance:	
ADMR	Absorption detected magnetic resonance
ALC-MuSR	Avoided level crossing MuSR
BP	Breit-Pauli
CPMG	Carr-Purcell-Meiboom-Gill
CW, cw	Continuous wave
DEER	Double electron electron resonance
DQC-ESR (EPR)	Double quantum coherence ESR (EPR)
ED-EPR (EchoEPR)	Echo-detected EPR
ELDOR	Electron electron double resonance
EMR	Electron magnetic resonance
ENDOR	Electron nuclear double resonance
ENTOR	Electron nuclear triple resonance
EPR	Electron paramagnetic resonance

(continued)

Table G6 (continued)

Abbreviation	Name or description
EPR-COSY	EPR correlation spectroscopy
EPR-SECSY	EPR spin echo correlated spectroscopy
ESE	Electron spin echo
ESEEM	Electron spin echo envelope modulation
ESR	Electron spin resonance
ESTN	Electron spin transient nutation
FID	Free induction decay
FT	Fourier transform
HF, hf	Hyperfine
HF-EPR (ESR)	High frequency EPR (ESR)
HFC, hfc (Hfi or Hfs)	Hyperfine coupling (interaction or structure)
HYSCORE	Hyperfine sublevel correlation
IHC	Isotropic hyperfine coupling
LF-MuSRx	Longitudinal (magnetic) field muon spin-relaxation
MIDP	Microwave induced delayed phosphorescence
MRFM	Magnetic resonance force microscopy
MW, mw	Micro wave
MuSR (μSR)	Muon spin rotation
NMR	Nuclear magnetic resonance
NMRD	Nuclear magnetic relaxation dispersion
NQC, Nqc	Nuclear quadrupole coupling
OD(N)MR	Optically detected (nuclear) magnetic resonance
PELDOR	Pulsed electron electron double resonance
QC-ENDOR (NMR)	Quantum computing ENDOR (NMR)
QTM	Quantum tunneling of magnetization
RF, rf	Radio-frequency
SHF, shf	Super-hyperfine
SMM	Single-molecule magnet
SO(MF)	Spin-orbit (meanfield)
SOO	Spin-other-orbit
SS/EPR dosimeters	Solid state EPR dosimeters
TF	Transverse-field
TPPI	Time proportional phase increment
Quantum chemistry:	
AMFI	Atomic mean field
B3LYP	Becke, three-parameter, Lee-Yang-Parr
CAS	Complete active space
CC	Coupled-cluster
CI	Configuration interaction
CNDO	Complete neglect of differential overlap
CP	Car–Parrinello
CP(CM)	Conducter-like polarized (continuum method)
CP(KS)	Coupled-perturbed (Kohn-Sham)
DFT	Density functional theory
DIM	Diatomics-in-molecules
DKH	Douglas-Kroll-Hess

(continued)

Table G6 (continued)

Abbreviation	Name or description
DZ(P)	Double-zeta (plus polarization)
GGA	Generalized gradient approximations
GIAO	Gauge including atomic orbitals
HDV	Heisenberg-Dirac-Van Vleck
HF	Hartree-Fock
HOMO	Highest occupied molecular orbital
IEF	Integral equation formalism
IGLO	Individual gauges for localized orbitals
INDO	Intermediate neglect of differential overlap
J-T	Jahn-Teller
L(S)DA	Local (spin) density approximation
LUMO	Lowest unoccupied molecular orbital
MCSCF	Multi-configuration SCF
MD	Molecular dynamics
MM	Molecular mechanics
MO	Molecular orbital
MP	Møller-Plesset
MRCI	Multi-reference configuration-interaction
MRMP2	Second-order multi-reference Møller–Plesset
NBMO	Non-bonding molecular orbital
NDDO	Neglect of diatomic differential overlap
PCM	Polarizable continuum models
QM/MM	Quantum-mechanics/molecular-mechanics
(Q)RO	(Quasi) restricted orbital
ROHF	Restricted open-shell Hartree-Fock
SAC-CI	Symmetry-adapted cluster configuration interaction
SCF	Self-consistent field
SCIPCM	Self-consistent isodensity PCM
SCRF	Self-consistent reaction field
SD(T)	Single, double (and perturbative triple)
SECI (CIS)	Single excitation configuration interaction
SO-CI	Spin–orbit configuration interaction
SOMO	Singly occupied molecular orbital
SOS	Sum-over-states
TZ	Triple-zeta
UDFT	Uncoupled density functional theory
UHF	Unrestricted Hartree-Fock
ZFS	Zero-field splitting
ZORA	Zero order regular approximation
ZPVE	Zero point vibrational energy
Chemistry and biochemistry:	
2-MTHF	2-Methyltetrahydrofuran
$AlPO_4$	Aluminum orthophosphate
ArO	Phenoxide
a-Si:H	Hydrogenated amorphous silicon

(continued)

Table G6 (continued)

Abbreviation	Name or description
BQ	1,4-Benzoquinone
BSS	Benzylsuccinate synthase
CU	Coupling unit
CuHis	Copper(II)-histidine
Cyt	Cytochrome
DCMU	3-(3,4-Dichlorophenyl)-1,1-dimethylurea
DMBQ	2,3-Dimethyl-1,4-benzoquinone
DMC	2,3-Dimethylenecyclohexane-1,4-diyl
DME	Dimethylether
DMEQ	2,3-Dimethyl-5-ethyl-1,4-benzoquinone
DMNQ	2,3-Dimethyl-1,4-naphthoquinone
DPNO	Diphenylnitroxide
DQ	Duroquinone: 2,3,5,6-tetramethyl-1,4-benzoquinone
DTBN	di-tert-Butyl nitroxide
Et_3N	Triethylamine
FA	Ferredoxin A
FB	Ferredoxin B
Freon-11	Fluorotrichloromethane (CCl_3F)
Freon-113	1,1,2-Trifluoro-1,2,2-trichloroethane (CCl_2FCClF_2)
Freon-114B2	1,2-Dibromotetrafluoroethane (CF_2BrCF_2Br)
GO	Galactose oxidase
GT	Gauche-trans
HAS	Human serum albumin
HCA II	Human carbonic anhydrase II
IN	Iminonitroxide
MES	2-(n-Morphorino)ethansulfonic acid
MTBE	Methyl tert-butyl ether
NADP	Nicotinamide adenine nucleotide phosphate
NAG	n-Acetyl-glycine radical
NN	Nitronyl nitroxide
NO	tert.-Butyl-nitroxide
NQ	1,4-Naphthoquinone
OEC	Oxygen-evolving complex
P680	Pigment 680 nm
P700	Pigment 700 nm
PE	Polyethylene
PFL	Pyruvate formate lyase
PQ	Plastoquinone
Pr_3N	Tripropylamine
PS	Photosynthetic reaction center
Q	Quinone
Q_K	Phylloquinone
QOX	Quinol oxidase
Rg	Rare gases
RNR	Ribonucleotide reductase
RO•	Alkoxy radicals

(continued)

Table G6 (continued)

Abbreviation	Name or description
RO_2•	Organic peroxyl radical
Rps	Rhodpseudomonas
S_H2	Bimoleclar homolytic substitution
Tempone	4-Oxo-2,2,6,6-tetramethylpiperidine-N-oxyl
TME	Tetramethyleneethane
TMM	Trimethylenemethane
TMQ	2,3,5-Trimethyl-1,4-benzoquinone
TMS	Tetramethylsilane
TPA	Triphenylamine
TPM	Triphenylmethyl
Tris	Tris(hydroxylmethyl)aminomeethane
Trp	Tryptophan
USQ	Ubisemiquinone
VCP	Vinyl cyclopropane
V-O	Vacancy-oxygen (complex)
VOCs	Volatile organic compounds
VP	Versatile peroxidase
VZ	Verdazyl
WOC	Water oxidizing complex
ZSM	Zeolite socony mobil
Others:	
CNOT	Controlled-not
CORBA	Common object request broker architecture
ETE	Extended time excitation
EXAFS	Extended X-ray absorption fine structure
FCC (fcc)	Face centered cubic
FFT	Fast Fourier transform
FTIR	Fourier transform infrared
HCP, hcp	Hexagonal closed-packed
IAEA	International atomic energy agency
IDAS	International dose assurance service
IP	Ionization potential
LET	Linear energy transfer
MBE	Molecular beam epitaxy
NIST	National institute for standards and technology
NPL	National Physical Laboratory
NSERC	Natural Sciences and Engineering Research Council of Canada
PL	Photo-luminescence
PPTV (pptv)	Parts-per-trillion-by-volume
QC	Quantum computing
QIP	Quantum information processing
SDC	Super dense coding
SQUID	Superconducting quantum interference device
SS/ES	Solid state electron spectroscopy
UV/VIS	Ultraviolet ultraviolet/visible (absorption spectroscopy)
XANES:	X-ray absorption near edge structure

Table G7 Magnetic properties of stable isotopes [a, b, c]

Isotope	Atomic number (Z)	Natural abundance (%)	Nuclear spin (I)	Nuclear g-factor (g_N)
^{1}H	1	99.985	0.5	5.58569
^{2}H	1	0.0148	1	0.85744
^{3}He	2	0.00014	0.5	−4.25525
^{6}Li	3	7.5	1	0.82205
^{7}Li	3	92.5	1.5	2.17096
^{9}Be	4	100	1.5	−0.785
^{10}B	5	19.8	3	0.60022
^{11}B	5	80.2	1.5	1.79242
^{13}C	6	1.11	0.5	1.40482
^{14}N	7	99.63	1	0.40376
^{15}N	7	0.366	0.5	−0.56638
^{17}O	8	0.038	2.5	−0.75752
^{19}F	9	100	0.5	5.25773
^{21}Ne	10	0.27	1.5	−0.4412
^{23}Na	11	100	1.5	1.47839
^{25}Mg	12	10	2.5	−0.34218
^{27}Al	13	100	2.5	1.4566
^{29}Si	14	4.67	0.5	−1.1106
^{31}P	15	100	0.5	2.2632
^{33}S	16	0.75	1.5	0.42911
^{35}Cl	17	75.77	1.5	0.54792
^{37}Cl	17	24.23	1.5	0.45608
^{39}K	19	93.26	1.5	0.26099
^{40}K	19	0.0117	4	−0.32453
^{41}K	19	6.73	1.5	0.14325
^{43}Ca	20	0.135	3.5	−0.37641
^{45}Sc	21	100	3.5	1.35906
^{47}Ti	22	7.4	2.5	−0.31539
^{49}Ti	22	5.4	3.5	−0.31548
^{50}V	23	0.25	6	0.55659
^{51}V	23	99.75	3.5	1.46836
^{53}Cr	24	9.5	1.5	−0.3147
^{55}Mn	25	100	2.5	1.3819
^{57}Fe	26	2.15	0.5	0.1806
^{59}Co	27	100	3.5	1.318
^{61}Ni	28	1.13	1.5	−0.50001
^{63}Cu	29	69.2	1.5	1.484
^{65}Cu	29	30.8	1.5	1.588
^{67}Zn	30	4.1	2.5	0.35031
^{69}Ga	31	60.1	1.5	1.34439
^{71}Ga	31	39.9	1.5	1.70818
^{73}Ge	32	7.8	4.5	−0.19544
^{75}As	33	100	1.5	0.95965
^{77}Se	34	7.6	0.5	1.0693

(continued)

Table G7 (continued)

Isotope	Atomic number (Z)	Natural abundance (%)	Nuclear spin (I)	Nuclear g-factor (g_N)
^{79}Br	35	50.69	1.5	1.40427
^{81}Br	35	49.31	1.5	1.51371
^{83}Kr	36	11.5	4.5	−0.2157
^{85}Rb	37	72.17	2.5	0.54125
^{87}Rb	37	27.83	1.5	1.83427
^{87}Sr	38	7	4.5	−0.24291
^{89}Y	39	100	0.5	−0.27484
^{91}Zr	40	11.2	2.5	−0.52145
^{93}Nb	41	100	4.5	1.3712
^{95}Mo	42	15.9	2.5	−0.3656
^{97}Mo	42	9.6	2.5	−0.3734
^{99}Ru	44	12.7	2.5	−0.249
^{101}Ru	44	17	2.5	−0.279
^{103}Rh	46	100	0.5	−0.1768
^{105}Pd	46	22.2	2.5	−0.256
^{107}Ag	47	51.83	0.5	−0.22725
^{109}Ag	47	48.17	0.5	−0.26174
^{111}Cd	48	12.8	0.5	−1.19043
^{113}Cd	48	12.2	0.5	−1.2454
^{113}In	49	4.3	4.5	1.22864
^{115}In	49	95.7	4.5	1.23129
^{115}Sn	50	0.38	0.5	−1.8377
^{117}Sn	50	7.75	0.5	−2.00208
^{119}Sn	50	8.6	0.5	−2.09456
^{121}Sb	51	57.3	2.5	1.3455
^{123}Sb	51	42.7	3.5	0.72876
^{123}Te	52	0.89	0.5	−1.4736
^{125}Te	52	7	0.5	−1.7766
^{127}I	53	100	2.5	1.1253
^{129}Xe	54	26.4	0.5	−1.55595
^{131}Xe	54	21.2	1.5	0.46124
^{133}Cs	55	100	3.5	0.73785
^{135}Ba	56	6.59	1.5	0.55884
^{137}Ba	56	11.2	1.5	0.62515
^{138}La	57	0.089	5	0.74278
^{139}La	57	99.911	3.5	0.7952
^{141}Pr	59	100	2.5	1.6
^{143}Nd	60	12.2	3.5	−0.3076
^{145}Nd	60	8.3	3.5	−0.19
^{147}Sm	62	15.1	3.5	−0.2322
^{149}Sm	62	13.9	3.5	0.1915
^{151}Eu	63	47.9	2.5	1.389
^{153}Eu	63	52.1	2.5	0.6134
^{155}Gd	64	14.8	1.5	−0.1723

(continued)

Table G7 (continued)

Isotope	Atomic number (Z)	Natural abundance (%)	Nuclear spin (I)	Nuclear g-factor (g_N)
^{157}Gd	64	15.7	1.5	−0.2253
^{159}Tb	65	100	1.5	1.342
^{161}Dy	66	19	2.5	−0.189
^{163}Dy	66	24.9	2.5	0.266
^{165}Ho	67	100	3.5	1.192
^{167}Er	68	22.9	3.5	−0.1618
^{169}Tm	69	100	0.5	−0.466
^{171}Yb	70	14.4	0.5	0.9885
^{173}Yb	70	16.2	2.5	−0.27195
^{175}Lu	71	97.39	3.5	0.63943
^{176}Lu	71	2.61	7	0.452
^{177}Hf	72	18.6	3.5	0.2267
^{179}Hf	72	13.7	4.5	−0.1424
^{181}Ta	73	99.9877	3.5	0.67729
^{183}W	74	14.3	0.5	0.23557
^{185}Re	75	37.4	2.5	1.2748
^{187}Re	75	62.6	2.5	1.2878
^{187}Os	76	1.6	0.5	0.1311
^{189}Os	76	16.1	1.5	0.488
^{191}Ir	77	37.3	1.5	0.097
^{193}Ir	78	62.7	1.5	0.107
^{195}Pt	78	33.8	0.5	1.219
^{197}Au	79	100	1.5	0.09797
^{199}Hg	80	16.8	0.5	1.01177
^{201}Hg	80	13.2	1.5	−0.37348
^{203}Tl	81	29.5	0.5	3.24451
^{205}Tl	81	70.5	0.5	3.2754
^{207}Pb	82	22.1	0.5	1.1748
^{209}Bi	83	100	4.5	0.938
^{235}U	92	0.72	3.5	−0.11

[a]Raghavan P (1989) At. Data Nucl. Data Tables 42:189
[b]http://ie.lbl.gov/toipdf/mometbl.pdf
[c]Values for the isotropic and anisotropic hyperfine couplings of the isotopes are reported in (Weil JA, Bolton JR (2007) Electron paramagnetic resonance: elementary theory and practical applications, 2nd ed. Wiley)

Index

A. Lund and M. Shiotani (eds.), *EPR of Free Radicals in Solids I*, Progress in Theoretical Chemistry and Physics 24, DOI 10.1007/978-94-007-4893-4,